

Developments in Geotechnical Engineering

A. Murali Krishna
Arindam Dey
S. Sreedeepr *Editors*

Geotechnics for Natural and Engineered Sustainable Technologies

GeoNEst

Developments in Geotechnical Engineering

Series editors

Braja M. Das, Henderson, USA
Nagaratnam Sivakugan, Townsville, Australia

This series on Geotechnical Engineering has been initiated to provide an integrated platform for publishing in all areas of geotechnics and their applications to engineering problems. The series focuses on the topics that have garnered recent interest from a large research audience, including, but not limited to, saturated and unsaturated soils, expansive soils, geosynthetics, marine geotechnics, and soil improvement. This series includes monographs, textbooks, and references in the general area of Geotechnical Engineering. The books in this series will serve researchers, practitioners, and students alike.

More information about this series at <http://www.springer.com/series/13410>

A. Murali Krishna · Arindam Dey
S. Sreedeepl
Editors

Geotechnics for Natural and Engineered Sustainable Technologies

GeoNEst



Springer

Editors

A. Murali Krishna
Department of Civil Engineering
Indian Institute of Technology Guwahati
Guwahati, Assam
India

S. Sreedep
Department of Civil Engineering
Indian Institute of Technology Guwahati
Guwahati, Assam
India

Arindam Dey
Department of Civil Engineering
Indian Institute of Technology Guwahati
Guwahati, Assam
India

ISSN 2364-5156

ISSN 2364-5164 (electronic)

Developments in Geotechnical Engineering

ISBN 978-981-10-7720-3

ISBN 978-981-10-7721-0 (eBook)

<https://doi.org/10.1007/978-981-10-7721-0>

Library of Congress Control Number: 2017962052

© Springer Nature Singapore Pte Ltd. 2018

This work is subject to copyright. All rights are reserved by the Publisher, whether the whole or part of the material is concerned, specifically the rights of translation, reprinting, reuse of illustrations, recitation, broadcasting, reproduction on microfilms or in any other physical way, and transmission or information storage and retrieval, electronic adaptation, computer software, or by similar or dissimilar methodology now known or hereafter developed.

The use of general descriptive names, registered names, trademarks, service marks, etc. in this publication does not imply, even in the absence of a specific statement, that such names are exempt from the relevant protective laws and regulations and therefore free for general use.

The publisher, the authors and the editors are safe to assume that the advice and information in this book are believed to be true and accurate at the date of publication. Neither the publisher nor the authors or the editors give a warranty, express or implied, with respect to the material contained herein or for any errors or omissions that may have been made. The publisher remains neutral with regard to jurisdictional claims in published maps and institutional affiliations.

Printed on acid-free paper

This Springer imprint is published by Springer Nature

The registered company is Springer Nature Singapore Pte Ltd.

The registered company address is: 152 Beach Road, #21-01/04 Gateway East, Singapore 189721, Singapore

Foreword

Since the advent of soil mechanics as a separate discipline in Civil Engineering (through the contribution of Terzaghi on **effective stress concept**), more and more phenomena have come to light which could not be explained by the basic laws of mechanics and hydraulics. Greater industrialization has led to land use irrespective of its suitability. Therefore, different ground improvement techniques have evolved, resulting in the development of several techniques of handling soils for desired purposes. One of the major areas of a rapid development is **Environmental Geotechnique and other similar subjects of practical significance**.

The Indian Geotechnical Society as part of their regular activity has been organizing regularly annual conferences since 1960 with the first Asian Regional Conference, organized at New Delhi. Different local chapters of IGS have taken responsibility of organizing the annual conferences every year in the month of December without fail. One such annual conference is being organized by the Guwahati Chapter this year (2017).

The organizing committee has deliberately chosen the theme topics such as Geoenvironmental Engineering, Ground Improvement Techniques, Soil Dynamics and Earthquake Engineering, Behaviour of Unsaturated Soils, Geohydrology, Dam and Embankment Engineering, Rock Mechanics, Tunnelling and Underground Structures, Uncertainties Risk and Reliability in Geotechnical Engineering, Transportation Geotechnique, Computational Geomechanics and Geotechnical Modelling, Marine Geotechnique, Geosynthetic Engineering, along with conventional topics such as Earth-Retaining Structures, Slope Stability, Foundations in Difficult Soils and Geotechnical and Geophysical Investigations.

It is heartening to note that significant contributions have been received on all the topics and are being brought out as a **Springer Publication** during the conference with all the keynote and subtheme contributions.

The book “Geotechnics for Natural and Engineered Sustainable Technologies: GeoNEst” is being brought out as Springer book series “Developments in Geotechnical Engineering” (Eds: A. Murali Krishna, Arindam Dey and S. Sreedeeep).

This book will be a useful reference material for both postgraduate courses and further research programmes.

Bangalore, India

A. Sridharan, Ph.D. (Purdue), DSc (IISc)
President, IGS, 1997 and 1998, Formerly Professor
of Civil Engineering, Indian Institute of Science

Foreword from the IGS President

The edited volume on “Geotechnics for Natural and Engineered Sustainable Technologies: GeoNEst” is an outcome of the Indian Geotechnical Conference held in the Indian Institute of Technology Guwahati during 14–16 December 2017. The compilation has excellent contributions in the areas of subsurface investigations, modelling of soil structure interactions, use of EPS foam to reduce lateral pressures, comprehensive characterization of municipal solid waste, unsaturated soils, cracks and fractures in rocks, retrofitting of structures, failure analysis of landfills, study of ground motions for intra-plate regions for earthquake resistant design, uncertainties in site characterization using surface wave techniques and their effects on ground response, impact of flooding on highways, framework for sustainability and resilience in geotechnical engineering, case studies on offshore geotechnics, forensic study on the causes of failure of stone columns, runout of flow landslides and geocell applications.

The contributions are timely and address contemporary issues and challenges in geotechnical engineering. I congratulate the authors of articles and editors of the volume for their initiative in bringing a very useful contribution to the geotechnical engineering practice.

Bangalore, India

Prof. G. L. Siva Kumar Babu
President, Indian Geotechnical Society
Professor, Indian Institute of Science

Editorial Preface

In the recent decades, India has experienced tremendous boom towards urbanization resulting in a rapid change in the socio-economic structure of the country. In order to cater the needs of millions, engineering sector has been flourishing beyond its limits. The need for the development has long crossed the metropolitan city limits and has transgressed in the difficult terrains of the country. As a consequence, natural and engineered technologies are continually evolving in research and practice leading to opening up of several new vistas of implementation, application and development. However, the need for the hour is not only to quickly provide the short-term supplies and solutions, but also to present long-term sustainable solutions to enhance the performance life of the adopted developmental solutions. In this regard, it is also important to focus on the culminating natural and anthropogenic disasters and develop procedures to minimize them. Since almost a hefty share of such disasters involve the geomaterials such as soils, rocks and the present-day advanced composite materials, it is immensely important to visit the domain of geotechnical engineering with a critical emphasis given to the sustainable approaches to natural and engineered geotechnical technologies. This thought avenues have brewed the concept of Geotechnics for Natural and Engineered Sustainable Technologies (GeoNEst) to be taken up as the theme of the Indian Geotechnical Conference 2017 (IGC-2017). In this regard, the basic concept is presented as a congregation of several subthemes, each of which is targeted to a specific and important issue of geotechnical engineering research and practice.

This book titled *Geotechnics for Natural and Engineered Sustainable Technologies (GeoNEst)* is the congregation of the expert deliberations made at the Indian Geotechnical Conference 2017 (IGC-2017) held on 14–17 December 2017 at IIT Guwahati, India. A total of 29 eminent researchers and practitioners contributed to the fortification of the current state of the art and practice, thus paving the avenues towards the future research in the purview of the theme of the conference and its various crucial subthemes. The book is orchestrated with 29 chapters describing various vistas of natural and engineered sustainable geotechnical engineering technologies.

Chapter “Addressing Sustainable Technologies in Geotechnical and Geoenvironmental Engineering” addresses the theme of the conference in describing the **sustainability issues** of geotechnical and geoenvironmental engineering problems and their contribution to the climate change and global environmental impacts due to the usage of a substantial amount of material and energy. Chapter “Geotechnics of Soft Ground” elucidates the geotechnical characteristics and **behaviour of soft ground** which are commonly improved by preloading accompanied by prefabricated vertical drains (PVDs) or load-displacement piles. Chapter “Soil–Structure Interaction Analysis of Pile Foundations Subjected to Dynamic Loads” explains the **dynamic soil–structure interaction (SSI) analysis of pile-supported structures**. Dynamic response of single and group piles, embedded in clay soil having varying consistencies, has been explained with the aid of sophisticated finite element analyses. Chapter “Cascaded Recycle of Waste Tires —Some Novel Approaches Toward Sustainable Geo-Construction and Climate Change Adaptation” describes a novel approach towards sustainable geotechnical engineering through the usage and **application of recycled waste tyres** for various disaster mitigation techniques. Experience of such approach adopted in Japan shares the benefit of using tyre-derived materials towards sustainable geotechnical applications. Chapter “Static and Seismic Slope Safety Displacement-Based Criterion for Seismic Analysis” describes the application of displacement-based criterion to ascertain the **static and seismic slope safety**. The intricate description provides a basis for better approach to understanding the development of critical mechanisms and post-seismic damage incurred in the slopes due to a seismic event. Chapter “On the Use of Scaled Model Tests for Analysis and Design of Offshore Wind Turbines” describes the application of scaled model tests for the analysis and design of **offshore wind turbines**. The challenges in designing such foundations are described, and in this regard, the rationale for conducting scaled model tests is provided. Scaling issues are discussed in lieu of proposing a methodology to scale the model tests for predicting the long-term consequences from the prototypes. Chapter “Modeling and Behavior of Geosynthetics-Reinforced Foundation” efficiently describes the importance of **geosynthetic-reinforced foundations** and provides a treatise on the modelling and behaviour of such foundation systems. The state-of-the-art development of the analytical techniques commonly used to delineate the behaviour of such foundations based on lumped parameter modelling is presented. Chapter “Image-Based Characterization Techniques for Geotechnical Applications” presents the **advanced image-based characterization techniques** utilizing the sophisticated digital technologies for geotechnical characterization. The importance and benefit of such techniques are illustrated through various applications.

Chapter “Geotechnical Challenges in Tunnelling Through Weak Rocks” details the challenges associated with **tunnelling in weak rocks** involving tunnel instability, rock mass yielding and excessive deformation resulting out of squeezing

rocks. Chapter “[Reliability and Accuracy of Seismic Tests in Geotechnical Site Characterization](#)” reports the reliability and accuracy associated with the **geophysical site characterization**. Based on the experimental findings from selected reference sites, the intra- and inter-methods variability for reliability assessment has been elucidated. Chapter “[Soil–Bentonite Cutoff Walls for Geoenvironmental Containment](#)” presents the application of **soil–bentonite cut-off walls in geo-environmental containment** by the prevention of the migration of mobile contaminant in the aquifer. The factors affecting the hydraulic conductivity of the barriers, self-recovery of permeability due to hydraulic fracturing and the role of chemical diffusion on the transport of mobile contaminants through the soil-bentonite walls are explained. Chapter “[Development of Underground Tunnel Construction Technology in Weak Rock](#)” describes the **underground tunnel construction** technology through the weak rocks and unfavourable geological conditions. Detailing of the support system is presented with rock bolt and steel pipe grouting reinforcements. Elaborations of the presupported tunnelling method (PSTM) and tubular roof construction method (TRcM) in soft ground are presented in relation to the field monitoring results.

Chapter “[Subsurface Investigation—Integrated and Modern Approach](#)” presents the problems associated with conventional practice of **surface exploration** and highlights the importance and utility of various modern and integrated techniques of subsurface investigation to estimate the required geotechnical properties for design and performance assessment. Chapter “[Modeling Soil–Foundation Interaction and Beyond](#)” discusses the **soil–foundation interaction** problem in relation to the seismic pile installation through numerical and centrifuge model studies. Chapter “[Effect of Long-Term Performance of EPS Geofoam on Lateral Earth Pressures on Retaining Walls](#)” describes **influence of the EPS geofoam** on the reduction of lateral earth pressures on instrumented non-yielding rigid model retaining walls in terms of the short- and long-term static and traffic loading scenarios. Chapter “[Comprehensive Characteristics of Fresh and Processed MSW Generated in Kanpur City](#)” describes the compressive characteristics of **fresh and processed municipal solid waste (MSW)** generated in Kanpur City through their gradation, compaction and compressibility behaviour. Chapter “[Physico-Chemical Effects on Behaviour of Unsaturated Soils](#)” describes the effect of physico-chemical factors on the structure, compressibility and collapse **behaviour of compacted soils**. Chapter “[Crack Initiation—Propagation and Failure Modes in Rocks](#)” illustrates the problem of **crack initiation in rocks** leading to the variety of propagation and failure modes along with various fracture patterns in the rocks based on laboratory investigations and numerical simulations. Chapter “[Retrofitting of N–W Corner of Kolkata High Court Heritage Building Through Micropiles and Grouting](#)” describes a case study of **retrofitting of the Kolkata High Court heritage building** with the aid of micropiles and grouting to prevent the distresses originating from the sequential differential settlement of the building structure. Chapter “[Meethotamulla Landfill Failure Analysis: A Probabilistic Approach](#)” describes a **forensic study** related to

the catastrophic failure of Meethotamulla landfill at Colombo, based on a probabilistic approach. Chapter “[Determination of Anelastic Attenuation Factor \(\$Q\$ \) and Decay Factor \(\$K\$ \) from Ground Motion Records of the Intra-plate Region](#)” illustrates the necessity of evaluation of the anelastic attenuation and decay factors for inferring source properties, **ground motion simulations and hazard analysis**. Chapter “[Uncertainties in Site Characterization Using Surface Wave Techniques and Their Effects on Seismic Ground Response](#)” illustrates the **uncertainties associated with the non-destructive geophysical exploration** approach for site characterization using surface wave techniques and their effects on the seismic ground response analysis. Chapter “[Impact of Flooding on Roadways](#)” showcases the **impact of flooding on roadways**, emphasizing on the extent of damage induced in the granular base and asphalt mix layers. Chapter “[A Quantitative Framework for Sustainability and Resilience in Geotechnical Engineering](#)” highlights a qualitative framework for **sustainability and resilience in geotechnical engineering**. The importance of considering sustainability in conjunction with resilience in infrastructure asset management is illustrated through driver-pressure-state-impact-response (DPSIR) framework.

Chapter “[Case Studies—Prediction of Offshore Jack-up Leg Penetrations](#)” presents selected practical case studies related to the prediction of **offshore jack-up leg penetrations**. The importance of a good prediction of the spudcan bearing resistance in problematic soil profile in shedding light on the precautionary measures to be adopted by the rig contractors for facilitating the safe installation of the spudcans is highlighted. Chapter “[Forensic Study on the Causes of Failure of Stone Columns Under Water Storage Tanks and Possible Remedial Measures](#)” presents the outcome of **forensic investigation** conducted to comprehend the causes of failure of stone column-supported water storage tanks.

Chapter “[Runout of Flow Landslides](#)” describes the **runout of landslide masses** and its impact on the risk assessment and management of flow landslides. Empirical and analytical techniques developed to dynamically compute the depth of moving material and shear layers have been presented. Chapter “[Quantification of Soil State Variables Using Electromagnetic Methods](#)” elucidates the **application of electromagnetic methods** to quantify the soil state variables, namely the water content and porosity, of the unsaturated granular and cohesive soils. Chapter “[Diverse Applications of Geocells for Highways—Two Case Studies from the North-East](#)” highlights selected case studies from the North-East India in explaining the diverse **applications of geocells for highways**. The importance of using these sustainable exclusions in the subgrade layers of the roadways and embankment slopes in enhancing the load-bearing capacity and erosion protection efficacies is emphasized.

We sincerely thank and appreciate the efforts of all the expert contributors in formulating the chapters. We also thank the reviewers and Springer team for giving valuable inputs for finalizing the manuscripts. We are positive and hopeful that the contents of this book will serve as a promoter and catalyst in opening up new vistas

in geotechnical engineering related to the natural and engineered technologies, thus propagating the basic motivation of GeoNEst. It is believed that the ideas shared herein will pave the pathway for collaborative implementations of sustainable geotechnical engineering approaches in the future, which is the prime need of today. The editors would like to thank Springer for publishing these important contributions and aiding to spread the conglomerated ideas through this book.

Guwahati, India

A. Murali Krishna
Arindam Dey
S. Sreedeep

Contents

Addressing Sustainable Technologies in Geotechnical and Geoenvironmental Engineering	1
Krishna R. Reddy and Girish Kumar	
Geotechnics of Soft Ground	27
Madhav Madhira and Venkata Abhishek Sakleshpur	
Soil-Structure Interaction Analysis of Pile Foundations Subjected to Dynamic Loads	45
A. Boominathan, Ramon Varghese and Srilakshmi K. Nair	
Cascaded Recycle of Waste Tires—Some Novel Approaches Toward Sustainable Geo-Construction and Climate Change Adaptation	63
Hemanta Hazarika, Hidetoshi Yokota, Shigeki Endo and Tota Kinoshita	
Static and Seismic Slope Safety Displacement-Based Criterion for Seismic Analysis	83
Saraha K. Sarma	
On the Use of Scaled Model Tests for Analysis and Design of Offshore Wind Turbines	107
Subhamoy Bhattacharya, Georgios Nikitas and Saleh Jalbi	
Modeling and Behavior of Geosynthetics-Reinforced Foundation	131
Sarvesh Chandra	
Image-Based Characterization Techniques for Geotechnical Applications	145
Gali Madhavi Latha, Prashanth Vangla and Nimisha Roy	
Geotechnical Challenges in Tunnelling Through Weak Rocks	163
Mahendra Singh	

Reliability and Accuracy of Seismic Tests in Geotechnical Site Characterization	187
Sebastiano Foti and Federico Passeri	
Soil–Bentonite Cutoff Walls for Geoenvironmental Containment	207
Takeshi Katsumi, Atsushi Takai and Toru Inui	
Development of Underground Tunnel Construction Technology in Weak Rock	225
Eun Chul Shin, Jeong Jun Park and Arum Lee	
Subsurface Investigation—Integrated and Modern Approach	245
P. Anbazhagan	
Modeling Soil–Foundation Interaction and Beyond	259
Subhadeep Banerjee	
Effect of Long-Term Performance of EPS Geofoam on Lateral Earth Pressures on Retaining Walls	271
Satyanarayana Murty Dasaka and Vinil Kumar Gade	
Comprehensive Characteristics of Fresh and Processed MSW Generated in Kanpur City	291
S. Rajesh	
Physico-Chemical Effects on Behaviour of Unsaturated Soils	303
T. Thyagaraj	
Crack Initiation—Propagation and Failure Modes in Rocks	317
V. B. Maji and Sivakumar G.	
Retrofitting of N–W Corner of Kolkata High Court Heritage Building Through Micropiles and Grouting	329
Satyendra Mittal and G. L. Sivakumar Babu	
Meethotamulla Landfill Failure Analysis: A Probabilistic Approach	341
B. Munwar Basha and K. V. N. S. Raviteja	
Determination of Anelastic Attenuation Factor (Q) and Decay Factor (K) from Ground Motion Records of the Intra-plate Region	353
Neelima Satyam, Shambhavi Dube, Raj Banerjee, Srijit Bandyopadhyay, G. R. Reddy, Suzette Payne and Justin Coleman	
Uncertainties in Site Characterization Using Surface Wave Techniques and Their Effects on Seismic Ground Response	371
Ravi S. Jakka and Narayan Roy	
Impact of Flooding on Roadways	385
Rajib Basu Mallick, Mingjiang Tao and Nivedya M. K.	

A Quantitative Framework for Sustainability and Resilience in Geotechnical Engineering	399
Dipanjan Basu and Mina Lee	
Case Studies—Prediction of Offshore Jack-up Leg Penetrations	413
C. R. Parthasarathy	
Forensic Study on the Causes of Failure of Stone Columns Under Water Storage Tanks and Possible Remedial Measures	423
Kaushik Bandyopadhyay	
Runout of Flow Landslides.....	433
J. Kim, Z. Q. Liu, S. Lacasse, S. Nordal and V. Thakur	
Quantification of Soil State Variables Using Electromagnetic Methods	447
Alexander Scheuermann, Thierry Bore, Partha Narayan Mishra, Habibullah Bhuyan, Guanxi Yan, Tilman Bittner and Rolf Becker	
Diverse Applications of Geocells for Highways—Two Case Studies from the North-East	457
Shahrokh P. Bagli	

About the Editors

Dr. A. Murali Krishna is an Associate Professor in the Department of Civil Engineering, Indian Institute of Technology Guwahati. He obtained his Ph.D. degree from IISc Bangalore; M.Tech. degree from IIT Kanpur; and B.Tech. degree from SV University, Tirupati. His research interests include earthquake geotechnics, geosynthetics and ground improvement, site characterization and numerical and physical modelling of geotechnical structures. He has published 140 technical papers in international/national journals and conference/seminar proceedings including chapters. He is a recipient of the BRNS Young Scientist Research Award, BOYSCAST Fellowship and HERITAGE Fellowship. He is currently an “executive member” of IGS and has been a member of TC 203 of ISSMGE since 2011. He is actively associated with IGS Guwahati Chapter, organizing local activities/workshops and IGC-2017. He has organized national and international workshops and short courses. He is a reviewer for several national and international journals.

Dr. Arindam Dey is an Assistant Professor in the Geotechnical Engineering Division, Department of Civil Engineering, Indian Institute of Technology Guwahati. He obtained his Ph.D. and M.Tech. degrees from IIT Kanpur and his B.Tech. degree from Jadavpur University, Kolkata. His research interests include geotechnical earthquake engineering, geosynthetics engineering, ground improvement, characterization of geomaterials, geophysical investigation, foundation engineering, slope stability and landslide analysis, rock mechanics and numerical modelling of geotechnical structures. He has published 135 technical papers in international/national journals and conference/seminar proceedings including books, chapters and technical reports. He has received research awards from IGS and ISSMGE. He is a recipient of the “Fellowship for Young Indian Researchers from the Ministry of Italy”. He has been involved in organizing national and international workshops and short courses. He is currently the Honorary Secretary of IGS Guwahati Local Chapter and has been actively involved in organizing local activities/workshops and the GeoNEst, IGC-2017. He has delivered several invited

lectures in India and abroad and is a reviewer for several national and international journals.

Dr. S. Sreedeep is currently a Professor in the Geotechnical Engineering Division, Department of Civil Engineering, Indian Institute of Technology Guwahati. He obtained his Ph.D. and M.Tech. degrees from IIT Bombay and B.Tech. degree from Calicut University. His research interests include behavioural studies of unsaturated geomaterials, hazardous waste management, utilization of waste materials and bio-geotechnology. He has published 170 technical papers in international/national journals and conference/seminar proceedings. He was a recipient of the Shamsher Prakash Research Award for Geotechnical Engineering in 2014. He is a member of ASCE, ASTM, IACMAG, IGS and TC 106 of ISSMGE. He is a reviewer for several national and international journals.

Addressing Sustainable Technologies in Geotechnical and Geoenvironmental Engineering

Krishna R. Reddy and Girish Kumar

Abstract Geotechnical and geoenvironmental engineering, which constitutes one of the major tasks of the infrastructure and construction projects, is one of the main contributors to the climate change and other global environmental impacts, due to the use of large amounts of materials and energy. One of the most effective ways to address these challenges is to have the environmental implications integrated into the decisions of a geotechnical/geoenvironmental project. In this regard, the application of life cycle assessment (LCA) has gained major impetus to evaluate the environmental sustainability of such projects. LCA is a comprehensive method for assessing a range of environmental impacts across the full life cycle of a geotechnical and geoenvironmental project, from raw material acquisition, material manufacturing and transport, construction, use and maintenance, and final disposal/recycling. LCA can be challenging due to limited reliable or relevant inventory of data for the assessment. However, it is a systematic and well-accepted tool to develop/design environmentally sustainable geotechnical and geoenvironmental projects. In addition, a triple bottom line assessment which further involves evaluating the economic and social sustainability aspects of the project along with the LCA is essential to holistically evaluate and identify the effectiveness of a geotechnical and geoenvironmental project toward sustainability. This paper presents a review of few studies that demonstrate the application of LCA and triple bottom line assessment to some of the common geotechnical and geoenvironmental projects. The study underscores the importance of LCA in identifying the critical materials and/or operations for the resulting environmental impacts and helps explore different options to improve the net environmental and socioeconomic benefits.

K. R. Reddy (✉) · G. Kumar

Department of Civil and Materials Engineering, University of Illinois at Chicago, 842 West Taylor Street, Chicago, IL 60607, USA
e-mail: kreddy@uic.edu

G. Kumar

e-mail: gkumar6@uic.edu

Keywords Life cycle assessment • Sustainability • Geotechnical engineering
Geoenvironmental engineering • Triple bottom line assessment

1 Introduction

The exploding population growth that leads to several adverse environmental impacts such as depletion of natural resources, increased waste generation, increased pollution, damage to ecosystem, loss of biodiversity, economic disparities, and social injustice has been a serious concern in recent years. In addition to this, the global climate changes leading to extreme weather patterns have gained wide attention from the past two decades. These challenges have been the major impetus to think of what is now widely known as the concept of sustainability or sustainable development. The term sustainability was first introduced by the World Commission on Environment and Development in their report “Our Common Future” where they defined sustainability as “development that meets the needs of the present generation without compromising the ability of future generations to meet their own needs” (UN 1987). Although this definition serves its intended purpose and urges the need for incorporating sustainability on a global level, it does not reflect the scope of sustainability evaluation at a local or a project level. The objectives of sustainability may vary for different scales (global, regional, local, and project levels). In this regard, American Society of Civil Engineers (ASCE) came up with a functional definition that defines sustainability as “A set of environmental, economic, and social conditions—the Triple Bottom Line—in which all of society has the capacity and opportunity to maintain and improve its quality of life indefinitely, without degrading the quantity, quality or the availability of natural, economic, and social resources” (ASCE 2009). This definition facilitates in incorporating the essential requirements to realize sustainability and its benefits at a project level.

Furthermore, to emphasize on the need for meeting the sustainability objectives at a project level, the ASCE Policy 418 (ASCE 2016) promotes sustainable development in engineering projects through their principle of “doing the right project” which entails that the environmental, economical, and social impacts are assessed and are made known to the community served by the project, before any decision is made. In addition, the policy also promotes the idea of “doing the project right” which requires that the project shall be planned by looking holistically at the life cycle stages (from concept to demolition and reuse) along with educating the stakeholders about the social, economic, and environmental benefits of the project.

In the context of civil engineering infrastructure, the geotechnical and geo-environmental projects account for a significant amount of energy and material consumption as the projects involve extensive use of earth and its resources. Hence, a major intervention in these projects with regard to environmental impacts can greatly contribute to the overall development toward sustainability. Current

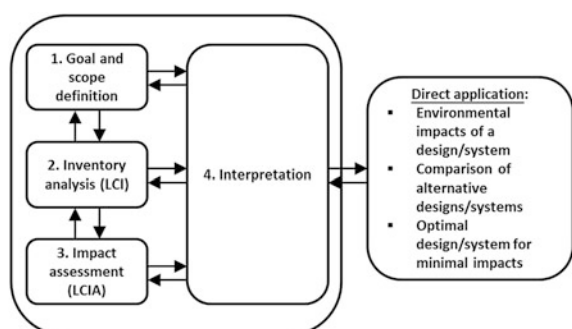
practices in geotechnical and geoenvironmental engineering involve the design of the projects optimized based on the cost and ease of implementation, time for implementation, regulatory compliance, and physical or environmental risks while satisfying the technical needs (codal provisions) with acceptable safety factors. Although these factors are essential, it is imperative to consider broader environmental, economic, and social impacts across the entire life cycle of the project, within a well-defined scope, in order to mitigate the aforementioned global environmental challenges. In addition to mitigating the environmental impacts, the life cycle thinking on a project often leads to innovative solutions (designs) which are technically sound as well as cost-effective. A holistic assessment of the sustainability of a project is complete if the economic and social impact assessment and its consequences are given due consideration along with the environmental impacts. This would further lead to making right decisions and thereby contributing toward global substantiality goals.

In recent years, there has been a growing interest and awareness to involve life cycle approach in the design of civil infrastructure, especially with the buildings. However, a few efforts have been made in incorporating life cycle assessment and sustainability evaluation into conventional geotechnical and geoenvironmental projects. This study presents a review of few such published studies that perform LCA and/or triple bottom line assessment on common geotechnical and geoenvironmental projects. The importance of performing sustainability assessment is emphasized, and its implications on the sustainable development at a project level are highlighted.

2 Life Cycle Assessment (LCA)

LCA is a tool to assess the environmental impacts associated with a project across its entire life cycle (from raw material acquisition, through construction and use, and final disposal/recycling of waste). A schematic representation of the framework of LCA is shown in Fig. 1.

Fig. 1 Life cycle assessment framework



LCA provides a means to identify, quantify, and interpret the resources and energy flows at each life cycle stage within a defined scope of the project. It has a well-established standard methodology developed by International Organization for Standardization (ISO 14040/44) which describes the procedure to be followed to perform the LCA (ISO 2006a, b). LCA involves four iterative phases: (1) goal and scope definition, (2) life cycle inventory analysis (LCI), (3) life cycle impact assessment (LCIA), and (4) interpretation of the results.

2.1 Goal and Scope

This phase of LCA essentially includes a statement of the purpose of the analysis, and this phase also mandates to identify the intended application and the intended audience to whom the results of the analysis apply. The functional unit and the system boundaries necessary to meet the goal are also defined in this phase. The functional unit of the LCA refers to a representative unit (can be smaller than the actual entity) which forms the basis for comparison between two alternatives performing a common function. The potential environmental impacts (emissions to air, water, and soil) of the project are evaluated as a proportional share of the full emission from each process in the life cycle associated with the functional unit (Finnveden et al. 2009).

2.2 Life Cycle Inventory Analysis (LCI)

This phase of LCA involves a systematic and detailed collection of the input (in the form of resource and energy used) and output (in the form of emissions and other environmental implications) associated with each process over the entire life cycle, corresponding to the functional unit. Setting up an appropriate inventory of data for different processes within the system boundary is challenging. Many databases have been developed over the years, and these databases are often integrated with the LCA software tools that aid in the data compilation and analysis.

2.3 Life Cycle Impact Assessment (LCIA)

This phase entails understanding and evaluating the magnitude and significance of the potential environmental impacts of all the inputs and outputs of each stage in the life cycle of the system under study. This includes the environmental impacts associated with the raw material extraction, material manufacturing, construction, use, and disposal/recycling. The life cycle impact assessment performs the interpretation of the inventory results and their potential impacts on the entities that

needs to be protected such as human health and environment. Generally, the impacts to human health and environment are modeled based on the knowledge about the interrelationship between interventions in the form of resource extraction, emissions, land use, and their impacts to human health and environment (Finnveden et al. 2009).

2.4 *Interpretation*

The main and unique feature of LCA is that it provides an opportunity to identify the sources of high environmental impacts arising from each life cycle stage and mitigate those impacts by exploring other alternatives that have lower environmental impacts. This phase of LCA is the interpretation, and the decisions from this phase can be included at each of the other phases to dynamically assess and minimize the environmental impacts of a project.

3 Sustainability (Triple Bottom Line) Assessment

The LCA is typically restricted to the standardized assessment of environmental impacts associated with the entire life cycle of the project. However, sustainability is broader than just environmental implications, and in order to realize the true impacts of the project, it is essential to add the social and economic aspects into the scope of the project over its entire life cycle. This is often referred to as the triple bottom line or the three pillars of sustainability. A narrow interpretation of just the environmental aspects alone is now replaced by the wider and more holistic interpretation with the consideration on the long-term consequences of the impacts on social and economic front. However, in order to determine the sustainability associated with a project, it is essential to have tools, metrics, and indicators that can quantify the impacts associated with each pillar and thereby help in making right decisions in the project.

LCA provides a standard framework to assess the environmental sustainability of a project. There are several tools (software) with well-accepted impact assessment methods that aid in quantifying the environmental impacts into different impact categories (e.g., cumulative energy, global warming, ozone depletion, fossil fuel depletion, eutrophication, human health, acidification, land use) and thereby help in identifying the major contributing factors to the environmental impacts over the entire life cycle. Quantification of these environmental impacts is well-established in the scientific literature, and several databases are available for use.

Economic sustainability assessment of the project is often regarded to account for direct costs arising over the entire life cycle (material costs, construction and operational costs, transportation costs, energy costs, and disposal/recycling costs),

and the total costs form the most common indicator of economic impacts. In addition to the direct costs, there are several indicators that cover and express the total economic impacts holistically such as the indirect costs (e.g., implications of climate change on economic damages) and benefits (e.g., employment opportunities and human capital), project life span, and flexibility among others. Life cycle cost analysis (LCCA) is one of the most common methods used to evaluate the direct costs and benefits associated with the project over its entire life cycle. However, there is no well-established metrics that can represent the indirect costs or benefits in a way that the stakeholders can easily understand and make decisions.

Social sustainability evaluation and its quantification, for a project, are challenging when compared to environmental and economic impact assessment. It is essential to actively engage communities and the stakeholders in the development of engineering solutions to account for social implications of the project and address the issues well before the project implementation. Most of the engineering projects are largely driven by economic considerations and rarely include impacts on the workers on an individual level and other broader societal consequences. There exists no single general tool or metrics that can fairly evaluate the potential social impacts and implications of a project and quantify it. The social impacts often tend to be subjective, since the perception of social impacts is variable, and hence, there is usually no general conclusion over social sustainability. But, if included, it adds validity to the overall sustainability of the project.

4 Case Studies

There has been a very limited effort to incorporate the life cycle thinking and the triple bottom line concept into the geotechnical and geoenvironmental engineering practice. However, there is a growing interest in recent years toward life cycle assessment-driven decision-making in such projects, resulting in technically sound solution while meeting sustainability objectives based on broader environmental, economic, and social considerations (Goldenberg and Reddy 2014, 2017; Giri and Reddy 2014; Reddy and Giri 2015). In this study, few case studies that discuss the use of LCA and sustainability evaluation in conventional geotechnical and geoenvironmental projects are briefly discussed. Some of the major conclusions of the studies and their implications on sustainable engineering in practice are highlighted.

4.1 *LCA of Soil Stabilization*

Lime stabilization is one of the most common techniques in practice for ground improvement. It essentially involves the addition of binders such as lime, cement, and gypsum to enhance the strength, stiffness, and other properties of soil. Lime

stabilization, although being a cost-effective solution to ground improvement, can have huge environmental implications associated with the production of lime to improve large volumes of soil. da Rocha et al. (2016) investigated the environmental impacts of stabilization of dispersive clayey soil with different dosages of lime to attain target strength, using LCA. The stabilization of the soil (in Paraguayan Chaco) was intended to convert the dispersive clayey soil to a non-dispersive soil for its use in construction of dams, embankments, pavements, and other purposes.

The technical design to achieve target strength after the stabilization was based on the adjusted porosity–binder ratio ($\eta/(L_{iv})^{0.16}$), where η is the porosity of the blend and L_{iv} is the volumetric lime content, and this ratio relates to the unconfined compressive strength of the soil–lime blend, after a certain curing time (Consoli et al. 2016). Five different target porosity–binder ratios that correspond to five different values of unconfined compressive strength (UCC) were considered in this study (Table 1). For each of the five ratios defined, three different percentages (dosage) of lime (3, 5, and 7%) at the corresponding three different dry densities (γ_d) of the soil–lime blend were proposed to achieve each of the five targeted UCC strength, thus creating five groups. This resulted in a total of 15 different blends which were evaluated for their environmental impacts using the standard LCA framework. A detailed explanation on the basis for the technical design can be found elsewhere (da Rocha et al. 2016; Consoli et al. 2009, 2016).

The goal of the study by da Rocha et al. (2016) was to perform LCA and evaluate the potential environmental impacts of one cubic meter (functional unit) of different soil–lime blends for its application in a road embankment. The results from the LCA on these blends are compared within each group and also between

Table 1 Dosage options considered for LCA by da Rocha et al. (2016)

Group	Dosage option	γ_d (kN/m ³)	η (%)	Lime (%)	L_{iv} (%)	$\eta/(L_{iv})^{0.16}$
B	B3	17.28	36.75	3	1.94	33.07
	B5	16.52	39.47	5	3.03	
	B7	16.00	41.32	7	4.03	
C	C3	17.50	35.94	3	1.96	32.27
	C5	16.75	38.61	5	3.07	
	C7	16.24	40.42	7	4.09	
D	D3	18.20	33.37	3	2.04	29.78
	D5	17.50	35.88	5	3.21	
	D7	17.02	37.58	7	4.28	
E	E3	18.63	31.79	3	2.09	28.26
	E5	17.96	34.19	5	3.29	
	E7	17.50	35.82	7	4.40	
F	F3	19.00	30.45	3	2.13	26.98
	F5	18.35	32.76	5	3.36	
	F7	17.91	34.33	7	4.51	

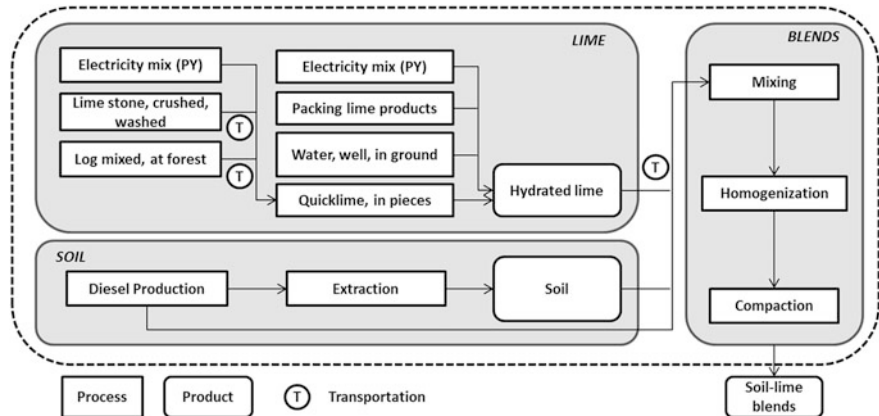


Fig. 2 Schematic of the system boundaries for LCA on soil blends (da Rocha et al. (2016))

the five different groups to identify the best means to perform lime stabilization that results in lower environmental impacts. The scope of the LCA involves mainly lime production, soil excavation, lime transportation, soil transportation, and blending process (mixing, homogenizing, and compacting). The use/maintenance and disposal/recycling stages of the life cycle were not considered in the scope of the LCA. Figure 2 shows a schematic representation of the system boundaries considered for LCA by da Rocha et al. (2016). OpenLCA, a free LCA software, was used by the authors to perform the LCA. A detailed discussion on the LCI, the databases for input/output for different processes and materials, and the LCIA methods used are reported in da Rocha et al. (2016).

4.1.1 Results

The impact assessment method developed by Centre of Environmental Science of Leiden University was used to evaluate the environmental impacts. The environmental impacts were expressed in terms of acidification potential, eutrophication potential, climate change, photochemical oxidation, depletion of abiotic resources, ozone depletion potential, and embodied energy (based on cumulative energy demand) over the entire life cycle. In this paper, only the results pertaining to the global warming potential and the embodied energy are presented for all the soil-lime blends. Figure 3 shows the total energy consumption (in MJ) and greenhouse gas (GHG) emissions (in CO_2 eq.) for each dosage option evaluated. It is found from the LCA results in Fig. 3 that the blends that required the least percent of lime to achieve target strength contributed the least toward total energy consumption and GHG emissions over the entire life cycle of its production. The total energy consumption and GHG emissions increased with both the higher percent of lime dosage and increasing density. However, the proportions in which energy demand

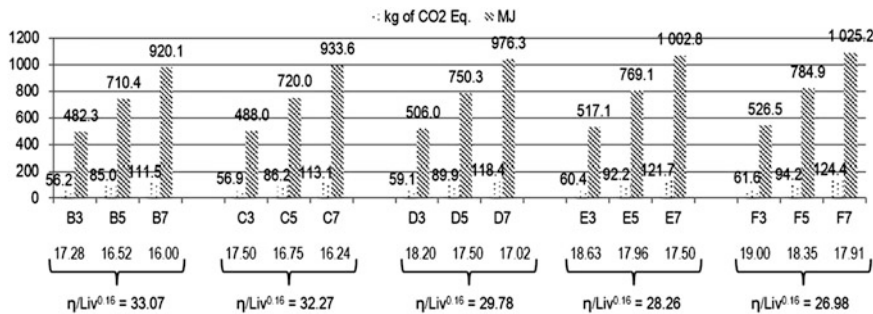


Fig. 3 Total GHG emission and energy consumption for each blend (da Rocha et al. 2016)

and GHG emissions increase are higher for increasing lime percentages than increasing density.

This indicates that the energy expended in preparing the soil-lime blend (mixing, homogenizing, and compacting) to achieve a higher density (leading to a lower porosity) does not contribute substantially to the environmental impacts when compared to the energy used in production and transportation of lime alone. Moreover, the production of lime is highly energy- and carbon-intensive process which leads to higher environmental impacts.

The study also showed that the environmental impact categories namely photochemical oxidation, embodied energy, and global warming potential were more pronounced when compared to other impact categories, across all the blends examined and lime production alone contributed to more than 75% of these impacts. Hence, an environmentally sustainable design (that consumes less energy and has less global warming potential) for soil stabilization could be obtained by using lower dosage of lime and compacting the blend to achieve a higher density, while meeting the target strength required. A detailed discussion on the results on different impact categories and the contribution of each process in the life cycle toward those environmental impacts are presented in da Rocha et al. (2016). Although this analysis may seem trivial, the implications of such analysis using LCA are more beneficial in designing a project from an environmental impact perspective.

4.2 LCA of Ground Improvement Methods

Ground improvement (GI) is one among the many other avenues for sustainable development in geotechnical engineering. There have been many studies that evaluate and compare the environmental impacts of different GI alternatives for different purposes (Harbottle et al. 2007; Jefferson et al. 2010; Egan and Slocombe 2010; Shillaber et al. 2015a, b). One such study that includes both environmental and

economic sustainability assessment is the study by Raymond et al. (2017). This study was intended to evaluate an environmentally and economically sustainable GI method for its applicability at the Treasure Island, California, to increase the soil's resistance to liquefaction under seismic loads. The goal and scope of the study by Raymond et al. (2017) was to evaluate the environmental and economic impacts of five GI methods namely deep soil mixing (DSM), vibro replacement (VR), vibro compaction (VC), deep dynamic compaction (DDC), and the installation of earthquake drain (EQD), which were considered to be viable options for Treasure Island redevelopment project. The technical design or the performance criterion of the GI was set to achieve a normalized SPT blow count of 15 or greater ($(N_1)_{60} \geq 15$) after the treatment. A functional unit of 25,000 m³ (50 m × 50 m × 10 m) of treated soil meeting the specified performance criterion was considered for the comparison of the LCA results of all the five GI methods. The scope or the system boundary of the LCA (Fig. 4) included the environmental impacts associated with raw material extraction, materials processing, manufacturing, transportation, equipment and vehicle mobilization and use, fuel production and consumption, and construction operations.

The LCA performed does not include the environmental impacts due to manufacturing of the equipment/vehicles, the use/maintenance phases, and the final disposal or recycling of the materials. A life cycle inventory of the input (quantifying resources) and output (quantifying emissions) flows for each of the GI methods was developed over the entire life cycle as described by the scope in Fig. 4. The data for the life cycle inventory was based on various LCI databases (in GaBi, Ecoinvent and National Renewable Energy Laboratory US LCI), published LCA studies and the EMFAC and OFFROAD transportation modeling programs. A detailed explanation on the various sources of data for the LCI on all the materials and processes considered is presented by Raymond et al. (2017).

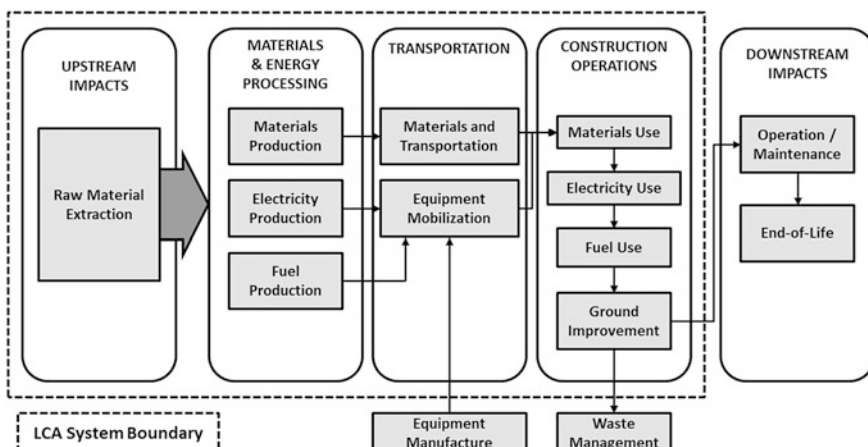


Fig. 4 Schematic of the system boundary for the LCA (Raymond et al. 2017)

The life cycle impact assessment was performed using the Tool for the Reduction and Assessment of Chemical and other Environmental Impacts (TRACI), an impact assessment method developed by USEPA (Bare 2002), to evaluate the potential impacts to environment and human health due to each of the GI methods. The environmental impacts were expressed in terms of several impact categories namely energy consumption (in GJ), global warming potential (GWP in CO₂ eq.), acidification potential (AP in hg SO₂ eq.), and photochemical oxidation potential (smog formation in tonnes of O₃). In addition to the environmental impacts, the study included an assessment of the indirect economic costs incurred by a GI method based on the carbon emissions due to each of the GI methods. This indirect cost is called the social cost of carbon (SCC) and is defined as an estimate of the monetized damages associated with an incremental increase in carbon emissions in a given year. The SCC integrates different climatic processes and economic growth, and interacts between the climate and the global economy to reflect the climatic impacts in terms of economic damages/costs. Although this does not account for all the economic and social issues associated with a GI method, it does help in evaluating the broader and long-term consequences of the different GI methods and thereby on the decision-making of the most appropriate GI method to be used. A detailed explanation on the method used for evaluating SCC is reported in Raymond et al. (2017).

4.2.1 Results

The results from the TRACI showed that for the given volume of the soil (25,000 m³), the DSM method had the highest environmental impact among all the methods considered. The LCA results showed that the high environmental impacts with the DSM method are predominantly due to the use of portland cement, the production of which is a highly energy-intensive process. About 95% of GWP for the DSM method was related to the cement manufacturing, and hence, a major intervention to improve the environmental sustainability of DSM is possible by using alternate materials in place of cement that can produce the same or better performance as that of the cement. The environmental impacts associated with VR, VC, DDC, and EQD are mainly determined by the transportation distances (emissions due to production and fuel consumption for transport) and the fuel consumption by equipment used for different site operations. The results for all the environmental impacts, along with the cost of implementing the GI method to treat 25,000 m³ of soil, for the five GI methods assessed are shown in Fig. 5 (a higher value indicates more negative impacts).

Based on the results (Fig. 5), vibro replacement (VR) was found to have the second highest environmental impact next to DSM. However, the environmental impacts of VR method are considerably lower than those of DSM. The project cost was found to be highest for DSM, followed by EQD method and the VR method.

A sensitivity analysis was performed to evaluate the significance of the materials used and the transportation distances involved in the entire life cycle of GI on the

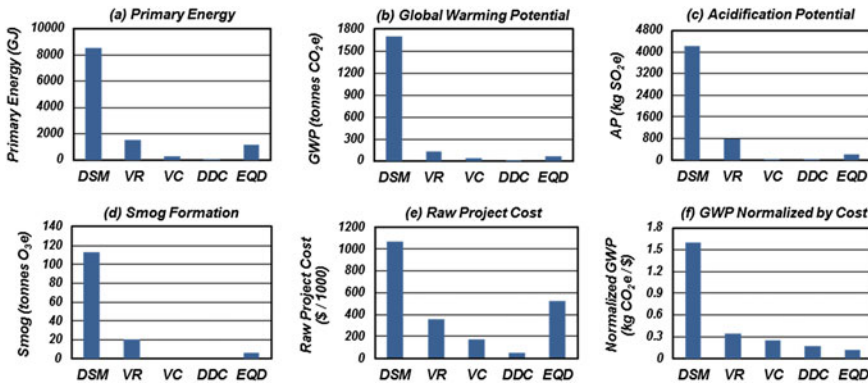


Fig. 5 LCIA results of all the GI methods for **a** primary energy, **b** global warming potential, **c** acidification potential, **d** smog formation potential, **e** raw project cost, **f** GWP normalized by cost of the corresponding GI method (Raymond et al. 2017)

environmental impacts. In addition, the sensitivity analysis would aid in determining the reliability of the results of LCA while considering the uncertainty associated with the assumptions made on transport distances. The sensitivity analysis included the effect of use of recycled materials (slag cement or recycled aggregate in place of portland cement) in different percentages of replacement (25, 50, and 75%) to determine the extent of GHG emissions reduction. Furthermore, the use of recycled crushed aggregate, from a nearby road construction site, in place of virgin aggregates was assessed for VR method and its effect on the environmental impacts was examined. In addition to the use of alternate materials, the influence of transport distances was evaluated for DSM, VR, and EQD methods.

The results of the sensitivity of DSM and VR to the use of recycled materials showed that the use of recycled materials can significantly reduce the GHG emissions. A 50% replacement of portland cement with the slag cement in DSM method decreased the GHG emissions by 42%. Likewise, the use of recycled aggregates in place of virgin aggregates for VR method reduced the GHG emissions by 45%. The sensitivity analysis on the transport distances showed that transportation distances had huge influence on the GHG emissions for VR method. However, the variation in distances had moderate impact for the EQD method and had very low impact for the DSM method. The detail results on sensitivity analysis are shown in Raymond et al. (2017).

Finally, the baseline results obtained from the LCA on a functional unit of just 25,000 m³ of soil were upscaled and applied to the area of the Treasure Island site (1.1 million m³ of soil). But here, a combination of GI methods in several scenarios was examined for the possible redevelopment of the site. A total of five scenarios including the scenario proposed by the ENGEO consulting engineers in 2011 were evaluated. The proportions of the volume of the soil treated by different GI methods in each of the scenarios are shown in Table 2.

Table 2 Treasure Island ground improvement scenario analysis (Raymond et al. 2017)

GI method	Proposed plan by ENGEO	Scenario 1	Scenario 2	Scenario 3	Scenario 4
DSM (%)	10.4	0.0	0.0	0.0	10.4
VR (%)	0.0	10.4	10.4	10.4	0.0
VC (%)	9.1	0.0	65.0	9.1	80.5
DDC (%)	80.5	80.5	0.0	80.5	0.0
Earthquake drains (%)	0.0	9.1	24.6	0.0	9.1
<i>Impact category</i>					
Primary energy (GJ)	447,427	158,038	279,035	122,349	543,447
GWP (tonnes CO ₂ e)	83,047	10,834	24,512	10,067	96,187.0%
AP (tonnes SO ₂ e)	2.00	0.01	0.61	0.36	2.10
Smog (tonnes O ₃ e)	53.08	0.40	16.92	9.74	56.06
SCC-3% avg (2015\$/tonne CO ₂ e)	\$3,737,099	\$487,546	\$1,103,023	\$453,003	\$4,328,401

The scenario analysis showed that the most environmentally and economically preferable combination of GI methods would include VR, DDC, and VC methods in the proportions mentioned in Table 2. Furthermore, the authors stated that if scenario 3 were to be executed instead of the proposed scenario by ENGEO in 2011, it would result in a savings of \$3.3 million. Finally, the authors concluded that the best combination does not include DSM, since DSM contributes substantially higher to the GHG emissions than any other method in any case. The results presented in the study by Raymond et al. (2017) may not be idealized, since the LCA was conducted for the specific project conditions. However, a life cycle assessment of this kind (including the economic implications due to the environmental impacts) could be conducted to any GI project or any other geotechnical project in general and the results from such analysis could be used to plan an effective approach to execute the project in a way that is less harmful to human health and environment.

4.3 Sustainability Assessment of Retaining Wall Systems

Construction of earth retaining wall (ERW) systems is one of the most common projects in geotechnical engineering as it forms an essential component of roadway/embankment design, soil excavations, slope stabilization, and other infrastructure. Several different ERW systems exist, and each type has its own pros and cons based on its applicability. Broadly, there are two main ERW systems used in practice, the conventional walls (gravity and cantilever type) and the mechanically stabilized earth (MSE) walls. However, one could design and use either wall systems to attain the intended or target performance as necessary. There are few studies in the

literature that investigate the cost-effectiveness of MSE walls over conventional wall types (Koerner and Soong 2001; Jones 1996; Khan and Sikder 2004; Tanyu et al. 2008; Berg et al. 2009). Some studies performed LCA on different ERW systems (Soga et al. 2011; Inui et al. 2011), while some other studies evaluated the overall sustainability of the two wall types based on triple bottom line framework, but with some simplifications (Giri and Reddy 2015; Lee and Basu 2015).

Furthermore, Damians et al. (2016a) performed the life cycle assessment of different types of retaining wall systems constructed to different heights for the same target performance and concluded that the environmental impacts decreased in the order of gravity, cantilever, steel MSE, and polymeric MSE wall types. Most of the abovementioned studies did not investigate the different wall types for their economic and social implications of choosing one over the other in a project. Hence, a holistic consideration of the broader environmental, economic, and social issues is lacking. In this regard, Damians et al. (2016b) performed a sustainability assessment using the triple bottom line framework to evaluate the overall sustainability of the four wall types (gravity, cantilever, steel MSE, and polymeric MSE) and four different wall heights (3, 5, 10, and 15 m).

The technical design for the three wall types (see Fig. 6) was based on the stability analysis of the retaining wall using the recommendations given in American Association of State Highway and Transportation Officials (AASHTO 2014) and American Concrete Institute (ACI 2002). The functional unit for comparing and/or analyzing the environmental impacts for the four wall types was defined as the entire wall height running 1 m in length along the wall face. A detailed explanation on the geometry of the walls, ground conditions, material properties used in the stability analyses is reported in Damians et al. (2016a, b). The scope of the sustainability assessment included all the materials and processes from the raw material acquisition till the end of construction phase. The use/maintenance and the disposal/recycling phases were not included in the assessment. The design life of the walls was assumed to be 100 years.

The SimaPro software v8.0.2 was used for the LCA and LCI of the input and the output flows in terms of resources and emissions, respectively, that are taken from the Ecoinvent v3.1 database available in the SimaPro software. The ReCiPe method with the hierarchist theory option was used for the environmental impact assessment. A detailed list of the inventory and the assumptions made in the study are presented in Damians et al. (2016a). A total of seven midpoint impact categories (climate change, ozone depletion, human toxicity, photochemical oxidation, acidification, freshwater eutrophication, marine eutrophication) and three endpoint impact categories (human health, ecosystem diversity, resource depletion) used by the ReCiPe method as the environmental impact indicators were evaluated in this study. In addition, the cumulative energy demand model which is also available in SimaPro software was used to evaluate the energy consumption over the entire life cycle of each wall option. An explanation on the differences between the midpoint and endpoint indicators, the corresponding impact categories and their units is presented elsewhere (Damians et al. 2016a, b; Goedkoop et al. 2008; Frischknecht et al. 2007).

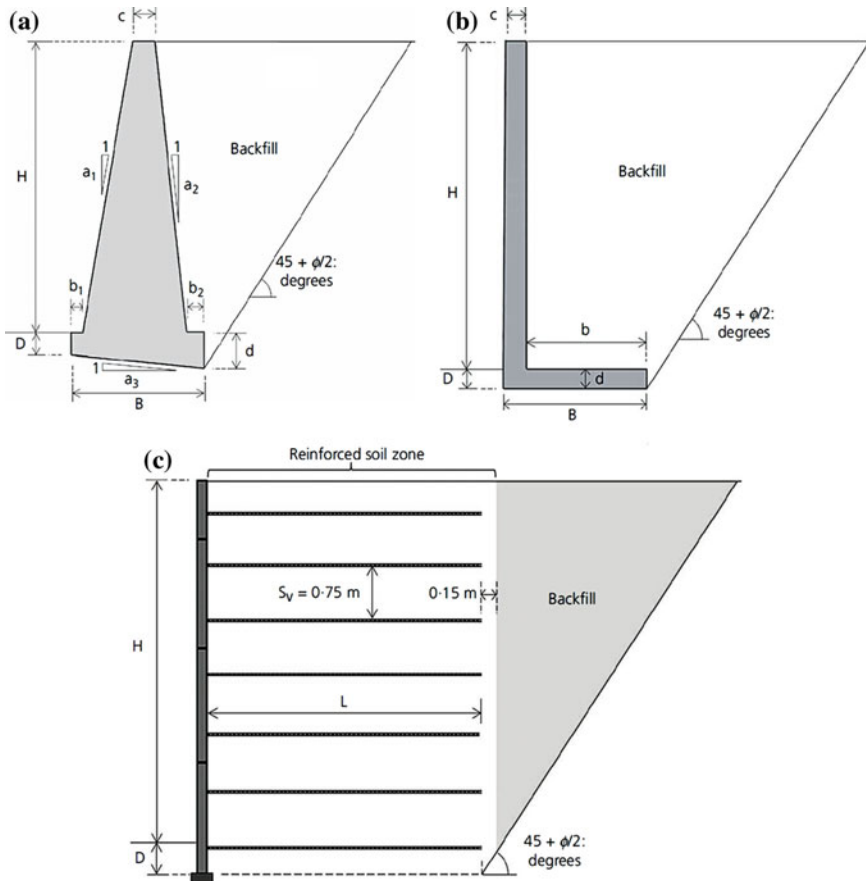


Fig. 6 Schematic of a gravity, b cantilever, c MSE wall types (Damians et al. 2016b)

The economic assessment was based on the direct costs associated with the materials, transportation, and time of operation of equipment used for the construction. The unit cost of the materials and operations was taken from a construction materials' database used in Barcelona, Spain (Itec 2014). Furthermore, a probabilistic approach was adopted to account for the uncertainty due to material losses and costs to estimate the final costs of each wall types. Finally, the societal impact assessment was carried out by the means of a survey form, identifying the key indicators for social sustainability quantification, developed using the inputs from a group of 200 graduate and 50 undergraduate students enrolled in a geotechnical engineering design class. The indicators were further refined by the authors of the study based on their experience with actual ERW projects. The final list of indicators were grouped into five criteria categories. An integer scoring system from 1 to 5, with the higher number for better Mives outcomes for each indicator, was used for quantifying the relative benefits of each option under the

different indicators considered. The final survey form used for actual evaluation of the social sustainability of the different wall options was filled by the same 250 students and ten experienced ERW designers. The final scores were aggregated and weighted as described in the original paper by Damians et al. (2016b).

In this study, a sustainability assessment model based on value theory and multi-attribute assumptions was implemented using the value integrated model for sustainable evaluation (Mives) methodology/software tool (Josa et al. 2008). The objective of this program was to quantify the overall sustainability through multi-criteria analysis so as to end up with a single numerical score that is helpful for objective decision-making among different alternatives. The process involves assigning the value functions to each of the indicator value obtained from the assessment of each triple bottom pillar. This is performed in order to convert the indicator values in different units to a dimensionless number between 0 and 1 to help in comparing the values in different pillars. Thereafter, each value at the indicator level (for different indicators) is multiplied with appropriate indicator weighting factors and added to achieve a criterion value for each indicator level. The value at the criterion level is multiplied with weighting factor for each criterion and added to obtain the value at each requirement level. Finally, the weighting values are multiplied to the values at each requirement level to obtain the final Mives score for the option being assessed. This final score indicates the value corresponding to the combined results from the assessment of the option under each pillar of sustainability. A thorough explanation on the procedure of the multi-criteria analysis using the value function approach is presented in Damians et al. (2016b)

4.3.1 Results

The results for the environmental sustainability assessment of the different wall options as obtained using the ReCiPe impact assessment method are shown in Fig. 7. Figure 7 shows the two midpoint indicators namely the global warming potential and the cumulative energy demand as they are the most familiar quantities for environmental impact evaluations.

The results show that in each of the impact categories, the conventional wall types (gravity and cantilever) have higher negative environmental impact than the MSE wall types. In addition, the environmental impacts were found to increase nonlinearly with the increasing wall height. However, the change (increase) in the impacts (CO_2 eq. and GJ) is drastic for conventional wall types and this is because of the fact that with increasing height of the conventional wall types, the steel reinforcement required to assure the required flexural strength also increases. Furthermore, the use of soil backfill in place of concrete as a major structural component of the retaining wall system resulted in lower environmental impacts as the emissions from the production of concrete, which are considerably high, are eliminated.

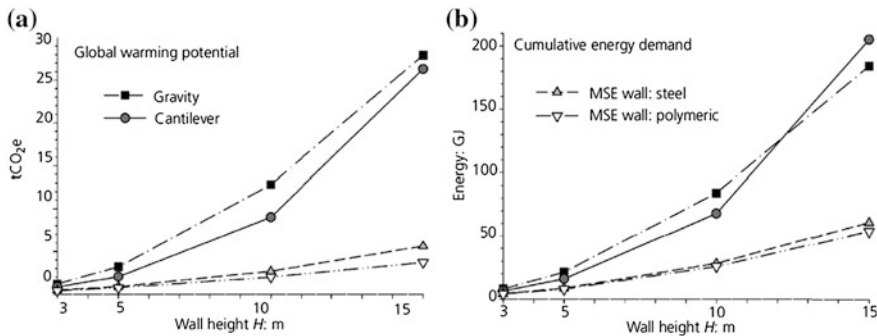


Fig. 7 Environmental impact results for **a** global warming potential, **b** cumulative energy demand for different wall options with varying heights (Damians et al. 2016b)

Figure 8 shows endpoint impact in terms of human health, ecosystem diversity, and depletion of natural resources aggregated into a single score for different wall types with varying height. The relative contributions of each endpoint impact category are also shown in Fig. 8. It is intuitive to expect the impacts to be higher for higher value of the wall height. For each impact category, the impacts decrease in the order of gravity, cantilever, steel-reinforced MSE, and polymeric reinforced MSE wall types except for 15 m of wall height where cantilever wall has higher environmental impacts than the gravity wall. It is also found that for any case, a large proportion of damages (40–51%) are associated with human health. It is followed by depletion of natural resources in most of the cases.

Figure 9 shows the total cost of different wall types as a function of wall heights along with the relative contributions of labor costs, equipment costs, material costs, and transportation costs to the total costs. It can be seen that for a lower wall height (3 m), the conventional wall types happen to be the preferred option (30% less expensive) from an economic perspective. Interestingly, for a wall height of 5 m the four wall options happen to be equally economical and the total cost incurred is effectively the same. However, as the wall height increases the MSE wall types turn out to be the best options with low total costs and the MSE wall with polymeric reinforcement happens to be slightly more cost-effective than the MSE wall with steel reinforcement. On the other hand, the gravity and cantilever wall are approximately 20 and 70% more expensive than the MSE walls for a wall height of 15 m. The greater cost for cantilever wall is again due to the high amount of steel reinforcement needed to support the wall from flexure.

Figure 9 indicates that the gravity and cantilever wall types are more labor-intensive when compared to MSE walls. However, the MSE wall types happen to incur a significant portion of the total costs due to transportation for the distances chosen in this study. For the wall heights of 10 and 15 m, the cost of materials consistently had the highest contribution among all the sectors of the total costs, regardless of the wall type.

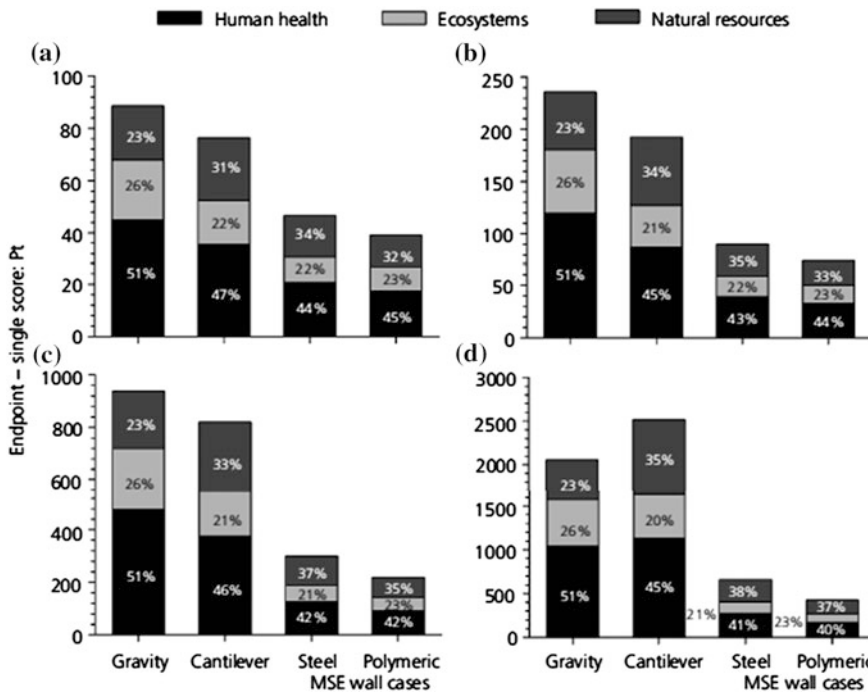


Fig. 8 Endpoint single score results and relative contributions for all wall types and wall heights **a** $H = 3$ m; **b** $H = 5$ m; **c** $H = 10$ m; **d** $H = 15$ m (Damians et al. 2016b)

Figure 10a shows the endpoint score at the requirement level obtained after applying the weighting using the value function to transform it to a dimensionless number for sustainability assessment as described earlier, briefly. Based on the weighting factors and the value function, it is observed that the MSE wall types are generally the best options from an environmental impact perspective. In particular, the MSE wall with polymeric reinforcement is found to be the best option for wall heights less than 12 m. Likewise, Fig. 10b shows the transformed value of the economic indicators (costs) at the requirement level for different wall types after applying the value function. The results in Fig. 10b show that the value of the indicator scores depends on the value function and the criterion adopted for transforming the costs to reflect their economic feasibility.

As mentioned earlier, the social sustainability assessment of the different wall types was based on the survey that included 17 indicators under 5 criteria categories. The survey was taken by 200 graduate students, 50 undergraduate students, and 10 ERW designers, and the weighting factors for the final values obtained at the requirement level were 30, 20, and 50%, respectively. The final computed values were found to be 0.53, 0.54, 0.57, and 0.58 for the gravity, cantilever, MSE-steel, and MSE polymeric wall, respectively. From the sample population that took part in the survey, it can be interpreted that the overall preference of one wall type over the

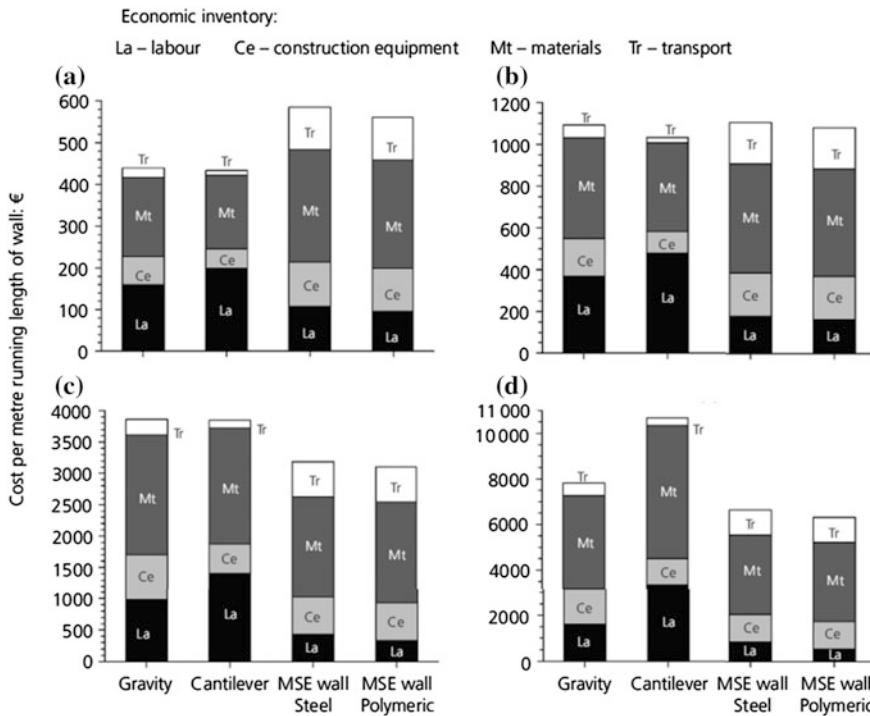


Fig. 9 Total costs for different wall options and different wall heights: **a** $H = 3$ m; **b** $H = 5$ m; **c** $H = 10$ m; **d** $H = 15$ m (Damians et al. 2016b)

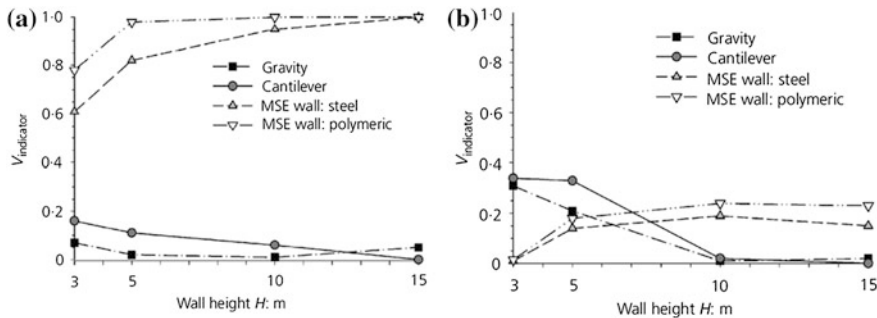


Fig. 10 Indicator results at the requirement level for different wall types and heights for **a** environmental impacts and **b** economic impacts (Damians et al. 2016b)

other was not significant. However, the results could also be influenced by the weighting factors used to arrive at the final values. In general, it was observed that the MSE wall types were preferred over the conventional wall types.

Finally, the overall sustainability assessment for the different wall types and wall heights was based on the final Mives scores after applying the weighting preferences to favor one of the three pillars based on the stakeholders' interests. A total of four weighting scenarios were considered; however, only one case, the reference case with equal weighting to each pillar, is discussed here. Based on the equal preference (33%) to each pillar of sustainability, it can be concluded that the MSE wall types are consistently a better option than the conventional wall types. However, the final scores and thereby the decisions for different wall options can significantly be affected by the weighting preferences. A detailed discussion on the results for each of the scenarios and the explanation on the results are presented in Damians et al. (2016b).

4.4 Sustainability Assessment of Landfill Cover Systems

In a municipal solid waste (MSW) landfill, final cover system forms an integral part of the engineered landfill as it is designed to minimize the infiltration of water into the waste in order to prevent the generation of landfill leachate. In addition, it acts as a barrier and reduces the landfill gas (LFG) emissions, predominantly methane (CH_4) and carbon dioxide (CO_2), into the atmosphere. The final cover system is usually accompanied with LFG collection system. However, there still exist some fugitive LFG emissions that are not targeted by the gas collection system. In this regard, landfills alone are reported to be the third largest source of CH_4 emissions into the atmosphere (USEPA 2011).

The subtitle D regulations recommend a minimum design requirement on the various components of the final cover system for MSW landfills to minimize the infiltration into the waste mass. In recent years, biocovers that involve the addition of organic amendments to the cover soil in order to promote microbial oxidation of methane have been widely investigated. This helps mitigate methane emissions into the atmosphere. However, the design of such biocovers is critical since it has to meet the performance of a subtitle D cover system while achieving optimum methane oxidation. The resulting net environmental impact and benefits of the biocovers are not known. In this regard, Sadasivam and Reddy (2014) conducted a site-specific LCA for the chosen landfill site in the Chicago metropolitan area and evaluated the overall sustainability of the two cover systems (subtitle D cover and the biocover) using the triple bottom line framework. The Countryside Landfill in Illinois was chosen to design the two cover systems and analyze the sustainability metric for the site-specific information. A schematic of the two cover systems is shown in Fig. 11.

The landfill cover design for the two cover systems was based on the California Landfill Methane Inventory Model (CALMIM). CALMIM is a field-validated model that predicts the methane emissions based on site-specific input data on cover parameters and the weather parameters for a user-defined location. More about the analysis performed using CALMIM and the assumptions made for obtaining the final design of the two cover systems based on annual methane emissions are

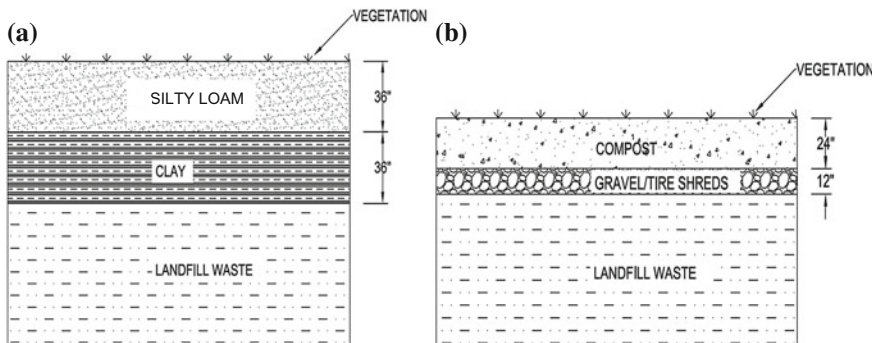


Fig. 11 Schematic of cover systems: **a** final cover system as per Illinois administrative code and **b** compost-based biocover

reported in Sadasivam and Reddy (2014). The functional unit of the assessment was taken as 1 acre (0.4 ha) of the landfill site for comparing the impacts of both the cover systems. The subtitle D cover was designed to meet the federal and the Illinois Environmental Protection Agency (IEPA) which required a two-layer system (low-permeability layer overlain by an erosion layer) with each layer being 90 cm thick (Sharma and Reddy 2004). The biocover generally consists of a compost layer overtopping a gas diffusion layer of at least 15 cm thick (Huber-Humer et al. 2008). This gas diffusion layer can be a variety of materials including wood chips, pebbles, gravel, or tire shreds. The system boundary for the sustainability assessment included the manufacturing of cover components, transportation of cover materials to the site, placement of the cover materials on site, and the monitoring of the cover. The design life of both the cover systems was assumed to be 50 years from the time of its placement.

The life cycle inventory related to the input materials and other processes (e.g., transport) associated with each of the cover systems over the entire life cycle (defined by the scope) are presented in Sadasivam and Reddy (2014). The Ecoindicator-99(E) v2.08 method available in SimaPro LCA software tool was used to perform the LCA of the two cover systems. The environmental impacts assessed by the Ecoindicator-99 method were expressed in terms of several midpoints (climate change, ozone depletion, carcinogens, acidification, ecotoxicity, land use, radiation, respiratory inorganics and organics) and endpoint indicators (damage to human health, ecosystem quality, and depletion of natural resources). Furthermore, the environmental sustainability assessment was conducted for five different cover options (three options for subtitle D cover and two options for biocover) which are (1) subtitle D cover assuming clay was not obtained from a quarry or mine and existed in a stockpile on site, (2) subtitle D cover assuming vegetative cover soil (silty loam) and clay obtained from a mine, (3) subtitle D cover assuming silty loam and clay obtained from a quarry, (4) biocover assuming tire shreds as the gas diffusion layer, and (5) biocover assuming gravel as the gas diffusion layer.

The economic assessment of the two cover systems was based on the direct costs associated with the materials, transportation, and the cover installation operations. The unit costs for each material and operation are reported in Sadasivam and Reddy (2014). The social sustainability assessment of the two cover systems was based on a qualitative and quantitative method in accordance with the United Nations Environment Program (UNEP) and the Society of Environmental Toxicology and Chemistry (SETAC) framework for Methodological Sheets for Social LCA (Benoit-Norris et al. 2011). A binary scoring system of "0" (for no negative impact) and "1" (for a negative impact) for a specific set of indicators relevant to the cover systems was used for quantifying the social sustainability of the two cover systems. The indicators were distributed among four categories of social impact namely the workers, consumers (the residents), local community, and the society. The cover system that yields least number of cumulative points after scoring was regarded as more socially sustainable option. Finally, the overall sustainability assessment was based on simple ranking system with the two cover systems ranked under each pillar of sustainability. The cover system which is the most sustainable under at least two pillars of sustainability is regarded as the most sustainable option.

4.4.1 Results

The environmental impact assessment results from SimaPro using the Ecoindicator-99 method for all the five scenarios tested are shown in Fig. 12. The plot shows the midpoint level impact categories under a single score for each of the scenarios examined. Based on the total environmental impacts including all the impact categories, it is observed that the compost-based biocover with the tire shreds as the drainage layer has the lowest overall environmental impacts. This is due to the fact that the tire shred is a waste material that is reused and thereby eliminating the emissions related to the use of virgin natural materials/resources (gravel). The second best option was found to be compost-based biocover with gravel as drainage material.

The most environmentally unsustainable option was found to be the subtitle D cover system with the clay obtained from mine or quarry.

The specific impact categories that contributed the most toward the total environmental impacts were the respiratory inorganics and the depletion of fossil fuels. The installation of cover being a labor-intensive process, the high impacts due to respirator inorganics correspond to the damage to human health, especially workers involved in the installation process and the people residing close to the landfill site. In addition, the high fuel consumption relating to the depletion of resources corresponds to the extensive transportation involved in hauling the materials and operation of the equipment for cover installation operations (spreading and compaction).

The results from the economic assessment based on the costs associated with materials, site installation operations, and transportation of materials indicate that the total cost incurred by the two cover systems was comparable with the subtitle D

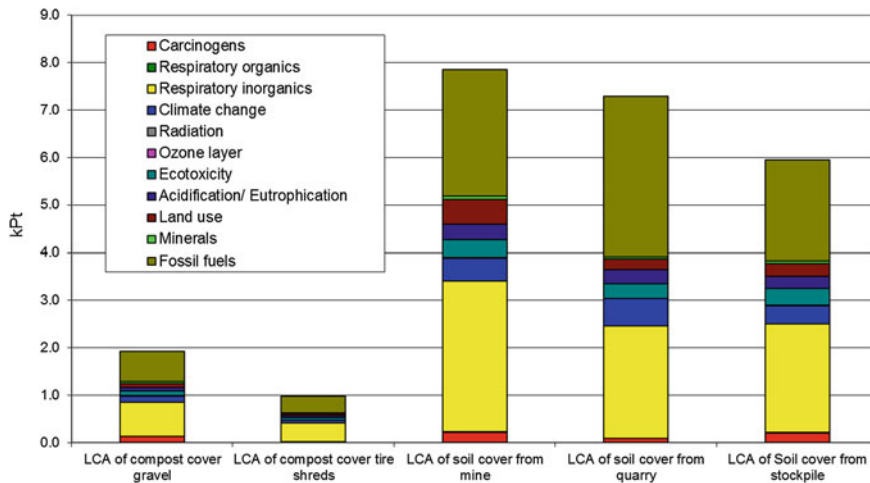


Fig. 12 Single score plot for the environmental impacts of the five cover system scenarios examined (Sadasivam and Reddy 2014)

cover (\$101,640) being slightly more expensive than the biocover system (\$98,432). However, the authors also noted that the availability of the compost that might lead to hauling of compost from far locations, thereby incurring more cost for transport can change the results. A summary of the unit costs used for the economic assessment is reported in Sadasivam and Reddy (2014).

The social sustainability assessment of the two cover systems based on the specific indicators and metrics (see Table 4 in Sadasivam and Reddy 2014) indicated that the biocover system with the least cumulative points was regarded the better option when compared to subtitle D soil cover system. The authors of the study also noted that the subtitle D cover could possibly have negative social impacts due to the excavation and use of silty clay soils that could otherwise be used for agricultural purposes, and in this sense, biocover was found to be favorable to the workers in terms of eliminating the need for such soils and thereby happened to be the most effective option. Since the compost-based biocover system was found to be sustainable under each of the environmental, economic, and social pillars of sustainability, it was regarded the most sustainable option in comparison with the subtitle D soil cover system. Such a triple bottom line analysis could be applied to any other geoenvironmental projects (Goldenberg and Reddy 2014, 2017; Giri and Reddy 2014; Reddy and Giri 2015), and the decisions of the project based on such assessment would result in technically sound, environmentally friendly, and cost-effective design solutions.

5 Discussion and Conclusions

Currently, in the geotechnical and geoenvironmental practice there is rarely any notion of sustainability associated with the design and planning of the project. The environmental, economic, and social implications due to the materials, operations, equipment, the construction, disposal, and reuse/recycling involved in a project are not accounted/realized in the project design and implementation. This inadvertently accumulates and adds to the existing scenario of global environmental challenges including global warming, climate change, and depletion of natural resources. There are very limited studies in the literature on incorporating sustainability objectives and performing LCA and sustainability assessment to the geotechnical and geoenvironmental projects. Until recently, the advent of strict regulations and the drive toward sustainable development have led to increased awareness toward life cycle based analysis of the geotechnical and geoenvironmental systems.

This study presents an overview of the use of LCA and sustainability assessment techniques to design an environmentally, economically, and socially sustainable design solution in geotechnical and geoenvironmental projects. A review of few of the recently published studies involving the LCA and triple bottom line assessment of geotechnical and geoenvironmental systems is presented. The published studies that are discussed in this paper incorporated LCA framework set forth by ISO 14040/44. In addition to the environmental sustainability assessment, some studies also addressed the economic and social impacts of the respective project to holistically evaluate the overall sustainability of the project. Some of the studies also included the multi-criteria decision analysis to analyze the sustainability and identify the most sustainable alternative among the options examined. Although there is a lack of strong generality and standardization with the metrics in completely evaluating the social and economic impacts, the relative comparisons of the different alternatives under the same assumptions would provide reasonably valid results which could aid in better decision-making on the projects. In addition, performing LCA and/or sustainability assessment helps in identifying the key areas contributing to the major environmental, economic, and/or social impacts and thereby provides the opportunity to explore innovative and cost-effective solutions to combat and reduce those high impacts. The studies presented in this paper demonstrate how LCA and sustainability assessment techniques/methods can be applied to geotechnical and geoenvironmental projects and potentially help in effective project planning and decision-making in the projects while contributing to the global sustainable development.

References

ASCE. (2009). *Code of ethics*. http://www.asce.org/uploadedFiles/About_ASCE/Ethics/Content_Pieces/CodeofEthics2006.pdf. Accessed on May 22, 2017.

ASCE. (2016). *Policy statement 418: The role of the civil engineer in sustainable development*. <http://www.asce.org/issues-and-advocacy/public-policy/policy-statement-418—the-role-of-the-civil-engineer-in-sustainable-development/>. Accessed on May 22, 2017.

Bare, J. C. (2002). TRACI. *Journal of Industrial Ecology*, 6(3–4), 49–78.

Benoit-Norris, C., Vickery-Niederman, G., Valdivia, S., Franz, J., Traverso, M., Ciroth, A., et al. (2011). Introducing the UNEP/SETAC methodological sheets for subcategories of social LCA. *The International Journal of Life Cycle Assessment*, 16(7), 682–690.

Berg, R. R., Christopher, B. R., & Samtani, N. C. (2009). *Design of mechanically stabilized earth walls and reinforced soil slopes—Volume II*. National Highway Institute, Federal Highway Administration, Washington, DC, USA, No. FHWANHI-10-025.

Consoli, N. C., da Silva Lopes, L., Jr., & Heineck, K. S. (2009). Key parameters for the strength control of lime stabilized soils. *Journal of Materials in Civil Engineering*, 21(5), 210–216.

Consoli, N. C., Samaniego, R. A. Q., & Villalba, N. M. K. (2016). Durability, strength, and stiffness of dispersive clay–lime blends. *Journal of Materials in Civil Engineering*, 28(11), 04016124.

da Rocha, C. G., Passuello, A., Consoli, N. C., Samaniego, R. A. Q., & Kanazawa, N. M. (2016). Life cycle assessment for soil stabilization dosages: A study for the Paraguayan Chaco. *Journal of Cleaner Production*, 139, 309–318.

Damians, I. P., Bathurst, R. J., Adroguer, E. G., Josa, A., & Lloret, A. (2016a). Environmental assessment of earth retaining wall structures. *Environmental Geotechnics*.

Damians, I. P., Bathurst, R. J., Adroguer, E. G., Josa, A., & Lloret, A. (2016b). Sustainability assessment of earth-retaining wall structures. *Environmental Geotechnics*.

Egan, D., & Slocombe, B. (2010). Demonstrating environmental benefits of ground improvement. *Ground Improvement. Proceedings of the Institution of Civil Engineers*, 163(1).

Finnveden, G., Hauschild, M. Z., Ekval, T., Guinée, J., Heijungs, R., Hellweg, S., et al. (2009). Recent developments in life cycle assessment. *Journal of Environmental Management*, 91(1), 1–21.

Frischknecht, R., Jungbluth, N., Althaus, H. J., Bauer, C., Doka, G., Dones, R., et al. (2007). *Implementation of life cycle impact assessment methods*. Swiss centre for life cycle inventories, Dübendorf, Switzerland. Ecoinvent Report No. 3, v2.0. <http://www.ecoinvent.org/>. Accessed May 22, 2017.

Giri, R. K., & Reddy, K. R. (2014). LCA and sustainability assessment for selecting deep foundation system for high-rise buildings. In *ICSI 2014: Creating infrastructure for a sustainable world* (pp. 621–630).

Giri, R. K., & Reddy, K. R. (2015). Sustainability assessment of two alternate earth-retaining structures. In *IFCEE 2015* (pp. 2836–2845).

Goedkoop, M., Heijungs, R., Huijbregts, M., et al. (2008). *ReCiPe 2008: A life cycle impact assessment method which comprises harmonised category indicators at the midpoint and the endpoint level, Report I: Characterisation*. Ministerie van Volkshuisvesting, Ruimtelijke Ordening en Milieubeheer, The Hague, Netherlands. <http://www.lcia-recipe.net/>. Accessed on May 22, 2017.

Goldenberg, M., & Reddy, K. R. (2014). Sustainability assessment of excavation and disposal versus in situ stabilization of heavy metal-contaminated soil at a superfund site in Illinois. In *Geo-Congress 2014: Geo-characterization and modeling for sustainability* (pp. 2245–2254).

Goldenberg, M., & Reddy, K. R. (2017). Sustainability assessment of conventional and alternate landfill cover systems. In *Geotechnical frontiers 2017* (pp. 323–332).

Harbottle, M. J., Al-Tabbaa, A., & Evans, C. W. (2007). A comparison of the technical sustainability of in situ stabilisation/solidification with disposal to landfill. *Journal of Hazardous Materials*, 141(2), 430–440.

Huber-Humer, M., Gebert, J., & Hilger, H. (2008). Biotic systems to mitigate landfill methane emissions. *Waste Management and Research*, 26(1), 33–46.

Inui, T., Chau, C., Soga, K., Nicolson, D., & O’Riordan, N. (2011). Embodied energy and gas emissions of retaining wall structures. *Journal of Geotechnical and Geoenvironmental Engineering*, 137(10), 958–967.

Itec (Catalonia Institute of Construction Technology). (2014). *Banco estructurado de datos de elementos constructivos (BEDEC)*. Catalonia institute of construction technology, Barcelona, Spain. <http://itec.es/nouBedec.e/>. Accessed May 22, 2017 (in Spanish).

ISO. (2006a). ISO 14040 International standard. In: *Environmental management—Life cycle assessment—Principles and framework*. International organization for standardization, Geneva, Switzerland.

ISO. (2006b). ISO 14044 International standard. In: *Environmental management—Life cycle assessment—Requirements and guidelines*. International organization for standardization, Geneva, Switzerland.

Jefferson, I., Gaterell, M., Thomas, A. M., & Serridge, C. J. (2010). Emissions assessment related to vibro stone columns. *Proceedings of the Institution of Civil Engineers-Ground Improvement*, 163(1), 71–77.

Jones, C. J. F. P. (1996). *Earth reinforcement and soil structures*. London, UK: Thomas Telford.

Josa A, San José T and Cuadrado J (2008) El caso de la EHE. In *Jornada sobre sostenibilidad en la tecnología del hormigón: MIVES, una Herramienta de Apoyo a la Toma de Decisiones* (pp. 84–95). Barcelona, Spain (in Spanish).

Khan, A. J., & Sikder, M. (2004). Design basis and economic aspects of different types of retaining walls. *Journal of Civil Engineering (IEB)*, 32(1), 17–34.

Koerner, R. M., & Soong, T. Y. (2001). Geosynthetic reinforced segmental retaining walls. *Geotextiles and Geomembranes*, 19(6), 359–386.

Lee, M., & Basu, D. (2015). Sustainability assessment of mechanically stabilized earth walls. In *CD Proceedings of 15th Pan-American Conference on Soil Mechanics and Geotechnical Engineering, Buenos Aires, Argentina* (pp. 830–837). IOS, Amsterdam, Netherlands.

Raymond, A. J., Pinkse, M. A., Kendall, A., & DeJong, J. T. (2017). Life cycle assessment of ground improvement alternatives for the Treasure island, California, redevelopment. In *Geotechnical frontiers 2017* (pp. 345–354).

Reddy, K. R., & Giri, R. K. (2015). Assessing sustainability of ground improvement methods: quantitative triple bottom line framework and case study. In *Infrastructure development for environmental conservation and sustenance 28–30 October, 2015* (Vol. 35).

Sadasivam, B. Y., & Reddy, K. R. (2014). Sustainability assessment of Subtitle D cover versus biocover for methane oxidation at municipal solid waste landfills. In *Geo-congress 2014: Geo-characterization and modeling for sustainability* (pp. 3807–3816).

Sharma, H. D., & Reddy, K. R. (2004). *Geoenvironmental engineering: Site remediation, waste containment, and emerging waste management technologies*. Wiley.

Shillaber, C. M., Mitchell, J. K., & Dove, J. E. (2015a). Energy and carbon assessment of ground improvement works. I: Definitions and background. *Journal of Geotechnical and Geoenvironmental Engineering*, 142(3), 04015083.

Shillaber, C. M., Mitchell, J. K., & Dove, J. E. (2015b). Energy and carbon assessment of ground improvement works. II: working model and example. *Journal of Geotechnical and Geoenvironmental Engineering*, 142(3), 04015084.

Soga, K., Chau, C., Nicholson, D., & Pantelidou, H. (2011). Embodied energy: Soil retaining geosystems. *KSCE Journal of Civil Engineering*, 15(4), 739.

Tanyu, B. F., Sabatini, P. J., & Berg, R. R. (2008). *Earth retaining structures*. US department of transportation, federal highway administration, Washington, DC, USA, FHWA-NHI-7-071.

UN. (1987). World commission on environment and development. In *Our common future* (p. 27). Oxford: Oxford University Press.

USEPA. (2011). *Municipal solid waste generation, recycling, and disposal in the United States: Facts and figures for 2010*. EPA-530-F-11-005, Washington, DC.

Geotechnics of Soft Ground

Madhav Madhira and Venkata Abhishek Sakleshpur

Abstract Geotechnical practice conventionally involves investigating a site to characterize it through: (1) in situ testing and (2) laboratory testing of so-called undisturbed samples, and then synthesizing the results to predict the overall response of the ground to engineering intervention. In the recent past, several case studies have been reported in the literature, particularly of soft ground improved by preloading with prefabricated vertical drains (PVDs), with time-settlement plots obtained from data recorded by settlement gauges installed at different depths in the ground. In addition, several load-displacement responses of piles are also available in the literature. This paper complements the above approach of element response to gross one by analyzing the response of the ground to arrive at its gross engineering properties or characteristics. Methods to estimate the compression index, C_c , and the coefficient of radial consolidation, c_r , by back-analysis of observed time-settlement plots of PVD-improved ground are illustrated. Furthermore, an approach to predict the magnitude of desiccation of weathered crust, and quantify the non-homogeneity of soft ground with respect to C_c , is presented. The c_r values estimated from three case histories compare reasonably well with those given by Hansbo (2005). Lastly, a method to estimate the initial shaft and base stiffnesses and the ultimate shaft and base resistances of a pile foundation is presented by considering the soil-pile response to be hyperbolic. Predictions compare well with results obtained from pile load tests (PLTs) performed at three different locations in India.

Keywords Compression index • Radial consolidation coefficient
Pseudo-overconsolidation • Inflection point method • Winkler model
Pile-soil stiffness and ultimate strength

M. Madhira (✉)

Department of Civil Engineering, JNTU & IIT, 500034 Hyderabad, TS, India
e-mail: madhavmr@gmail.com

V. A. Sakleshpur

Lyles School of Civil Engineering, Purdue University, 47907 West Lafayette, IN, USA
e-mail: svabhi.92@gmail.com

1 Introduction

Soft ground, widespread throughout the world along deltaic and coastal regions, is highly compressible with high natural moisture content (close to the liquid limit), low undrained shear strength and low hydraulic conductivity. As a result, ground improvement by preloading with prefabricated vertical drains (PVDs) is frequently carried out to accelerate the consolidation of soft ground, increase its shear strength, and minimize the settlement of the structure built over it. The compression index, C_c , and the coefficient of radial consolidation, c_r , are important geotechnical parameters for estimation of primary consolidation settlement and time taken for completion of primary consolidation, respectively, of PVD-improved ground. Conventional laboratory-based methods for calculating C_c have certain demerits, such as sample disturbance caused during transportation of Shelby tubes from the site, lack of proper care while conducting the experiment, time constraints, and high apparatus cost. To overcome these difficulties, several researchers have proposed single-parameter and multi-parameter correlations for C_c in terms of liquid limit, w_L , natural water content, w_n , initial void ratio, e_0 , and plasticity index, PI (Tiwari and Ajmera 2012; McCabe et al. 2014; Lee et al. 2015; Baroni and Almeida 2017; Kootahi and Moradi 2017).

The Rowe cell (Rowe and Barden 1966) with radial drainage, used to determine c_r , is a stress-controlled test that is usually performed at a load increment ratio of 1. However, the value of c_r obtained from this test may not be reliable for highly sensitive clays. An alternate laboratory approach to evaluate c_r is to estimate the coefficient of consolidation for vertical flow, c_v , from one-dimensional oedometer tests and then multiply c_v by a certain factor to obtain c_r . However, the size of the soil sample in these elemental tests is relatively small when compared to the actual thickness of the deposit, and thus the value of c_r measured in the laboratory may not be truly representative of the entire soil layer in the field (Charan and Madhav 2016).

This paper summarizes methods to estimate C_c and c_r from observed time-settlement plots for points located at different depths in a thick compressible deposit improved with PVDs. The magnitude of desiccation of weathered crust is evaluated by means of a pseudo-overconsolidation ratio (pseudo-OCR), and the non-homogeneity of soft ground with respect to the compression index is illustrated. Two approaches for estimation of c_r from observed time-settlement plots are summarized: (1) based on Asaoka's method (Asaoka 1978) and (2) based on inflection point method (Cour 1971; Robinson 1997a, b; Mesri et al. 1999; Sinha et al. 2007). The effect of surcharge application in the form of ramp loading is incorporated into these methods. The values of c_r estimated from three case histories, using these methods, are compared with those given by Hansbo (2005). Lastly, a method to estimate the initial shaft and base stiffnesses and the ultimate shaft and base resistances of a pile foundation is presented considering the soil–pile response to be hyperbolic. Predictions compare well with results obtained from pile load tests (PLTs) performed at three different sites in India.

2 Estimation of C_c from Observed Time–Settlement Plots

The primary consolidation settlement of soft soil is typically estimated by considering the soil to be either normally consolidated ($OCR = 1$) or overconsolidated ($OCR > 1$) based on its geology and stress history. The primary consolidation settlement, S , for a single, thick, compressible soil layer is

(a) For normally consolidated (NC) soil (i.e. $\sigma'_{v0} = \sigma'_{vp}$ and $\sigma'_v \geq \sigma'_{vp}$)

$$S = \frac{C_c}{1 + e_0} H \log\left(\frac{\sigma'_v}{\sigma'_{v0}}\right) \quad (1)$$

(b) For soil that is initially overconsolidated (OC) but becomes normally consolidated (NC) after the stress increment (i.e. $\sigma'_{v0} < \sigma'_{vp} \leq \sigma'_v$)

$$S = \frac{C_s}{1 + e_0} H \log\left(\frac{\sigma'_{vp}}{\sigma'_{v0}}\right) + \frac{C_c}{1 + e_0} H \log\left(\frac{\sigma'_v}{\sigma'_{vp}}\right) \quad (2)$$

where σ'_{v0} = initial vertical effective stress at mid-depth, σ'_{vp} = preconsolidation pressure, σ'_v = current vertical effective stress at mid-depth = $\sigma'_{v0} + \Delta\sigma$, $\Delta\sigma$ = stress increment, C_c = compression index, C_s = swelling or recompression index, e_0 = initial void ratio, and H = layer thickness.

Rewriting Eqs. (1) and (2) in terms of the compression index for each sublayer, i (Madhav et al. 2015)

$$C_{c,i} = \frac{\Delta S_i (1 + e_{0,i})}{\Delta H_i \log\left(\frac{\sigma'_{v,i}}{\sigma'_{v0,i}}\right)} \quad (\text{for NC soil}) \quad (3)$$

$$C_{c,i} = \frac{\Delta S_i (1 + e_{0,i})}{\Delta H_i \left[\frac{C_{s,i}}{C_{c,i}} \log\left(\frac{\sigma'_{vpi}}{\sigma'_{v0,i}}\right) + \log\left(\frac{\sigma'_{v,i}}{\sigma'_{vpi}}\right) \right]} \quad (\text{for initial OC then NC soil}) \quad (4)$$

From Eqs. (3) and (4), the compression index, $C_{c,i}$, of each sublayer can be estimated from known values of ΔS_i . The non-homogeneity of the deposit in terms of the compression index, if any, can thus be determined by plotting the values of $C_{c,i}$ versus depth for all the sublayers.

2.1 Second Bangkok International Airport (SBIA)

The subsoil profile at the SBIA site (Fig. 1) is relatively uniform and consists of a top 2.0-m-thick weathered crust, followed by a 6.0-m-thick very soft clay layer and

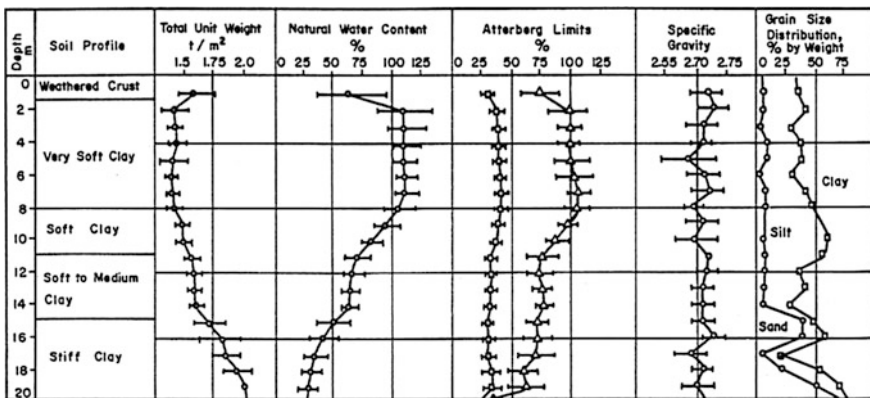


Fig. 1 Typical subsoil profile in Bangkok plain (Balasubramaniam et al. 2007)

a 3.0-m-thick soft clay layer. Below the soft clay layer lies a 4.0-m-thick layer of soft to medium clay followed by a stiff clay layer down to a depth of 20 m. The natural water content of the very soft clay layer is greater than 100% and is as high as the liquid limit. Hence, ground improvement by preloading with PVDs was adopted at the site. Figure 2 shows the observed time-settlement curves at different depths below the centre of the surcharge fill.

The final settlements near the ground surface, and at different depths, are read from Fig. 2. The settlement, ΔS_i , of each sublayer, i , is estimated as the difference

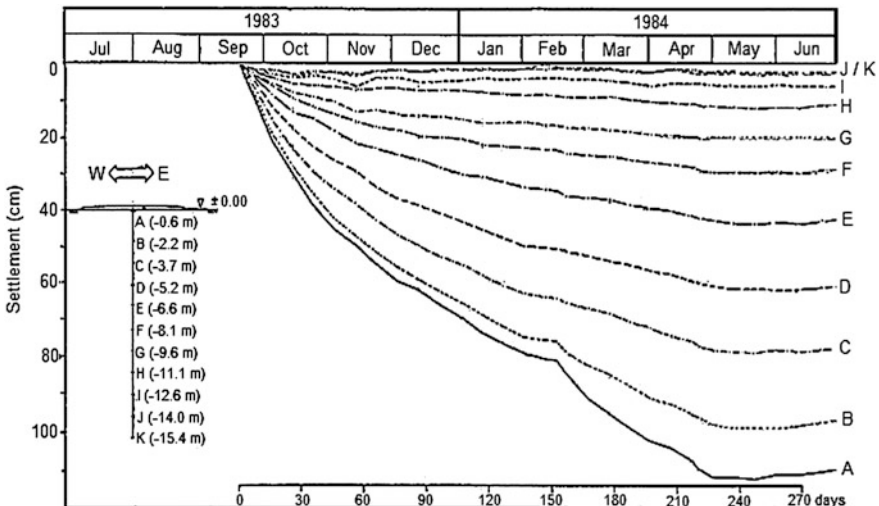


Fig. 2 Settlement versus time at different depths below centre of surcharge fill (modified from Madhav and Srikanth 2014)

between the settlements at two consequent depths (Madhav and Srikar 2014). The compression index, $C_{c,i}$, of each sublayer can then be estimated based on the corresponding saturated unit weight, γ_{sat} , and natural water content, w_n , of the sublayer (Fig. 1).

The variation of compression index with depth for the SBIA site is shown in Fig. 3. The compression index decreases from 0.87 at 4.5 m depth to as low as 0.05 at 15 m depth due to the increase in fine sand content in the soil. The relatively small value of compression index ($C_c = 0.27$) in the top 2-m-thick weathered crust is possibly due to desiccation. Alternate cycles of heating and cooling, and wetting and drying, can cause the soil to shrink and expand, leading to desiccation, which in almost all clays, leads to an increase in strength. However, an alternate approach is to consider the layer to have attained pseudo-overconsolidation, somewhat akin to the idea proposed by Bjerrum (1972). The magnitude of desiccation can be quantified in terms of pseudo-OCR using Eq. (4). To do that, it is first presumed that the desiccated layer was initially normally consolidated and had the same compression index ($C_c = 0.64$) as that of the NC clay layer below it. Next, for a given C_s/C_c ratio, the OCR ($= \sigma'_{vp}/\sigma'_v$) in Eq. (4) is varied to yield different values of C_c (Table 1). It can be observed that for OCR = 2.5–3.0 and $C_s/C_c = 0.1$, the corresponding value of C_c lies between 0.62 and 0.71. If the matching is carried out for a higher value of C_c of 0.87, then the OCR of the desiccated layer is definitely greater than 3.0. Thus, it is now possible to assign a specific value of OCR to a desiccated layer, or in other words, it can be stated that the degree of desiccation can be quantified.

Fig. 3 Compression index versus depth at SBIA site (modified from Madhav and Srikar 2014)

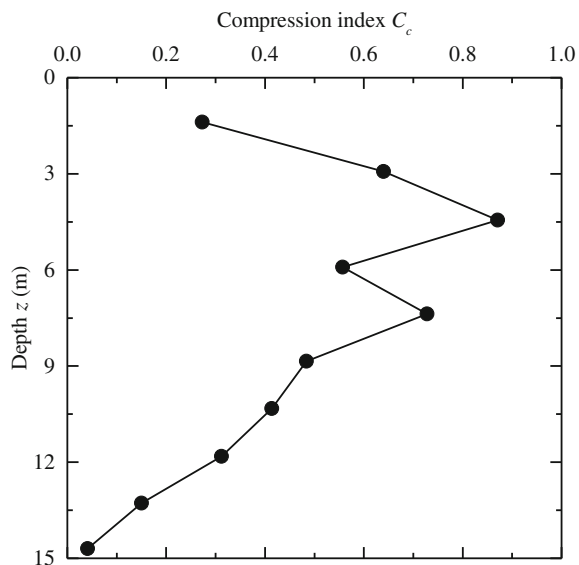


Table 1 Pseudo-OCR of desiccated layer (Madhav and Srikar 2014)

OCR (pseudo)	Compression index C_c		
	$C_s/C_c = 0.05$	$C_s/C_c = 0.10$	$C_s/C_c = 0.15$
1.5	0.406	0.400	0.394
2.0	0.531	0.514	0.499
2.5	0.650	0.618	0.588
3.0	0.763	0.710	0.664

3 Estimation of c_r from Observed Time–Settlement Plots

Barron (1948) presented the first exhaustive solution to the problem of consolidation of a soil cylinder encompassing a central vertical drain. Barron's classical theory enables one to solve the problem of radial consolidation under two conditions: (i) free strain, with the vertical surface stress being constant but with non-uniform surface displacements during the consolidation process, and (ii) equal strain, with non-uniform vertical surface stresses but with uniform surface displacements as

$$\frac{\partial u}{\partial t} = c_r \left[\left(\frac{\partial^2 u}{\partial r^2} \right) + \frac{1}{r} \frac{\partial u}{\partial r} \right] \quad (5)$$

where u = excess pore pressure at radial distance, r , from the centre of the unit cell at time, t , after an instantaneous increase of total vertical stress. The solution of Eq. (5) for monotonic loading with no smear and no well resistance is (Barron 1948)

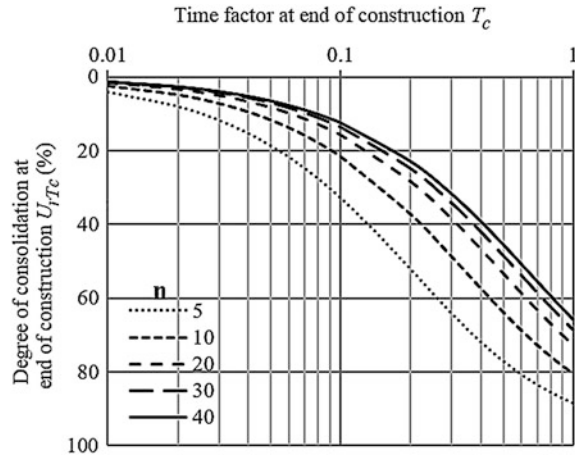
$$U_r = 1 - \exp \left(\frac{-8T_r}{m} \right) \quad (6)$$

$$m = \frac{n^2}{n^2 - 1} \ln(n) - \frac{3n^2 - 1}{4n^2} \quad (7)$$

where U_r = average degree of consolidation for radial flow, T_r = non-dimensional time factor for radial flow = $(c_r \times t)/d_e^2$, n = drain spacing ratio = d_e/d_w , d_w = equivalent diameter of drain = $2(a + b)/\pi$ (Hansbo 1979), a = width of band drain, b = thickness of band drain, and d_e = equivalent diameter of unit cell = 1.13 s and 1.05 s for drains installed in square and triangular patterns, respectively, where s is the centre-to-centre spacing of the drains.

The solution for equal strain, radial consolidation under construction or ramp loading with no smear is (Olson 1977)

Fig. 4 U_{rTc} versus T_c for different values of n (modified from Charan and Madhav 2015)



$$U_r = \frac{T_r - \frac{[1-\exp(-AT_r)]}{A}}{T_c} \quad (\text{for } T_r \leq T_c) \quad (8)$$

$$U_r = 1 - \frac{1}{AT_c} [\exp(AT_c) - 1] \exp(-AT_r) \quad (\text{for } T_r \geq T_c) \quad (9)$$

where T_c = non-dimensional time factor at the end of construction, and $A = 2/m$. Figure 4 shows the degree of consolidation, U_{rTc} , at the end of construction, estimated from either Eq. (8) or Eq. (9) by equating T_r and T_c , versus the time factor at the end of construction, T_c , for different values of n . As expected, U_{rTc} increases with T_c but decreases with n .

3.1 Based on Asaoka or Hyperbola Methods

From a given time-settlement plot, the final settlement, S_f , is estimated using either Asaoka's method or Hyperbola method. Knowing the settlement, S_{Tc} , at the end of construction, t_c , the degree of consolidation, U_{rTc} , can be determined by dividing S_{Tc} with S_f . The time factor, T_c , corresponding to the end of construction can thus be obtained from the estimated value of U_{rTc} and the known value of n (Fig. 4). The coefficient of radial consolidation is then estimated from the known values of t_c , T_c , and d_e as $c_r = (T_c \times d_e^2)/t_c$.

3.2 Based on Inflection Point Method

The prediction of final settlement by Asaoka's method is affected by the period of assessment after surcharge placement, and the time interval used for the assessment. For small time intervals, it becomes difficult to assess the best-fit line through the data points, whereas a larger time interval would require a long-term monitoring program to assess the best-fit line. The prediction of final settlement by the hyperbolic method is also affected by the period of assessment after surcharge placement. These difficulties can be overcome with the inflection point method by plotting time on a logarithmic scale versus the slope of the U - $\log T_r$ curve on a linear scale. The inflection point is the point at which the slope of the degree of radial consolidation, dU_r/dT_r , at any time factor, T_r , is maximum.

Figure 5 illustrates the variation of dU_r/dT_r with radial time factor, T_r , for different values of T_c at $n = 10$. It is observed that for a given value of n , the inflection point is independent of T_r for $T_c > 0.01$. The value of T_r corresponding to the inflection point, T_{inf} , can be used to determine c_r from observed time-settlement plots. Figure 6 shows that the radial time factor, T_{inf} , at the inflection point increases non-linearly with the drain spacing ratio, n . Figure 7 presents the variation of the maximum slope of the U - $\log T_r$ curve with the time factor at the end of construction, T_c , for different values of n . The maximum slope increases with T_c but decreases with n .

To apply the inflection point method, one must first obtain the settlements ($S_1, S_2, S_3, \dots, S_i, S_{i+1}, \dots$) at corresponding times ($t_1, t_2, t_3, \dots, t_i, t_{i+1}, \dots$) from the observed time-settlement plot, such that $t_{i+1} - t_i$ is constant. The final settlement, S_f , can be estimated using Asaoka or Hyperbola method. The degree of radial

Fig. 5 dU_r/dT_r versus T_r —effect of T_c for $n = 10$ (modified from Charan and Madhav 2016)

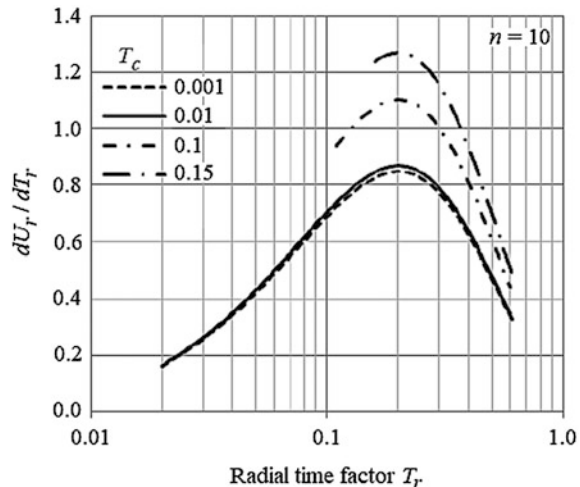


Fig. 6 Inflection time factor T_{inf} versus n (modified from Charan and Madhav 2016)

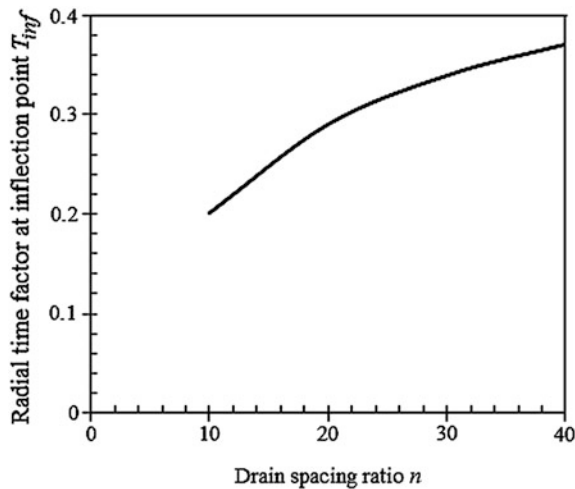
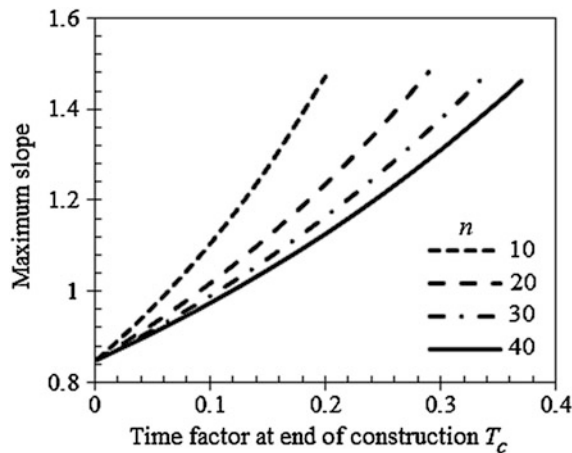


Fig. 7 Maximum slope versus T_c —effect of n (modified from Charan and Madhav 2016)



consolidation, U_r , estimated at each time interval, is plotted against time on log scale. The slope, $dU_r/d\log\Delta t$, of the degree of consolidation for a small interval of time, Δt , is then determined and plotted against time on log scale. Thereafter, a second-order polynomial curve is fitted to the data points. The time, t_{inf} , corresponding to the peak of the polynomial curve is the time at the inflection point, and the corresponding time factor, T_{inf} , can be obtained from Fig. 6 for the known value of n . Thus, the coefficient of radial consolidation can be calculated from the known values of t_{inf} , T_{inf} and d_e as $c_r = (T_{\text{inf}} \times d_e^2)/t_{\text{inf}}$.

3.3 Analysis of Case Histories

Table 2 summarizes the application of the aforesaid methods for prediction of c_r of PVD-improved ground from three case histories. The predicted values of c_r are compared with the corresponding values given by Hansbo (2005). The predicted c_r value based on Asaoka's method, for the Stockholm Arlanda airport site, is 18% lower than that stated by Hansbo (2005), whereas the estimated c_r value for the SBIA site is 20% higher (based on Asaoka's method) and 55% lower (based on inflection point method) than that of Hansbo (2005). The predicted c_r value for the Ska-Edeby site is 52% lower (based on Asaoka's method) and 4.5% higher (based on inflection point method) than that of Hansbo (2005). It should be noted that the values given by Hansbo (2005) are based on curve fitting to the complete time-settlement plot.

4 Estimation of Pile Shaft and Base Responses from Pile Load Test (PLT) Data

The ultimate capacity of a pile is typically estimated by considering the strengths and unit weights of the surrounding soil layers, overburden pressure, and other relevant parameters. However, the estimated pile capacity may differ from the measured capacity in the field because the actual values of soil strength/stiffness, lateral earth pressure coefficient, pile-soil interfacial friction angle, and geo-stratification, may differ from those used in design. Thus, estimation of axial capacity of a pile involves considerable uncertainty in the selection of appropriate geotechnical design parameters. Moreover, the design rules are not always consistent with the pile installation procedures/processes involved. This section presents an approach to estimate the ultimate pile shaft and base resistances and the initial pile shaft and base stiffnesses from PLT data.

4.1 Problem Definition and Formulation

Figure 8 depicts a single, rigid pile of diameter, d , and length, L , subjected to an axial compressive load, P . The pile-soil system is modelled in terms of a Winkler-type model with different non-linear responses for both the shaft and base resistances. The pile load, shaft resistance, and base resistance, versus displacement curves are all assumed to be hyperbolic (Fig. 9). The initial slopes of the curves in Figs. 9a–c represent the pile stiffness, k_p , shaft stiffness, k_t , and base stiffness, k_b , respectively. The ultimate capacity, shaft resistance, and base resistance of the pile, are denoted by P_{ult} , τ_{max} , and q_u , respectively.

Table 2 Estimation of c_r of PVD-improved ground based on Asaoka's method and inflection point method (adapted from Charan and Madhav 2015, 2016)

Case history	PVD dimensions (mm)	PVD spacing and installation pattern	n	p_v (kPa)	S_f (m)	t_c (days)	S_{Te} (m)	U_{Trc} (%)	T_c	$c_r (m^2/yr)$ Asaoka's method	t_{inf} (days)	T_{inf}	$c_r (m^2/yr)$ Inflection point method	$c_r (m^2/yr)$ Hansbo (2005)
Stockholm Arlanda Airport	$a = 100$ $b = 4$	$s = 0.9$ m (triangular)	14.27	400	2.80	171	2.2	78.6	1.12	2.13	—	—	—	2.6
Ska-Edeby	$a = 100$ $b = 4$	$s = 0.95$ m (triangular)	15.07	40	0.315	40	0.015	4.7	0.024	0.217	190	0.25	0.47	0.45
SBIA, Bangkok	$a = 100$ $b = 4$	$s = 1$ m (square)	17.07	80	1.51 (CSC) 1.78 (TSC)	220	0.86 (CSC) 1.08 (TSC)	56.9 (CSC) 60.6 (TSC)	0.53 (CSC) 0.60 (TSC)	1.12 (CSC) 1.27 (TSC)	315 (CSC) y300 (TSC)	0.27 (CSC) 0.42 (TSC)	0.40 (CSC) 0.42 (TSC)	0.93 (CSC and TSC)

Note a = width of PVD, b = thickness of PVD, s = centre-to-centre spacing of PVDs, n = drain spacing ratio = d_d/d_w , p_v = maximum value of applied total stress due to preloading, S_f = final settlement from Asaoka's method, t_c = time taken for preload construction, S_{Te} = settlement at end of preload construction, U_{Trc} = degree of radial consolidation at end of preload construction, T_c = time factor at end of preload construction, c_r = coefficient of radial consolidation, t_{inf} = time corresponding to inflection point, T_{inf} = time factor corresponding to inflection point, CSC = consolidation settlement curve, and TSC = total settlement curve

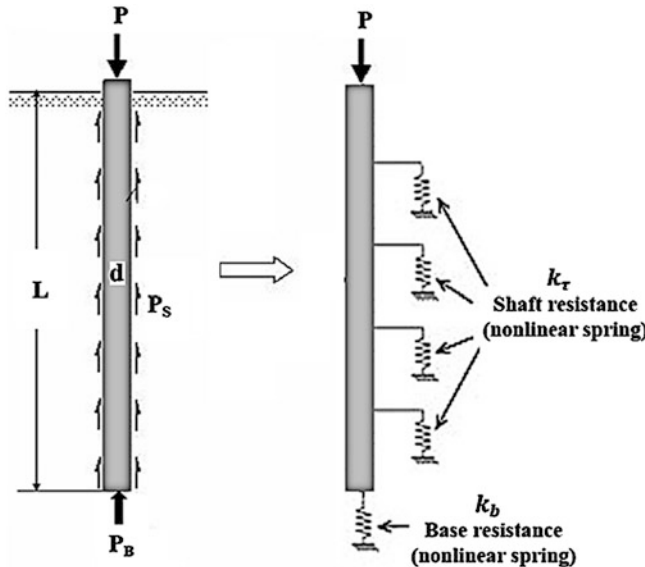


Fig. 8 Definition sketch of pile–soil system modelled using non-linear Winkler springs (Kiran et al. 2017)

The applied load, P , on the pile corresponding to a displacement, δ , can be expressed as the sum of the shaft and base resistances as (Kiran et al. 2017)

$$P = k_p \delta = \tau \pi d L + q \frac{\pi d^2}{4} \quad (10)$$

where $\tau = k_\tau \delta$ and $q = k_b \delta$. The ultimate capacity, P_{ult} , of the pile can be expressed as the sum of the ultimate shaft and base resistances as

$$P_{\text{ult}} = \tau_{\max} \pi d L + q_u \frac{\pi d^2}{4} \quad (11)$$

The loads, P_1 and P_2 , corresponding to displacements, δ_1 and δ_2 , are expressed as

$$P_1 = \frac{k_\tau \delta_1}{1 + \frac{k_\tau}{\tau_{\max}} \delta_1} \pi d L + \frac{k_b \delta_1}{1 + \frac{k_b}{q_u} \delta_1} \frac{\pi d^2}{4} \quad (12)$$

$$P_2 = \frac{k_\tau \delta_2}{1 + \frac{k_\tau}{\tau_{\max}} \delta_2} \pi d L + \frac{k_b \delta_2}{1 + \frac{k_b}{q_u} \delta_2} \frac{\pi d^2}{4} \quad (13)$$

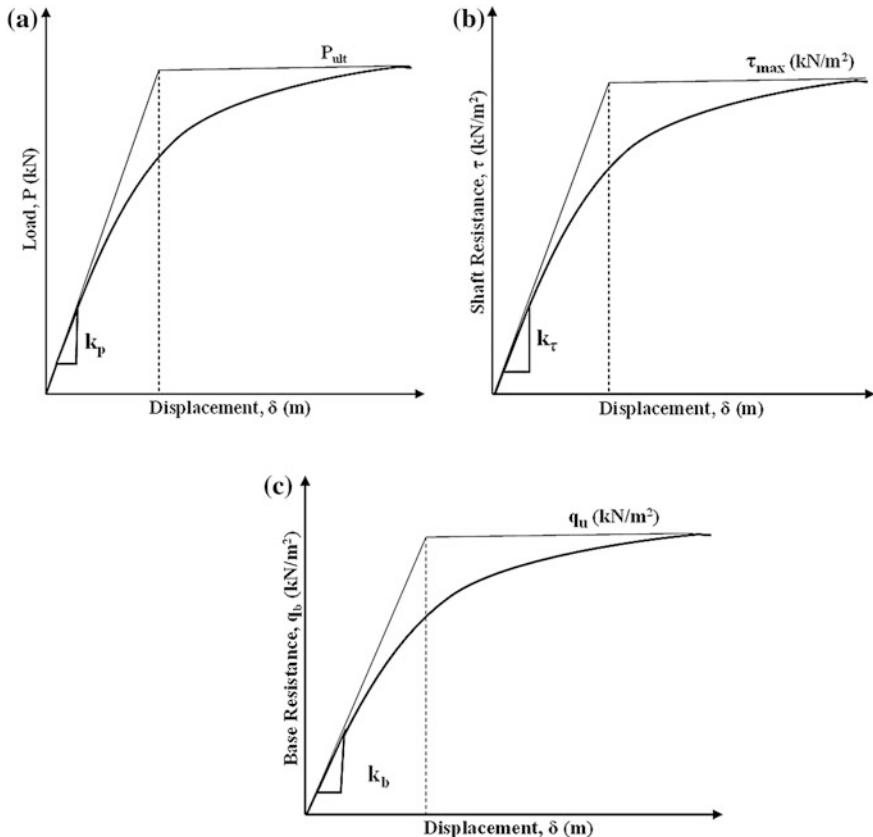


Fig. 9 **a** Typical pile load–displacement curve and assumed, **b** shaft, and **c** base resistance versus displacement curves (Kiran et al. 2017)

Normalizing Eqs. (10)–(13) with the cross-sectional area of the pile, A_b ($= \pi d^2/4$), and subsequently simplifying them, results in the following expressions

$$d_1 = C_1 k_\tau + C_2 \tau_{\max} \quad (14)$$

$$d_2 = C_3 k_\tau + C_4 \tau_{\max} \quad (15)$$

where

$$d_1 = \frac{P_1^*}{\delta_1} - \frac{k_p^* P_{\text{ult}}^*}{A_1} \quad (16)$$

$$d_2 = \frac{P_2^*}{\delta_2} - \frac{k_p^* P_{\text{ult}}^*}{A_2} \quad (17)$$

$$C_1 = \frac{4L}{d} \left\{ \frac{\tau_{\max}}{\tau_{\max} + k_{\tau} \delta_1} - \frac{P_{\text{ult}}^*}{A_1} + \frac{4L \tau_{\max}}{d A_1} \right\} \quad (18)$$

$$C_2 = - \frac{4L}{d A_1} k_{\text{p}}^* \quad (19)$$

$$C_3 = \frac{4L}{d} \left\{ \frac{\tau_{\max}}{\tau_{\max} + k_{\tau} \delta_2} - \frac{P_{\text{ult}}^*}{A_2} + \frac{4L \tau_{\max}}{d A_2} \right\} \quad (20)$$

$$C_4 = - \frac{4L}{d A_2} k_{\text{p}}^* \quad (21)$$

$$A_1 = \left(P_{\text{ult}}^* - \frac{4L}{d} \tau_{\max} \right) + \left(k_{\text{p}}^* - \frac{4L}{d} k_{\tau} \right) \delta_1 \quad (22)$$

$$A_2 = \left(P_{\text{ult}}^* - \frac{4L}{d} \tau_{\max} \right) + \left(k_{\text{p}}^* - \frac{4L}{d} k_{\tau} \right) \delta_2 \quad (23)$$

where $P_1^* = P_1/A_{\text{b}}$, $P_2^* = P_2/A_{\text{b}}$, $P_{\text{ult}}^* = P_{\text{ult}}/A_{\text{b}}$ and $k_{\text{p}}^* = k_{\text{p}}/A_{\text{b}}$. Equations (14) and (15) can be solved for the shaft stiffness, k_{τ} , of the pile as

$$k_{\tau} = \frac{C_4 d_1 - C_2 d_2}{C_1 C_4 - C_2 C_3} \quad (24)$$

The ultimate shaft resistance, τ_{\max} , of the pile can be estimated from the following expression

$$\tau_{\max} = \frac{\left\{ P_2^* A_2 - \left(\frac{k_{\text{p}}^*}{k_{\tau}} - \frac{4L}{d} \right) P_{\text{ult}}^* k_{\tau} \delta_2 \right\}}{\left\{ \frac{4L}{d} \left(A_2 - k_{\text{p}}^* \delta_2 + \frac{4L}{d} k_{\tau} \delta_2 \right) \right\}} \quad (25)$$

Equations (14) and (25) are solved iteratively to obtain the shaft stiffness, k_{τ} , base stiffness, k_{b} , ultimate shaft resistance, τ_{\max} , and ultimate base resistance, q_{u} , of the pile.

4.2 Comparison with PLT Data and IS:2911

The load-displacement plot for an initial PLT carried out on a pile for a major bridge at Dharaikuri, West Bengal, is shown in Fig. 10a. The length and diameter of the pile are 24 m and 1 m, respectively. Based on linear regression over the approximated linear portion of the curve, the ultimate pile capacity, P_{ult} , is 15.8 MN and the initial stiffness, k_{p} , of the pile is 1666 MN/m. The estimated shaft and base

Fig. 10 Comparison of measured and predicted pile load–displacement curves for PLT at **a** Dharaikuri, **b** Mahananda, and **c** Karala

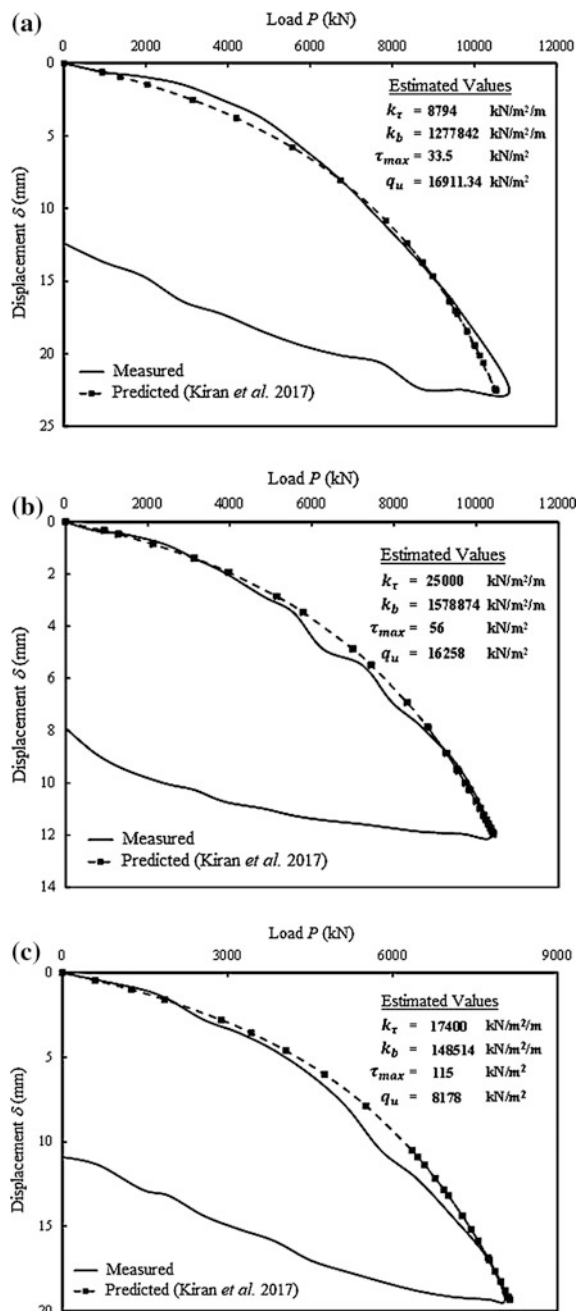


Table 3 Summary of ultimate shaft and base resistances estimated by Kiran et al. (2017) and IS:2911 for the test piles under study

PLT location	Average N value along pile shaft		N value at pile tip		Estimated values (Kiran et al. 2017)		τ_{\max} from IS:2911 (kPa)	q_u from IS:2911 (MPa)
	SPT N	Corrected N''	SPT N	Corrected N''	τ_{\max} (kPa)	q_u (MPa)	$N''/0.5$	$13 N''/L/B$
Dharaikuri	81	44	100	51	34	16.9	88	15.9
Karala	54	29	81	38	115	8.2	58	12.8
Mahananda A1	84	49	99	45	56	16.3	98	14.0
Mahananda A2	63	33	100	49	56	16.3	66	15.3

stiffness and resistance parameters, k_t , k_b , τ_{\max} , and q_u , are 8.8 MN/m^3 , 1277.8 MN/m^3 , 33.5 kPa , and 16.9 MPa , respectively. As expected, the predicted pile load–displacement curve, based on the aforesaid parameters, compares very well with the measured curve (Fig. 10a).

Figure 10b compares the measured and predicted load–displacement curves for PLT carried out at a bridge site across the river Mahananda. The length and diameter of the pile are 24 m and 1 m, respectively. The estimated ultimate capacity, P_{ult} , and initial stiffness, k_p , of the pile are 16.3 MN and 3125 MN/m , respectively, based on which the corresponding values of the parameters k_t , k_b , τ_{\max} , and q_u , contributing to the pile response are 25 MN/m^3 , 1578.9 MN/m^3 , 56 kPa , and 16.3 MPa , respectively. Similarly, Fig. 10c compares the measured and predicted load–displacement curves for PLT carried out at a bridge site across the river Karala. The length and diameter of the pile are 26 m and 1 m, respectively. The estimated ultimate capacity, P_{ult} , and initial stiffness, k_p , of the pile are 15 MN and 1428 MN/m , respectively. The parameters, k_t , k_b , τ_{\max} , and q_u , governing the pile response are computed to be 17.4 MN/m^3 , 148.5 MN/m^3 , 115 kPa , and 8.2 MPa , respectively. Table 3 summarizes the data collected from the three PLT sites and compares the estimated results with those obtained from the Indian standard code IS:2911 based on the standard penetration resistance, N . The predicted q_u values are comparable with those of IS:2911 but the τ_{\max} values are overestimated by IS:2911.

5 Concluding Remarks

Traditionally, the compression index, C_c , and the coefficient of radial consolidation, c_r , are estimated from the results of laboratory tests on relatively small soil samples, and subsequently extrapolated for the entire thickness of the soil layer in the field.

In this paper, alternate approaches to estimate these parameters by back-analysis of observed time-settlement plots of PVD-improved ground are presented. The relatively low C_c value for the weathered crust at the SBIA site is attributed to desiccation, which is quantified in terms of pseudo-OCR. The c_r values estimated using Asaoka's method and the inflection point method for the case histories analyzed in this paper (Stockholm Arlanda airport, Ska-Edeby and SBIA) are compared with those given by Hansbo (2005) based on curve fitting to the complete time-settlement plots. Finally, a non-linear, hyperbolic, Winkler-based approach to estimate the initial shaft and base stiffnesses and the ultimate shaft and base resistances of a pile from PLT data is presented. The predicted pile load-displacement curves compare well with the measured curves obtained from the Dharaikuri, Mahananda, and Karala test sites. It is now possible to estimate the shaft and base stiffnesses and resistances of a pile as installed, from an initial pile load test, so that they can be compared with the design values. A large PLT database can be built for all such cases to help revise some of the provisions of the Indian standard code for more efficient pile design.

Acknowledgements The contributions of V. Venkata Charan, G. Srikan, and K. Vijay Kiran, former graduate students at JNTU, Hyderabad, and B. Vidyaranya, Engineering Manager, L&T, Mumbai, are gratefully acknowledged.

References

Asaoka, A. (1978). Observational procedure of settlement prediction. *Soils and Foundations*, 18 (4), 87–101.

Balasubramaniam, A. S., Huang, M., Bolton, M., Oh, E. Y. N., Bergado, D. T., & Phienwej, N. (2007). Interpretation and analysis of test embankments in soft clays with and without ground improvement. *Geotechnical Engineering Journal of the SEAGS & AGSSEA*, 38(3), 235–254.

Baroni, M., & Almeida, M. S. S. (2017). Compressibility and stress history of very soft organic clays. In *Proceedings of the ICE-Geotechnical Engineering*. 170(2), 148–160.

Barron, R. A. (1948). Consolidation of fine-grained soils by drain wells. *Transactions of ASCE*, 113(1), 718–742.

Bjerrum, L. (1972). Embankments on soft ground. In *Proceedings of Specialty Conference on Performance of Earth and Earth-Supported Structures*. ASCE, Purdue University, pp. 1–54.

Charan, V. V. & Madhav, M. R. (2015). Method for estimation of coefficient of consolidation for radial flow from in-situ time-settlement plots. In *Proceedings of 50th Indian Geotechnical Conference (IGC)*. Pune, India, Paper No. 309, pp. 1–8.

Charan, V. V. & Madhav, M. R. (2016). Estimation of coefficient of consolidation with radial flow by inflection method from in-situ time-settlement plots. In *Proceedings of 4th International Conference on New Developments in Soil Mechanics and Geotechnical Engineering*. pp. 591–598. Nicosia, North Cyprus.

Cour, F. R. (1971). Inflection point method for computing c_v . *Journal of the Soil Mechanics and Foundations Division, ASCE*, 97(5), 827–831.

Hansbo, S. (1979). Consolidation of clay by band-shaped prefabricated drains. *Ground Engineering*, 12(5), 16–25.

Hansbo, S. (2005). Experience of consolidation process from test areas with and without vertical drains. In B. Indraratna & J. Chu (Eds.), *Ground Improvement—Case Histories* (Vol. 3, pp. 3–49). UK: Elsevier.

IS:2911 (Part 1/Sec 2) (1979). Code of practice for design and construction of pile foundations—bored cast in-situ piles. Bureau of Indian Standards, New Delhi, India.

Kiran, K. V., Madhav, M. R., & Vidyaranya, B. (2017). Estimation of shaft and base responses from pile load test. In *Proceedings of 7th Conference on Deep Foundation Technologies for Infrastructure Development in India (DFI-India 2017)*. Chennai, India (in press).

Kootahi, K., & Moradi, G. (2017). Evaluation of compression index of marine fine-grained soils by the use of index tests. *Marine Georesources and Geotechnology*, 35(4), 548–570.

Lee, C., Hong, S.-J., Kim, D., & Lee, W. (2015). Assessment of compression index of Busan and Incheon clays with sedimentation state. *Marine Georesources and Geotechnology*, 33(1), 23–32.

Madhav, M. R., & Srikanth, G. (2014). Estimation of compression index from in-situ time-settlement plots. In *Proceedings of Indian Geotechnical Conference (IGC)*. Kakinada, India, pp. 1485–1489.

Madhav, M. R., Charan, V. V., & Srikanth, G. (2015). Estimation of non-homogeneities in in-situ compressibility and consolidation parameters of soft ground. In *Proceedings of International Conference on Geotechnical Engineering (ICGE)*. Colombo, Sri Lanka, pp. 267–270.

McCabe, B., Sheil, B. B., Long, M. M., Buggy, F. J. & Farrell, E. R. (2014). Empirical correlations for the compression index of Irish soft soils. *Proceedings of the ICE—Geotechnical Engineering*, 167(6), 510–517.

Mesri, G., Feng, T. W., & Shahien, M. (1999). Coefficient of consolidation by inflection point method. *Journal of Geotechnical and Geoenvironmental Engineering*, ASCE, 125(8), 716–718.

Olson, R. E. (1977). Consolidation under time dependent loading. *Journal of Geotechnical Engineering Division*, ASCE, 103(1), 55–60.

Robinson, R. G. (1997a). Consolidation analysis by an inflection point method. *Geotechnique*, 47(1), 199–200.

Robinson, R. G. (1997b). Determination of radial coefficient of consolidation by the inflection point method. *Geotechnique*, 47(5), 1079–1081.

Rowe, P. W., & Barden, L. (1966). A new consolidation cell. *Geotechnique*, 16(2), 162–170.

Sinha, A. K., Havanagi, V. G., & Mathur, S. (2007). Inflection point method for predicting settlement of PVD improved soft clay under embankments. *Geotextiles and Geomembranes*, 25(6), 336–345.

Tiwari, B., & Ajmera, B. (2012). New correlation equations for compression index of remolded clays. *Journal of Geotechnical and Geoenvironmental Engineering*, ASCE, 138(6), 757–762.

Soil-Structure Interaction Analysis of Pile Foundations Subjected to Dynamic Loads

A. Boominathan, Ramon Varghese and Srilakshmi K. Nair

Abstract Soil-structure interaction (SSI) analysis has been recognized to be an essential step in the design of important structures. With the advent of powerful computers, SSI analysis capabilities have increased by leaps and bounds. This article presents recent research on dynamic SSI analysis of pile-supported structures using direct- and substructure-based numerical techniques. Dynamic response of pile foundations is a frequency-dependent problem. Experimental studies as well as numerical simulations, discussed in the article, reveal characteristics of single and group piles under dynamic loads. It was observed that dynamic lateral stiffness of piles is reduced significantly by cyclic loading. Peak displacement amplitude of pile-clay system, under dynamic loads, was observed to decrease significantly when consistency of clay changes from soft to medium stiff. Finite element analyses were able to simulate the frequency response of a single pile, with admissible accuracy. Flexible volume substructuring using the program SASSI 2010, for seismic response of pile foundations, is discussed with two case studies. The substructure-based SASSI analysis is found to produce results which are in agreement with analytical and experimental results. However, the choice of analyses tools for pile-supported structures is to be made after weighing the computational cost and complexity of numerical models.

Keywords SSI · Pile foundation · Seismic response · Substructuring method
SASSI

A. Boominathan (✉) · R. Varghese · S. K. Nair
Department of Civil Engineering, Indian Institute of Technology Madras,
Chennai, India
e-mail: boomi@iitm.ac.in

1 Introduction

Foundations are quite frequently required to transmit dynamic loads, some of which are transient like wind loads, earthquake, and blast loads, and some others are sustained for a long duration like dynamic loads from machines. When a foundation is subjected to dynamic loads, the dynamic interaction between the foundation and soil affects the response of the foundation, leading to soil–structure interaction (SSI).

Piles act as major vibration transmission paths in machine foundations. Complexity of an SSI analysis can depend on how accurately nonlinear behavior of pile and soil, as well as interfaces, is modeled. The stiffness of the pile in the lateral direction is very low in comparison with its vertical stiffness; hence, the lateral capacity/stiffness of the pile governs the design in most cases, where the lateral loads are dominant (Boominathan et al. 2015). Dynamic response of pile in lateral direction due to dynamic load at pile head would be influenced mostly by the top few meters of soil below ground. The primary objective of an equipment foundation design would be to meet the stipulated performance criteria. However, most often, intensity of the equipment excitation is not generally large enough to develop inelasticity in soil, and analysis methods which are easily applied to elastic media can be and have been employed with a fair degree of accuracy.

Seismic response of piles has received large attention in recent years. Analytical methods for Seismic Soil–Pile–Superstructure Interaction (SSPSI) are available at various levels of sophistication. A wide range of field and laboratory experiments has been reported in the literature and has been used to validate analytical methods. El-Marsafawi et al. (1992) evaluated theoretical analysis methods using comparisons with dynamic tests on pile groups. The conclusion that was arrived at was that linear theory gave reasonable estimate for stiffness of single and group piles. However, damping was overestimated by most analytical techniques. Static interaction factors in the analyses were observed to produce an approximate estimate of dynamic group stiffness in the low frequency range, for small pile groups. The stiffness may be underestimated in other cases.

The use of finite element and finite difference techniques for soil–structure interaction effects on seismic response of structures began in the 1970s. The ‘new age’ in SSI began with pioneering works by Dyatlovitsky (1966), Lysmer et al. (1981), Kausel et al. (1975), Luco (1974), Wolf (1985), and several others. Finite element modeling of an infinite soil medium requires special boundary conditions that would mimic an infinite medium. Several techniques have been used to simulate the semi-infinite halfspace in FE models. Kelvin elements that contain springs and dashpots connected in parallel can be attached to a boundary in order to simulate an infinite medium. These elements basically absorb energy that reaches the boundaries and account for radiation damping in the soil–foundation system. Dashpot and spring coefficients for transmitting boundary were developed by Novak and Mitwally (1988). Viscous elements proposed originally by Lysmer and Kuhlemeyer (1969) for shallow foundations are used when the loads in the problem

are purely dynamic in nature. Infinite elements can also be employed in FE analysis (Zienkiewicz et al. 1985; Chadwick et al. 1999; Kim and Yun 2000).

Recent studies on dynamic and seismic response of pile foundations using physical modeling and numerical methods are presented in this paper.

2 Numerical Methods for SSI Analysis

SSI analysis techniques with varying degree of sophistication have been proposed by researchers over the past decades. Simple analogs and empirical relations form the most basic analysis methods. For instance, shallow foundations can be approximated with lumped springs with an assumption that the foundation is supported by a homogeneous elastic, semi-infinite medium. Pile foundations can be approximated as beams with Winkler-type springs and dampers in which the configurations of the springs and dampers widely vary depending on researchers. The most comprehensive approach to solve the nonlinear SSI problem, however, will be finite element analysis or other discretization schemes like the finite difference method, boundary element method, or hybrid methods that involve a mix of these. The advantage of such methods is that complex structural configurations and soil layers can be explicitly modeled. Broadly, most numerical SSI methods fall under categories of direct and substructure methods.

The direct method SSI analysis accounts for the inertial and kinematic interaction simultaneously with the entire soil-structure system modeled as finite element model. The direct method can incorporate advanced nonlinear material and interface models for both soil and structure. Solution of equations of motion can be in frequency domain or time domain. However, nonlinear analysis involving step-by-step integration of the equation of motion is carried out only in time domain, and the method involves introduction of artificial boundaries at the sides of the soil, so as to minimize effect of wave reflections.

Substructure method divides the problem into substructures that can be conveniently analyzed using appropriate methods and then superposed to obtain the final response. The method assumes linear soil and structural behavior, and it can be solved in frequency domain. The fundamental idea is to perform the analysis of the interaction problem in several steps and to use the most amenable solution in each step, requiring as a result less computer time and storage than in the case of a complete analysis in a single step (Villaverde 2009). Substructure-based methods are in some cases over 100 times faster than direct methods. For example in programs such as SASSI, impedances of the substructure are evaluated first, considering layered soil. The complex impedances are then used in the dynamic analysis of structure-foundation model. However, linear analysis is the drawback of this technique. Current developments in computer programs include iterative nonlinear interpolation procedures, to enhance the linear substructure-based analysis (Ghiocel 2015).

The SASSI program has often been used for three-dimensional seismic soil-structure interaction (SSI) analysis of nuclear reactor buildings. The program can address wave propagation effects in unbounded soil media and account for non-linear soil using strain-compatible soil modulus and damping properties. Soil layers are formulated as horizontal viscoelastic layers in the program. Strain-compatible dynamic soil properties can be included in the analysis by employing computer codes such as SHAKE (Schnabel 1972).

3 Dynamic Response of Single and Group Piles

Dynamic lateral stiffness of piles is an important parameter in design of foundations for dynamic loads. Boominathan et al. (2015) compared the lateral dynamic response of a full-scale pile from experiment with a nonlinear finite element model. Forced vibration tests were carried on single piles in two different locations in India. 3D nonlinear FE analysis of single piles was carried out using ABAQUS. Elasto-plastic Drucker–Prager model was used for soil elements. The interface between soil and pile was modeled using the penalty contact method. Frequency response as well as lateral dynamic stiffness evaluated using criteria stipulated in IS 9716-1981, obtained from the FEA, was in good agreement with experimental values.

Dynamic tests on model single pile in clay have been reported by Ayothiraman and Boominathan (2006) and Boominathan and Ayothiraman (2007). A laboratory scale setup was fabricated to prevent reflection of stress waves from the boundary of the test tank (Fig. 1). The pile was excited at the free head using an electrodynamic exciter with frequencies ranging from 2 to 50 Hz. An equivalent 2D FEA model was then developed in the program PLAXIS. Mohr–coulomb elasto-plastic model with interface reduction factor for interfaces was employed in the model. The FE analysis was found to overestimate amplitudes near resonance. Estimated

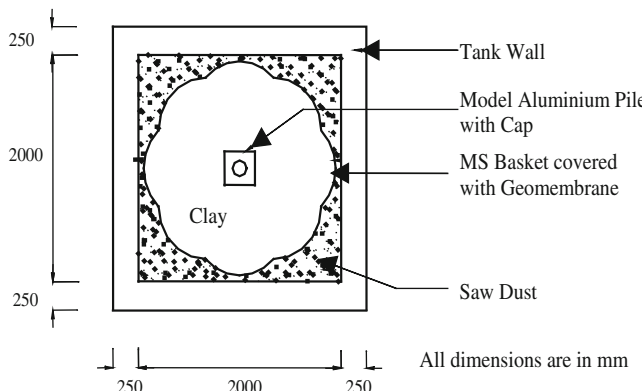


Fig. 1 Elastic halfspace simulation minimizing wave reflection (after Boominathan and Ayothiraman 2007)

Fig. 2 Experimental setup for cyclic test
(Chandrasekaran et al. 2010)



bending moment was found to be in good agreement with experimental result for short pile of length to diameter (l/d) ratio of 20. Although the model fairly predicts the location of maximum bending moment, a large difference in magnitude was observed for long piles with l/d ratio of 40.

Experimental study on the effect of cyclic lateral load on three different model pile groups was carried out by Chandrasekaran et al. (2010). A photograph of the cyclic testing experimental setup is presented in Fig. 2. The study concluded that cyclic loading reduces lateral capacity of pile groups significantly. A plot of average load per pile versus pile head deflection for a 3×3 pile group obtained from the experiment is presented in Fig. 3. A $p-y$ curve method-based numerical simulation was performed using the program GROUP, for the pile groups. It was observed that load-deflection curves obtained by using inbuilt p -multipliers based on static tests could not match experimental curves. However, dynamic p -multipliers obtained from experimental results when plugged into the program gave close match with experimental curves.

Boominathan et al. (2013) discussed case studies on dynamic response of piles in India. Full-scale steady state forced vibration test stipulated in IS 9716 was followed in the tests. A simulation of the forced vibration test was performed using FEA using ABAQUS. The finite element discretization of the pile-soil system is presented in Fig. 4. The lateral stiffness was then estimated using FEA with good agreement. The DYNA 5 program was used to estimate dynamic vertical and lateral stiffness of piles, which in turn were used in a FEA to determine natural frequencies of the fan foundation system.

Fig. 3 Load deflection behavior of 3×3 pile group at different numbers of cycles (Chandrasekaran et al. 2010)

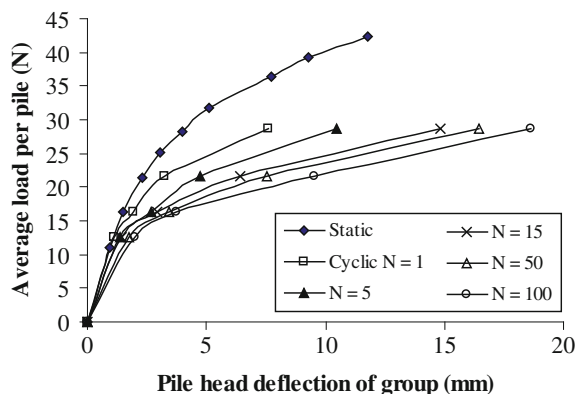
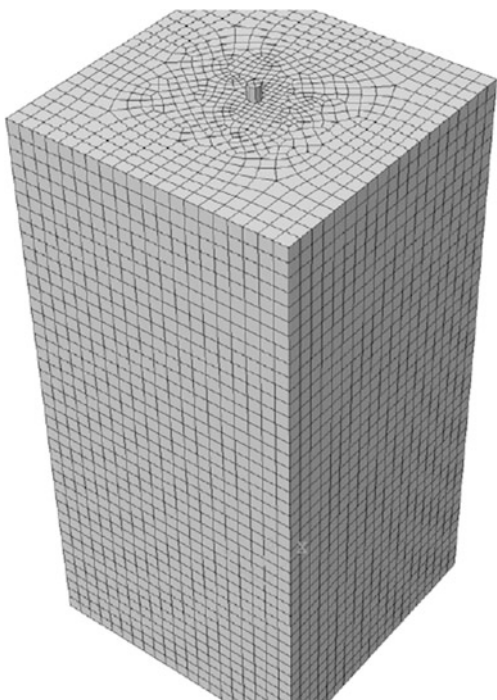


Fig. 4 Finite element model of the single pile–soil system (Boominathan et al. 2013)



Ayothiraman and Boominathan (2013) observed from laboratory model tests that the depth of fixity for single pile in clay increases under dynamic loads. An increase of the order of 1.5–2.7 times depth of fixity under static loads was observed. Nonlinear soil behavior was found to have influence in the low frequency to resonance region. The degree of nonlinearity was found to increase with increasing consistency of clay. Magnification in peak displacement amplitude of pile under dynamic loads was observed to reduce significantly as consistency of



Fig. 5 Experimental setup for lateral dynamic load test (Chandrasekaran et al. 2013)

clay changes from soft to medium stiff state. An empirical equation (Eq. 1) was proposed to estimate the ratio of effective pile length under dynamic and static lateral loads.

$$\frac{L_{fd}}{L_{fs}} \approx 5.91 \left(\frac{E_p}{G_s} \right)^{-0.12} \quad (1)$$

Chandrasekaran et al. (2013) presented results from 1g experimental model studies on various pile groups. The authors reported strong profound increase in nonlinear behavior of pile groups in clay with increasing magnitude of applied dynamic lateral load. Higher loads result in an increase in hysteretic damping of the soil induced by development of large-amplitude shear strain and excess pore pressure. Subramanian and Boominathan (2016) studied lateral dynamic response of model 1×2 batter pile group embedded in soft homogeneous clay. The natural frequency of batter piles was found to be higher than vertical piles by 34%, implying that they possess greater lateral stiffness. Bending strain in vertical piles was observed to be similar, but in the case of batter piles, the pile in compression carried less bending strain compared to the pile in tension. The study confirmed findings of earlier researchers that batter piles carried lesser bending strains. The reduction in bending strains was found to increase with batter angle (Fig. 5).

4 Seismic Response of Pile and Piled Raft Foundations

Seismic response of pile foundations has been receiving attention after observed pile damage and failure during major earthquakes including Alaska (March 27, 1964), Niigata (June 16, 1964), San Fernando (February 9, 1971), Mexico City (September 19, 1985), Kobe (January 17, 1995). Pile foundations are known to filter out low period components of ground motion, induce a rotational component at the head, and develop internal kinematic bending moment and shear forces, during earthquakes (Mylonakis et al. 1997). In addition to numerical methods, there exist simplified methods to estimate kinematic pile bending moments in layered soils (Dobry and O'Rourke 1983; Nikolaou et al. 2001; Mylonakis 2001). Importance of kinematic bending moments has been identified and stipulated by design codes such as Eurocode 8 and NEHRP 2000. Analysis of composite foundations like the piled raft requires three-dimensional numerical models to account for various interactions (Katzenbach and Choudhury 2013). Seismic response of piled rafts has been studied by researchers, using direct- and substructure-based numerical methods (Kumar et al. 2016; Mayoral et al. 2009; Nakaia et al. 2004).

Substructure-based seismic SSI analysis of pile foundations, using the program SASSI, is discussed for three different cases. The substructuring method is simple for cases in which the structure and the foundation interface boundary are on the surface of the foundation medium. Based on how rigorously the interaction at the soil and structure interface degrees of freedom is considered, substructuring methods can be classified into four types, namely rigid boundary method, the flexible boundary method, the flexible volume substructuring method (FVSM), and the substructure subtraction method.

In the FVSM technique, the soil–foundation system is partitioned into three substructures as presented in Fig. 6. The partitioning in SASSI program (Lysmer et al. 1981) is done in such a way that interaction occurs in all nodes of the embedded parts of the foundation, and the mass, damping, and stiffness matrices of the foundation are reduced by the corresponding properties of the excavated mass of soil. The substructuring in the SASSI code is formulated using the complex

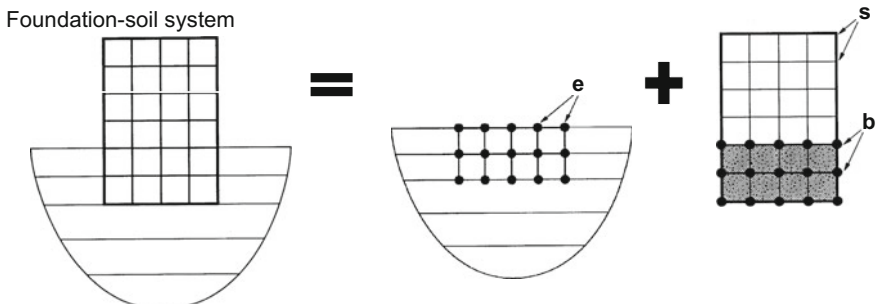


Fig. 6 Substructuring in FVSM (from Ostadan and Deng 2012)

response method and finite element technique. Soil model consists of viscoelastic horizontal layers resting on a viscoelastic halfspace. Horizontal layering and linear material model are inherent limitations of the SASSI methodology.

$$\begin{bmatrix} C_{ss} & C_{sb} \\ C_{bb} & (C_{bb} - C_{ee} + X_{ee}) \end{bmatrix} \begin{Bmatrix} u_s \\ u_e \end{Bmatrix} = \begin{Bmatrix} 0 \\ X_{ee}u'_e \end{Bmatrix} \quad (2)$$

The governing equation that is solved for seismic response problem is presented as Eq. 2, in which X_{ff} represents the impedance matrix of free field substructure, C represents complex frequency-dependent stiffness matrix, and subscripts s , b , and e refer to degrees of freedom for nodes at the superstructure, basement, and excavated soil, respectively.

4.1 Kinematic Seismic Response of Single and Group Piles

The kinematic interaction, in general, refers to the wave passage problem, the scattering of seismic rays by a rigid inclusion. In the present study, kinematic response of a free-headed single pile embedded in homogeneous elastic halfspace was carried out using SASSI 2010 program. The length to diameter ratio of pile was 20. Two cases of soil profiles, one with ratio of pile modulus to soil Young's modulus (E_p/E_s) of 1000 and another one with 10,000, were considered. A 3D model of the pile was developed using eight noded brick elements in SASSI 2010 as illustrated in Fig. 7. Near-field soil elements were not explicitly modeled. The

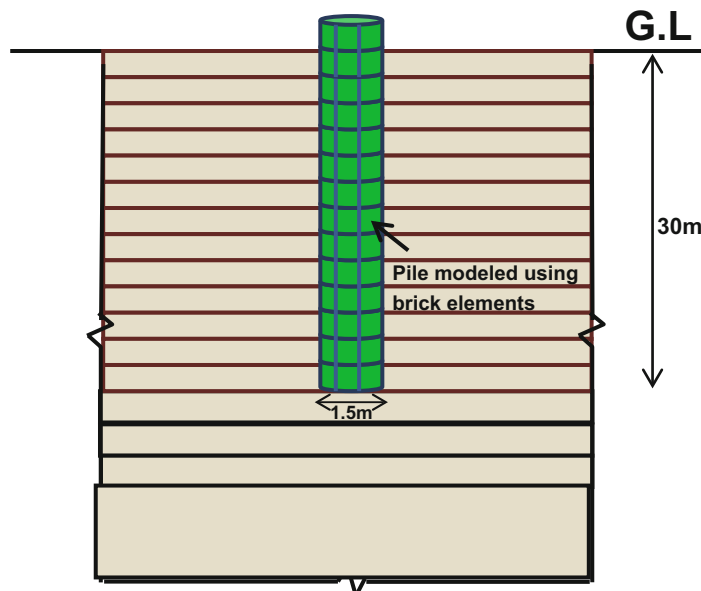


Fig. 7 Free-headed single pile in homogeneous elastic halfspace

control point was kept at the ground level, and the impedance calculation was done for 85 frequencies. The kinematic response factor for horizontal displacement, I_u along the direction of motion, defined as the ratio of pile head displacement (U_p), to free field displacement (U_{ff}), is then extracted from the program. The factor I_u is plotted against dimensionless frequency defined as in Eq. (4).

$$I_u = \frac{|U_p|}{U_{ff}} \quad (3)$$

$$a_o = \omega d / V_s \quad (4)$$

The kinematic response factors for the single proposed by Fan et al. (1991) based on the solution to three-dimensional boundary value problems by Kaynia and Kausel (1982) is also presented in Fig. 8. It can be easily noticed from Fig. 8 that the SASSI-based kinematic response factor matches well with that proposed by Fan et al. (1991) for soft soil site conditions ($E_p/E_s = 10,000$) but is slightly higher than Fan et al. (1991) factors for stiff soil site conditions ($E_p/E_s = 1000$).

Another study was done for fixed head pile group embedded in homogeneous soil and subjected to vertically propagating waves. A 2×2 pile group (Fig. 9) was analyzed in SASSI using FVSM technique, and results are compared with those reported by Fan et al. (1991). The soil profile with the ratio of elastic pile modulus to soil elastic modulus (E_p/E_s) as 10,000 and ratio of pile spacing to diameter as 5 was selected. The pile group as well as near-field soil is modeled using 3D eight noded brick elements as shown in Fig. 10. Near-field soil elements were modeled to simulate pile-soil-pile interactions. In this case, pile head fixity was modeled by applying rotational restraint and rigid links connections at the top surface of piles. Control point was set at the ground level. Analysis was performed for a set of 40 frequencies.

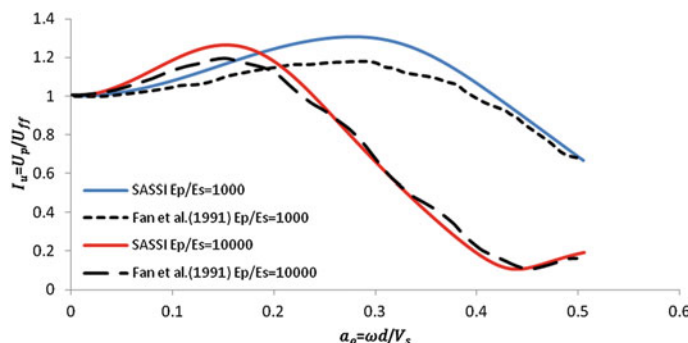
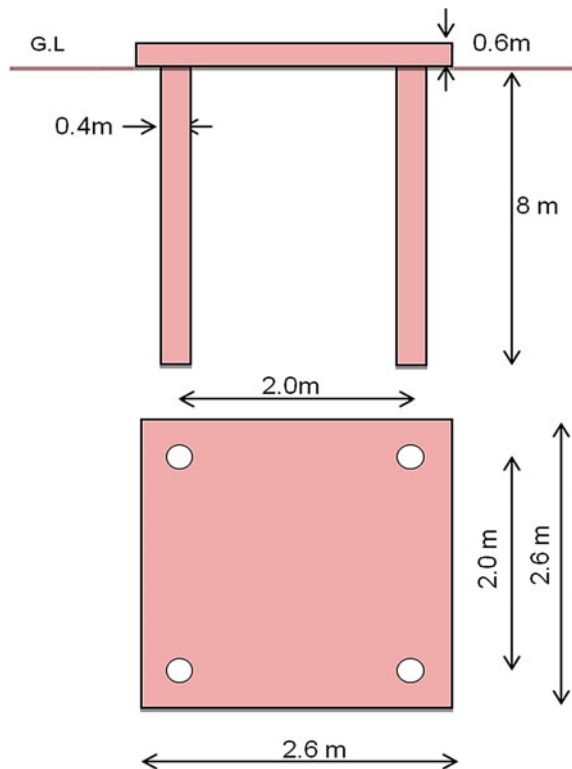


Fig. 8 Kinematic response factor I_u versus dimensionless frequency

Fig. 9 Schematic diagram showing details of pile group



Output was obtained as ratio of translation at the pile cap to the free field displacement which is the kinematic response factor I_u . Figure 11 shows the comparison of results obtained from SASSI analysis with Fan et al. (1991). It can be observed from Fig. 9 that the shape of kinematic factor curve obtained from SASSI 2010 is similar to that of obtained from Fan et al. (1991) but the values are matching only at low frequencies.

4.2 Seismic Response of a Piled Raft Foundation in Soft Clay

Seismic response of piled raft (PR) clay system was studied by Banerjee (2009) by conducting centrifuge shake table tests. In the present study, a three-dimensional SASSI model is developed for a piled raft with the intention of simulating the centrifuge experiment. Prototype dimensions of the raft are 12.5 m \times 7.5 m \times 0.5 m, with four piles of diameter 0.9 m and length of 13 m as shown in Fig. 12a. Flexural rigidity of the piles in prototype scale is 10308351 kNm². Vertical load of

Fig. 10 Finite element mesh showing piles and near-field soil elements modeled using brick elements

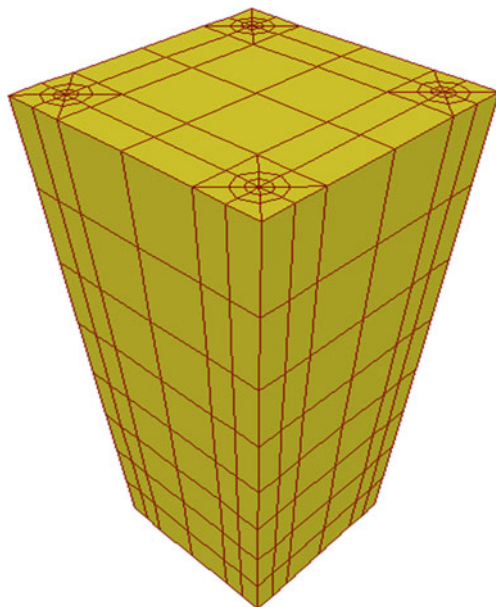
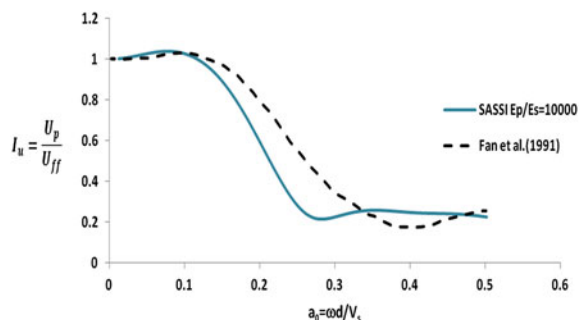


Fig. 11 Variation of kinematic response factor with dimensionless frequency for pile group



605 tonnes was applied on the top of raft using steel plates to simulate load from steel plates placed over the raft in the experiment. Soil used in the experiment was homogeneous soft kaolin clay that had a bulk unit weight of 16 kN/m³, liquid limit of 80%, plastic limit of 35%, and water content of 66% (Banerjee et al. 2014). Increase in low strain shear modulus, G_{\max} , was assumed to follow Eq. (5), proposed by Banerjee (2009).

$$G_{\max} = 2060p^{0.653} \quad (5)$$

There are several methods of modeling piles using finite elements for SASSI. Volume elements like brick elements can be used to model the entire volume of pile. Other techniques include beam elements, central beam and rigid links, and

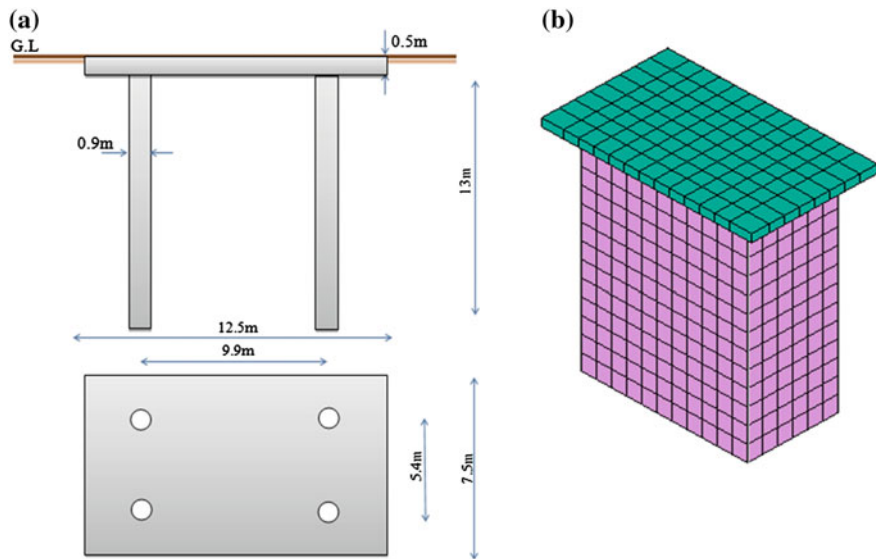


Fig. 12 **a** Details of the piled raft system and **b** finite element mesh showing raft and *inter-pile* elements

special *inter-pile* elements (Ostadian and Deng 2012). In this present study, piles are modeled as *inter-pile* elements in SASSI 2010. This pile model consists of a beam element that is assigned flexural rigidity of the pile and volume elements around the beam that models its volume. The finite element mesh of the model is presented in Fig. 12b.

The input motion applied to the soil layer below the foundation was the same as that used in the experiment. The time history with peak acceleration of 0.053g, used in the experiment, was applied as input motion. Time history and Fourier spectra of the input motion are presented in Fig. 13. To compensate for the linear soil model, equivalent linear ground response analysis was performed using the program SHAKE 2010 using modulus reduction and damping curves reported by Banerjee (2009). The strain-compatible modulus and damping obtained from SHAKE 2010 are then used as input for the SSI analysis.

Response spectrum and Fourier spectrum obtained from the simulation and experiments are presented in Fig. 14a, b, respectively. The simulation was found to reproduce all dominating peaks in the spectra. The highest spectral ordinate was observed at 1.46 s, in the experiment, and the simulation results follow the peak very closely. Low period response is found to be amplified by the simulation at around 0.5 s. The peak acceleration value recorded at the top of raft was 0.57 m/s^2 in the simulation, compared to a peak acceleration of 0.69 m/s^2 observed from experiment. Amplification in Fourier amplitude of 24% and a de-amplification of 47% were observed at 4.5 and 2.1 s, respectively.

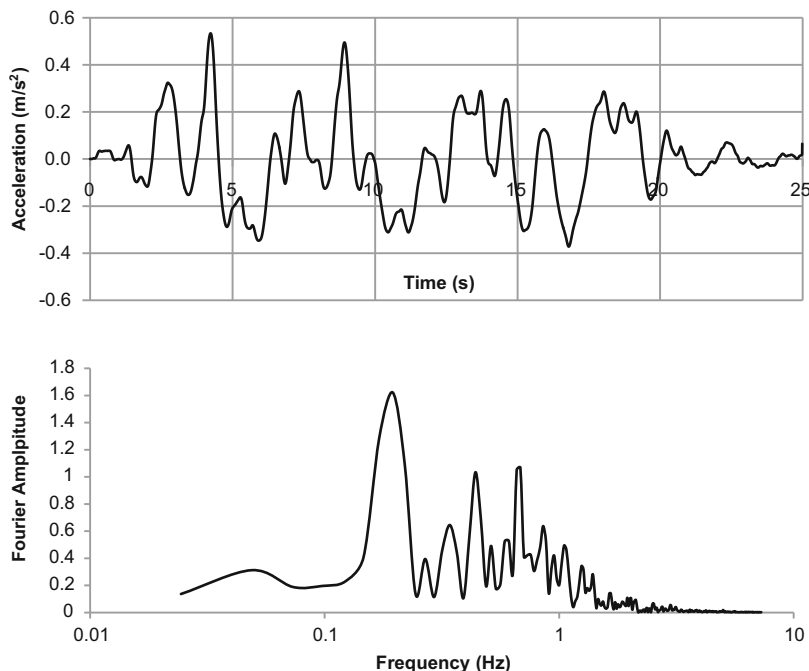


Fig. 13 Time history and Fourier spectrum of input motion

5 Conclusions

Soil–pile structure interaction is a complicated phenomenon with group interaction playing a profound role. Dynamic response of pile groups differs from static response and needs to be addressed as a frequency-dependent problem. Effective pile length and location of bending moment have been found to vary when loading becomes dynamic in nature. Static p – y curves were found to be inadequate to reproduce load deflection and bending moment curves after dynamic loading. Nonlinearity of response of pile groups in clay is found to increase with magnitude of load and consistency of clay. Batter piles were found to exhibit higher natural frequencies and lateral stiffness compared to their vertical counterparts.

Numerical methods of varying complexity and rigorousness are available for dynamic SSI analysis of pile foundations. Numerical simulation of dynamic pile–soil response, using finite element method, has been found to reproduce response curves in many cases.

Seismic pile–soil–pile interaction is also known to be a frequency-dependent phenomenon. The kinematic response factor evaluated using SASSI was found to match well with analytical solutions, for the single pile case. Kinematic interaction factor for the 2×2 group was found to vary with analytical solution at higher frequencies. A simulation of a centrifuge test on a clay-piled raft system was found

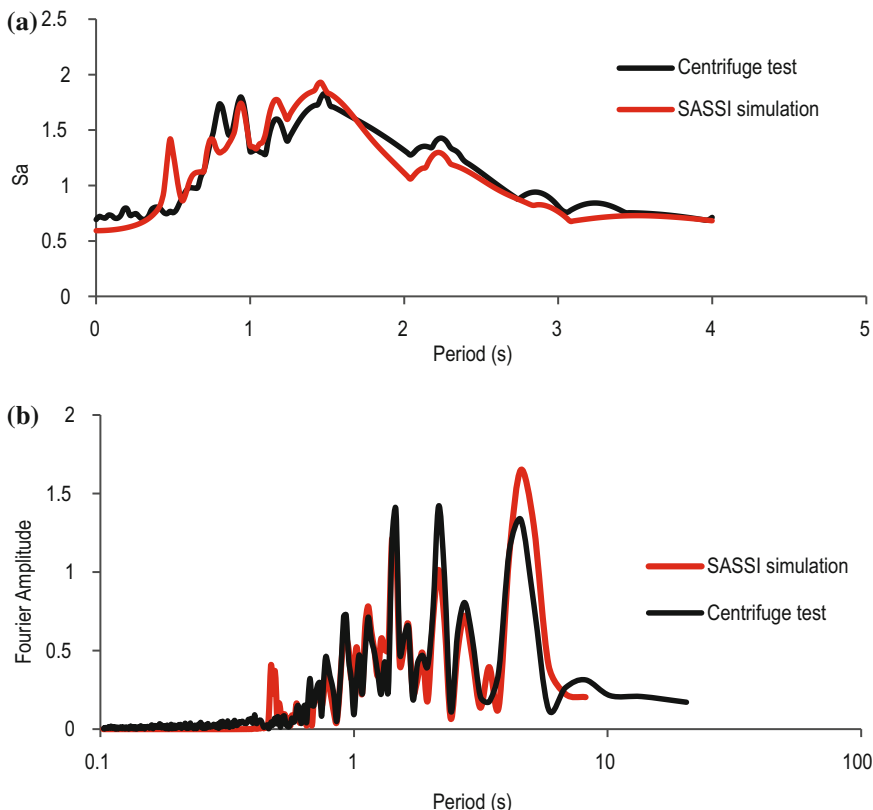


Fig. 14 **a** Response spectrum and **b** Fourier spectrum obtained at top of raft

to match well with experimental results. Substructure-based numerical methods can be employed to estimate both foundation input motions after kinematic interaction and structural response due to seismic SSI.

Acknowledgements The authors are thankful to Dr. Subhadeep Banerjee, Indian Institute of Technology Madras, for providing centrifuge shake table data on piled raft foundations and valuable comments.

References

Ayothiraman, R., & Boominathan, A. (2006). Observed and predicted dynamic lateral response of single pile in clay. *Soil and Rock Behaviour and Modelling*, 150, 367–374, ASCE Geotechnical Special Publication.

Ayothiraman, R., & Boominathan, A. (2013). Depth of fixity of piles in clay under dynamic lateral load. *Geotechnical and Geological Engineering*, 31, 447–461.

Banerjee, S. (2009). Centrifuge and numerical modelling of soft clay-pile-raft foundations subjected to seismic shaking. Doctoral dissertation, NUS, Singapore.

Banerjee, S., Goh, S. H., & Lee, F. H. (2014). Earthquake induced bending moment in fixed head piles in soft clay. *Géotechnique*, 64(6), 431–446.

Boominathan, A., & Ayothiraman, R. (2007). Measurement and analysis of horizontal vibration response of pile foundations. *Shock and Vibration*, 14(2), 89–106.

Boominathan, A., Kumar, K., & Zhussupbekov, A. (2013). Dynamic responses of piles—case studies in India. In *Proceedings of 7th International Conference on Case Histories in Geotechnical Engineering*, Chicago, USA. Paper No. OSP-1, April 29–May 4.

Boominathan, A., Krishna Kumar, S., & Subramanian, R. M. (2015). Lateral dynamic response and the effect of weak zone on the stiffness of full scale single piles. *Indian Geotechnical Journal*, 45(1), 43–50.

Chadwick, E., Bettess, P., & Langhrouche, O. (1999). Diffraction of short waves modelled using new mapped wave envelop finite and infinite elements. *International Journal of Numerical Methods in Engineering*, 45(3), 335–354.

Chandrasekaran, S. S., Boominathan, A., & Dodagoudar, G. R. (2010). Experimental investigations on the behavior of pile groups in clay under lateral cyclic loading. *Geotechnical and Geological Engineering*, 28, 603–617.

Chandrasekaran, S. S., Boominathan, A., & Dodagoudar, G. R. (2013). Dynamic response of laterally loaded pile groups in clay. *Journal of Earthquake Engineering*, 17(1), 33–53.

Dobry, R., & O'rourke, M. J. (1983). Discussion of "Seismic Response Of End-bearing Piles" by Raul Flores-Berrones and Robert V. Whitman (April, 1982). *Journal of Geotechnical Engineering*, 109(5), 778–781.

Dyatlovitsky, L. (1966). The dynamic elasticity problem solution using the finite difference method. *Applied Mechanics*, 2(10), 118–123.

El-Marsafawi, H., Han, Y. C., & Novak, M. (1992). Dynamic experiments on two pile groups. *Journal of Geotechnical Engineering, ASCE*, 118(4), 576–592.

Fan, K., Gazetas, G., Kaynia, A., Kausel, E., & Ahmed, S. (1991). Kinematic seismic response of single piles and pile groups. *Journal of Geotechnical Engineering*, 117(12), 1860–1879.

Ghiocel Predictive Technologies, Inc. (2015). ACS SASSI-An advanced computational software for 3D dynamic analyses including SSI effects, ACS SASSI version 3 manuals. March 31.

IS 9716. (2003). Guide for lateral dynamic load test on piles. Bureau of Indian Standards, New Delhi.

Kausel, E., Roesset, J. M., & Waas, G. (1975). Dynamic analysis of footings on layered media. *Journal of Engineering Mechanics, ASCE*, 101, 679–693.

Kaynia, A. M., & Kausel, E. (1982). Dynamic stiffnesses and seismic response of pile groups. Research report, Department of Civil Engineering, MIT, Cambridge, Massachusetts.

Katzenbach, K., & Choudhury, D. (2013). ISSMGE combined pile-raft foundation guideline. Deep foundations, International Society for Mechanics and Geotechnical Engineering, London, 1–28.

Kim, D., & Yun, C.-B. (2000). Time-domain soil structure interaction analysis in two-dimensional medium based on analytical frequency-dependent infinite elements. *International Journal of Numerical Methods in Engineering*, 47(7), 1241–1261.

Kumar, A., Choudhury, D., & Katzenbach, R.: Effect of earthquake on combined pile-raft foundation. *International Journal of Geomechanics, ASCE*, 16(5) (2016).

Luco, J. E. (1974). Impedance functions for a rigid foundation on a layered medium. *Nuclear Engineering and Design*, 31, 204–217.

Lysmer, J., & Kuhlemeyer, R. L. (1969). Finite dynamic model for infinite media. *Journal of Engineering Mechanics Division*, 95(4), 859–878.

Lysmer, J., Tabatabaei-Raissi, M., Tajirian, F., Vahdani, S., & Ostadan, F. (1981). SASSI: A system for analysis of soil-structure interaction.

Mayoral, J. M., Alberto, Y., Mendoza, M. J., & Romo, M. P. (2009). Seismic response of an urban bridge support system in soft clay. *Soil Dynamics and Earthquake Engineering*, 29(5), 925–938.

Mylonakis, G. (2001). Simplified model for seismic pile bending at soil layer interfaces. *Soils and Foundations*, 41(4), 47–58.

Mylonakis, G., Nikolaou, A., & Gazetas, G. (1997). Soil-pile-bridge seismic interaction: Kinematic and inertial effects. Part I: Soft soil. *Earthquake Engineering and Structural Dynamics*, 26(3), 337–359.

Nakaia, S., Katoa, H., Ishidaa, R., Manob, H., & Ngatac, M. (2004). Load bearing mechanism of piled raft foundation during earthquake. In *Proceedings of 3rd UNJR Workshop on Soil-Structure Interaction*, March 29–30.

Nikolaou, S., Mylonakis, G., Gazetas, G., & Tazoh, T. (2001). Kinematic pile bending during earthquakes: Analysis and field measurements. *Geotechnique*, 51(5), 425–440.

Novak, M., & Mitwally, H. (1988). Transmitting boundary for axisymmetrical dilation problems. *Journal of Engineering Mechanics*, 114 (1).

Ostadian, F., & Deng, N. (2012). SASSI 2010, User's Manual. Geotechnical Engineering Division, Civil Engineering Department, University of California, Berkeley.

Schnabel, P. B. (1972). SHAKE a computer program for earthquake response analysis of horizontally layered sites. EERC Report, University of California, Berkeley.

Subramanian, R. M., & Boominathan, A. (2016). Dynamic experimental studies on lateral behaviour of batter piles in soft clay. *International Journal of Geotechnical Engineering*, 10 (4), 317–327.

Villaverde, R. (2009). Fundamental concepts of earthquake engineering. CRC Press, January 16.

Wolf, J. P. (1985). Dynamic soil structure interaction. In Prentice-Hall International Series in civil engineering and engineering mechanics.

Zienkiewicz, O. C., Bando, K., Bettess, P., Emson, C., & Chiam, T. C. (1985). Mapped finite element methods for exterior wave problems. *International Journal of Numerical Methods in Engineering*, 21(7), 1229–1251.

Cascaded Recycle of Waste Tires—Some Novel Approaches Toward Sustainable Geo-Construction and Climate Change Adaptation

Hemanta Hazarika, Hidetoshi Yokota, Shigeki Endo
and Tota Kinoshita

Abstract For sustainable development, it is necessary that various stakeholders, whose needs match, come together and make accelerated efforts toward realizing a recycle economy through active promotion of recycling of industrial by-products or waste. This paper describes some of the research on the effective use of by-products/wastes of other industries in the field of geotechnical engineering with special emphasis on geo-disaster reduction. Recycling of waste tires and disaster mitigation in the context of Japanese experiences are focused here, and various disaster reduction techniques developed in Japan using tire-derived materials are described.

Keywords Cascaded recycle · Earthquake · Horizontal inclusion
Liquefaction · Vertical inclusion · Waste tires

1 Introduction

Recently, concerns are growing regarding climate change-induced disasters associated with global warming, and the approaches and efforts to reduce emissions of CO₂ have been implemented through the collaboration of industry, government, and academia. The recycling of the waste discharged by either human or industrial activities as geomaterials is one of these approaches. However, rather than mere recycling, *Cascaded Recycling* of such products is encouraged these days as it leads to substantial reduction of CO₂ emission to the atmosphere. Figure 1 explains the concept of cascaded recycle in the case of waste tire recycling. In Japan, the volume of waste tires generated in the year 2014 has been increased by 2 million from the previous year. The trend of recycling efforts during 2009–2015

H. Hazarika (✉)

Kyushu University, Fukuoka, Japan
e-mail: hazarika@civil.kyushu-u.ac.jp

H. Yokota · S. Endo · T. Kinoshita
Bridgestone Corporation, Tokyo, Japan

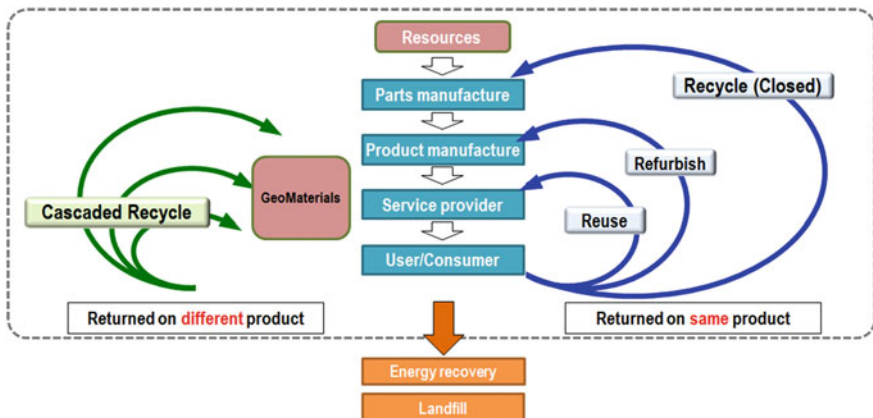


Fig. 1 Concept of cascaded recycling of waste tires

(Japan Automobile Tyre Manufacturers Association 2016) shows that at least 59% of the scrap tires were used for energy recovery (thermal recycling). The rests were reused either through returning on the same product (material recycling) or through returning on different products (cascaded recycling).

Global statistics on waste tires also presents a similar scenario. About 1 billion waste tires are generated every year in different parts of the world. Most of those waste tires are either burnt to produce energy or landfilled. Thermal recycling, however, is harmful to the environment because it releases more CO₂ compared to the other efforts of recycling, such as material recycling and cascaded recycling. In order to encourage the recycling of waste tires that minimize the CO₂ release, utilization of such industrial by-product in cascaded form (returning on different product) is gaining attention in recent years. It is, therefore, necessary to shift the share of recycling from thermal to cascaded recycling. When recycled in cascaded form they can be called tire-derived geomaterials (TDGMs). Besides its low-carbon-released characteristics when used as geomaterials, the other advantageous material characteristics of TDGM are as follows: lightweight, excellent vibration absorption capacity, and high permeability. In addition, these materials are non-dilatant in nature unlike other granular geomaterials (Hazarika 2013). Owing to these characteristics, they can replace other conventional materials (such as gravel), in applications such as drainage, leachate, reinforcement, and so on.

On the other hand, in recent years, the world has seen large-scale earthquake-induced hazards or climate change-related hazards. Especially, in Japan, such natural hazards are too frequent in recent years. Also, in most of the developing countries, where the infrastructure development is still in infancy, adequate and cost-effective disaster mitigation efforts are urgently needed. The key issues in most of the developing countries are the balance between the cost and the increased burden to environment while undertaking any infrastructural projects.

In this paper, recycling of waste tires and disaster mitigation in the context of Japanese experiences were focused, and few geo-disaster reduction techniques developed in Japan using TDGM are described.

2 Brief Review of Research on TDGM in Geotechnical Applications

For the past one decade, research related to the utilization of tires in construction projects has been gaining momentum. Due to their advantageous physical and mechanical characteristics, TDGM either in the form of shreds, chips, or crumbs have been used as fill material for embankments (Humphrey 2008), as fill material behind retaining walls and abutments (Garcia et al. 2012; Hartman et al. 2013; Reddy and Krishna 2015), as base isolation for buildings (Tsang 2008), as liquefaction prevention material, and as lining in tunnel construction (Kim and Konagai 2001). The environmental aspects of such materials were thoroughly reviewed by Edil (2008).

On the other hand, the Japanese research covers a wide range of waste tire utilization. Few examples of those include the following: use of whole tires or in conjunction with other granular materials or use of tire chips and tire shreds (Hazarika et al. 2012c; Niiya et al. 2012; Karmokar et al. 2006; Kikuchi et al. 2008). Also, tire chips mixed with cement-treated clay was used as a sealing material at a waste disposal sites in Tokyo Bay (Mitarai et al. 2006). Use of tire chips as a material to prevent liquefaction in soil also was experimented by Yasuhara et al. (2010) and Uchimura et al. (2008). In the following section, few innovative techniques toward geohazards mitigation using TDGM in the context of Japanese scenario have been briefly introduced followed by the verification of those techniques in the next sections.

3 Techniques of Geohazards Mitigations Using TDGM

3.1 *Protection of Quay Wall During Earthquake (Vertical Inclusion)*

During the 1995 Hyogo-ken Nanbu Earthquake, many waterfront retaining walls were reported to be tilted in the seaward direction, while soil liquefaction was also observed in the backfill soil (Inagaki et al. 1996). A technique to protect retaining wall from such damage was developed and validated through experimental investigations, which were reported in Hazarika et al. (2006, 2008, 2010, 2012a, b, c, d). The technique, named Structural Stability And Flexibility during Earthquakes using Tyres (SAFETY), consists of a compressible inclusion made of tire chips, which

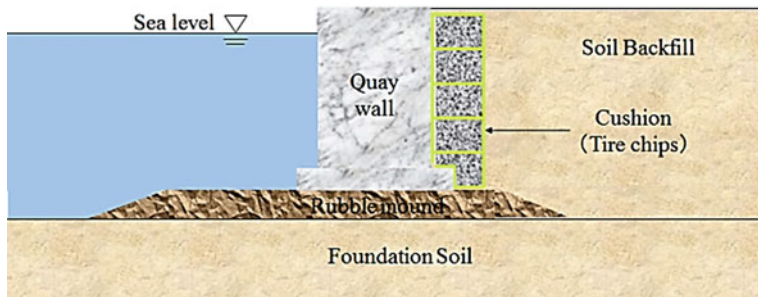


Fig. 2 Quay wall with tire chips cushion as backfill (Hazarika et al. 2008)

was placed as a cushion behind the retaining wall as can be seen in Fig. 2. The purpose of the installation of such cushion behind the quay wall was to absorb the impact due to an earthquake and at the same time restricting the displacement of structures.

However, in order to optimize the amount of tire chips to be used in making the cushion, some percentage of sand or gravel can be mixed with tire chips by enclosing the mixture inside geotextile bags and then placing those behind the structure. This kind of mixing and confining technique saves the amount of tire chips/tire shreds to be used in a project. At the same time, it also reduces any unwanted vertical settlement due to vertical load coming from the structure on the backfill, since tire-derived materials have high compressibility. In addition, mixing and confining of the materials before placing makes the execution easier and faster.

In the backfills of waterfront retaining structures, which are susceptible to liquefaction, vertical drain installation in the backfill was proposed (Hazarika 2012; Hazarika et al. 2012d). Vertical reinforcing inclusion, thus, refers to the cushion and vertical drains which are made of highly permeable tire chips and are placed vertically as part of backfill material. The vertical drains can quickly dissipate the generated excess pore water pressure during earthquake. The schematic diagram of SAFETY technique is shown in Fig. 3. The drains can also be made of mixtures of tire chips and gravel in an optimum mixing percentage, as both the materials possess almost identical permeability.

3.2 Protection of Seawall During Tsunami

Many seawalls were damaged during 2011 off the Pacific Coast of Tohoku Earthquake and resulting tsunami. Examples of failures of many seawalls and breakwaters during that disaster are reported in Hazarika et al. (2012a, b). Any countermeasures, to protect seawalls from future damage during tsunami, require the knowledge of damage mechanism of seawalls due to tsunami. When tsunami overflows the seawall it collides with the seawall foundation, and due to rapid

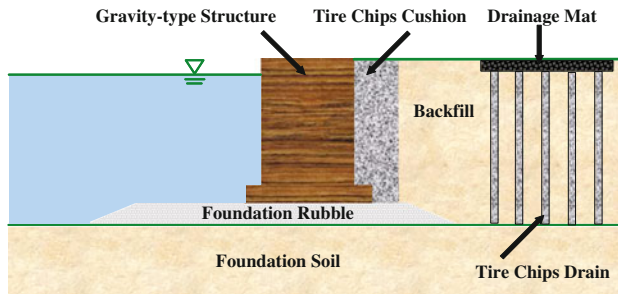
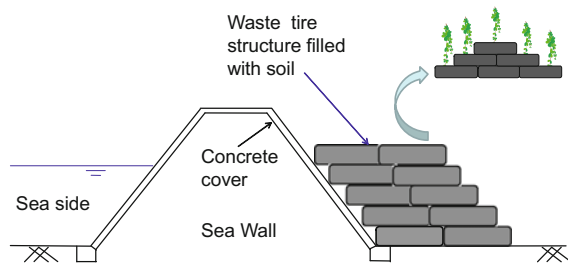


Fig. 3 Vertical inclusion technique (Hazarika 2012)

Fig. 4 Protection of seawall by using whole tires (Hazarika and Fukumoto 2016)

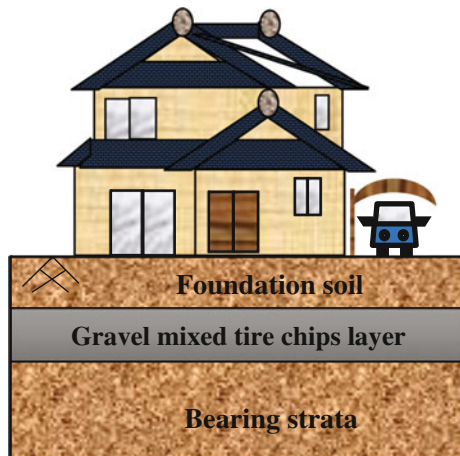


overflow, the soils of the seawall embankment are scoured due to the impact of water resulting in outflow of the concrete panel covering of embankment. On the other hand, when the tsunami returns to sea, the force of backwash hits the seawall with a huge impact force, and as a result seawall collapses completely due to reduced strength of the foundation and the structure. Therefore, to protect seawall from damage due to tsunami, we need to adopt two countermeasures simultaneously: (a) protection of soils behind the seawall due to tsunami impact force and (b) protection of concrete cover behind the seawall due to force of backwash. To protect seawall from impact force of tsunami, a new concept of using waste tire (a resilient material) structures behind seawall was developed (Hazarika and Fukumoto 2016), which is shown in Fig. 4. Considering the aesthetic, the tires can be planted with suitable plants to preserve the greenery (Hazarika et al. 2016).

3.3 Protection of Residential Building During Earthquake (Horizontal Inclusion)

To prevent vibration-induced and liquefaction-induced damage of residential buildings during earthquakes, it is important to adopt low-cost ground improvement technique, since house owners cannot afford to go for the expensive ground improvement techniques applied in conventional infrastructural projects. One such

Fig. 5 Protection of residential building using horizontal inclusion (Hazarika et al. 2009)



low-cost technique has been developed which utilizes tire chips mixed gravel under the foundation of residential housing, which is shown in Fig. 5 (Hazarika et al. 2009; Hazarika and Abdullah 2015). Horizontal reinforcing inclusion, thus, refers to a layer made of tire chips and gravel which are placed horizontally as shown. Mixture of gravel and tire chips layers along with geogrid reinforcement (if necessary) provides sufficient bearing capacity to the foundation that otherwise has to rest on highly compressible tire chips layer.

4 Validation of Vertical Inclusion Technique

4.1 Test Cases and Test Procedures

Experimental verification of this technique was made by conducting 1g shaking table test using the large three-dimensional underwater shaking table assembly belonging to the Port and Airport Research Institute (PARI), Japan. The circular shaking table of diameter 5.65 m is mounted on a 15 m long, 15 m wide, and 2-m-deep water pool. Details of the shaking table assembly and the model construction procedures used in this study can be found in Hazarika et al. (2006), (2008), Iai and Sugano (2000) and Sugano et al. (1996).

A caisson type quay wall was used in this testing, which was placed in a soil box of 4 m long, 1.25 m wide, and 1.5 m deep. Four different models were constructed in which each of the models differs on the selection of backfill material as shown in Fig. 6. In Case 1A, a conventional caisson with gravel as part of the backfill was used. In Case 1B, the entire gravel backfill was substituted by tire chips. A layer of gravel was placed on top of the tire chips to prevent any uplifting of tire chips during earthquake due to their low weight. Case 2A is the case in which the top half

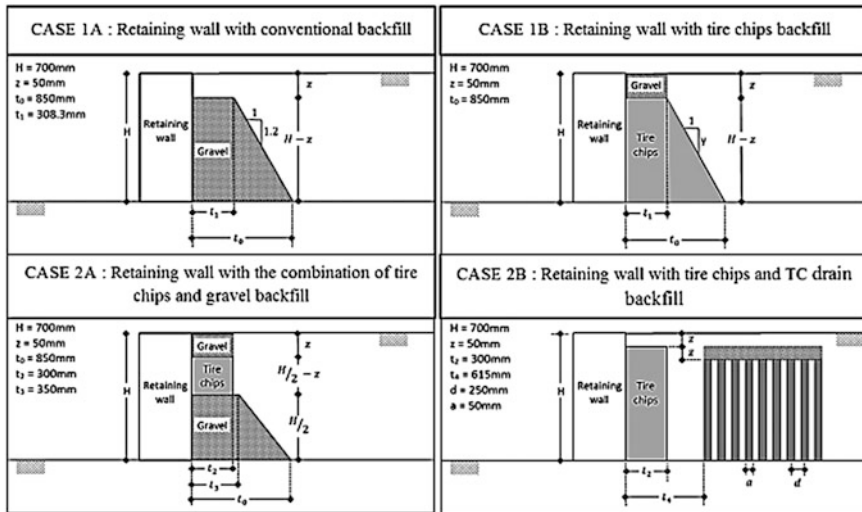


Fig. 6 Models used in the shaking table experiment

of the gravel in Case 1A was replaced by tire chips. In Case 2B, a compressible inclusion and a series of vertical drains made of tire chips were installed as part of the backfill as explained in Fig. 3 in the section above. A total of 23 vertical drains of diameter 50 mm were installed with a spacing of 210–250 mm in triangular pattern. To ensure proper water drainage during earthquake loading, on top of the entire drains a 50-mm-thick gravel layer underlying a 50-mm-thick soil cover was laid. This later also could prevent any uplifting of the tire chips drain. A cross-sectional view of this case is shown in Fig. 7.

The test models consist of 0.1-m-thick bedrock layer, 0.45-m-thick dense seabed layer (relative density of 78.59%), 0.1-m-thick foundation rubble, and 0.85-m-thick backfill soil (relative density of 45.95%). Saturation of the backfill was achieved by elevating the water level up to 1.3 m at a slow rate, after constructing and instrumenting the models.

Scaling law for model to prototype ratio of 1/10 was selected in this study. The similitude of various parameters in 1g gravitational field was calculated based on the soil–structure–fluid system proposed by Iai (1989). The models shown in Fig. 6 were subjected to an actual earthquake loading (the N–S component of the strong motion acceleration record at the Port Island, Kobe, Japan, during the 1995 Hyogo-ken Nanbu Earthquake).

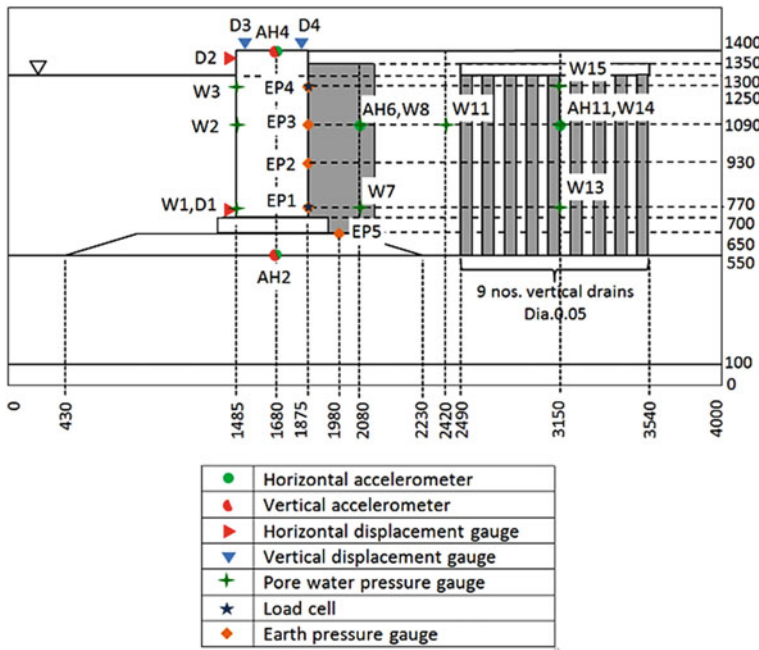


Fig. 7 Cross section and instrumentations of the models used in the experiment (all dimensions are in mm)

4.2 Test Results

Figure 8 shows the time histories of horizontal displacement experienced by the caisson during the test duration at the top (D2) and bottom (D1) of the caisson. Negative signs of the horizontal displacement indicate that the displacement was toward the sea. It can be seen that the residual displacement of the retaining wall with conventional backfill (Case 1A) was 9.1 and 7.8 mm at the top and the toe, respectively. Replacing the rubble backfill with tire chips (Case 1B) helps reducing the amount of residual displacement by almost 50% where the displacements recorded were 4 and 3.3 mm at the same points. The combination of tire chips and rubble as backfill material (Case 2A) also shows some reduction in the residual horizontal displacement compared to the conventional case. The vertical inclusion technique (Case 2B) yields similar residual horizontal displacement as in the case of Case 1B (Fig. 9).

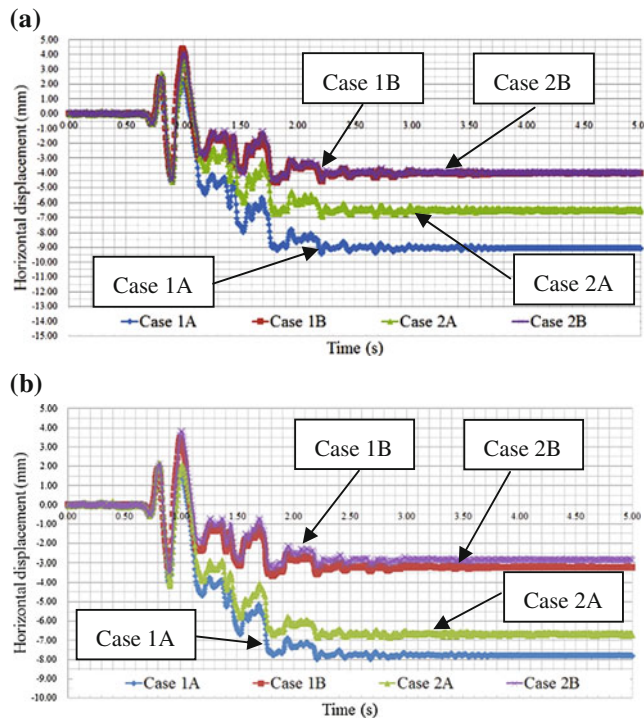


Fig. 8 Comparison of the horizontal displacements of the caissons. **a** At the top of the caisson (D2 of Fig. 7). **b** At the bottom of the caisson (D1 of Fig. 7)

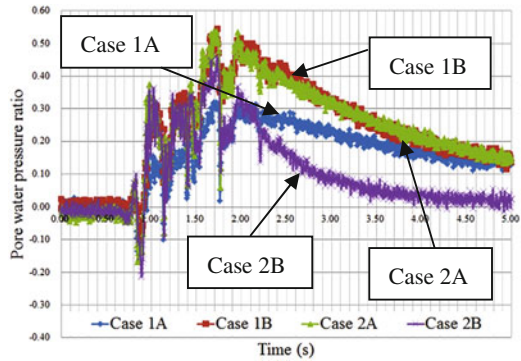
5 Validation of Seawall Protection Technique

To evaluate the tsunami impact force absorption and the load dispersion effect of the protective tire structures explained in Fig. 4, Tsunami overflow tests (TOTs) were conducted by placing model tires behind the seawall in various configurations and different filling conditions of tires.

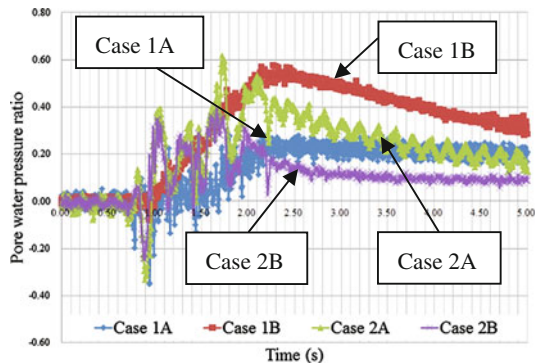
5.1 Test Model and Test Conditions

A new apparatus for TOT was developed by the research group of adaptation to global geo-disaster and environment at Kyushu University. In this apparatus, a model soil box made of acryl (1200 mm in length, 300 mm in width, and 1000 mm in height) was used to reproduce the overflow phenomenon of tsunami. The schematic diagram of the apparatus developed in this research is shown in Fig. 10.

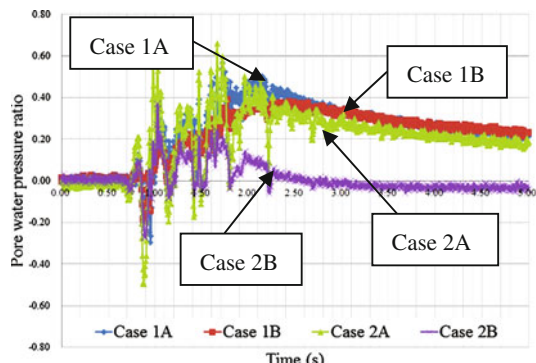
Fig. 9 State of the pore water pressure dissipation with time in the four cases



(a) W13 (Backfill bottom)



(b) W14 (Mid-height of the backfill)



(c) W15 (Top of the backfill)

The model seawall (height 60 cm and crown width 12 cm) is placed inside the soil box. There is a hinge gate above the model seawall that stores water and can reproduce the overflow phenomenon of tsunami.

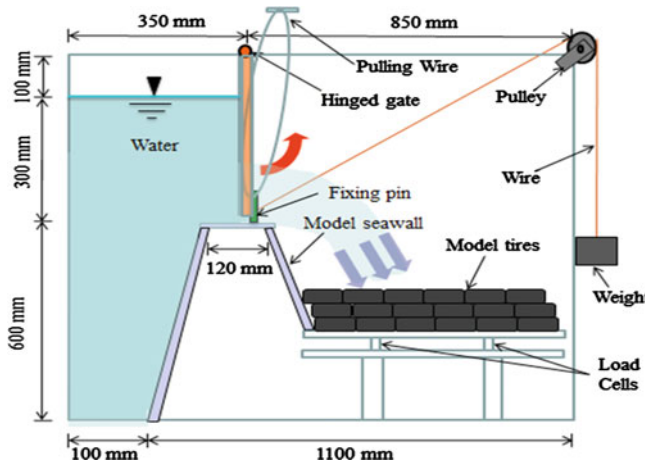
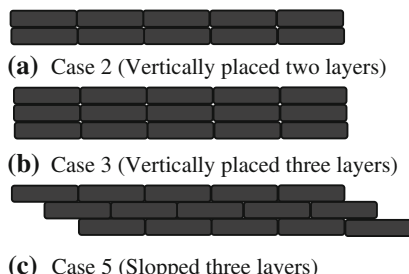


Fig. 10 Tsunami overflow testing (TOT) apparatus (Hazarika and Fukumoto 2016)

It was expected that the ability of tires to reduce the impact force of tsunami will be different according to the number of tire layers, types of filling material, and style of tire placing (configurations). Therefore, the following test cases were examined as explained in Fig. 11. Vertically laying cases (Case 2: two layers, Case 3: three layers) and alternately laying case (Case 5: slopped three layers). Three different filling conditions of tire were examined: (1) hollow tire (without any filling) (2) tire filled with Masado (decomposed granite soils abundant in Kyushu area, Japan), and (3) tire filled with tire chips (TCs) of maximum grain size 2 mm.

In the tests, model tires with outer diameter 85 mm, inner diameter 45 mm, and thickness 21 mm were used instead of actual tires. There are five load tables (Table 1 to 5) in the landside of the apparatus shown in Fig. 10. Each load table is supported with two load cells as shown in the figure. In the data analysis of this test, average value of the two load cells (in each table) was taken, and then the maximum values of those were determined.

Fig. 11 Test cases



5.2 Test Results

Figure 12 shows the calculated values of the water impact force against the time of overflow. Two typical cases are shown in the figure. One with no tire placed on the back of seawall, and the other is the case of seawall reinforced by slopped three layers of tires (Case 5 of Fig. 11). Comparison of the results shows that there is a considerable reduction (more than one third) of the impact force due to tire placement.

Comparisons were also made for the magnitude of impact force for different filling conditions of tires, as indicated in Fig. 13. This figure shows the variation of impact loads due to Case 5 (three-layered slope arrangement) for the different filling conditions. It can be observed that the impact force is reduced when the model tires are introduced behind the seawall in all the filling conditions of tires. This figure indicates that the impact force is reduced to some extent when hollow tires (without any filling materials) are placed behind the seawall. The impact force is further reduced when the tire chips-filled or the soil-filled model tires are used. In addition, the reduction is faster (time taken to reach the steady state is smaller) in these two cases (filled tires). The reduction percentage is found to be different depending on the filling materials of the tires. Tires filled with soils lead to the significant decrease of the impact load as compared to tires filled with pure tire chips. Therefore, it can be said that, instead of using pure tire chips, mixing tire chips with soils can be a viable alternative when applying the technique in actual field conditions.

From aesthetic point of view, filled tires on the back of a seawall are not appealing. Therefore, cultivation of suitable plants inside actual tires (used passenger car tire) was done in field using a yard inside the Ito campus of Kyushu University. Field test shows that the greening effect could be maintained in all the seasons in a year by appropriate selection and plantation of trees inside the tires. The details of those field tests can found in Hazarika et al. (2016).

Fig. 12 Comparison of impact force of tsunami with and without tires

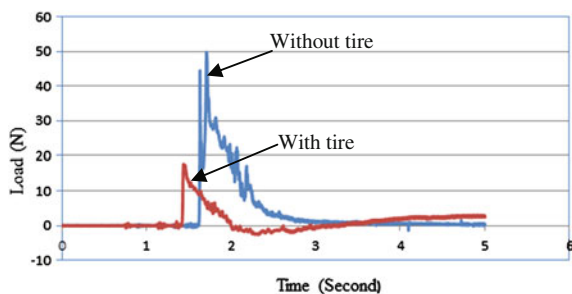
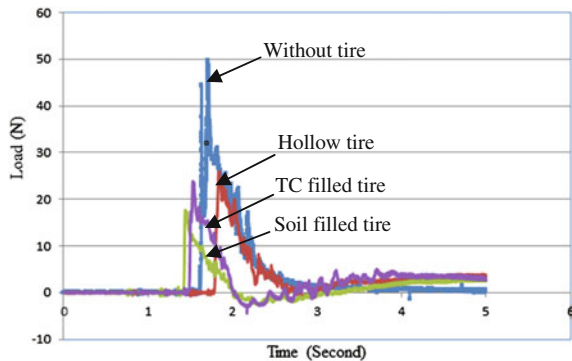


Fig. 13 Comparison of impact force of tsunami for different filling conditions of tires



6 Validation of Horizontal Inclusion Technique

6.1 Model Shaking Table Test

A series of 1g model shaking table tests were performed, using the shaking table assembly of Kyushu University, to evaluate the technique described in Fig. 5. The test model (prototype to model ratio of 20) is shown in Fig. 14. Model test box was 600 mm in length, 300 mm in width, and 500 mm in height. Toyoura sand was used as foundation soils of a model house. Pure tire chips (2 mm in size) or tire chips mixed gravel (size almost similar to tire chips) was used as the horizontal inclusion. Adjusting the height of the ground in the soil box up to 300 mm, the relative density of base layer and the layer containing horizontal inclusion was adjusted to be around 50%. The layer immediately below the foundation was made of gravel, which represents the top layer of foundation with some sort of soil improvement.

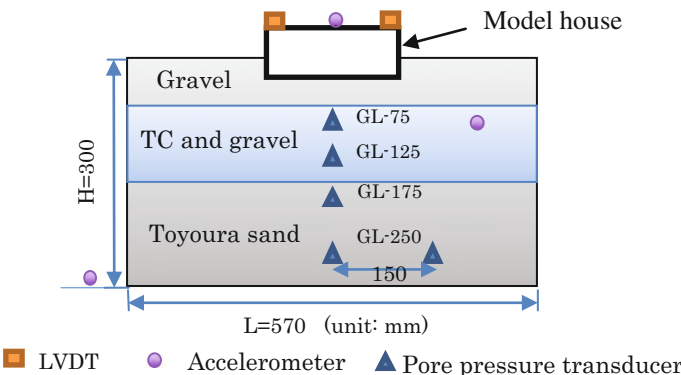


Fig. 14 Model for 1g shaking table test

A total of seven test cases were examined under three different conditions of the horizontal inclusion, which are shown in Table 1. In the Table, Case 0 represents the conventional foundation soil. Case 1, Case 2-1, and Case 2-2 represent the cases in which the thickness of horizontal inclusion was 10 cm. Case 3-1 and Case 3-2 represent the conditions in which the thickness of horizontal inclusion was reduced to 5 cm. Finally, in Case 4, the reinforced layer was located between the upper and lower sand layers. In the table, TC refers to tire chips and gf (gravel fraction) refers to the percentage of gravel in the mixture by volume. Gravel fractions (gf) of 30, 50, and 70% were used.

A sinusoidal acceleration of 300 Gal with 3 Hz frequency was imparted into the model for 45 s, and the responses were measured using the LVDT, accelerometers, and pore water transducers, which were installed at various locations within the foundation soils shown in Fig. 14.

6.2 Test Results

The maximum of excess pore water pressure ratios at various depths within the foundation soils are shown in Fig. 15. In the unreinforced foundation (Case 0) the excess pore water pressure exceeds 1.0 at all the depths indicating liquefaction in the foundation soils. Except for Case 4, in all the other cases the liquefaction was restrained in the reinforced layer. While Case 2-1 is the most effective in restraining liquefaction, Case 2-2 and Case 3-2 also display no liquefaction in all throughout the depth. These results imply that when the thickness of reinforced layer is 10 cm, liquefaction can be prevented using the proposed horizontal inclusion technique. However, when the layer thickness is reduced to 5 cm, the gravel fraction has to be over 70% to ensure its function. This may be attributed to the lightweight nature of tire chips, which may not exert enough overburden pressure on the layers underneath.

The average final settlements of the model house due to the cyclic loading for each case are shown in Fig. 16. From this figure, it is clear that the settlement of the house reinforced by pure tire chips (10-cm-thick inclusion) can be reduced to half

Table 1 Different configurations of the model test

Depth (mm)	Case 0	Case 1	Case 2-1	Case 2-2	Case 3-1	Case 3-2	Case 4
50	Gravel	Gravel	Gravel	Gravel	Gravel	Gravel	Gravel
100	Sand	Pure TC	TC + gravel (gf = 50%)	TC + gravel (gf = 30%)	TC + gravel (gf = 50%)	TC + gravel (gf = 70%)	Pure sand
150					Sand	Sand	TC + gravel
200		Sand	Sand	Sand			Sand
250							
300							

Fig. 15 Liquefaction potentials of the foundation in each case

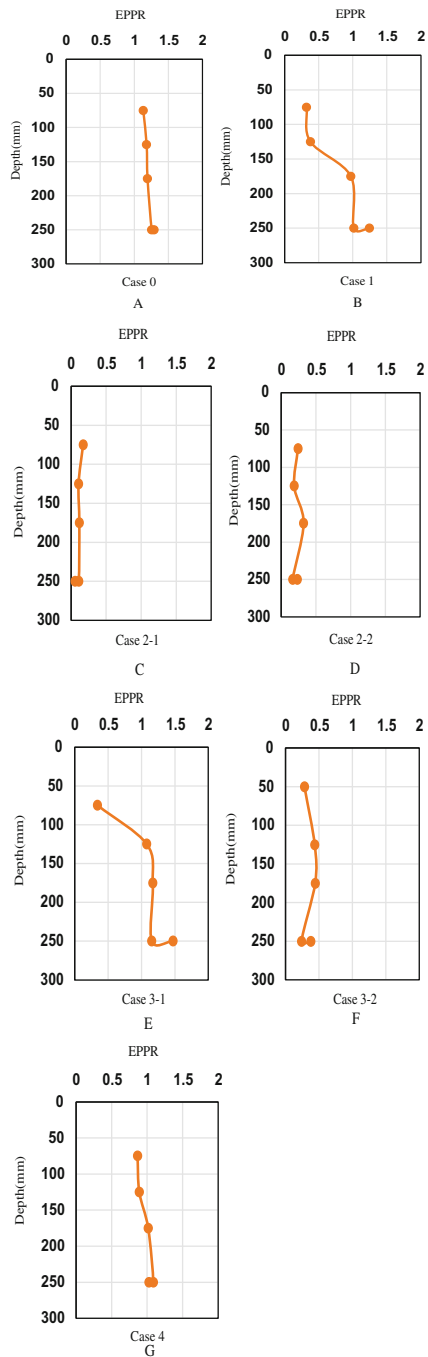
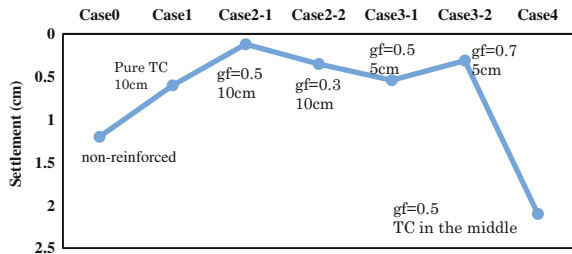


Fig. 16 Comparisons of the settlement of model house in each case



that of the non-reinforced foundation. However, when comparing with the gravel-mixed tire chips reinforced foundation (10-cm-thick inclusion), it can be observed that the settlement of the house was reduced further to half as compared to the foundation reinforced with pure tire chips. This implies that mixing gravel to tire chips can decrease the differential settlement due to enhanced bearing capacity.

In addition, the settlement decreases with the increase in the thickness of reinforced layer and the amount of gravel fraction. Furthermore, Case 2-1, in which the reinforced layer thickness was 10 cm and gravel fraction was 50%, the settlement is significantly less. In Case 4, the settlement was found to be even larger than the unreinforced foundation. This implies that this particular pattern of reinforcement is not appropriate for the model considered in this study. In other words, the location and thickness of the horizontal inclusion are also important design consideration in this technique.

7 Concluding Remarks

The following are the some of the main conclusions derived from this research.

1. The use of pure tire chips or in combination with gravel as part of the backfill improves the performance of the structure during an earthquake.
2. Significant lowering of the pore water pressure buildup within the backfill could be achieved in the case of backfill improved by vertical inclusion technique.
3. The tsunami impact force behind sea walls can be reduced considerably by placing filled whole tires (with a suitable filling material) to protect the damage of such structures from impact force and resulting scouring and erosion.
4. Tires must be filled with soils (or with other materials) to provide certain stiffness, so that they would be able to absorb the impact force of tsunami.
5. In the case of horizontal inclusion technique, tire chips was found to be an excellent liquefaction mitigating material, However, due to its' lightweight nature, it may also cause unexpected settlement of the structure. When the reinforced layer is mixed with gravel, the shear stiffness in reinforced layer will be increased, and thus, the settlement will be decreased.

- When the thickness of reinforced layer is 10 cm (2 m in prototype) and gravel fraction is 50%, the technique yields the best performance, as the rise of excess pore water pressure could be significantly restrained. This ultimately leads to the reduction of earthquake-induced settlement of the structure.

Application of the geo-disaster mitigation techniques discussed here is expected to contribute toward reducing the global warming by cutting down the release of greenhouse gas through cascaded recycling of waste tires, and thus, could be an effective adaptation measure against climate change. The techniques also possess tremendous potentials for adopting in developing and emerging economies, where alarming rate of car usage as the mode of commuting is already creating problems of stockpiling and illegal dumping, which in turn are placing a huge burden on our environment. Through a judicious decision during design process, if the cost reduction can be additionally achieved through use of such materials in geotechnical constructions, establishment of groundbreaking adaptive technology will not be a distant dream.

References

Edil, T. B. (2008). A review of environmental aspects and environmental applications of shredded scrap tires. In H. Hazarika & K. Yasuhara (Eds.), *Scrap tire derived geomaterials-opportunities and challenges* (pp. 3–18). London: Taylor & Francis Group.

Garcia, M., Pando, M. A., & Tempest, B. (2012). Tire derived aggregates as a sustainable recycled material for retaining wall backfills. In *International Conference on Sustainable Design and Construction* (pp. 542–552), Missouri, USA.

Hartman, D., Ledezma, M., Xiao, M., & Zoghi, M. (2013). Shake table test of MSE wall with tire derived aggregates (TDA) backfill. In *Geo-Congress 2013* (pp. 1168–1177), USA.

Hazarika, H. (2012). Earthquake resistant reinforcement of coastal structure using recycle material from waste tires. *Expected Materials for the Future*, 12(4), 34–41. (In Japanese).

Hazarika, H. (2013). Paradigm shift in earthquake induced geohazards mitigation—Emergence of nondilatant geomaterials. In *Keynote Lecture for the Annual Conference of Indian Geotechnical Society*, Roorkee, India: CD-ROM.

Hazarika, H., & Abdullah, A. (2015). Improvement effects of two and three dimensional geosynthetics used in liquefaction countermeasures. In *Proceedings of the 15th Asian Regional Conference of ISSMGE*, Fukuoka, Japan: CD-ROM.

Hazarika, H., & Fukumoto, Y. (2016). Sustainable solution for seawall protection against tsunami-induced damage. *International Journal of Geomechanics*, 16(5), [https://doi.org/10.1061/\(ASCE\)GM.1943-5622.0000687](https://doi.org/10.1061/(ASCE)GM.1943-5622.0000687).

Hazarika, H., Hara, T., & Fukumoto, Y. (2016). Resilient and sustainable geotechnical solution: Lessons learned from the 2011 great east Japan disaster. In G. L. S. Babu, S. Saride, & B. M. Basha (Eds.), *Sustainability issues in civil engineering* (Chapter 9, pp. 125–151). USA: Springer.

Hazarika, H., Igarashi, N., & Yamagami, T. (2009). Evaluation of ground improvement effect of tire recycle materials using shaking table test. In *Proceedings of the 64th Annual Conference of Japan Society of Civil Engineers* (pp. 931–932) (In Japanese).

Hazarika, H., Kasama, K., Suetsugu, D., Kataoka, S., & Yasufuku, N. (2012a). Damage to geotechnical structures in waterfront areas of northern Tohoku due to the March 11, 2011 tsunami disaster. *Indian Geotechnical Journal, Indian Geotechnical Society*, 43(2), 137–152.

Hazarika, H., Kataoka, S., Kasama, K., Kaneko, K., & Suetsugu, D. (2012b). Compound geotechnical disaster in Aomori prefecture and northern Iwate prefecture due to the earthquake and tsunami. *Japanese Geotechnical Journal, Japanese Geotechnical Society*, 7(11), 13–23. (in Japanese).

Hazarika, H., Kohama, E., & Sugano, T. (2008). Underwater shake table tests on waterfront structures protected with tire chips cushion. *Geotechnical and Geoenvironmental Engineering (ASCE)*, 134(12), 1706–1719.

Hazarika, H., Kohama, E., Suzuki, H., & Sugano, T. (2006). Enhancement of earthquake resistance of structures using tire chips as incompressible inclusion. *Report of the Port and Airport Research Institute*, 45(1), 3–28.

Hazarika, H., Otani, J., & Kikuchi, Y. (2012c). Evaluation of tyre products as ground improving geomaterials. *Ground Improvement, Institute of Civil Engineers, UK*, 165(G11), 1–16.

Hazarika, H., Yasuhara, K., Kikuchi, Y., Karmokar, A. K., & Mitarai, Y. (2010). Multifaceted potentials of tire-derived three dimensional geosynthetics in geotechnical applications and their evaluation. *Geotextiles and Geomembranes*, 28, 303–315.

Hazarika, H., Yasuhara, K., Kikuchi, Y., Kishida, T., Mitarai, Y., & Sugano, T. (2012d). Novel earthquake resistant reinforcing technique (SAFETY) using recycled tire materials. *Geotechnical Engineering Magazine of Japan Geotechnical Society*, 60(9), 30–31. (in Japanese).

Humphrey, D. N. (2008). Tire derived aggregate as lightweight fill for embankments and retaining walls. In H. Hazarika & K. Yasuhara (Eds.), *Scrap tire derived geomaterials—Opportunities and challenges* (pp. 59–81). London: Taylor & Francis Group.

Iai, S. (1989). Similitude for shaking table tests on soil-structure-fluid Model in 1g gravitational field. *Soils and Foundations, Japanese Geotechnical Society*, 29(1), 105–118.

Iai, S., & Sugano, T. (2000). Shake table testing on seismic performance of gravity quay walls. In *Proceedings of the 12th World Conference on Earthquake Engineering*, Paper No. 2680.

Inagaki, H., Iai, S., Sugahano, T., Yamazaki, H., & Inatomi, T. (1996). Performance of caisson type quay walls at Kobe port. *Soils and foundations* (pp. 119–136), Special Issue, Japanese Geotechnical Society.

Japan Automobile Tyre Manufacturers Association. (2016). *Tyre industry of Japan*. Retrieved from http://www.jatma.or.jp/media/pdf/tyre_industry_2016.pdf.

Karmokar, A. K., Takeichi, H., Kawaida, M., Kato, Y., Mogi, H., & Yasuhara, K. (2006). Study on thermal insulation behavior of scrap tire materials for their use in cold region civil engineering applications. In *Proceedings of the 60th Japan Society of Civil Engineers Annual Meeting* (pp. 851–852), Tokyo, Japan.

Kikuchi, Y., Sato, T., Nagatome, T., Mitarai, T., & Morikawa, Y. (2008). Change of failure mechanism of cement treated clay by adding tire chips. In *Proceedings of the 4th Asian Regional Conference on Geosynthetics* (pp. 374–379), Shanghai.

Kim, D. S., & Konagai, K. (2001). Key parameters governing the performance of soft tunnel coating for seismic isolation. *Earthquake Engineering and Structural Dynamics*, 30(9), 1333–1343.

Mitarai, Y., Yasuhara, K., Kikuchi, Y., & Karmokar, A. K. (2006). Application of cement treated clay added with tire chips to the sealing materials of coastal waste disposal site. In *Proceedings of the 6th International Congress on Environmental Geotechnology* (Vol. 1, pp. 757–764), Cardiff, UK.

Niiya, F., Hazarika, H., Yasufuku, N., & Ishikura, R. (2012). Cyclic frictional behavior of two and three dimensional geosynthetics used in liquefaction countermeasure. In *Proceedings of the 5th Taiwan-Japan Joint Workshop on Large Earthquakes and Heavy Rainfall*, Tainan, Taiwan: CD-ROM.

Reddy, S. B., & Krishna A. M. (2015). Recycled tire chips mixed with sand as lightweight backfill material in retaining wall applications: An Experimental Investigation. *International Journal of Geosynthetics and Ground Engineering*. <https://doi.org/10.1007/s40891-015-0036-0>.

Sugano, T., Morita, T., Mito, M., Sasaki, T., & Inagaki, H. (1996). Case studies of caisson type quay wall damage by 1995 Hyogo-ken Nanbu Earthquake. In *Proceedings of the 11th World Conference on Earthquake Engineering*, Paper No. 765.

Tsang, H. (2008). Seismic isolation by rubber-soil mixtures for developing countries. *Earthquake Engineering and Structural Dynamics*, 37, 283–303.

Uchimura, T., Chi, N. A., Nirmalan, S., Sato, T., Meidani, M., & Towhata, I. (2008). Shaking table tests on effect of tire chips and sand mixture in increasing liquefaction resistance and mitigating uplift of pipe. In H. Hazarika & K. Yasuhara (Eds.), *Scrap tire derived geomaterials—Opportunities and challenges* (pp. 179–186). London: Taylor & Francis Group.

Yasuhara, K., Komine, H., Murakami, S., Miyota, S., & Hazarika, H. (2010). Mitigation of liquefaction using tire-chips as a gravel drain. In *Proceedings of the 6th International Congress on Environmental Geotechnics*. India: CD-ROM.

Static and Seismic Slope Safety

Displacement-Based Criterion for Seismic Analysis

Sarada K. Sarma

Abstract Methods of slope stability analyses for static and seismic conditions are discussed. The ideas of factor of safety, critical acceleration and critical slip surface are examined. The idea of displacement of slopes during earthquakes is also discussed; it is emphasised that displacements are a better criterion for seismic design of slopes. Post-seismic large displacement of slopes is examined in a test case.

Keywords Slope safety • Analysis technique • Factor of safety
Critical acceleration • Critical surface • Sliding displacements • Multi-block sliding

1 Introduction

Slopes fail when the shear strength of soils along the slip surface is not sufficient to resist the net force trying to drive the soil mass down the slope. The net force is mainly coming from the gravity and the seismic loads, but also there may be other forces trying to either support the soil mass or add to the driving force. The shear strength of the soil is provided by the cohesion and the internal friction of the material, but the strength is affected by the pore water pressure present in the soil. There are alternative ways to analyse the safety of a slope, whether it is for static or for seismic conditions. It is possible to use methods like finite element and finite difference which use numerical techniques to determine the stresses and strains in the slope. Alternatively, it is possible to use simple methods like the limit equilibrium analysis technique which gives a measure of the safety of the slopes in terms of stresses on possible slip surfaces but does not give any idea about the stresses and strains inside the slope. The use of the finite element method locates the most likely surface to fail but does not provide the factor of safety directly. However, the strength reduction technique can be utilised to determine this factor. Limit equilibrium technique, associated with multi-block sliding, can be used to

S. K. Sarma (✉)
Civil & Environmental Engineering, Imperial College, London, UK
e-mail: s.sarma@imperial.ac.uk

determine large displacements along slip surfaces but such displacements cannot be determined successfully with finite element technique.

2 Triggering Factors for Slope Failures

The triggering factors can be natural or man-made. While man-made factors can be controlled, we can do nothing about the natural factors other than taking measures to stop or minimise the effects. The factors mentioned here may not be exhaustive but are the important ones. The natural factors are: (1) earthquakes, (2) rainfall, (3) toe cutting by natural causes such as river erosion. The man-made factors are: (4) toe cutting for road construction and house building, (5) loading on the ridge of the slope, (6) reservoir building such as for dams.

Earthquakes affect the slopes in different ways. The application of seismic motion produces inertia forces, both horizontal and vertical which increase the driving loads on the slopes. At the same time, it may increase the pore water pressures in the soil due to cyclic loading; this in turn reduces the shearing strength of the soil. The rainfall on the slope and on the ridge of the slope allows water to flow into the soil, thereby producing seepage pressures which increase the pore water pressures which in turn reduce the strength of the soil. The effect of the rainfall will depend on the degree of saturation of the soil prior to the rainfall. In mountainous regions, flowing rivers cut into the slopes, causing erosion which in turn removes the support provided by the toe to the slope. Also, this reduces the total available shear strength on the slip surface. The same effect can be seen in seashores and in shores of lakes. The same effect of toe cutting by river erosion is also caused by toe cutting of the slopes for road construction, house building, etc. Loading on the ridge of the slope, very close to the edge, may also add to the driving force on the slope. This effect is generally considered as bearing capacity failure near slopes. Far away from the edge of the slope, the loading will not have such effect on the slope. Reservoirs at the toe of the slope, whether produced by dam building or natural lakes, may produce hydro-dynamic pressures on the slopes during earthquakes which add to the driving force. The reservoir water, without any earthquake, supports the slope. Also, new reservoirs change the pore water pressures in the slope which changes the strength. Reservoirs in the higher reaches cause flow of water into slopes in the lower reaches, which in turn increases the pore water pressures in the soil, thus reducing the strength of the soil.

Thus, slope failures are caused either by increasing the driving forces on the slope or by reducing the supporting load and/or by decreasing the strength of the soil or both.

3 Inertia Forces in the Slope Due to Earthquakes

The inertia forces on the slope due to earthquakes can be determined, if the dynamic response of the slope to the earthquake can be solved. We must remember that soil is a nonlinear inelastic material. Finite element or finite difference solutions can provide such an answer with some simplifications to the boundary conditions. An analytical solution to this problem does not exist, even for linear elastic materials. However, there are simplified solutions for symmetric wedges representing dams, Seed and Martin (1966) and Ambraseys and Sarma (1967). These simplified solutions give some idea of how a slope responds. We can get an idea of the complexities of the problem from the following wave propagation mechanism shown in Fig. 1.

The figure shows a vertically propagating SV wave (with incoming horizontal particle motion only), producing both horizontal and vertical motions in the slope through reflected P and SV waves. Any wave, whether it is a P wave or an S wave, when it impinges on an inclined surface (inclined to the direction of propagation of the wave), produces both P and S waves. The directions of these reflected waves depend on the velocities of the corresponding waves. There are critical and super-critical conditions, when an S wave impinging on a steeper inclination cannot produce a P wave and it results in complex situations. The datum line is not a boundary in this figure but a line to measure the time from. The incoming SV waves from below arrive at the datum line at the same time. The long arrows show wave propagation directions, while the short arrows show the particle motions. The particle motion for the P waves is parallel to the wave direction while that for SV waves is normal to the wave direction. The particle motions at any point, at any instant of time, will be the combined effect of motions of all waves arriving at the point at that time, Sarma and Irakleidis (2008). The results from response of embankment dams and field evidence of ground motions in slopes show that the motions are amplified from the base towards the crest near

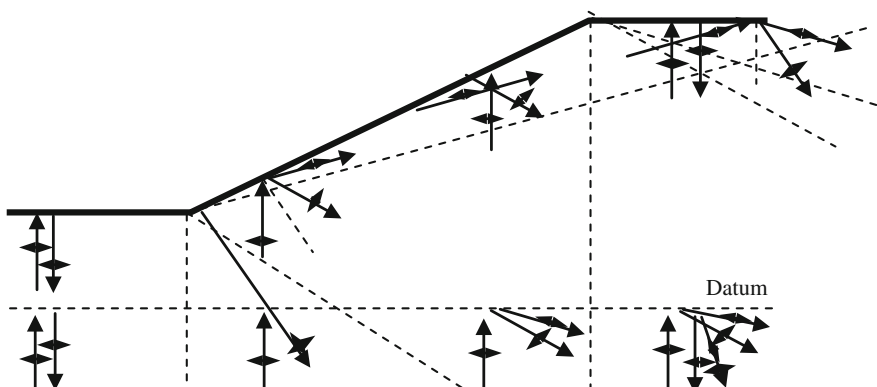


Fig. 1 Wave propagation in a slope subjected to a vertically travelling SV wave

the slope, Faccioli et al. (2002). Numerical analysis of the problem shows similar effects, Bouckovalas and Papadimitriou (2005).

4 Concept of the Average Acceleration

Since the earthquake accelerations on a slope vary from point to point, it is necessary to define an average acceleration on a mass of soil in the slope involved in sliding. This average acceleration depends on the input acceleration, geometry and material properties of the slope materials all of which contribute to the response of the soil mass, and the geometry of the slip surface. The average acceleration concept is not necessary while using nonlinear, inelastic, dynamic finite element method as it gives the stresses and strains in the slope directly. But, this concept becomes necessary when the limit equilibrium technique is used for the seismic analysis of slopes.

The concept is easily understood when analytical solution to the dynamic problem is available, for example, in the case of one-dimensional earth dams. In this case, the dam is represented by a symmetric triangular wedge, of homogeneous visco-elastic material, resting on a rigid base. The base is subjected to horizontal ground accelerations varying with time. The response shows that accelerations within the body of the dam at any time vary with height but are constant in a horizontal line. The response depends on the dam height and the shear wave velocity of the material, which provides the natural periods of the dam. There is a fundamental period, and the higher-mode periods are functions of the fundamental period.

Figure 2 shows such a dam, and the response acceleration is given by $\ddot{U}(y, t)$. A possible slip surface is shown in the slope. A thin horizontal strip confined between the free surface and the slip surface at a given height is shown in the figure, which has a mass dm . This mass when multiplied by the acceleration at the given height gives a force, which can be integrated between the base of the slip surface and the top of the dam, which results in the total inertia force on the slipping mass. The total force divided by the total mass between the same limits gives an average acceleration. This average acceleration is a function of time and looks and behaves like any acceleration record. This record has a peak value, which we designate as $k_m g$, where g is the acceleration due to gravity and k_m is the average peak seismic coefficient. Within this framework, kg is the average acceleration at any time, which is shown as A_x in Fig. 2.

In the limit equilibrium method of seismic slope stability analysis, we use this average acceleration, assumed to be a constant for the mass involved.

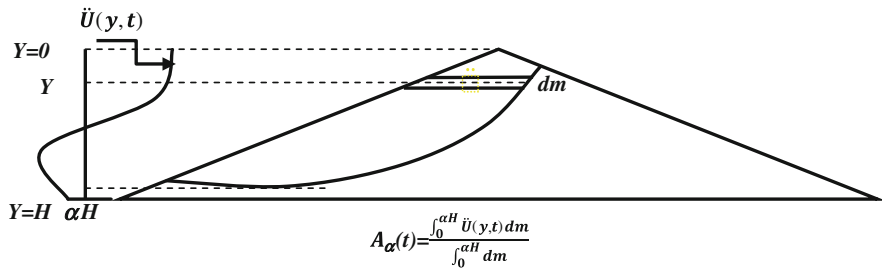


Fig. 2 Average acceleration ($A_x = kg$) in an embankment dam subjected to horizontal ground motion as a function of time

5 Basics of the Limit Equilibrium Technique in Slope Stability Analysis

Figure 3 shows a slope and a possible slip surface in it. In this figure, W is the weight of the soil above the slip surface, kW is a horizontal load, σ_n is the normal stress and τ is the shear stress on the slip surface. The horizontal load usually represents the inertia of the soil mass due to an average earthquake acceleration kg , but it can also be any other horizontal load. Water in the slope, if any, will produce pore water pressure in the soil, which will affect the strength but not the equilibrium stresses.

The idea of the limit equilibrium method is to find σ_n and τ , which varies from point to point on the slip surface, so that the mass of soil contained within the slip surface and the free surface is in equilibrium. It is to be noted that these stresses cannot be determined exactly, other than through a stress-strain analysis like using finite element methods. Limit equilibrium technique tries to estimate these stresses using reasonable assumptions following some acceptability criteria. The first criterion is that the effective normal stress on the slip surface and on the interslice boundaries must be compressive since soil cannot take tension. The second

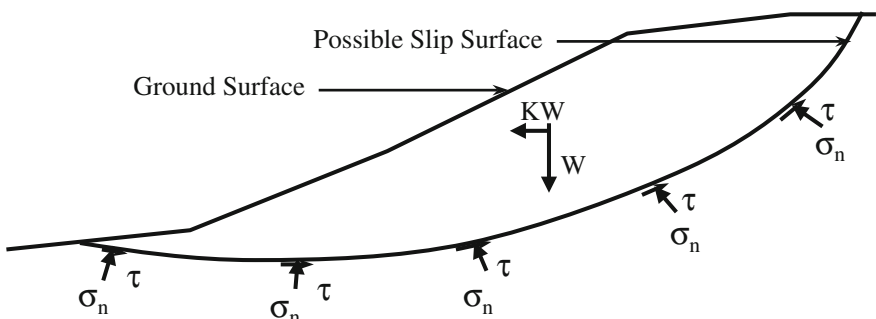


Fig. 3 Schematic slope and a possible slip surface

criterion is that the shear stresses on the slip surface and on the interslice boundaries have directions as shown in the figure to satisfy kinematics of the sliding condition. The third criterion is that the implied stresses within the body of the mass do not violate the failure criterion of the soil.

Method of slices with the limit equilibrium technique is a way of estimating the normal stresses on the slip surface, with some errors associated with the unknown interslice forces. Different methods, available in the literature, differ in the way the normal stresses; i.e. the errors associated with the interslice forces are estimated and therefore give different answers, when equilibrium of the soil mass is achieved. So long as the estimates are reasonable, the results should be similar and one method cannot be said to be more accurate compared to another. In theory, there are infinite solutions to a given problem in this kind of analysis. If for some reason, such as convenience of solution, the equilibrium is not established, then the methods should not be compared. At the end, it is the third criterion, i.e. the implied stresses inside the soil mass do not violate the failure criterion of soil, and dictates whether the solution is good. Quite often, it is not possible to obtain a perfectly acceptable solution and it is left to the analyst to decide the acceptability.

The shear strength of soil is defined by the Mohr–Coulomb criterion:

$$\tau_f = c' + (\sigma_n - u)\tan\phi' \quad (1)$$

where

τ_f	Shear strength
σ_n	Total normal stress
u	Pore water pressure
$(\sigma_n - u) = \sigma'_n$	Effective normal stress
ϕ'	Angle of internal friction in terms of effective stresses
c'	Effective cohesion

The shear stress τ at the base of the slice is assumed to be a fraction of the shear strength, τ_f , so that

$$\tau = \tau_f/F$$

F is termed the **Factor of Safety**. It is implied that F is applied to both c' and $\tan\phi'$.

It is assumed that F is same along the slip surface. For a stable mass, F is greater than one and it varies along the slip surface. However, a constant F is not a bad assumption. When F equals one, it is a critical situation. If the soil is such that it does not lose strength after failure, such as in dry loose sands, then the assumption of constant F along the slip surface is true when F equals one. But for brittle soils, such as over consolidated clay, where there is drop of strength after failure, there is the progressive failure situation and in such a case, the constant F may not be a good assumption.

The limit equilibrium technique of slope stability analysis is quite well known, such as Bishop's rigorous method (1955), Janbu's method (1957), Morgenstern's and Price's method (1965), Spencer's method (1973), Sarma's method (1973, 1979a) and many more. All of these methods, except Sarma (1979a, b), use vertical slices. Sarma (1979a, b) uses slices which are not vertical and the sides of the slices are not parallel either. Of these, Janbu's method, M&P's method and both of Sarma's method use distinctly different assumptions regarding the interslice forces; Spencer's assumption is same as M&P's, but the technique of solving the equilibrium equations is different. Sarma (1973) method and Bishop's rigorous method have the same assumption regarding interslice forces, but the technique of solving the equilibrium equations is completely different. Sarma (1979a, b) method is in a class of its own, where the assumptions regarding the interslice forces and the technique of solutions are different.

6 Assumptions in the Vertical Slice Method Regarding Interslice Forces

Figure 4 shows a vertical slice inside the sliding mass with the forces acting on it. E is the interslice thrust, and X is the interslice shear force. N is the normal force and T is the shear force on the base of the slice which are the integrals of σ_n and τ over the length of the base of the slice, respectively. These forces are unknown and the solution technique is to determine these forces from the equilibrium conditions of all such slices, forming the sliding mass. The known forces are the weight w and the horizontal force kw on the slice. If there are other known forces, then these should be included as well. The idea is to find a value of F , the factor safety, which is introduced in the definition of τ . In order to find a solution, it is necessary to make some assumptions regarding the interslice forces. One of the outcomes of the method of slices is that an extra unknown has to be introduced in the assumptions

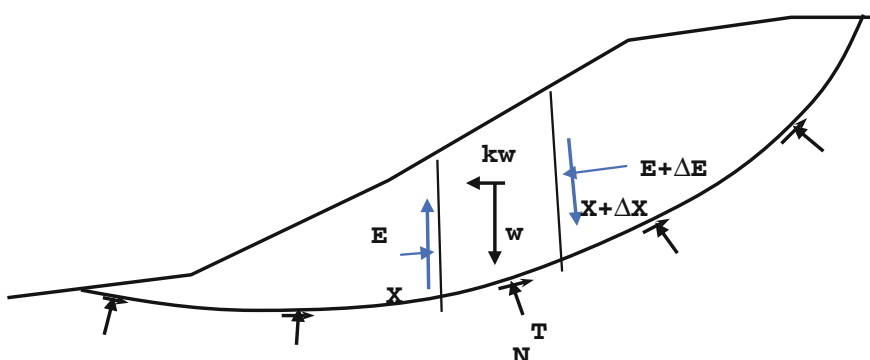


Fig. 4 A vertical slice in a slipping mass of soil in a slope

which scale the assumed values of the interslice forces or iterate the assumed values to maintain equilibrium. Otherwise, complete equilibrium cannot be established.

In Janbu's method, the assumption is that the point of application of the interslice thrust E is some known value z . Note that he did not introduce an unknown parameter in his assumption and therefore does not satisfy equilibrium exactly but the error is such that it can be ignored.

In M&P's method, the assumption is that $X = \lambda f_x E$, where λ is the unknown parameter to be determined along with F and f_x is an arbitrarily chosen known function. In Spencer's method, the assumption is same as in M&P's method but f_x is chosen as 1 and λ is replaced by $\tan \theta$. However, with this assumption, it is easier to solve the equilibrium equations. In Sarma (1973) method, $X = \lambda Q_x$, where λ is the unknown parameter to be determined and Q_x is a chosen function. In this method, Q_x is a defined function based on soil properties and the geometry of the slice. In Bishop's rigorous method, the assumption is $X = Q_x$ where Q is an arbitrarily chosen function without the unknown parameter and therefore requires iterations on the function Q to satisfy equilibrium.

Sarma (1973, 1979a, b) methods differ from other slice method in the sense that the equilibrium equations are solved to determine the critical horizontal acceleration factor instead of the factor of safety. The factor of safety is determined by changing the soil parameters by a factor F and determining the critical acceleration factor for the reduced strength, thus producing a relationship between the earthquake acceleration and the factor of safety.

Sarma (1979a, b) method is different from all other slice method in the sense that the slices are not vertical and the sides of the slices are not parallel. The assumption regarding the interslice forces is that these are also in limiting equilibrium state in all the slice boundaries. This assumption is consistent with the fact that when the applied horizontal acceleration equals the critical one, slide movement starts to occur.

The method of slices is not the only one in trying to estimate the normal stresses. Sarma (1979b) suggested a direct way of estimating the normal stresses. This stress depends on the soil parameters, pore water pressures and the geometry of the slip surface. This is shown in the equation below:

$$\sigma'_n = \lambda [\gamma h(1 - r_u) \cos \phi' - c'(\sin \beta + \sin \phi')] \frac{\cos \phi'}{1 + \sin \beta \sin \phi'} \quad (2)$$

where

σ'_n Normal effective stress at a point on the slip surface

γ Unit weight of the soil above the point (average)

h Height of the soil column above the point

r_u Pore pressure ratio = $u/\gamma h$

u Pore pressure on the slip surface at the point

ϕ' Angle of internal friction in terms of effective stresses of the soil on the slip surface

- c' Cohesion in terms of effective stresses
- β Inclination of the slip surface to the horizontal at the point.
- λ A constant to be determined from the equilibrium of the whole mass along with factor of safety or critical acceleration.

This equation is derived by assuming that the effective vertical stress at a point is equal to the effective overburden pressure at the point and the slip surface is at limiting equilibrium. For equilibrium, the normal stress, the shear stress which depends on the normal stress and the pore water pressure are integrated along the slip surface, which can easily be done by considering continuous piece-wise linear slip surface if the slip surface is not integrable as a single function.

In all of these methods, the implied stresses in the body of the slope are only checked and used to accept or discard the solution. More often than not, the solutions are accepted even though the criteria are not completely satisfied.

Sarma (1979a, b) method is later extended by Sarma and Tan (2006), to make use of the acceptability criterion directly to determine the slip surface and the critical acceleration factor. This solution shows, Tan and Sarma (2008), that if the acceptability criterion is satisfied, then the limit equilibrium solution is as good as that obtained from finite element method. This method was termed as extended limit equilibrium method.

7 Pore Water Pressures

In discussing soil strength, pore water pressures play a very important role. Pore water pressures in slopes can be steady-state or/and transient. The steady-state condition can be of two kinds. The first is the hydro-static condition. This is due to external water as in a reservoir or due to ground water table. The second is the steady-state seepage condition. This is due to steady flow of water through the slope from a higher reservoir to a lower reservoir. The transient pore water pressure is caused by the loading of saturated soil in undrained condition. This is the excess pore water pressure in the soil. This pore pressure dissipates through the soil with time ending in the steady-state condition. In the case of isotropic undrained loading, the excess pore pressures are recoverable. But in the case of anisotropic loading, part of the pore pressures due to the deviatoric loading are non-recoverable. Therefore, pore pressures increase through repeated anisotropic loading. For example, when a soil mass is subjected to an earthquake strong motion, there is not enough time for the excess pore pressure to dissipate during the earthquake and therefore the condition is undrained even for highly permeable soils. The excess pore pressures generated through cyclic loading may cause liquefaction of loose cohesionless soils during earthquakes. If liquefaction happens in a slope during earthquakes, we will see very large displacements. Even for very mild slopes, this may cause displacements which are termed lateral spreading. Loading of clays is considered undrained in short time (short time may be days or much longer).

Laboratory tests on loose cohesionless soils show such results of pore pressure rise in cyclic loading, Seed and Idriss (1982).

8 Displacement Criterion of Slopes for Seismic Conditions

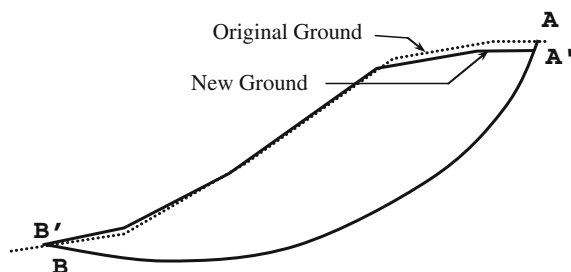
The term, “factor of safety”, is in constant use as a measure of safety of the slope since the First International Conference on Soil Mechanics in 1936 but Fellenius (1927) probably used it first, but, his own translation to English was “Degree of Security”.

This term has served its purpose well. There was no other attempt to look for another criterion until by Newmark in 1965 while trying to define safety of slopes under seismic conditions. He noticed that during earthquakes, even though the factor of safety of a slope may become less than one intermittently there is not enough time for the mass to move downhill. Therefore, a factor of safety less than one does not constitute failure in the true sense. He used the relative “*displacements*” of the sliding mass (relative to the main body of the slope) as a measure of the safety of the slope; see Fig. 5. Displacement-based safety analyses are superior as displacements are directly related to the damage caused by slope instability and additionally can incorporate in their estimate the possible changes of soil strength with distance moved.

9 Critical Acceleration

The displacement analysis in stability problems requires an estimate of the ***critical earthquake acceleration*** for the slope. The critical acceleration is similar in nature as the factor of safety. This is defined as the horizontal acceleration required to produce a factor of safety equal to one. Earthquake acceleration smaller than the critical implies a factor of safety greater than one, and conversely, acceleration bigger than the critical implies a factor of safety smaller than one. The critical acceleration is determined the same way as the factor of safety. Any slope stability

Fig. 5 Relative displacements of the sliding mass (AA' or BB' represents the relative displacement—note that AA' and BB' may not be equal)



analysis technique, which determines factor of safety, can be used to compute the critical acceleration by iterative technique. Sarma (1973) and Sarma (1979a, b) are two methods in which the critical accelerations are determined directly and the factor of safety by iterations. Charts of critical accelerations were produced for homogeneous slopes similar to the stability charts for factor of safety, Pratter (1979), Lighthall (1979) and Sarma (1999). Sarma (1975), (1988) showed how the excess pore water pressures generated by earthquakes can be taken into account in deriving the critical accelerations.

Since the true failure surface is generally not a plane and Newmark model requires an estimate of an equivalent plane, Sarma (1975) made the only attempt at defining such a plane. The equivalent plane was defined by the direction of the sum of the shear force vectors on the slip surface at the critical state.

10 Critical Slip Surface

The determination of the factor of safety or the critical acceleration is linked to the determination of the critical slip surface. The critical surface can be defined as that surface along which a slip will take place given the right circumstances. In the factor of safety (F) approach, the right circumstance will be if the strength of soil is less by the factor F than that assumed for the analysis. In the critical acceleration ($k_c g$) approach, the right circumstance will be if the earthquake acceleration is bigger than the critical with the given strength of the soil. The two surfaces defined in the two approaches are not the same, even though they are practically very similar. In the normal practice, the critical surface is found by analysing many surfaces and then selecting the one with the minimum value of either the factor of safety or the critical acceleration. Many different searching techniques are used for this purpose. The extended limit equilibrium method, Sarma and Tan (2006), finds the critical acceleration and the critical surface at the same time. In this method, the acceptability criterion, i.e. the implied stresses inside the soil mass do not violate the failure criterion of the soil, is used explicitly to determine both the critical acceleration and the critical surface at the same time. Tan and Sarma (2008) verified this technique by comparing with solutions using finite element method; see Fig. 6a, b.

11 Sliding Displacement Analysis

11.1 Single Block on a Single Plane

Newmark (1965) used a very simple technique that of a block of soil moving on an inclined plane, Fig. 7, to assess the displacements during an earthquake.

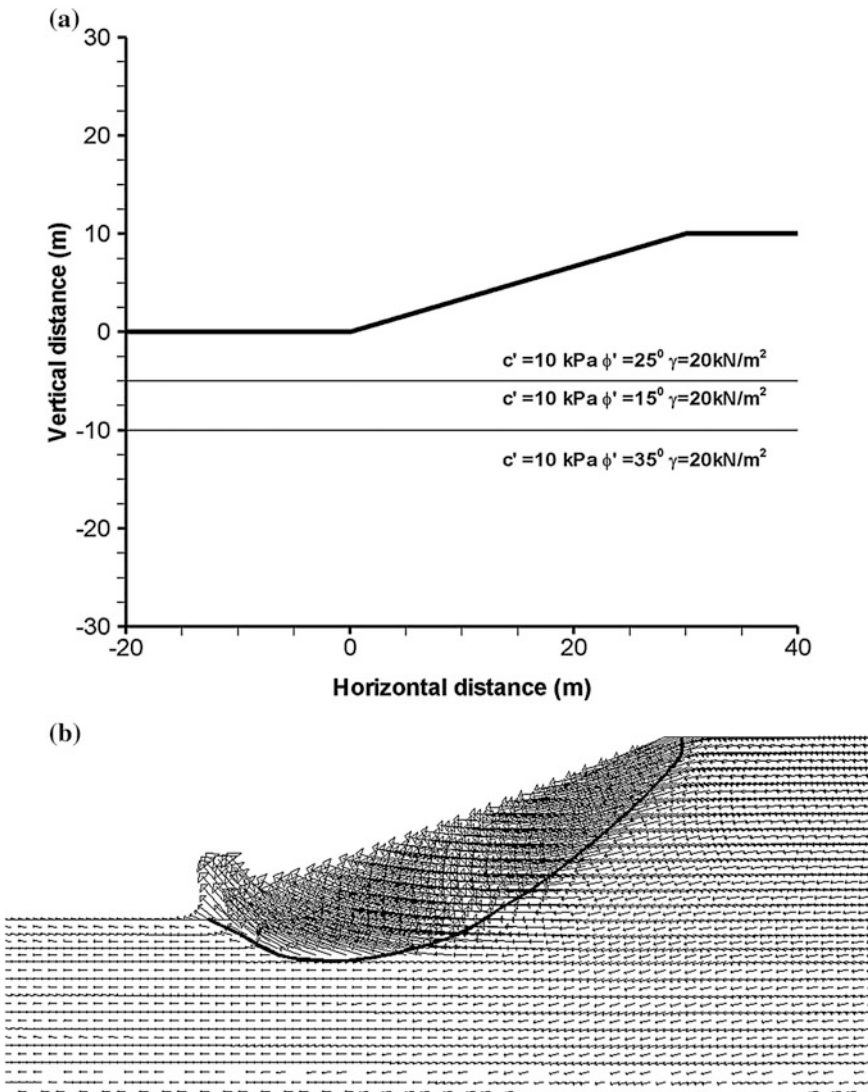


Fig. 6 **a** Geometry and material properties of the non-homogeneous slope. **b** Non-homogeneous slope, FE verification. $k_c = 0.26$ versus 0.254 (FE), firm line shows the slip surface found by using the extended limit equilibrium method. Tan and Sarma (2008)

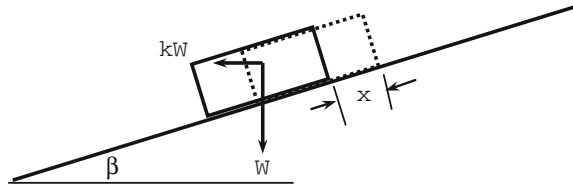
The mechanics of the sliding block is very simple.

D Driving force down the slope = $W(\sin \beta + k \cos \beta)$

R Resisting force = $[W(\cos \beta - k \sin \beta) - U] \tan f' + c'L$

where

Fig. 7 Equivalent sliding block model (x represents the relative displacement)



U Force due to pore water pressure

and

L Length of the block (represents the length of the slip surface)

We define a critical horizontal acceleration $k_c g$ so that due to its application on the mass of soil, the block is in limiting equilibrium; i.e. $D_c = R_c$. Subscript c refers to the critical condition. If we assume that, during sliding, the soil parameters and pore water pressures do not change, and equal to those at limiting condition, then k_c remains constant. The equation of motion of the sliding block can be written as follows:

$$\frac{W}{g} \ddot{x} = D - R = \frac{W \cos(\phi' - \beta)}{\cos(\phi')} (k - k_c) \quad (3)$$

$$k_c = \tan(\phi' - \beta) - U \frac{\sin \phi'}{\cos(\phi' - \beta)} + c' L \frac{\cos \phi'}{\cos(\phi' - \beta)} \quad (4)$$

where

x Relative displacement. Dots represent differentiation with respect to time.

Note that k is a function of time, representing average seismic acceleration factor.

If the soil parameters and/or the pore pressures change during sliding, then k_c also becomes a function of time.

The parameters of the sliding block are chosen, so that the critical acceleration for the real slip surface of the slope matches that of the sliding block. The main parameters controlling sliding displacements are: (1) the ratio k_c/k_m , (2) the value of k_m , (3) the duration of pulses or the peak velocity of the record or the peak displacements. There are various equations and charts, Ambraseys (1972), Sarma (1975), Franklin and Chang (1977), Ambraseys and Menu (1988), Sarma (1988), Sarma and Kourkoulis (2004) which give an estimate of the displacements during an earthquake. There are many other such estimates in the literature. Sarma and Kourkoulis looked at the various parameters of the earthquake record, which affect the computed displacements. The amount of displacement which can be considered as safe depends on the serviceability of the type of structure after the earthquake and the risk associated with failures.

Pitilakis (2001) and Stamatopoulos and Stamatopoulos (2001) provide some idea of the displacements that could be considered as safe in slopes and in other related structures.

11.2 Non-planar Sliding Surfaces for Displacements

There have been a few attempts to improve the basic Newmark concept. These attempts were in computing the displacements (a) along non-planar surfaces, discussed below, (b) when the soil strength along the slip surface changes significantly with shear displacements and (c) when the dynamic response of the sliding mass is included, Bray and Travasarou (2007).

Sarma (1981) used circular arc slip surfaces, since such a surface is the only non-planar surface on which rigid body motions can take place keeping the moving part and the fixed part of the slope in contact with each other. Displacements along any other non-planar surface require internal deformation of the rigid block. Logarithmic spiral curve appears to be the most critical slip surface in a static analysis. It is easy to determine the critical acceleration for this slip surface. Ling and Leshchinsky (1995) used this surface to compute the displacement by considering moment equilibrium about the centre of the spiral. According to the formulation of Ling and Leschinsky, the centre of gravity of the sliding mass remains at the same distance from the centre of the spiral during rotation. Therefore, any displacement, however small, will disconnect the sliding body from the main body of the slope. Therefore, the sliding block analogy fails. The dilatancy of the soil allows the upper part of the slope to keep in contact with the main body of the slope in straining before failure. But, the soil cannot expand to keep the sliding part in contact with the fixed part of the slope during sliding and therefore needs internal deformation. The computed displacement by this method does not represent the reality of the situation any better than the plane equivalent sliding block model. The two-block sliding model was used by Zarabi (1979) and is reported in detail in Whitman (1979) in connection with retaining wall problems. In this model, the mass of the wall and that of the soil remain unchanged during motion. Since the wall and the soil move in different directions, the equilibrium requires the instantaneous critical acceleration to change during motion. Therefore, the thrust on the wall changes. This change of thrust is considered in the analysis. Stamatopoulos (1992), based on the initial idea of Prof. Whitman, produced a model of two-block sliding uniformly on two different planes, taking into account the internal deformations. He also used the concept of mass transfer between blocks, the upper block becoming smaller while the lower block grows, providing more resistance to sliding. In his formulation, the geometry of the blocks is kept very simple for ease of computation. Ambraseys and Srbulov (1995) extended the Stamatopoulos (1992) model by introducing non-uniform motion. Stamatopoulos (1996) introduced the model of a chain of linked blocks sliding down a slope assuming the transfer of mass from the top-most block to the bottom-most block, and the intermediate

blocks remain unaffected. In this model, no internal deformations are considered, the chain-links being connected together by frictionless hinges. The chain is considered to be of uniform cross section.

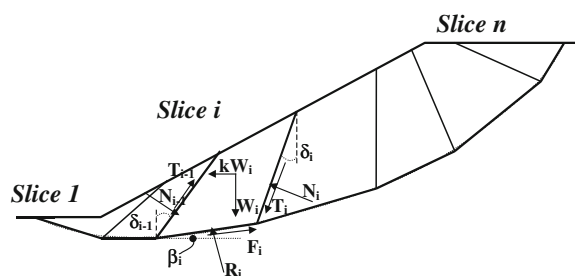
12 Multi-block Sliding Model

A new model was developed by Sarma and Chlimintzas (2001), which can be considered as an extension of the Ambraseys and Srbulov model. This is a multi-block model, where each block is able to move on its own plane keeping in contact but sliding along the sides of neighbouring blocks. This method takes into account the effect of internal deformation and transfer of mass between successive blocks. It is assumed that during sliding, the base and the internal sliding boundaries remain fixed in place while the soils move past these boundaries. The ultimate result is to define a deformed shape of the sliding mass. Depending on the toe situation, this model can accumulate mass at the toe, which in turn provides extra resistance to displacement, or lose mass in the toe-block. This model is suitable for computing co-seismic and post-seismic sliding displacements.

The starting point of this model is that a slope fails when a kinematic mechanism develops within the possible sliding mass, thus forming a general slip surface along with internal failure surfaces, Fig. 8.

For this part of the analysis, Sarma (1979a, b) method is used. This method derives a critical acceleration for the slope for failing along the critical slip surface and at the same time determines the kinematic mechanism of failure. This mechanism is transformed into the multi-block sliding model shown in Fig. 9. The model shows rigid blocks sliding on the slip surface. The rigid rod connecting two blocks is fixed on the one end and slides on the side of the neighbouring block. This allows the blocks to remain in contact with the slip surface as well as with its neighbouring blocks. Since the rods do not deform, the displacement of one block defines the displacements of others as shown in Fig. 10 and therefore it is a motion with single degree of freedom. The displacements of two neighbouring blocks are related by the following: $h = u_i \cos(\delta_i + \beta_i) = u_{i+1} \cos(\delta_i + \beta_{i+1})$; see Fig. 10. Therefore, for

Fig. 8 A slip surface in a slope showing the kinematic slip mechanism



vertical slice boundaries, when δ is zero for all slices, the horizontal displacement is common to all blocks.

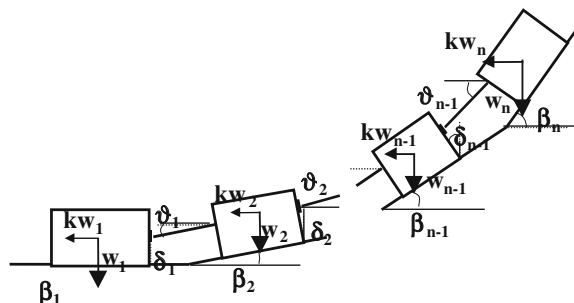
In this model, the blocks themselves are assumed rigid and the boundaries are fixed in space. Each block trying to slide past a boundary merely gives up a part of its mass to the neighbouring block. The model of mass transfer is explained in Fig. 11. The figure shows how the geometry of the blocks changes. Due to the displacement u_{i+1} of the block $i + 1$, the area JICE wants to occupy the area J'CC'E' but the slip surface does not allow this position. The model assumes that the part JICE, moving from one slope segment to another, deforms in such a way that in the new position it is in full contact with the slip surface, its side boundaries are E''C'' and J'C and the ground surface line is continuous. The new position of the deformed shape is J'CC"E", and the new ground surface line is a'E"J'b'. The area (or mass) that is removed from block $i + 1$ is enclosed by CC'C'' and is equal to the area defined by the new position J'E'E'' which is added to the block i . This implies that the area J'CC'E' has undergone a shear deformation in a direction parallel to the interslice surface. This model allows the change of contact forces, particularly the resistance offered by the cohesion. This also allows blocks to disappear when the whole block passes through a boundary. The equation of motion of this system can be found in Chlimintzas (2003).

Within this concept, we may visualise two situations. The first is a small displacement model, and the second is a large displacement model.

12.1 Small Displacement Model

When the displacements are small, compared to the size of the blocks, the transfer of mass and the change of geometry are negligible. Therefore, if the strength parameters do not change, the critical acceleration does not change. Therefore, the problem reverts to an equivalent single-block sliding on an equivalent plane surface same as the original Newmark model.

Fig. 9 Equivalent rigid multi-block sliding model



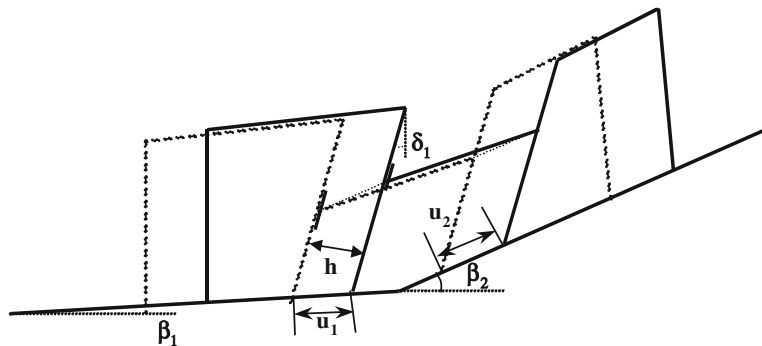


Fig. 10 Relationship between movements of neighbouring blocks

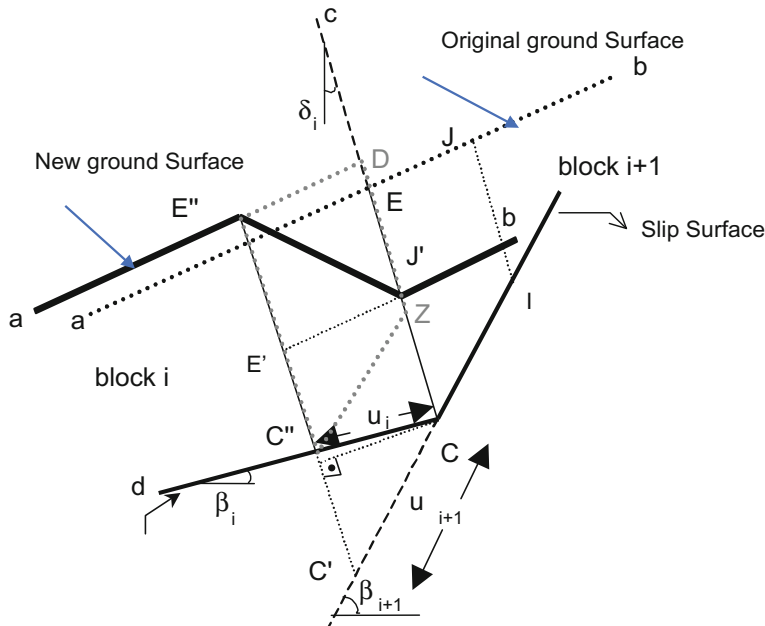


Fig. 11 Mechanism of mass transfer and the geometry change

12.2 Large Displacement Model

In this model, during sliding, the change of mass is taken into account. Due to the change of mass, the equation of motion becomes nonlinear and the solution is found numerically only. It is assumed that during a small time step, the mass remains constant and therefore can be solved. But the mass and the corresponding critical acceleration are updated at the end of each time step. Change of mass may create a

more stable configuration, and the sliding motion may stop. In the case of the simple plane sliding block, a statically unstable condition will produce infinite displacement while the mass transfer model may stop the motion at some time. Figure 12 shows a result of such analysis. In this figure

AD Original ground surface

A'F''H'E''J'D' New ground surface

ABCD Original slip surface

A'ABCD' New slip surface

Note u_1 , u_2 and u_3 are different from but related to each other.

12.3 The Toe Problem

In the large displacement model, the generation of a stable configuration will depend on the toe situation. In Fig. 13, three alternative toe situations are shown. Note the differences between the slope angle and the angle of the slip surface at the exit point. The mass of soil exiting through the toe will find itself hanging in the air.

In the case (a), the mass of this hanging part of the soil is likely to be lost;

In the case (b), the mass of soil may provide some resistance to movement but small;

In the case (c), the mass of soil will provide resistance to movement. An additional slice can be considered which can grow from zero mass at the beginning, providing increasing resistance with time (Fig. 15).

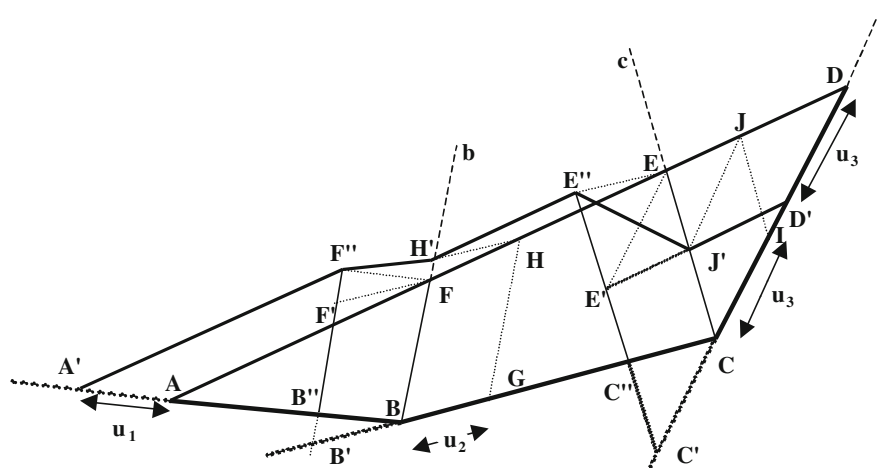


Fig. 12 Geometry changes and mass transfer in a three-block system with straight ground surface

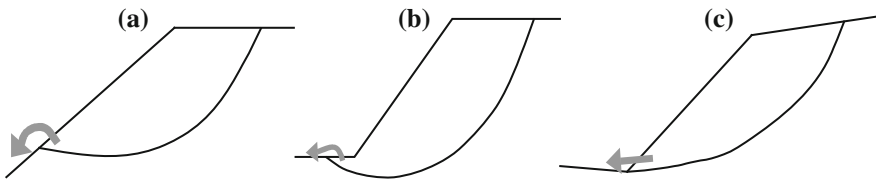


Fig. 13 Alternative toe situations

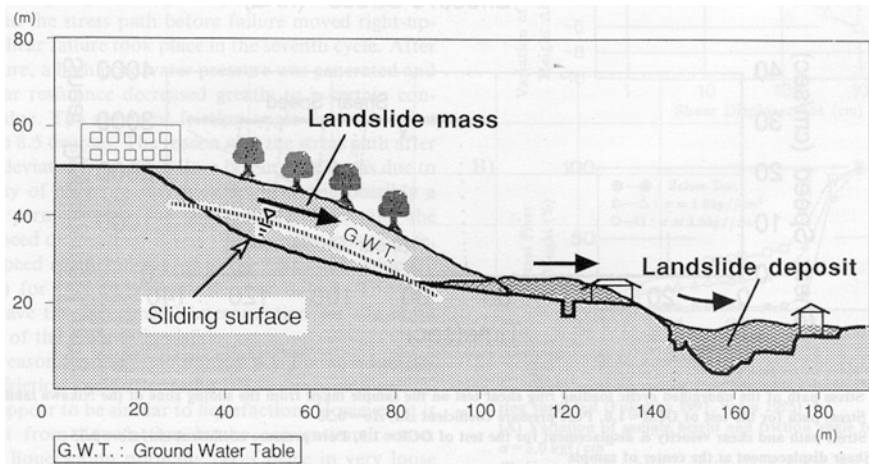


Fig. 14 Nikawa landslide, Kobe earthquake (after Sassa et al. 1996)

12.4 Test Case for Large Displacement Model: Example of a Slope Failure in Hyogoken-Nambu (Kobe) Earthquake on 17 January 1995 in Japan

Figure 15 shows three computed displacements and the corresponding change in the slope after sliding. Cases a and b show the deformed shapes when no toe loss is included. Case a uses vertical slices, and case b uses inclined slices obtained from Sarma (1979a, b) analysis. Case c includes the toe loss, and the toe situation is according to that existed before sliding. The results show that when toe loss is included and the strength is appropriate, large displacements of a sliding mass can be modelled correctly. In a design problem, the strength is unknown for this kind of situation and can only be guessed.

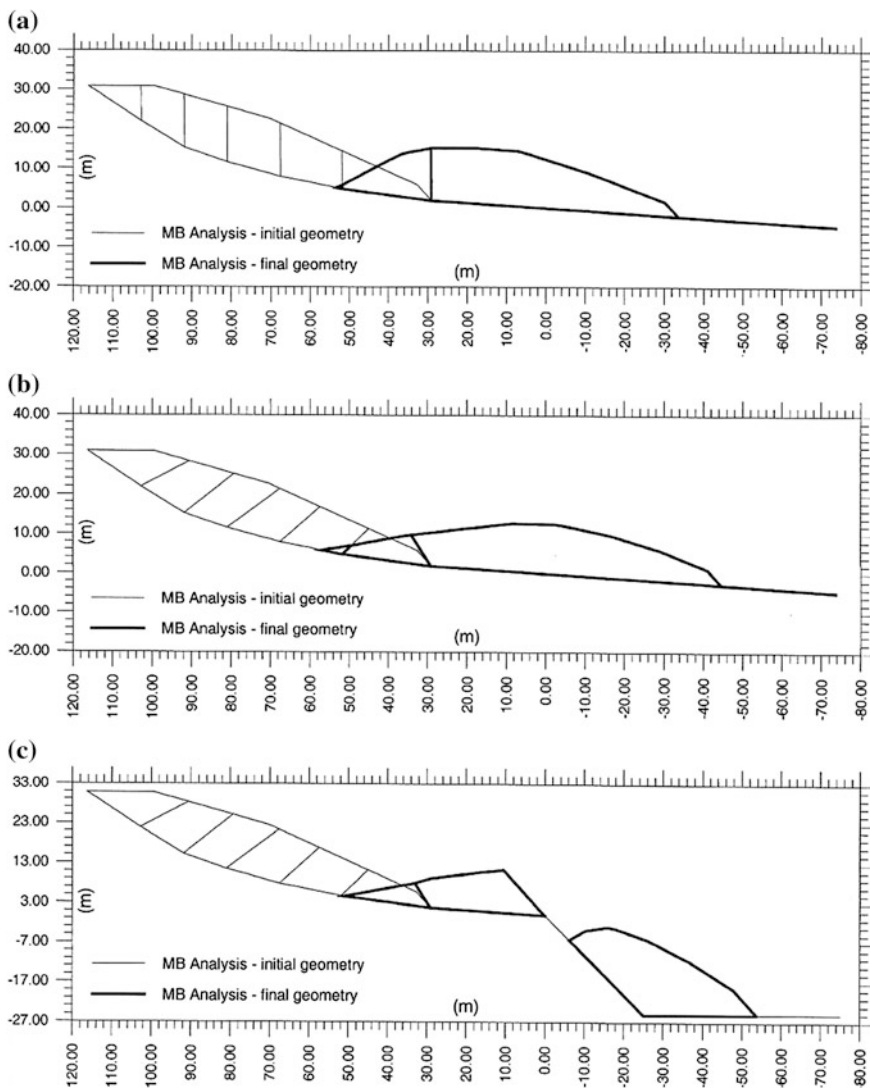


Fig. 15 Nikawa landslide, Kobe earthquake, computed displacements (after Chlimintzas (2003), p. 174)

13 Finite Element Verification of Accuracy of Sliding Displacement Model

The multi-block sliding model is extensively used and modified by Stamatopoulos and his colleagues. They have looked at the change of strength of the materials on the slip surface when displacements are involved, Stamatopoulos (2009, 2015).

Stamatopoulos (2017) [personal communication] has carried out finite element verification of co-seismic displacements. He has found that when only the bed-rock accelerations are used, then the sliding block displacements do not agree well with the FE displacements. But, when the response of the structure is considered in the sliding block analysis, as in computing the average accelerations, then the two displacements agree very well and the multi-block model produces considerably better results compared to the single sliding block model. He has considered two cases, one of a gravity retaining wall, Stamatopoulos et al. (2006), and the second of a rock slope with a plane dense sandy interface (personal communication).

14 Conclusions

1. Assessment of seismic slope safety requires the determination of the ground motion (accelerations) in the slope.
2. Seismic displacement is a better criterion for assessment of safety than factor of safety.
3. Soil parameters should be determined with as much accuracy as possible.
4. For small seismic displacements, relative to the length of the slide, mass transfer can be ignored and the single sliding block model can be used without significant difference in the results.
5. When large displacements are involved, the results produced by neglecting mass transfer become increasingly conservative.
6. Aseismic or post-seismic slides are generally induced by severe reduction of shear strength and not by application of inertia forces. Once motion has begun, only the rearrangement of the material to a more stable geometry can cause it to stop.
7. The developed multi-block model represents a dynamic limiting equilibrium method of slices technique. It provides a simple but comprehensive method to assess the sensitivity of slopes to seismic loads and estimate the magnitude of the expected displacements.
8. Unlike some other sliding block models, the present model allows internal shear movements to happen and energy to be dissipated along internal shear surfaces.

Acknowledgements I wish to thank Dr. Constantinos Stamatopoulos for reading through the manuscripts, correcting it where necessary and providing me with his most recent unpublished work on finite element verification of sliding displacements.

References

Ambraseys, N., & Sarma, S. K. (1967). The response of earth dams to strong earthquakes. *Geotechnique*, 17(3), 181–213, 181–213.

Ambraseys, N. (1972). Behaviour of foundation materials during strong earthquakes. In Proceedings of the 4th European Symposium Earthquake Engineering (Vol. 7, pp. 11–12). London.

Ambraseys, N., & Menu, J. (1988). Earthquake induced ground displacements. *Earthquake Engineering Straight Dynamic*, 16(7), 985–1006.

Ambraseys, N., & Srbulov, M. (1995). Earthquake induced displacements of slopes. *Soil Dynamic and Earthquake Engineering*, 14, 59–71.

Bishop, A. W. (1955). The use of slip circle in the stability analysis of slopes. *Geotechnique*, 5(1), 7–17.

Bouckovalas, G., & Papadimitriou, A. (2005). Numerical evaluation of slope topography effects on seismic ground motion. *Soil Dynamic and Earthquake Engineering*, 25, 547–558.

Bray, J. D., & Travasarou, T. (2007). Simplified procedure for estimating earthquake-Induced deviatoric slope displacements. *Journal Geotechnical and Geoenvironmental Engineering*, ASCE, 133(4), 381–392.

Chlimintzas, G. O. (2003). *Seismic displacements of slopes using multi-block sliding technique*. PhD Thesis, Imperial College, London.

Faccioli, E., Vanini, M., & Frassine L. (2002). Complex site effects in earthquake ground motion, including topography. In *Paper No. 844, 12th European Conference on Earthquake Engineering*, Elsevier Ltd.

Fellenius, W. (1927). *Erdstatische Berechnungen* (calculation of stability of slopes). W. Ernst und Sohn, Berlin (Revised edition 1939).

Franklin, A. G., & Chang, F. K. (1977). *Earthquake resistance of earth and rockfill dams: Permanent displacements of embankments by Newmark sliding block analysis*. Misc. Paper, US Corps of Engineers, Vicksburg, Mississippi, USA.

Janbu, N. (1957). Earth pressure and bearing capacity calculations by generalised procedure of slices. In *Proceedings of the 4th International Conference on Soil Mechanics and Foundation Engineering* (Vol. 2, 207–212).

Lighthall, P. (1979). *Dimensionless charts for critical acceleration and static stability of earth slopes*. MSc dissertation Imperial College Civil Engineering Department Soil Mechanics and Engineering. SEIS. Section London SW7.

Ling, H. I., & Leshchinsky, D. (1995). Seismic performance of simple slopes. *Soils and Foundations*, 35(2), 85–94.

Morgenstern, N., & Price, V. (1965). The analysis of the stability of general slip surfaces. *Geotechnique*, 15(1), 79–93.

Newmark, N. (1965). Effects of earthquakes on dams and embankments. *Geotechnique*, 15, 139–160.

Pitilakis, K. (2001). *Final report of project: Seismic ground displacements as a tool for town planning, design and mitigation*. Work performed by Aristotle University of Thessaloniki, under the grant of the European Commission, agreement No. ENV4-CT97-0392.

Pratter, E. G. (1979). Yield acceleration for seismic stability of slopes. *Journal of GT Division ASCE*, 105(GT5), 682–687.

Sarma, S. K. (1973). Stability analysis of embankments and slopes. *Geotechnique*, 23(3), 423–433.

Sarma, S. K. (1975). Seismic stability of earth dams and embankments. *Geotechnique*, 4, 743–761.

Sarma, S. K. (1979a). Stability analysis of embankments and slopes. *Journal of the Geotechnical Engineering Division, ASCE*, 105(GT12), 1511–1524.

Sarma, S. K. (1979b). *Response and stability of earth dams during strong earthquakes*. Misc. Paper GL-79-13, Grant Agreement NO. DAERO-75-G-010, Geotechnical Laboratory, US

Army Corps of Engineers Waterways Experiment Station, PO Box 631, Vicksburg, Miss 39180.

Sarma, S. K. (1981). Seismic Displacement Analysis of Earth Dams. *Journal of Geotechnical Engineering Division ASCE*, 107, GT12.

Sarma, S. K. (1988). Seismic response and stability of earth dams. In A. Kordze (Ed.), *Seismic risk assessment and design of building structures* (pp. 143–160). Omega Scientific.

Sarma, S. K. (1999). Seismic slope stability—The critical acceleration. In Seco e Pinto (Ed.), *Earthquake Geotechnical Engineering* (pp. 1077–1082). Balkema, Rotterdam. *Proceedings of the 2nd International Conference on Earthquake Geotechnical Engineering*, Lisbon, Portugal.

Sarma, S., & Chlimintzas, G. (2001). Co-seismic and post-seismic displacements of slopes. In *15th International Conference Soil Mechanics and Geotechnical Engineering, Lessons Learned from Recent Strong Earthquakes, Earthquake Geotechnical Engineering Satellite Conference*, Istanbul, Turkey.

Sarma, S. K., & Irakleidis, A. (2008). A simplified method of analysis for the seismic response of slopes. In *3rd Pan Hellenic conference on Earthquake Engineering & Engineering Seismology*, Athens.

Sarma, S., & Kourkoulis, R. (2004). Investigation into the prediction of sliding block displacements in seismic analysis of earth dams. In *Proceedings of the 13th WCEE*, paper no 1957, Vancouver, Canada.

Sarma, S. K., & Tan, D. (2006). Determination of critical slip surface in slope analysis. *Geotechnique*, 56(8), 539–550.

Sassa, K., Fukuoka, H., Scaracia-Mugnosa, G., & Evans, S. (1996). Earthquake induced landslides—Distribution, motion and mechanisms. In *Hyogoken-Nambu Earthquake* (pp. 53–64). Soils and Foundations, Special (January 1996) issue on Geotechnical aspects of the January 17, 1995.

Seed, H. B., & Idriss, I. M. (1982). Ground motions and soil liquefaction during earthquakes. Earthquake Engineering Research institute Monograph, Oakland, USA

Seed, H. B., & Martin, G. (1966). The seismic coefficient in earth dam design. *Journal of SMFE Division ASCE*, 92, SM3.

Spencer, E. (1973). Thrust line criterion in embankment stability analysis. *Geotechnique*, 23(1), 85–100.

Stamatopoulos, C. (1992). Analysis of a slide parallel to the slope. In *Proceedings of the 2nd Greek National Conference of Geotechnical Engineering*, 1, 481–488 (in Greek).

Stamatopoulos, C. (1996). Sliding system predicting large permanent co-seismic movements of slopes. *EESD*, 25(10), 1075–1093.

Stamatopoulos, C., & Stamatopoulos, C. K. (2001). *Final report of project: Seismic ground displacements as a tool for town planning, design and mitigation*. Work performed by Kotzias Stamatopoulos co. under the grant agreement of the European Commission project ENV4-CT97-0392.

Stamatopoulos, C., Velgaki, E., Modaressi, A., & Lopez-Caballero, F. (2006). Seismic displacements of gravity walls by a two-body model. *Bulletin of Earthquake Engineering, Springer*, 4(3), 295–318.

Stamatopoulos, C. (2009). Constitutive modelling of earthquake induced slides on clays along slip surfaces. *Landslides*, 6(3), 191–207.

Stamatopoulos, C. (2015). *Constitutive and multi-block modelling of slides on saturated sands along slip surfaces*. Soils and Foundations, The Japanese Geotechnical Society (in press).

Tan, D., & Sarma, S. K. (2008). Finite element verification of an enhanced limit equilibrium method for slope analysis. *Geotechnique*, 58(6), 481–488.

Whitman, R. V. (1979). Dynamic behavior of soils and its application to civil engineering projects. State of the art reports and special lectures. In *6th Panamerican Conference on Soil Mechanics and Foundation Engineering* (pp. 59–105). Lima, Peru, December.

Zarabi-Kashami, K. (1979). *Sliding of gravity retaining walls during earthquakes considering vertical acceleration and changing inclination of failure surface*. SM Thesis, Department of Civil Engg. MIT.

On the Use of Scaled Model Tests for Analysis and Design of Offshore Wind Turbines

Subhamoy Bhattacharya, Georgios Nikitas and Saleh Jalbi

Abstract Large-scale offshore wind farms have emerged as a critical renewable energy technology to reduce greenhouse gas (GHG) emission and autonomy in energy production. Each of these wind farms consists of many wind turbine generators (WTG) mounted on a support structure and is capable of generating up to (as we write the paper) 1.2 GW of power. These are relatively new technological advancements which are installed in harsh offshore environments. Naturally, the design of foundations for such structures is challenging. Furthermore, WTG support structures due to its shape and form (heavy rotating mass at the top of a slender tower) are dynamically sensitive in the sense that the natural frequency of such system is very close to the forcing frequencies acting on them. The aims of this keynote lecture are as follows: (a) summarise the loads acting on the structure together with its associated complexity; (b) discuss the challenges in designing such foundations; (c) describe the rationale behind scaled models tests that supported the development of offshore wind turbine design philosophy; (d) draw parallel with other geotechnical scaled model tests and discuss the scaling issues; (e) propose a method to scale the model tests for predicting prototype consequences. While there is no track record of long-term performances of these new structures, design and construction of these must be carried out for 25–30 years and it is argued that scaled model tests are necessary. Finally, the lecture concludes that well thought out scaled models tests can be effective in predicting the long-term issues and engineers need to learn from other disciplines.

Keywords Offshore wind turbines · Technology readiness level (TRL)
Monopiles · Dynamic soil-structure interaction

S. Bhattacharya (✉) · G. Nikitas · S. Jalbi
University of Surrey, Guildford, UK
e-mail: S.Bhattacharya@surrey.ac.uk; Subhamoy.Bhattacharya@gmail.com

1 Introduction

Offshore wind farm is a recent innovation and holds promise in tackling global challenges of combating climate change and clean air. These new technologies are scalable with each of these modern wind farms capable of generating over 1.2 GW of power. Figure 1 shows the installed wind farm in Europe together with the generating capacity of the countries as of 2016. Recently, Denmark produced 120% of the country's power requirements through wind and the excess 20% power were exported to the neighbouring countries. China, though started very late compared to Europe, made remarkable progress, and the ambition is to generate 30 GW of power by 2020 from offshore wind, for further details, see Bhattacharya et al. (2017). In this context, it is important to highlight the advantages of offshore wind farms given the consensus reached on climate change agreement by the nations of the world at the twenty-first meeting of the Conferences of the Parties (COP 21). The advantages of offshore wind are highlighted through an example from the UK. Further details can be found in Bhattacharya (2017) and Bhattacharya et al. (2017).

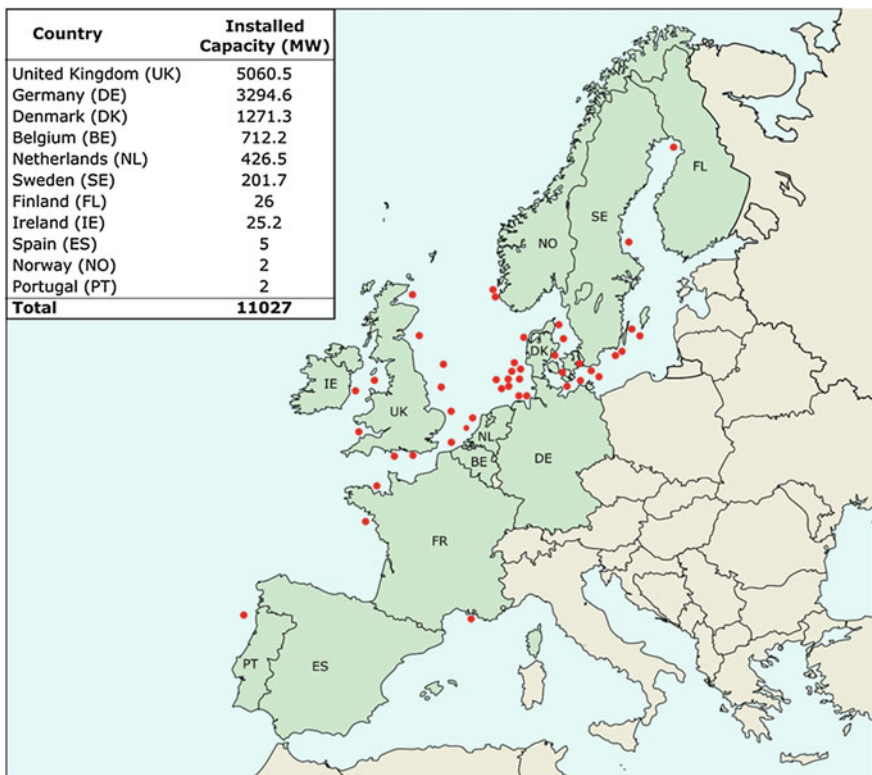


Fig. 1 Wind farms in Europe

In a recent policy and legislation discussion, there is a commitment to completely take off petrol and diesel vehicles from UK road by 2040 and to be replaced by electric vehicles. Therefore, there will be an additional 30 GW electricity requirement, and two options are considered here: ten large sized Nuclear Power Plants (NPP) costing circa 25 Billion USD each and taking approximately 20 years to construct one of them. On the other hand, 30 GW electricity can be produced using 5000 offshore turbines of 6MW and typical cost of each turbine is about 6–8 million USD. Furthermore, it takes about 6–9 months to construct a wind farm. Figure 2 shows a photograph of a wind farm where an array of wind turbines can be observed. A typical wind farm consists of inter-array electric cable joining the turbines which in turn is connected to an offshore substation. A further export cable transmits the power from offshore station to the onshore grid, see Fig. 3 for a schematic view and layout of an offshore wind farm.

Before the details of engineering of these systems are discussed, it is considered useful to discuss the sustainability of wind resources as it is often claimed that wind does not blow all the time.



Fig. 2 Photograph of a wind farm

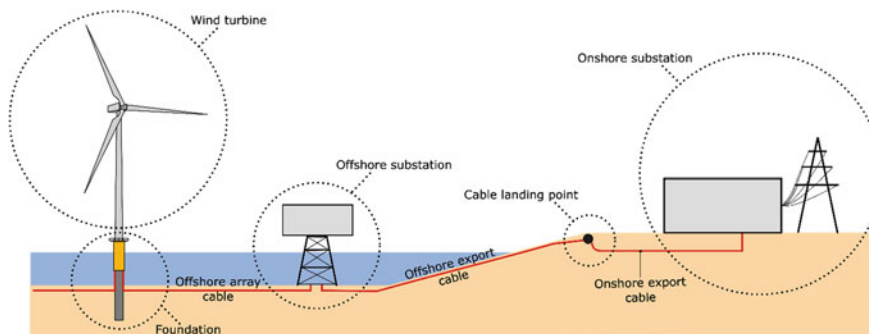


Fig. 3 Overview of wind farm

Wind, essentially an atmospheric air in motion, is a secondary source of energy and is dependent on the sun. The electromagnetic radiation of the sun unevenly heats the surface of the earth and creates a temperature gradient in the air, thereby also developing a density and pressure difference. The disparity in differential heating of the surface of the earth is also a result of specific heat and absorption capacity of the materials such as sand, clay, intermediate and mixed soils, rocks, water. This also results in differential heating of air in different regions and also at different rates. The physical process or mechanism that governs the air flow is convection. Common examples are land and sea breezes in coastal regions. The direction and velocity of wind is partly influenced by the rotation of the earth, topography of the earth surface, and thus, coastal areas are attractive locations for harvesting wind power. This above discussion shows the sustainability of the wind resource as it is related to the sun and earth's motion.

Figure 4 shows the development of wind turbines from 3 to 8 MW, and it may be observed that with the rated capacity, the height of the tower increases and the top mass also increases. Research and design are underway to develop 20 MW turbine. In a recent development, floating wind turbine has been installed in Scotland and Fig. 5 shows the schematic view of the system.

Foundations constitute the most important design consideration and often determine the financial viability of a project. Typically, foundations cost 25–34% of the whole project, and there are attempts to get the costs down. Many aspects must be considered while choosing and designing the foundation for a particular site. They include: ease to install under most weather conditions, varying seabed conditions, aspects of installation including vessels and equipment required and local regulations concerning the environment (noise). Figure 6 shows the various types of foundations commonly used today for different depths of water. Monopile (Fig. 6c), gravity-based foundations (Fig. 6b) and suction caissons (Fig. 6a) are currently being used or considered for water depths of about 30 m. For water depth between 30 and 60 m, jackets or seabed frame structures supported on piles or caissons are either used or planned. Floating system is being considered for deeper waters, typically more than 60 m. However, selection of foundations depends on seabed, site conditions, turbine and loading characteristics and the economics and

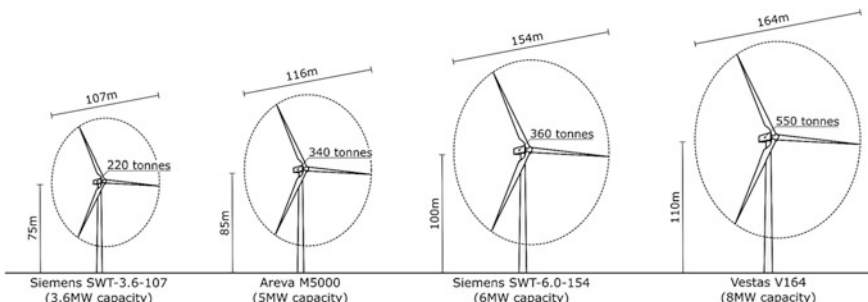


Fig. 4 Gradual development of offshore wind turbines

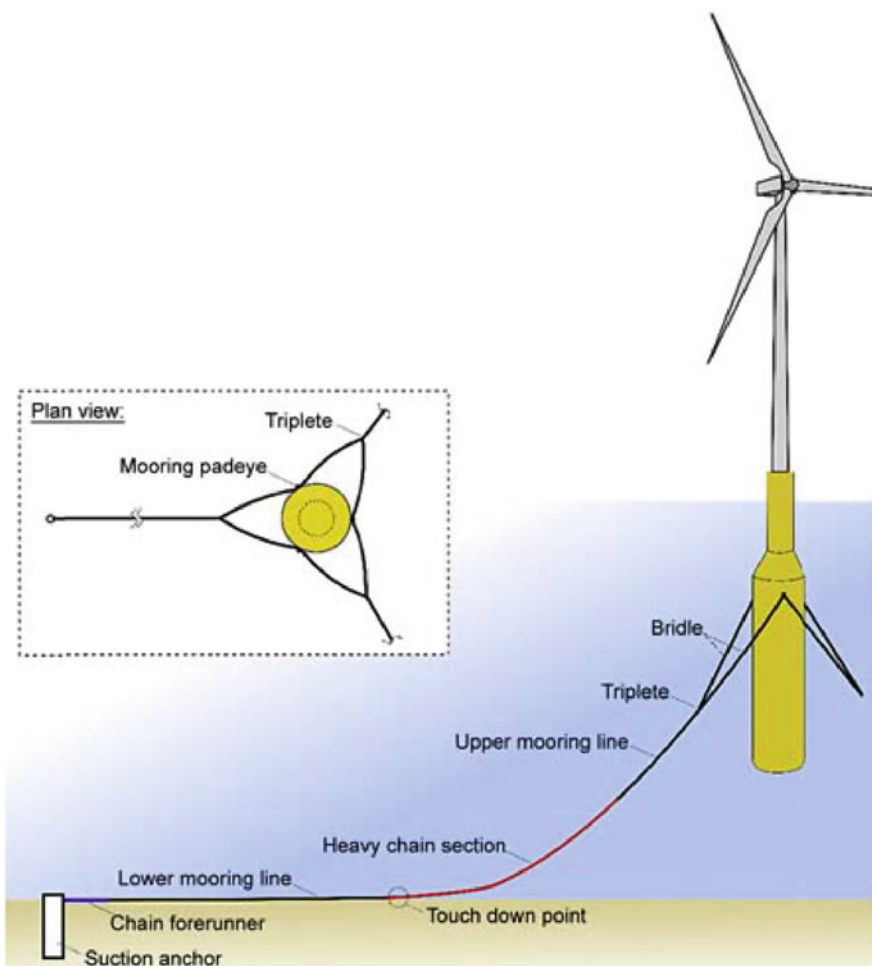


Fig. 5 Details of Hywind floating offshore wind turbine

not always on the water depth. Monopile is a large diameter column inserted deep into the ground and is the most used foundation so far in the offshore wind industry.

While the structure looks very simple, it is more complex than one can imagine and the primary reason is due to a heavy rotating mass acting the top of a slender tower. Based on Fig. 4, for 8 MW turbine, there is 550 tonnes of mass and out of which circa 90 tonnes is rotating. Figure 7 shows a mechanical model of a wind turbine system supported on monopile together with nomenclature of different components. In the model, the foundation is replaced by a set of four springs: Vertical spring (K_V having the units of MN/m), lateral (K_L having the units of MN/m), rotational/rocking (K_R having the units GNm/rad) and cross-coupling (K_{LR} having the units of GN). It may be noted that the torsional spring is not

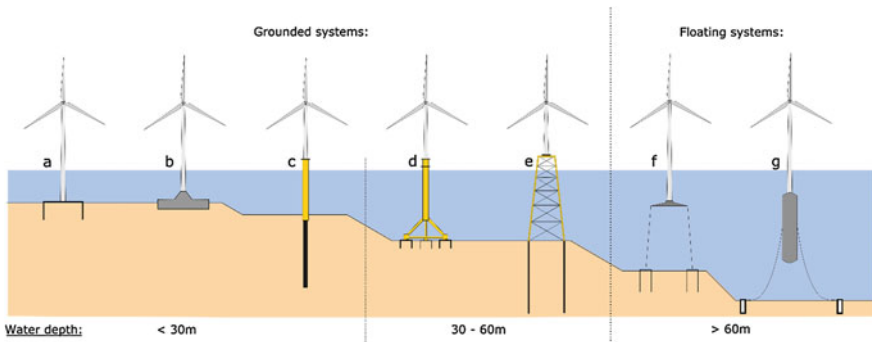


Fig. 6 Different foundations to support offshore wind turbines based on water depths

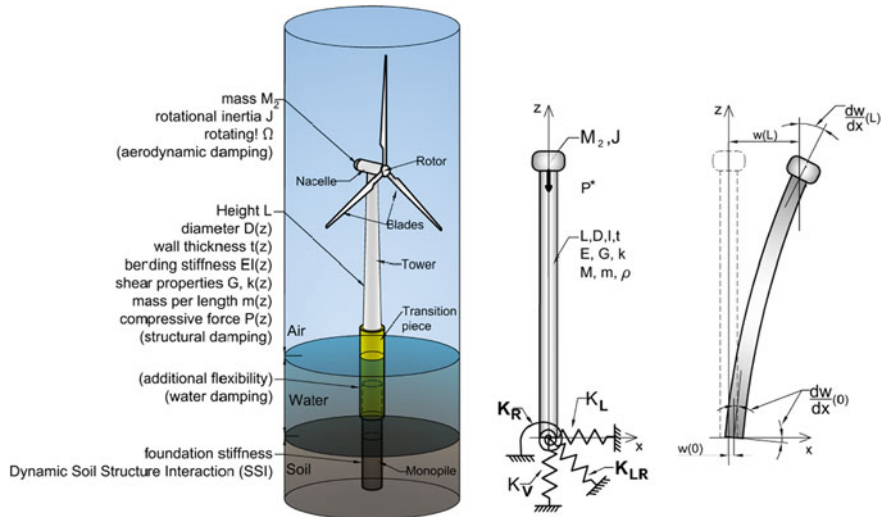


Fig. 7 Offshore wind turbine system with structural model, see Arany et al. (2015a, b)

included as the effect of torsional loads is minimal due to the yaw bearing at the top of the tower which supports the rotor-nacelle assembly (RNA). Different loads acting on the turbine can be visualized in Fig. 8. The loading on an offshore wind turbine is quite complex and is described in the next section. However, detailed discussion on loading together with the method to calculate them can be found in Arany et al. (2015a, b, 2017).

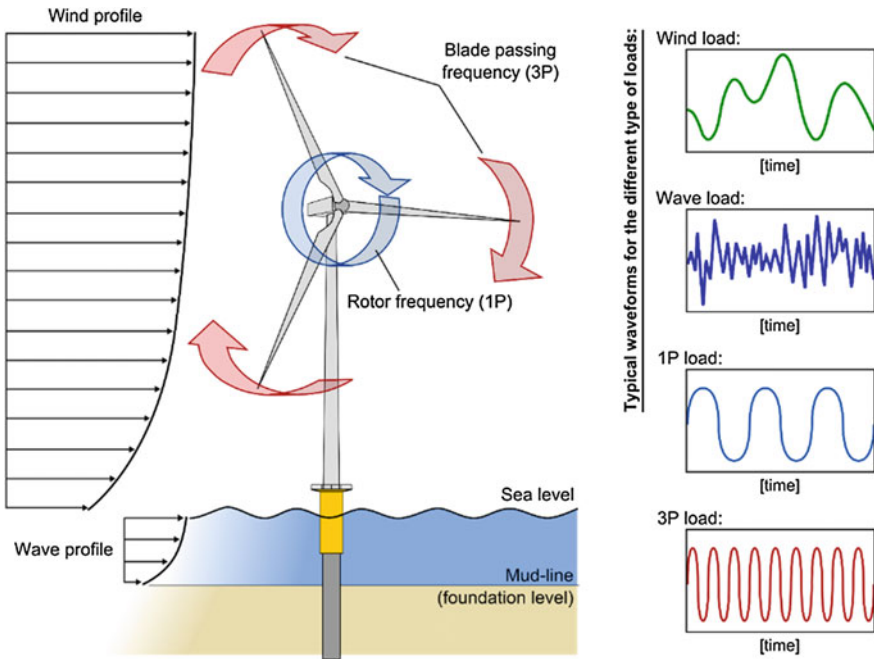


Fig. 8 Typical loads acting on an offshore wind turbine

2 Complexity of Loading

Offshore wind turbines are characterized by a unique set of cyclic and dynamic loading conditions and are schematically depicted in Fig. 8. These include: (i) load produced by the turbulence of the wind, whose amplitude is function of the wind speed; (ii) load caused by waves crashing against the substructure, whose magnitude depends on the height and period of waves; (iii) load caused by mass and aerodynamic imbalances of the rotor, whose forcing frequency equals the rotational frequency of the rotor (referred to as 1P loading in the literature); (iv) loads in the tower due to the vibrations caused by blade shadowing effect (referred to as 3P loading in the literature), which occurs as each blade passes through the shadow of the tower.

The loads imposed by wind and wave are random in both space (spatial) and time (temporal); as a result, these are better described statistically by using the Pierson–Moskowitz wave spectrum and Kaimal wind spectrum, shown in Fig. 9. 1P and 3P will be a range of frequency depending on the turbine type and the operating range. Figure 9 shows the range of frequencies for NREL 5 MW turbine. It is clear from the frequency content of the applied loads that the designer in order to avoid the resonance of the OWT has to select a design frequency that lies outside the ranges of forcing frequencies. Specifically, the Det Norske Veritas (DNV) code

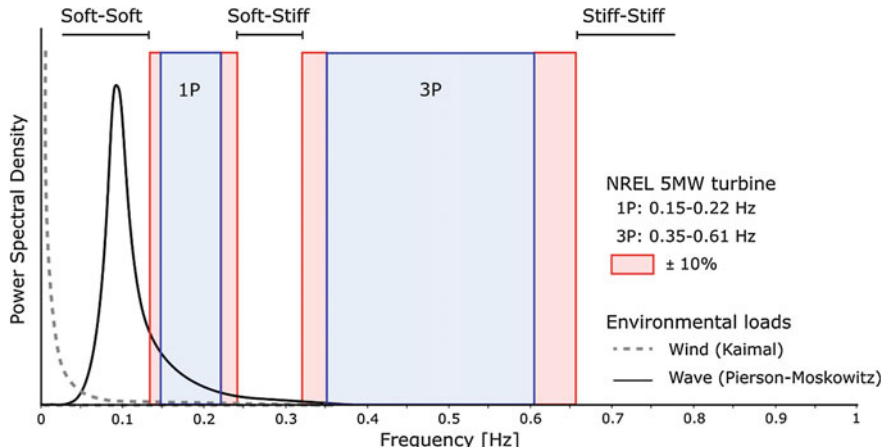


Fig. 9 Qualitative power spectrum of main forcing frequencies and different design approaches considering a NREL 5 MW wind turbine

recommends that in order to avoid resonance, the natural global frequency of the wind turbine should be at least $\pm 10\%$ away from the main forcing frequencies, i.e. wind, wave, 1P and 3P. Three design approaches are possible: soft-soft (natural frequency $< 1P$), soft-stiff (natural frequency between 1P and 3P) and stiff-stiff (natural frequency $> 3P$). Current design approach is *soft-stiff*, and the target natural frequency of the whole wind turbine system is between 1P and 3P. It is therefore clear that the natural frequency of the whole system is very close to forcing frequencies making it dynamically sensitive.

Based on the above discussion on the loading of an offshore wind turbine structure and the natural frequency of the whole system, it is clear that the following interactions are possible:

1. Aerodynamic interaction due to the wind passing through the blades. It may be noted that the loads at the hub are ultimately transferred to the foundations.
2. Hydrodynamic interaction due to the waves slamming the substructure.
3. Due to the controlling action of the wind turbine, i.e. yaw and pitching action, the wave and wind load may act in different directions. For a fully developed sea, the wave will act in the direction of the wind. However, in order to maintain a constant power, there will be controlling action of the turbine and the turbine may not face the wind directly causing a wind-wave misalignment.
4. Cyclic as well as dynamic soil-structure interaction due to the cyclic loads acting on the foundation.

3 Issues in Geotechnical Analysis and Design

Offshore wind turbines are a relatively new innovation with no track record of long-term performance. It is required to design these structures for 25–30 years, and it is being expected to produce power for the entire design life. However, there are uncertainties related to long-term performances which can be described as *known-unknowns*, and there may be *unknown-unknowns*. Some of these aspects are described below.

Soil-structure interaction (SSI) can be cyclic as well as dynamic and will affect the following. The three main uncertainties in terms of long-term design issues can be summarized as follows:

1. The load acting on a wind turbine foundation is not symmetric two-way cyclic but biased one-way cyclic, and as a result, there is the chance of progressive tilting. The real question is whether the foundation will *tilt* progressively under the combined action of millions of cycles of loads arising from the environment (wind, wave) as well as on-board machineries (rotor frequency-1P and blade passing frequency-2P/3P). Figure 10 shows a simplified estimation of the midline bending moment acting on a monopile type foundation following Bhattacharya et al. (2017). It is clear that the cyclic load is asymmetric which depends on the site condition, i.e. relative wind and wave component. If the foundation tilts more than the allowable set by the turbine manufacturer, it may be considered failed based on Serviceability Limit State (SLS) criteria. This may also make the warranty of the turbine null and void.
2. Repeated cyclic or dynamic loads on a soil cause alteration in the properties which in turn can alter the stiffness of foundation. A change in support stiffness (i.e. the foundation and Fig. 7 is referred in this regard) may cause a change in

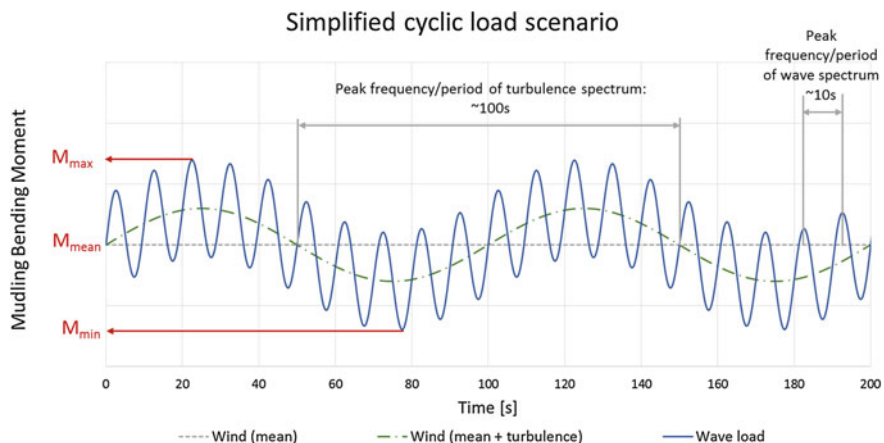


Fig. 10 Simplified bending moment profile at the mudline level for a monopile-supported wind turbine

natural frequency, which can lead to a shift from the design/target value. As a result, the system may get closer to the forcing frequencies. This issue is particularly problematic for soft-stiff design (i.e. the natural or resonant frequency of the whole system is placed between upper bound of 1P and the lower bound of 3P) as any increase or decrease in natural frequency will impinge on the forcing frequencies and may lead to unplanned resonance. This may lead to loss of years of service, which is to be avoided.

3. Wind and wave loads may act in different directions, and one of the uncertainties is predicting the long-term behaviour of the turbine taking this misalignment into consideration. While the blowing wind creates the ocean waves and ideally they should act collinearly. However, due to operational requirements (i.e. to obtain steady power), the rotor often needs to feather away from the predominant direction (yaw action) which creates wind-wave misalignment.

3.1 *Need for Scaled Model Testing*

As mentioned before, these are new structures with no track record of long-term performance. It is therefore important to predict the long-term issues so that appropriate maintenance issues may be planned to reduce loss of revenue due to downtime. For example, a crack in a blade can lead to misalignment in the whole wind turbine leading to higher 1P load. Replacement of a blade or maintenance can be expensive as it involves an offshore vessel and downtime of the turbine. Again, the turbine structure may be exposed to extreme storm events when the loads will be much higher than the operational loads. Following the storm event, the load levels will be back to operational and it is necessary to predict if the deformation during the storm levels to ensure trouble-free operation. Another aspect that makes this problem unique is the multiple cyclic/dynamic loads acting on the foundation. Each of the four main loads described in Fig. 8 has unique frequency, magnitude and applies different number of cycles. Wind thrust and waves will apply larger loads. As water depths increase, the wave load will increase. The wind thrust load depends on the blade diameter. On the other hand, the 1P and 3P loads are orders of magnitude lower but will apply a large number of cycles to the foundation.

It is therefore essential to understand the mechanisms that may cause the change in dynamic characteristics of the structure or the scenarios under which there will tilt and if it can be predicted through analysis. It is important to also learn from other disciplines if similar problem exists. Section 1.5 takes an example from aerospace engineering from a well-known problem known as “*ground resonance*” which is quite similar to this problem in the sense that a heavy rotating mass acts on the top of a beam.

An effective and economic way to study the behaviour (i.e. understand the physics behind the real problem) of an engineering system is by carefully

conducting designed scaled model tests in laboratory conditions. These tests can be repeated by changing the parameters, and different phenomenon can be identified. For the problem in hand, the main objective is to simulate (as realistically as possible) the application of millions of loading cycles by keeping constant the similitude relations. One of the important conditions that must be preserved is the dynamic sensitive nature of the structure.

Based on the discussion in the earlier section of the wind turbine structure and the loading, it is clear that the behaviour of offshore wind turbine is *Aero-Hydro-Cyclic & Dynamic-Soil-Structure-Interaction*. Arguably, this is one of the most complex interaction problems. Ideally, aerodynamic problems are better modelled in a wind tunnel and hydrodynamic problems are studied in wave tank. On the other hand, cyclic and dynamic soil-structure interaction problems are best studied in a geotechnical centrifuge. Therefore, one can argue the best way to model the problem is place a wind tunnel and a wave tank onboard the geotechnical centrifuge and it is currently impossible. It has been pointed out in the literature that parasitic (unwanted) vibrations of a geotechnical centrifuge prevent modelling the cyclic and dynamic foundation-soil interaction.

One of the ways to study these complex interactions is to use intelligence to identify the important interactions that can solve the various *known-unknowns*. In the course of the experimental investigation, it is hoped that some of the *unknown-unknowns* may also be identified.

It is considered important to list the design challenges:

1. Prediction of foundation stiffness both for small amplitude and large amplitude vibrations and deformations. The small amplitude vibration is required for natural frequency estimate of the whole system. This needs to be compared with target natural frequency. Furthermore, the natural frequency will need to be used in conjunction with the forcing frequencies (mainly due to wave, 1P and 3P) for calculating the dynamic loads.
2. The foundation stiffness at large amplitude vibration is needed for estimating the deformation of the foundation under operational and storm loading.
3. Changes in foundation stiffness due to episodes of storm loading and wind-wave misalignment.

The cost of foundations is typically 25–35% of the overall cost of an offshore wind farm project. In order to reduce the levelized cost of energy (LCOE), new cost-effective types foundations are being proposed. However, before any new type of foundation can be used in a project, a thorough technology review is often carried out to de-risk it and in order to protect the interest of the stakeholders. For a wind farm project, the major stakeholders are the developer, the insurance company. Taking the concepts from aerospace industry, European Commission defines this through technology readiness level (TRL) numbering starting from 1 to 9, further details of which can be found in Nikitas et al. (2016). One of the initial TRL is the proof of concept which is verification of the technology validation in the laboratory environment. This would mean conforming to the fundamental principles through

Table 1 Definition of TRL

TRL level as European Commission
TRL-1: Basic principles verified
TRL-2: Technology concept formulated
TRL-3: Experimental proof of concept
TRL-4: Technology validated in lab
TRL-5: Technology validated in relevant environment
TRL-6: Technology demonstrated in relevant environment
TRL-7: System prototype demonstration in operational environment
TRL-8: System complete and qualified
TRL-9: Actual system proven in operational environment

testing as experiments are essentially a very small prototype. Scaled model testing can be used in such cases and will bring out the limitations of any design and makes one think to improve (Table 1).

3.2 What Can Be Learnt from Other Similar Problems

Figure 11 shows two models: (a) a model of a helicopter as it lands on a surface; (b) wind turbine structure together with the support system. Figure 12 shows an experiment whereby the helicopter collapsed due to resonance type failure. Depending on the rotational speed of the blades, the helicopter can be set to resonance leading to failure. As a wind turbine system is quite similar, one can conclude that a wind turbine system can resonate if the RPM of the rotor matches with the natural frequency of the whole system. Therefore, the essential calculations

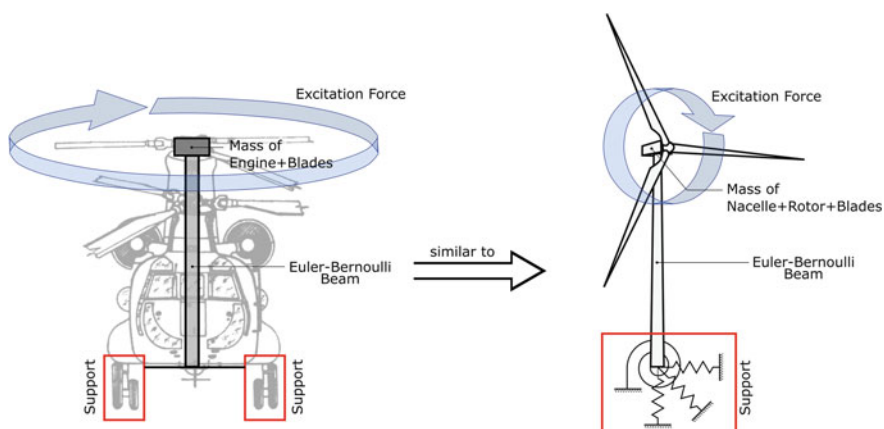


Fig. 11 Comparison of resonance phenomenon in a helicopter with OWT



Fig. 12 Ground resonance due to a helicopter

are as follows: predicting the natural frequency of the whole system and that calculations need stiffness of the foundation at its core. Following Fig. 9, it is clear that for soft-stiff system, the natural frequency of the whole system will be very close to 1P and 3P requires. It is therefore essential to predict the damping of the whole system, and higher damping is necessary. There are many sources of damping in a real wind turbine system, and they are as follows: soil (hysteresis and radiation), material of the tower, connections details, aerodynamic, hydrodynamic and external dampers (if any).

In this context, the importance of scaled model tests can be highlighted. Through a series of tests, the damping of various materials can be studied. For example, same scaled model can be used to carry out tests in different types of soils such as clays (low, medium and high plasticity), sand (loose, medium and dense sand), intermediate soils (for example, silty sand, sandy silt) to study the effect of damping.

4 Scaled Model Tests

Offshore wind turbines are relatively new structures without any track record of long-term performance. Therefore, the uncertainties of their long-term response pose additional challenges to developers and designers of offshore wind farms.

In fact, monitoring of a limited number of installed wind turbines has indicated a gradual departure of the overall system dynamics from the design requirements, which may lead to amplification of the dynamic response of the turbines, leading to larger tower deflections and/or rotations beyond the allowable limits tolerated by manufacturer. The latter is often considered responsible for the damage observed in gearboxes and other electrical rotating equipment. Before detailed discussion is carried out on scaled tests, it is important to highlight the spirit of the scaled model tests.

4.1 Spirit Behind the Scaled Model Tests

It is instructive to take a simple example to explain the spirit of the scaled model tests. Suppose, if we are asked to predict the age of the earth based on a simple model test, the first objective is to understand the mechanisms/process behind the formation. In this context, it is important to highlight the principles used by Kelvin (1862) to carry out the calculations: It was assumed that earth was formed from a completely molten object, and the age was determined by the amount of time it would take for the near surface to cool to its present temperature. The governing mechanism here is the *heat flow* from inside to outside.

A simple analogy is the boiling of an egg where the heat flows from outside to inside. Taking inspiration from a similar geotechnical problem of pile driving in clay (i.e. radial consolidation) and making bold simplifications, the governing non-dimensional group is as follows: $\frac{C_h t}{D^2}$ where C_h is coefficient of consolidation, t is the time, and D is pile diameter. If it is assumed similar fluid in egg and earth, one can get the following similarity: $\frac{t_{\text{earth}}}{D_{\text{earth}}^2} \equiv \frac{t_{\text{egg}}}{D_{\text{egg}}^2}$ (Fig. 13).

If we use the values of earth diameter and typical egg sizes and assume that it takes 3 min to boil an egg, one can get the following as time to cool the earth.

$$t_{\text{earth}} \equiv t_{\text{egg}} \frac{D_{\text{earth}}^2}{D_{\text{egg}}^2} = 3 \text{ min} \times \left[\frac{6371 \times 10^6 \text{ mm}}{25 \text{ mm}} \right]^2 = 1.95 \times 10^{17} \text{ min}$$

The model tests predict about 371 billion years, whereas the actual is about 4.54 billion years. It may be noted that the shape of the egg is not same as the earth, and we used the same fluid coefficients for egg and earth. Another interesting fact is that there was heat generation due to nuclear reaction within the earth and therefore additional factors.



Fig. 13 Spirit of a model test: modelling age of the earth

4.2 Physical Modelling of Offshore Wind Turbines

As mentioned in the Sect. 2, offshore wind turbines are subjected to a complex set of loading due to wind, wave and onboard machinery (1P and 2P/3P). Apart from the environmental loading and due to the necessity of maintaining a constant RPM for the generator, different control system acts in the Nacelle which does yaw action or a pitch action. These may cause wind and wave misalignment which makes the foundation loads estimation challenging. Therefore, physical modelling of offshore wind turbine needs to incorporate as much as possible all such details. Figure 14

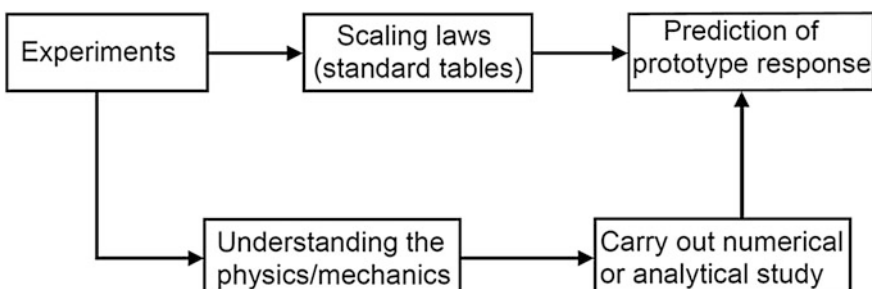


Fig. 14 Reflective loop for physical modelling

shows two approaches widely used: (a) use of standard tables for scaling which is very typical of centrifuge modelling. In such cases, if it is found that a certain parameter is scaled by N^4 , model observation can be multiplied by N^4 to predict the prototype; (b) use experiments to study the mechanics of the problem treating the model as a prototype in its own right. The model may be imperfect in the sense that it doesn't represent a realistic prototype but the intention of the experiments is to find the laws that govern the behavior under scrutiny. In the second approach, once the physics of the problem is understood, the prototype response can be predicted by applying the identified laws in a suitable way.

Bhattacharya et al. (2011, 2013a, b) and Lombardi et al. (2013) shows that the second method is well-suited for investigating the dynamics of offshore wind turbines, which involves complex dynamic wind–wave–foundation–structure interaction. In a wind tunnel, the aerodynamic effects are modelled efficiently and correctly (as far as practicable) and in the wave tank the hydrodynamic loads and scouring can be modelled. In a geotechnical centrifuge, one can model the stress level in the soil but the model package must be rotated at a high RPM which will bring in unwanted vibrations in the small-scale model. Ideally, a tiny wind tunnel together with a tiny wave tank onboard a geotechnical centrifuge may serve the purpose but this is not viable and will add more uncertainty to the models than it tries to unearth. A model need not be more complex and often simple experiments can unearth the governing laws. It must also be mentioned that there will be cases where the scaling laws may not be satisfied rather violated and these must be recognized by the experimenter. Such violation (for example the case of low effective stress in a 1-g scaled model) needs to be tackled in a different way and previous researchers used non-dimensional groups. Some specific issues must be mentioned in relation to the problem of offshore wind turbines:

- (a) The small-scale model must be subjected to multiple frequencies of loading and the dynamics of the problem must be preserved. This will ensure appropriate dynamic soil-structure interaction and the strain level in the soil around a foundation must be maintained i.e. a mix of small strain and large strain.
- (b) Repeated vibration (regular + irregular) of the foundation will induce cyclic strains in the supporting soil and the experiments need to capture the changes in soil stiffness and the associated effects. For example, it is necessary to ascertain if the cyclic strains would develop and accumulate pore pressures around the soil and its impact on the overall dynamics of the system.

The readers are referred to Bhattacharya et al. (2011) and Lombardi et al. (2013) to see the method of obtaining similitude relations for monopile supported wind turbines and the particular problem of Dynamic Soil-Structure-Interaction of monopile supported wind turbines. The scaling laws related to multiple foundation supported wind turbine is different and can be found in Bhattacharya et al. (2013b).

4.3 Example of Scaled Model Tests

This section of the paper takes some examples of scaled model tests of offshore wind turbines. Further details of the tests together with procedure can be found in Bhattacharya et al. (2013a, b) and Lombardi et al. (2013). Figure 15 shows some of the test set-ups developed to study the problems. The main aim of the tests is to identify scenarios when the wind turbine system can fail in various limit states: *Ultimate Limit State* (ULS), *Serviceability Limit State* (SLS) and *Fatigue Limit State* (FLS). Figure 16 shows observed collapse of monopile-supported wind turbine in sandy soils together with the limit states that needed to be avoided. Further details of the design limit states can be found in Arany et al. (2017). Some of the identified soil-structure interactions are as follows (Fig. 17):

- (1) Long-term behaviour of offshore wind turbines supported on monopiles is strongly affected by the level of strain generated in the soil adjacent the foundation. Larger strains result in higher variation in foundation stiffness and therefore the natural frequency of the system will also vary. Evidently, the potential change in vibration characteristics has to be appropriately taken into account in design and prediction of the long-term performance of offshore wind turbines.
- (2) Figure 18 shows a schematic representation of the change in natural frequency with number of cycles. Generally, it has been observed that natural frequency of monopile-supported wind turbine increased in sand due to the densification of the soil. On the other hand, natural frequency of wind turbines in clay decreased and is dependent on strain level in the soil next to the pile.
- (3) Figure 19 shows a schematic representation of the soil-structure interaction as understood from the scaled model tests. In general, there are two types of interaction: (a) fatigue type i.e. cycles of loading which may lead to strain



Fig. 15 Examples of scaled model tests; **a** monopile-supported wind turbine with blades; **b** asymmetric tripod-supported wind turbine where the RNA mass is simulated by a top mass; **c** model of a floating turbine

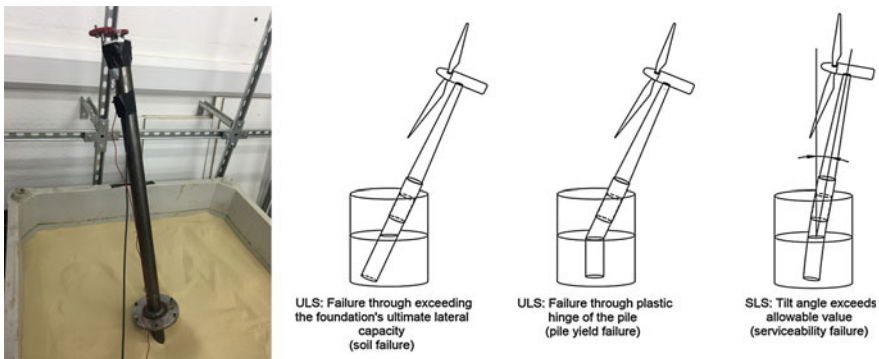


Fig. 16 Simulated collapse of monopile-supported offshore wind turbine and what to avoid? Collapse of monopile-supported wind turbine in sand

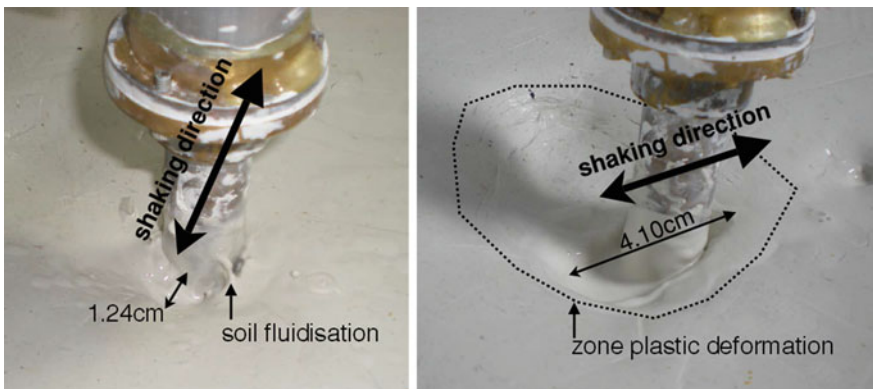


Fig. 17 Collapse of monopile-supported wind turbine in kaolin clay. Due to high strain in the soil next to the pile, the clay fluidized

accumulation; (b) resonance type whereby there will be densification of the soil. The above two mechanisms compete and the long-term performance depends of the combined effects of the two mechanisms.

4.4 Multiple Support Supported Offshore Wind Turbines

Offshore wind farm projects are increasingly turning to alternative foundations which include jacket and multipod foundations. The scaling relations required to investigate such foundations need to take into account the geometric arrangement (i.e. characterizing the asymmetry). The rules of similarity between the model and

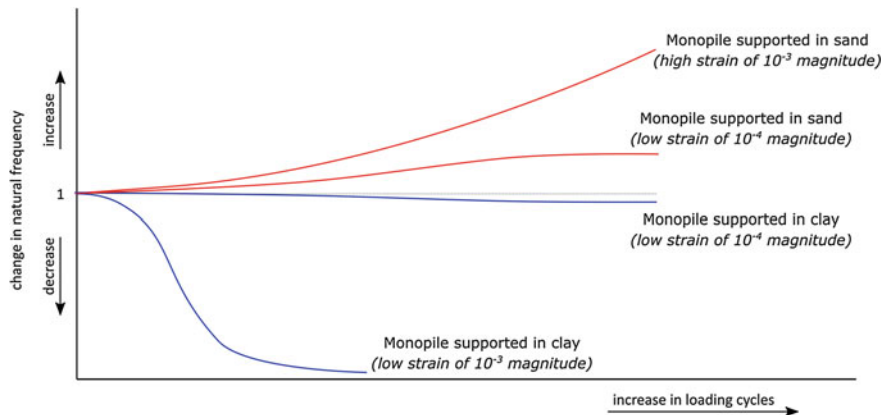


Fig. 18 Change in natural frequency of monopile-supported wind turbine in sands and clays, see Bhattacharya et al. (2011)

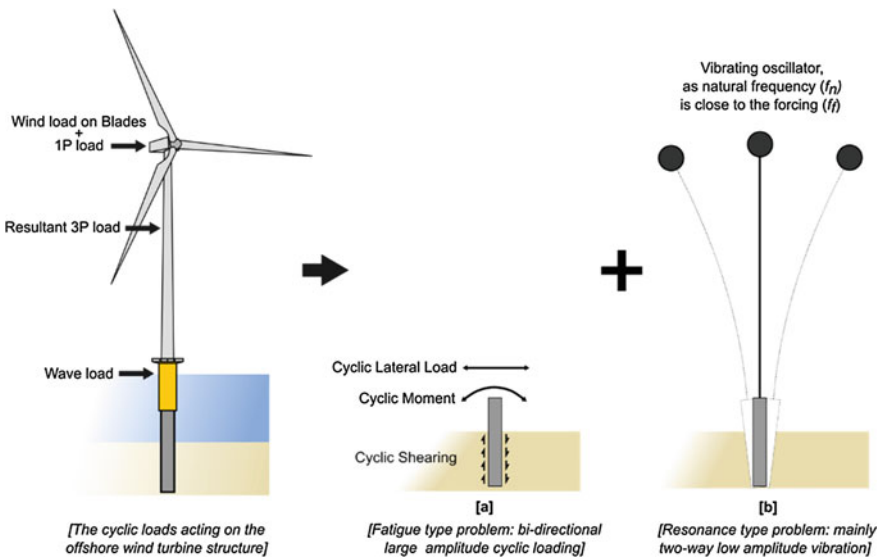
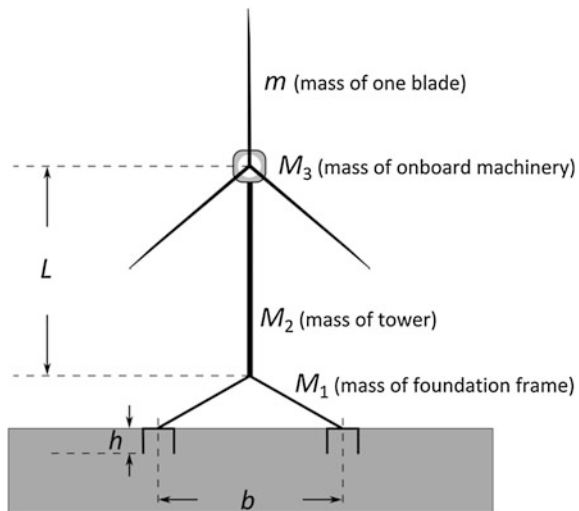


Fig. 19 Breakdown of soil-structure interaction of offshore wind turbines into two types of problems, see Nikitas et al. (2016, 2017)

prototype that need to be maintained are as follows: (a) the dimensions of the small-scale model need to be selected in such a way that similar modes of vibration will be excited in model and prototype. It is expected that rocking modes will govern the multipod (tripod or tetrapod suction piles or caissons) foundation, and as a result, relative spacing of individual pod foundations (*b* in Fig. 20) with respect to the tower height (*L* in Fig. 20) needs to be maintained. This geometrical scaling is

Fig. 20 Schematic diagram for multipod foundation wind turbines



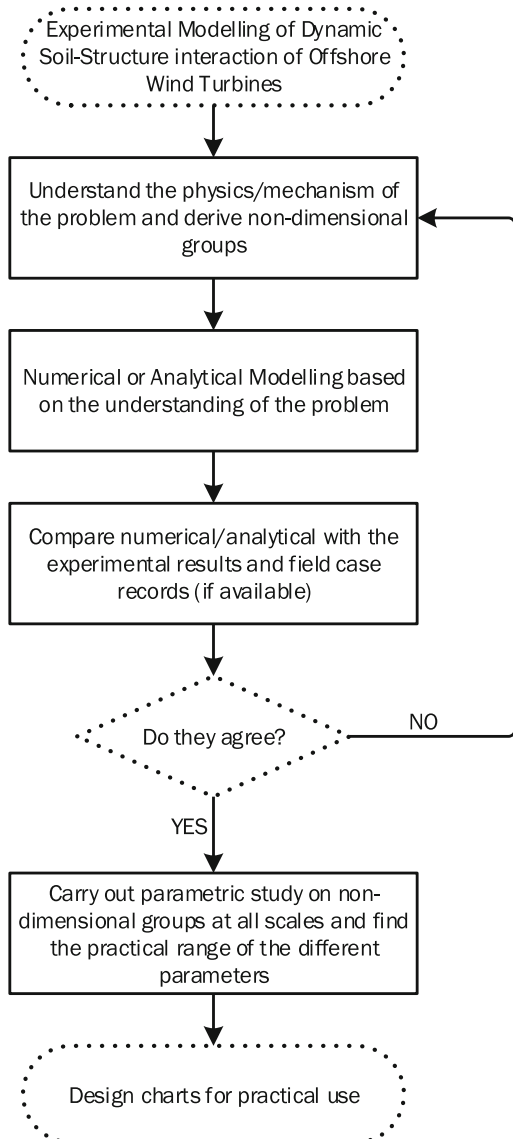
also necessary to determine the point of application of the resultant force on the model. The aspect ratio of the caisson (diameter to depth ratio) should also be maintained to ensure the pore water flow is reproduced.

A series of tests were carried by Bhattacharya et al. (2013a, b) and Bhattacharya (2014) to investigate the dynamics and long-term performance of small-scale offshore wind turbines models supported on multipod foundations. Figure 15b shows the asymmetric model arrangement in a typical set-up. The results showed that the multipod foundations (symmetric or asymmetric) exhibit two closely spaced natural frequencies corresponding to the rocking modes of vibration in two principle axes. Furthermore, the corresponding two spectral peaks change with repeated cycles of loading, and they converge for symmetric tetrapods but not for asymmetric tripods. From the fatigue design point of view, the two spectral peaks for multipod foundations broaden the range of frequencies that can be excited by the broadband nature of the environmental loading (wind and wave), thereby impacting the extent of motions. Thus, the system lifespan (number of cycles to failure) may effectively increase for symmetric foundations as the two peaks will tend to converge. However, for asymmetric foundations, the system life may continue to be affected adversely as the two peaks will not converge. In this sense, designers should prefer symmetric foundations to asymmetric foundations

5 Summary and Conclusions

Offshore wind turbines are relatively a new innovation and is considered as a reliable and cheap source of power. These are now sited in deeper waters and in many numbers to form a wind farm for economic viability. Design of foundations

Fig. 21 Flowchart showing the usefulness of scaled laboratory testing



for such structures are complex and challenging. These are to be designed for lifetime of 25–30 years and there is no track record of long term performance. One of the uncertainties are long term performance of these structures and to find out under what condition, there can be an issue that can jeopardize the operation. To supplement the design, small scale experimental studies can be carried out to understand the governing laws and mechanics of the problem. This keynote lecture addresses the complex dynamic soil-structure interaction problems for offshore wind turbines and lessons learnt from the small-scale tests.

Mechanics-based non-dimensional groups or similitude relations need to be derived in order to study the various aspects of this problem. Figure 21 shows a flowchart showing the usefulness of scaled model tests in the sense that design chart can be developed. For unknown problems, the governing laws are identified through scaled model tests and subsequently verified/validated where possible or where data exists. Numerical or analytical methods can then be formulated to incorporate the identified laws. It is often useful to plot data from numerical and experimental in a non-dimensional form using the mechanics based non-dimensional groups to find any anomaly. If there are discrepancies, it must be addressed. Problems may exist in non-linearity problem where advanced finite element analysis data can be useful. Finally, using the practical range of parameters, one can develop useful design charts.

Acknowledgements The first author would like to thank the support from EPSRC, RWE Innogy, VJ Tech for carrying out the research.

References

Arany, L., Bhattacharya, S., Adhikari, S., Hogan, S. J., & Macdonald, JHG. (2015a). An analytical model to predict the natural frequency of offshore wind turbines on three-spring flexible foundations using two different beam models. *Soil Dynamics and Earthquake Engineering*, 74:40–5. <https://doi.org/doi:10.1016/j.soildyn.2015.03.007>.

Arany, L., Bhattacharya, S., Macdonald, J., & Hogan, S. J. (2015b). Simplified critical mudline bending moment spectra of offshore wind turbine support structures. *Wind Energy*, 18, 2171–2197.

Arany, L., Bhattacharya, S., Macdonald, J. H. G., & Hogan, S. J. (2016). Closed form solution of Eigen frequency of monopile supported offshore wind turbines in deeper waters incorporating stiffness of substructure and SSI. *Soil Dynamics and Earthquake Engineering*, 83, 18–32. <https://doi.org/10.1016/j.soildyn.2015.12.011>.

Arany, L., Bhattacharya, S., Macdonald, J., & Hogan, S. J. (2017). Design of monopiles for offshore wind turbines in 10 steps. *Soil Dynamics and Earthquake Engineering*, 92, 126–152.

Bhattacharya, S. (2014). *Challenges in the design of offshore wind turbine foundations*. IET: Engineering and Technology Reference.

Bhattacharya, S. (2017). *Chapter 12: Civil engineering aspects of a wind farm and wind turbine structures*. Wind Energy Engineering: A Handbook for Onshore and Offshore Wind Turbines Hardcover. Elsevier. ISBN:9780128094518.

Bhattacharya, S., Cox, J., Lombardi, D., & Muir Wood, D. (2013a). Dynamics of offshore wind turbines supported on two foundations. *Geotechnical engineering: Proceedings of the ICE*, 166 (2), 159–169.

Bhattacharya, S., Lombardi, D., & Wood, D. M. (2011). Similitude relationships for physical modelling of monopile-supported offshore wind turbines. *International Journal of Physical Modelling in Geotechnics*, 11(2), 58–68.

Bhattacharya, S., Nikitas, N., Garnsey, J., Alexander, N. A., Cox, J., Lombardi, D., et al. (2013b). Observed dynamic soil–structure interaction in scale testing of offshore wind turbine foundations. *Soil Dynamics and Earthquake Engineering*, 54, 47–60.

Bhattacharya, S., Wang, L., Liu, J., & Hong, Y. (2017). *Civil engineering challenges associated with design of offshore wind turbines with special reference to China*. Chapter 13 of Wind

Energy Engineering A Handbook for Onshore and Offshore Wind Turbines Academic Press (Elsevier), pp. 243–273.

Guo, Z., Yu, L., Wang, L., Bhattacharya, S., Nikitas, G., & Xing, Y. (2015). Model tests on the long-term dynamic performance of offshore wind turbines founded on monopiles in sand. *ASME Journal of Offshore Mechanics and Arctic Engineering*, 137(4). <https://doi.org/10.1115/1.4030682>.

Lombardi, D., Bhattacharya, S., & Muir, Wood D. (2013). Dynamic soil-structure interaction of monopile supported wind turbines in cohesive soil. *Soil Dynamics and Earthquake Engineering*, 49, 165–180.

Nikitas, G., Arany, L., Aingaran, S., Vimalan, J., & Bhattacharya, S. (2017). Predicting long term performance of offshore wind turbines using cyclic simple shear apparatus. *Soil Dynamics and Earthquake Engineering*, 92, 678–683.

Nikitas, G., Vimalan, N. J., Bhattacharya, S. (2016). An innovative cyclic loading device to study long term performance of offshore wind turbines. *Soil Dynamics and Earthquake Engineering*, 82, 154–160.

Yu, L., Wang, L., Guo, Z., Bhattacharya, S., Nikitas, G., Li, L., et al. (2015). Long-term dynamic behavior of monopile supported offshore wind turbines in sand. *Theoretical and Applied Mechanics Letters*, 5(2), 80–84.

Modeling and Behavior of Geosynthetics-Reinforced Foundation

Sarvesh Chandra

Abstract Use of geosynthetic-reinforced granular beds is getting very popular over the last two to three decades. The cost of geosynthetics has gone done many fold as it is produced in large scales. This has necessitated development of analytical tools for design of reinforced granular beds resting on soft soils which have low bearing capacity and cause large settlements. Some of the basic modeling elements used for modeling soil behavior are being used to develop more complex models for representing reinforced granular bed behavior. This paper reviews the development that has taken place in this area during last three decades. The focus is more on the mechanical models developed for representing the behavior of geosynthetic-reinforced foundation beds. There are models developed for single and multiple layers of reinforcement. These models take into consideration factors such as compressibility of granular material, extensible and inextensible reinforcements, interfacial friction between the geosynthetic reinforcement and the soil, pretension in the reinforcement, time-dependent behavior of the soft soil, shear modulus of the granular bed, the creep behavior of reinforcement, flexural rigidity of the reinforcement, and nonlinear behavior of granular material and soft clay. Most of these models are not yet validated in the field conditions. The major reason for lack of this is that the models are having far too many parameters, and the values of these parameters for any site are not available. Parametric studies carried out using these models have improved the understanding of the behavior of reinforced foundations considerably.

Keywords Reinforcement · Granular beds · Modeling · Soft soil Settlement

S. Chandra (✉)

Department of Civil Engineering, GLA University, Mathura 281406, India
e-mail: sarviitk@gmail.com

1 Introduction

One of the major challenges in the design of foundations is that the behavior of materials like soil and rocks cannot be modeled precisely. The nature and variation of rock or soil underlying most of the structures are neither homogeneous nor isotropic. Unlike the concrete or steel, the behavior of granular materials is more complex and depends on various factors like minerals, grain size and shape, distribution of grain sizes, density, water content, pore pressure, stress history. The material properties of these materials depend on the past and present stress conditions and may change under the superimposed loads.

It is a major challenge to represent the behavior of such materials in mathematical form. The problem is further complicated when there is an inclusion in these materials and two- or three-dimensional problems are handled. There are generally two approaches adopted for the idealization of materials like soil to represent its behavior in mathematical form. The first approach, generally termed as continuum approach, in which the soils are idealized as a continuum and its response is expressed through constitutive equations. In the second approach, termed as modeling approach, the behavior of soils can be represented by mechanical models, mathematical models, or numerical models. This paper focuses on the modeling approach as it is applied to reinforced granular beds. In the following paragraphs, some important mechanical models have been discussed.

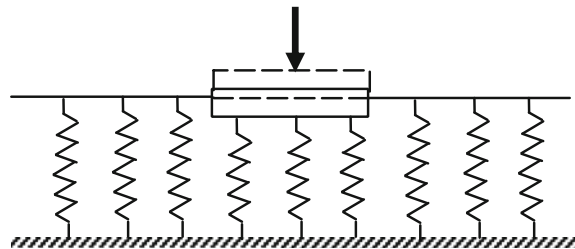
1.1 Winkler Model (1867)

Winkler proposed that the deflection of soil medium at any point on the surface is directly proportional to the stress applied at that point. It is independent of the stresses applied at other locations. In this model, soil is idealized as a system of mutually independent, discrete linearly elastic springs with a spring constant k . Therefore, the stress at any point on soil surface can be represented by

$$q(x, y) = k \times w(x, y) \quad (1)$$

where $w(x, y)$ is the deflection. In this model as the springs are independent, deflections are confined to loaded regions only and also the displacements will be constant whether the soil is subjected to an infinitely rigid load or a uniform flexible load. Another limitation of the model is that it gives linear elastic response, where actual soil behavior cannot be represented as linear elastic. The variation in the properties of the soil strata with depth and time is not considered in this model at all (Fig. 1).

Terzaghi (1955) defined the spring constant of soil by a term coefficient or modulus of subgrade reaction. This spring constant or modulus of subgrade reaction can be determined by plate load test in the field. The ratio of the subgrade reactive

Fig. 1 Winkler model

pressure at any point immediately below the foundation and settlement of that point can be defined as modulus of subgrade reaction K_s . The unit of K_s is usually $\text{kN/m}^2/\text{m}$ or $\text{MN/m}^2/\text{m}$. The sizes of the foundations are very large as compared to the plates used for plate load tests. The correction for plate size must be applied to the K_s as follows:

For granular soils:

$$K_s = K_{s1} \left[\frac{B + 0.305}{2B} \right]^2 \quad (2)$$

where

K_s = Modulus of subgrade reaction of foundation of width, B.

K_{s1} = Modulus of subgrade reaction of a long plate of width, 0.305 m.

For cohesive Soils:

$$K_s = K_{s1} \frac{0.305}{B} \quad (3)$$

When square plate of width 0.305 m size is used in plate load test, \bar{K}_{s1} shall be used instead of K_{s1} . In addition to correction for size, correction for shape of plate and embedment depth are also required to be incorporated into the plate load test data.

Soil may exhibit considerable interaction action among its elements; therefore, the discrete springs (Winkler model) cannot simulate actual behavior of the soil. To overcome such shortcoming, improved two-parameter models which permit interaction among the springs were proposed. They include models like Filonenko-Borodich model (1940), Hetenyi model (1946), Pasternak model (1954).

1.2 Pasternak Model (1954)

This model assumes the existence of shear interaction between the spring elements. The spring elements are connected to a layer of incompressible vertical elements

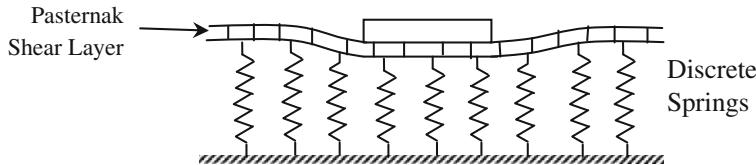


Fig. 2 Pasternak model

which deform in transverse shear only. The response function for Pasternak model is given by:

$$q(x, y) = K_s \times w(x, y) - G_p \nabla^2 w(x, y) \quad (4)$$

For an isotropic shear layer, $G_x = G_y = G_p$ (shear modulus of the layer) (Fig. 2).

In addition to these models, various other models have been proposed by several researchers like Kerr (1965), Reissner (1955), Vlasov and Leontiev (1966). A common feature of these models is that a parameter, in addition to the subgrade reaction parameter, is employed to simulate the behavior of soil. Inclusion of the second parameter can improve the accuracy of the simulation, but such approaches suffer from the drawback that the parameters are difficult to determine.

2 Development of Models for Reinforced Soils

Soil reinforcement has become a major part of geotechnical practice over the last 40 years, and its use is growing rapidly as worldwide development of infrastructure poses an increasing demand for land reclamation and utilization of soft foundation soils. In many practical situations in the field, the response of soft foundation soils can be improved considerably by placing an engineered granular fill containing single or multiple layers of geosynthetic reinforcement on top of it.

The use of geosynthetic reinforcements reduces the settlement of the soft ground under loading, distributes the loads uniformly over a wider area, and prevents nonuniform sinking of the granular material into the ground. The modeling and analyses of such reinforced foundations are relatively more complex and challenging. The use of geosynthetic-reinforced granular fill over soft soil effectively reduces the settlement and increases the bearing capacity. Many researchers have studied behavior of such reinforced foundation beds.

One of the most significant works in this direction was done by Madhav and Poorooshahab in 1988. In this paper, they extended the Pasternak model by including a layer of geosynthetics as a membrane embedded in shear layer and proposed a three-parameter mechanical model for geosynthetic-reinforced granular fill-soft soil system. The granular fill, the soft subgrade, and the geosynthetic reinforcement were idealized by Pasternak shear layer, a layer of Winkler springs, and a rough

membrane, respectively. The results at small displacement indicated that the effect of granular fill was more significant than that of the membrane in reducing the settlements of the reinforced soft soil system. The effect of providing geosynthetic reinforcement is significant at higher loads. This paper gave a new insight for the development of models for reinforced granular beds resting on soft soils.

Bourdeau (1989) formulated a two-dimensional plane strain numerical model to assess the tensile membrane action in a two-layer soil system reinforced by a geotextile. The model considered the static equilibrium of an elastic membrane placed at the interface between a granular base and a compressible subgrade. The theory of stochastic stress diffusion in particulate media was used to describe the transmission of load through the gravel base, and a Winkler model was assumed for the subgrade. The model incorporated a Mohr–Coulomb criterion for the frictional interaction at the gravel–fabric interface, and it allowed for incomplete anchorage. The results showed that the performance of high tensile modulus fabrics was affected to a higher degree by an incomplete anchorage than lower modulus fabrics.

Madhav and Poorooshasp (1989) investigated the effect of membrane in increasing the confining stress in the granular material with a consequent increase of the shear modulus (G) for a Pasternak-type foundation model. Analysis of a simple Pasternak-type foundation with variable G showed a significant reduction in the overall settlements as well as in the differential settlements due to the increased shear moduli. It was pointed out that extending the reinforcement beyond $2B$ (width of the footing) on either side of the center of footing has less effect on settlements within the loaded region.

Ghosh and Madhav (1994a) proposed a new three-parameter model incorporating the nonlinearities in the load-settlement and the shear stress–strain responses of soft clay and granular fill, respectively, for the analysis of a reinforced granular fill-soft soil system. The improvements in the settlement behavior are significant with respect to stiffness of granular fill, when the soil is softer, and with respect to interfacial friction, when the fill material is less stiff. The improvement in settlement response due to reinforcement is of the same order, and over and above the effect of granular fill.

Ghosh and Madhav (1994b) developed a mathematical model for the analysis of a reinforced foundation bed by incorporating the confinement effect of a single layer of reinforcement. It was quantified in terms of the average increase in confining pressure due to the reinforcement from which modified shear stiffnesses of the granular soil surrounding the reinforcement were obtained. The parametric studies for a plane strain case showed that the confining effect significantly improves the load-carrying capacity of the foundation. The confining effect is more pronounced when the shear stiffness of the granular fill is large. From the study, it was concluded that the modified shear stiffness below the center of the footing increases by two to five times the initial value of shear stiffness.

Ghosh and Madhav (1994c) proposed a new model for a reinforced shallow foundation bed by incorporating the “rough membrane” element for single layer reinforcement. Mechanics of the rough membrane element with the assumption of horizontal shear stress transfer at the soil/reinforcement interfaces were explained

and formulated. The model was generalized by incorporating nonlinear response of the soft soil and of the granular fill under plane strain loading conditions. The membrane effect was quantified in terms of the improvement in the load-settlement responses of the composite foundation system over the unreinforced one. From the parametric studies, it was revealed that reinforcement in tension spreads the load over a larger area, leading to a reduction in the settlement beneath the footing. It was also found out that a reinforcement length of $3B$ is sufficient to improve the foundation response to a significant degree.

Shukla and Chandra (1994a, b) proposed a generalized mechanical foundation model (Fig. 3) for the analysis of geosynthetic-reinforced granular fill-soft soil systems. The geosynthetic reinforcement layer, the granular fill layer, and the soft soil were idealized by a stretched rough elastic membrane, a Pasternak shear layer with stiffer springs, and Winkler springs and dashpot, respectively. The model considers, simultaneously, several factors governing its behavior, such as the compressibility of the granular fill, the compaction of granular fill, the time-dependent behavior of soft soil, and prestress in the geosynthetic reinforcement, besides the material and soil-geosynthetic interface characteristics. The effect of compaction of the granular fill was incorporated in the model by considering an appropriate shear transfer mechanism at the fill-geosynthetic interface. It was observed from the study that the compressibility of the granular fill has an appreciable influence on the settlement response of the geosynthetic-reinforced granular fill-soft soil system as long as the stiffness of the granular fill is less than approximately 50 times that of the soft soil. The major limitation of this model was that there were too many parameters involved in model. The procedure for determining the model parameters from laboratory or field tests is not very well established.

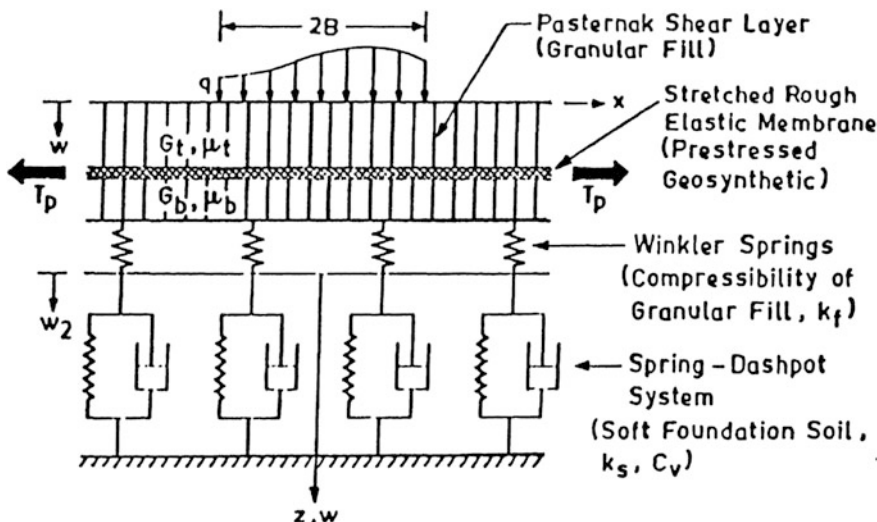


Fig. 3 A generalized model for reinforced granular beds resting on soft clay

Yin (1997a) proposed a one-dimensional mathematical model for geosynthetic-reinforced granular fill over soft soil subjected to vertical surcharge loading. This paper suggested a new approach of deformation compatibility condition in the model which eliminates the model parameters that are required to calculate the shear stresses between the top and bottom granular fill layers and the geosynthetic layer and makes it possible to include the geosynthetic stiffness in the model. A finite element analysis (FE) was established for the same problem using a FE program SIGMA/W (1995). The settlement and mobilized tension computed using the model shows better agreement with the results of finite element model than the other one-dimensional models. It was also seen that the settlement is slightly reduced within the loaded region and the mobilized tension slightly increases, due to an increase in the stiffness of geosynthetic reinforcement.

Yin (1997b) extended the model further by incorporating the nonlinear behavior of the granular fill and soft soil. A hyperbolic function represents the nonlinear shear stress-shear strain behavior of the granular fill and the soft soil. The study showed that the behavior of granular fill and soft soil was significantly affected by the ultimate shear strength of the granular fill (τ_u) and ultimate bearing capacity of the soft soil (q_u), respectively. Further, it was observed that the settlement increases with the decreasing values of q_u and τ_u . The mobilized tension in the geosynthetic reinforcement increases with the decreasing q_u values and increasing τ_u values.

Yin (2000a) derived governing differential equations for a reinforced Timoshenko beam on an elastic foundation for modeling geosynthetic-reinforced foundation soils or pavement. An analytical solution was obtained for a point load on infinite Timoshenko beam on elastic foundation. Influence of the location, tension, and shear stiffness of reinforcement on settlement of the beam and reinforcement tension force was studied. A finite element (FE) model was established for the same infinite beam problem. Results from the TB model (Timoshenko beam on elastic foundation) were compared with the results from the FE model and from the PB (the Winkler model, based on the pure bending theory). It was found that results from the proposed TB model show good agreement with the results from the FE model as compared with the results from the PB model. The TB model is particularly useful in modeling a reinforced beam with or without considering the reinforcement shear stiffness.

Yin (2000b) suggested a method for obtaining closed-form solutions for a reinforced Timoshenko beam on an elastic foundation subjected to any pressure loading. The solution can be used to calculate settlement, rotation, tension, bending moment, and shear force of the beam. The parametric study showed that the settlement without geosynthetic shear stiffness is larger than that with geosynthetic shear stiffness. The settlement and rotation decrease as tension stiffness of the geosynthetic reinforcement increases, while bending moment, tension, and shear force increase as tension stiffness increases.

Zhan and Yin (2001) developed a two-dimensional analytical model based on elastic theory for modeling soil-geosynthetic interaction for a geosynthetic layer of finite length embedded horizontally between granular fill and soft soil ground. The soil-geosynthetic interaction was analyzed in both the vertical and horizontal

directions. The vertical and the horizontal soil-geosynthetic interactions were modeled using Winkler springs and horizontal shear springs, respectively. The geosynthetic reinforcement was assumed to be elastic and only resisted tension without bending and shearing resistance. The results from the proposed analytical model were compared with the results of rigorous two-dimensional finite difference analysis using Fast Lagrangian Analysis of Continua (FLAC). Based on the parametric study it was observed that the geosynthetic reinforcement is most effective when it is placed at 0.35–0.70B (B is the width of the footing) below ground. A geosynthetic length of 2.5–3B would be economical and effective in improving soft ground. An increase in interface shear modulus and geosynthetic stiffness also improves soft ground.

Nogami and Yong (2003) studied the response of geosynthetic-reinforced geomedium subjected to structural loading by considering each soil layer by a system of an infinite number of closely spaced one-dimensional columns connected with horizontal springs. The governing differential equations for the geomedium were obtained and solved by iterative finite difference method. This model can also be used for inhomogeneous soil medium and soil reinforced with multiple layers of geosynthetic reinforcements considering linear stress-strain variation of soil. The results obtained by this approach when compared with the results of finite element studies match closely for small strain levels, but for large strain levels a large discrepancy between the values has been observed. They further observed that for higher loading intensity when three reinforcement layers are placed within the soft soil without any gravel layer, the response of the reinforced bed is better than the same when a single reinforcement layer is placed within the gravel layer. However, no significant difference in the response of the reinforced beds was observed for smaller loads.

Maheshwari et al. (2004) presented a mechanical model to estimate the flexural response of beams resting on reinforced granular beds. The reinforcing elements (such as geogrids) were idealized as beam with smooth surface characteristics. The lower poor strata and the upper dense soil were modeled as Winkler springs of different stiffness. It was observed that for the given range of parameters, the normalized deflection of the upper and lower beams remains unaffected if the normalized length ratio of beams exceeds 1.5. Further, it was observed that the combined response of the model is significantly affected by various parameters such as the ratio of flexural rigidity of upper and lower beam, the ratio of stiffness of upper and lower soil layers, the ratio of the length of upper and lower beams, and placement depth of the reinforcement.

Deb et al. (2006) studied the response of single and multilayer geosynthetic-reinforced granular fill-soft soil system using a lumped parameter modeling approach (Fig. 4). The effect of inclusion of stone columns and geosynthetic creep on the settlement response was also included in the analysis. The reinforced granular fill-soft soil system was idealized by nonlinear spring or spring-dashpot system, granular fill by Pasternak shear layer, stone columns with stiffer Winkler springs, and geosynthetic reinforcements by rough elastic membranes. Both extensible and inextensible reinforcements had been modeled. Plane strain

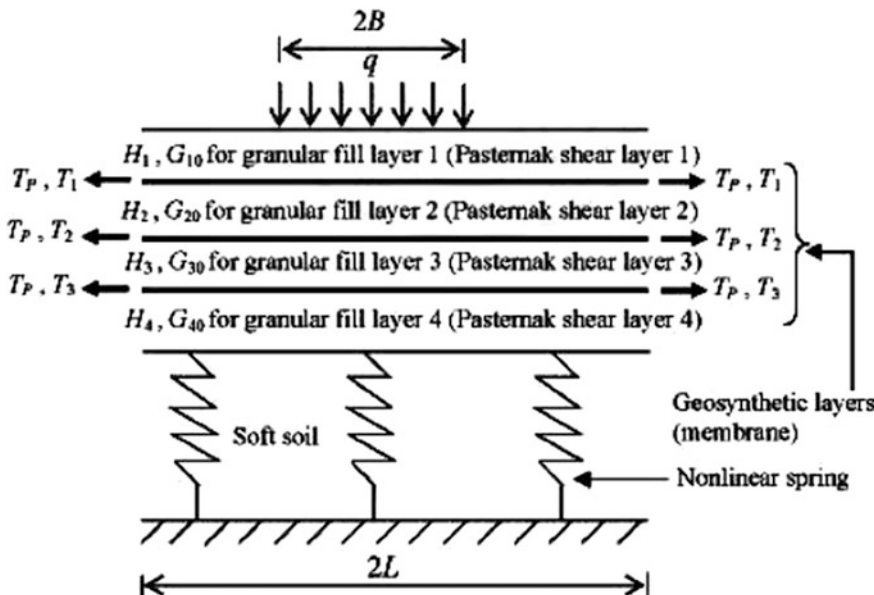


Fig. 4 Model for multilayer-reinforced granular bed

condition had been considered for the loading and reinforced foundation soil system. The numerical solutions were obtained by an iterative finite difference scheme, and the results were presented in a nondimensional form. In addition to the above, a numerical study has also been conducted using the Fast Lagrangian Analysis of Continua (FLAC) program which simulates the behavior of the structures specially built of soil and rock. It had been observed that there is a significant reduction in the settlement when multilayer geosynthetic reinforcement was used. In case of inextensible reinforcements, as the number of reinforcement layer is increased the settlement is decreased with a decreasing rate, but in case of extensible reinforcements the reduction rate is almost constant.

From the literature review it has been observed that placement of granular fill containing single or multiple layer of geosynthetic over soft soil is very effective to improve the bearing capacity of the soft foundation soil and reduce the excessive settlement of the structures constructed on soft soil.

Deb et al. (2007) studied the response of multilayer geosynthetics-reinforced granular fill-soft soil system. The effect of stone column inclusions and geosynthetic creep on the settlement response was also included. A lumped parameter modeling approach was adopted. The reinforced granular fill-soft soil system was idealized by mechanical elements, such as soft soil by nonlinear spring of spring-dashpot system, granular fill by Pasternak shear layer, stone columns with stiffer Winkler springs, and geosynthetics reinforcements by elastic rough membranes. The time-dependent behavior (creep) of the geosynthetics reinforcements

was idealized by standard linear solid (SLS) model. The equations governing the response of the proposed foundation models were derived with the general assumption that the geosynthetic reinforcement layers were rough enough to develop full frictional resistance even at negligibly small displacement. A plane stress condition was considered for the loading and the reinforced foundation soil system. Numerical solutions were obtained by an iterative finite difference scheme.

Deb (2008) presented an analysis to predict the behavior of a geosynthetic-reinforced granular fill over soft soil improved with stone columns (Fig. 5). Granular fill was idealized by Pasternak model; reinforcement was considered as rough membrane; stone column was modeled by stiffer springs; and soft soil was idealized by Kelvin–Voigt model to represent its consolidation behavior.

Shahu and Hayashi (2009) presented a rational analysis of an extensible sheet reinforcement subjected to a high oblique end force assuming a nonlinear elasto-plastic vertical stress–displacement relationship for the backfill soil and a nonlinear elasto-plastic shear stress–displacement relationship for the soil–reinforcement interface. Few important findings of the analysis were that the analysis gives the value of reinforcement stiffness factor above which the extensible reinforcement will act as inextensible one.

Dey (2009) did lumped parameter modeling, in which the granular beds are represented by Winkler springs, the viscoelastic compressible medium is represented by a four-parameter Burger element, and the footing and the reinforcement are represented by beams. Taking into account the nonlinear and viscoelastic behavior of the underlying soil, a generalized method to analyze and predict the flexural response of footings resting on unreinforced and reinforced foundation beds was developed.

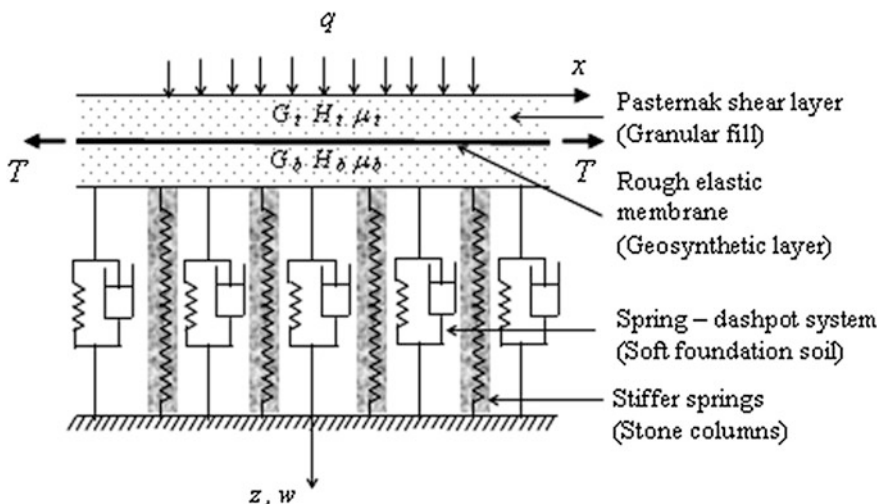


Fig. 5 Foundation model for reinforced granular bed resting on stone column-reinforced soft soil

Parvathi (2011) studied the analysis of viscoelastic foundations and prediction of its flexural response. The soil was modeled as a tension membrane which inter-connects the Burger model (five-parameter model). It was visualized as modified Filonenko-Borodich model. Winkler springs were replaced by viscoelastic Burger model. So time-dependent behavior as well as continuity of stress beyond the loading area was achieved, and flexural responses were found out. The model is ideally suited for representing cohesive soil like clay.

Zhao et al (2016) proposed a model to be used for roads to be constructed on reinforced granular beds. In this model, the pavement of a road is idealized as a long and thin Euler–Bernoulli beam and the reinforced granular bed which has reinforced layer embedded in it is idealized as Timoshenko beam and the foundation soil is simulated by Pasternak model. An analytical solution is obtained, and the results are compared with the results obtained by finite element method. The results are also compared for two cases when the granular fill is idealized by Pasternak model and when the granular fill represented by a Winkler model. From this study it was concluded that shear modulus of the granular material and the stiffness of the beam have significant effect on the response of the model.

Mohan et al (2016) reviewed various models for geosynthetic-reinforced granular beds and suggested an approach useful for design of reinforced earth wall. An extensible reinforcement subjected to oblique forces was considered embedded in granular material having nonlinear behavior of the backfill. A nonlinear relationship for the interface shear stress mobilized was also considered in the analysis. This study may be useful for internal design of reinforced earth walls.

Some of the models mentioned above have been used for the design of railway tracks resting on reinforced granular beds under static and moving loads. One such attempt was made in a paper published by Rajesh et al (2015). In this paper, the ballast and sub-ballast layer have been idealized by Pasternak shear layer (Fig. 6). To incorporate the compressibility of the ballast and sub-ballast layer, a layer of stiff Winkler springs has been connected to the bottom of the lower Pasternak shear layer. The load coming on the reinforced granular layer is taken from the distribution of axle load to five sleepers. A pseudo-static approach has been used for moving load of a train.

The geosynthetic layer is represented by a stretched rough elastic membrane. Soft soil subgrade has been represented by the Burger element, which is a combination of Kelvin–Voigt element and Maxwell element arranged in series. Burger model has been adopted because of the flexibility it provides and also due to its generalized nature. The Burger model is capable of representing all the deformation phenomena occurring in a viscoelastic subgrade when subjected to loading and unloading process.

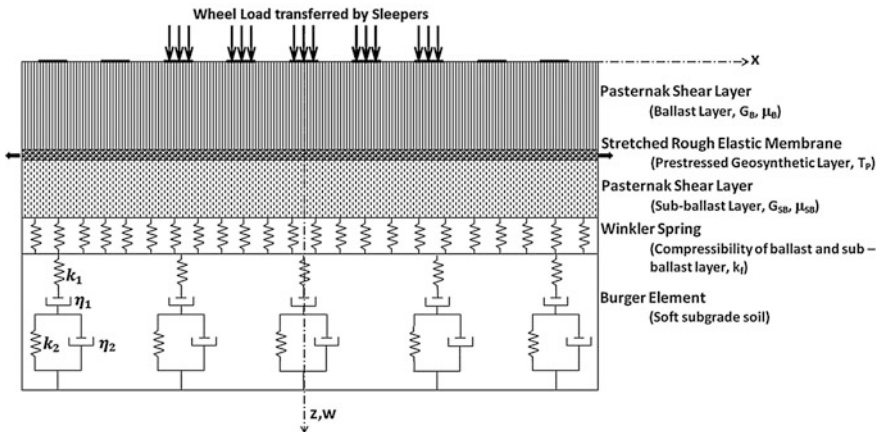


Fig. 6 Proposed foundation model for the railway track system

3 Summary/Conclusion

It has been a common practice for long to put a sand layer on top of weaker soils to spread the load over wider area and thus taking care of low bearing capacity of loose deposits and to reduce settlement. Reinforcing the sand layer serves the same purpose with much lesser thickness of granular layer. The reinforced layer has an advantage over unreinforced granular layer due to the fact that the reinforcement placed in the granular layer through the interfacial friction mobilized on the interface can create confining effect. Use of multiple layers of reinforcement is also very common, but using more than three layers of reinforcement is not of much advantage.

There have been many attempts in the past to model the behavior of reinforced granular beds resting on soft soil. The models proposed have several parameters involved in the governing equation of the model which are difficult to obtain in field situations. In many finite element studies, the reinforcement has been modeled as an elastic membrane and the interfacial elements are introduced to represent soil-reinforcement interaction. There are several studies where the results obtained by modeling approach have been compared with the results of finite element studies. However, there is no study where the results obtained by modeling approach are validated from field tests or observations in the field. Therefore, these models so far have only limited applications in the field.

References

Bourdeau, P. L. (1989). Modelling of membrane action in a two-layer reinforced soil system. *Computers and Geotechnics*, 7, 19–36.

Deb, K., Chandra, S., & Basudhar, P. K. (2006). Nonlinear analysis of multilayer extensible geosynthetic-reinforced granular bed on soft soil. *Geotechnical and Geoogical Engg*, 25(1), 11–23.

Deb, K., Dey, A., Chandra S. (2007). Modeling of Layered Soil System, 1st Indian Young Geotechnical Engineers Conference, Hyderabad, India, 2–3rd March, 2007, pp. 50–55.

Deb, K. (2008). Modelling of Granular bed-stone column-improved soft soil. *International Journal for Numerical and Analytical Methods in Geomechanics*, 32(10), 1267–1288.

Dey, A. (2009). Nonlinearly elastic and viscoelastic unreinforced and reinforced foundation beds: Modeling and model parameter estimation. (*Ph.D. Thesis*). Department of Civil Engineering, Indian Institute of Technology, Kanpur, India.

Filonenko-Borodich, M. M. (1940). Some approximate theories of the elastic foundation. *Uchenye Zapiski Moskovskogo Gosudarstvennogo Universiteta Mekhanika*, 46, 3–18. (in Russian).

Ghosh, C., & Madhav, M. R. (1994a). Settlement response of a reinforced shallow earth bed. *Geotextiles and Geomembranes*, 13, 643–656.

Ghosh, C., & Madhav, M. R. (1994b). Reinforced Granular fill-soft soil system: Confinement effect. *Geotextiles and Geomembranes*, 13, 727–741.

Ghosh, C., & Madhav, M. R. (1994c). Reinforced granular fill-soft soil system: Membrane effect. *Geotextiles and Geomembranes*, 13, 743–759.

Hetényi, M. (1946). *Beams on elastic foundation*. Ann Arbor: The University of Michigan Press.

Kerr, A. D. (1965). A study of a new foundation model. *Acta Mechanica*, 1, 135–147.

Madhav, M. R., & Poorooshshab, H. B. (1988). A new model for geosynthetic reinforced soil. *Computers and Geotechnics*, 6(4), 277–290.

Madhav, M. R., & Poorooshshab, H. B. (1989). Modified pasternak model for reinforced soil. *International Journal of Mathematical Modelling*, 12(12), 1505–1509.

Maheshwari, P., Basudhar, P. K., & Chandra, S. (2004). Analysis of beams on reinforced granular beds. *Geosynthetics International*, 11(6), 470–480.

Mohan, A., Darsan, A., Nair, A. S., Morris, S. M., & Vaishnavi, L. K. (2016). Reinforced granular foundation beds- a review. *international journal of innovative research in science, engineering and technology. Special Issue*, 5(14), 321–328.

Nogami, T., & Yong, T. Y. (2003). Load-Settlement analysis of geosynthetic-reinforced soil with a simplified model. *Soils and Foundations*, 43(3), 33–42.

Parvathi, G. S. (2011). *Analysis of beams on viscoelastic foundations and model parameter estimation (M.Tech. thesis)*. Department of Civil Engineering, Indian Institute of Technology, Kanpur, India.

Pasternak, P. L. (1954). *On a new method of analysis of an elastic foundation by means of two foundation constants*. Moscow (in Russian): Gosudarstvennoe Izdatelstvo Liberaturi po Stroitelstvu Arkhitektury.

Rajesh, S., Choudhary, K., & Chandra, S. (2015). A generalized model for geosynthetic reinforced railway tracks resting on soft clays. *International Journal for Numerical and Analytical Methods in Geomechanics*, 39(3), 310–326.

Reissner, E. (1955). Stresses in elastic plates over flexible foundations. *Journal of the Engineering Mechanics Division Proceedings ASCE*, 81, Paper No. 690.

Shukla, S. K., & Chandra, S. (1994a). The effect of prestressing on the settlement characteristics of geosynthetic-reinforced soil. *Geotextiles and Geomembranes*, 13, 531–543.

Shukla, S. K., & Chandra, S. (1994b). A generalized mechanical model for geosynthetic-reinforced foundation soil. *Geotextiles and Geomembranes*, 13, 813–825.

Terzaghi, K. (1955). Evaluation of coefficients of subgrade reaction. *Geotechnique*, 5, 297–326.

Vlasov, V. Z. & Leontiev, N. N. (1966). Beams, Plates and Shells on Elastic Foundation, Israel Program of Scientific Translations, NTIS No. N67-14238.

Winkler, E. (1867). In *Die Lehre von der Elastizität und Festigkeit* (p. 182). Domonicus: Prague.

Yin, J. H. (1997a). Modelling geosynthetic-reinforced granular fills over soft soil. *Geosynthetics International*, 4(2), 165–185.

Yin, J. H. (1997b). A nonlinear model of geosynthetic-reinforced granular fill over soft soil. *Geosynthetics International*, 4(5), 523–537.

Yin, J. H. (2000a). Comparative modeling study of reinforced beam on elastic foundation. *Journal of Geotechnical and Geoenvironmental Engineering Division*, ASCE, 126(3), 265–271.

Yin, J. H. (2000b). Closed-Form solution for reinforced timoshenko beam on elastic foundation. *Journal of Engineering Mechanics Division*, ASCE, 126(8), 868–874.

Zhan, C. H., & Yin, J. H. (2001). Elastic analysis of soil-geosynthetic interaction. *Geosynthetics International*, 8(1), 27–48.

Zhao, L. S., Zhou, W. H., Fatahi, B., Li, X. B., & Yuen, K. V. (2016). A dual beam model for geosynthetic-reinforced granular fill on an elastic foundation. *Journal of Applied Mathematical Modelling*, 40, 9254–9268.

Image-Based Characterization Techniques for Geotechnical Applications

Gali Madhavi Latha, Prashanth Vangla and Nimisha Roy

Abstract Recent advances in digital technology led to great improvement in understanding and solving many geotechnical engineering problems. This paper presents few important image-based techniques for precise characterizations, applicable to geotechnical engineering and demonstrates the same. Some of the important applications discussed in this paper are particle shape characterization of granular materials, quantification of surface roughness of sand particles, measurement of shear band thickness in direct shear tests and correlating it to the shear strength of soils, and microtopographical analysis of geosynthetic surfaces to understand shear-induced surface changes and correlating them to their interface shear behavior. While experimental measurements fall short to render required accuracy to these problems, image-based studies offer better visualization of underlying mechanisms along with accurate quantifications.

Keywords Image analysis · Image segmentation · Optical methods · Shape analysis · Interface

1 Introduction

Sieve analysis has been traditionally used for particle size characterization. Since the shape of the sieve openings is entirely different from the numerous possible shapes of soil particles, there is always a compromise on the measured size of the particles through sieves. Sieve analysis provides a single size for a particle, irrespective of its shape. The shape of the particles, which is one of the important parameters of grains that govern their kinematic and shear behavior, is ignored in most of the geotechnical analyses and designs, since its quantification is complex. Recent developments in digital technology have facilitated procurement of sufficient information through visual inputs. Image-based shape characterization

G. M. Latha (✉) · P. Vangla · N. Roy
Department of Civil Engineering, IISc, Bangalore 560012, India
e-mail: madhavi@civil.iisc.ernet.in

provides complete details of the grain boundary, including its dimensions and shape, resulting in more accurate and meaningful description of grain geometry, which can be used to understand its kinematic and shear behavior.

In conventional geotechnical testing, many instruments are used to measure deformations in soils during loading. The linear variable differential transformers (LVDTs), typically used to measure deformations, have accuracy less than $\pm 1 \mu\text{m}$, and the measurements are limited to a specific area where they are fixed. On the other hand, Image-based methods can capture the complete deformation field around an object by tracking several points on it. Also, formation of shear bands can be visualized through a series of images during deformation, and the shape and thickness of shear bands can be quantified by applying special algorithms to the images. These shear bands can then be used to understand the movement of particles during shear and use this information to understand the underlying shearing mechanisms. Commercial cameras and light sources are the only components needed for image-based methods to obtain the entire deformation field with relatively high precision. Hence, accurate measurements can be obtained at a cheaper cost.

Indiscriminate selection of soil type or geosynthetics for any geotechnical engineering application could lead to complications because the physical and functional properties of these materials vary substantially across the same group. It is extremely important that the geosynthetics should provide adequate grip with neighboring soils and generate necessary amount of friction when they are sheared or displaced along the interface, for applications like retaining walls and containment systems lined with geomembranes. The resistance offered at the interface of soil-geosynthetics hugely depends upon on the morphological properties of particulate materials and surface characteristics of geosynthetics. Characterization of morphological properties of granular soils/particulate materials and understanding the behavior of soil-geosynthetics interfaces through image-based techniques are an evolving interest among many geotechnical fraternities.

The contents of this paper mainly focus on the image-based techniques used for size and shape characterization of granular materials, estimation of shear band thickness, and estimation of shear-induced surface changes in geomembranes.

2 Background

The most widely acknowledged and accepted definition of particle shape by researchers is the one given by Barrett (1980), who clearly stated that shape comprises of three independent multi-scale components: form (macro-scale), roundness (meso-scale), and surface texture (micro-scale). The most popular means to assess particle shape is by the use of conventional methods based on ocular inspection of grains using descriptors like rounded, subrounded, angular, and subangular to define it based on visual reference charts. However, these methods have been criticized due to the subjectivity in their measuring techniques, giving

rise to user-dependent results. The advancement in computer vision and imaging techniques has led researchers to develop image-based methods for characterization of shape in the recent past. Notwithstanding the efforts, most image-based methods used for quantification of particle shape do not yield reliable results as they deviate from the conventional and most well-accepted definitions formulated by researchers in the past (Krumbein and Sloss 1951 for sphericity; Wadell 1932 for roundness; Lees 1964 for angularity), due to the difficulties involved in automating them.

Failure in granular materials is usually represented by the formation of intense localized shear zones or bands at the shearing plane in a particulate material (internal) or at the interface of particulate and continuum materials. The intense localized shearing includes interparticle slip and dilation, which is attributed to the particle rearrangement, slip and rotation (Desrues et al. 1996). Evolution of shear zones can be closely associated with the stress-strain behavior. Thus, understanding and measurement of the internal and interface shear zone formation provide insights into the fundamental mechanism underlying the shear behavior. Thickness of the internal shear zone is mainly a function of mean particle size (Hartley 1982; De Jaeger 1991), and interface shear zone is a function of mean particle size of the particulate material and roughness of the continuum material (Paikowsky et al. 1995; DeJong et al. 2000).

Various measurement techniques were used by earlier researchers to measure the internal and interface shear zone/band formation during shearing. The techniques like gamma-rays, stereophotogrammetry/false relief stereophotogrammetry (Butterfield et al. 1970; Desrues and Duthilleul 1984; Desrues and Viggiani 2004), and X-ray computed tomography (Desrues et al. 1991, 1996) were used to completely characterize the shear band formation by measuring the deformations prior to the onset of shear band and during the formation of shear band until its complete formation and geometry and orientation of the shear band. Recent developments in digital image processing introduced more efficient methods such as the digital images correlation (DIC) and the particle image velocimetry (PIV), which were used many researchers (White et al. 2001; Wolf et al. 2003; DeJong et al. 2003; Rechenmacher and Finno 2004; Réthoré et al. 2007) to characterize the internal and interface shear band formations. Few other techniques like capturing the images through a transparent side wall of sand sample consisting of artificial colored columns of sand along with uncolored sand (Sadrekarimi and Olson 2010) were also used to study shear zone formation. This technique can be used to find the final thickness of the shear zone or continues formation of shear zone without disturbing the sample.

The detailed analysis of the shearing mechanisms and stress-strain behavior at interfaces is possible only through proper quantification of the morphological properties of particulate materials and surface features of the continuum material. There are numerous classes of methods coined in literature to define particle shape based on verbal descriptions, visual comparisons, empirical results, single-number classification methods, functional, analytical and image-based methods (Sozer 2005), which led to the evolution of many shape parameters/descriptors. Despite the prevalence of so many methods and the importance of particle shape in

geotechnical engineering, a universally accepted method that quantifies shape accurately and precisely is still lacking. It is because of this reason that particle shape is not given enough importance in engineering considerations.

In recent years, microtopographical analysis of shear-induced surface changes in the smooth geomembrane by particulate has gained significant interest among the geotechnical community (Dove and Frost 1999; Lee and Kagbo 2002; Alshibli and Alsaled 2004; Dove et al. 2006; Fuggle 2011; Frost et al. 2012). This type of studies is helpful to get clear insights to understand the underlying shearing mechanism of particulate–continuum interfaces such as sand-geomembrane and sand-steel; these types of interfaces are often seen in many geotechnical structures. The surface changes in the smooth interfaces like geomembrane often studied using various contact and non-contact techniques. Most often measurements using stylus profilometer or image-based optical profile microscopy (OPM) techniques are used to quantify the roughness of the geomembrane (Dove and Frost 1996, 1999). Stylus profilometer is a contact-based technique that gives only the 2D information of the surface profile traced by the stylus tip on the materials. Dove et al. (1996) used atomic force microscopy (AFM) to measure the 3D surface roughness of the geomembrane from the examination of microtopography, at a scale comparable to fine-grained soil particles. However, the scan area of the sample for the measurement in this method is only $10 \mu\text{m}^2$, limiting the applicability of this method to fine-grained soil particles and smooth geomembranes. The methods like stylus profilometer, OPM, and AFM may not provide detailed information of the surface because the measurements are non-continuous and made at specific locations or less scan area.

Literature suggests that advanced image-based methods are needed for accurate measurement of size and shape of particulate materials, shear band analysis, and shear-induced surface in the smooth continuum material to gain more insights in this area of research. These kinds of approaches can also greatly facilitate to develop more sophisticated constitutive models to precisely predict macro stress–strain response of soils alone or soil-smooth continuum material.

3 Estimation of Shear Band Thickness

Numerous researchers have studied the shear zone formations in granular materials when tested alone or interfacing with man-made materials. In this study, to capture the shear band formation, images through a transparent side wall of direct shear box consisting of sand sample with artificially colored columns of sand along with uncolored sand are taken. A large-scale conventional direct shear test setup with shear box dimensions 300 mm (length) \times 300 mm (breadth) \times 80.5 mm (height) was modified into a large symmetric loading interface direct shear setup for this study (Vangla and Latha 2016). In a symmetric loading direct shear test arrangement, upper half of the shear box is rigidly fixed to the load plate and is constrained against the rotation to create a uniform stress state inside the box. To fill the colored

sand, metal sheets bent in the shape of a channel were attached temporarily at specific spacing to the transparent side of the shear box and colored sand was filled along these channels to create bands up to certain height, while the gaps between the bands contain uncolored sand. The metal sheets were then carefully withdrawn while ensuring that the bands remain intact and distinct from the surrounding sand. Remaining space of the box above the colored bands was completely filled with uncolored sand using regular sand pluviation to a relative density of 90%. Photographs of deforming sand shear box were taken continuously during the test at an interval of 0.5 mm. However, images taken before the commencement of shearing and at the end of the test when the box was displaced by 20 mm were used for the image analysis. Shear bands were analyzed using image segmentation technique, which works on the technique of pixel classification. As explained above, colored sand bands were used in the tests to follow the locus of sand particles in this band during shearing to assess and analyze the movements. When the digital image containing sand of natural color with few bands of different color is analyzed in image segmentation, the digital image is partitioned into multiple segments based on the color contrast. The objective of image segmentation is to convert the digital image into something that is more meaningful and easier to analyze (Shapiro and Stockman 2001). Pal and Pal (1993) reviewed various image segmentation techniques in detail.

The segmented picture is then used to locate the boundaries of the colored columns before and after the test. The segmented image is a binary image, which is represented by typically two colors which are black and white. The RGB (red, green, blue) color for the white is (1, 1, 1) and black is (0, 0, 0), and they are indexed as 1 and 0, respectively, for each pixel. A MATLAB algorithm was written for tracing the boundaries of colored bands in segmented pictures. Figures 1 and 2 present shear band analysis of sand alone shear test of coarse sand (CS, D₅₀ is 3 mm) in direct shear tests and interface direct shear tests of CS with three wire meshes WM1, WM2, and WM3 with varying aperture size (spacing between two consecutive plain weave wire strands) 0.2, 0.9, and 3 mm, respectively. In these tests, specially designed clamps were used to fix the wire meshes efficiently to the rigid base, avoiding elongation of the meshes during shear. As observed from Figs. 1 and 2, the variation of shear band thickness of different types of interfaces and sand alone is precisely captured using image segmentation technique.

4 Size and Shape Characterization of Particulate Materials

Barrett (1980) clearly stated, “Form, roundness and surface texture are essentially independent properties of shape because one varies widely without necessarily affecting the other two properties”. Sphericity is recognized as only one aspect of the form (Wadell 1932, 1933). Barrett’s study classified all three components of

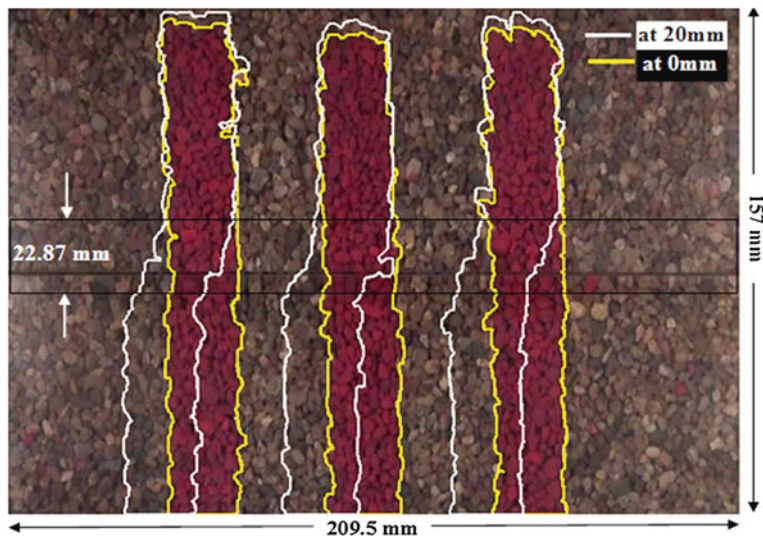
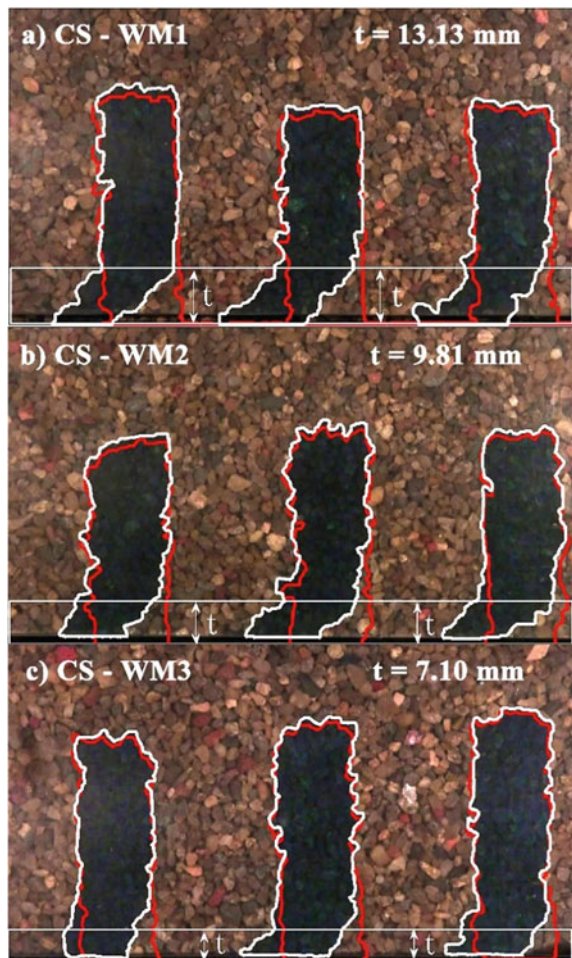


Fig. 1 Estimation of shear band thickness (after Vangla and Latha 2015)

particle shape—form, roundness, and surface texture into three different scales with respect to the particle size as shown in Fig. 3. In addition to these three parameters, one more parameter called as angularity is also often used to characterize the particle shape. This parameter is not just an antithesis of roundness but a distinct concept (Lees 1964).

Several researchers have attempted to characterize the particle shape of sand particles by various methods including projection methods, standard shape comparison methods, functional methods, and fractal methods (Sozer 2005), which led to the evolution of many shape parameters/descriptors. Despite the availability of many methods, no method has been accepted as standard, because of conceptual and practical deficiencies. A new computational method which overcomes the limitations of existing methods is developed (Nimisha 2017) to quantify sphericity, roundness, angularity, and roughness of sand particles without any requirement of manual intervention. The method is implemented in three steps in MATLAB. In the first step, filtering techniques are employed on segmented 2D image projections of particles to remove high-frequency components of noise and roughness after converting the boundary profile of the image into the frequency domain using Fourier transforms. This process is also used to quantify roughness of the particle outline. The second stage implements an algorithm developed to identify “corners” along the particle outline free from micro-scale features and to fit the most appropriate circle in each corner for the quantification of roundness as per Wadell’s concept. In case of angularity, the corners information and their curvature using the radius of the best fit circles are used to determine the degree of angularity (A) of the particle according to the concept put forth by Lees (1964). The third stage deals with the quantification of form or sphericity of the particle using computational geometry.

Fig. 2 Shear bands in interface direct shear tests
a CS-WM1, **b** CS-WM2,
c CS-WM3 (after Vangla and Latha 2016)



4.1 Roughness

To determine the roughness of a particle, its outline is extracted after segmenting its image into a binary image through image segmentation process. This outline comprises of micro- to macro-level features of the particle including noise due to aliasing effect by the square pixels tessellation. To determine the roughness of the particle, the existing noise has to be removed from the outline. For this purpose, the outline is opened up at a constant interval of 0.0017 radians (0.1°) in clockwise direction from its centroid, which is named as raw profile. The raw profile in the spatial domain is transformed into the frequency domain subsequently by the use of fast Fourier algorithm. The frequency domain comprises different wavelength components of the raw profile corresponding to various aspects of particle shape,

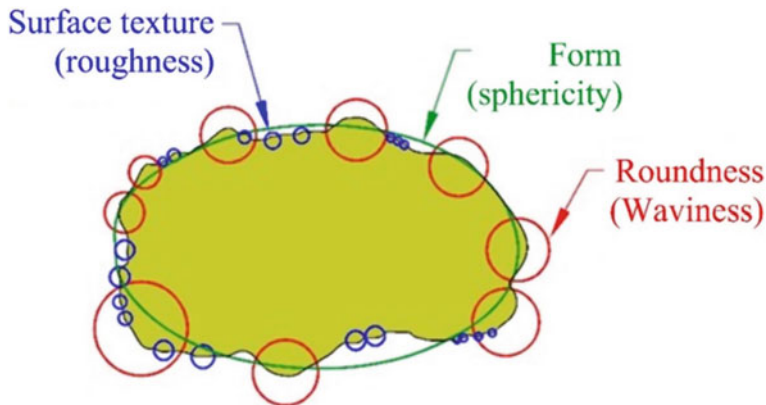


Fig. 3 Particle shape characterization at different scales (after Barrett 1980; Mitchell and Soga 2005)

viz. roughness corresponding to small wavelength component, roundness corresponding to medium wavelength component, and form corresponding to high-wavelength component. This information is very useful to suppress or retain the selected wavelength components by applying filters before reconstructing the particle outline for further findings. A low-pass Gaussian regression filter used is applied to remove the noise features and roughness features to obtain a mean profile of raw profile. Having established the roughness free profile, root mean squared roughness (R_q) can be computed as:

$$R_q = \sqrt{\frac{\sum_{k=1}^n (y_{kr} - y_{ks})^2}{n}} \quad (1)$$

where y_{kr} is the value of the k th coordinate of the raw profile, y_{ks} is the value of the k th coordinate of the smoothed profile, and n is the total number of points in the profile. The R_q is scale-dependent value, which increases with the increase in particle size. Therefore, to obtain R_q which is free from this scale dependence, it is normalized with length (L) of the particle, which is called as normalized roughness (NR_q), expressed in percentage.

$$NR_q = \frac{R_q}{L} \quad (2)$$

4.2 Roundness

The course of automating the procedure of determining roundness of a particle as per Wadell (1932) involves four main steps; these steps are performed on smoothened particle outline (free from noise and roughness features). The first step involves identification of dominant points along the particle outline. The dominant points also known as significant points, relevant points, points of interest, or corner points (Morgera 2012) are identified by liner polygonal approximation method. An algorithm is written for this purpose and is implemented in MATLAB. The algorithm involves detecting boundary points at maximum distance (d) from a defined vector, starting from the vector representing the length of the particle, and iterating to obtain vectors formed by joining end points of the previous vector and the detected boundary points at maximum distances from it on either side, until d is greater than a predefined threshold value n . Here, n is a variable parameter, the value of which, is calculated by several trials to be 0.09% of the maximum dimension of the particle. In the second step, the detected dominant points along the particle outline are used to identify the corner portions of the particle. An algorithm was written and implemented in MATLAB to identify the corners, which are concave inward portions present along the particle outline. In the third step, the maximum inscribed circle is found. For each pixel inside the boundary of the soil particle, the minimum distance to particle boundary is computed, which produces a distance contour map. The pixel with the maximum stored distance is the center of the maximum inscribed circle, and the stored distance is its radius. The final step is to fit the best circle in each corner so as to determine its radius of curvature. The radius of curvature is determined at every point of each corner using a modified double derivative formula (Eq. 3), to take into account the uneven spacing of discrete points along a closed boundary. Let the first point of the curve be (x_s, y_s) , the middle point be (x_m, y_m) at a finite difference k with respect to the first point and at a finite difference h with respect to the end point (x_e, y_e) . Considering these points, the double derivative formula can be modified as follows by incorporating the average weightage of h and k (both represent a small change in x).

$$f''(x) = \frac{k \times (y_e - y_m) + h \times (y_s - y_m)}{k \times h \times \left(\frac{h+k}{2}\right)} \quad (3)$$

where $h = x_e - x_m$, $k = x_m - x_s$.

The above double derivative formula results in many circles at each corner. The best fit circle among these circles is the one, which is tangential to the local maxima of the corner and touches the maximum number of points along the corner boundary. Roundness can now be computed using Wadell's definition as follows:

$$R = \frac{\sum_{r=1}^n D_r}{D_i} \quad (4)$$

where D_r is the diameter of the r th circle, n is the total number of circles, and D_i is the diameter of the inscribed circle.

4.3 Angularity

Lees (1964) coined the degree of angularity (A) of all corners of a particle as follows:

$$A = \sum (180^\circ - a) \times \frac{x}{r} \quad (5)$$

where a is the measured angle between the planes bounding a corner, x is the distance of the tip of the corner from the center of the maximum inscribed circle C , and r is the radius of the maximum inscribed circle as discussed above. The angles formed by the planes bounding the determined corners are computed in accordance with Lees definition which follows a different procedure for corners having radius of curvature (r_c) lesser than half the radius of curvature of the maximum inscribed circle r than those corners with r_c greater than half of r . In the former case, tangents are drawn at the end points of each corner and their intersecting angle is stored as a . The distance between C and the farthest point (maxima) of each corner is computed as x . In the latter case, tangents are drawn at the dominant points adjacent to each end point of the corner and at the point where this tangent diverges away from the curvature of the corner. The angle of intersection of these two lines at both ends of such corners is recorded as a . Both the ends of such corners are considered as separate corners, and x is computed separately for both the cases by calculating the distance between the maxima of each corner end and C . The values of a and x of each corner can be substituted in Eq. (5) and summed up for all the corners to arrive at the value of angularity of the particle. Hence, this algorithm is in accordance with Lees (1964) method as it successfully automates the procedure of computing angularity and eliminates the need for manual calculation and approximations based on the visual observations.

4.4 Shape Analysis of Real Particles

The new computational methods discussed in above sections are adopted for shape analysis of two sand groups: angular coarse sand (ACS: particle size 2–4.75 mm) and coarse sand (CS: particle size 2–4.75 mm). Both these sands are classified as

poorly graded sands (SP) as per unified soil classification system. The sand belonging to the category CS is river sand taken, whereas sand belonging to category ACS is quarry sand. SEM images of randomly selected 30 particles of each type of sand were taken for shape analysis in this study. Particles from CS have average NR_q value of 0.05, whereas ACS particles have exhibited higher average NR_q value of 0.10. The average value of roundness is 0.28 for CS, classifying it as subangular (roundness between 0.25 and 0.35) as per Powers (1953). Angular coarse sand has average roundness value of 0.18, classifying it as angular (roundness between 0.17 and 0.25) as per Powers (1953). The crushed angular coarse sand exhibited higher average angularity value of 1453 and falls in more angular class of Lees (1964) chart as compared to CS, which has average angularity value of 925. The average value of sphericity for coarse sand is 0.82, whereas angular coarse sand has average sphericity value of 0.74. The reference chart provided by Krumbein and Sloss (1951) classifies ACS into the more angular, rougher, and less spherical category as compared with CS, which matches with visual observations. Figure 4 shows the shape parameters of two typical particles of both the groups. The yellow lines indicate the corners with radius of curvature greater than that of maximum inscribed circle of the particle.

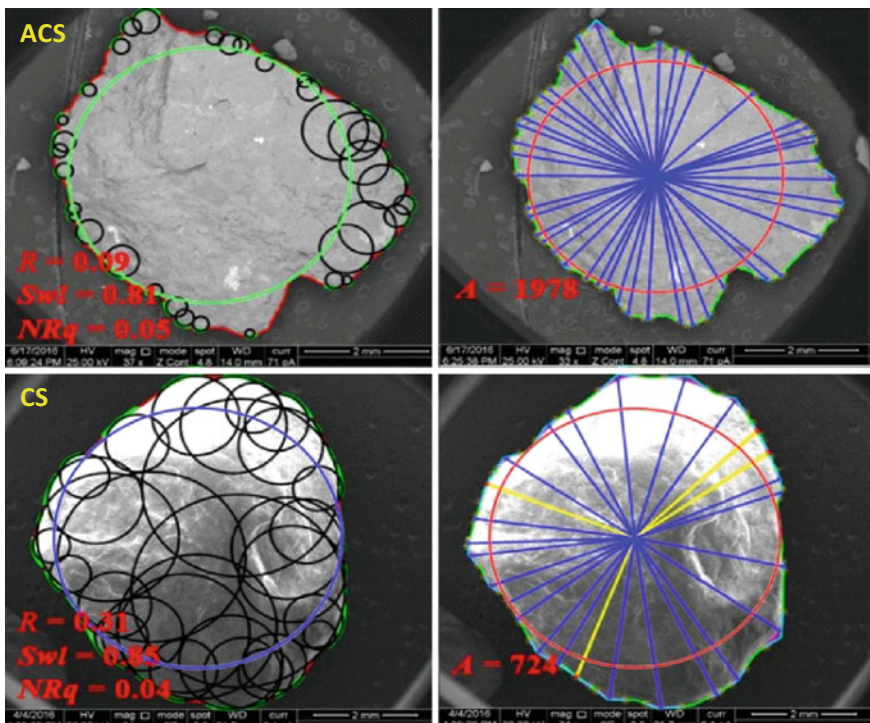


Fig. 4 Shows SEM images of typical sand particles of both groups used for shape analysis along with their normalized roughness, roundness, angularity, and sphericity values

5 Estimation of Shear-Induced Surface Changes in Smooth Geomembrane

The applicability of 3D optical profilometer for surface roughness characterization of sands, unsheared and sheared smooth geomembrane and the usefulness of surface roughness studies for understanding the interface shear behavior of sand-smooth geomembrane are presented in this section. The 3D optical profilometer is an advanced profilometer which works on coherence correlation interferometry (CCI); it has several advantages over contact systems including the elimination of surface damage, speedy and continuous surface roughness measurements, which could lead to generate the complete topography of the scanned surface in 3D form to visualize the features for qualitative and quantitative understanding as well. More details about the instrument and sample preparation of sands and geomembrane for surface roughness studies can be seen in Vangla and Latha (2017). The sand samples for surface roughness studies were randomly selected. The measured/scanned surface of a sample comprises of form, waviness, and roughness. Since the roughness of the sample is of specific interest for the characterization of the surface, the waviness and form have to be removed from the measured surface by applying filters. The removal of form and waviness from the measured surface is illustrated with Fig. 5, which presents the components of the measured surface of angular coarse sand (ACS). Figure 5a presents 3D topography of the scanned ACS sample whose dimension is 0.8 mm × 0.8 mm; this comprises of all three components such as form, waviness, and roughness. A second order polynomial, which is practically sufficient in most cases, was used for the form removal as shown in Fig. 5b. Figure 5c presents the form free measured surface, from this waviness is removed by 32 μm × 32 μm cutoff wavelength using areal Gaussian filter shown in Fig. 5d. Figure 5e presents the surface roughness of the ACS particle.

Surface roughness through areal measurement is S_a , which is the average surface roughness. Average surface roughness (S_a) is the arithmetic average of the absolute values of profile height deviations recorded within the evaluation area and measured from the mean surface area, which is a horizontal plane. S_a values were quantified for each sand particle surface using each Gaussian filter, to understand the effect of waviness cutoff wavelength on the surface roughness measurements of sand particles. The variation of S_a values obtained for all two sand particles with increase in cutoffs has almost liner increasing trend as shown in Fig. 6.

It is obvious that the surface roughness values are greatly influenced by the waviness cutoff chosen. Differentiating between roughness and waviness is very difficult when the waviness is complex. In case of sand particles, the inherent curvature which can come into the scan area makes the selection of waviness cutoff difficult. However, at the 32 μm × 32 μm areal cutoff wavelength, the 3D topographical measurement seems to be flat and free from waviness and form compared to the 3D topographical views obtained at other cutoff wavelengths. Hence, the filter size of 32 μm × 32 μm seems to be appropriate for all two sand particles.

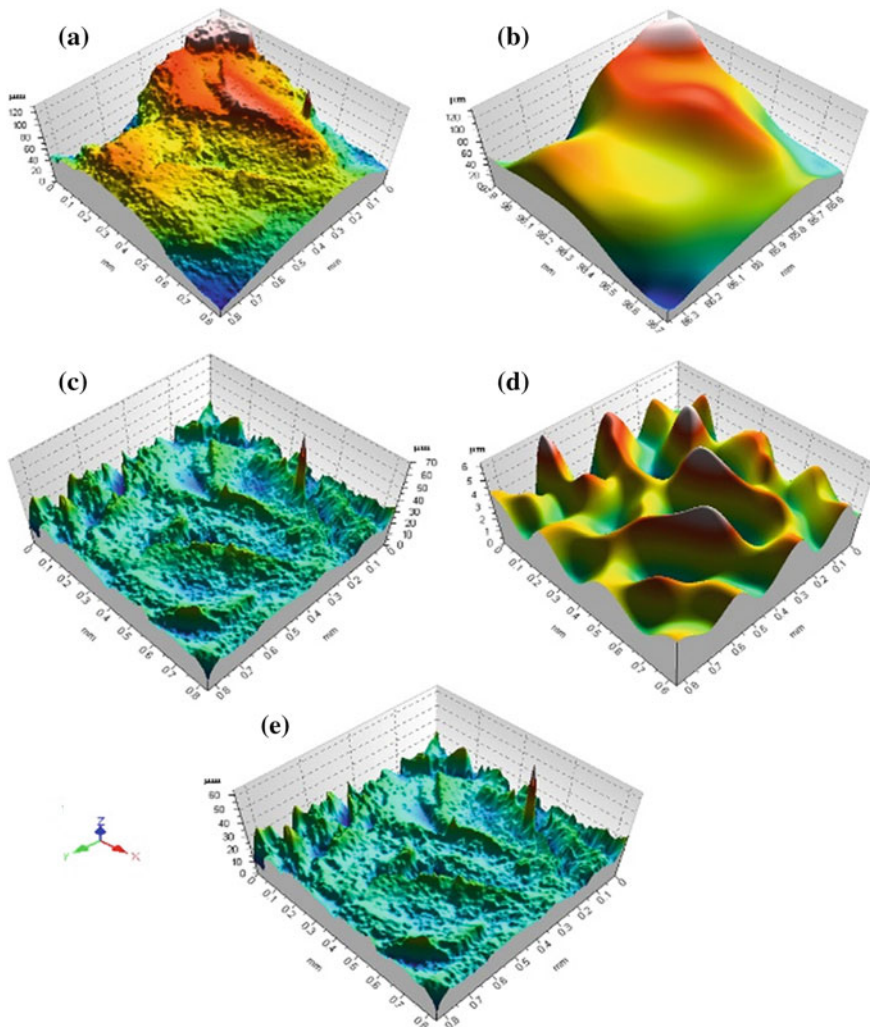
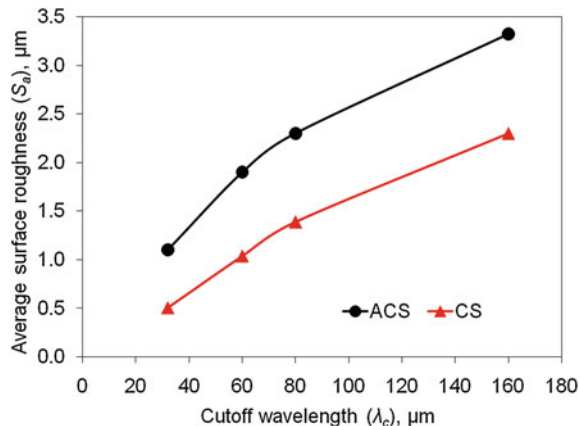


Fig. 5 Filtering of the measured surface **a** measured surface of the GM surface, **b** form to be removed, **c** surface texture of GM after form removal, **d** attenuated waviness, **e** surface roughness area profile

However, these values are highly subjective and should be evaluated for each case separately based on visual observations and by multiple measurements on small scan areas. From the Fig. 6, one can observe that ACS particle obtained higher S_a value at all cutoff wavelength compared to CS, indicating that ACS particle is more rough compared to CS. The visual and microscopic observations are also in agreement with the surface roughness studies carried out on ACS and CS.

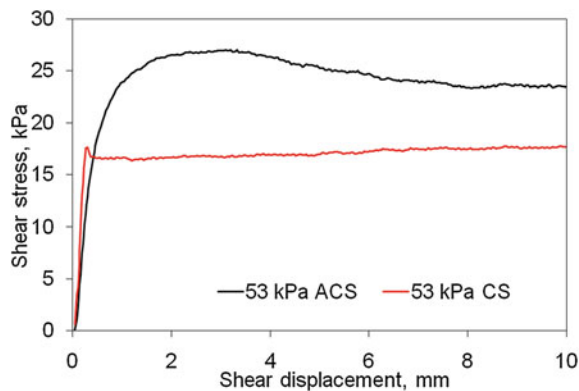
Fig. 6 Variation of average surface roughness (S_a) with cutoff wavelength



Interface shear tests were carried out at three different normal stresses 23, 37, and 53 kPa on sand-smooth geomembrane interfaces. Angular coarse sand (ACS) and coarse sand (CS) were selected to understand the effect of particle shape on the interface shear behavior since these two sands have same particle size range but entirely different particle shape. The typical shear stress–shear displacement response of ACS-GM and CS-GM interfaces at 53 kPa normal stress is shown in Fig. 7. The ACS-GM interface showed a peak friction angle of about 27° and post-peak friction angle of about 25° . In case of CS-GM interface, the friction angle and post peak friction angle are reduced to about 18.7° and 18.6° , respectively. From these values and from the Fig. 7, it is clear that angular coarse sand has offered higher shear stress compared CS. Relative density of sand was 70% in all these tests, and initial void ratios were calculated to be higher for ACS. These results demonstrate that the particle shape of sand is highly influential in governing the interface shear strength compared to the initial void ratio or packing of particles in a sand sample. ACS and CS are classified as angular and subangular based on their sphericity and roundness values. Also, ACS particles are rough compared to CS particles. Higher angularity and more roughness of ACS particles are responsible for higher shear resistance of ACS-GM interfaces.

These interface shearing mechanisms are understood through the surface roughness studies carried out on unsheared and sheared geomembrane using 3D optical profilometer. The surface roughness of the virgin/unsheared geomembrane was investigated by measuring roughness of five GM samples of size $14\text{ mm} \times 3.5\text{ mm}$ cut from five different locations of the geomembrane role. Average value of S_a obtained by measurements on these five samples was $0.08\text{ }\mu\text{m}$. The cutoff wavelength used in case of unsheared and sheared geomembrane is 2.5 mm to attenuate the waviness, decided based on several trials with different cutoff wavelengths. Topographical studies to measure the surface changes were carried out on representative geomembrane samples sheared by ACS and CS.

Fig. 7 Shear stress–shear displacement response of ACS-GM and CS-GM interfaces at 53 kPa normal stress



The average surface roughness (S_a) obtained for ACS-GM and CS-GM interfaces is 1.09 and 0.77 μm , respectively. From these values, it is evident that ACS has induced higher surface changes than CS, resulting in relatively higher interface shear resistance. Figures 8 and 9 present the shear-induced surface changes in smooth geomembrane measured through 3D optical profilometer after it is sheared by ACS and CS, respectively. The 3D topographical images shown in these figures are the typical regions that have deeper and intense grooves, which were extracted from the actual scanned sample 14 mm \times 3.5 mm. The preprogrammed routine in the software also allows the extraction 2D profiles from the specific locations from the scanned surface as shown in Figs. 8 and 9.

Fig. 8 Shear-induced surface changes by ACS **a** typical 3D topographical view of GM, **b** 2D profile extracted at the specific location

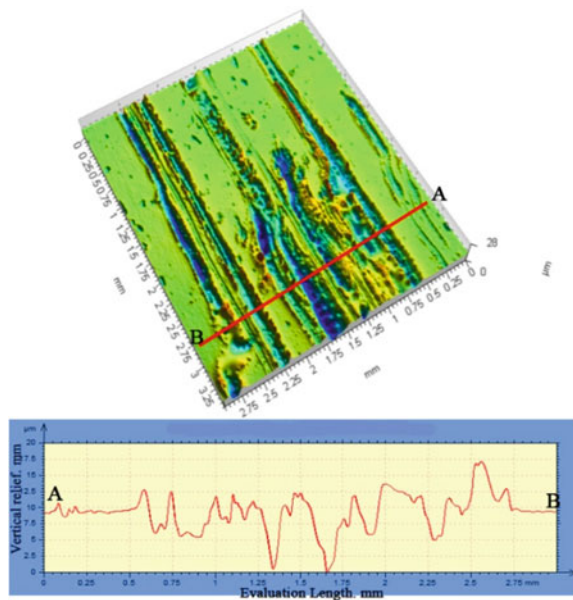
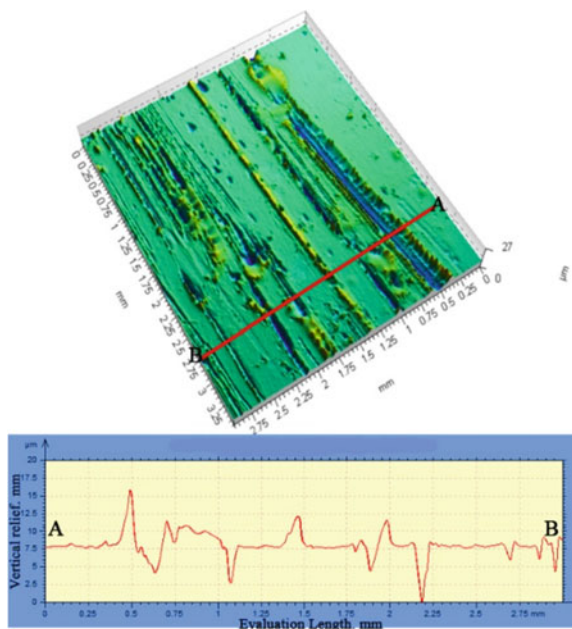


Fig. 9 Shear-induced surface changes by CS **a** typical 3D topographical view of GM, **b** 2D profile extracted at the specific location



6 Summary

This paper describes some of the image-based techniques used for geotechnical characterizations. Specific techniques developed for granular particle shape characterization, shear band analysis, surface roughness measurements for sand and geosynthetics, and microtopographical analysis of geomembrane surfaces are explained and demonstrated for real materials and tests. These image methods offer accurate, quick, and spatially distributed measurements compared to conventional measurement techniques using contact-based transducers.

References

Alshibli, K. A., & Alsaleh, M. I. (2004). Characterizing surface roughness and shape of sands using digital microscopy. *Journal of Computing in Civil Engineering*, 18(1), 36–45.

Barrett, P. J. (1980). The shape of rock particles, a critical review. *Sedimentology*, 027(3), 291–303.

Butterfield, R., Harkness, R. M., & Andrews, K. Z. (1970). A stereo-photogrammetric method for measuring displacement fields. *Géotechnique*, 20(3), 308–314.

De Jaeger, J. (1991). *Influence de la morphologie des sables sur leur comportement mécanique*. Doctoral dissertation, Université Catholique de Louvain, 3 tomes.

DeJong, J. T., Frost, J. D., & Sacs, M. (2000, November). Relating quantitative measures of surface roughness and hardness to Geomaterial interface strength. In *Proceedings of Geo-Eng 2000 Conference*. Sydney: CDROM.

DeJong, J. T., Randolph, M. F., & White, D. J. (2003). Interface load transfer degradation during cyclic loading: a microscale investigation. *Soils and Foundations*, 43, 91–94.

Desrues, J., & Duthilleul, B. (1984). Mesure du champ de déformation d'un objet plan par la méthode stéréophotogrammétrique de faux relief. *Journal de mécanique théorique et appliquée*, 3(1), 79–103.

Desrues, J., & Viggiani, G. (2004). Strain localization in sand: An overview of the experimental results obtained in Grenoble using stereophotogrammetry. *International Journal for Numerical and Analytical Methods in Geomechanics*, 28(4), 279–321.

Desrues, J., Chambon, R., Mokni, M., & Mazerolle, F. (1996). Void ratio evolution inside shear bands in triaxial sand specimens studied by computed tomography. *Géotechnique*, 46(3), 529–546.

Desrues, J., Mokni, M., & Mazerolle, F (1991). Tomodensitométrie et localisation dans les sables. In *Proceedings, 10th ECSMFE, Florence* (pp. 61–64). Balkema: Rotterdam.

Dove, J. E., & Frost, J. D. (1996). A method for measuring geomembrane surface roughness. *Geosynthetics International*, 3(3), 369–392.

Dove, J. E., & Frost, J. D. (1999). Peak friction behavior of smooth geomembrane-particle interfaces. *Journal of Geotechnical and Geoenvironmental Engineering*, 125(7), 544–555.

Dove, J. E., Bents, D. D., Wang, J., & Gao, B. (2006). Particle-scale surface interactions of non-dilative interface systems. *Geotextiles and Geomembranes*, 24(3), 156–168.

Dove, J. E., Frost, J. D., & Dove, P. M. (1996). Geomembrane microtopography by atomic force microscopy. *Geosynthetics International*, 3, 227–245.

Frost, J. D., & Han, J. (1999). Behavior of interfaces between fiber-reinforced polymers and sands. *Journal of geotechnical and geoenvironmental engineering*, 125(8), 633–640.

Frost, J. D., Kim, D., & Lee, S. W. (2012). Microscale geomembrane-granular material interactions. *KSCE Journal of Civil Engineering*, 16(1), 79–92.

Fuggle, A. R. (2011). *Geomaterial gradation influences on interface shear behavior*. PhD Dissertation, School of Civil and Environmental Engineering, Georgia Institute of Technology, Atlanta.

Hartley, S. (1982). *Shear bands in sand*. Part II: Project Report, Department of Engineering, University of Cambridge, UK.

Krumbein, W. C., & Sloss, L. L. (1951). Stratigraphy and sedimentation. *Soil Science*, 71(5), 401.

Lee, S. W., & Kagbo, S. (2002). Strain induced changes in geomembrane surface topography. *Geosynthetics International*, 9(1), 21.

Lees, G. (1964). The measurement of particle shape and its influence in engineering materials. *Journal of the British Granite and Whinstone Federation, London*, 4(2), 1–22.

Mitchell, J. K., & Soga, K. (2005). *Fundamentals of soil behavior* (3rd ed.). New York, USA: Wiley.

Morgera, A. (2012). *Dominant points detection for shape analysis*. Doctoral dissertation, University of Cagliari, Italy.

Nimisha, R. (2017). *Shape characterization of granular particles using image based techniques*. Ph.D. Thesis, Indian Institute of Science, Bangalore, India.

Paikowsky, S. G., Player, C. M., & Connors, P. J. (1995). A dual interface apparatus for testing unrestricted friction of soil along solid surfaces. *Geotechnical Testing Journal, ASTM*, 18(2), 168–193.

Pal, N. R., & Pal, S. K. (1993). A review on image segmentation techniques. *Pattern Recognition*, 26(9), 1277–1294.

Powers, M. C. (1953). A new roundness scale for sedimentary particles. *Journal of Sedimentary Research*, 23(2), 117–119.

Rechenmacher, A., & Finno, R. (2004). Digital image correlation to evaluate shear banding in dilative sands. *Geotechnical Testing Journal, ASTM*, 27(1), 13–22.

Réthoré, J., Hild, F., & Roux, S. (2007). Shear-band capturing using a multiscale extended digital image correlation technique. *Computer Methods in Applied Mechanics and Engineering*, 196 (49), 5016–5030.

Sadrekarimi, A., & Olson, S. M. (2010). Particle damage observed in ring shear tests on sands. *Canadian Geotechnical Journal*, 47(5), 497–515.

Shapiro, L. G., & Stockman, G. C. (2001). *Computer vision*. New Jersey: USA, Prentice-Hall.

Sozer Z. B. (2005). *Two-dimensional characterization of topographies of geomaterial particles and surfaces*. Doctoral dissertation, Georgia Institute of Technology, Atlanta, USA.

Vangla, P., & Latha, G. M. (2015). Influence of particle size on the friction and interfacial shear strength of sands of similar morphology. *International Journal of Geosynthetics and Ground Engineering*, 1(6), 1–12.

Vangla, P., & Latha, G. M. (2016). Effect of particle size of sand and surface asperities of reinforcement on their interface shear behaviour. *Geotextiles and Geomembranes*, 44(3), 254–268.

Vangla, P., & Latha, G. M. (2017). Surface topographical analysis of geomembranes and sands using 3D optical profilometer. *Geosynthetics International*, 24(2), 151–166.

Wadell, H. (1932). Volume, shape, and roundness of rock particles. *The Journal of Geology*, 40 (5), 443–451.

Wadell, H. (1933). Sphericity and roundness of rock particles. *The Journal of Geology*, 41(3), 310–331.

White, D. J., Take, W. A., Bolton, M. D., & Munachen, S. E. (2001, August). A deformation measuring system for geotechnical testing based on digital imaging, close-range photogrammetry, and PIV image analysis. In *Proceedings of the 15th International Conference on Soil Mechanics and Geotechnical Engineering (XVth ICSMGE)* (Vol. 1, pp. 539–542).

Wolf, H., König, D., & Triantafyllidis, T. (2003). Experimental investigation of shear band patterns in granular material. *Journal of Structural Geology*, 25(8), 1229–1240.

Geotechnical Challenges in Tunnelling Through Weak Rocks

Mahendra Singh

Abstract Engineers associated with construction of tunnels in weak rocks are frequently met with geotechnical problems like instability of tunnels, yielding of the rock mass and excessive deformations due to squeezing. The problems are induced due to redistribution of in situ stresses around tunnel periphery caused by excavation of the tunnel. It is a challenging task to have proper understanding of the geotechnical issues before starting the excavation. The present chapter discusses some of the most challenging geotechnical issues which can be resolved in advance with characterisation of the rock mass at the site. These issues include assessing rock mass strength subject to given confining pressure for unreinforced and bolted rock mass, assessment of squeezing potential, assessment of tunnel deformation and expected support pressure. If adequate understanding on these issues is available with the designers, proper strategies may be formulated to handle problems at construction stage.

Keywords Squeezing tunnels · Failure criterion · Tunnel deformation · Support pressure · Rock bolt · Weak rock

1 Introduction

Geotechnical engineers working in hydropower and transportation engineering sectors often deal with construction of tunnels in rocks. During planning, design and construction of tunnels, geotechnical engineering plays the most important role as an inadequate understanding of geotechnical aspects may result in serious cost implications. The geology in the Himalayan region is extremely fragile and full of surprises. The rock masses invariably exhibit structural discontinuities like joints, bedding planes, foliations, shear zones and varying degree of weathering. The rock masses are characterised with low strength, high deformability and anisotropy in

M. Singh (✉)

Department of Civil Engineering, IIT Roorkee, Roorkee 247667, India
e-mail: singhfce@iitr.ac.in; msingh.civil@gmail.com

engineering behaviour. Tectonic stresses are always present in the region. The stress regime changes due to excavation of tunnel, and a complex interaction of rock mass and tunnels support occurs. It is very important to foresee the problems likely to be caused due to redistribution of stresses. Once the expected engineering behaviour is adequately predicted, the strategies can then be formulated to cope up with the problems at the construction stage.

In general, it is common to use the term “weak rock” to represent the behaviour of the “rock mass” as a whole. The overall behaviour of the rock mass is governed jointly by the characteristics of intact rock substance and the geological discontinuities present in the rock mass. In addition, the scale of the problem affects the behaviour of the tunnel in the rock mass.

The basic aim of the geotechnical design in tunnelling is to utilise the rock itself as a principal structural material without creating much disturbance during excavation process with minimum addition of concrete and steel support. The instability may be due, but not limited, to: (a) geological structural features, i.e. joints, foliations, bedding planes, shear zones and faults, (b) excessive high stresses due to tectonic activity, (c) weathering of rock materials or swelling minerals and (d) excessive ground water pressure. The potential failure mechanism plays key role in geotechnical design of the tunnels. The failure may be due to structurally controlled failure mechanism which prevails at shallow depths where structural discontinuities, e.g. joints, bedding planes and foliations dominate the engineering behaviour. Stress-induced failure occurs at relatively greater depths.

The Himalayan geology is so varying and full of surprises that it is never possible to get full information in advance. Though preliminary investigations are done at the initial stage itself, it is very challenging at the tender stage to exactly quantify the problems likely to be encountered during tunnel construction. The geotechnical model needs to be updated during construction and adequate arrangements are required to accommodate the changes in the support system as the construction progresses. Sufficient understanding and comprehension is required at the design stage itself before starting the construction. Some of the challenges to be handled by the geotechnical engineers, especially for weak rock masses, are as follows:

- i. Determination of stresses around tunnels,
- ii. Rock mass strength, failure criteria for jointed rocks and behaviour of jointed rocks reinforced with rock bolts,
- iii. Assessment of squeezing potential,
- iv. Assessment of tunnel closure,
- v. Assessment of ultimate support pressure.

The present chapter discusses how reliable estimates of geotechnical design parameters can be made at the design stage itself to tackle the problems during construction. This chapter is focussed on characterisation and classification-based approaches which are simple in use in the field. In addition, this chapter concerns the instability issues only. Seepage problems, numerical analysis, detailed design of support system and construction strategies in the field are beyond the scope of the present chapter.

2 Stresses Around Tunnels

Excavation of tunnel disturbs the in situ stress state and redistributes stresses around the tunnel periphery. Closed-form solutions are available for standard shapes of tunnels to get stress distribution around tunnels (Obert and Duvall 1967). Figure 1 shows typical variation of radial and circumferential stresses in an elastic rock mass due to excavation of a circular tunnel in a rock mass subjected to hydrostatic stress state. Hoek (2007) has discussed how deformation and displacements occur as construction progresses. It is observed by Hoek (2007) that the radial displacement starts at a distance equal to about one half the tunnel diameter ahead of the advancing face and reaches its final value at about one and half tunnel diameter behind the face. The tunnel deformation analysis can be done if the rock mass properties and in situ stress values are known. A simple analysis of tunnel deformation for a circular tunnel (Fig. 2) subject to hydrostatic in situ stress (p_o) and internal support pressure (p_i) is given by Hoek (2007). For simplicity, a linear failure criterion was assumed for the rock mass as follows:

$$\sigma_1 = \sigma_{cm} + k\sigma_3 \quad (2.1)$$

Fig. 1 Stress distribution around a circular tunnel (in situ stresses: hydrostatic)

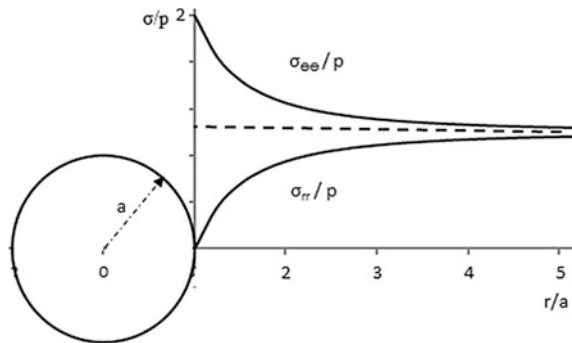
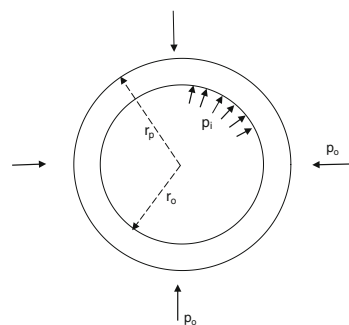


Fig. 2 A circular tunnel subject to internal pressure and hydrostatic in situ stress



where σ_{cm} is the uniaxial compressive strength of the rock mass given as follows:

$$\sigma_{cm} = (2c \cos \phi) / (1 - \sin \phi) \quad (2.2)$$

and k is the slope of σ_1 versus σ_3 line and is given as follows:

$$k = (1 + \sin \phi) / (1 - \sin \phi) \quad (2.3)$$

σ_1 is the major principal stress at failure; σ_3 is confining stress at failure; and c and ϕ are Mohr–Coulomb shear strength parameters.

If the internal support pressure p_i is sufficiently large (greater than the critical support pressure p_{cr}), no failure occurs, and the behaviour of the rock mass surrounding the tunnel is elastic. The critical support pressure can be obtained as follows (Hoek 2007):

$$p_{cr} = (2p_o - \sigma_{cm}) / (1 + k) \quad (2.4)$$

However, if the internal support pressure is not sufficient enough, the rock mass fails and the radius r_p of the plastic zone around the tunnel may be obtained as follows:

$$r_p = r_o \left[\frac{2(p_o(k-1) + \sigma_{cm})}{(1+k)((k-1)p_i + \sigma_{cm})} \right]^{\frac{1}{(k-1)}} \quad (2.5)$$

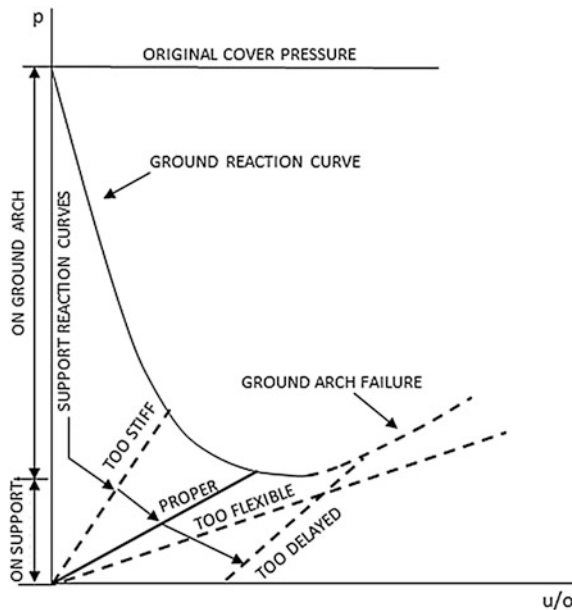
The total inward radial displacement of the tunnel wall, u_{ip} , may be obtained as follows:

$$u_{ip} = \frac{r_o(1+v)}{E} \left[2(1-v)(p_o - p_{cr})(r_p/r_o)^2 - (1-2v)(p_o - p_i) \right] \quad (2.6)$$

where E and v are modulus of elasticity and Poisson's ratio of the rock mass.

For designing appropriate support system, rock mass–tunnel support interaction analysis is carried out for the particular support system adopted. A case of squeezing ground condition is presented in Fig. 3 (Hoek and Brown 1982). The plot shows variation of support pressure, p , with tunnel wall displacement, u . If the support system is too flexible, it will offer relatively little resistance even after deforming to very large extent. On the other hand, if the support system is too stiff, it will attract very high stresses and may yield. It is not only important to have a proper type of support; equally important is the decision when to apply the support. If the supports are employed too early, they will attract high stresses and may yield. If the supports are too delayed, large deformations would have occurred and rock mass would have failed. For a proper economical, safe and efficient design, the supports installed should be neither too early, nor too late and at the same time, neither too rigid nor too stiff compared with the stiffness of the rock mass.

Fig. 3 Rock mass–tunnel support interaction analysis (Hoek and Brown 1982)



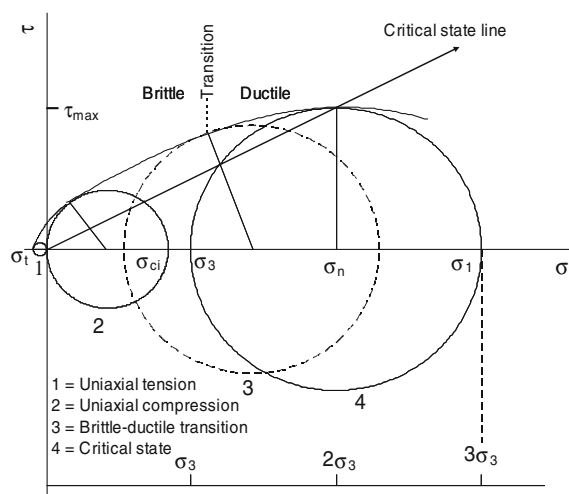
3 Rock Mass Strength and Failure Criteria

While performing rock mass–tunnel support interaction analysis, the designer needs to assess the rock mass strength subject to the prevailing confining pressure. An accurate determination of the rock mass strength is therefore the backbone of the analysis and design. In the simple analysis presented in the preceding section, simple linear strength behaviour of the rock mass was considered. In reality, the strength behaves in a nonlinear manner; i.e. the principal stress at failure is a nonlinear function of confining pressure. A suitable nonlinear strength criterion is used for this purpose. A number of strength criteria are available in the literature (Hoek and Brown 1980; Ramamurthy 1993; Ramamurthy and Arora 1994; Singh and Singh 2012), and the use of any criterion may be a matter of choice. The criterion should, however, be simple in use; its parameters should carry physical meaning, and the designer should be able to easily obtain these parameters. The criterion parameters should be robust; i.e. their values should not vary when amount of input data, which is given to obtain input parameters, is varied. Conventional Mohr–Coulomb failure criterion (linear form) is the most widely used failure criterion and fulfils the requirement of an ideal failure criterion except that it is linear criterion. This criterion has been extended to take care of nonlinearity in strength behaviour, and modified Mohr–Coulomb (MMC) criterion has been suggested (Singh and Singh 2005, 2012; Singh et al. 2011, 2015; Singh 2016). It is reported that the MMC criterion parameter ϕ is the most robust (Shen et al. 2014) parameter as compared to other criterion parameters. A brief description of the MMC criterion is presented in the following.

3.1 Modified Mohr–Coulomb (MMC) Criterion for Jointed Rocks

The MMC criterion derives its base from Barton's critical state concept for rocks. A rock tested under low confining pressure fails in a dilatant and brittle manner due to opening up of the pre-existing microcracks resulting in high value of instantaneous friction angle ϕ . For tests at higher confining pressure, the tendency of dilation is suppressed and the failure mechanism shifts from brittle to ductile and a relatively lower value of ϕ is obtained. If confining pressure is increased further, the rock becomes completely ductile; at sufficiently high confining pressure, the rock enters the critical state (Fig. 4). The tangential gradient of the envelope is steep at low confining pressure and tends to become asymptotic to a horizontal line at critical state. Barton (1976) states “critical state for an initially intact rock is defined as the stress condition under which Mohr envelope of peak shear strength of the rocks reaches a point of zero gradient. This condition represents the maximum possible shear strength of the rock. For each rock, there will be a critical effective confining pressure above which the shear strength cannot be made to increase”. This characteristic of Mohr failure envelope approaching horizontal has been used to define the correct shape of the failure criterion (Singh and Singh 2005; Singh et al. 2011, 2015; Singh 2016), and the conventional Mohr–Coulomb criterion was modified to incorporate nonlinearity in strength behaviour. Based on statistical back analysis of large number of triaxial test data, it was also shown by Singh et al. (2011) that for the application of MMC criterion, the critical confining pressure of an intact rock may be taken nearly equal to its UCS, σ_{ci} . The modified Mohr–Coulomb (MMC) criterion was thus expressed as follows:

Fig. 4 Barton's critical state concept for rocks (Singh et al. 2011)



$$(\sigma_1 - \sigma_3) = \sigma_{ci} + \frac{2 \sin \phi_{i0}}{1 - \sin \phi_{i0}} \sigma_3 - \frac{1}{\sigma_{ci}} \frac{\sin \phi_{i0}}{(1 - \sin \phi_{i0})} \sigma_3^2 \text{ for } 0 \leq \sigma_3 \leq \sigma_{ci} \quad (3.1)$$

where σ_1 is the major principal stress at failure; σ_3 is the minor principal stress at failure; ϕ_{i0} is the friction angle of intact rock at very low confining pressure ($\sigma_3 \rightarrow 0$); and σ_{ci} is UCS of the intact rock given as follows:

$$\sigma_{ci} = \frac{2c_i \cos \phi_{i0}}{1 - \sin \phi_{i0}} \quad (3.2)$$

where c_i is the cohesion of the intact rock.

The expression for differential stress at failure ($\sigma_1 - \sigma_3$) is applicable up to critical confining pressure $\sigma_3 = \sigma_{ci}$. Beyond this point, the differential stress ($\sigma_1 - \sigma_3$) becomes constant as per the critical state concept (Barton 1976).

Figure 5 shows results from triaxial tests conducted on jointed rock by Brown (1970). The variation of shear strength indicates that jointed rocks also follow critical state concept. It is observed that at sufficiently high confining pressure the Mohr failure envelopes of jointed and intact rocks merge with each other. Singh and Singh (2012) employed the critical state concept to suggest a nonlinear strength criterion for jointed rocks. The suggested strength criterion for jointed rock along with the failure criterion of intact rock is shown in Fig. 6. Based on analysis of a compiled database comprising of more than 730 triaxial test data for a variety of rocks ($\sigma_{ci} = 9.5\text{--}123$ MPa) from the worldwide literature, Singh and Singh (2012) suggested that critical confining pressure of jointed rocks may also be taken nearly equal to UCS of intact rock, σ_{ci} , for the application of the proposed criterion. Consequently, the MMC criterion “single parameter form” for jointed rocks was expressed as follows:

Fig. 5 Mohr failure envelopes for intact and jointed specimens (Source Singh and Singh 2012; redrawn from Brown 1970)

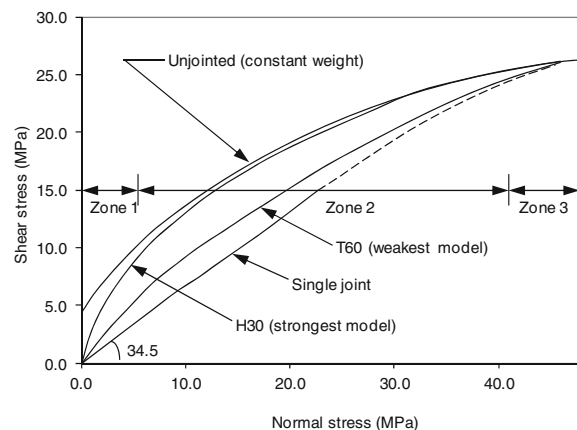
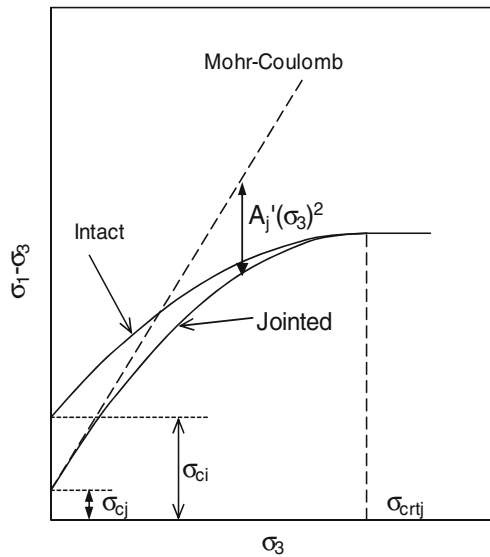


Fig. 6 Modified Mohr–Coulomb criteria for intact and jointed rocks (Singh and Singh 2012)



$$(\sigma_1 - \sigma_3) = \sigma_{cj} + \frac{2 \sin \phi_{j0}}{1 - \sin \phi_{j0}} \sigma_3 - \frac{1}{\sigma_{ci}} \frac{\sin \phi_{j0}}{(1 - \sin \phi_{j0})} \sigma_3^2 \text{ for } 0 \leq \sigma_3 \leq \sigma_{ci} \quad (3.3)$$

where σ_{cj} is the UCS of the rock mass; ϕ_{j0} is the friction angle of the rock mass corresponding to very low confining pressure range ($\sigma_3 \rightarrow 0$) and can be obtained as follows:

$$\sin \phi_{j0} = \left[(1 - SRF) + \frac{\sin \phi_{i0}}{1 - \sin \phi_{i0}} \right] \Big/ \left[(2 - SRF) + \frac{\sin \phi_{i0}}{1 - \sin \phi_{i0}} \right] \quad (3.4)$$

where SRF is strength reduction factor = σ_{cj}/σ_{ci} .

Few triaxial tests on intact rock are required to get parameter ϕ_{i0} . If triaxial test data on intact rock is not available, the following nonlinear form of the criterion may be used as an alternative (Singh and Rao 2005a):

$$(\sigma_1 - \sigma_3) = \sigma_{cj} - 2A_j \sigma_{ci} \sigma_3 + A_j \sigma_3^2 \text{ for } 0 \leq \sigma_3 \leq \sigma_{ci} \quad (3.5)$$

where A_j is an empirical criterion parameter and may be estimated from the experimental value of σ_{ci} , using the following expressions:

$$\text{For average prediction of } \sigma_1 \quad A_j = -1.23(\sigma_{ci})^{-0.77} \quad (3.6)$$

$$\text{For lower bound prediction of } \sigma_1 \quad A_j = -0.43(\sigma_{ci})^{-0.72} \quad (3.7)$$

The designer may use the lower bound prediction. However, a parametric analysis by varying the strength values from low to average prediction gives a good insight into behaviour of the rock mass.

3.1.1 Assessment of σ_{cj} in Field

An important input to the MMC criterion is the UCS of the rock mass, σ_{cj} . The values of σ_{ci} and ϕ_{i0} will be available from laboratory tests on intact rocks; however, determination of σ_{cj} is a difficult task. Major factors that govern σ_{cj} are intact rock strength σ_{ci} , discontinuity characteristics, kinematics and possible failure mode. Rock mass classification systems are frequently used in the field to assess the rock mass strength. Table 1 presents some of the approaches available from the literature. Amongst rock mass classification systems, the Q system is widely used for tunnelling projects in India. The following expressions may be used to assess σ_{cj} from Q :

Singh et al. (1992)

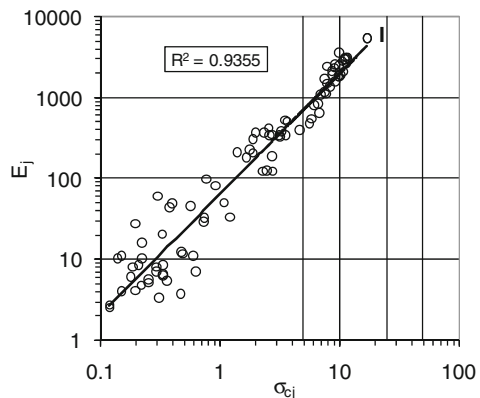
$$\sigma_{cj} = 7\gamma Q^{1/3} \text{ MPa} \quad (\text{for } Q < 10, 2 < \sigma_{ci} < 100 \text{ MPa, SRF} = 2.5) \quad (3.8)$$

Table 1 Approaches for assessing UCS of jointed rocks

Author(s)	Relation
Yudhbir and Prinzl (1983)	$\sigma_{cj}/\sigma_{ci} = \exp[7.65 \times (\text{RMR} - 100)/100]$
Ramamurthy et al. (1985), Ramamurthy (1986)	$\sigma_{cj}/\sigma_{ci} = \exp\{(\text{RMR} - 100)/18.75\}$
Trueman (1988), Asef et al. (2000)	$\sigma_{cj} = 0.5 \exp(0.06 \text{RMR}) \text{ MPa}$
Kalamaras and Bieniawski (1993)	$\sigma_{cj}/\sigma_{ci} = \exp\{(\text{RMR} - 100)/24\}$
Sheorey (1997)	$\sigma_{cj}/\sigma_{ci} = \exp\{(\text{RMR} - 100)/20\}$
Aydan and Dalgic (1998)	$\sigma_{cj}/\sigma_{ci} = \text{RMR}/\{\text{RMR} + 6(100 - \text{RMR})\}$
Zhang (2010)	$\sigma_{cj}/\sigma_{ci} = 10^{(0.013\text{RQD}-1.34)}$
Ramamurthy (1993), Ramamurthy and Arora (1994)	$\sigma_{cj}/\sigma_{ci} = \exp(-0.008J_f)$
Hoek and Marinos (2000)	$\sigma_{cj} = (0.0034m_i^{0.8}) \sigma_{ci}[1.029 + 0.025e^{-0.1m_i}]^{\text{GSI}}$ m_i = Hoek-Brown constant
Singh (1997), Singh et al. (2002)	$\sigma_{cj}/\sigma_{ci} = \exp(-aJ_f)$; $a = 0.0123$ for splitting, 0.010 for shearing, 0.0250 for rotation and 0.0180 for sliding

Major source Zhang (2010)

Fig. 7 Jointed rock positions on Deere–Miller classification chart (Singh and Rao 2005b)



Barton (2002)

$$\sigma_{cj} = 5\gamma \left(\frac{Q\sigma_{ci}}{100} \right)^{1/3} \text{ MPa} \quad (3.9)$$

where γ is the unit weight of the rock mass in gm/cc and σ_{cj} and σ_{ci} are in MPa.

It may be noted that the best estimates of rock mass strength, σ_{cj} , can only be made in the field through large-size field-testing by loading the mass up to failure. It is, however, extremely difficult, time consuming and expensive to load a large volume of jointed mass in the field up to ultimate failure. Singh (1997), Singh and Rao (2005b) have discussed that a better alternative is to get the deformability properties of rock mass by stressing a limited area of the mass up to a certain stress level and then relate the ultimate strength of the mass to the laboratory UCS of the rock material through a strength reduction factor, SRF. It has been shown by Singh and Rao (2005b) that when jointed rock positions are plotted on Deere and Miller (1966) classification chart, the points lie around an empirical line passing through the intact rock position (Fig. 7). The gradient of this empirical line defines a correlation between strength and modulus values of intact and jointed rocks. The modulus reduction factor, MRF, and the strength reduction factor, SRF, are correlated with each other by the following expression approximately:

$$\text{SRF} = (\text{MRF})^{0.63} \quad (3.10)$$

$$\Rightarrow \sigma_{cj}/\sigma_{ci} = (E_j/E_i)^{0.63} \quad (3.11)$$

where SRF is the ratio of rock mass strength to the intact rock strength; MRF is the ratio of rock mass modulus to the intact rock modulus; σ_{cj} is the rock mass strength; σ_{ci} is the intact rock strength; E_j is the elastic modulus of rock mass; and E_i is the intact rock modulus available from laboratory tests.

The elastic modulus of rock mass, E_j , may be obtained in the field by conducting uniaxial jacking tests (IS:7317 1974) in drift excavated for the purpose. The test consists of stressing two parallel flat rock faces (usually the roof and invert) of a drift by means of a hydraulic jack (Mehrotra 1992). The stress is generally applied in two or more cycles, and the second cycle of the stress deformation curve is recommended for computing the field modulus as follows:

$$E_j = \frac{m(1 - v^2)}{\sqrt{A}\delta_e} \quad (3.12)$$

where E_j is the elastic modulus of the rock mass in kg/cm^2 ; v is Poisson's ratio of the rock mass ($=0.3$); P is the load in kg; δ_e is the elastic settlement in cm; A is the area of plate in cm^2 ; and m is an empirical constant ($=0.96$ for circular plate of 25 mm thickness).

The results obtained through this approach are likely to be more realistic as inputs are directly derived from the field data. The size of the drift should be sufficiently large as compared to the plate size so that there is little effect of confinement. The confinement may result in overprediction of the modulus values.

3.2 Effect of Rock Bolting on Rock Strength

Rock bolts are widely used to reinforce the rock mass for stabilising tunnels. Numerical methods are the best answer to assess strength of bolted rock. However, numerical modelling is relatively expensive and time consuming and should therefore be preferred at the final stage of design. Srivastava and Singh (2015) have suggested a simple empirical approach to assess approximately the strength of fully grouted passive rock bolts. The approach is based on outcome of laboratory tests conducted on jointed rock specimens with and without rock bolts. The rock mass strength is considered to be governed by the shear strength of the joints present in the mass. The shear strength of a single joint in the mass (without rock bolt) is expressed as follows:

$$\tau_f = c_j + \sigma_n \tan(\phi_j) \quad (3.13)$$

where c_j = cohesion of the joint and ϕ_j = friction angle of the joint.

When rock mass is reinforced with bolts, the strength of a series of joints in the mass is represented as follows:

$$\tau_f = c_{j_mass} + \sigma_n \tan(\phi_{j_mass}) \quad (3.14)$$

where c_{j_mass} and ϕ_{j_mass} are the cohesion and friction angle along joints in the mass.

It was observed by Srivastava and Singh (2015) that when rock mass is reinforced with fully grouted rock bolts, there is substantial improvement in the cohesion of the joints; however, the friction angle remains almost unchanged. The cohesion enhancement (CE) caused by bolting was expressed as follows:

$$CE = c_{j_mass} - c_j \quad (3.15)$$

where c_{j_mass} is the cohesion of series of joint in mass and c_j is the cohesion of a single joint.

The cohesion enhancement is a measure of improved shear strength of joints which depends on the amount of steel, geometry of rock mass and configuration of bolt pattern. The amount of steel was represented by the term per cent area ratio, A_r , given by the following:

$$A_r = (A_b/A) \times 100\% \quad (3.16)$$

where A_b = total cross section area of bolts and A = area of mass on shearing plane.

While considering geometry, the representative rock block dimension (D_b) and bolt spacing (S_b) were found to affect the strength enhancement. If the block dimension is small and bolt spacing is large, the enhancement will be low, whereas if the block dimension is large and the bolt spacing is relatively small, the enhancement can be expected to be high. To account for the importance of the block dimension and bolt spacing, a number N (spacing ratio) was defined as follows:

$$N_b = S_b/D_b \quad (3.17)$$

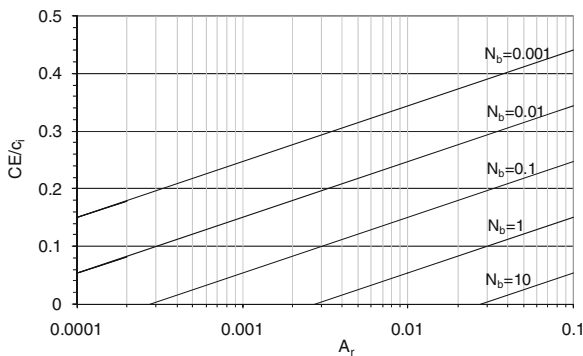
where $S_b = \sqrt{(\text{Area of shearing plane})/(\text{Number of bolts})}$, $D_b = (\text{volume of representative block})^{1/3}$.

The cohesion enhancement due to provision of rock bolts was obtained from laboratory test data and was plotted (as a fraction of intact rock cohesion) against the quantity A_r/N . The following correlation was obtained for the cohesion enhancement for the given amount of steel, bolt spacing and representative rock block dimension:

$$(CE)/c_i = (c_{j_mass} - c_j)/c_i = 0.04 \ln(A_r/N_b) + 0.24 \quad (3.18)$$

A ready-to-use chart was produced by Srivastava and Singh (2015) to assess the cohesion enhancement (Fig. 8) depending on amount of steel, bolt spacing and representative block dimension. The cohesion enhancement can be readily used to find out the enhanced rock mass strength σ_{cj} in MMC criterion for incorporating the effect of rock bolts on strength behaviour of rock mass.

Fig. 8 Chart for computing cohesion enhancement
(Srivastava and Singh 2015)



4 Assessment of Squeezing Potential of Tunnels in Weak Rocks

Squeezing of tunnels is a common phenomenon in tunnels excavated in weak rocks. Barla (2001) has defined squeezing as large time-dependent convergence during tunnel excavation. A particular combination of induced stresses and material properties may induce squeezing conditions. Excessive deformations may occur and continue over a long period of time. Identification of squeezing potential is the first step towards the successful design and construction of tunnels in weak rocks. Some of the approaches used for identifying the squeezing potential are presented in brief in the following sections. The approaches have been grouped into two broad categories, i.e. empirical and semi-empirical approaches.

4.1 Empirical Approaches

4.1.1 Singh et al. (1992) Approach Based on *Q* System

Singh et al. (1992) analysed 39 case histories, on squeezing and non-squeezing conditions, and plotted tunnel depth against rock mass quality *Q* (Barton et al. 1974). A clear-cut demarcation line differentiating squeezing cases from non-squeezing cases was observed, and the condition for squeezing found as follows:

$$H \geq 350Q^{1/3} \quad (4.1)$$

where *H* is tunnel depth in m.

4.1.2 Goel et al. (1995) Approach Based on Rock Mass Number

Difficulty is generally faced in assigning correct rating to the parameter SRF in Q system. To avoid this problem, Goel et al. (1995) suggested a rock mass number N , defined as stress-free Q ; i.e. Q with SRF = 1.

$$N = (Q)_{\text{SRF}=1} \quad (4.2)$$

Considering the tunnel depth H (m), the tunnel span or diameter B (m) and the rock mass number N from 99 tunnel sections, Goel et al. (1995) plotted the available data on a log–log diagram between N and $HB^{0.1}$. The following correlations were suggested:

For squeezing conditions

$$H \gg (275N^{0.33})B^{-1} \text{ (m)} \quad (4.3)$$

For non-squeezing conditions

$$H \ll (275N^{0.33})B^{-1} \text{ (m)} \quad (4.4)$$

4.1.3 Dwivedi (2014) Approach Based on Q , N and Joint Factor

Recently Dwivedi (2014) collected data for more than 180 tunnel sections for the various ground conditions. Rock mass quality was obtained by computing Q (Barton et al. 1974), N (Goel et al. 1995) and joint factor J_f (Arora 1987; Ramamurthy and Arora 1994; Singh 1997; Singh et al. 2002, 2004). The value of joint factor will vary along the periphery of the tunnel. For simplicity, the joint factor was obtained at springing level (element A, Fig. 9). Apparent dip of the joint as obtained in the plane normal to tunnel axis was considered to get the joint inclination parameter of the joints. The conditions for different ground conditions were expressed as given in Table 2.

4.2 Semi-empirical Approaches

4.2.1 Rock Mass Strength-Based Approaches

The excavation of a tunnel redistributes the stresses in the tectonically stressed rock mass. The tangential stresses around the tunnel periphery may become large and in the absence of adequate support, may exceed the uniaxial compressive strength of the rock mass. The rock mass at the periphery may fail, and the broken zone may

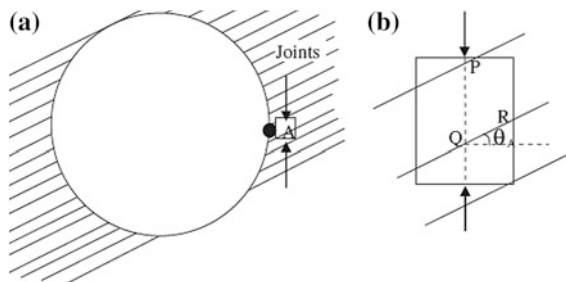


Fig. 9 Computation of joint factor: **a** rock mass element “A” near springing level. **b** Apparent dip of joints for element “A”

Table 2 Ground conditions based on Q , N and J_f (Dwivedi 2014)

Ground condition	Based on Q	Based on N	Based on J_f
Self-supporting	$H < 191(Q/D)^{0.642}$	$H < 127(N/D)^{0.9087}$	$HD < 170009e^{-0.025J_f}$
Non-squeezing	$H < 722(Q/D)^{0.34}$	$H < 466(N/D)^{0.3176}$	$HD < 170234e^{-0.017J_f}$
Squeezing	$H > 722(Q/D)^{0.34}$	$H > 466(N/D)^{0.3176}$	$HD > 170234e^{-0.017J_f}$
Rock-burst	$H > 635(Q/D)^{-0.27}$ and $Q/D > 0.08$	$H > 1035(N/D)^{-0.096}$ and $N/D > 0.14$	$HD > 4189e^{0.0049J_f}$

progress slowly in the radial direction, giving rise to time-dependent large-tunnel convergence. The rock-mass-strength-based approaches attempt to “quantify” squeezing potential by comparing the rock mass strength with the overburden stress at the tunnel depth.

Jethwa et al. (1984) defined an index “competency factor” as the ratio of uniaxial compressive strength of rock mass to overburden stress γH . The competency factor was used to define squeezing potential, and a classification for squeezing potential was suggested as shown in Table 3.

Table 3 Classification of squeezing potential (Jethwa et al. 1984)

$\sigma_{cm}/(\gamma H)$	Squeezing type
<0.4	Highly squeezing
0.4–0.8	Moderately squeezing
0.8–2.0	Mildly squeezing
>2.0	Non-squeezing

Where σ_{cm} = rock mass uniaxial compressive strength; γ = rock mass unit weight; H = tunnel depth below surface

Table 4 Squeezing levels defined by Hoek and Marinos (2000)

Class	Squeezing level	Tunnel strain (%)
1	Few support problems	$\varepsilon_t \leq 1$
2	Minor squeezing	$1 < \varepsilon_t \leq 2.5$
3	Severe squeezing	$2.5 < \varepsilon_t \leq 5.0$
4	Very severe squeezing	$5.0 < \varepsilon_t \leq 10.0$
5	Extreme squeezing	$10.0 < \varepsilon_t$

Hoek and Marinos (2000) also used the ratio of rock mass uniaxial compressive strength σ_{cm} to the in situ stress p_o to define tunnel squeezing potential. An approximate relationship was suggested based on axisymmetric finite element analysis to assess the tunnel strain for in situ stresses p_o and support pressures p_i as follows:

$$\varepsilon_t(\%) = 0.15(1 - p_i/p_o)(\sigma_{cm}/p_o)^{-(3p_i/p_o + 1)/(3.8p_i/p_o + 0.54)} \quad (4.5)$$

The squeezing level was classified as given in Table 4.

4.2.2 Strain-Based Approaches

Aydan et al. (1993) Approach

Rather than comparing the rock mass strength with the in situ stress, some investigators find it more convenient to compare the strains or deformations to quantify the squeezing potential. It is argued by Singh et al. (2007) that the approach of comparing the strain and not the strength is advantageous as the deformations are easy to measure in the field. The field engineer can easily observe deformations and modify the support system during the progress of the project. Aydan et al. (1993) have used analogy between the stress-strain response of rock in laboratory and the tangential stress-strain response around tunnels to define squeezing potential. Five distinct states of stress-strain response were expressed during loading of a specimen at low confining stress (Fig. 10). Expressions were suggested to obtain the normalised strain levels as follows:

$$\eta_p = \varepsilon_p/\varepsilon_e = 2\sigma_{ci}^{-0.17}, \quad \eta_s = \varepsilon_s/\varepsilon_e = 3\sigma_{ci}^{-0.25}, \quad \eta_f = \varepsilon_f/\varepsilon_e = 5\sigma_{ci}^{-0.32} \quad (4.6)$$

If the strain level around a circular tunnel in a hydrostatic stress field is ε_0^a , and elastic strain limit for the rock mass is ε_0^e , the ratio of ε_0^a to ε_0^e gives an indication of the squeezing potential in the tunnel. A classification of squeezing potential was suggested as shown in Table 5 (Aydan et al. 1993). The squeezing potential was divided into five classes.

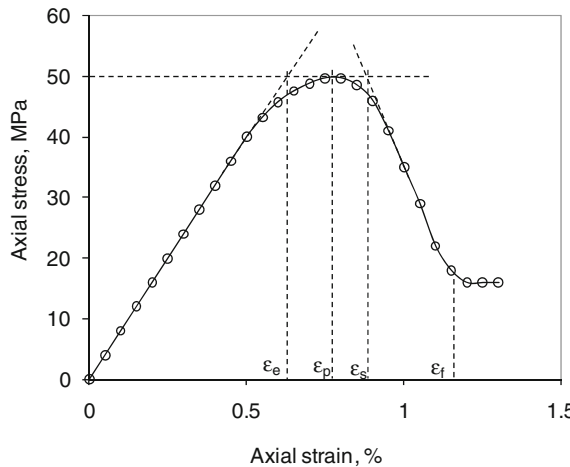


Fig. 10 Idealised strain levels used for defining squeezing levels (Aydan et al. 1993)

Table 5 Classification of squeezing behaviour according to Aydan et al. (1993)

Class	Squeezing degree	Symbol	Theoretical expression
1	Non-squeezing	NS	$\epsilon_0^a/\epsilon_0^e \leq 1$
2	Light squeezing	LS	$1 < \epsilon_0^a/\epsilon_0^e \leq \eta_p$
3	Fair squeezing	FS	$\eta_p < \epsilon_0^a/\epsilon_0^e \leq \eta_s$
4	Heavy squeezing	HS	$\eta_s < \epsilon_0^a/\epsilon_0^e \leq \eta_f$
5	Very heavy squeezing	VHS	$\eta_f < \epsilon_0^a/\epsilon_0^e$

Note ϵ_0^a is the tangential strain around a circular tunnel in a hydrostatic stress field and ϵ_0^e is the elastic strain limit for the rock mass

Critical-Strain-Based Approach (Singh et al. 2007)

The critical strain is defined as an empirical level of tangential strain at the periphery of the tunnel above which construction problems are likely to occur. Sakurai (1997) used critical strain to define various warning levels for severity of construction in a tunnel. Aydan et al. (1993) and Hoek (2001) considered critical strain value equal to 1% as a thumb rule. It has, however, been observed that there are some tunnels which suffered strains as high as 4% but did not exhibit stability problems (Hoek 2001). Singh et al. (2007) suggested that the critical strain should not be taken as 1%, rather it should depend on the properties of the intact rock material and jointed rock mass. Based on laboratory experiments on large number of rock mass specimens, Singh et al. (2007) suggested the following relationship for computing critical strain, ϵ_{cr} .

Table 6 Squeezing potential in tunnels (Singh et al. 2007)

Class	Squeezing level	Tunnel strain (%)
1	No squeezing	$SI \leq 1.0$
2	Light squeezing	$1.0 < SI \leq 2.0$
3	Fair squeezing	$2.0 < SI \leq 3.0$
4	Heavy squeezing	$3.0 < SI \leq 5.0$
5	Very heavy squeezing	$5.0 < SI$

$$\varepsilon_{cr}(\%) = \frac{\sigma_{ci}}{E_{tj}^{0.37} E_i^{0.63}} \times 100 \quad (4.7)$$

where E_{tj} and E_i are the tangent moduli of rock mass and intact rock, respectively.

To assess rock mass modulus E_{tj} , one can use Q system and strength reduction factor. The following two alternative expressions were then obtained for critical strain.

$$\varepsilon_{cr}(\%) = 31.1 \frac{(\sigma_{ci})^{1.6}}{E_i^{0.6} Q^{0.2}} \quad (4.8)$$

and

$$\varepsilon_{cr}(\%) = 5.84 \frac{(\sigma_{ci})^{0.88}}{E_i^{0.63} Q^{0.12}} \quad (4.9)$$

To define squeezing potential, Singh et al. (2007) suggested that the observed or expected strain may be obtained either from numerical modelling or preferably from actual monitoring in the field. The squeezing index, SI, may then be obtained as follows:

$$SI = \frac{\text{Observed or expected strain}}{\text{Critical strain}} \quad (4.10)$$

A classification was suggested to quantify the squeezing potential (Table 6) which can be used to classify the squeezing potential based on the index SI. Based on the expected squeezing levels, the strategies may be formulated to face the construction problems.

5 Prediction of Tunnel Deformation

Deformations are major concern in case of tunnels excavated through weak rocks. If proper counter measures to install sufficient supports are not taken in time, excessive deformations may occur leading to instability problems. A prior

Table 7 Tunnel deformation based on Q and J_f (Dwivedi 2014)

Ground condition	Based on Q	Based on J_f
Non-squeezing	$\frac{u_p}{a} = \frac{0.0046\sigma_v}{Q^{0.5}(K+7)} + 0.0004$	$\frac{u_p}{a} = \frac{3 \times 10^{-10}\sigma_v(J_f)^3}{K+6} + 0.0003$
Squeezing	$\frac{u_p}{a} = \frac{0.0191\sigma_v Q^{-0.2}}{K+1} + 0.0025$	$\frac{u_p}{a} = \frac{5 \times 10^{-10}\sigma_v(J_f)^3}{K+0.5} + 0.0052$

knowledge of deformation level is therefore very essential to keep contingency plans ready in advance. An empirical approach to assess likely tunnel deformation that has been suggested recently is presented in the following section.

Dwivedi et al. (2013) have compiled a database of case histories from hydroelectric projects. Rock mass characteristics were defined either by Q or joint factor J_f . Attempts were made to find correlations amongst the deformation u_p , support stiffness K , in situ stress σ_v (MPa), tunnel radius a and rock mass characteristics J_f or Q for squeezing and non-squeezing ground conditions. The relationships so obtained are presented in Table 7.

6 Prediction of Support Pressure

The adequacy of the tunnel support system will depend on the ultimate support pressure and capacity of the support to resist that pressure. Various correlations are available in the literature to estimate the support pressure for squeezing and non-squeezing ground conditions.

Jethwa et al. (1984) used an analytical closed-form solution for a circular tunnel under a hydrostatic stress field and data from in situ monitoring and suggested expression for the ultimate rock pressure p_u on the tunnel lining in terms of peak and residual friction angles of the rock mass as shown in Fig. 11. The rock mass was considered to be elastic–plastic ideally brittle model with a Mohr–Coulomb strength criterion with known values of shear strength parameters for peak and residual conditions.

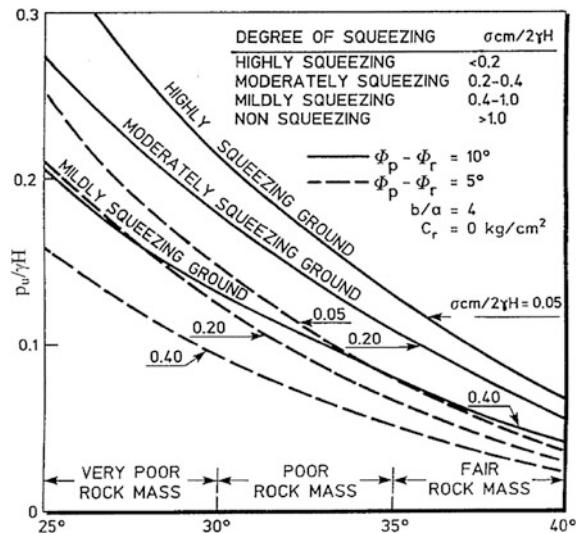
Grimstad and Barton (1993) suggested an empirical approach for estimation of roof support pressure, P_u , for squeezing and non-squeezing conditions in tunnels using rock mass quality, Q , as follows:

$$P_u = \frac{0.2\sqrt{J_n}}{3J_r} Q^{-1/3} \quad (6.1)$$

where P_u is the tunnel support pressure, MPa; J_n , the joint set number; J_r , the joint roughness number; and Q , the rock quality index.

Goel (1994) has suggested a correlation for support pressure, P_e , for non-squeezing ground based on rock mass number N as

Fig. 11 Support pressure as per Jethwa et al. (1984) approach



$$P_e = \frac{0.07H^{-0.1}a^{-0.1}}{N^{0.33}} + 0.022 \quad (6.2)$$

Goel (1994), based on case histories of 63 tunnels, concluded that the effect of tunnel size and depth of overburden is less in non-squeezing conditions, but it is significant in squeezing conditions. The following empirical correlation was suggested for prediction of ultimate support pressure in squeezing ground conditions:

$$P_N = (f/30)10^{\frac{H^{0.6}a^{0.1}}{50N^{0.33}}} \quad (6.3)$$

where P_N = tunnel support pressure in MPa; f = correction factor for tunnel closure (Goel 1994); H = depth of tunnel (m); a = radius of tunnel (m); and N is rock mass number.

Bhasin and Grimstad (1996) took into consideration the size of the tunnel suggested the following correlation for poor quality brecciated rock mass.

$$P_b = \frac{0.04}{J_r} D Q^{-1/3} \quad (6.4)$$

where P_b defines the ultimate tunnel support pressure, MPa; D is the diameter or span of the tunnel (m); J_r is the joint roughness number; and Q is the rock quality index.

Recently Dwivedi (2014) analysed data of 35 tunnel sections from 10 different tunnelling projects for non-squeezing ground conditions. The following correlation has been suggested to estimate support pressure based on joint factor.

$$P_e = 10^{-6} \sigma_v \left(\frac{7 \times 10^{-4} J_f^3}{d^{0.2}} + 4058 \right) \quad (6.5)$$

where P_e = ultimate support pressure in non-squeezing ground, MPa; σ_v = vertical in situ stress (0.027H), MPa; and d = radial tunnel deformation (%).

Dwivedi et al. (2014) analysed deformation data of several squeezing tunnels. Variation of deformation with joint factor was studied. The following correlation for predicting ultimate support pressure for squeezing ground condition was suggested:

$$P_s = 9.23 \times 10^{-3} \sigma_v \left[(J_f^3 \sigma_h^{0.1}) \left/ \left(10^7 \sigma_{ci}^{0.1} \left(d^{0.2} + \frac{J_f}{1434} \right) \right) \right]^{1.7} \quad (6.6)$$

where P_s = predicted support pressure, MPa; σ_v = vertical in situ stress (0.027H), MPa, σ_{ci} = uniaxial compressive strength of intact rock, MPa; σ_h = horizontal in situ stress, MPa; and d = radial tunnel deformation (%).

7 Concluding Remarks

Geotechnical issues are the most dominating aspects which cause delay and cost escalation in tunnelling projects, especially in weak rocks. The major issues are estimation of rock mass strength, suitable nonlinear failure criterion, assessment of squeezing potential, likely tunnel deformation and support pressure for various ground conditions. In the present chapter, a brief description has been given as to how reliable information can be generated based on simple characterisation of rock mass and classification techniques which are very easy to use in the field. A nonlinear strength criterion (MMC criterion) has been discussed. The criterion has the advantage in that the conventional parameters c and ϕ are retained as such. Correlations have been suggested to assess squeezing potential, tunnel deformation and support pressure based on rock mass quality Q , rock mass number N and joint factor J_f .

The empirical correlations are based on certain assumptions about the shape of the tunnel and in situ stress state. It is recommended that if significant problems are foreseen, detailed rock mass–tunnel support interaction analysis (2D and 3D) should be carried out using computer software for the actual shape of tunnel and the in situ stress state to arrive at final solution. The geotechnical model should be constantly updated as additional information is gathered during progress of tunnel and modifications in the support system should be made accordingly.

Acknowledgements This author would like to put on record his sincere thanks to his teachers Prof. T. Ramamurthy, Prof. K.S. Rao and Prof. K.G. Sharma, all from IIT Delhi and his mentor Prof. Bhawani Singh from University of Roorkee for their contributions in explaining basics of

Rock Engineering to the author. Thanks are also due to Prof. M.N. Viladkar and Prof. N.K. Samadhiya, both from IIT Roorkee for helping in understanding the geotechnique of tunnel engineering. The Ph.D. students namely Dr. B.K. Agrawal, Dr. Ajit Kumar, Dr. Jaysing Choudhari, Dr. Ajay Bindlish, Dr. R.D. Dwivedi, Dr. Harsh Verma, Dr. L.P. Srivastava and Dr. Dharmendra Shukla have immensely contributed on the subject matter through their Ph.D. work. The author sincerely thanks them all.

References

Arora, V. K. (1987). *Strength and deformational behaviour of jointed rocks* (Ph.D. thesis). IIT Delhi, India.

Asef, M. R., Reddish, D. J., & Lloyd, P. W. (2000). Rock-support interaction analysis based on numerical modeling. *Geotechnical and Geological Engineering*, 18, 23–37.

Aydan, O., Akagi, T., & Kawamoto, T. (1993). The squeezing potential of rocks around tunnels: Theory and prediction. *Rock Mechanics and Rock Engineering*, 26(2), 125–143.

Aydan, O., & Dalgic, S. (1998). Prediction of deformation behavior of 3-lanes Bolu tunnels through squeezing rocks of North Anatolian Fault Zone (NAFZ). In *Proceedings of Regional Symposium on Sedimentary Rock Engineering* (pp. 228–233), Taipei.

Barla, G. (2001). Tunnelling under squeezing rock conditions. *Tunnelling mechanics*. In D. Kolymbas (Ed.), *Eurosommer-school in tunnel mechanics*, Innsbruck, 2001 (pp. 169–268). Berlin: Logos Verlag. Available at: http://ulisse.polito.it/matdid/1ing_civ_D3342_TO_0/Innsbruck2001.PDF.

Barton, N. (1976). Rock mechanics review: The shear strength of rock and rock joints. *International Journal of Rock Mechanics and Mining Science and Geomechanics Abstracts*, 13 (9), 255–279.

Barton, N. (2002). Some new Q-value correlations to assist in site characteristics and tunnel design. *International Journal of Rock Mechanics and Mining Sciences*, 39, 185–216.

Barton, N., Lien, R., & Lunde, J. (1974). Engineering classification of rock masses for the design of tunnel support. *Rock Mechanics*, 6(4), 183–236.

Bhasin, R., & Grimstad, E. (1996). Use of stress-strength relationship in the assessment of tunnel stability. *Tunnelling and Underground Space Technology*, 11(1), 93–98.

Brown, E. T. (1970). Strength of models of rock with intermittent joints. *Journal of Soil Mechanics & Foundations Div, Proceedings of the ASCE*, 96(SM6), 1935–1949.

Deere, D. U., & Miller, R. P. (1966). *Engineering classification and index properties for intact rock*, Technical Report No. AFNL-TR-65-116. New Mexico: Air Force Weapons Laboratory.

Dwivedi R. D. (2014). *Behaviour of underground excavations in squeezing ground conditions* (Ph. D. thesis). IIT Roorkee, Roorkee, India.

Dwivedi, R. D., Singh, M., Viladkar, M. N., & Goel, R. K. (2013). Prediction of tunnel deformation in squeezing grounds. *Engineering Geology*, 161, 55–64.

Dwivedi, R. D., Singh, M., Viladkar, M. N., & Goel, R. K. (2014). Estimation of support pressure during tunnelling through squeezing grounds. *Engineering Geology*, 168, 9–22.

Goel R. K. (1994). *Correlations for predicting support pressures and closures in tunnels* (Ph.D. thesis). University of Nagpur, India, 310 p.

Goel, R. K., Jethwa, J. L., & Paithankar, A. G. (1995). Indian experiences with Q and RMR systems. *Tunnelling and Underground Space Technology*, 10(1), 97–109.

Grimstad, E., & Barton, N. (1993). Updating the Q-System for NMT. In *Proceedings of the International Symposium on Sprayed Concrete—Modern Use of Wet Mix Sprayed Concrete for Underground Support* (pp. 46–66). Fagernes, Oslo: Norwegian Concrete Association.

Hoek, E. (2001). Big tunnels in bad rock. *ASCE Journal of Geotechnical and Geoenvironmental Engineering*, 127(9), 726–740.

Hoek, E. (2007). Tunnels in weak rock. *Practical Rock Engineering*. <https://www.rocsience.com/learning/hoek-s-corner/books>.

Hoek, E., & Brown, E. T. (1980). Empirical strength criterion for rock masses. *Journal of Geotechnical and Geoenvironmental Engineering Div, ASCE*, 106(GT9), 1013–1035.

Hoek, E., & Brown, E. T. (1982). *Underground excavations in rock*. London: The Institution of Mining and Metallurgy, 527 p.

Hoek, E., & Marinos, P. (2000). Predicting tunnel squeezing problem in weak heterogeneous rock masses. *Tunnels and Tunnelling International*, 32(11), 45–51 & 32(12), 34–36.

IS:7317. (1974). *Code of practice for uniaxial jacking test for modulus of deformation of rocks*. Manak Bhawan, New Delhi: Bureau of Indian Standard.

Jethwa, J. L., Singh, B., & Singh, B. (1984). Estimation of ultimate rock pressure for tunnelling under squeezing rock conditions—A new approach. In E. T. Brown & J. A. Hudson (Eds.), *Design and Performance of Underground Excavations, ISRM Symposium* (pp. 231–238), Cambridge.

Kalamaras, G. S., & Bieniawski, Z. T. (1993). A rock mass strength concept for coal seams. In: *Proceedings of 12th Conference Ground Control in Mining* (pp. 274–283). Morgantown.

Mehrotra V. K. (1992). *Estimation of engineering parameters of rock mass* (Ph.D. thesis). University of Roorkee, Roorkee, India.

Obert, L., & Duvall, W. I. (1967). *Rock mechanics and the design of structures in rock*. USA: John Wiley & Sons Inc.

Ramamurthy, T. (1986). Stability of rock mass, 8th I.G.S. annual lecture. *Indian Geotechnical Journal*, 16(1), 1–75.

Ramamurthy, T. (1993). Strength and modulus response of anisotropic rocks. In: *Comprehensive rock engineering* (Vol. 1, pp. 313–329), UK: Pergamon Press.

Ramamurthy, T., & Arora, V. K. (1994). Strength prediction for jointed rocks in confined and unconfined states. *International Journal of Rock Mechanics and Mining Sciences & Geomechanics Abstracts*, 31(1), 9–22.

Ramamurthy, T., Rao, G. V., & Rao, K. S. (1985). A strength criterion for rocks. In *Proceedings of the Indian Geotechnical Conference* (Vol. 1, pp. 59–64), Roorkee.

Sakurai, S. (1997). Lessons learned from field measurements in tunneling. *Tunnelling and Underground Space Technology*, 12(4), 453–460.

Shen, J., Jimenez, R., Karakus, M., & Xu, C. (2014). A simplified failure criterion for intact rocks based on rock type and uniaxial compressive strength. *Rock Mechanics and Rock Engineering*, 47(2), 357–369.

Sheorey, P. R. (1997). *Empirical rock failure criteria*. Rotterdam: Balkema.

Singh, B., Jethwa, J. L., Dube, A. K., & Singh, B. (1992). Correlation between observed support pressure and rock mass quality. *Tunnelling and Underground Space Technology*, 7(1), 59–74.

Singh, M. (1997). *Engineering behaviour of jointed model materials* (Ph.D. thesis). IIT Delhi, India.

Singh, M. (2016). Use of critical state concept in determination of triaxial and polyaxial strength of intact, jointed and anisotropic rocks. In X.-T. Feng (Ed.), *Rock mechanics and engineering* (Vol. 1, pp. 479–502, Chapter-17), USA: CRC Press.

Singh, M., Raj, A., & Singh, B. (2011). Modified Mohr-Coulomb criterion for non-linear triaxial and polyaxial strength of intact rocks. *International Journal of Rock Mechanics and Mining Sciences*, 48(4), 546–555.

Singh, M., & Rao, K. S. (2005a). Bearing capacity of shallow foundations in anisotropic non Hoek-Brown rock masses. *ASCE Journal of Geotechnical and Geo-environmental Engineering*, 131(8), 1014–1023.

Singh, M., & Rao, K. S. (2005b). Empirical methods to estimate the strength of jointed rock masses. *Engineering Geology*, 77(1–2), 127–137.

Singh, M., Rao, K. S., & Ramamurthy, T. (2002). Strength and deformational behaviour of jointed rock mass. *Rock Mechanics and Rock Engineering*, 35(1), 45–64.

Singh, M., Rao, K. S., & Ramamurthy, T. (2004). Engineering behaviour of jointed rock mass. *Indian Geotechnical Journal*, 34(2), 164–198.

Singh, M., Samadhiya, N. K., Kumar, A., Kumar, V., & Singh, B. (2015). A nonlinear criterion for triaxial strength of inherently anisotropic rocks. *Rock Mechanics and Rock Engineering*, 48(4), 1387–1405.

Singh, M., & Singh, B. (2005). A strength criterion based on critical state mechanics for intact rocks. *Rock Mechanics and Rock Engineering*, 38(3), 243–248.

Singh, M., & Singh, B. (2012). Modified Mohr-Coulomb criterion for non-linear triaxial and polyaxial strength of jointed rocks. *International Journal of Rock Mechanics and Mining Sciences*, 51, 43–52.

Singh, M., Singh, B., & Choudhari, J. (2007). Critical strain and squeezing of rock mass in tunnels. *Tunnelling and Underground Space Technology*, 22(3), 343–350.

Srivastava, L. P., & Singh, M. (2015). Effect of fully grouted passive bolts on joint shear strength parameters in a blocky mass. *Rock Mechanics and Rock Engineering*, 48(3), 1197–1206.

Trueman, R. (1988). *An evaluation of strata support techniques in dual life gateroads* (Ph.D. thesis). University of Wales, Cardiff.

Yudhbir, W. L., & Prinzl, F. (1983). An empirical failure criterion for rock masses. In *Proceedings of 5th International Congress on Rock Mechanics* (Vol. 1, pp. B1–B8). Melbourne.

Zhang, L. (2010). Estimating the strength of jointed rock masses. *Rock Mechanics and Rock Engineering*, 44, 391–402.

Reliability and Accuracy of Seismic Tests in Geotechnical Site Characterization

Sebastiano Foti and Federico Passeri

Abstract Geophysical surveys, and specifically seismic tests, provide powerful tools for geotechnical site investigation. Indeed, they cover the whole range of soils and rocks, independently of particle size, and provide data in the natural state for the characterization at different scales. Assessment of the reliability of the most popular techniques is therefore of primary importance for static and seismic applications. This chapter reports some data from recent experiments devoted to reliability assessment at some reference sites, where intra-method and inter-method variability has been studied. The propagation of the measured uncertainties in soil porosity assessment and seismic ground response analyses is also considered to provide an insight on the consequences in the practice of geotechnical engineering.

Keywords Site characterization · Seismic waves · Geophysical surveys · Rayleigh waves · MASW · Porosity

1 Introduction

The role of geophysical surveys in geotechnical site characterization has been steadily increasing over time in the past decades. Indeed, the development of reliable and affordable instrumentations has gone together with the recognition of the relevance of geophysical parameters in describing the behavior of soils and rocks.

Geophysical tests are based on the measurement of a natural field or of the response of the ground to an induced perturbation (e.g., a mechanical wave or an electromagnetic wave). The data are then interpreted to derive the values of a given geophysical parameter and their variability in the subsoil.

S. Foti (✉) · F. Passeri
Politecnico di Torino, Turin, Italy
e-mail: sebastiano.foti@polito.it

F. Passeri
e-mail: federico.passeri@polito.it

The main advantage of geophysical surveys is that the subsoil is investigated in its natural state, with a measurement that is inherently non-destructive (even though in some methods it may be necessary to “invade” the medium in order to place the measuring devices). Moreover, no restrictions are applicable on the basis of the nature of the subsoil, as soils can be tested independently of their particle size distribution and rocks independently of their state of fracturation. On the other side, the main issue is related to the necessity of adopting a non-trivial framework for the interpretation of the measured quantities and the need for adequate expertise. Very often, geophysical methods rely on the solution of inverse problems, which are inherently ill-posed according to the Hadamard’s definition (Hadamard 1902). The consequence is the solution non-uniqueness, i.e., several solutions honor equally well the available experimental data and it is not possible to identify a single set of model parameters.

Geophysical surveys may provide relevant information in engineering and environmental applications according to the significance of the specific geophysical parameters under investigation. Indeed, they can provide information on the subsoil geometry under the condition that different layers are characterized by different geophysical parameters. This is, for example, the case for alternate layers of clayey and sandy materials, which can be easily reconstructed by electrical resistivity tomography (ERT) as their electrical conductivity is significantly different. On the other side, the influence of pore fluid on electromagnetic wave propagation may help to discriminate soil conditions in environmental and hydrogeological applications.

Among geophysical surveys, seismic tests play a fundamental role as they allow the direct estimation of the subsoil mechanical properties and stratigraphic conditions. Indeed, the velocity of propagation of seismic waves is directly linked to the mechanical response of the medium. In the most common interpretation framework (i.e., wave propagation in a linear elastic continuum), the velocity of propagation is linked to the elastic parameters by the following simple relationships:

$$M = \rho V_p^2 \quad (1)$$

$$G = \rho V_s^2 \quad (2)$$

where ρ is the mass per unit volume; V_p is the velocity of propagation of compressional waves; V_s is the velocity of propagation of shear waves; M is the longitudinal (oedometric) modulus, and G is the shear modulus.

Other, more realistic, models may be adopted depending on the target of the analysis. For example, if the dissipative properties of the subsoil are to be investigated, linear viscoelastic models are appropriate, at least for the small strain level. In this framework, the velocity of propagation is a complex value and the attenuation of wave amplitudes can be analyzed to estimate material damping ratio (Lai 2015).

A very appealing framework for the interpretation of seismic measurements is provided by the theory of propagation of wave in linear elastic saturated porous media (Biot 1956a, b). In particular, reference is herein made to the low-frequency range as the testing frequencies on sites are such that it applies even for coarse-grained materials (Foti et al. 2002). According to Biot theory, three types of body waves are generated in a fluid saturated porous medium: a shear wave and two compressional waves. However, the compressional wave of the second type (also known as Biot's wave) is always slower than the compressional wave of the first kind; hence, it is of little practical interest for geophysical measurements as the first arrival is always associated with the compressional wave of the first type. Under the hypothesis of incompressible soil grains, the velocity of propagation of the first compressional wave and of the shear wave can be written as:

$$V_P = \sqrt{\frac{(K^{SK} + \frac{4}{3} \cdot G) + \frac{K^F}{n}}{(1 - n) \cdot \rho^S + n \cdot \rho^F}} \quad (3)$$

$$V_S = \sqrt{\frac{G}{(1 - n) \cdot \rho^S + n \cdot \rho^F}} \quad (4)$$

with: ρ^S , grain density; ρ^F , water density; K^F , water bulk modulus; K^{SK} , soil skeleton bulk modulus; G , shear modulus; n , porosity.

The above formulas show some interesting features. First, the velocity of propagation of the compressional wave is strongly influenced by the pore fluid and its deformability. Indeed, the stiffness of the solid skeleton, which is of primary importance for geotechnical applications, is masked by the presence of the pore fluid. For this reason, V_P measurements are often considered of little interest for the characterization of uncemented shallow soil deposits. However, the bulk stiffness of the pore fluid is dramatically influenced by the presence of even small quantities of gas; hence also for saturation very close to one, the V_P is consistently lower than the velocity in a saturated medium. The identification of unsaturated zones is therefore easily accomplished with V_P measurements and can provide very relevant insight, for example, dealing with liquefaction phenomena as they are inhibited by even very small quantities of gas (Jamiolkowski 2014).

Contrarily, the presence of the pore fluid has almost no influence on the measured shear wave velocity, since the shear modulus is not affected by the presence of the fluid. In fact, the change in apparent density has only a minor effect on V_S . However, for unsaturated soils, literature examples showed that the velocity of propagation of shear waves is affected by suction (Cho and Santamarina 2001; Oh and Vanapalli 2011).

Biot's theory can also be used to predict soil porosity values on the basis of the velocity of propagation of seismic waves in saturated soils (Foti et al. 2002). Section 4 will be devoted to uncertainties in this specific application. However, this approach cannot be used for unsaturated soils. In this case, additional information is

indeed required. For example, Cosentini and Foti (2014) proposed an approach based on combined seismic and electrical measurements to assess ground conditions in terms of soil porosity and degree of saturation.

Back to conventional interpretation of shear wave velocities with the linear elastic model of continuum mechanics, it is necessary to remark that the in situ measured V_S is relative to the very small strain range and hence the small strain shear modulus G_0 is obtained with Eq. 2. For engineering applications, it is therefore necessary to adopt appropriate procedures aiming at accounting for nonlinear response of soils to external loads. Typically, this is achieved with two broad categories of numerical methods:

- EQuivalent Linear methods (EQL), in which linear (visco-)elastic solutions are considered and the (visco-)elastic moduli are iteratively corrected for specific induced strain levels (i.e., nonlinear response levels);
- Fully Nonlinear methods (NL), in which more sophisticated constitutive models are adopted to simulate in a consistent manner the response over the whole strain range of interest.

A well-known example of the equivalent linear procedure was originally proposed in the code SHAKE for the analysis of seismic ground response (Schnabel 1972). The implications of parameters variability in this approach will be discussed in Sect. 5. On the other side, a systematic review of nonlinear methods is provided in (Stewart and Kwok 2008) and interesting results are given in recent benchmark projects (Régnier et al. 2016, 2018).

However, for both equivalent linear and fully nonlinear methods, the small strain shear modulus is a parameter of paramount importance to obtain reliable and accurate results, since it represents the “starting point” for each analysis (Passeri et al. 2017).

Shear wave velocity is therefore a parameter that quantifies the mechanical behavior of geomaterials and it is strongly dependent not only on the mineralogy but also on the state parameters. The velocity of propagation can be expressed as

$$V_S = A F_e \left(\frac{\sigma'_0}{p_a} \right)^\beta \quad (5)$$

in which A is an experimental parameter that accounts for grain properties, F_e is a function of the void ratio e and grain shape, σ'_0 is the confining effective stress, p_a is a reference confining pressure (usually the atmospheric pressure), and β is an experimental exponent that accounts for stress dependency. Several formulations for F_e have been proposed in the literature, as summarized by (Mitchell and Soga 2005).

Accounting for the dependence of V_S on state parameters and soil fabric, its direct use has been also proposed for several applications:

- Soil liquefaction assessment via simplified procedures based on empirical correlations for the evaluation of the Cyclic Resistance Ratio (CRR), after

normalization to account for the state of stress (Andrus and Stokoe 2000; Kayen et al. 2013);

- Assessment of sample quality on the basis of comparison between the values measured on site and the values obtained in the laboratory (Jamiolkowski 2012);
- Assessment of the effectiveness of ground improvement treatments (Andrus et al. 1998; Raptakis 2012).

The above applications require reliable and accurate measurements of V_S , which must be obtained by in situ direct measurements, i.e., by means of geophysical tests (Stewart et al. 2014). Empirical correlations to estimate V_S from penetration resistance, undrained strength or other test results should be used with extreme caution and only for preliminary estimates. Indeed, a close inspection of the datasets from which they have been obtained reveals the very large uncertainties associated with the estimated values.

The present chapter is devoted to a discussion of uncertainties in geophysical surveys and, specifically, in seismic tests commonly adopted for the measurement of seismic wave velocities. After a brief discussion on the type and sources of uncertainties in geophysical tests, the most popular techniques are briefly introduced with specific reference to the source of uncertainty for each of them. Thereafter, two applications are presented to discuss the propagation of uncertainties: the estimation of soil porosity from measured seismic velocities on the basis of the Biot's theory and seismic ground response analyses.

2 Uncertainties and their Sources

In general terms, we define the accuracy of a method as its capability to provide an estimate that is as much as possible close to the “true” value of the investigated parameter.

On the other hand, the precision of a given method is associated with the possibility of getting consistent and repeatable measurements of the parameter of interest. Indeed, the precision aims at obtaining similar results with a repetition of the same test on the same sample (i.e., repeatability).

In this respect, the accuracy is very difficult to assess since the true value of the parameter is unknown. For this reason, very often the performances of a given geophysical method are studied with synthetic cases in which the benchmark is a numerical simulation with a set of known model parameters. However, this strategy is not fully satisfactory, as the uncertainties in data acquisition are not considered, and they can be very relevant. The other possibility is given by a comparison of the results by different techniques, although such comparisons are rarely fully representative of the actual accuracy. Indeed, one of the techniques has to be assumed as the ground truth. Moreover, most often it is not possible to derive general conclusions from such comparisons as different techniques explore different portions of the subsoil. This is, for example, the case when in-hole and surface measurements are compared one to the other (e.g., Garofalo et al. 2016b).

The precision in terms of repeatability of a given measurement is in principle easier to assess than accuracy. However, several blind tests performed in the past have shown that it is difficult to assure that measurements are actually performed in exactly the same conditions, especially when dealing with natural systems. Moreover, an assessment of a representative statistical sample is typically prevented by the limited possibility to get repeated and consistent measurements, due to the cost of each acquisition and interpretation.

In terms of uncertainty that affects the reliability of a geophysical test, it is important to clearly separate two broad categories: epistemic uncertainties and aleatory variabilities. The former is associated with an incomplete knowledge of the system, with the hypotheses that are introduced during the interpretation (i.e., adopted model), and with measurement errors. The second represents the natural randomness of subsoil conditions, for example, in terms of lateral heterogeneities of ground properties across the site of interest footprint. Epistemic uncertainties can be handled and reduced with additional data/knowledge, but are difficult to properly quantify. Contrarily, aleatory variability represents something more complex due to natural system and phenomena unpredictability that cannot be reduced.

A clear separation of the two contributions is unfortunately very difficult to implement and a lumped uncertainty is therefore typically considered. However, for some specific issues, the observed uncertainty can be referred to a predominant category of the two above. For example, the defective of the triggering system in a cross-hole test can be associated straightforwardly with epistemic uncertainty in resulted V_S profiles. On the other hand, uncertainties associated to the non-uniqueness of the solution in the surface wave inverse problem are the effects of a combined contribution of both epistemic uncertainties and aleatory variability. In fact, in this case the epistemic uncertainty is introduced in the obtained V_S profiles by the non-uniqueness of the solution and the choice of model parameters (e.g., Poisson ratios and layer thicknesses). On the other hand, the experimental dispersion curve is dependent on the response of a large soil deposit volume and represents an average of the soil response across several meters (Teague et al. 2017).

Hence, epistemic uncertainties in experimental data derive from several elements, among which the most relevant are as follows:

- (1) The availability of high-quality instrumentation;
- (2) The validity of the model assumptions adopted for the interpretation and for the implementation of the tools;
- (3) Skills and expertise of the technicians and analysts who execute the measurement and the interpretation.

The third point is often taken for granted, but actually should not be overlooked. Indeed, also for the increasing availability of affordable equipment, unskilled operators are often entering the market. In fact, processing and interpretation of geophysical data require a deep knowledge of the underlying theoretical background.

3 Seismic Methods

Seismic surveys include a large variety of methods conceived to measure the velocity of propagation of the seismic waves. In practice, what we measure is not the wave velocity of propagation, but the wavefield associated with the propagation of mechanical disturbances. The wavefield is measured by detecting ground motion at one or more locations. It is thereafter analyzed to estimate the local values of wave propagation velocities and the boundaries between subsoil portions characterized by different velocities (i.e., seismic layers).

Seismic surveys can be grouped into two broad categories depending on the position of measuring equipment:

- Invasive tests;
- Non-invasive tests.

The first category is often addressed as borehole methods since receivers and/or sources are placed in the subsoil, typically within holes. However, invasive measurements can be performed by taking the receivers in the subsoil with the rods used for cone penetration tests or dilatometer tests (respectively in the so-called Seismic Cone SCPT and Seismic Dilatometer SDMT tests).

Non-invasive tests are also addressed as surface tests; however, this name can be associated with surface wave analysis, which actually is only a specific type of non-invasive tests.

In the present chapter, we consider the most popular methods in the geotechnical and seismic application: cross-hole tests (CHT), down-hole tests (DHT), P-S suspension logging, and surface wave methods (SWM).

In the following, the basic of each technique is summarized with a special focus on the main source of uncertainties for each of them.

3.1 Cross-Hole Tests

The cross-hole method (Fig. 1a) is described in ASTM standard 4428/4428 M. The epistemic uncertainties in the cross-hole testing are related to the evaluation of the arrival times in the recorded traces and of the local distance between the boreholes at each depth (Jamiolkowski 2012). Moreover, the accuracy of the trigger system (in the case of the two-hole testing setup) and the interpretative model inadequateness may play an important role in the estimation of test results uncertainty. Indeed, a deficiency in the trigger system can lead to a systematic bias in the interpretation of arrival times and it represents a typical example of epistemic uncertainties. Finally, the cross-hole test assumes the homogeneity of the deposit at a given depth, hence a locally simple stratigraphic condition. If these assumptions are not confirmed, the obtained V_s profile might be influenced by epistemic uncertainties.

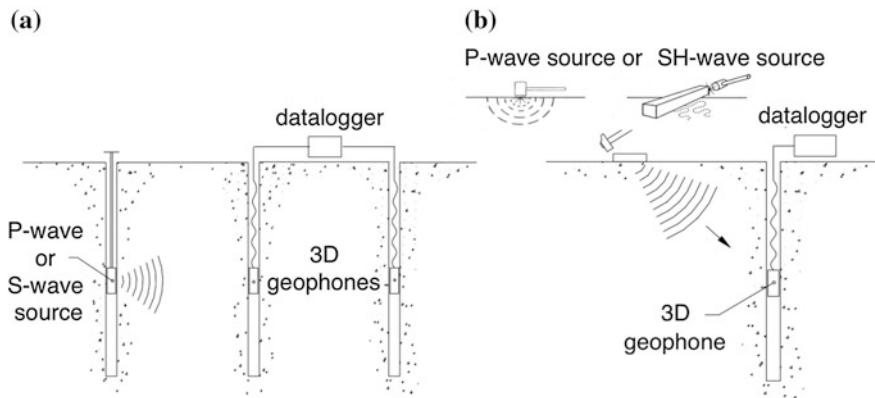


Fig. 1 **a** Cross-hole test CHT; **b** down-hole test DHT

3.2 Down-Hole Tests

The down-hole test (Fig. 1b) is the most used invasive method (ASTM standard 7400-07) (Butcher et al. 2005). Down-hole data can be processed by using four different approaches: (1) the true interval method, (2) the pseudo-interval method, (3) the linear interpolation over homogeneous layers method, or (4) the curved seismic ray paths inversion. The true interval method is the simplest approach, with the epistemic uncertainties mainly due to the determination of arrival times and some epistemic uncertainty due to assumptions regarding the wave path (particularly near the surface). The pseudo-interval method is influenced by greater uncertainties, as the consistency and repeatability of the triggering system from depth to depth can at times result in large changes in velocity over short distances. The linear interpolation over homogeneous layers method guarantees the stability of the solution, as it is a robust estimation over a larger set of experimental data; however, the result strongly depends on the preliminary choice of layer discretization. Finally, the curved ray paths approach requires the solution of a complex inverse problem and the non-uniqueness of the solution may severely affect the final result.

3.3 P-S Suspension Logging

The suspension P-S velocity logging was developed in the mid-1970s to answer the need for a technique that could measure seismic shear wave velocities in deep, uncased boreholes, by researchers at the OYO Corporation of Japan (Kaneko et al. 1990). The equipment is usually made up of a probe, containing a source and two receivers spaced 1 m apart inside of a casing with rubber membranes isolating the source and the two receivers. The whole assembly is suspended by a cable in a

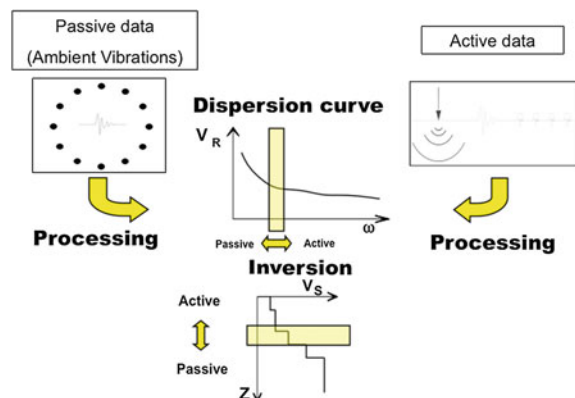
fluid-filled borehole. The probe is lowered into the borehole to the sample depth, where the source generates a pressure wave in the borehole fluid (mud or water) that is in turn coupled to the borehole wall. The sampled material includes the soil near the borehole interface. P-S suspension logging can provide high-resolution (typically 1 m) sampling and can be used to large depths (up to 1000 m). Since the waves spend their entire travel path near the borehole wall, the testing should be performed in uncased boreholes whenever possible. A significant disadvantage regards the possible detection of tube waves, which can lead to misinterpretation of the velocities, resulting in a systematic overestimation of V_s (i.e., epistemic uncertainty). This problem is particularly pronounced with heavy casing and thick grout, whereas it decreases in importance for PVC casing with thin grout and uncased boreholes.

3.4 Surface Wave Analysis

Surface Wave Methods (SWM) have grown in popularity over the past 25 years due to the time and cost savings they can provide (Socco et al. 2010; Foti et al. 2011). In general, even if different data analysis techniques and equipment can be used, surface wave testing is organized in three different steps (see Fig. 2): (1) field data acquisition; (2) dispersion curves extraction; (3) inversion process (Foti et al. 2014).

An initial distinction is due to the type of sources used for the generation of Rayleigh wave field in the test. Active sources are generally impact sources (hammers or large falling weights), seismic guns, explosives, or continuous sources (electromagnetic shakers or Vibroseis™). Ambient vibrations are generated by passive sources such as human activities (e.g., traffic on highways, construction activities) and/or natural events (e.g., wind, ocean waves). Ambient vibrations are also collected for single-station HVSR (Horizontal to Vertical Spectral Ratio,

Fig. 2 Surface wave analysis (active and passive data)



or simply H/V) analyses (Nakamura 1989; Bard et al. 2010). If the HVSR curve exhibits a sharp, well-defined peak, then the frequency at which this peak occurs ($f_{0,HV}$) may be used to approximate the fundamental shear wave resonant frequency at that location. Surface wave testing guidelines developed through the InterPACIFIC project encourage the combined use of both active and passive surface wave methods whenever possible (Foti et al. 2017). A wealth of information and pertinent references on active and passive surface wave methods may be found in these guidelines.

Typically, a stack of linear elastic and homogeneous layers is used in the inversion process and the result is biased if the soil deposit does not resemble reasonably a 1D, layered medium. In addition, the mathematical ill-posedness of the inverse problem causes the non-uniqueness of the solution, which is a further uncertainty (both epistemic and aleatory) leading to geophysical equivalence problems (Foti et al. 2009). Because of the non-unique, mixed determined and ill-posed nature of the nonlinear inverse problem (Foti et al. 2014), these analyses require specific expertise.

4 Uncertainties in Soil Porosity

Porosity is widely recognized as a key parameter as it affects the mechanical and hydraulic response of soils. A crucial issue in its determination is typically represented by the difficulties in collecting high-quality undisturbed samples for coarse-grained soils (Jamiolkowski 2012) or for deep formations. Usually, in geotechnical engineering, the relative density of sands is obtained through empirical correlations with in situ tests, whose reliability is not easily assessed. Foti et al. (2002) proposed an approach for porosity assessment on the basis of measured seismic wave velocity by adopting the formulation by Biot (1956b) for linear elastic, isotropic, and fully saturated porous media. Indeed, combining Eqs. 3 and 4, soil porosity n can be indeed written as (Foti et al. 2002):

$$n = \frac{\rho^S - \sqrt{(\rho^S)^2 - \frac{4 \cdot (\rho^S - \rho^F) \cdot K^F}{V_p^2 - 2 \cdot \left(\frac{1 - \nu^{SK}}{1 - 2 \cdot \nu^{SK}} \right) \cdot V_S^2}}}{2 \cdot (\rho^S - \rho^F)} \quad (6)$$

where ν^{SK} is the Poisson ratio of the (evacuated) soil skeleton. The reliability of the estimate has been studied by Foti and Passeri (2016) by considering an error propagation procedure for Cross-Hole tests. Their analysis showed that the critical parameters are the P-wave travel time (t_p), the distance between the holes (d), the compressional wave velocity in the fluid (V_w), and the Poisson's ratio of the (evacuated) solid skeleton. Uncertainties on the other parameters are negligible.

Repeated measurements of cross-hole experimental data were obtained at the site of the Zelazny Most tailing dam in two different campaigns in 2011 and 2014

(Callerio et al. 2013; Jamiolkowski 2012, 2014; Jamiolkowski and Masella 2015). Measurements of P and S seismic wave propagation were constantly repeated to enlarge the statistical sample. Specifically, travel time measurements and boreholes deviation surveys were repeated to statistically evaluate mean values and related uncertainties in terms of standard deviations.

An example is reported in Fig. 3, with the velocity profiles (Fig. 3a) and the estimated porosity according to Eq. 6 (Fig. 3b). In Fig. 3c and d, the coefficients of variation (CoV) and the calculated percentage uncertainty propagated on n are shown for each parameter. Figure 3d shows that the propagated percentage error on n due to t_p is one order lower than the uncertainty due to d , V_w , or v^{SK} . In any case, the uncertainty associated with each parameter is limited to values lower than 7%. In this case, Poisson ratio of the solid skeleton was set to a standard range according to literature ($v^{SK} = 0.25 \pm 0.1$).

5 Uncertainties in V_S Profiles and Their Implications on Seismic Ground Response Analyses

In static problems, the uncertainties associated with the evaluation of ground parameters are often circumvented by adopting caution estimates, for example, for strength and/or deformability. However, when dealing with dynamic systems, the establishment of a caution (i.e., a priori conservative) estimate is often not practicable. For example, in ground response analyses, an overestimation of V_S may result in reduced impedance contrasts and hence less amplification. Contrarily, an

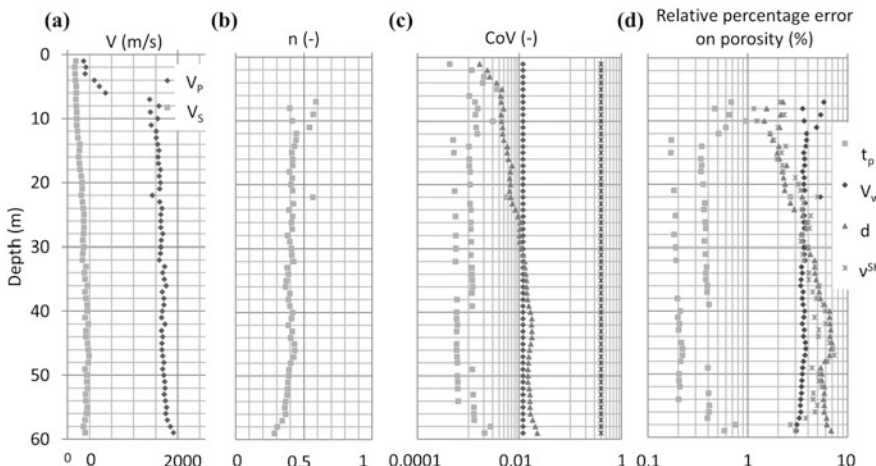


Fig. 3 **a** Velocities profiles, **b** estimated porosities, **c** coefficients of variation, **d** relative percentage errors on porosity

underestimation could represent a very deformable system and, since the dissipation of energy increases nonlinearly with shear strains, it may lead to an over-damped response of the system resulting in an underestimation of the ground motion.

Specifically, the shear wave velocity model is recognized as the most influent element in ground response analyses (Idriss 2004; Rathje et al. 2010).

For the aforementioned reasons, uncertainties in V_S model need to be explicitly evaluated. Several blind comparative studies have been performed around the world in recent years to assess the reliability of V_S profiles obtained with borehole and surface geophysical methods. Some of these blind tests were focused only on surface wave methods as in the SESAME (Site Effects aSsessment from Ambient noise) (Bard and SESAME Participants 2004) and in the NERIES-JRA4 (Bard et al. 2010; Di Giulio et al. 2012) projects. Other blind tests for surface wave analysis on a common dataset are documented by Cornou et al. (2006), dealing with different methods for the analysis of ambient vibrations; Tran and Hiltunen (2011) for linear arrays of active and passive acquisitions; (Cox et al. 2014) for combined active and passive data.

In the following, two blind tests will be specifically considered: one in Mirandola (Italy), the other in South Korea. At both sites, multiple realizations of invasive and non-invasive tests have been performed to assess the intra-method and inter-method variability. In the following, a selected set of profiles from each case study is used to investigate the propagation of uncertainties on ground response analyses by means of linear viscoelastic transfer functions. A thorough assessment considering also the nonlinear response is reported by Passeri et al. (2017).

The Mirandola site was investigated within the InterPACIFIC project (Intercomparison of methods for site parameter and velocity profile characterization) in which three sites were investigated to cover different geological conditions. Specifically, Mirandola was chosen as a representative of the “soft-soil” class, Grenoble in France for the “stiff-soil” class with a quite deep bedrock and Cadarache in France as a “hard-rock” site, being placed on an outcropping cretaceous limestone. Full details on the tests at the three sites and on the observed variability are reported by Garofalo et al. (2016a, b).

The Mirandola site is very close to the location of a station of the Italian strong-motion network that recorded the earthquake sequence of 2012. Two boreholes were drilled down to 123-m depth and arranged for the execution of seismic measurements. Subsequently, the holes have been used for the installation of a permanent down-hole array composed of three triaxial geophones at different depths (Laurenzano et al. 2017).

In the following, only the V_S profiles that clearly identified a marked impedance contrast at depth are considered in order to evaluate comparable viscoelastic transfer functions for the site. This criterion provides 8 V_S profiles from invasive tests and 12 V_S profiles from non-invasive tests (Fig. 4a and b). For invasive tests, the teams reported very similar V_S profiles (Fig. 4a), except for two profiles that show a thin, marked increase of velocities at around 80 m depth. Both of these V_S profiles were obtained with P-S suspension logging. Close to a depth of 75 m, all

teams identified a low-velocity layer. Likewise, every team estimated the depth to bedrock between 115 and 125 m below the ground surface. Figure 4b presents the V_s profiles determined by 12 teams analyzing non-invasive data. As expected, none of the non-invasive analysts identified the thin, low-velocity layer at about 75 m and the variability of the bedrock depth and bedrock shear wave velocity is larger than for invasive tests. In particular, three profiles (Q, S, and V) report high bedrock velocities that could influence the ground response: profile Q presents a stiff shallow bedrock; profile V presents an outlier velocity value (3490 m/s); profile S

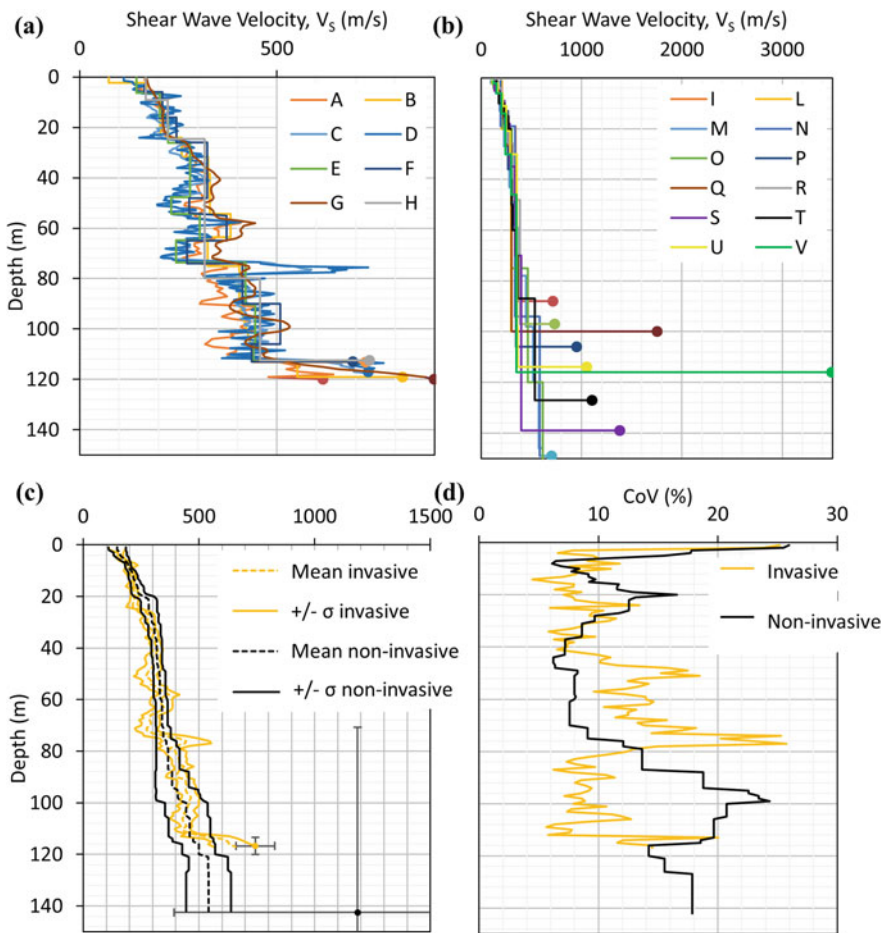


Fig. 4 **a** Invasive and **b** non-invasive test results for Mirandola, **c** mean and \pm one standard deviation V_s profiles (dashed and solid lines, respectively) and bedrock depth/ V_s (markers and error bars, respectively) for the invasive and non-invasive results, **d** coefficients of variation for invasive and non-invasive tests

presents intermediate values for both depth and V_s with respect to Q and V. On the other hand, profiles M and O identify the bedrock at high depth.

Figure 4c presents the mean and the mean \pm one standard deviation V_s profiles for invasive and non-invasive methods. For the bedrock, depth and velocity mean and standard deviation are presented as points and error bars. Figure 4d presents a coefficient of variation (CoV) (i.e., standard deviation divided by the mean) for the invasive and non-invasive V_s soil profiles. At depths less than 80 m, the mean of the V_s soil profiles for invasive and non-invasive tests is similar, showing consistency in the inter-method comparison. However, as expected, the non-invasive test reduction in resolution with depth produces an increase of V_s variability at large depths, especially for the identification of the seismic bedrock.

The linear viscoelastic theoretical transfer function (TF) for each V_s profile are presented in Fig. 5a. The fundamental resonant frequency is between 0.7 and 1 Hz. The amplitudes of the transfer functions are not realistic since an arbitrary small strain damping ratio value was chosen. However, comparable values among the 20 V_s profiles were obtained, with the exception of Q, S, and V, which have either stiffer bedrock or a deeper depth to bedrock than the other V_s profiles.

Tarabusi and Caputo (2017) used passive microtremors to investigate the natural frequencies at the Mirandola area. Their results are compared to the linear viscoelastic analysis results in Fig. 5b, which includes all the data in Fig. 5a zoomed on the fundamental resonant frequency. The fundamental elastic resonance frequencies (i.e., the ones related to bedrock impedances) for the different V_s profiles consistently approximate the experimental HVSR values, except for the V_s profiles Q, S, and V that fall out of the mean \pm 1 standard deviation range.

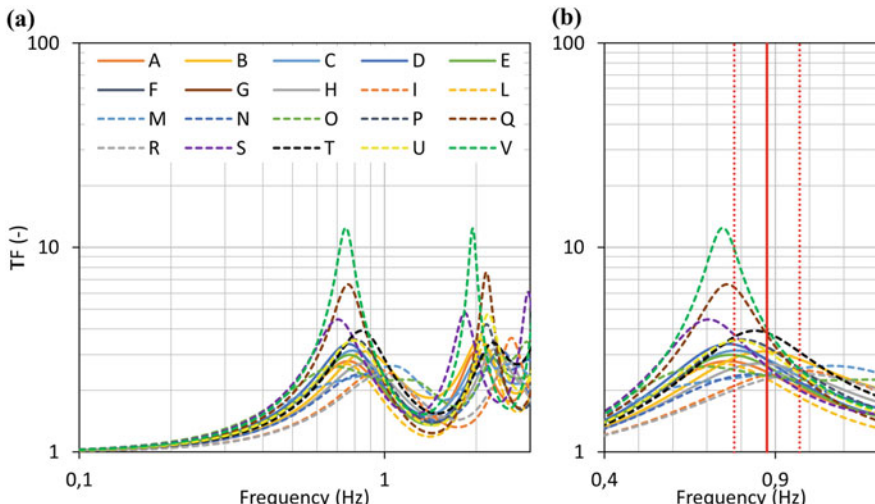


Fig. 5 **a** Invasive and non-invasive profiles viscoelastic transfer functions for Mirandola and **b** comparisons between simulated viscoelastic transfer functions and HVSR mean peak and standard deviation for the Mirandola area (Tarabusi and Caputo 2017)

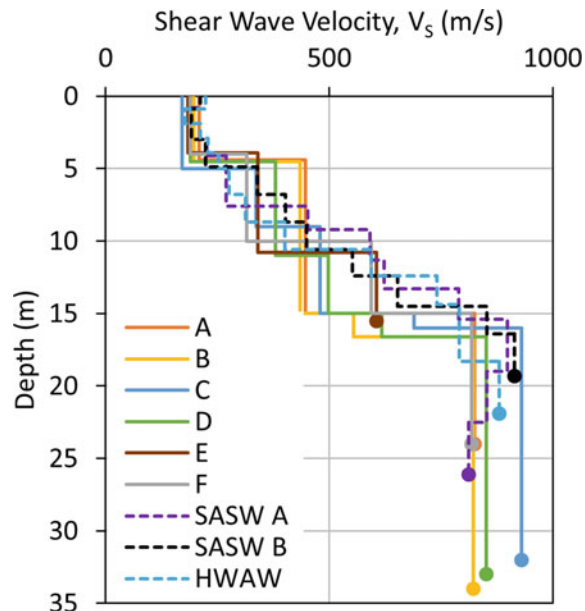
The second case study is located in South Korea, at the Pyeong-taek side of the Seohae Grand Bridge. The geotechnical survey was carried out between piers number 27 and 28 under the bridge, along with the highway layout. Kim et al. (2013) provide a detailed description of measurement methods and of the Round Robin Test (RRT).

This site has been chosen because of the very different geological and geomechanical characteristics, compared to the Mirandola subsoil conditions. Indeed, it is characterized by a very shallow (around 20 m) bedrock, mainly consisting of a weathered-soft rock interface. For this reason, a high fundamental resonant frequency is expected.

A selection of the data collected by Kim et al. (2013) is used for the present study and the V_s profiles are reported in Fig. 6. With solid lines are given the DH results obtained with the linear interpolation over homogeneous layers method, whereas the dashed-line profiles represent the non-invasive test results. In particular, a selection of 6 down-hole tests and 3 non-invasive tests is considered. DH results obtained by inversion of the curved ray paths method were discarded because of the large variability observed in the results. In addition, even if a large number of non-invasive profiles were available, only the results for which the experimental dispersion curve was estimated over a sufficient frequency range for the characterization of the whole deposit were selected. For the present case study, a robust statistical sample is therefore not available (i.e., small amount of intra-method data).

Figure 6 shows a good consistency for the intra- and inter-method shear wave velocities comparison. In the first 5 m, the invasive results provide almost identical

Fig. 6 Invasive (DH) and non-invasive profiles at the Seohae Grand Bridge site



V_S values as non-invasive, even if a denser layer discretization was adopted for non-invasive tests. Between 5 and 10 m, larger values of V_S are obtained from invasive tests than from non-invasive results. Conversely, between 10 and 15 m non-invasive tests seem to detect stiffer layers than invasive tests since a continuous V_S increase is obtained, likely due again to the larger number of layers in the inversion process.

Finally, the bedrock variabilities are relevant. In particular, the E down-hole profile does not reach the conventional seismic bedrock velocity ($V_S > 800$ m/s) and it locates the last interface at around 11 m. In addition, the C profile presents an unusual bedrock impedance, with a sharp increase from 498 to 930 m/s at 15 m depth. The other 4 DH profiles are in agreement with each other both for depth and bedrock velocity (ranging from 818 to 930 m/s). Non-invasive tests are also consistent for the intra-method bedrock comparison, except for the SASW A, which gives a V_S inversion at 19 m, decreasing the V_S from 899 to 812 m/s. Even if 30 m depth were not reached for many profiles, it is possible to classify the Seohae Grand Bridge site as class C ($V_{S,30}$ between 360 and 760 m/s for NEHRP regulations) if the final/bedrock layer is extrapolated down to 30 m.

The preliminary intra- and inter-method ground response variability is shown in Fig. 7 by using linear viscoelastic transfer function (TF). Both invasive and non-invasive results appropriately reproduce fundamental resonance peaks and amplitudes; however, initial intra- and inter-method dissimilarities can be assessed. Amplitudes range from 2.5 (E) to 4 (C), whereas resonance frequencies vary between 6.2 Hz (C) and 7.7 Hz (E). As discussed in the previous paragraph, profile C detected a large impedance increase at 15 m depth, almost doubling the V_S value. For this reason, the viscoelastic transfer function shows a peak that reaches a value

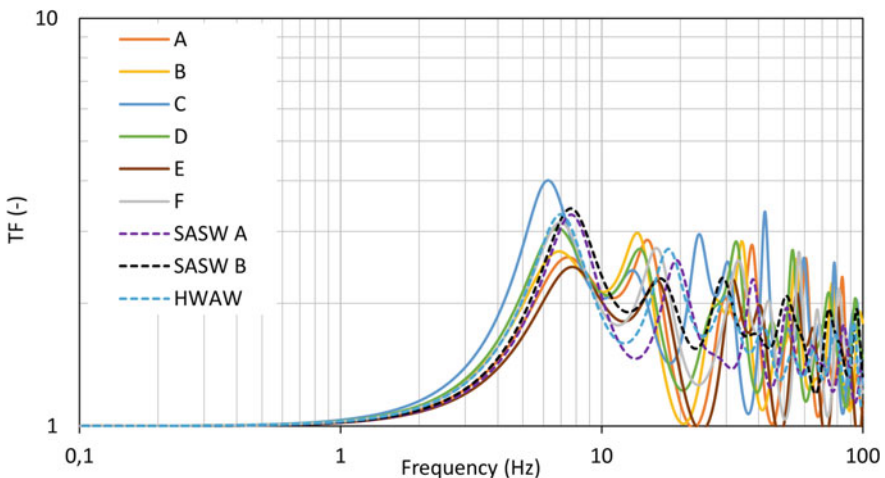


Fig. 7 Viscoelastic transfer functions for invasive and non-invasive tests at Seohae Grand Bridge site

of 4 and a lower resonant frequency is observed. Contrarily, the E profile is the one with shallow impedance contrast and lower bedrock shear wave velocity, which produces a lower peak and a global stiffer profile (i.e., higher resonance frequency).

6 Summary

Geophysical tests, which are soundly based on the theory of wave propagation, can provide relevant information for site characterization not only for seismic projects. Uncertainties on the evaluation of seismic velocities have been discussed in the present note, reporting some results from recent blind exercises in which geophysical measurements have been reiterated at some reference sites, aiming at assessing the contribution of epistemic uncertainties. It is shown that, with good quality measurements and careful interpretation, coefficients of variations of less than 15–20% can be expected. These uncertainties should be adequately taken into account for applications that make use of measured shear wave velocities. Two examples are reported to show how these uncertainties are mapped into uncertainties in specific applications: the evaluation of soil porosity and the analysis of seismic ground response.

In general, uncertainties are often overlooked in conventional approaches for site characterization. Specifically, geotechnical site investigations often rely on the use of empirical correlations, which hide large uncertainties on top of the experimental uncertainties in the execution of the test itself. On the other side, laboratory tests, which are apparently performed under very controlled conditions, are indeed affected by severe uncertainties associated to sample disturbance. Most times, cost issues avoid these uncertainties to be explicitly evaluated.

In the Authors' opinion, the whole community should devote a significant effort in research to provide adequate tools for a rigorous inclusion of uncertainties in standard practice for geotechnical engineering at large. It is also broadly acknowledged that deterministic approaches lead to inconsistent, non-rigorous, and erroneous response for static and dynamic analyses. Then probabilistic approaches and systematic hazard assessments must be adopted, especially in Geotechnical Earthquake Engineering. In this probabilistic framework, a precise evaluation of all the epistemic uncertainties and aleatory variabilities involved (i.e., not only the ones in V_S profile that represent only a portion of the total) has always to be carried out, in order to provide a consistent outcome.

References

Andrus, R. D., & Stokoe, K. H. (2000). Liquefaction resistance of soils from shear-wave velocity. *Journal of Geotechnical and Geoenvironmental Engineering*, 126, 1015–1025.

Andrus, R., Chung, R., & Stokoe, K. H. (1998). Delineation of densified sand at treasure island by SASW testing in geotechnical site characterization. In *Proceedings of the First International Conference on Site Characterization (Isc '98)* (pp. 459–64).

Bard, P., & Participants, SESAME (2004). The SESAME project: An overview and main results. In *Proceedings of 13th World Conference on Earthquake Engineering*, Vancouver, Bc, Canada, August (pp. 1–6).

Bard, P.-Y., Cadet, H., Endrun, B., Hobiger, M., Renalier, F., Theodulidis, N., et al. (2010). From non-invasive site characterization to site amplification: Recent advances in the use of ambient vibration measurements. In *Earthquake Engineering in Europe*. Berlin: Springer.

Biot, M. A. (1956a). Theory of propagation of elastic waves in a fluid-saturated porous solid. I. Low-frequency range. *The Journal of the Acoustical Society of America*, 28, 168–178.

Biot, M. A. (1956b). Theory of propagation of elastic waves in a fluid-saturated porous solid. II. Higher frequency range. *The Journal of the Acoustical Society of America*, 28, 179–191.

Butcher, A., Campanella, R., Kaynia, A., & Massarsch, K. (2005). Seismic cone downhole procedure to measure shear wave velocity—A guideline prepared by ISSMGE TC10: Geophysical testing in geotechnical engineering. In *Proceedings of the 16th International Conference on Soil Mechanics and Geotechnical Engineering*, Osaka, Japan.

Callero, A., Janicki, K., Milani, D., Priano, S., & Signori, M. (2013). Cross-hole tests at Zelazny most tailings pond, Poland—highlights and statistical interpretation of results. In *Near Surface Geoscience 2013-19th Eage European Meeting of Environmental and Engineering Geophysics*.

Cho, G. C., & Santamarina, J. C. (2001). Unsaturated particulate materials—particle-level studies. *Journal of Geotechnical and Geoenvironmental Engineering*, 127, 84–96.

Cornou, C., Ohmberger, M., Boore, D., Kudo, K., & Bard, P-Y. (2006). Derivation of structural models from ambient vibration array recordings: Results from an international blind test. In *Proceedings of the Third International Symposium on the Effects of Surface Geology on Seismic Motion*, Grenoble, France.

Cosentini, R. M., & Foti, S. (2014). Evaluation of porosity and degree of saturation from seismic and electrical data. *Geotechnique*, 64, 278–286.

Cox, B., Wood, C., & Teague, D. (2014). Synthesis of the UTexas1 surface wave dataset blind-analysis study: Inter-analyst dispersion and shear wave velocity uncertainty. In *Geo-Congress 2014: Geo-Characterization and Modeling for Sustainability* (pp. 850–859).

Di Giulio, G., Savvaidis, A., et al. (2012). Exploring the model space and ranking a best class of models in surface-wave dispersion inversion: Application at European strong-motion sites. *Geophysics*, 77, B147–B166.

Foti, S., Comina, C., Boiero, D., & Socco, L. (2009). Non-uniqueness in surface-wave inversion and consequences on seismic site response analyses. *Soil Dynamics and Earthquake Engineering*, 29, 982–993.

Foti, S., Garofalo, F., et al. (2017). Guidelines for the good practice of surface wave analysis. A product of the Interpacific project. *Bulletin of Earthquake Engineering*, on line first. <https://doi.org/10.1007/s10518-017-0206-7>.

Foti, S., Lai, C. G., & Lancellotta, R. (2002). Porosity of fluid-saturated porous media from measured seismic wave velocities. *Géotechnique*, 52, 359–373.

Foti, S., Lai, C. G., Rix, G. J., & Strobbia, C. (2014). *Surface wave methods for near-surface site characterization*. United States: CRC Press.

Foti, S., Parolai, S., Albarello, D., & Picozzi, M. (2011). Application of surface-wave methods for seismic site characterization. *Surveys in Geophysics*, 32, 777–825.

Foti, S., & Passeri, F. (2016). Reliability of soil porosity estimation from seismic wave velocities. In *Isc5-International Conference on Geotechnical and Geophysical Soil Characterisation, Gold Coast*, Australia (Vol. 1, pp. 425–430).

Garofalo, F., Foti, S., et al. (2016a). InterPACIFIC project: Comparison of invasive and non-invasive methods for seismic site characterization. Part I: Intra-comparison of surface wave methods. *Soil Dynamics and Earthquake Engineering*, 82, 222–240.

Garofalo, F., Foti, S., et al. (2016b). InterPACIFIC project: Comparison of invasive and non-invasive methods for seismic site characterization. Part II: Inter-comparison between surface-wave and borehole methods. *Soil Dynamics and Earthquake Engineering*, 82, 241–254.

Hadamard, J. (1902). Sur Les Problèmes Aux Dérivées Partielles Et Leur Signification Physique. *Princeton University Bulletin*, 49–52.

Idriss, I. (2004). Evolution of the state of practice. In *International Workshop on the Uncertainties in Nonlinear Soil Properties and Their Impact on Modeling Dynamic Soil Response*, Pacific Earthquake Engineering Research Center, Richmond, California.

Jamiolkowski, M. (2012). Role of geophysical testing in geotechnical site characterization. *Soils and Rocks International Journal of Geotechnical and Geoenvironmental Engineering*, 2: 117–137.

Jamiolkowski, M. (2014). Soil mechanics and the observational method: Challenges at the Zelazny most copper tailings disposal facility. *Géotechnique*, 64, 590–618.

Jamiolkowski, M., & Masella, A. (2015). Geotechnical characterization of copper tailings at Zelazny most site. *Keynote Lecture, DMT*, 15, 25–42.

Kaneko, F., Kanemori, T., & Tonouchi, K. (1990). Low-frequency shear wave logging in unconsolidated formations for geotechnical applications. In *Geophysical Applications for Geotechnical Investigations*. United States: ASTM International.

Kayen, R., Moss, R., et al. (2013). Shear-wave velocity-based probabilistic and deterministic assessment of seismic soil liquefaction potential. *Journal of Geotechnical and Geoenvironmental Engineering*, 139, 407–419.

Kim, D., Park, H., & Bang, E. (2013). Round Robin test for comparative study of in-situ seismic tests. *Geotechnical and Geophysical Site Characterization*, 4, 1427–1434.

Lai, C. G. (2015). Non-conventional methods for measuring dynamic properties of geomaterials. In *Proceedings of 6th International Conference on Earthquake Geotechnical Engineering*, Christchurch, New Zealand (pp. 1–4).

Laurenzano, G., Priolo, E., et al. (2017). Site response estimation at Mirandola by virtual reference station. *Bulletin of Earthquake Engineering*, 15, 2393–2409.

Mitchell, J. K., & Soga, K. (2005). *Fundamentals of soil behavior*. New Jersey: Wiley.

Nakamura, Y. (1989). A method for dynamic characteristics estimation of subsurface using microtremor on the ground surface. *Railway Technical Research Institute, Quarterly Reports*, 30.

Oh, W., & Vanapalli, S. (2011). The relationship between the elastic and shear modulus of unsaturated soils. In E. Alonso and A. Gens (Eds.), *Unsaturated Soils, Proceedings of the 5th International Conference on Unsaturated Soils* (pp. 341–346).

Passeri, F., Foti, S., Cox, B., & Rodriguez-Marek A. (2017). Influence of estimated epistemic uncertainties in shear wave velocity models on ground response analyses. *Earthquake Spectra (Submitted to)*.

Raptakis, D. G. (2012). Pre-loading effect on dynamic soil properties: Seismic methods and their efficiency in geotechnical aspects. *Soil Dynamics and Earthquake Engineering*, 34, 69–77.

Rathje, E. M., Kottke, A. R., & Trent, W. L. (2010). Influence of input motion and site property variabilities on seismic site response analysis. *Journal of Geotechnical and Geoenvironmental Engineering*, 136, 607–619.

Régnier, J., Bonilla, L. F., et al. (2016). International benchmark on numerical simulations for 1D, nonlinear site response (Prenolin): Verification phase based on canonical cases. *Bulletin of the Seismological Society of America*, 106, 2112–2135.

Régnier, J., Bonilla, L. F., et al. (2018). Prenolin: International benchmark on 1D nonlinear site response analysis—validation phase exercise. *Bulletin of the Seismological Society of America*. <https://doi.org/10.1785/0120170210>

Schnabel, P. B. (1972). *Shake a computer program for earthquake response analysis of horizontally layered sites* (EERC Report). Berkeley: University of California.

Socco, L. V., Foti, S., & Boiero, D. (2010). Surface-wave analysis for building near-surface velocity models—established approaches and new perspectives. *Geophysics*, 75, a83–a102.

Stewart, J. P., & Kwok, A. O. (2008). Nonlinear seismic ground response analysis: Code usage protocols and verification against vertical array data. In *Geotechnical Earthquake Engineering And Soil Dynamics IV*. United States: American Society of Civil Engineers.

Stewart, J. P., Afshari, K., & Hashash, Y. M. (2014). Guidelines for performing hazard-consistent one-dimensional ground response analysis for ground motion prediction. *Peer Rep*, 16.

Tarabusi, G., & Caputo, R. (2017). The use of HVSR measurements for investigating buried tectonic structures: The Mirandola anticline, Northern Italy, as a case study. *International Journal of Earth Sciences*, 106, 341–353.

Teague, D. P., Cox, B., & Rathje, E. M. (2017). Measured vs. predicted site response at the garner valley downhole array considering shear wave velocity uncertainty from borehole and surface wave methods. *Soil Dynamics And Earthquake Engineering (Submitted to)*.

Tran, K. T., & Hiltunen, D. R. (2011). An assessment of surface wave techniques at the Texas A&M national geotechnical experimentation site. In *Geo-Risk 2011: Risk Assessment and Management*. United States: American Society of Civil Engineers.

Soil–Bentonite Cutoff Walls for Geoenvironmental Containment

Takeshi Katsumi, Atsushi Takai and Toru Inui

Abstract Cutoff walls used for prevention of the migration of mobile contaminants in the aquifer must maintain high barrier performance for a long period. Soil–bentonite (SB), which is a mixture of in situ soil and bentonite, has many advantages as a barrier material such as appropriate deformability, homogeneity, and material stability because the SB consists only of inorganic soils. To ensure the long-term durability of the SB cutoff walls, various aspects such as performance of constructed barriers and post-construction maintenance need to be clarified. For a decade or more, the authors have studied factors affecting hydraulic conductivity (k) of SB, self-recovery in the k values against occurrence of hydraulic fractures, the feasibility of on-site quality assessment using the piezocone test, and the role of chemical diffusion in transport of mobile substances through SB cutoff walls. These approaches revealed that the k of the SB is affected by chemicals in groundwater and the content of bentonite powder. The piezocone test seems to be a suitable tool for detection of a lean-mix part in the cutoff walls and for measurement of on-site k values. The effect of chemical diffusion on transport of mobile substances is not negligible because the relative concentration of a chemical substance attained 0.26 after 50 years only by the chemical diffusion when not considering adsorption onto soil particles.

Keywords Containment · Barrier performance · Bentonite · Chemical diffusion · On-site quality

1 Introduction

The generation of waste materials, toxic chemicals, and other hazardous materials has become one of the most emergent problems to which society should find solutions not only in Japan but in the world. The disposal and dumping of such

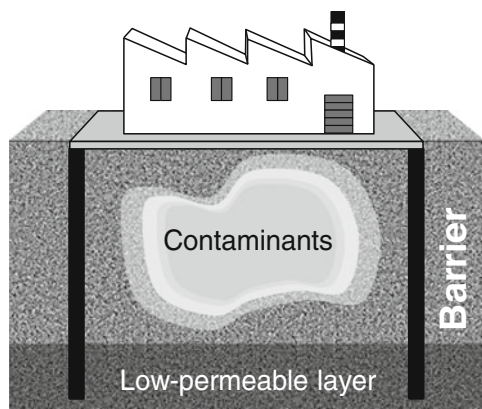
T. Katsumi (✉) · A. Takai · T. Inui
Kyoto University, Kyoto, Japan
e-mail: katsumi.takeshi.6v@kyoto-u.ac.jp

materials caused geoenvironmental problems, typified by contamination in the subsurface ground. For the positive utilization of such contaminated land space, various treatment techniques have been developed in these decades. Although excavation of the contaminated soil and subsequent disposal to landfills are one of the most conclusive methods in terms of complete removal of contaminants, this method is usually expensive due to landfill cost, and more importantly nothing else that contaminants are just transferred to a different place. Thus, more reasonable and environmentally friendly countermeasures with less transference of contaminants are required.

In view of this, in situ containment of contaminants using vertical cutoff walls with steel sheet piles or low-permeable earthen materials is an effective method to prevent the migration of mobile contaminants in the aquifer, as shown in Fig. 1 (Evans 1994; Yeo et al. 2009). To ensure strict isolation of the contaminants from surrounding environment, high barrier performance of cutoff walls must be maintained for a long period. Soil–bentonite (SB) is widely used because of low hydraulic conductivity (k) and appropriate deformability (e.g., Grube 1992). In addition, homogeneity of the SB cutoff walls can be expected, and material deterioration would not occur because the SB consists only of inorganic soils (Takai et al. 2016).

Low k of the SB attributes to the swelling characteristics of amended bentonite. Since the swelling characteristics of bentonite are strongly affected by chemicals and bentonite cannot swell sufficiently against solutions that have high concentration of inorganic chemicals or nonpolar liquids (Norrish and Quirk 1954), effect of chemicals in the groundwater on the barrier performance of bentonitic materials, either cutoff walls or clay liners, have been of great concern (e.g., Shackelford et al. 2000; Katsumi et al. 2007, 2008a, b, c; Ishimori and Katsumi 2012; Tang et al. 2014; Sato et al. 2017). Another concern regarding containment barriers is the assurance of homogeneity in hydraulic barrier performance. The hydraulic barrier performance in field should be verified after installation, since the on-site k may vary from predetermined laboratory k because of scale effect, natural variability in

Fig. 1 Schematic view of in situ containment of ground contaminants (Takai et al. 2016)



the base soils, accumulation of soil particles at the bottom, etc. Chemical diffusion also plays an important role in transport of mobile substances in the ground. Since the effect of diffusion on chemical transport is relatively large in low-permeable materials such as SB, chemical diffusion should be taken into consideration when evaluating hydraulic barrier performance of SB (Shackelford 2014).

This paper discusses barrier performance of SB cutoff walls from the viewpoints of factors affecting a k value and self-recovery against hydraulic fractures, as well as the feasibility of on-site quality assessment using the piezocene test (CPTU). SB cutoff wall installation method was proposed by Kamon et al. (2006) and Katsumi et al. (2008). Hydraulic conductivity values for the SB specimens with various additive contents of bentonite powder and chemical concentrations in permeant and in soil pore water were evaluated. The self-recovery capacity of the SB was evaluated by using specimens having an interface or a hole in the direction of permeation. CPTU, which can obtain the physical properties—corrected cone resistance (q_c), sleeve friction (f_s), and pore pressure (u)—of the ground of concern, is widely applied on-site investigations to estimate the soil profiles. Thus, CPTU can be expected to detect the zone with lean-mix of bentonite in SB walls from the CPTU data and to assess in situ k value during pauses in cone penetration. CPTU using a large-scale soil tank filled with various compositions of SB which simulate a heterogeneous wall was conducted. The role of chemical diffusion in transport of mobile substances was numerically assessed after determination of effective porosity and an effective diffusion coefficient through a series of experiments.

2 SB Cutoff Wall Installation Method

In this study, the SB cutoff wall installation method proposed by Kamon et al. (2006) and Katsumi et al. (2008) is considered. This method employs the trench cutting and re-mixing deep wall (TRD) method. First, the trench is cut with supplying bentonite slurry to maintain the workability of the in situ soil as shown in Fig. 2 (e.g., Katsumi et al. 2008). Second, bentonite powder is added to the soil–slurry mixture and re-mixed in the trench after the base machine is transferred back to the initial position. The advantage of employing the TRD method is to construct a cutoff wall of high homogeneity even in layered soils, since the cutter post which advances horizontally through the layers excavates, injects slurry or powder from its head, and mixes the soil, forming a continuous wall (e.g., Kamon et al. 1998; Katsumi et al. 2003).

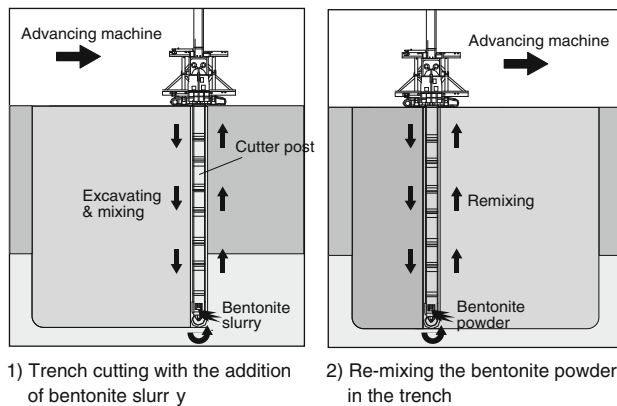


Fig. 2 Installation of SB cutoff walls by TRD method (Katsumi et al. 2008)

3 Hydraulic Conductivity of SB

3.1 Preparation of SB

Two soils used as base soil of SB in the experiments are summarized in Table 1. Composite soil is a mixture of sandy gravel and volcanic cohesive soil by a ratio of 25:4 in weight. Silica sand #7 is a commercially available geomaterial. The concentration of chemicals in pore water was adjusted with distilled water, calcium chloride (CaCl_2) solutions, artificial seawater, and heavy fuel oil A.

Specimen preparations were based on the procedures to simulate these construction processes in the laboratory. First, water contents of the sandy gravel, volcanic cohesive soil, and silica sand were adjusted to 27, 70, and 26%, respectively. Second, 10%-concentration bentonite slurry was mixed with the soil for 2 min to obtain 150-mm flow value of the soil–slurry mixture according to JIS R 5201. Finally, bentonite powder was added with proportions of $25\text{--}150 \text{ kg/m}^3$ and re-mixed using the soil mixer for 2 min.

Table 1 Basic properties of soils used

	Composite soil	Silica sand
Particle density (g/cm^3)	2.72	2.68
Grain size (%)		
Gravel [2 mm]	5.6	0
Sand [75 μm –2 mm]	70.8	99.6
Silt and clay [–75 μm]	23.6	0.4
Permeability (m/s)	1.5×10^{-7}	3.9×10^{-5}

3.2 Hydraulic Conductivity Test Using a Flexible-Wall Permeameter

In all tests, flexible-wall permeameters (shown in Fig. 3) were used to minimize leakage along a side wall of a specimen, according to ASTM D5084. After a SB specimen was pre-consolidated at 39.2 kPa in a conventional consolidation test apparatus and saturated using a vacuum deaerator for at least 2 days, the specimen with a height of approximately 2.0 cm and a diameter of 6.0 cm was placed between deaerated filter papers, geotextiles, and plastic caps with holes to connect the tubes. A confining pressure of 30 kPa and a hydraulic gradient of approximately 50 were applied during permeation.

In a series of the hydraulic conductivity test, effects of chemicals in inflow and in situ groundwater were assessed. For evaluating the effect of chemicals in inflow groundwater, bentonite in SB was initially hydrated with groundwater at a site of concern containing no chemicals, whereas swelling of bentonite was impeded when in situ groundwater contains chemicals with a relatively high concentration. CaCl_2 solution, artificial seawater, heavy fuel oil A, and 50% ethanol were used as original pore water and as permeant. CaCl_2 solution was selected because Ca^{2+} is present in many cases in natural aqueous system as well as in water discharged from industrial processes. Seawater and heavy fuel oil A were used to evaluate the performance of the SB near seashore and at an oil-contaminated site, respectively. The effect of the content of bentonite powder (C_{BP}) was also studied in a range from 50 to 150 kg/m^3 .

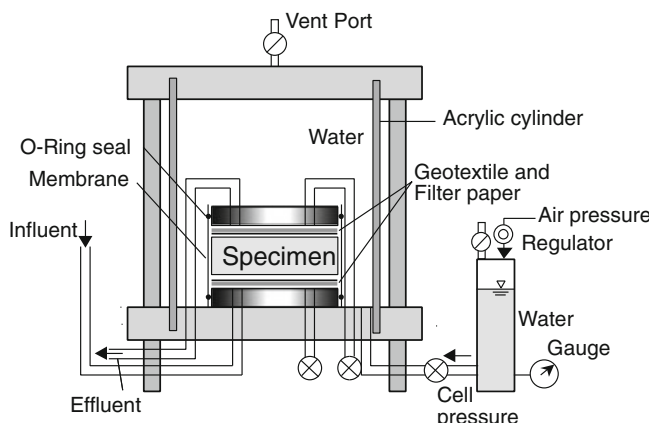


Fig. 3 Diagram of a flexible-wall permeameter

3.3 Chemical Compatibility

Figure 4 illustrates the k values for $C_{BP} = 100 \text{ kg/m}^3$ with different chemical conditions in the permeant (Kamon et al. 2006). Permeation with 0.1 M (=mol/L) CaCl_2 solution provided 3.5 times higher k value than the case with distilled water, while the difference in k is negligible for higher CaCl_2 concentration than 0.1 M. SB achieved the low k of $1.2 \times 10^{-10} \text{ m/s}$ even against the seawater. Hydraulic conductivity value with 50% ethanol permeation is almost equal with the value with distilled water permeation. Intrinsic permeability values are $5.0 \times 10^{-20} \text{ m}^2$ against 50%-ethanol permeation and $3.0 \times 10^{-20} \text{ m}^2$ against distilled water permeation. Therefore, the primary effect of organic solvent on hydraulic barrier performance is negligible. In conclusion from these experimental results, increase in the k of SB is not significant with any permeant if the bentonite in SB is initially well hydrated with soil pore water.

Figure 5 illustrates k values of SB made with $C_{BP} = 100 \text{ kg/m}^3$ for different chemicals in pore water present in the original soil. The higher k values were obtained with the higher CaCl_2 concentrations. The k increased linearly in association with CaCl_2 concentration ranging from 0 to 0.05 M. The k value higher than $1.0 \times 10^{-9} \text{ m/s}$ was obtained for 0.1 M. When the pore water was replaced with seawater, the k of SB reached the same values as in the case of 0.05 M CaCl_2 . When heavy fuel oil A is contained in base soil, SB exhibited very low k values due to both the hydrophobicity of oil and the swelling of bentonite.

The k values for various bentonite powder contents, C_{BP} , with different CaCl_2 concentrations in soil pore water are illustrated in Fig. 6. The higher C_{BP} results in the lower k , even when the CaCl_2 concentrations in the pore water were high (0.05 or 0.1 M). Even for the CaCl_2 concentration of 0.1 M, the k was lower than $1.0 \times 10^{-9} \text{ m/s}$ when $C_{BP} = 150 \text{ kg/m}^3$. These low hydraulic conductivity values are attributed to the shorter distance of montmorillonite layers by adding the larger amount of bentonite powder. From these experimental results, when the SB cutoff

Fig. 4 k values versus types of permeant (edited after Takai et al. 2013)

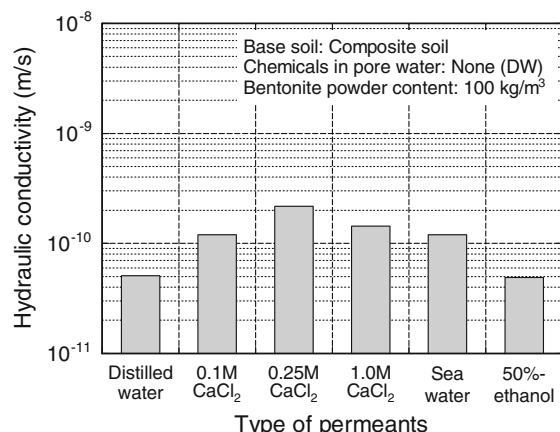


Fig. 5 k values versus types of soil pore water (edited after Takai et al. 2013)

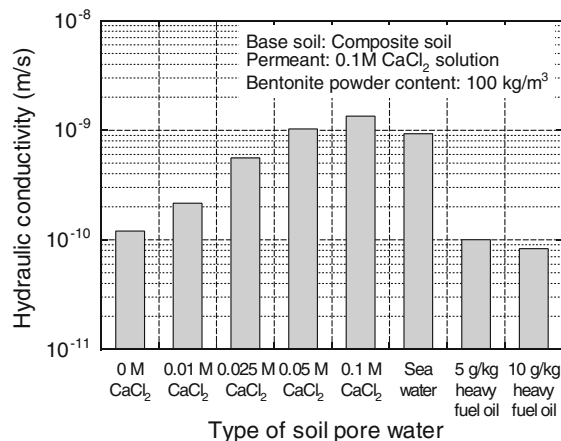
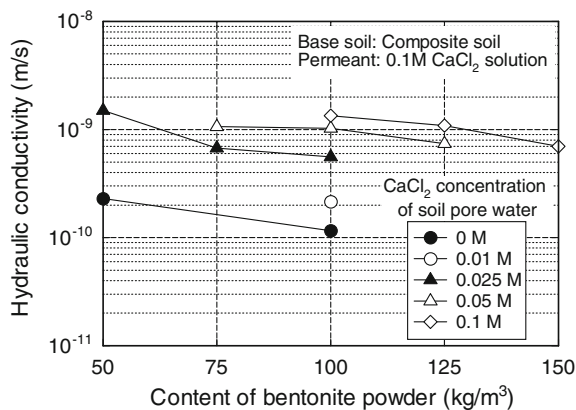


Fig. 6 Effects of additive content of bentonite powder and CaCl_2 concentrations in pore water (edited after Takai et al. 2013)



walls are installed at a site where the inorganic chemical concentration of the groundwater is high, the hydraulic barrier performance can be enhanced by adding a larger amount of bentonite. Under prehydrated condition (CaCl_2 concentration in pore water = 0 M), a k lower than 1.0×10^{-9} m/s was achieved with 50 kg/m³ additive content of powder bentonite for the composite soil used in this study.

3.4 Self-recovery in K

Since SB maintains appropriate deformability unlike solidified materials, SB cutoff walls can deform as conforming to adjacent ground. This is an important function of SB because the SB cutoff walls may follow the ground deformation and maintain its soundness even when earthquake occurs. Besides, even if hydraulic fractures

occur in the direction of permeation, self-sealing capability of SB attributed to the deformability and the swelling of bentonite can be expected. To assess this function, SB specimens with a hydraulic fracture—an interface or a hole—were also subjected to permeation. For the preparation of specimens having an interface, the cylindrical specimen demolded after pre-consolidation was diametrically halved. After the two semicircular specimens were attached again, the specimen was subjected to permeation. To prepare specimens with a hole, a stainless bar with a diameter of 2.0 mm was penetrated at the center of specimen in the direction of the permeation. These procedures for preparation of specimens with a fracture are shown in Fig. 7. The k of SBs with a hydraulic fracture was calculated with the section area of specimen ($\approx 28.27 \text{ cm}^2$) and the volume of effluent as the apparent k on the assumption of Darcian flow in the specimen.

Figure 8 illustrates temporal changes in apparent k of the specimens with and without an interface. In the case that the CaCl_2 concentration is 0.02 M, significant increase in apparent k value was observed at the beginning of permeation when the specimen had an interface. However, even in such case, the apparent k decreased with time and converged within several times to the k of undamaged SB after 40 h or more. Since there was no significant difference between the cases with and without an interface when the CaCl_2 concentration of soil pore water was 0.05 M, it can be assumed that the permeated volume through the interface is not much compared to total flux through the specimen when the k of undamaged SB is relatively high. Figure 9 shows mean k after 40 h for the specimens without a fracture, with an interface, and with a hole. As seen in this figure, when CaCl_2 concentration in pore water was 0 or 0.02 M, mean k of specimen with an interface and with a hole increased several times higher than those of undamaged SBs. Although this indicates that flow volume through the fractures was relatively larger than that through sound planes, the presence of fractures causes no significant change in flux through the whole domain. These observations confirm that

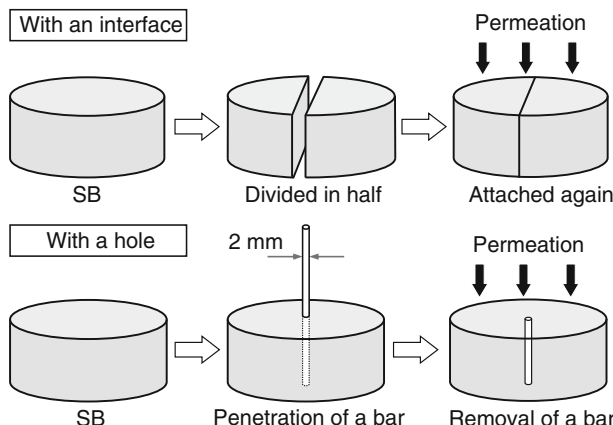


Fig. 7 Preparation of SB specimens having an interface and a hole (edited after Takai et al. 2014)

Fig. 8 Apparent k of SBs with and without an interface (edited after Takai et al. 2014)

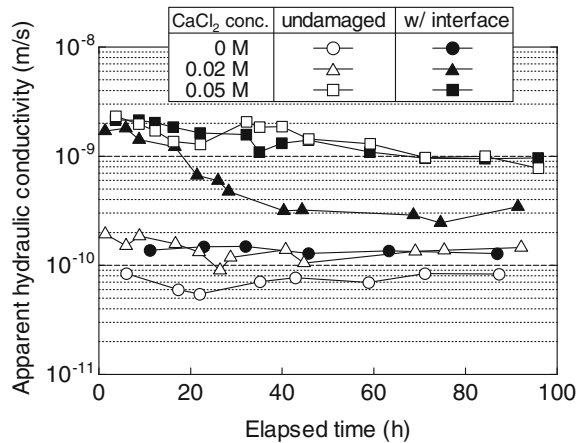
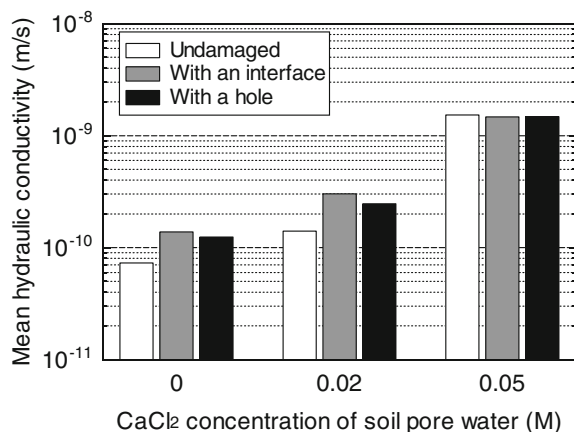


Fig. 9 Comparison of mean k with and without a fracture



bentonite particles in SB were dispersed into the permeant due to high dispersivity and re-swelled to the permeant within the fractures. Furthermore, the interface was firmly attached and the hole shrank by confining pressure during permeation because of the deformability of SB. Thus, even if fractures appear in SB cutoff walls after an earthquake, the SB can recover its k under a certain level of overburden pressure regardless of CaCl_2 concentration in pore water at the site of concern.

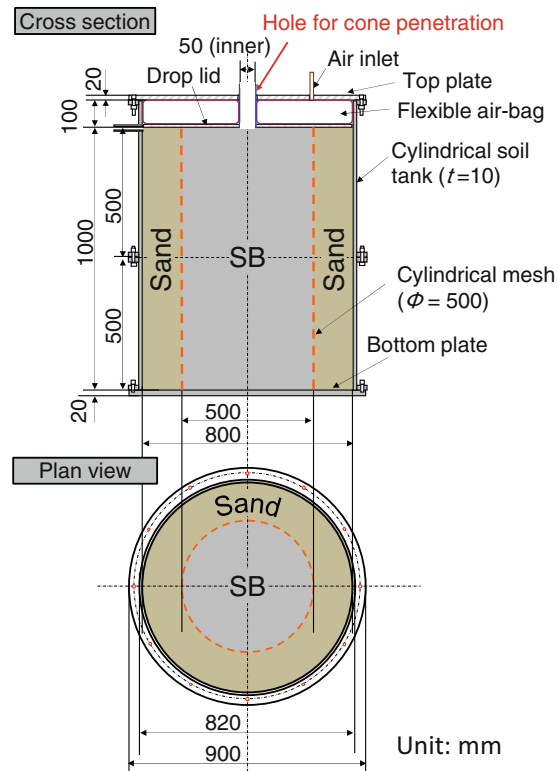
4 On-site Quality Assessment Using CPTU

The feasibility of using the CPTU in quality assessment of SB cutoff walls was studied using a large-scale soil tank in the laboratory. There are several advantages of using CPTU in the measurement of k of vertical barriers: It is fast, cost-effective,

and reliable, and provides a profile of k versus depth. This latter point is important for the confirmation of the high hydraulic barrier performance of cutoff walls because the k values for samples taken during construction are not continuous and a limited number of k values must represent the quality of whole cutoff walls. One disadvantage is that the CPTU permeates only a small volume of material relative to other in situ test methods (Joshi et al. 2010).

The probe used in this study has a diameter of 35.6 mm (=10 cm² in its section area), and the ceramic filter for pore pressure measurement is located on a shoulder of the cone tip. One thermometer and two inclinometers are also embedded in the probe. The detailed view of large-scale soil tank used for CPTU is shown in Fig. 10. The soil tank has 1.0 m in inner diameter and 0.8 m in height. A self-standing steel mesh with 0.5 m diameter was set in the center of soil tank. The cylindrical mesh isolated the SB layer from the surrounding soil, and it allowed drainage from SB layer during cone penetration. Rubber packing was placed at each contacting face (upper and lower tank, or with top/bottom plates) to avoid water leakage from the connection parts. A circular hole of 5.0 cm diameter is equipped on the top steel plate for cone penetration. Air pressure can be supplied to the surface of the soil layer via a flexible air bag to avoid any volume change of the soil

Fig. 10 Schematic diagram of large-scale soil tank

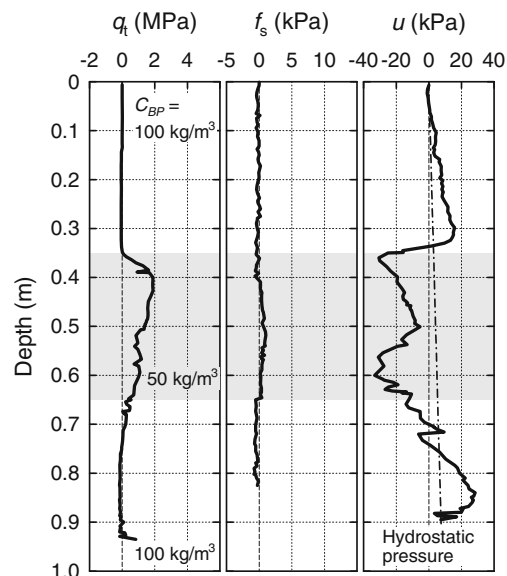


layers. To transport the air pressure equally on the surface, a drop lid with a circular hole for cone penetration was placed between the soil surface and the air bag. During the cone penetration, the specimen was loaded with an air pressure of 30 kPa. The mean wet density of surrounding sand layer was 2.00 Mg/m³, while that of SB layers were approximately 1.82 Mg/m³ and 1.88 Mg/m³ for SB with 50 kg/m³ and 100 kg/m³, respectively. After the tank was left for several hours with a loading pressure of 30 kPa, the cone probe was manually pushed into the soil using guiding equipment, and the penetration depth was recorded with a depth recorder placed on the top plate. At certain depths, penetration was suspended to conduct pore pressure dissipation test for k value assessment. The target rate of penetration was set up to 1.0 cm/s to enhance the precision of detection, while a penetration rate of 2.0 cm/s is commonly used for the field investigations.

In practical applications, bentonite powder is normally added at a proportion of 100 kg/m³, provided the cation concentration in the groundwater is low enough to allow for the sufficient swelling of bentonite. Thus, hereafter, SB with 100 kg/m³ of bentonite powder will be referred to as rich SB mixture and SB with less amount of bentonite powder (smaller C_{BP}) as lean SB mixture.

Profiles of CPTU measurements with penetration depth are shown in Fig. 11. This figure illustrates q_t , f_s , and u , respectively, from left to right. In this test condition, an SB layer with 50 kg/m³ bentonite powder was sandwiched between SB layers with 100 kg/m³ bentonite powder. The result clearly confirms that the q_t values in the middle layer consisting of SB with $C_{BP} = 50$ kg/m³ are larger than those in the top and bottom layers consisting of SB with $C_{BP} = 100$ kg/m³. In the middle layer, the q_t values attain approximately 1.9 MPa and, in the top and bottom layer, approximately 0.1 MPa regardless of the depth. Extremely low q_t values

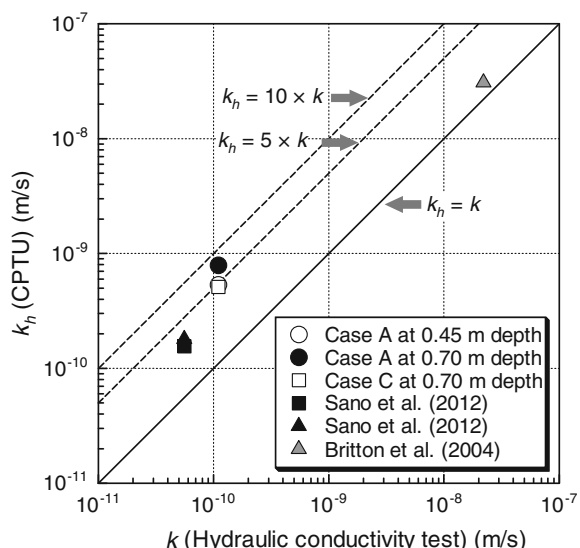
Fig. 11 Profiles of CPTU with penetration depth (Takai et al. 2016)



attribute to SB's high flexibility and softness, which are specific characteristics of SB. In contrast, since an SB with 50 kg/m³ bentonite powder is classified as sandy gravel (SG) according to JGS 0051 (2009) due to a clay fraction of less than 6%, the strength characteristics of silica sand became predominant. The f_s values are very small regardless of the depth. Pore water pressure values also have an obviously different trend in the middle layer and in the top and bottom layers. Although u values increase with the penetration depth until the probe reaches a boundary at around 0.35 m depth, those drastically decrease and become negative values in the middle layer probably due to positive dilatancy during the cone penetration. Although excess pore water pressure was generated in the top and bottom layers, u values in the middle layer are negative throughout the whole layer. Generally, q_t and f_s from sand stratum are higher than those from silty soil and/or clay stratum due to their large particle sizes. Besides, pore water pressure may decrease with less fine particle content. Therefore, considering that cutoff walls are mainly constructed in the sand stratum, the behavior of partial lean-mix SB in cutoff walls may be strongly affected by the characteristics and types of the on-site soil. Although further studies should focus on the sources of the variation in u values during CPTU, these results indicate that CPTU can detect a lean-mix part in a horizontal direction in SB cutoff walls from the data profiles, as long as the mechanical properties of SB are responsive to C_{BP} within the range of the design values.

Pore water pressure values were recorded at 1 s intervals at a certain depth after cone penetration was suspended. Figure 12 illustrates the relationship between k_h values obtained from the pore pressure dissipation test during CPTU with 50% dissipation and that values obtained from hydraulic conductivity test with 30 kPa confining pressure, with results of previous research conducted on SBs with different base soils (Sano et al. 2012) and pilot-scale SB backfill with different

Fig. 12 Comparison of k_h from CPTU and k from laboratory hydraulic conductivity test (Takai et al. 2016)



bentonite contents (Britton et al. 2004). For the calculation of k_h values, an I_r value of 3.3 and m_v values of 7.43×10^{-4} and $8.59 \times 10^{-4} \text{ m}^2/\text{kN}$ measured in the process of conventional consolidation test were applied for SBs with 50 and 100 kg/m^3 bentonite powder, respectively. It can be observed that the k_h values measured by the pore pressure dissipation test have good correlation with the k values measured by hydraulic conductivity test. The overall trend of this relationship is that the k_h values from CPTU are larger than those from hydraulic conductivity tests. This difference may well be explained by the permeation of the piezocone: It permeates only a small volume of liquid in a ceramic filter, whereas a sufficient volume of permeant is continuously supplied during the hydraulic conductivity test. Another possible reason is that water penetration in the hydraulic conductivity test is one-dimensional, while the pore water pressure during CPTU dissipates three-dimensionally, and horizontal dissipation is also affected by drainage from sandy layer around the SB layer. Nonetheless, it is possible to obtain the k value by implementation of the pore pressure dissipation test within a difference of one order of magnitude. These observations confirm that k of SB can be approximately estimated by the pore pressure dissipation test. This fact suggests that the operation of the pore pressure dissipation test is suitable for the QC/QA of hydraulic barrier performance immediately after the installation of SB cutoff walls. The hydraulic barrier performance of SB cutoff walls can be assessed within one order of magnitude difference, within a short period of time, and with spatial continuity, by the pore pressure dissipation test during CPTU.

5 Role of Chemical Diffusion

For measurement of diffusion parameters, advection–diffusion test using a thin vertical column was conducted (Takai et al. 2017). Silica sand-based SB with C_{BP} of 50 kg/m^3 was filled into an acrylic cell with a diameter of 10.0 cm and a height of 1.5 cm to achieve a porosity of 0.47 between porous stones and filter papers. An SB with 50 kg/m^3 bentonite powder was selected in this research because an SB with 100 kg/m^3 , a normal proportion in practical application, has extremely low k and needed very long test period. After the specimen was saturated by injecting distilled water from a bottom port, 0.05 M NaCl solution was circulated in a top porous stone with a peristaltic pump to keep the concentration gradient constant. A bottle connected to bottom ports was lowered to apply a water level difference of 90 cm. The mass and the Cl^- concentration of effluent were measured once at 24 h intervals. Cl^- concentration, which is not adsorbed onto soil particles, was measured, and the test was continued for 10–15 days. In this study, the mass transport parameters were determined by fitting analytical results to experimental ones regarding the mass flux of Cl^- leaching out from the bottom porous stone. Analytical results were obtained using Dtransu-2D, which is a two-dimensional advection–dispersion analysis program. A one-dimensional model which represents the SB specimen and the bottom porous stone in the diffusion test system was used.

Each mesh has 1 mm thickness. Input k was an average one obtained during the test with a constant hydraulic gradient of 20 in consideration of an upward osmotic pressure caused by the concentration difference. Dispersion coefficient was set to 0 because the model was so thin and advective velocity in the SB can be negligible because of low k . A retardation factor of 1 and an attenuation coefficient of 0 were applied because Cl^- is not adsorbed. A breakthrough curve obtained from the numerical analysis was shifted so that the initial rise in the Cl^- concentration coincides with the experimental one. Based on results of sensitivity analysis, effective diffusion coefficient, D_e , and effective porosity, n_e , of the SBM were determined with two significant digits so that the residual sum of squares at the initial three days becomes minimum. As a result, k , n_e , and D_e of the silica sand-based SB with C_{BP} of 50 kg/m^3 were calculated to be $5.8 \times 10^{-10} \text{ m/s}$, 0.22, and $3.0 \times 10^{-10} \text{ m}^2/\text{s}$, respectively.

By using these parameters and hydraulic conductivity values, solute transport through a SB wall for up to 100 years was evaluated. Figure 13 illustrates three possible scenarios of hydraulic conditions on site which are: (1) advection and diffusion in the opposite direction, (2) only diffusion, and (3) advection and diffusion in the same direction. The chemical diffusion drives mobile substances only toward outside the cutoff walls because the concentration of toxic elements should be relatively high inside the cutoff walls. Horizontal mass transport of substances was numerically evaluated under these conditions by using an analytical model shown in Fig. 14, which simulates the SB cutoff wall and an adjacent saturated sandy ground with a horizontal length of 10 m outward from the outer border of the cutoff wall. Thickness of the cutoff wall was 55 cm which corresponds to a typical

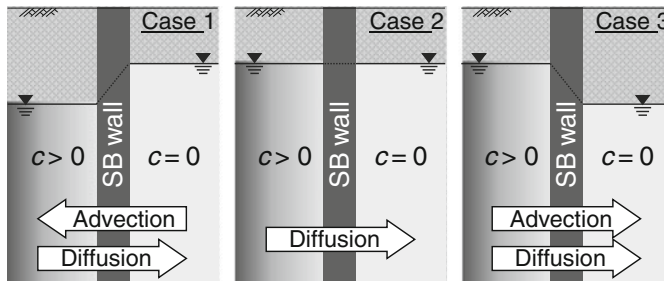


Fig. 13 Possible scenarios of groundwater condition

Fig. 14 Analytical model used

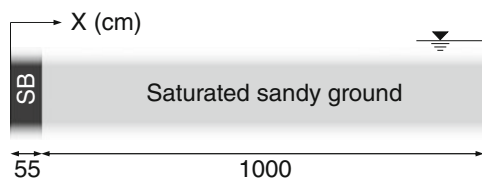
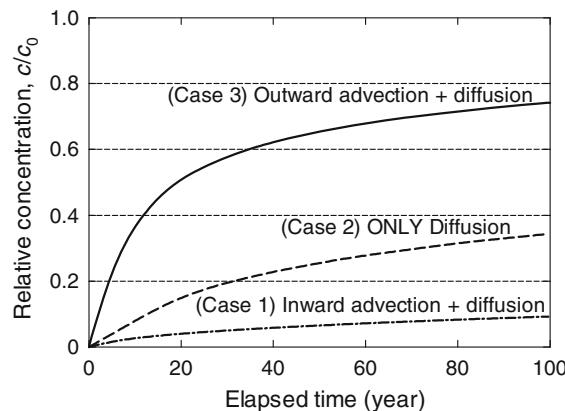


Fig. 15 Transport of mobile substances



thickness on site. Sorption of the substances onto soil particles was not considered in this analysis. In the model, the SB cutoff walls and the sandy ground were divided into 1 cm and 10 cm thickness, respectively. A difference in the ground-water level was set to 55 cm, which corresponds to a hydraulic gradient of 1. Input k , D_e , and n_e of the SB cutoff wall were 5.8×10^{-10} m/s, 3.0×10^{-10} m²/s, and 0.2, respectively, based on experimental results. The diffusion coefficient of Cl^- ion in water of 2.0×10^{-9} m²/s was input as the D_e of the sandy ground n_e of 0.2 and k of 1.0×10^{-5} m/s were used.

Figure 15 shows temporal change in relative concentration, which is a concentration normalized by the inflow concentration, at the outer boundary of the SB wall. The relative concentration after 50 years was 0.07, 0.26, and 0.66 in case 1, 2, and 3, respectively. Since influence of the advection is relatively large, the transport of contaminants can be restrained by preventing the advection with maintaining the inside groundwater level lower than the outside. Since the relative concentration in 50 years was 0.26 even in the case 2, the influence of diffusion is not negligible on the mass transport. However, the fact that the relative concentration can be lowered to 0.07 when maintaining the groundwater level inside the cutoff wall lower than the one of the outside, control of groundwater level is effective to prevent the migration of mobile contaminants for a long period.

6 Conclusions

In this paper, long-term durability of SB cutoff walls used for ground contamination was discussed from the viewpoints of factors affecting a k value, self-sealing capability, and the chemical diffusion on transport of mobile substances. The conclusions are summarized as follows:

- (1) Sufficient hydration of bentonite in SB can maintain a low k against permeation of any chemical solutions, whereas calcium ions in soil pore water have more significant influence. Even when cations exist in pore water with a relatively high concentration, the k can be enhanced by mixing a higher content of bentonite powder.
- (2) Even if hydraulic fractures appear in the SB cutoff walls after an earthquake, self-sealing hydraulic barrier performance would not be significantly affected under a certain level of overburden pressure regardless of CaCl_2 concentration in pore water at the site of concern.
- (3) The k_h measured by the pore pressure dissipation test showed a good correlation with those measured by the laboratory hydraulic conductivity test, with a difference of less than one order of magnitude. Thus, the dissipation test seems to be a suitable tool to be used in the process of quality assurance of the hydraulic barrier performance of SB cutoff walls.
- (4) Although influence of chemical diffusion is not negligible in transport of mobile substances in the ground, the concentration can be lowered when maintaining the inside groundwater level lower than the outside one.

Acknowledgements The authors would like to express their appreciation to Professor M. Kamon (Research Institute for Environmental Geotechnics), Mr. S. Araki (Raito Kogyo Co., Ltd.), and Professor M. Mimura (Graduate School of Engineering, Kyoto University) for their helpful advice and suggestions on this study. Special thanks are due to Mr. M. Yoshimura and Mr. T. Terao (Soil and Rock Engineering Co., Ltd., Japan), and former and current students at Kyoto University. This work was supported by JSPS KAKENHI Grants-in-Aid for Scientific Research (Nos. 22360185, 24760379, and 15H02264).

References

Britton, J. P., Filz, G. M., & Herring, W. E. (2004). Measuring the hydraulic conductivity of soil-bentonite backfill. *Journal of Geotechnical and Geoenvironmental Engineering*, 130(12), 1250–1258.

Evans, J. C. (1994). Hydraulic conductivity of vertical cutoff walls. In D. E. Daniel & S. J. Trautwein (Eds.), *Hydraulic conductivity and waste contaminant transport in soils, ASTM STP 1142* (pp. 79–94). Philadelphia: ASTM.

Grube, W. E. (1992). Slurry trench cut-off walls for environmental pollution control. In D. B. Paul, R. R. Davidson, & N. J. Cavalli (Eds.), *Slurry walls: design, construction, and quality control, ASTM STP 1129* (pp. 69–77). Philadelphia: ASTM.

Ishimori, H., & Katsumi, T. (2012). Temperature effects on the swelling capacity and barrier performance of geosynthetic clay liners permeated with sodium chloride solutions. *Geotextiles and Geomembranes*, 33, 25–33, Elsevier.

Joshi, K., Kechavarzi, C., Sutherland, K., Ng, M. Y. A., Soga, K., & Tedd, P. (2010). Laboratory and in situ tests for long-term hydraulic conductivity of a cement-bentonite cutoff wall. *Journal of Geotechnical and Geoenvironmental Engineering, ASCE*, 136, 562–572.

Kamon, M., Ohta, H., Aoi, M., & Asada, S. (1998). Development of new river protection method by continuous inclined diaphragm wall. In P. S. Séco e Pinto (Ed.), *Environmental geotechnics* (pp. 35–38). Rotterdam: Balkema.

Katsumi, T., Ishimori, H., Ogawa, A., Maruyama, S., & Fukagawa, R. (2008b). Effects of water content distribution on hydraulic conductivity of prehydrated GCLs against calcium chloride solutions. *Soils and Foundations, JGS*, 48(3), 407–417.

Katsumi, T., Ishimori, H., Ogawa, A., Yoshikawa, K., Hana-maoto, K., & Fukagawa, R. (2007). Hydraulic conductivity of nonprehydrated geosynthetic clay liners permeated with inorganic solutions and waste leachates. *Soils and Foundations, JGS*, 47(1), 79–96.

Katsumi, T., Ishimori, H., Onikata, M., & Fukagawa, R. (2008c). Long-term barrier performance of modified bentonite materials against sodium and calcium permeant solutions. *Geotextiles and Geomembranes*, 28, 14–30, Elsevier.

Kamon, M., Katsumi, T., Inui, T., Ogawa, Y., & Araki, S. (2006). Hydraulic performance of soil-bentonite mixture barrier. In H. R. Thomas (Ed.), *SICEG Environmental Geotechnics* (pp. 733–740). London, UK: Thomas Telford Publishing.

Katsumi, T., Kamon, M., Inui, T., & Araki, S. (2008a). Hydraulic barrier performance of SBM cut-off wall constructed by the trench cutting and re-mixing deep wall method. In M. V. Khire, A. N. Alshawabkeh, & K. R. Reddy (Eds.), *Geo-congress 2008: Geotechnics of waste management and remediation, GSP 177* (pp. 628–635). New Orleans: ASCE.

Katsumi, T., Kamon, M., Watanabe, M., Suminaga, I., & Fukagawa, R. (2003). Basic properties of soil-cement cut-off wall applied to waste containment barriers. In P. J. Culligan, H. H. Einstein, & A. J. Whittle (Eds.), *Soil and Rock America 2003* (pp. 1389–1395). Germany: VGE, Essen.

Norrish, K., & Quirk, J. (1954). Crystalline swelling of montmorillonite: Use of electrolytes to control swelling. *Nature*, 173, 255–257.

Sano, K., Takai, A., Inui, T., Katsumi, T., Kamon, M., Yoshimura, M., et al. (2012). Quality assessment of SBM cut-off wall using piezocone. *Proceedings of Geo-Environmental Engineering, 2012*, 171–178.

Sato, K., Razakamanantsoa, A. R., Barast, G., Djeran-Maigre, I., Katsumi, T., & Levacher, D. (2017). Comparison of prehydration and polymer adding effects on Na activated Ca-bentonite by free swell index test. *Applied Clay Science*, 142, 69–80, Elsevier.

Shackelford, C. D. (2014). The ISSMGE Kerry Rowe Lecture: The role of diffusion in environmental geotechnics. *Canadian Geotechnical Journal*, 51, 1219–1242.

Shackelford, C. D., Benson, C. H., Katsumi, T., Edil, T. B., & Lin, L. (2000). Evaluating the hydraulic conductivity of GCLs permeated with non-standard liquids. *Geotextiles and Geomembranes*, 18, 133–161, Elsevier.

Takai, A., Inui, T., Katsumi, T., Kamon, M., & Araki, S. (2013). Hydraulic barrier performance of soil bentonite mixture cutoff wall. In M. Manassero, A. Dominijanni, S. Foti, & G. Musso (Eds.), *Coupled phenomena in environmental geotechnics—from theoretical and experimental research to practical applications* (pp. 707–714). Torino: CRC Press.

Takai, A., Inui, T., Katsumi, T., Kamon, M., & Araki, S. (2014). Experimental study on the self-sealing capability of soil-bentonite mixture cutoff walls. In A. Bouazza, S. T. S. Yuen, & B. Brown (Eds.), *Proceedings of the 7th international congress on environmental geotechnics—lessons, learnings & challenges* (pp. 411–416). Melbourne: Engineers Australia.

Takai, A., Inui, T., & Katsumi, T. (2016). Evaluating the hydraulic barrier performance of soil-bentonite cutoff walls using the piezocone penetration test. *Soils and Foundations*, 56(2), 277–290.

Takai, A., Katsumi, T., Inui, T., & Kamon, M. (2017). Solute transport in soil-bentonite cutoff walls considering chemical diffusion. Nineteenth International Conference on Soil Mechanics and Geotechnical Engineering (in press).

Tang, Q., Katsumi, T., & Inui, T. (2014). Membrane behavior of bentonite-amended compacted clay. *Soils and Foundations, JGS*, 54(3), 329–344.

Yeo, S. S., Shackelford, C. D., & Evans, J. C. (2009). Hydraulic conductivity and compressibility of soil-bentonite backfill amended with activated carbon. *Journal of Geotechnical and Geoenvironmental Engineering*, 135(5), 664–672.

Development of Underground Tunnel Construction Technology in Weak Rock

Eun Chul Shin, Jeong Jun Park and Arum Lee

Abstract The construction of tunnel has a long history from the mining tunnel for minerals to underground passage for transportation. Most of tunnels are being constructed to pass through the high mountain to have a shortcut instead of taking a detour to reach the destination. The geological conditions in the area of tunnel construction work are not all the time favorable condition. The rock bolt and steel rib support systems for tunnel face are described. The tunnel construction in weak rock is described with rock bolt and steel pipe grouting reinforcement (NATM). The advantages and construction procedures of pre-supported tunneling method (PSTM) and tubular roof construction method (TRcM) in soft ground are presented with the detail schematic diagrams. In the latter part of this paper, the field application case histories of PSTM and TRcM are reported for the tunnel construction for road in weak rock and metro station in soft ground, respectively. The field monitoring results during the tunnel construction which underpass through 60-m-long existing railway tracks by using TRcM are also described.

Keywords Pre-supported tunneling method · Tubular roof construction method · NATM · Weak rock · Field monitoring work

E. C. Shin (✉) · A. Lee
Department of Civil and Environmental Engineering,
Incheon National University, Incheon, Republic of Korea
e-mail: ecshin@inu.ac.kr

A. Lee
e-mail: 94arum2@naver.com

J. J. Park
Incheon Disaster Prevention Research Center,
Incheon National University, Incheon, Republic of Korea
e-mail: smearjun@hanmail.net

1 Introduction

It is quite difficult work for making tunnel in the soft ground or partially weathered rock. The stability of tunnel is the priority in the construction of tunnel like this ground condition. The stability of tunnel construction in the densely populated urban area is largely depended upon the selection of excavation technique. The NATM is normally applied for the good rock condition with controlled rock blasting method as well as rock bolting system. Sometimes, rock blasting is caused by cracking the buildings above ground and subsidence of ground surface. The residents on the ground are frequently frightened due to the sudden shock of ground shaking and blasting noise. Terzaghi (1946) suggested the simplified diagram for the movement of loosened rock toward a tunnel and the transfer of load onto the surrounding rock as shown in Fig. 1. The height of loosened rock is expressed in H_p , and B_1 is the zone of rock in which movement occurred. H_t and B are the height and the width of tunnel, respectively. The overburden pressure W_1 is due to the weight of soil and rock above the loose rock line from c to d . The variation of pressure condition along the supporting methods is presented by Terzaghi (1946) for in situ rock conditions which are characterized as hard and intact rock to squeezing and swelling rocks. The height of loosened rock H_p is given for various in situ rock conditions and expressed in term of $(B + H_t)$. Merritt reported the tunnel support system for the variation of rock quality designation (Deere and Miller 1966) as well as tunnel width as shown in Fig. 2.

Fig. 1 Movement of loosened rock around tunnel

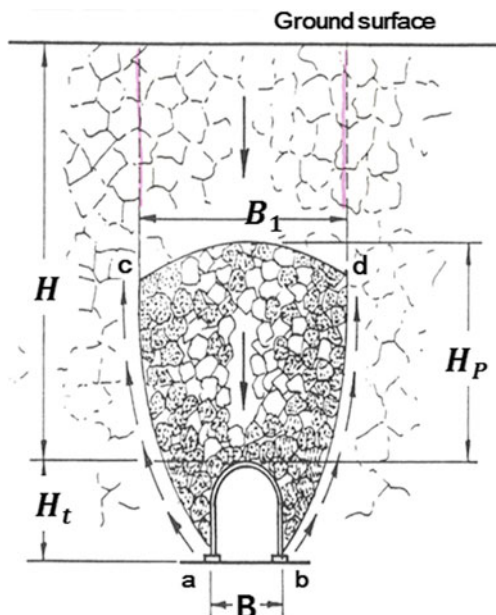
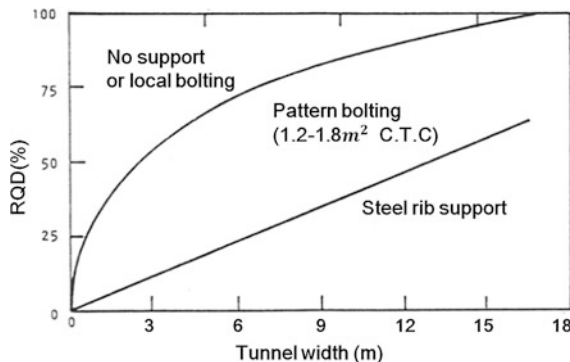


Fig. 2 Rock support system with variation of RQD

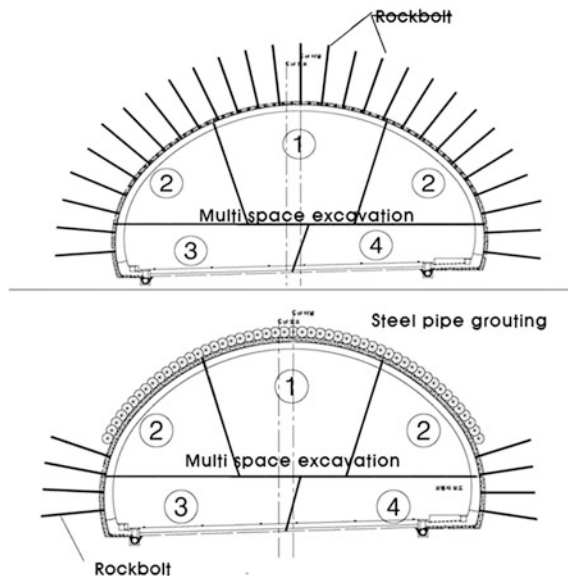


In this way, damage and collapse of tunnel surface are occurred during tunnel construction, causing settlement and depression on the ground surface, causing safety problems. Therefore, it is necessary to evaluate the construction procedures and field monitoring during the excavation of tunnel. In this paper, the tunnel construction methods by using NATM, PSTM, and TRcM are described with the detail sequence of tunnel construction. The construction case histories of PSTM and TRcM are presented with field monitoring works.

2 General Tunnel Method by NATM

New Austrian tunneling method (NATM) was developed by Ladislaus von Rabecewitz in Austria, 1948. The basic concept of NATM tunneling method is to design and construct a tunnel by installing the support material in an appropriate time to maintain the new equilibrium state of stress around tunnel. In other words, this method is based on the equilibrium theory that induces a new equilibrium state as elastic or elastic-plastic state contrary to the conventional tunnel which was designed based on the theory of relaxation load. The NATM method is based on the theory that tunnel fracture is caused by shear failure, and the relatively thin concrete lining is applied to the excavated ground using the mechanical properties of rock. Compared to existing tunneling method, it is an economical and stable tunneling method. In the NATM method, the shotcrete which is the primary support material is installed at the initial stage after tunnel excavation to settle the behavior of the rock mass in the ground initially. After installing the rock bolts, it is expected to prevent the loosening of the surrounding ground and sealing effect between the rocks. NATM is economical and stable method to install tunnels by analyzing the measurement results of installed instruments and judging the installation of secondary support materials. Cross-sectional diagram of NATM is shown in Fig. 3.

Fig. 3 Cross-sectional diagram of NATM



3 Pre-supported Tunneling Method

3.1 *Introduction of PSTM*

The basic concept and the case history of pre-supported tunneling method (PSTM) in weak weathered rock are presented in detail. The construction of tunnel in the weak weathered rock has a high collapse potential. The collapse potential can be much reduced with the reinforcement of upper layer around tunnel. The reinforcement methods of weak weathered rock are either combined rock nailing with pressurized grouting or rock bolt. The pipe roof method with combination of pressurized grouting is also applied around the tunnel where the soil condition is very weak. The tunnel construction project in urban area where the weak weathered rock is existed has several problems such as superstructures above ground surface, heavy traffic, road, limited working space, and pedestrian road. The ground reinforcement with combination of pre-nailing and pressurized grouting would be the solution to overcome fore-mentioned problems. In the construction work, residential house, office building, and so on are existed above ground surface. Thus, pre-nailing work can not be proceeded from the ground surface. The pre-nailing with the vertical spacing 1.5 m relative to the tunnel axis and 1.0 m horizontal spacing is installed during the underground excavation work with the help of pilot tunnel as shown in Fig. 4a. In the economical point of view, this method is much cheaper than that of pipe roofing method. The use of shield tunnel boring machine could be difficult because a shallow cover soil and also the weak fractured rock with groundwater table could be existed. The second step of PSTM is to drill the hole for

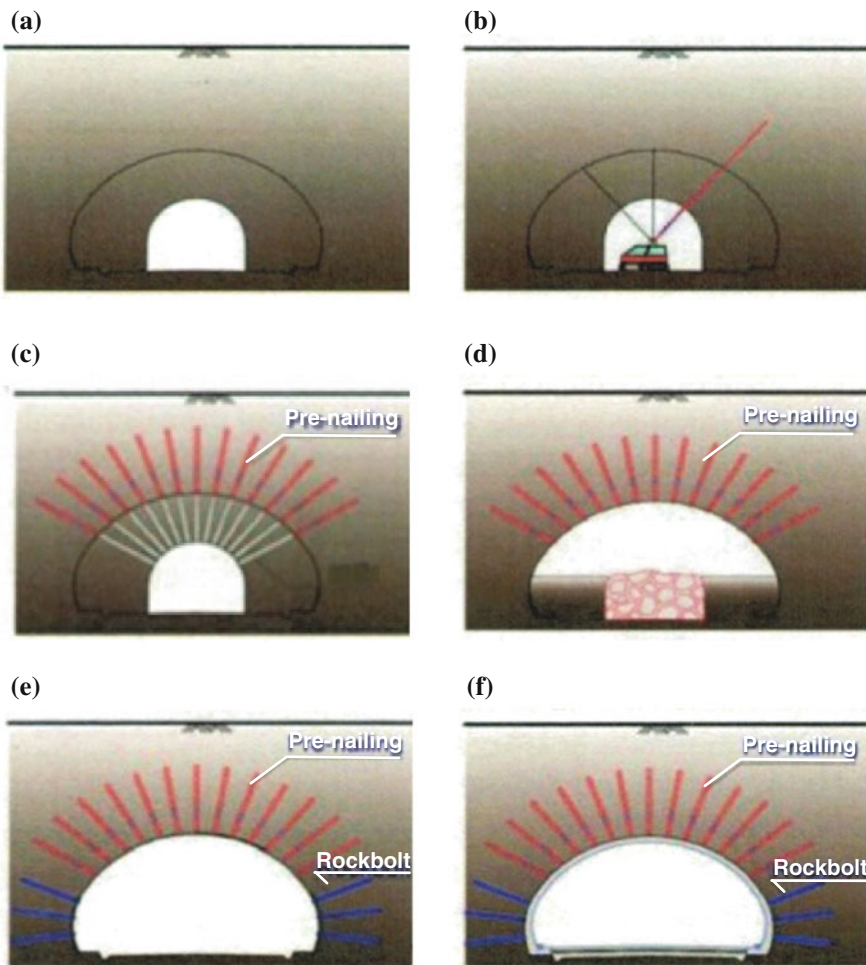


Fig. 4 Construction sequences of tunnel by using PSTM

installation of pre-nailing with grouting in the pilot tunnel as shown in Fig. 4b. Nails are normally installed as shown in Fig. 4c. After then, the pressurized grouting work is performed with using the enlarged packer to increase the grouting efficiency in the radial direction for the peripheral zone where the excavation will not be proceeded in Fig. 4d. The upper half part of main tunnel is excavated by using the ordinary excavation equipment for soil or adoption of blasting method for the rock. The nails are clamped with bearing plate which is connected on the steel rib. The lower half part of main tunnel is removed by using either the excavation equipment or rock blast method in Fig. 4e. The remaining part of un-nailing zone at the lower part of tunnel is reinforced with installation of rock bolts. In the final stage of PSTM as soon in Fig. 4f is combining pre-nailing with the steel rib and shotcrete

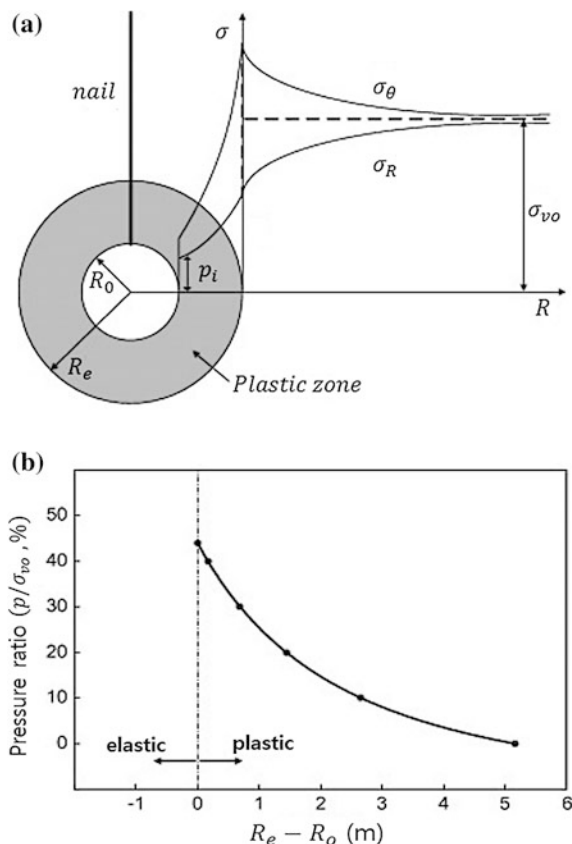
lining with the thickness of 25 cm. The shotcrete lining is applied in the first layer of 10 cm and the second layer of 15 cm.

According to the paper by Seo et al. (2014), the plastic range caused by the tunnel excavation can be evaluated using plastic deformation theory. The extent of the plastic range from the tunnel-excavation boundary, shown in Fig. 5a, can be evaluated using (Bray 1967)

$$R_e = R_o \left(\frac{\sigma_{vo}(1 - \sin \phi) - c(\cos \phi - \cot \phi)}{p + c \cot \phi} \right)^{\frac{1}{K_p-1}} \quad (1)$$

where R_o is the tunnel radius, σ_{vo} is the initial vertical stress, p is the support pressure, and K_p is the coefficient of passive earth pressure. Here, R_e is inversely proportional to the supporting pressure. The relationship between the supporting pressure and R_e is shown in Fig. 5b. Several supporting systems have been used to constrain the plastic deformation by using rock bolts with pressurized grouting, pipe roof method, and shotcrete with steel supporting element. Seo et al. (2014)

Fig. 5 Stresses around tunnel: **a** plastic range around tunnel, **b** relationship between support pressure and plastic range (Seo et al. 2014)



reported that the 40% of overburden pressure can be supported by the reinforcing elements by the results of numerical analysis for shallow tunnel.

3.2 Case Histories of PSTM

There are two types of reinforcement methods around tunnel in the weak weathered rock, that is, external method and internal method. The external method is normally used where the cover soil above the tunnel is weak and shallow, and there is no superstructure on the ground surface. Figure 6a shows the underground tunnel construction work with the existing road on the ground surface. The PSTM-external method would be suitable because the construction of tunnel would be possible without interruption of work due to not having an open-cut procedure. The weak weathered rock layer above the tunnel can be reinforced in advance by utilizing external soil nailing with pressurized grouting work from the ground surface to the tunnel section. Once the weak weathered rock is reinforced, a single large tunnel can be constructed instead of twin tunnels in one direction as shown in Fig. 6b. Adopting this method can reduce the construction cost and shorten the construction period. The safety of tunnel is also improved and reduced the maintenance cost of tunnel.

The tunnel named Daeri tunnel is located in the near Daegu City about 300 km south from Seoul in Korea. The purpose of Daeri tunnel is to access easily from Kyungbu Expressway to the industrial complex and save a travel time. The geological formations at the site consist of mostly weathered shale and partly granite. The upper layer of ground consists of weathered rock and has severe weak zone at the entrance and way out of tunnel. In this case, the PSTM was adopted with the use

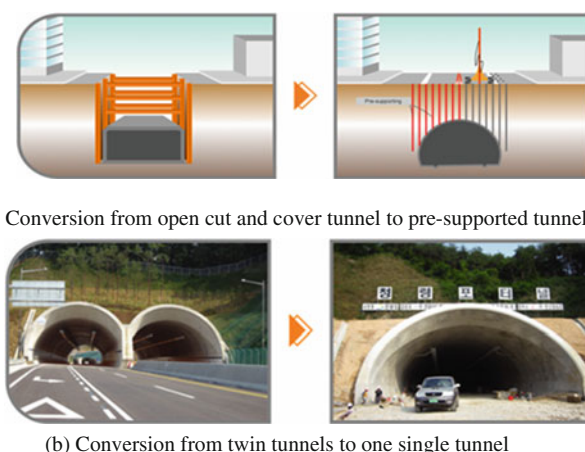


Fig. 6 Application of external reinforcement method for shallow tunnel construction

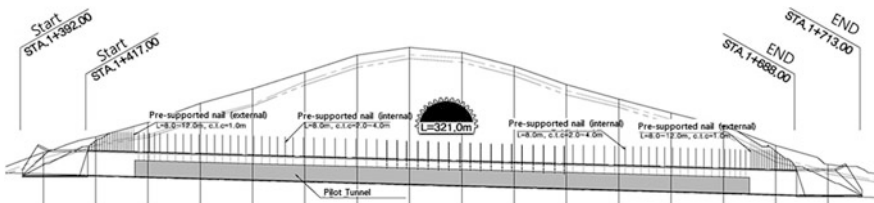


Fig. 7 Cross section of pre-supported tunnel method for Daeri tunnel



(a) External reinforcement method

(b) Internal reinforcement method

Fig. 8 Reinforcement method by using soil nailing with pressurized grouting

of external soil nailing reinforcement method at the inlet and outlet of tunnel. The internal pre-supported tunnel method using the pilot tunnel was adopted to facilitate the tunnel construction work. The cross section of Daeri tunnel is shown in Fig. 7. The view of external and internal reinforcement method with soil nailing and pressurized grouting works is shown in Fig. 8.

The construction of central part of tunnel was proceeded with the help of pilot tunnel. The soil nailing was installed from the pilot tunnel and pressurized grouting (Fig. 8) in the zone of non-excavated tunnel section as shown in Fig. 9. The section of tunnel can be enlarged by the blasting method.

Fig. 9 Large section of tunnel excavation with using pilot tunnel



4 Metro Tunnel Construction Work by TRcM

4.1 Site Condition and Construction Procedures of Tunnel

The number of population in Incheon Metropolitan city reaches more than 3 million people, and Incheon Metro line No. 1 which opened in October 1999 with the 31.1 km long was not enough to digest the demand of traffic volume. Therefore, a total of 29.2 km-long Incheon Metro line No. 2 was began from July 2009 and completed by June 2016. The civil engineering and construction expense was approximately 1.4 billion in USD. The Incheon Metro line No. 1 runs from northern part of Incheon to southern international business area called Songdo economic free zone, while the Incheon Metro line No. 2 runs from the northwestern part of Incheon to the middle-eastern part of Incheon region. The underground tunnel construction work for Incheon Metro line No. 2 was executed at the station No. 218 called Juan station where Seoul-Incheon Metro line No. 1 is situated on the ground level with the width of 60 m. The plan view and cross-sectional view are shown in Fig. 10. Most of the tunneling works were carried out by using NATM for the construction of Incheon Metro line No. 2, and sometimes pipe roof method was incorporated with NATM in the soft soil area at the upper layer of soil ground. The feasibility study for adoption of TRcM at this particular construction site was carried out by Shin (2011). The top view of Tubular Roof Construction Method (TRcM) cross section on railway Juan station is shown in Fig. 11. The soil profiles at the Juan station of Incheon Metro line No. 2 are tabulated in Table 1. From the visual observation at the construction site and based on the soil boring data in Table 1, the soil profiles consist of landfilled sand with the permeability of 9.0×10^{-4} cm/s, and clayey soil with the permeability of $3.0 \times 10^{-4} \sim 10^{-6}$ cm/s, consequently sandy layer ($k = 4 \sim 8.2 \times 10^{-4}$ cm/s), and weathered soil ($k = 3.0 \sim 5.1 \times 10^{-4}$ cm/s). This site has a particular problem to construct the metro station (Juan station) in underground which can facilitate the passengers to transfer from Incheon Metro line No. 2 to Seoul-Incheon Metro line No. 1 and vice versa. The soil layer in the upper 8 m has very soft to medium dense soil characteristics. The groundwater table is located at 2 m below the ground surface level.



Fig. 10 View of Incheon Metro line No. 2, 218 station (L: 1.271 km)



Fig. 11 The top view of Juan railway station for TRcM tunnel section

Table 1 Soil stratification with depth for Juan station

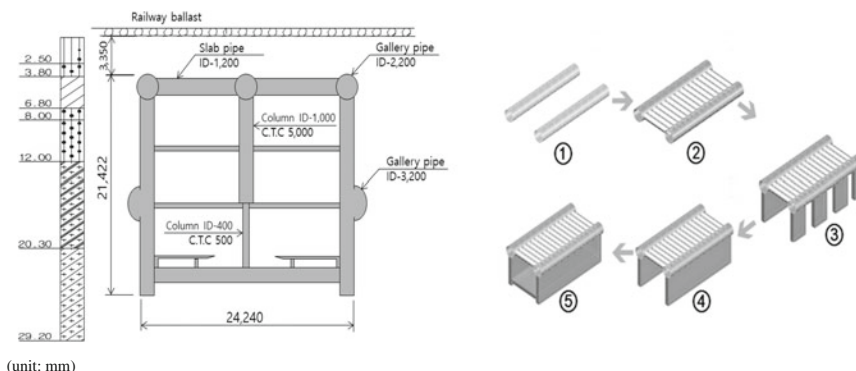
BH No.	Soil type	Depth (m)	SPT N value	Soil consistence
BH-6	Landfilled sand	0.0 ~ 5.1	7/30 ~ 12/30	Loose ~ medium dense
	Sedimentary clay	5.1 ~ 6.3	0/30 ~ 1/30	Very soft
	Sedimentary sand	6.3 ~ 7.5	13/30	Medium dense
	Weathered soil	7.5 ~ 16.4	9/30 ~ 50/14	Loose ~ very dense
	Weathered rock	16.4 ~ 19.8	50/9 ~ 50/4	Very dense
BH-7	Landfilled sand	0.0 ~ 2.5	2/30	Very loose
	Sedimentary clay	3.8 ~ 6.8	3/30 ~ 4/30	Soft
	Sedimentary sand	2.5 ~ 8.0	6/30 ~ 18/30	Loose ~ medium dense
	Weathered soil	8.0 ~ 12.0	26/30 ~ 50/24	Medium ~ very dense
	Weathered rock	12.0 ~ 20.3	50/10 ~ 50/2	Very dense
BH-8	Landfilled sand	0.0 ~ 2.0	3/30	Loose dense
	Sedimentary clay	2.0 ~ 6.7	2/30 ~ 4/30	Very soft ~ soft
	Sedimentary sand	6.7 ~ 7.6	50/7	Very dense
	Weathered rock	7.6 ~ 15.3	50/9 ~ 50/2	Very dense

The railway traffics between Seoul and Incheon passes through Juan station (seven lines and two platforms) are very heavy, and the thickness of top soil layer is only 3 m from roof top of Incheon Metro station line No. 2. The permeability of this layer is pretty high enough to draw down the groundwater table, and hence, the

railways on the ground level could be settled. The stability of the entire structural railroad bed could be a big problem.

The construction of tunnel by using TRcM technique gives several advantages such as railway traffic can be operated as usual during construction work of tunnel and the drawdown of groundwater table can also be controlled. Juan railway station has seven railways with two passenger platform which gives a trouble to inject a grout milk into the ground from the ground surface for prevention of groundwater drawdown. Because the metro line between Seoul and Incheon is Seoul–Incheon operating continuously with only 3 h interruption at night. The seepage water was prevented with the injection of grout milk at the top of inner gallery steel pipe during the press-in the large steel pipe. Fig. 12a shows the schematic diagram of cross section of Tubular Roof Construction Method (TRcM) tunnel method with soil profile. The construction consequence of Tubular Roof Construction Method (TRcM) is given in five steps as shown in Fig. 12b: ① Press-in the large steel gallery pipe by using a large hydraulic jack with reaction wall, ② Installed transversal slab with concrete filling and rebar, ③ Excavation soil in downward direction for trench with precast concrete wall, ④ Cast in concrete for continuous vertical wall formation, ⑤ Cast in concrete for bottom slab.

The roof structure of tunnel is formed with pressed-in steel pipe. The settlement and deformation of ground surface can be minimized due to the large steel casing pipe with help of grouting as well as rebar reinforcement. The excavation section for tunnel construction is minimized with the assurance of stability of tunnel. There is no vibration and also noise during construction of tunnel. The views of pressed-in the large steel gallery pipe and completion of column construction are shown in Fig. 13



(a) Cross-section of TRcM (unit: mm) (b) Construction procedures of TRcM

Fig. 12 Schematic design concept of tunnel construction by TRcM



(a) Pressed-in steel pipe

(b) Completed column

Fig. 13 Views of pressed-in steel gallery pipe and column construction

4.2 Field Monitoring of TRcM Construction Site

Various instruments at the field as shown in Fig. 14 were installed for measurement of ground settlement, groundwater level, settlement at ballast, inclination of temporary wall and existing building, and cracking on the platform and adjacent structures. The various fore-mentioned instruments and the location of each device installation and the content of measurement are described in Table 2 (Hanyang Construction Co., Ltd. 2014).

The in-ground inclinometer can measure the lateral deformation of ground along the deep excavated and pressed-in steel casing sections. The observation of ground water monitoring well can measure the fluctuation of ground water table inside the ground during the excavation and pressed-insteel casing for tunnel construction. The settlement plate of rail can detect the variations of rail deflection during the train in operation. The differential settlement of rail and also degree of settlement of rail can detect and hence the safety of train operation can be identified. The field measurements of rail and ballast settlement, and in-ground inclinometer are shown in Fig. 15a and b, respectively.

Table 2 Various instruments for field monitoring at TRcM construction site

Type of instrument	Location of installation	Number of installation	Symbol
In-ground inclinometer	Tunnel starting and ending points	5	Ⓐ
Groundwater level indicator	Tunnel starting and ending points	2	Ⓑ
Ballast settlement gage	Reinforced rails bound for Seoul and Incheon	46	Ⓒ
Ground settlement plate	Platform at tunnel starting and ending points	6	Ⓓ
Structural inclinometer	Platform and adjacent structures	6	Ⓔ
Crack gage	Platform and adjacent structures	18	Ⓕ

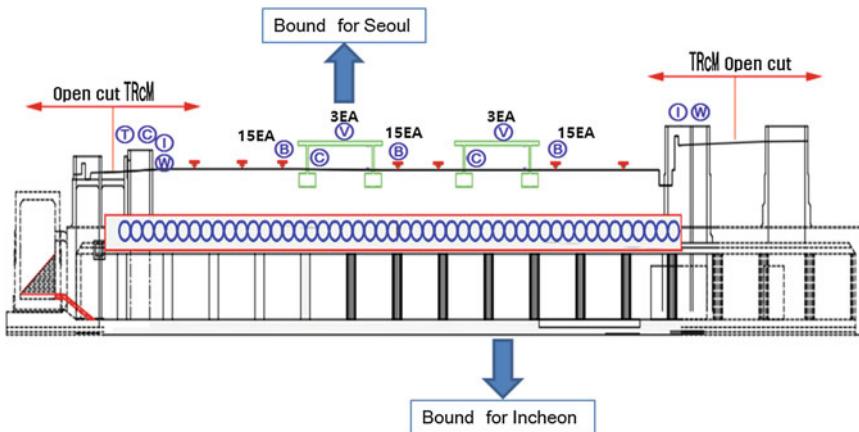


Fig. 14 Locations of various field measurements for TRcM tunnel section

The field measurement for TRcM construction section was conducted from December 2010 to October 31, 2014, and the excavation depth was reached at 26 m below ground level. The settlements on both rail and ballast are the most sensitive issue and monitored 24 h by means of the automatic instruments as well as visual observation by the safety guard people. Because Juan railway station is one of busy railway stations among Seoul–Incheon Metro line No.1, the thickness of top soil layer is only 3 m with soft and loose state soil, and sudden collapse of rail ballast or sinkhole could be happened due to excavation of soil or sudden drawdown of groundwater level during tunnel construction work. The rail and ballast are reinforced by using a steel beam along the railway in the section of TRcM construction area to cope with the local settlement. Totally, 46 ballast settlements were measured, and the final accumulated results of field measurement range from -2.424 to 1.000 mm by October 31, 2014. The control limit of ballast settlement is 20.2 mm which is based on the settlement limit of railroad bed as 7 mm per 10 m. The results of field measured settlement at three different locations of ballast from October 20, 2010 to November 8, 2010 are shown in Fig. 16. The settlement result shown in Fig. 16a, b is the location in the left side and right side of platform for the bound for Seoul. The settlement results shown in Fig. 16c are the location in the right side of platform for bound for Incheon. The soil excavation for TRcM tunnel construction was executed from the right side of the open-cut site, and hence, the settlement levels in Fig. 16c are slightly higher than those of other locations. The results of field measurement are far lower than that of the limited settlement criteria of 20.2 mm (Fig. 16).

A total of five in-ground inclinometers were installed at the tunnel starting point as well as tunnel ending point. The find excavation depth for TRcM tunnel construction site was 26 m below ground level while the installation depth of inclinometer was about 30 m. The result of lateral ground displacement by inclinometer located in Station 217E2 TRcM tunnel section are shown in Fig. 17 ($\delta_{\max} = 18.38$ mm). Some

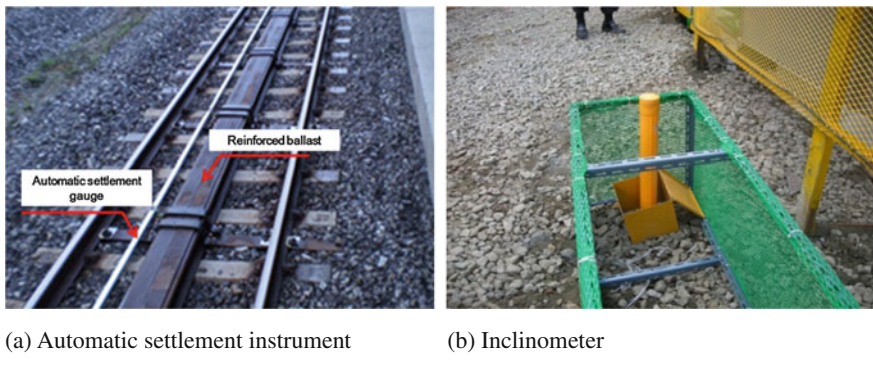


Fig. 15 Views of reinforced ballast with steel beam and field measurement

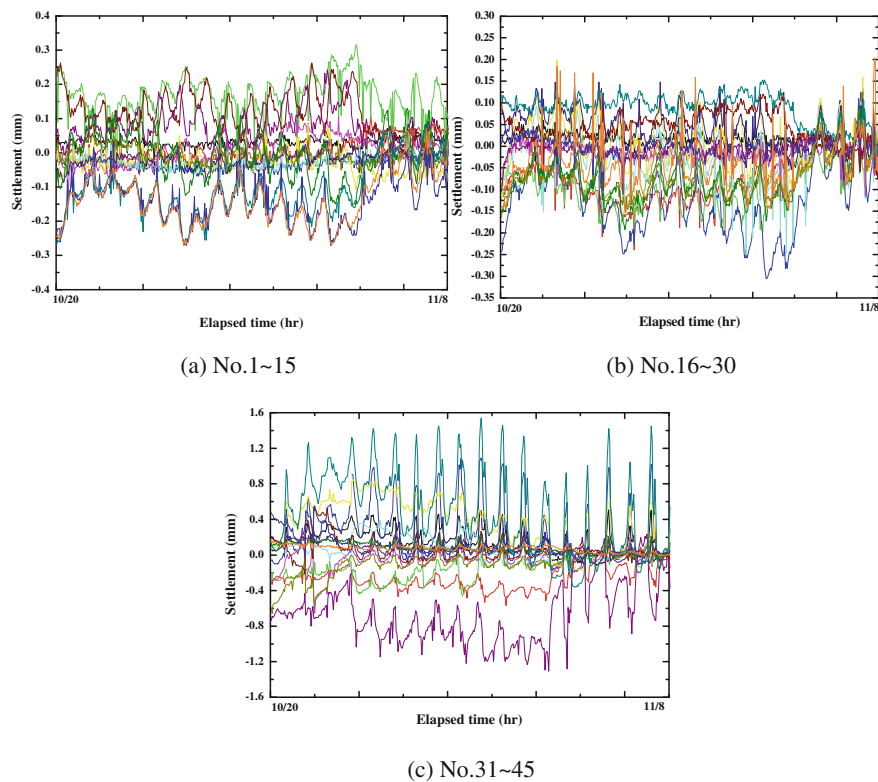
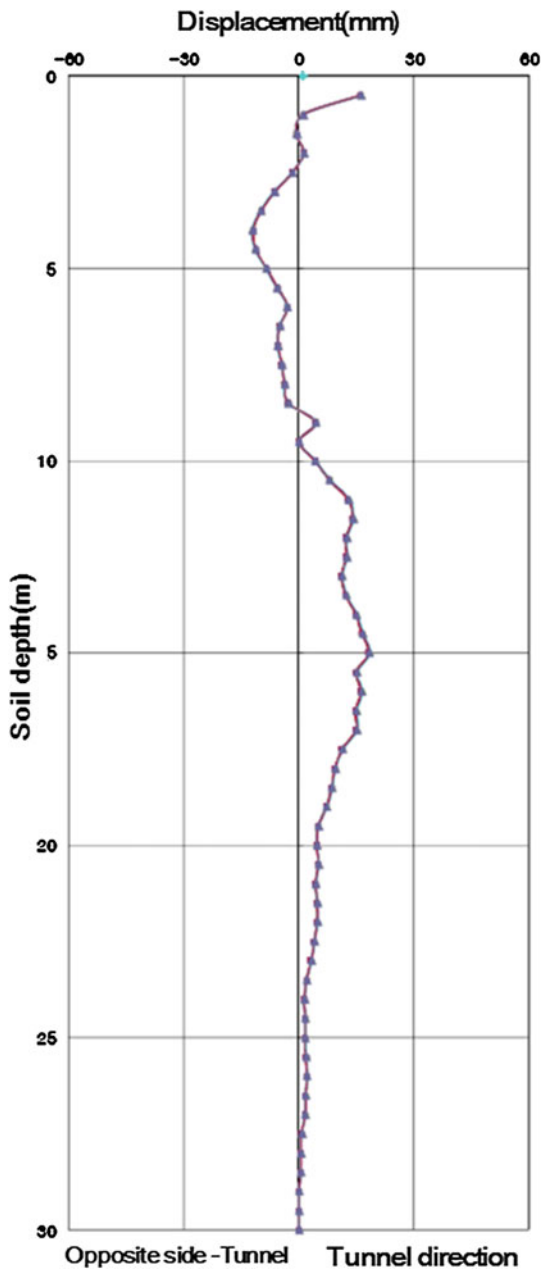


Fig. 16 Results of field settlement for ballast in railway

Fig. 17 Results of lateral ground displacement by inclinometer



variations of lateral displacements range from -12.03 to 21.23 mm. The lateral displacement of ground for rest of three locations (Station 218E1) shows very small magnitude of displacement ($\delta = -1.6 \sim 1.59$ mm). The maximum accumulated lateral displacement of ground from five different inclinometers is approximately $16.46 \sim 21.23$ mm which is far below than the first control limit of 52 mm.

The ground monitoring well was also installed at the similar location of in-ground inclinometer. The final groundwater levels were located at 21.46 and 21.51 m below ground level. The groundwater levels had been draw down to 11.79 and 11.84 m from the initial groundwater level. The groundwater level was rapidly drawn down in the periods from April 2011 to August 2011 due to extensive excavation of soft ground for the open-cut to create a space for the installation of TRcM construction equipment. Since then, the groundwater level shown in Fig. 18a remained as the steady state level. Comparison with the field measurement results of inclinometer, settlements at the ground surface and rail ballast, and cracking on the structures, the fluctuation of groundwater level was not much influenced on the deformation of TRcM construction section.

The ground surface settlement levels shown in Fig. 18b are the settlement measured at the railroad bed bound for Incheon. The settlement levels for three different locations are very similar to each other. The magnitude of settlement at the ground surface ranges from 15 to 19 mm which is far below than the first limit criteria of 32 mm.

The inclination of structures shown in Fig. 18c was measured on the platform bound for Seoul and Incheon. Because the concrete structures of platform adjacent to the railway can be more influenced due to train operation and tunnel excavation. The inclination of adjacent structures ranges approximately from -0.038 to 0.042 mm.

Totally, 18 structural crack gages were installed, and the magnitude of cracks ranges from -0.16 to 1.38 mm. Some places have reached the control limit. However, there is no place to increase the magnitude of crack continuously, and hence, it is reached as a steady state. The field measurement of structural crack is shown in Fig. 19a.

The deflection of TRcM structure was monitored for 18 sections and resulted from -4.0 to 1 mm which is much lower value than the control limit of 13.00 mm. Field measurement of structural deflection for TRcM is shown in Fig. 19b.

The deflection of beam at TRcM structure was monitored for 12 places and resulted from -0.0318 to 0.00667 mm. It is far below than that of limited value of 0.1 mm.

The rest of beams show very minimum deflection. The large magnitude of beam deflection at TRcM is shown in Fig. 19c.

Comprehensive field monitoring works were carried out to make sure the safety of TRcM tunnel construction site and maintain the normal operation of Seoul–Incheon Metro line No. 1. The results of field measurement for various instruments are tabulated in Table 3 and turned out that all measured values are fallen in control limits.

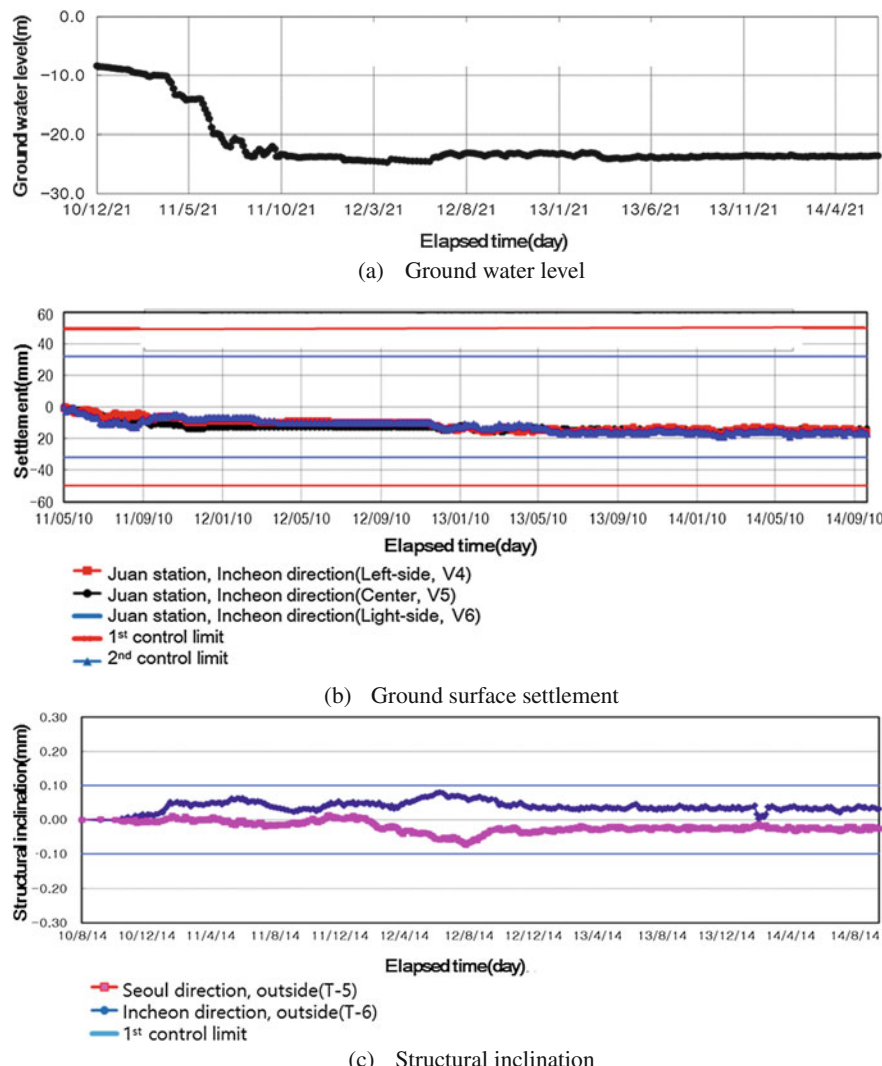


Fig. 18 Field monitoring results for groundwater level ground settlement and structural inclination

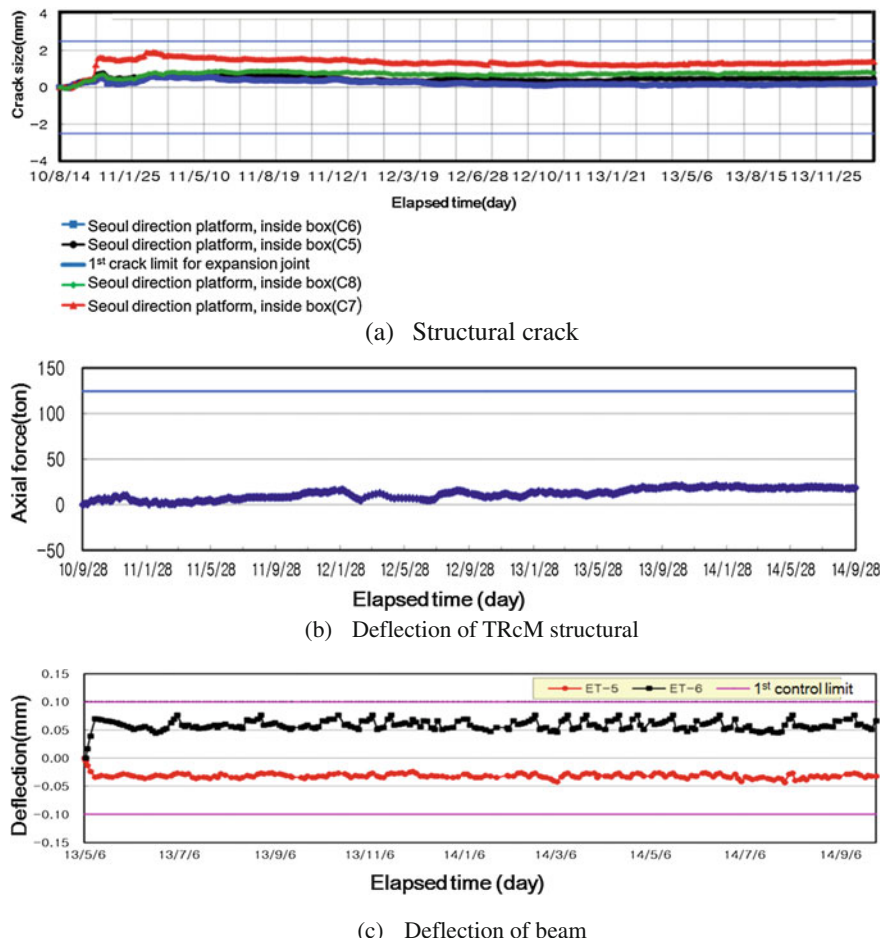


Fig. 19 Field monitoring results for structural cracking size, deflection of TRcM structure, and beam at TRcM

Table 3 Results of field measurement for various instruments

Type of instrument	Final value	Control limit
In-ground inclinometer (5 EA)	16.46 ~ 21.23 (mm)	52 mm ($\frac{1}{500} \times 26$ m)
Groundwater level indicator (2 EA)	-11.79 ~ 11.84 (m)	-
Ground settlement gage (6 EA)	-15 ~ 19 (mm)	32 mm
Ballast settlement gauge (46 EA)	-2.424 ~ 1.00 (mm)	20.1 mm
Structural inclinometer (6 EA)	-0.038 ~ 0.042 (mm)	0.1 mm
Crack gage (18 EA)	-0.16 ~ 1.38 (mm)	0.2 mm
Structural deflection of TRcM and inside of casing pipe (18 EA)	-4.0 ~ 4.0 (mm)	13.0 mm
Beam deflection TRcM (12 EA)	-0.0318 ~ 0.0667 (mm)	0.1 mm

5 Concluding Remarks

The stability of tunnel is the most important matter in the construction of tunnel in either weak rock or soft ground. The permanent support system during the construction of tunnel has been evolved from rock bolt to modern supporting systems with combination of soil nailing and pressurized grouting, and as well as with pipe roof structures. The methodology of tunnel construction has been developed such as NATM, PSTM, and TRcM.

The NATM technique has long been used because it is based on simple theory and easy to use by utilizing rock bolt or steel pipe grouting support system on the excavated rock face after blasting of rock.

The pre-supported tunneling method (PSTM) is very efficient method for both the weak rock and the tunnel has a shallow depth of top soil. It can be also very useful technology to construct the single large tunnel with the excavation of pilot tunnel. The time required to construct the large-scale tunnel is fast, and hence, it is cost-effective tunneling method.

The construction of tunnel by using Tubular Roof Construction Method (TRcM) can be done in the soft ground area, and also the top soil layer is relatively shallow. The construction procedures as well as field monitoring works with various measurement instruments are described with respect to the careful control of limited values. It is a useful technology to construct long-span tunnel ($L = 60$ m) in the soft ground under the heavy traffic load by the railways.

References

Bray, J. W. (2001). A study of jointed and fractured rock, II. Theory of limiting equilibrium. *Rock Mechanics and Engineering Geology*, 5, 197–216.

Deere, D. U., & Miller, R. P. (1996). Engineering classification and index properties for intact rock. In: Air Force Weapons Laboratory Technical Report, AFWL-TR-65-116, Kirtland Base, New Mexico, pp. 300.

Hanyang Construction CO., Ltd. (2014). Field Monitoring Report (August, September 2014) for Incheon Metro Line No. 2 construction site 210, 218 Station.

Hoek, E. (2001). Big tunnels in bad rock. *ASCE Journal of Geotechnical and Geoenvironmental Engineering*, 127(9), 726–740.

Seo, D. H., Lee, T. H., Kim, D. R., & Shin, J. H. (2014). Pre-nailing support for shallow soft-ground tunneling. *Tunneling and Underground Space Technology*, 42, 216–226, Elsevier.

Shin, E. C. (2011). Tunnel and temporary support system during Incheon Metro Line No. 2 Construction sites 209 and 210.

Terzaghi, K. (1946). Rock defects and loads on tunnel supports in R.V. proctor and T.L. White, Rock Tunneling with steel Supports, Commercial Shearing and Stamping Co., Youngstown, Ohio, USA.

Subsurface Investigation—Integrated and Modern Approach

P. Anbazhagan

Abstract Subsurface exploration is an indispensable component of any project and requires understanding of the engineering and geologic properties of the soil and rock strata and groundwater conditions that could be useful for the new design project and evaluate performance of the existing project for the retrofitting. Conventional way of drilling borehole, logging subsurface layer information with Standard Penetration Test N values measurement, and arriving at soil properties through laboratory experiments are useful for simple project up to some extent, but may not be always effective for subsurface investigation for unusual cases. This article presents problem associated with conventional practice of surface exploration in unusual cases in a modern geotechnical world. It also explains the integrated and modern approach that has been adopted to estimate required properties for the design and performance assessment by using advanced subsurface exploration methods available at Indian Institute of Science, Bangalore.

Keywords Subsurface exploration · Borehole · Geophysical investigation · MASW · Ground-penetrating radar

1 Introduction

Preliminary geophysical investigation of subsurface strata is important prior to tendering or execution of project and preparation of project plan of any construction. Such investigations help in proper planning, cost estimation, and time-bound project execution. The data from the investigation helps in identifying the types of geologic materials with engineering properties, their porosity, thickness, weathering condition for the design and planning of the project. These investigations predominantly help to plan excavation, to find out the volume of excavation material,

P. Anbazhagan (✉)

Department of Civil Engineering, Indian Institute of Science,
Bangalore 560012, India

e-mail: anbazhagan@iisc.ac.in; anbazhagan2005@gmail.com

to find out the type of material that needs to be excavated, properties for the foundation design, in situ dynamic properties for the seismic analysis, and also to estimate and control project cost. Proper subsurface exploration data helps to prepare Program Evaluation Review Technique (PERT) chart for project management and timely completion of the project. Inadequate, imprecise survey information can substantially impact the accuracy of estimation or bid analogous to a certain excavation project (Stump 2004). Also, such unexpected costs can weaken the financial viability of the contractor's business. Several examples can be quoted for delay and cost escalation due to improper/wrong subsurface explorations.

Even though several advancements have taken place in geophysical testing useful for subsurface investigation and to solve unusual cases, these techniques have poor reputation and have not been well accepted in geotechnical engineering due to very poor planning by engineers, ignorance of the techniques, and over-optimism by geophysicists. This paper presents selected study of integrated subsurface investigation using limited geotechnical and extensive geophysical investigation to solve some of the geotechnical problems. Further, modern method of testing for subsurface exploration methods, i.e., Standard Penetration Test (SPT) with hammer energy measurement for liquefaction assessment and Multichannel Analysis of Surface Wave (MASW) for the deep in situ shear wave velocity measurement in deep deposits, is discussed. In the integrated subsurface investigation, detailed ground-penetrating radar (GPR) survey with few SPT and MASW testing are carried out.

2 Geotechnical and Geophysical Methods

Several geotechnical and geophysical methods are useful for modern subsurface investigation. In this study, widely available, simple, and low-cost geotechnical and geophysical methods are used. A brief summary of geotechnical and geophysical methods used in the study are presented.

The Standard Penetration Test (SPT) is one of the oldest, most popular, and commonly used in situ tests for subsurface exploration in soil mechanics and foundation engineering because the equipments and test procedures are simple. SPT is performed by drilling out a borehole and driving a standard "split spoon" sampler using repeated blows of a 63.5-kg hammer falling through 762 mm. The hammer is operated at the top of the borehole. It is connected to the split spoon sampler by rods. The split spoon sampler is lowered to the bottom of the borehole. It is then driven by hammer blows to a total depth of 450 mm in three intervals of 150 mm for which the number of blows is counted. The penetration resistance (N) is the number of blows required to drive the split spoon for the last 300 mm of penetration. Since the soil is considered to have been disturbed during the first 150 mm penetration, the penetration resistance for this depth is disregarded. SPT N values are useful for seismic site characterization, site response, and liquefaction studies toward seismic microzonation. In most cases, the specific site response analysis, shear wave velocity, and

shear modulus (G_{\max}) of layers are estimated using relationships based on the SPT N values (Anbazhagan et al. 2012a). With time, many researchers have contributed to standardize and make SPT a more efficient ground exploration test. Various corrections have been proposed for getting corrected SPT N value of any site. Among all the corrections, energy correction is the most important. Measurement of hammer energy during SPT test is part of SPT testing in most of the western countries (ASTM D4633 2016; Anbazhagan et al. 2016), and there is a separate ASTM code (ASTM D6066 2011) to arrive at normalized N values for estimation of liquefaction potential. However, there is no such standard in the Indian code of practice for SPT testing and liquefaction assessment. Again, different code prescribes different energy correction to be applied even for same hammer and lift–release mechanism. This leads to non-uniform results. Energy correction is very important for getting true SPT N value of any site. The maximum theoretical energy transferred is 473.4 J. As the safety hammer energy widely used in the USA has approximate 60% energy transfer, to keep the earlier data and correlations useful and valid, 60% energy transfer was assumed as standard. But multiple codes for practice and authors have reported different energy values even for the same hammer and drop mechanism. This is mostly due to different types of rods, anvil, etc., used; local site conditions; efficiency and skill of operator, etc. Hence, it becomes impractical to rely on a single value provided by an author or code to get the true value of energy correction (Howie et al. 2003). In order to measure hammer energy in the SPT setup, a simple and cost-effective SPT-Hammer Energy Measuring Apparatus (HEMA) was developed by the Department of Civil Engineering, IISc, Bangalore. SPT-HEMA is capable of recording energy at below the anvil and above the sampler tube. Figure 1 shows typical instrument rod and schematic field setup. In the instrumented rod, the transducer records the stress variation while the accelerometer gives acceleration. These signals are received by a microcontroller which filters, amplifies the signals, and processes them via analog-to-digital convertor. A program on LabVIEW platform has been written to get velocity profile using acceleration data. The software uses Force-Velocity (FV) Method to integrate the product of force and velocity with respect to time as prescribed in ASTM D4633 to give final energy output.

The surface wave methods adopt these three basic steps: (1) Data acquisition, (2) Dispersion analysis, and (3) Generating the layered earth model considering shear and compressional wave velocities, thickness of layer, density and poisson's ratio, etc. Initially, surface wave methods were based on the fundamental mode (M_0) of wave and all other types of waves (higher modes, body waves, etc.) were ignored. Later, this method was evolved by Matthews et al. (1996) and called as Continuous Surface Wave (CSW) method. Investigators at the University of Texas, Austin, introduced a two receiver approach in the 80s, which was based on the Fast Fourier Transform analysis of phase spectra of surface waves generated by an impulsive source like the sledge hammer. Surface wave method then became a widely used approach among geotechnical engineers and researchers.

Two receiver surface techniques were called as Spectral Analysis of Surface Waves (SASW) (Heisey et al. 1982). The complete efficiency of the method was

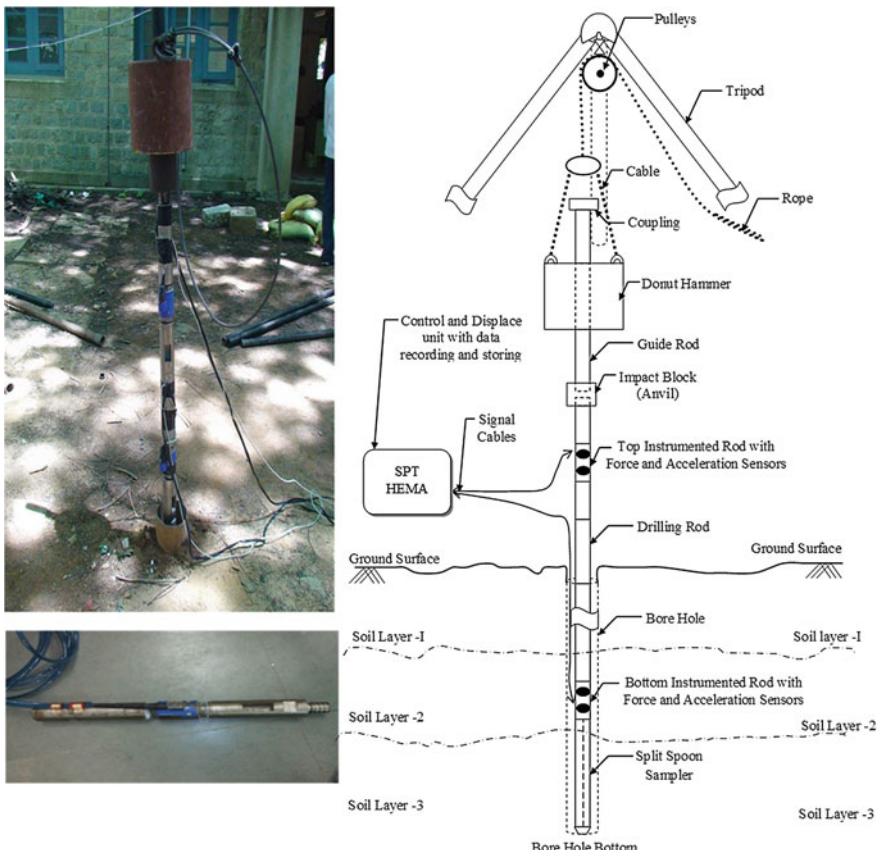


Fig. 1 Typical instrument rod and schematic field setup of SPT-Hammer Energy Measuring Apparatus (HEMA)

increased by: (1) Generating multi-frequency (not mono-frequency) waves simultaneously upon impact from the seismic source and (2) Separation involved in the subsequent data processing by using FFT. It was vastly superior compared to CSW method. This method termed as “MASW” (Multichannel Analysis of Surface Waves) by Park et al. (1999) in their publication on Geophysics became popular thereafter. The project actually started in the mid-90s at the Kansas Geological Survey (KGS) by geophysicists who had been utilizing the seismic reflection method in the oil industry to image the interior of the earth for depths of several kilometers called the high-resolution reflection method; it was used to image very shallow depths of engineering interest. MASW method involves the measurement and analysis of the generated seismic surface waves, the result of which is the shear wave velocity profile for the surveyed area. As shear wave velocity is one of the elastic properties which is comparable with Young’s Modulus, it can be used as a direct indicator of ground stiffness and consequently be used to derive the

load-bearing capacity. In this study, 24 channel Geode MASW systems with 4.5 and 2 Hz geophone cable of measuring shear wave velocity up to depth of 500 m by combining passive and active survey are used.

Ground Penetration Radar, also commonly known as: electromagnetic reflection (EMR); subsurface interface radar (SIR); geo-radar; subsurface penetrating radar; and soil radar, is an electromagnetic reflection method in which an electromagnetic signal is emitted via an emitter in the form of a built-in antenna into the structure under inspection (Fig. 2). As the properties of the materials vary in the substructures, the emitted waves undergo reflection. The receiver inbuilt in the antenna receives these reflected waves. These waves are recorded in the control unit, displayed on the monitor, and analyzed in the computer. Frequency of emitted and received electromagnetic waves plays an important role in resolution and depth of information. Using high-frequency antennas results in high-resolution data, but reduces the depth of penetration; whereas, low-frequency antennas provide greater depth of penetration at the expense of lower resolution. Dielectric property being one of the most crucial parameters in non-destructive techniques can be assessed from the received EM waves. Dielectric properties are usually influenced by the volumetric properties of the subsurface layers. The electric permittivity (dielectric constant) “ ϵ ” and the electric conductivity “ σ ” are petro-physical parameters, which determine the reflectivity of layer boundaries and penetration depth. GPR is a well-established non-destructive method for investigating the internal composition of many naturally occurring materials such as rocks, earth and gravel, and man-made materials like concrete, brick and asphalt.

GPR is being used to study the presence, depth, and lateral extent of each subsurface soil layers and is further used to classify soils (Anbazhagan, Amarajeevi, and Bharatha 2012b). Five different frequency antennas capable of detecting pen-size object to 20-m-size object below ground level and also possible to

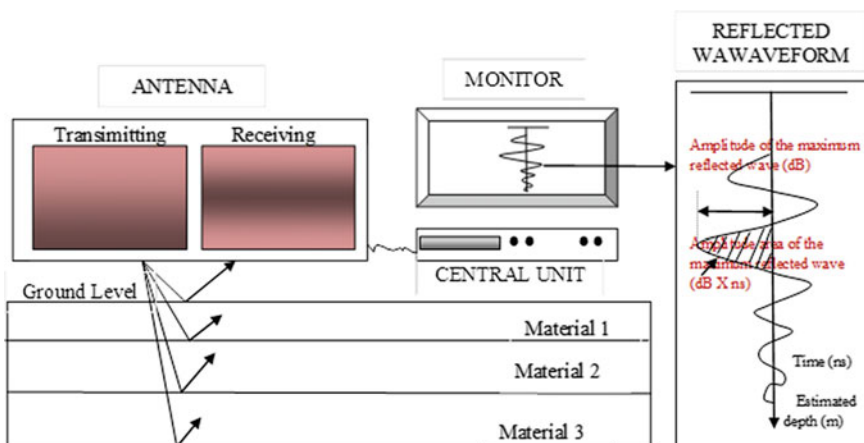


Fig. 2 Schematic ground-penetrating radar principle

investigate up to 50 m are used in this study. Most of the geotechnical investigations SPT, MASW, and GPR testing are being used independently for subsurface explorations and forensic geotechnical investigations. But limited studies were carried out by integrating these tests to obtain the subsurface data for the performance evaluation of geotechnical structures.

3 Integrated and Modern Subsurface Investigation

Subsurface investigation plays an important role by providing suitable data for design and performance assessment of geotechnical structures. The subsurface investigations can be carried out by geological, geophysical, and geotechnical methods. Many geophysical methods are engaged in the forensic investigation of geotechnical failures. In this study, seismic method of MASW, electromagnetic method of GPR, and limited drilling with SPT N measurement have been used to investigate the heterogeneous compaction, undulation subsurface, and karstic features in lateritic soil. Seismic methods are used to estimate the shear wave velocity of the subsurface layers and thereby Young's modulus and shear modulus. In this study, GPR has been used to identify the subsurface condition of the soil, thickness and homogeneity of the layers. The SPT results are used to get subsurface material type and depth, to compare with MASW result and to get in situ density.

Local site-specific soil conditions have great role in amplification and liquefaction due to an earthquake. Conventional MASW active survey with 4.5 Hz geophone survey is capable of shear wave velocity up to 50 m. In this study, modern approach of combined active and passive MASW survey with low-frequency geophone 2 Hz has been carried out to measure shear wave velocity more than 400 m in the deep soil deposit of Indo-Gangetic Basin (IGB). Shear wave velocity measured in this study is cross-correlated with drilled borehole up to depth of 350 m. Effect of hammer energy on liquefaction assessment and newly developed modern equipment SPT Hammer Energy Measurement Apparatus (SPT-HEMA) for the measurement delivered hammer energy below anvil and above split spoon sampler is also presented.

4 Subsurface Profiling for Excavation

Information about subsurface soil and rock layer are precisely required for proper planning and execution of excavation work in shallow bedrock sites, where variation of rock depth or boulder is found in smaller distance. Tender estimation prepared by conventional drilling was not able to identify variation of rock layers, and awarded work was stalled due to the presence of hard rock layer during excavation, which was not part of tender item (Anbazhagan et al. 2017a). Client approached and requested for quantity of excavation with possible cost and time

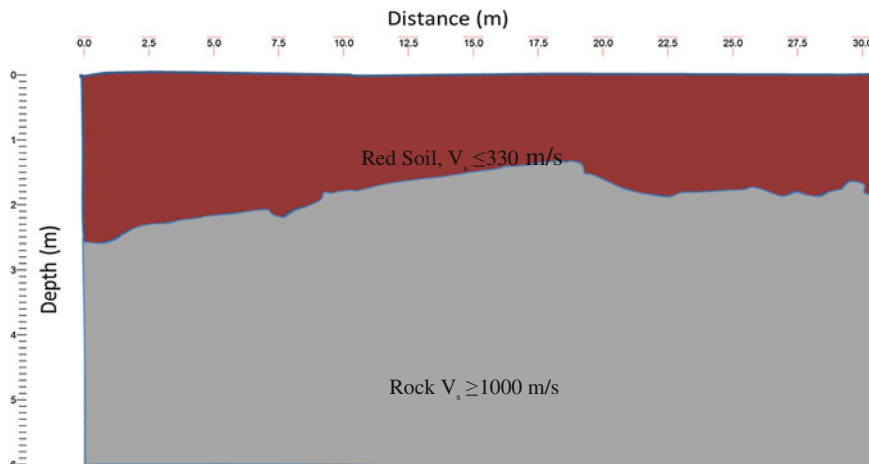


Fig. 3 Integrated subsurface profile for typical alignment for cost estimation

due to huge cost (about 50 lakhs) escalation demanded by contractor. MASW and GPR surveys were carried out in the study area and results were validated with excavated portion. Shear wave velocity from MASW was used to find out material stiffness, and GPR data was used to map variation of layer, i.e., thickness. Figure 3 shows integrated subsurface profile of typical alignment. A volume of soil and rock to be excavated was calculated and compared with the old estimated cost. The cost of excavation was obtained from integrated subsurface profile and compared with the tendered or estimated cost. In comparison (Table 1), it was found that the actual cost of excavation exceeded the estimated cost by 317.09%, which is more than twice the original estimated cost. From the results, it can be concluded that performing integrated subsurface prior to planning or executing a project provides knowledge of the geophysical or geotechnical properties of the site area which helps in estimating the exact cost of excavation, planning the orientation of the alignment, and efficient use of time, manpower, and machine; also accidental damage to subsurface utilities as well as excavation machinery can be avoided. More accurate volume calculation can be achieved by performing GPR surveys in the grid patterns for 3D sections (Anbazhagan et al. 2017a).

Table 1 Calculation of percentage escalation of actual cost from the estimated cost

	Earthwork (cum)	Rate (INR)	Rock (cum)	Rate (INR)	Total (INR)
Old estimated	405	245.00	0	—	99,225.00
In this study	151.875	245.00	253.125	1096.00	314,634.00

5 Floor Slab Settlement Due to Heavy Rain

Non-uniform settlement of reinforced cement concrete with polished stone floor slab and also rotation and tilting of machine foundations in 5000 m² industrial building were investigated using SPT and GPR survey. Site visit showed that heavy rain caused excessive settlement and tilting in a 95% finished building, roofing was completed, but rainwater gutter was under construction. Factory was constructed in undulating ground, and soil filling varies from 1 to 8 m, and most of the settlement tilting was noticed in soil fill area. GPR study has been carried out in systematic manner, and radargram showed homogenous and heterogeneous waveform due to subsurface. Typical GPR radargram showing uniform and non-uniform GPR waveform is shown in Fig. 4. In order to understand waveform due to change in soil moisture and density of site-specific soil, a model study has been performed. The study found that increase in moisture content reduces GPR wave amplitude and increases bulk density and dielectric constant. Uniform good reflected wave was observed in the uniform section, and scattered and non-uniform wave was observed in heterogeneous section. Figure 5 shows GPR model results with density and moisture content. GPR results are confirmed by measuring SPT N values in the heterogeneous location. Low SPT N value, i.e., <15 , was observed in heterogeneous section and higher SPT value, i.e., >18 , was observed in the uniform section. Integrated approach helped to complete investigation of larger area in short time with mapping of gap between floor slab and foundation with settled soil layer. Further area of heterogeneous zone due to settlement also arrived from GPR study. This investigation helped for effective repair and retrofits the distressed sections.

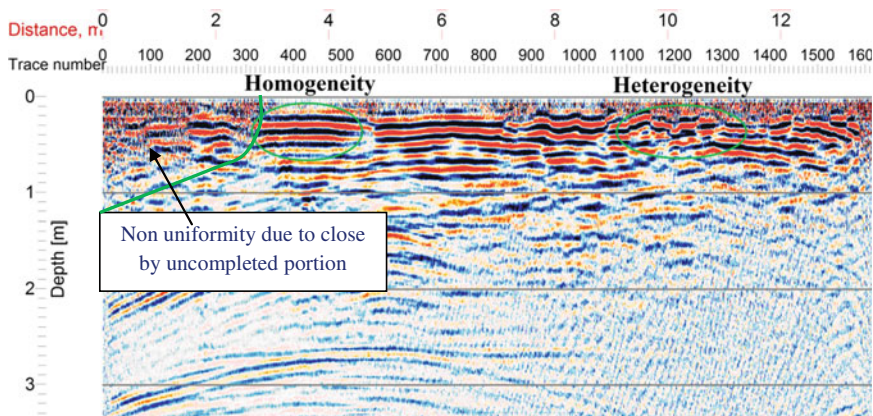


Fig. 4 Typical GPR radargram of the subsurface with varying moisture and density

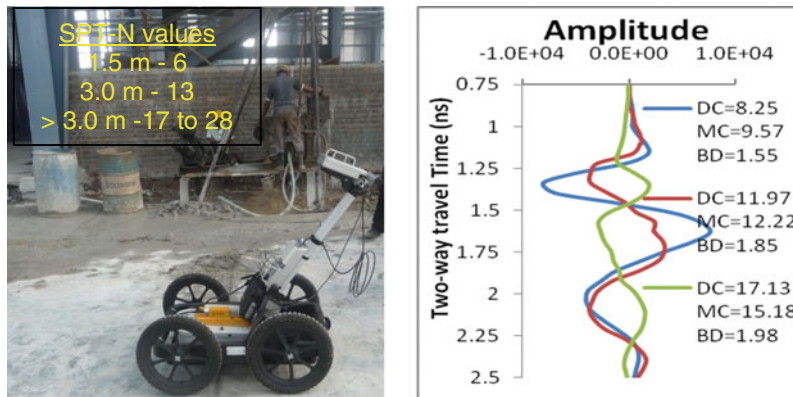


Fig. 5 Site photo and GPR wave trace for the different moisture content and density

6 Identification of Karstic Features in Lateritic Soil

Lateritic soils are widely spread across the southern and central parts of India. Lateritic formations usually have soft sediments entrapped between the hard-to-medium-soft lateritic rock, which are leached due to the ingress of water during rainy seasons creating hollow sections or cavities which span over large lengths.

Laterites are highly heterogeneous and prone to cavitation due to its weathering process; a sound knowledge of the subsurface condition is required before starting any construction. The integrated geotechnical and geophysical investigation has been carried out to identify the subsurface air cavities over large areas in mega project. Geophysical survey GPR and MASW techniques are used to identify the heterogeneities in lateritic soils and localized cavities. Initial GPR survey is carried out across the complete area at specific interval spacing and probable heterogeneous locations are identified. Detailed GPR and MASW surveys are carried out at probable stretches in close intervals. The anomalies in the GPR radargram are identified by visual inspection and trace amplitude approach. The results of the radar survey are cross-checked by generating 2D shear wave velocity profile adopting MASW. Typical radargram with trace amplitude and 2D shear wave velocity contrast due to cavity is shown in Fig. 6. This study shows that application of integrated geophysical techniques using GPR and MASW methods provides more promising results in comparison to only borehole methods for identification of cavities in highly heterogeneous soil type like laterite over large area in mega project (Anbazhagan et al. 2017b).

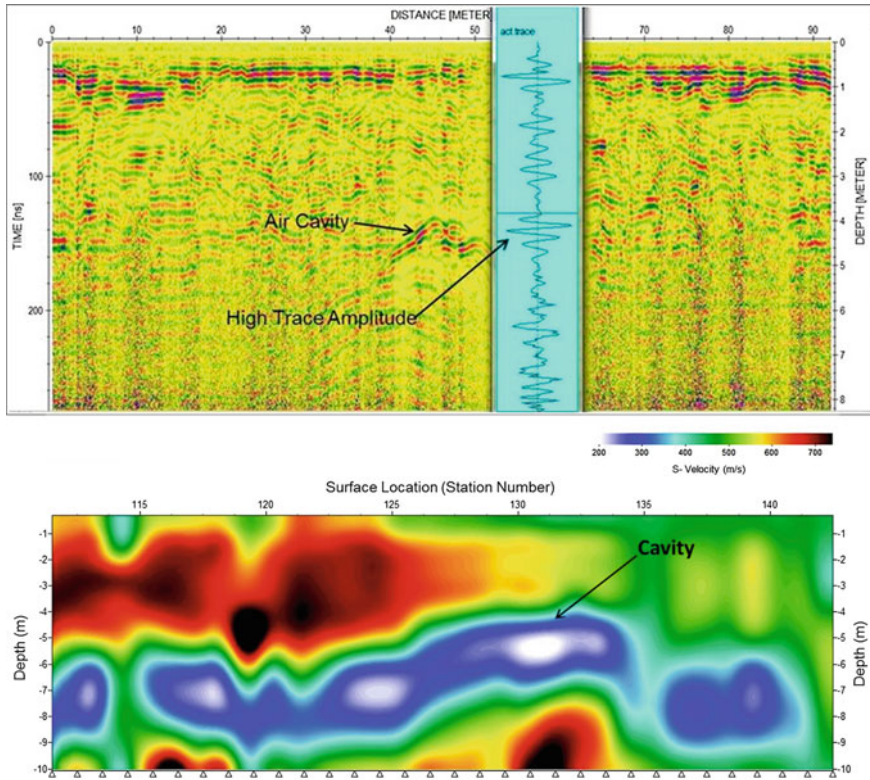


Fig. 6 Typical radargram showing cavity and confirmed 2D V_s profile

7 Study of Indo-Gangetic Basin Soil by Modern Approach

The high level of seismicity associated with the Himalayan tectonic province may cause huge site amplification and liquefaction in the loose Indo-Gangetic Basin (IGB) deep alluvial deposits. Few studies were carried out to characterize the IGB soil up to shallow depth, but a very limited attempt has been made to measure the dynamic properties of the deep soil column. Combined active and passive MASW using low-frequency geophones has been carried out in IGB, and shear wave velocity profile has been measured up to 500 m depth by this modern approach. V_s values up to 50 m were measured in the active survey. Low-frequency waves are generated by heavy excavator, and vehicular traffic has been used, and V_s values up to 500 m are measured by passive method. Measured shear wave velocity is compared with 350 m drilled log data, and bedrock depth matches with V_s values >800 m/s. Figure 7 shows typical shear wave velocity of deep soil deposit with borelog.

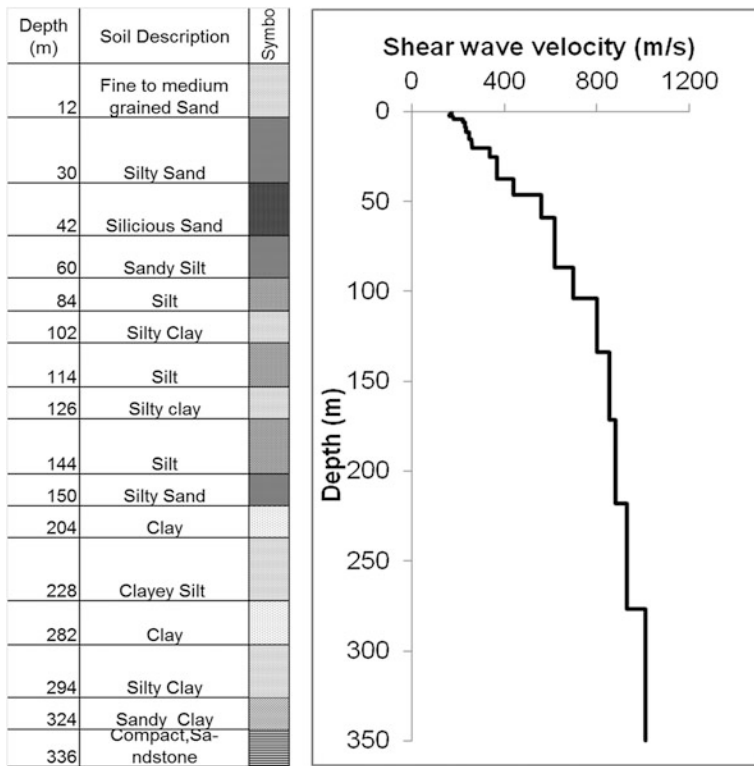
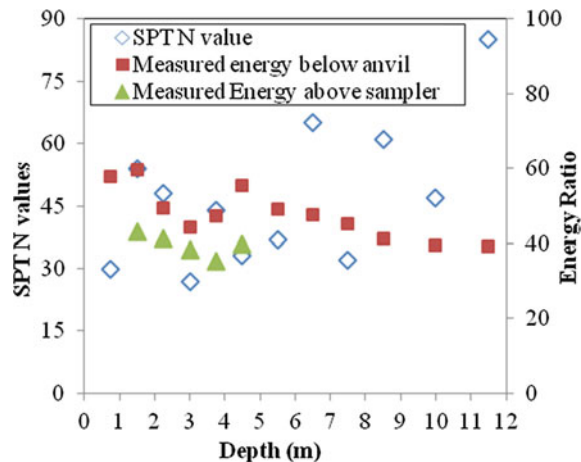


Fig. 7 Typical shear wave velocity measured by modern combined active and passive approach using 2 Hz geophones

Further, newly developed SPT-HEMA has been engaged to measure hammer energy delivered below anvil and above sampler. The study shows that typical donut hammer used in India has energy efficiency which varies from 68 to 40% and 62 to 38% close to sampler. Nearly 3–25% energy difference has been found between the energy measured just below the anvil and above the sampler. Typical variation of energy from a selected borehole with SPT N values are shown in Fig. 8. Thus, considering the whole dataset, the energy correction factor was found to vary from 0.65 to 1.15 below the anvil and from 0.58 to 1.03 above sampler. Typical borehole data has been taken, and effect of hammer energy on liquefaction potential has been estimated, and detailed calculation can be found in Anbazhagan et al. (2016). The actual energy transferred plays a very crucial role in assessment of liquefaction, and any uncertainty in energy transfer percentage leads to great uncertainties in the liquefaction potential of soil. This study shows that variations of hammer energy in liquefaction calculation may change soil layer category from liquefiable to non-liquefiable in the same borehole. Hence, it is recommended to use actual energy measurement setup at the site rather than using some arbitrary energy correction factor for finding liquefaction at any site.

Fig. 8 Hammer energy during SPT test using modern facility of SPT-HEMA



8 Summary

Here I have presented the recently completed and ongoing industrial and research work on geotechnical investigation. The effective planning and execution of civil construction project requires integrated subsurface investigation, so that project can be completed in time. Integrated subsurface investigation is not only useful for new project construction but also helps in forensic investigation of the geotechnical failure for effective retrofitting and restoration. I have also presented modern approach in investigating deep soil deposit in IGB and hammer energy measurement using indigenously developed SPT-HEMA and effect of hammer energy on liquefaction estimation.

Acknowledgements The author would like to thank the Science and Engineering Research Board (SERB), Department of Science and Technology (DST), India, for funding the projects titled “Measurement of shear wave velocity at deep soil sites and site response studies” Ref: SERB/F/162/15-2016 and “Development of correction factors for standard penetration test N values in India through energy measurement and field experiments—Step towards a reliable Liquefaction Potential Assessment” Ref: SERB/F/198/2017-18.

References

Anbazhagan, P., Aditya, P., & Rashmi, H. N. (2012a). Review of correlations between SPT N and shear modulus: A new correlation applicable to any region. *Soil Dynamics and Earthquake Engineering*, 36, pp. 52–69.

Anbazhagan, P., Agrawal, A., & Prakash, D. (2016). Effect of energy efficiency of hammer on liquefaction potential of soil. In *Proceedings of IGC* (pp. 15–17).

Anbazhagan, P., Divyesh, R., Athul, P., & Vidyaranya, B. (2017b). Identification of karstic features in lateritic soil by integrated geophysical approach. *Pure and Applied Geophysics (PAAG-D-17-00303)*.

Anbazhagan, P., Divyesh, R., & Madhura, H. (2017a). Integrated geophysical subsurface investigation for effective completion of the sewage pipeline project in the shallow bedrock region. *Consulting Ahead, 11*(1), pp. 55–67.

Anbazhagan, P., Amarajeevi, G., & Bharatha, T. P. (2012b). Study of ballast fouling in railway track formations. *Indian Geotechnical Journal, 42*(2), 87–99.

ASTM D4633. (2016). Standard test method for energy measurement for dynamic penetrometers. *American Society for Testing and Materials*.

ASTM D6066. (2011). Standard practice for determining the normalized penetration resistance of sands for evaluation of liquefaction potential. *American Society for Testing and Materials*.

Heisey, J. S., Stokoe II, K. H., & Meyer, A. H. (1982). Moduli of pavement systems from spectral analysis of surface waves. *Transportation Research Record, 852*, pp. 22–31 (Washington D.C).

Howie, J. A., Daniel, C. R., Jackson, R. S., & Walker, B. (2003). *Comparison of energy measurement methods in the standard penetration test*. Technical Report, U.S.: The University of British Columbia.

Matthews, M. C., Hope, V. S., & Clayton, C. R. I. (1996). The use of surface waves in the determination of ground stiffness profiles. *Proceedings of the Institution of civil Engineers: Geotechnical Engineering, 119*, 84–95.

Park, C. B., Richard, D., Miller, & Jianghai, X. (1999). Multichannel analysis of surface waves. *Geophysics, 64*, pp. 800–808.

Stump, G. (2004). Subsurface imaging system and method. United States Patent, Patent No. US 6701647B2.

Modeling Soil–Foundation Interaction and Beyond

Subhadeep Banerjee

Abstract This paper presents a study on seismic soil–pile installation using numerical modeling in conjunction with centrifuge model studies. The numerical analyses were conducted using ABAQUS with a hypoelastic constitutive model for the clay. Numerical analyses were used to extend the range of soil, pile, and ground motion parameters which could not be studied in centrifuge. The dimensionless parameters involving the major parameters such as pile modulus, soil modulus, slenderness ratio, natural frequencies of clay layer and pile-raft, superstructure mass, density of the soil and peak ground acceleration were obtained from the parametric studies. The relationships for the amplification of ground motions and the maximum bending moment in the pile were developed based on regression of the numerical data.

Keywords Earthquake · Piles · Clays · Amplification · Bending moment

1 Introduction

Many major cities such as Shanghai, Bangkok, Mumbai, Kuala Lumpur, Jakarta, and Singapore are built overlying soft problematic soils. As a result, many important inland and offshore structures such as bridges, port and harbors, tall structures like water tanks, chimney are supported on pile foundations to achieve the required load carrying capacity. In such situations, the response of pile and surrounding soil subjected to cyclic lateral loadings such as earthquakes, sea-waves, blasts is an important factor affecting the integrity of infrastructures. There is a significant history of observed soil–pile interaction under cyclic loading, has often resulted in pile and/or structural damage or failure. For instance, the potential significance of damage to piles was clearly demonstrated during the 1995 Kobe earthquake and more recent 2005 Sumatran earthquake.

S. Banerjee (✉)
IIT Madras, Madras, India
e-mail: subhadeep@iitm.ac.in

Since early 1970s various analytical procedures (Novak 1974; Dobry 1982; Shen and Teh 2004) and numerical simulations (Zhang et al. 2000; Nikolaou et al. 2001) have been developed for soil–pile interaction. In general, different types of constitutive relationships ranging from linear elastic to complex nonlinear elasto-plastic models were adapted to model stress–strain behavior of soil. However, most of those analytical or numerical techniques are often restricted to relatively idealized conditions. In view of that, the present paper details a few three-dimensional numerical analysis and parametric studies carried out on piles embedded in problematic soils.

2 Numerical Simulations of Seismic Clay–Pile–Raft Interaction

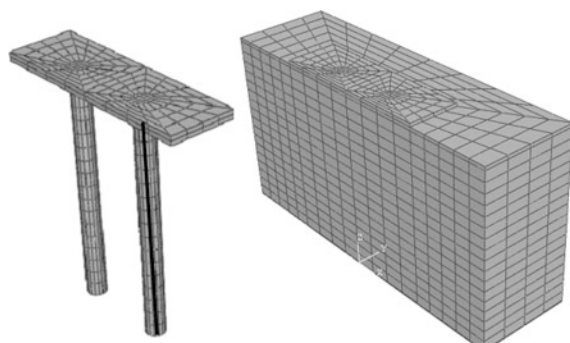
The first study describes the details and results of seismic effects on fixed-head, end-bearing piles installed through soft clay, using numerical modeling in conjunction with centrifuge studies. The numerical analyses were conducted using ABAQUS 6.7.1. The numerical analyses were extended to a range of soil, pile, and ground motion parameters to establish a framework for estimating earthquake-induced bending moments and amplification of seismic waves in fixed-head piles.

2.1 Numerical Model

The soil–pile–raft system was analyzed using a half-model consisting of 20-noded brick elements, Fig. 1.

The results of centrifuge experiments were used to validate the numerical simulations. Experiments were conducted using a laminar box cum shaking table assembly mounted on the NUS geotechnical centrifuge. The earthquake shaker consists of a laminar box seated on top a hydraulic actuator. To simulate laminar

Fig. 1 3-D half-model for soil–pile–raft analysis



movements, linear multi-point constraints were applied to the two vertical faces normal to the input motion, so that nodes at opposite ends of the domain and at the same depth move in unison with each other. In addition, the nodes on the vertical plane of symmetry were restrained against any horizontal displacements in the direction normal to this plane. The remaining three vertical faces, as well as the base of the mesh, were restrained against vertical motion.

The model pile-raft system comprises of four cylindrical model piles, each 260 mm long, connected to a 250 mm long \times 150 mm wide \times 10 mm thick steel plate which acts as a raft. The four piles are bolted to the steel plate so that the pile-head condition may be considered to be fixed. Three types of model piles, three different materials and of diameters 18 mm (0.9 m prototype), were used (Table 1). Superstructural masses were simulated by steel plates bolted on top of the raft, which impose a uniformly distributed load on the surface of the pile cap. In this study, up to six steel plates, each 1.9 kg mass, were added on the pile-raft system (In the prototype, Mass-1: 368 tonnes, Mass-2: 605 tonnes, and Mass-3: 863 tonnes).

The engineering properties of the kaolin clay as reported by Goh (2003) were adopted in the study and are shown in Table 2. The clay beds were prepared by consolidating clay slurry in the laminar box under 1 g preloading, followed by 50 g consolidation. The soft clay behavior was characterized using ABAQUS in-built hypoelastic stress–strain model that exhibits nonlinear, but reversible, stress–strain behavior even at small strains. Physically, the model considers the degradation of shear modulus of soil with respect to increasing shear strain within the soil mass.

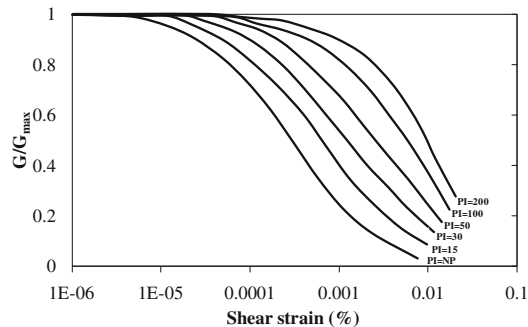
Table 1 Different types of piles used in the numerical simulations

Pile material	Length (m)	Dia. (m)	Slenderness ratio (l/r)	EI (kN/m ²)
Hollow stainless steel	13	0.9	28.89	3,545,002
Hollow stainless steel filled with PCC	13	0.9	28.89	4,285,785
Solid stainless steel	13	0.9	28.89	10,308,351

Table 2 Geotechnical properties of kaolin clay (After Goh 2003)

Properties	Range
Bulk unit weight (kN/m ³)	16
Water content (%)	66
Liquid limit (%)	80
Plastic limit (%)	40
Cohesion (kPa)	30
Young's modulus (MPa)	198
Compression index	0.55
Recompression index	0.14
Coefficient of permeability (m/s)	1.36×10^{-8}

Fig. 2 Modulus reduction curves proposed by Vucetic and Dobry (1991)



Vucetic and Dobry (1991) presented sets of design curves for variation of modulus reduction with strain amplitudes for different plasticity index (Fig. 2). These well-established data sets were used to derive the values of shear modulus corresponding to a specified strain and used as inputs to the constitutive model. The equivalent viscous damping of 10% is used in the analysis.

The input base motions were synthesized from ground motion response spectra of far-field Sumatran earthquakes measured by seismological stations in Singapore (Yu and Lee 2002; Banerjee et al. 2007) and are representative of the bedrock motions in Singapore due to far-field seismic events associated with the Great Sumatran Fault. The synthetic time histories were obtained by standard wave matching technique, where design response spectra were used as input. The final time histories were obtained by trial and matching with target time history. In the present paper, three ground motions are referred as PGA-1 (0.022g), PGA-2(0.07g), and PGA-3 (0.1g), respectively.

2.2 Soil–Pile Response

Figure 3a, b shows the acceleration time histories computed at the clay surface and top of the raft. For this numerical simulation, solid stainless steel piles with added mass were used. The model was subjected to the ground motion of PGA-3. By comparing the computed histories and corresponding response spectra at the clay surface and top of the raft with those of the input ground motion, it is evident that the amplification of ground motion occurred in both the clay and the structure as the seismic waves propagate upwards. However, despite being at the same elevation, there are differences noted between the acceleration histories computed at the clay and raft, which suggest that the raft does not move in tandem with the ground. Figure 3c is replotted in Fig. 3d with the amplification of the input ground motion (PGA-3) obtained by normalizing the spectral acceleration at the clay and raft with respect to the base response.

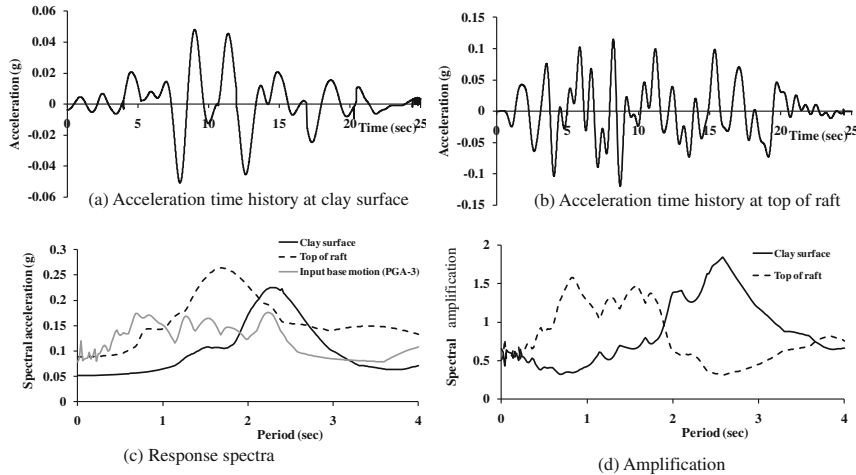


Fig. 3 Acceleration time histories, response spectra, and amplification

To measure the bending moment developed along the pile length, 3-noded beam elements were introduced along the centerline of the pile. The flexural rigidity of the beam was chosen as 10^6 times less than that of the pile so that the beam deformed freely without interfering with the structural response of the pile. The actual bending moment was obtained by multiplying computed beam moments by the scaling factor of 10^6 . Figure 4 shows that the maximum moment occurs near the pile-head reducing along the pile length to very small value near the pile tip.

2.3 Formulation of Dimensionless Parameters

In the present study, five dimensionless groups involving different parameters are identified as follows:

- (i) Stiffness ratio (T_p/T_s) is the ratio of the time period of the superstructure without the soil around it to that of the time period of the soil without any superstructure.

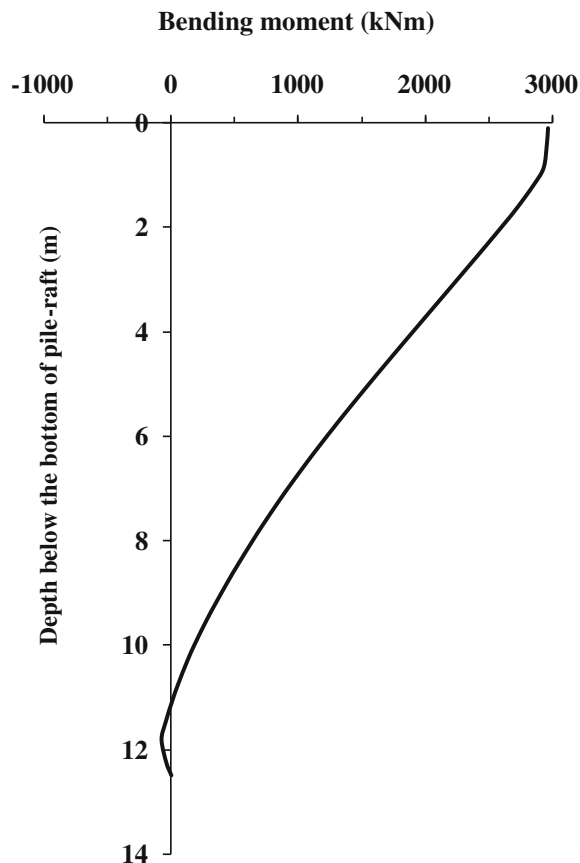
Time period of the superstructure is given by,

$$T_p = 2\pi \sqrt{\frac{mL_p^3}{3E_p I_p}} \quad (1)$$

where L_p is the length of pile, E_p is the modulus of elasticity, I_p is the moment of inertia, and m is the superstructure mass.

The time period of the soil layer is given by,

Fig. 4 Typical maximum bending moment profiles



$$T_s = \frac{4h}{\sqrt{\frac{G}{\rho}}} \quad (2)$$

where h is the height of the soil layer, G is the shear modulus of the soil layer, and ρ is the density of the soil layer.

- (ii) PGA is the peak ground acceleration of the base excitation expressed in terms of acceleration due to gravity (g).
- (iii) Mass ratio $(m/\rho r_p^3)$ is the ratio of mass of the superstructure to equivalent mass of soil. r_p is the radius of pile.
- (iv) Frequency ratio (f_b/f_0) where f_b is the predominant frequency of the input ground motions and f_o ($= 1/T_s$) is the natural frequency of the clay layer.
- (v) Slenderness ratio (L_p/d) is the ratio of the length of the pile to the diameter of the pile.

2.4 Parametric Study

A total of 27 numerical simulations involving three different pile types, superstructural masses and ground motions were carried out to establish semiempirical formulations for amplification at clay surface, top of raft, and maximum bending moment in pile.

Amplification at Clay Surface (A_s)

A detail regression analysis shows that the amplification at clay surface can be expressed as an exponential function (Fig. 5) of above-mentioned dimensionless groups as shown in Eqs. 3a and b.

$$A_s = 1.228 \times e^{57802x} \quad (3a)$$

$$x = \left(\frac{T_p}{T_s}\right)^{0.4} \times (PGA)^7 \times \left(\frac{m}{\rho r_p^3}\right)^{0.05} \times \left(\frac{f_b}{f_0}\right)^{0.6} \quad (3b)$$

It can be noted that the amplification at the clay surface primarily depend on PGA. It is also observed that the amplification at the clay surface increase with the decrease in clay stiffness.

Amplification at Top of Raft (A_r)

Amplification at the top of raft are expressed as a function of the amplification at the clay surface. Figure 6 shows the results of the regression analysis as follows:

$$A_r/A_s = 1.991 \times (A_s)^{-0.93} \quad (4)$$

From Eq. 4, it is noted that the amplification at the top of raft increase with the increase in the amplification at the clay surface.

Fig. 5 Semiempirical relationship for amplification at clay surface

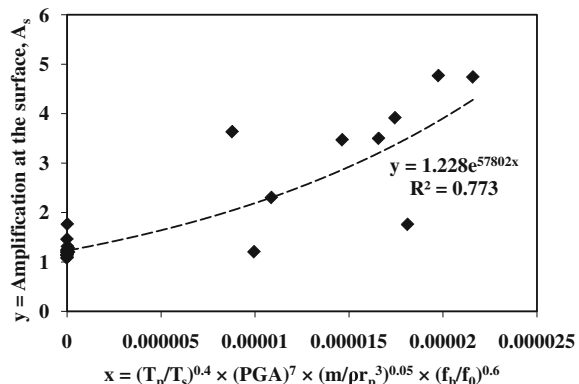


Fig. 6 Semiempirical relationship for amplification at the top of raft

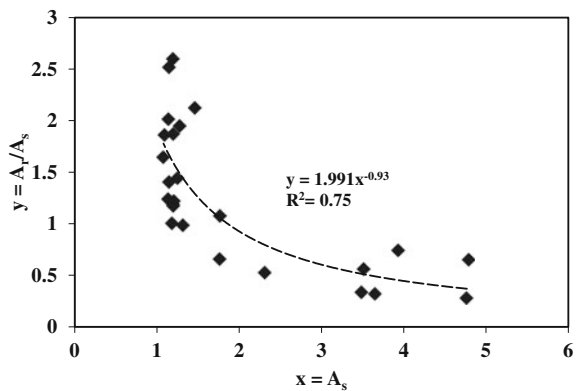
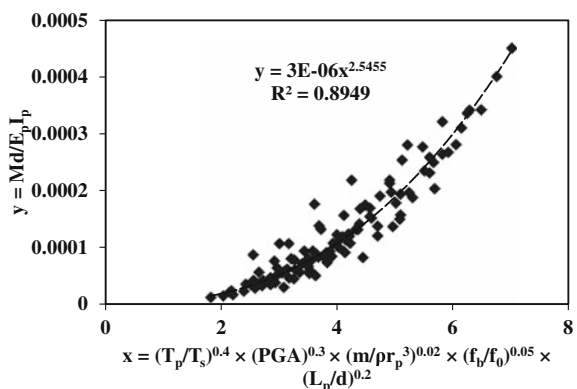


Fig. 7 Semiempirical relationship for maximum bending moment developed along the length of pile



Maximum Bending Moment Developed Along the Length of the Pile

The maximum moment is represented as a dimensionless formulation, $M_d/E_p I_p$ where M is the maximum moment, d is the diameter of the pile, $E_p I_p$ is the flexural rigidity of the pile. The semiempirical formulation of the maximum bending moment is obtained by regression analysis (Fig. 7) is as follows:

$$\frac{M_d}{E_p I_p} = 3 \times 10^{-6} \times \{z\}^{2.545} \quad (5a)$$

$$z = \left(\frac{T_p}{T_s}\right)^{0.4} \times (PGA)^{0.3} \times \left(\frac{m}{\rho r_p^3}\right)^{0.02} \times \left(\frac{f_b}{f_0}\right)^{0.05} \times \left(\frac{L_p}{d}\right)^{0.2} \quad (5b)$$

Equations 5a and b suggests that the maximum bending moment increases with the pile modulus, peak ground acceleration, and superstructural load.

2.5 Validation of the Proposed Formulations

Preceding discussion shows that the clay and pile response can be represented as semiempirical functions of dimensionless groups. The responses computed from the proposed relationships are compared with the results reported in the previous studies.

Comparison with the Centrifuge Tests Results by Banerjee (2010)

Banerjee (2010) reported a series of shaking table experiments conducted using geotechnical centrifuge at National University of Singapore. Input earthquake motions and the soil types are used as the same as that considered in the numerical simulations. The accelerometers and strain gauges were used to measure acceleration time histories and bending moments, respectively. Figure 8a presents the comparison of the results computed from the proposed semiempirical relationship with the results obtained from the centrifuge tests for the amplification at the clay surface. The figure shows that, despite the uncertainties involved in the centrifuge tests, the predicted results matched the test results with reasonable accuracy. Figure 8b shows the comparison between the computed and measured amplification at the top of raft. The figure shows that the proposed correlations compare satisfactorily PGA-2 (0.07g) and PGA 3 (0.1g), whereas the centrifuge results obtained from test with ground motion of PGA-1 (0.022g) tend to deviate from the prediction. However, the ground motion with PGA of 0.022g is too small to be a concern in the context of amplification.

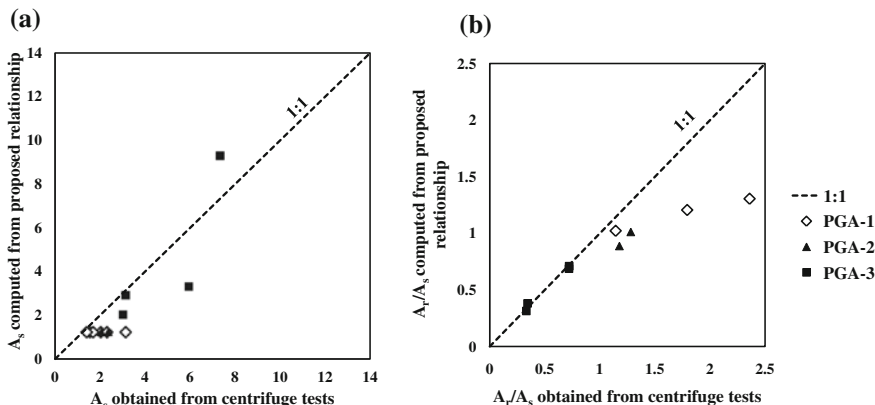


Fig. 8 Comparison of amplification at the **a** clay surface and **b** top of raft computed from proposed relationship with that obtained from centrifuge tests (Banerjee 2010)

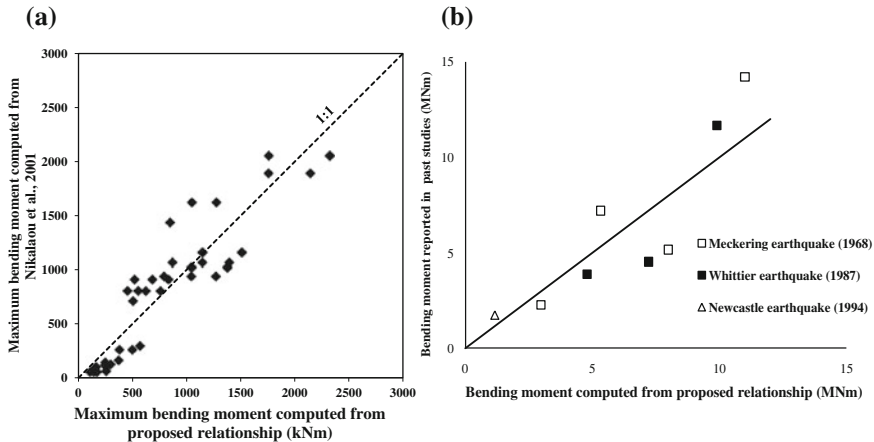


Fig. 9 Comparison between bending moments computed using proposed relationship with **a** Nikolaou et al. (2001) and **b** Poulos and Tabesh (1996)

Comparison with the Semiempirical Relationship Proposed by Nikolaou et al. (2001)

Nikolaou et al. (2001) developed a semiempirical relationship for maximum bending moment in piles embedded in layered soils (Eq. 6).

$$\max M \approx 0.042 a_s \rho_1 h_1 d^3 \left(\frac{l}{d} \right)^{0.3} \left(\frac{E_p}{E_1} \right)^{0.65} \left(\frac{V_1}{V_2} \right)^{-0.5} \quad (6)$$

where a_s is the free-field acceleration, ρ_1 is the density of topsoil (soil layer 1), h_1 is the height of the layer 1, l/d is the slenderness ratio of the pile, E_p is the modulus of elasticity of pile, E_1 is the modulus of elasticity of layer 1, V_1 and V_2 are the shear wave velocities of layer 1 and 2, respectively. It can be observed from Fig. 9a that the agreement between the proposed correlation and the formulation by Nikolaou et al. (2001) is fairly good. The slight deviations that is observed may be attributed to the effect of superstructure mass, which is not taken into account in the formulation by Nikolaou et al. (2001).

Comparison with the Analysis Reported by Poulos and Tabesh (1996)

Poulos and Tabesh (1996) presented an analysis for the seismic response of single piles ignoring inertia of piles. Figure 9b plots the bending moments computed from the proposed relationship along with Poulos' analysis. Figure shows that, in general, good agreement is achieved between the two analyses.

3 Concluding Remarks

The foregoing discussion suggests that the three-dimensional numerical analysis can be very effective to model complex soil–pile systems. It can also be found that the response of clay and piles subjected to seismic loading is affected by various factors such as pile modulus, soil modulus, slenderness ratio, natural frequencies of clay layer and pile-raft, superstructure mass, density of the soil and peak ground acceleration. The developed correlations are favorably validated with the previously published experimental results (Banerjee 2010) as well as the numerical analysis reported by Nikolaou et al. (2001) and Poulos and Tabesh (1996). However, it should be noted that the developed correlations are valid for fixed-head, end-bearing piles in homogenous clay. Further details of this study can be found in following literatures:

1. S Banerjee, M Joy & D Sarkar (2016). Parametric study and centrifuge-test verification for amplification and bending moment of clay–pile system subjected to earthquakes. *Geotechnical and Geological Engineering* 34 (6), 1899–1908.
2. S Banerjee & O N Shirole (2014). Numerical analysis of piles under cyclic lateral load. *Indian Geotechnical Journal* 44 (4), 436–448.
3. S Banerjee, S H Goh & F H Lee (2014). Earthquake-induced bending moment in fixed-head piles in soft clay. *Géotechnique* 64 (6), 431–446.

References

Banerjee, S., Goh, S. H., & Lee, F. H. (2007). Response of soft clay strata and clay-pile-raft systems to seismic shaking. *Journal of Earthquake and Tsunami*, 1(3), 233–255.

Banerjee, S. (2010). *Centrifuge and numerical modelling of soft clay-pile-raft foundations subjected to seismic shaking (Ph.D. thesis)*. National University of Singapore.

Dobry, R. (1982). Horizontal stiffness and damping of single piles. *Journal of Geotechnical and Geoenvironmental Engineering*, 108(GT3), 439–456.

Goh, T. L. (2003). Stabilization of an excavation by an embedded improved soil layer. Singapore: Ph.D. Thesis, National University of Singapore.

Nikolaou, S., Mylonakis, G., Gazetas, G., & Tazoh, T. (2001). Kinematic pile bending during earthquakes: Analysis and field measurements. *Géotechnique*, 51(5), 425–440.

Novak, M. (1974). Dynamic stiffness and damping of piles. *Canadian Geotechnical Journal*, 11(4), 574–598.

Poulos, H. G., & Tabesh, A. (1996). Seismic response of pile foundations—some important factors. In *Proceedings of 11th WCEE paper no. 2085*.

Shen, W. Y., & The, C. I. (2004). Analysis of laterally loaded piles in soil with stiffness increasing with depth. *Journal of Geotechnical and Geoenvironmental Engineering ASCE*, 130(8), 179–215.

Vucetic, M., & Dobry, R. (1991). Effect of soil plasticity on cyclic response. *Journal of Geotechnical Engineering ASCE*, 117(1), 89–107.

Yu, Y., & Lee, F. H. (2002). Seismic response of soft ground. In *Proceedings of physical modeling in geotechnics-ICPMG'02* (pp. 519–524). St. John's, Canada.

Zhang, F., Kimura, M., Nakai, T., & Hoshikawa, T. (2000). Mechanical behavior of pile foundations subjected to cyclic lateral loading up to the ultimate state. *Soils and Foundations*, 40(5), 1–17.

Effect of Long-Term Performance of EPS Geofoam on Lateral Earth Pressures on Retaining Walls

Satyanarayana Murty Dasaka and Vinil Kumar Gade

Abstract This paper presents short- and long-term influence of EPS geofoam to reduce static and traffic loading induced earth pressures on non-yielding rigid retaining walls. Grade III Indian standard sand and EPS15 geofoam (15 kg/m^3 density) are used in model studies, as backfill and compressible inclusion at the interface between the retaining wall and backfill, respectively. Short- and long-term static and traffic loading model tests are performed with and without presence of geofoam. Model retaining wall is instrumented with pressure sensors to measure the lateral earth pressure on wall. Plastic markers are placed along the width of model plate, geofoam, and sand backfill to measure the movement of wall, geofoam compression, and backfill settlement, respectively. Compressive creep (CC) strains of 3% are induced on geofoam samples to simulate pseudo-long-term (PLT) behavior of geofoam. Static and traffic loads are applied on backfill using Servo-hydraulic actuator and surcharge load distribution system. Lateral thrust isolation efficiencies of 55.1–64.2% and 60.6–69.4% are observed under static and traffic loading conditions, respectively, in the presence of geofoam. Higher lateral thrust isolation efficiency, geofoam compression and backfill settlements are observed from the pseudo-long-term static and traffic loading on retaining wall compared to respective initial tests.

Keywords Geofoam · Earth pressure · Isolation efficiency · Deformation

S. M. Dasaka (✉) · V. K. Gade

Department of Civil Engineering, Indian Institute of Technology Bombay,
Mumbai 400076, India
e-mail: dasaka@civil.iitb.ac.in

V. K. Gade

e-mail: gadevinilkumar23@gmail.com

1 Introduction

Economic and optimum design of retaining structures, silos, buried pipes, etc., mainly depends on amount and distribution of earth pressures acting on them. Earth retaining structures are part of several critical infrastructure facilities such as ports, bridges, highways, railways, underground structures and are constructed to support soil on one of its sides. They need to withstand pressures from retained material and surcharge pressures due to movement of vehicular traffic, loads from foundations of the adjacent buildings on their backfill, man-made and natural dynamic events. Evaluation of magnitude and distribution of earth pressure on retaining structures under different loading conditions is important as they influence the design decisions and overall economy of retaining structures. If lateral earth pressure acting on the retaining structure is higher, then retaining structures become too costly. Many researchers have come up with various techniques to reduce earth pressure on retaining wall. Lateral earth pressure from the backfill can be minimized by the controlled yielding method introducing the compressible layer behind the retaining wall, using lightweight backfill, or reinforced backfill. Compressible inclusion is any material that compresses readily, at least in one direction, under an applied stress or displacement compared to other materials in contact with. In the early twentieth century, bales of hay were used to induce vertical arching over buried pipes (Horvath 1996). Some of the compressible inclusions are geofoam, tire chips, glass-fiber, cardboard, and hay. However, behavior of these materials is unpredictable and moreover, glass-fiber is over-compressible and cardboard and hay are biodegradable with time (Horvath 1996). Geofoam is preferred as a compressible inclusion, as it does not suffer from the above shortcomings. The application of compressible inclusion such as EPS geofoam in rigid non-yielding retaining walls is known as the Reduced Earth Pressure (REP) concept and it consists of placing a relatively thin geofoam panel between the wall and the retained soil. EPS geofoam is an effective compressible inclusion than other inclusions used in civil engineering construction because of its multiple functions. EPS can be used either to reduce the load induced on the structure or to accommodate structural movements. EPS is especially a better and cost-effective alternative than to design the structure to withstand greater loads, as stated by Horvath (1998). Geofoam is one of the geosynthetic materials with considerable thickness compared to its length and width. In spite of wide advantages of geofoam (like readily compressible under applied loads, high stiffness to density ratio, etc.), its use is still very limited in construction projects.

2 Motivation and Objective

In view of the several advantages of geofoam, present study is aimed at understanding the behavior of geofoam on lateral earth pressure on rigid retaining walls. The objective of the present study is to verify the short- and long-term effectiveness

of geofoam in reducing the lateral earth pressure exerted on a rigid retaining wall subjected to static and traffic loading, through physical model studies.

3 Literature

Geofoam is a cellular in structure and lightweight material. The term geofoam is introduced by Horvath in 1992 (Athanasopoulos et al. 1999). Geofoam is any manufactured or synthetic material created by some internal expansion processes that result in a material with a texture of numerous, gas-filled cells. Cellular materials are efficient in load bearing because of their ability to support relatively large loads with relatively small amounts of material, whether they have closed or open cells. EPS geofoam advantages are: (Horvath 1994, 1995)

- least expensive by a significant margin (EPS15 approximately costs Rs. 2900/m³);
- uses eco-friendly blowing agent for manufacturing;
- does not release formaldehyde and other toxic gases;
- has predictable stress-strain behavior;
- lightweight material;
- inert in long-term burial conditions;
- easily shaped in field or prefabricated in required shapes;
- weather resistant;
- environmentally safe and does not produce leachate;
- exhibits high compressive strength to density ratio.

Different approaches, such as reinforced retaining walls (Saran et al. 1992; Garg 1998), use of recycled tire chips (Lee et al. 1999; Lee and Roh 2007), and use of compressible inclusion at the wall-backfill interface (Partos and Kazaniwsky 1987; Karpurapu and Bathurst 1992; Horvath 1995) have been found in the literature, which can be considered effective alternatives to conventional retaining walls retaining soil backfill. Compressible inclusions are ready to compress when lateral loads act on retaining wall.

Reduced earth pressure (REP) concept is illustrated in Fig. 1, and it is fundamental application of controlled yielding for rigid earth retaining walls. Earth retaining structure, as shown in Fig. 1, is any type of rigid retaining wall, such as gravity retaining wall, bridge abutment, basement wall. The working principle of compressible inclusion is illustrated in Fig. 2. Generally, the greater lateral movement of wall away from the backfill results in smaller lateral force acting on earth retaining structure. Displacement of geofoam compressible inclusion versus force behavior is reciprocal to the wall displacement versus force exerted in wall, as shown in Fig. 2. From Fig. 2, required minimum thickness of compressible inclusion to achieve active condition for at-rest retaining wall can be obtained, by relating the permissible deformation of compressible inclusion on wall and displacement corresponding to the intersection point.

Fig. 1 Conceptual illustration of components of reduced earth pressure (REP) concept (redrawn after Horvath 2000)

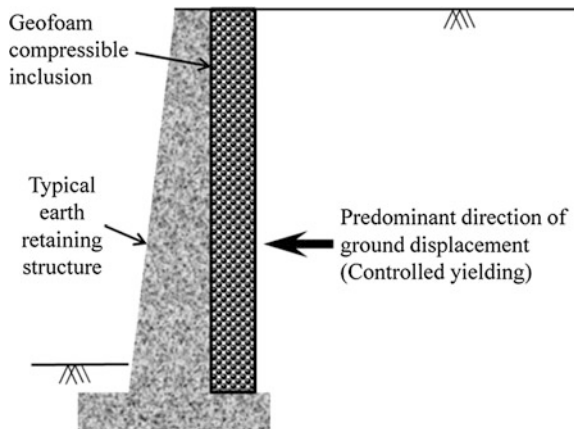
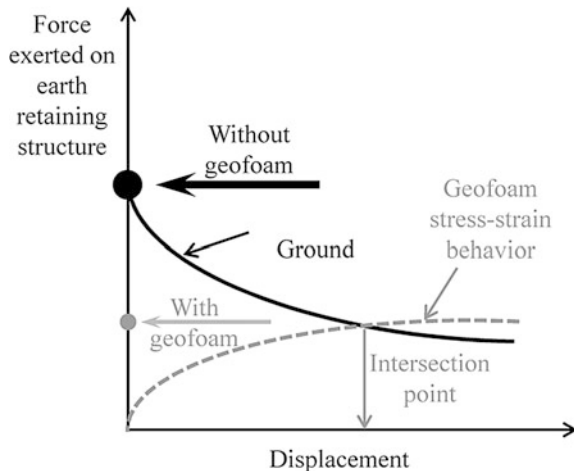


Fig. 2 Conceptual illustration of physical behavior of reduced earth pressure (REP) concept (redrawn after Horvath 2000)



4 Model Material and Preparation

In the present study, Indian Standard Grade III sand, commercially known as Ennore Grade III sand, is used as backfill in the retaining wall model studies. This sand is chosen in the present studies, as it is commercially available in required quantities. It is uniformly graded sand, and hence exhibits minimum possibility of segregation during pluviation. Moreover, the sand is well processed before packing, and hence its behavior can be well controlled. Expanded polystyrene geofoam (EPS) panels of $600\text{ mm} \times 300\text{ mm} \times 25$ or 50 mm thick and cubes of $100\text{ mm} \times 100\text{ mm} \times 100\text{ mm}$, are procured from M/S. Thermoshell Industries, Mumbai, India, are used to understand behavior of geofoam as compressible inclusion. Pictorial views of geofoam panel and cube sample are shown in Fig. 3. A loading plate of $150\text{ mm} \times 150\text{ mm} \times 6\text{ mm}$ is used to transfer the applied load

Fig. 3 Pictorial view of geofoam panel

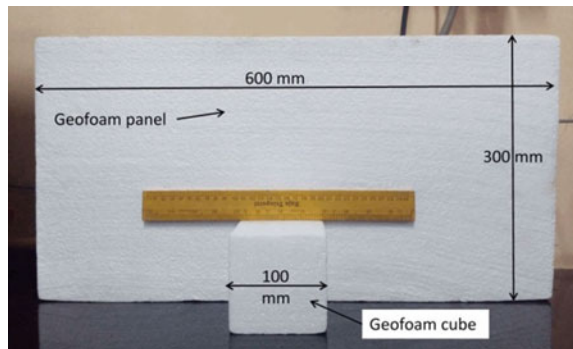
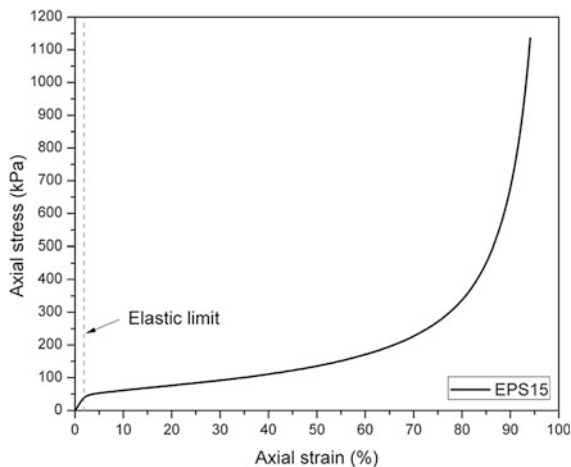


Fig. 4 Stress-strain response of EPS15 geofoam at 10%/min rate of strain



uniformly on geofoam sample. Strain rate of 10%/min is used to conduct the static compression tests of geofoam, which is considered as standard procedure (Horvath 1997; Stark et al. 2004; and ASTM D7180 2005). From static compression tests performed on EPS15, axial stress-strain behavior, Young's modulus (E) (1.99–2.28 MPa), compressive strength (σ_c) (63–70 kPa), yield strength (σ_y) (55 kPa), and elastic limit of geofoam are evaluated. Axial stress-strain behavior of EPS15 is shown in Fig. 4, and a bi-sigmoidal stress-strain relationship is observed.

For performing the retaining wall model tests, a container developed by Dave (2013) is used. Rigid container is made up of stainless steel and acrylic glass material. Internal dimensions of container are 1200 mm length, 305 mm width, and 700 mm height. One side of the container is fully covered with acrylic glass, which is transparent, and remaining three sides are made of stainless steel. Additional stiffeners are added to provide rigidity to the acrylic glass. Few tapped or threaded holes are made to the base of the container to place the model wall plate at desired location. Four wooden blocks of height equal to wall plate height and width equal

to the gap between the wall plate and edge of the container are used, to simulate the at-rest condition of the plate during the testing. To establish plane strain conditions in the backfill, lubricated polythene sheets are pasted on the inner sides of the wall container, as suggested by Tawfig and Caliendo (1993) and Fang et al. (2004). Before filling the sand in container, grease-lubricated 60- μm -thick polythene sheets of 120 mm wide are glued on the inner side of container wall, with an overlap 10 mm to provide continuity.

Dimensions of model wall plate are 700 mm height, 300 mm width, and 18 mm thick. Model wall is hinged at bottom, which is connected to bottom of the container with the help of two small fixtures. Six earth pressure cells (EPC) are instrumented to the model retaining wall plate along the centerline of plate at 100 mm c/c to measure the lateral earth pressure acting the model plate during the testing. Output from the all six pressure sensors is logged using the data logger at required intervals of time. The output response of each EPC is converted to earth pressure by applying the respective calibration factors. All these sensors are calibrated procedure and setup was adopted and developed by Gade and Dasaka (2017).

From image analysis movement of particles, deformation of retaining wall can be captured at multiple locations by placing plastic markers along the wall height and in soil. In the study, plastic markers of four different sizes are used. One set of markers pasted is permanently on the acrylic sheet with help of glue at four corners of the sand backfill or camera focus of view (FOV) in a rectangular pattern. Permanent marker positions are constant for all model studies and are backbone for image analysis. Second set of markers is placed along surface of backfill to measure the surface settlement of backfill. A layer of silicon grease is applied on face of movable markers before placing them near the acrylic sheet as it allows free movement of markers along with movements of sand particles. Third set of markers is placed along the interface between geofoam and backfill to measure the compression of geofoam. Fourth set of markers is placed along the thickness of model

Fig. 5 Details of rigid retaining wall model setup

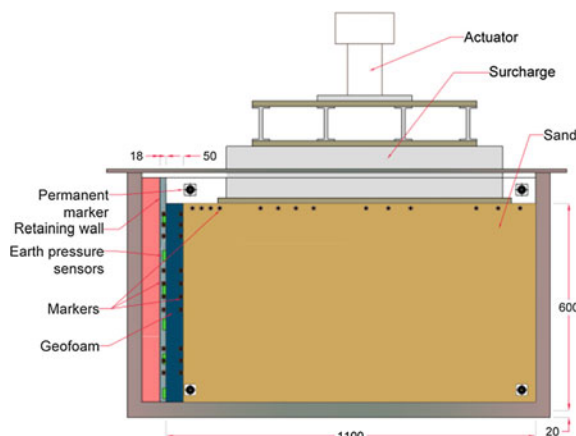
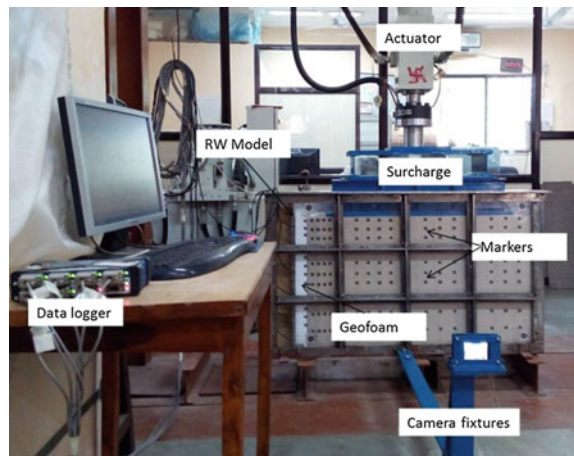


Fig. 6 Pictorial view of the model setup assembly



wall throughout the height of wall to monitor movement of wall. Schematic view of rigid retaining wall model along with sand backfill, geofoam, different types of markers, along with surcharge load are shown in Fig. 5. Pictorial view of the model setup including instrumentation, camera fixtures, and illumination setup are shown in Fig. 6.

Grade III sand is used as backfill in retaining wall model tests and sand beds are prepared at 65% relative density using mechanized traveling pluviator (MTP) developed by Gade and Dasaka (2016). In the study, each sand layer thickness is limited to 15 mm and to maintain each layer thickness uniformly, three scales of 60 cm length were pasted on the each long side of the container is helpful for maintaining the uniform thickness of sand layer. Once sand filling reaches to a height of 600 mm, sand surface is levelled by using the scrapper and brush, and cross-checked with spirit level. Levelling of sand surface is necessary to distribute uniformly applied surcharge load over the sand backfill. Afterwards, model tank is moved from sample preparation place to the actuator frame with the help of pallet truck. Afterwards, surcharge load distribution system is placed on the sand backfill and checked levelling of top surface of surcharge along the length and width direction.

5 Experimental Program

In the present study, short-term and long-term static and traffic loading model tests are performed on non-yielding retaining wall with and without various thicknesses (25, 50, and 75 mm) of EPS15 geofoam. For all the model tests, surcharge distribution system is placed at 150 mm away from the wall. Servo-hydraulic actuator is used for applying the static and traffic loading on retaining wall backfill. Suitable

surcharge loading distribution consists of solid steel plates and I sections is used for uniform distribution of loads from actuator to sand backfill.

5.1 Static Loading Model Tests

Static tests are performed retaining wall model tests with 43.09 kPa surcharge load are applied on backfill and load is maintained for 10 min. Static tests are performed without geofoam and 25, 50, and 75 mm thick EPS15 geofoam models. Lateral earth pressure measured on model retaining wall from the static tests is shown in Fig. 7. It is observed that with presence of geofoam (different thicknesses of geofoam) much lower pressure is experienced by model retaining wall compared to no-foam case. It is observed that 25 mm thick geofoam is more effective in reducing the lateral earth pressure on MRW compared to 50 and 75 mm.

From model tests, backfill settlements are quantified using image analysis of the images captured during the model testing at required time intervals. Backfill settlements in the presence of geofoam for various thicknesses of geofoam are shown in Fig. 8. For better comparison, backfill settlements for without geofoam case are also presented in Fig. 8. For better understanding, starting and end points of surcharge load distribution system are also shown in Fig. 8. It is observed from Fig. 8 that, lesser backfill settlements are observed for small thickness of geofoam and no-foam case experienced lower vertical settlements compared with geofoam cases.

From the image analysis, geofoam compression along the height of wall is also quantified from the face markers placed between geofoam and backfill as shown in Fig. 5. Here, compression of geofoam (δ) is reported in normalized geofoam compression (δ/H) form and it is defined as measured compression of geofoam from model tests divided by model height (H).

Fig. 7 Lateral earth pressure on retaining wall from static model tests

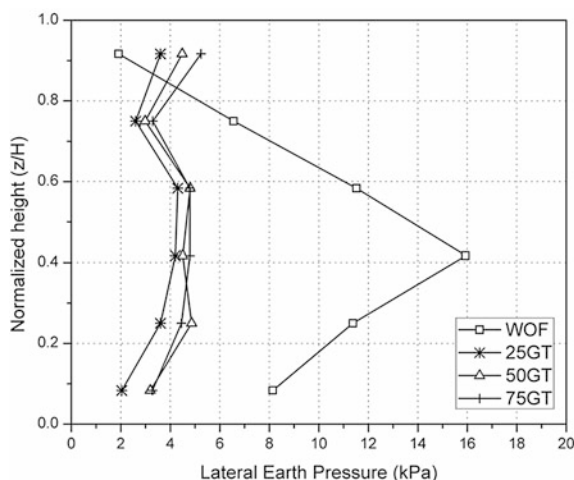


Fig. 8 Vertical settlements of static tests

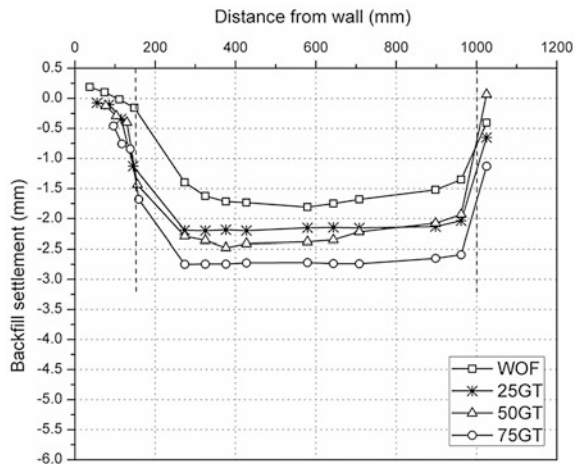
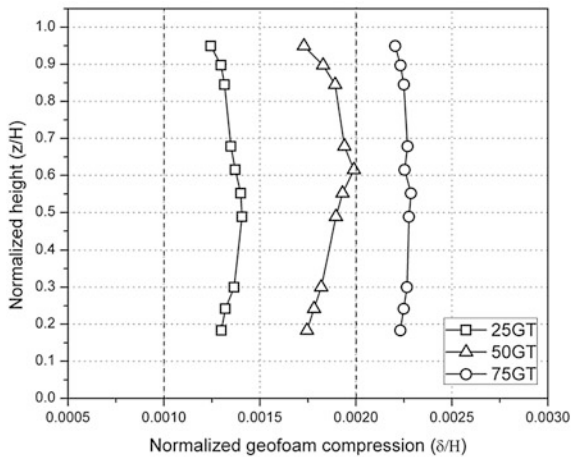


Fig. 9 Geofoam compression from static loading tests

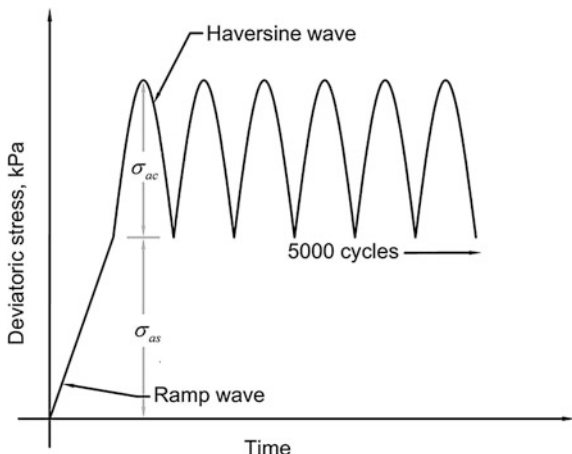


Geofoam compression along the height of wall with respect to time for the static surcharge load is shown in Fig. 9. In Fig. 9, two dotted lines correspond to $0.001 H$ and $0.002 H$ are plotted and they represent the minimum required wall displacement for achieving active condition for dense and medium sand backfills (Clough and Duncan 1991; Das 2010), respectively. Lower thickness of geofoam is resulted in lesser normalized geofoam compression from static model tests is observed.

5.2 Traffic Loading Model Tests

Bridge abutments, approach walls to bridge, and walls supporting railway tracks are some examples of non-yielding rigid retaining walls, which are subjected to

Fig. 10 Schematic representation of traffic load during model testing



vehicular cyclic loading in addition to static loads. These retaining walls must be designed to withstand the vehicular loads as well as the dead load (like pavement, subgrade, backfill, railway track). IRC:6 (2014) recommended to used load corresponding to 1.2 m of earth fill as cyclic load on retaining wall. Based on the literature review, the maximum traffic/cyclic load and dead load of 20 kPa (σ_{ac}) and 23.01 kPa (σ_{as}), respectively, are selected in the present study. Traffic loading model test comprises of two parts, firstly dead load is applied as rapid load in the form of ramp wave, then cyclic load of 5000 cycles is applied in the form of haversine wave. Schematic representation of traffic loading applied during the model testing is shown in Fig. 10.

Lateral earth pressure measured on model retaining wall from the traffic loading tests is shown in Fig. 11. Thickness of geofoam as insignificant effect on lateral earth pressure acting model wall compared to the pressure corresponding to no-foam case. From the traffic loading model tests, retaining wall is exhibited higher lateral earth pressure compared to the static surcharge model tests.

Backfill settlements and geofoam compression from the traffic loading tests are quantified similar to static tests and reported here. Backfill settlements of 10 Hz traffic loading tests with 25 and 50 mm EPS15 geofoam thicknesses are shown in Fig. 12. Similar to the static model tests traffic model tests also results in similar results. Lower the thickness of geofoam lesser vertical displacements in backfill. But, little higher backfill settlements were observed from traffic loading model tests compared to static model tests.

Geofoam compression in traffic loading tests with 25 and 50 mm EPS15 geofoam thicknesses is shown in Fig. 13. Normalized geofoam compression is smaller for the 25 mm thick geofoam compared to 50 mm thick geofoam irrespective density, however, for 25 mm thick geofoam percent geofoam compression crosses the elastic limit.

Isolation efficiency of geofoam in reducing the total lateral trust on retaining wall is evaluated. Total lateral thrust is calculated as area of the lateral earth pressure

Fig. 11 Lateral earth pressure on retaining wall from traffic loading model tests

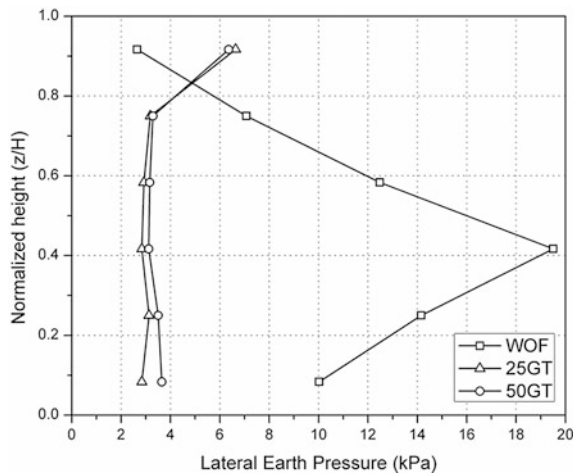


Fig. 12 Vertical settlements of traffic loading tests

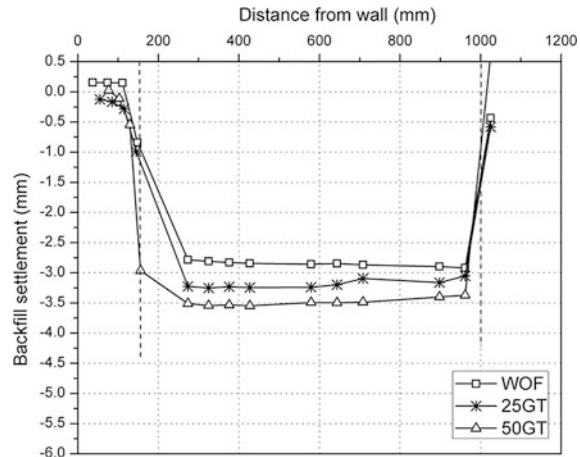
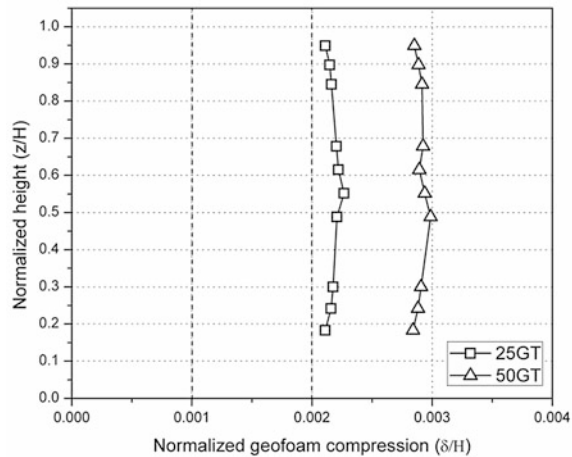


diagram from the model tests. Isolation efficiency is defined as the ratio of difference between total lateral thrust for no-geofoam case (T_{wof}) and geofoam case (T_{wf}) and the total lateral thrust for no-geofoam case (T_{wof}). This isolation efficiency term has been used by several researchers, such as Zarnani and Bathurst (2007), Ertugrul and Trandafir (2011), to understand the effect of thickness and density of geofoam in reducing the total lateral thrust on retaining wall.

$$I_T = \frac{T_{wof} - T_{wf}}{T_{wof}} \times 100 \quad (1)$$

Fig. 13 Geofoam compression from traffic loading tests



where

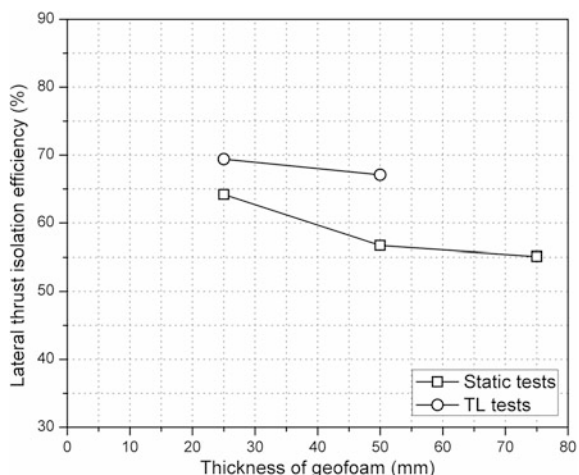
I_T Isolation efficiency, %,

T_{wof} Total lateral thrust on wall for no-geofoam case, kN/m,

T_{wf} Total lateral thrust on wall with geofoam inclusion, kN/m.

Lateral trust isolation efficiency of geofoam with respect to thickness of geofoam from static and traffic loading model tests is evaluated, as shown in Fig. 14. Lateral isolation efficiency of static model tests varies between 55.1 and 64.2%, and it increases for lower thickness of geofoam. Similarly from traffic loading tests, lateral thrust isolation efficiency is 60.6–69.4% observed. These results show that increase in thickness of geofoam does not significantly increase the isolation efficiency compared to overall isolation efficiency achieved. Higher lateral thrust isolation is observed from traffic loading model tests for respective thickness of EPS geofoam.

Fig. 14 Isolation efficiency of static and traffic loading



5.3 Pseudo-Long-Term Static Loading

To understand the long-term behavior of geofoam on lateral earth pressure acting on retaining wall, model tests are conducted by placing compressive creep sustained geofoam panels between model retaining wall and backfill. For evaluating the long-term effect on model retaining wall, geofoam panel needs to be compressed to the required compressive creep value before placing in the model. Pictorial view of developed setup for compressing the geofoam panel is shown in Fig. 15. Geofoam panel size used in the study is 600 mm × 300 mm × 25 or 50 mm (Height × width × thickness).

Geofoam panels are compressed to 3% compressive creep strain prior to placing them between the model retaining wall and backfill. Lateral earth pressure on retaining wall from pseudo-long-term static tests with 50 mm thickness of EPS15 geofoam is shown in Fig. 16. For better comparison, lateral earth pressure corresponding to initial or no compressive creep strain sustained samples is also shown in Fig. 16. With the use of compressive creep sustained geofoam samples, lower lateral earth pressure is measured compared to that of no compressive creep sustained geofoam model.

Geofoam compression along the height of backfill is quantified from image analysis for compressive creep sustained geofoam from the pseudo-long-term model static test is shown in Fig. 17. The geofoam compression is higher for compressive creep sustained geofoam compared to that no compressive creep sustained geofoam. Backfill settlements from the PLT static test are also quantified from the image analysis as shown in Fig. 18. The backfill settlements are higher for compressive creep sustained geofoam case compared to that of no compressive creep sustained geofoam.

Similar to initial traffic loading tests pseudo-long-term traffic loading tests are also performed on model retaining wall with 25 mm and 50 mm thick EPS15 geofoam. Lateral earth pressure from the pseudo-long-term traffic loading model tests are shown in Fig. 19. For comparison, respective lateral earth pressure acting on model retaining wall from initial traffic loading tests is shown in Fig. 19. From Fig. 19, it is observed that lesser lateral earth pressure on model wall from pseudo-long-term model tests compared to that of initial or non-compressive creep-induced model tests.

Fig. 15 Pictorial view of geofoam panel compression setup

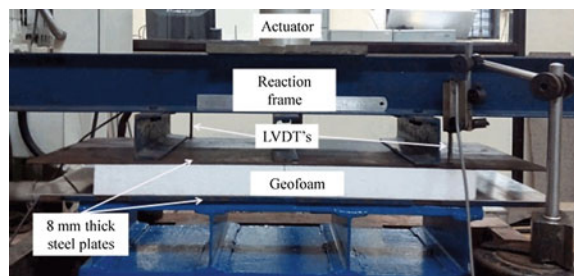


Fig. 16 Pseudo-long-term static lateral earth pressure

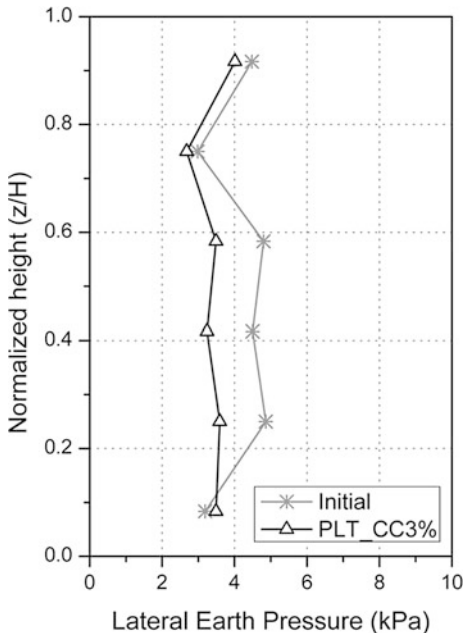
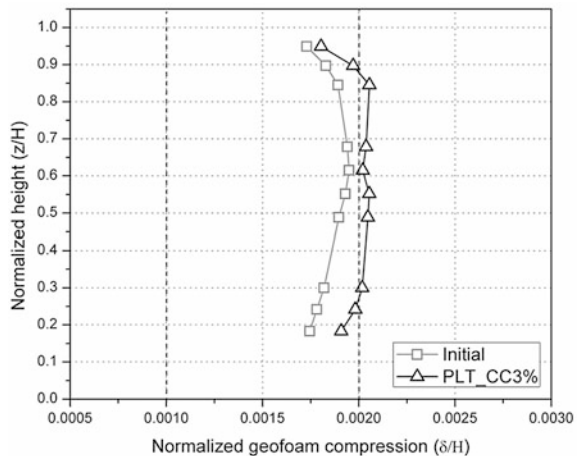


Fig. 17 Geofoam compression from pseudo-long-term static loading tests



Lateral thrust isolation efficiency as stated above is used to evaluate for pseudo-long-term static and traffic loading model tests and reported in Fig. 20. For better representation, lateral thrust isolation efficiencies of initial static and traffic loading are also shown in Fig. 20. It was observed that, irrespective of thickness of

Fig. 18 Vertical settlements of pseudo-long-term static loading tests

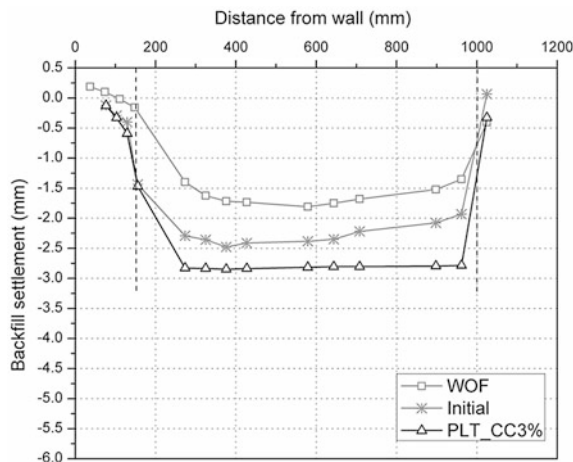
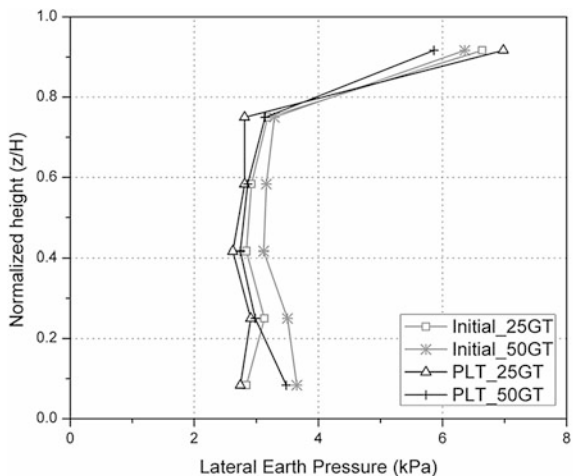


Fig. 19 Pseudo-long-term traffic loading lateral earth pressure



geofoam and type of loading pseudo-long-term lateral thrust isolation efficiency is higher compared to respective initial model tests, which means EPS geofoam is not only reducing the earth pressure acting on retaining wall in short duration of loading but also working actively in reducing the lateral earth pressure on wall for longer duration.

Geofoam compression and backfill settlements of pseudo-long-term traffic loading model tests are shown in Figs. 21 and 22, respectively. For comparison geofoam compression and backfill settlements of respective initial traffic loading tests, results are also shown in Figs. 21 and 22, respectively. Irrespective of

Fig. 20 Isolation efficiency of pseudo-long-term static and traffic loading tests

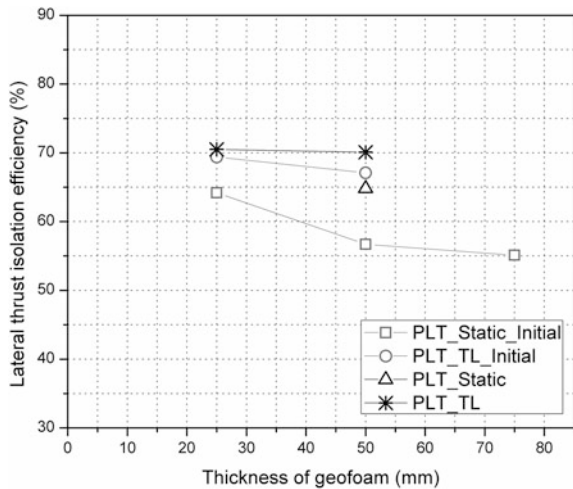
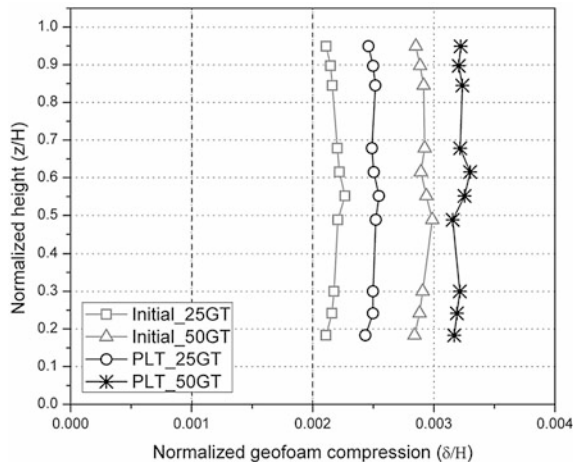


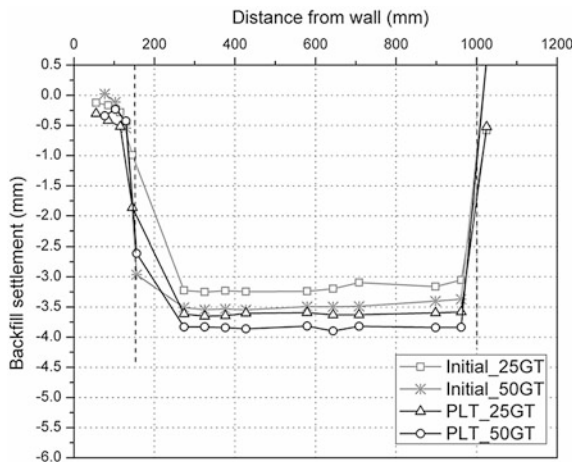
Fig. 21 Geofoam compression from pseudo-long-term traffic loading tests



thickness of geofoam, higher geofoam compression and backfill settlements are noticed from the pseudo-long-term model tests compared to respective initial traffic loading model tests.

Based on the results from the short-term and pseudo-long-term static and traffic loading tests, it is observed that higher horizontal geofoam compression leads to higher isolation efficiency of lateral thrust on the wall. Higher geofoam compression allows movement of backfill toward wall, and at this stage, full mobilization of stresses within soil takes place. This might be the reason behind reduction of lateral earth pressure on retaining wall using the geofoam panels.

Fig. 22 Vertical settlements of pseudo-long-term traffic loading tests



6 Conclusions

From the present study, following conclusions are drawn:

- Normalized geofoam compression along the height of wall increases with increasing thickness of geofoam. Backfill settlements are more in the case of geofoam compared to no-foam case and also, it increases with increase in thickness of geofoam.
- Isolation efficiency (Percentage of reduction of total lateral thrust on retaining wall) in the range of 55.1–64.2% and 60.6–69.4% is observed from static tests and traffic loading tests, respectively.
- Geofoam compression and backfill settlements are higher for traffic loading model tests compared to respective static model tests.
- Isolation efficiency from pseudo-long-term static and traffic loading tests on model rigid retaining walls is 8.1% and 1.1–3% higher from their respective short-term tests.

Finally, based on results of the extensive studies carried out in this work, it is noted that geofoam is highly beneficial in reducing the earth pressures on rigid non-yielding retaining walls. The main advantage of provision of geofoam layer at the wall-backfill interface is that the earth pressures will continuously decrease with elapsed time after construction of wall.

References

ASTM D7180-05 (2005) *Standard guide for use of expanded polystyrene (EPS) geofoam in geotechnical projects*. Annual book of ASTM Standards, ASTM Intl., West Conshohocken, PA.

Athanasiopoulos, G. A., Pelekis, P. C., & Xenaki, V. C. (1999). Dynamic properties of EPS geofoam: An experimental investigation. *Geosynthetics International*, 6(3), 171–194.

Clough, G. W., & Duncan, J. M. (1991). *Earth pressures, chapter in Foundation Engineering Handbook*, 2nd ed, edited by Hsai-Yang Fang (pp. 223–235). New York: van Nostrand Reinhold.

Das, B. M. (2010). *Principles of Geotechnical Engineering*, (7th ed). Cengage Learning.

Dave, T. N. (2013) *Performance evaluation of EPS geofoam inclusion to reduce static and dynamic earth pressures on rigid retaining walls*. PhD Thesis, Indian Institute of Technology Bombay, India.

Ertugrul, O. L., & Trandafir, A. C. (2011). Reduction of lateral earth forces acting on rigid non-yielding retaining walls by EPS geofoam inclusions. *Journal of Materials in Civil Engineering*, 23(12), 1711–1718.

Fang, Y. S., Chen, T. J., Holtz, R. D., & Lee, W. F. (2004). Reduction of boundary friction in model tests. *Geotechnical testing journal (ASTM)*, 27(1), 3–12.

Gade, V. K., & Dasaka, S. M. (2016). Development of a mechanized traveling pluviator to prepare reconstituted uniform sand specimens. *Journal of Materials in Civil Engineering*, (ASCE), 28 (2), 1–9. [https://doi.org/10.1061/\(ASCE\)MT.1943-5533.0001396](https://doi.org/10.1061/(ASCE)MT.1943-5533.0001396).

Gade, V. K., & Dasaka, S. M. (2017). Calibration of earth pressure sensors. *Indian Geotechnical Journal*. <https://doi.org/10.1007/s40098-017-0223-0>.

Garg, K. G. (1998). Retaining wall with reinforced backfill-a case study. *Geotextiles and Geomembranes*, 16, 135–149.

Horvath, J. S. (1994). Expanded polystyrene (EPS) geofoam: An introduction to material behavior. *Geotextiles and Geomembranes*, 23, 263–280. [https://doi.org/10.1016/0266-1144\(94\)90048-5](https://doi.org/10.1016/0266-1144(94)90048-5).

Horvath, J. S. (1995). *Geofoam geosynthetics*. Scarsdale, NY: Horvath Engineering.

Horvath, J. S. (1996). The compressible-inclusion function of EPS geofoam: an overview of concepts, applications, and products. In *Proceedings of International symposium on EPS Construction Method-ISEPS Tokyo'96*. Japan (pp. 71–81).

Horvath, J. S. (1998). The compressible inclusion function of EPS geofoam: an overview of concepts, applications, and products. *Res. Rpt. No. CE/GE-98*, 1. Manhattan College Civil Engineering Department, Bronx, NY.

Horvath, J. S. (1997). The compressible inclusion function of EPS geofoam. *Geotextile and Geomembrane*, 15(1–3), 77–120.

Horvath, J. S. (2000). Integral-abutment bridges: Problems and innovative solutions using EPS geofoam and other geosynthetics. *Res. Rpt. No. CE/GE-00*, 2. Manhattan college civil engineering department, Bronx, NY.

IRC:6. (2014). *Standard specifications and code of practice for road bridges, section: II—Loads and Stresses*. Indian Road Congress.

Karpurapu, R., & Bathurst, R. J. (1992). Numerical investigation of controlled yielding of soil-retaining wall structures. *Geotextiles and Geomembranes*, 11, 115–131.

Lee, H. J., & Roh, H. S. (2007). The use of recycled tire chips to minimize dynamic earth pressure during compaction of backfill. *Construction and Building Materials*, 21, 1016–1026.

Lee, J. H., Salgado, R., Bernal, A., & Lovell, C. W. (1999). Shredded tires and rubber-sand as lightweight material. *Geotechnical and Geoenvironmental Engineering*, 125(2), 132–141.

Partos, A. M. & Kazaniwsky, P. M. (1987). Geoboard reduces lateral earth pressures, In *Proceedings of Geosynthetics '87*, Industrial Fabrics Association International (pp. 628–639). New Orleans, LA: USA.

Saran, S., Garg, K. G., & Bhandari, R. K. (1992). Retaining wall with reinforced cohesionless backfill. *Journal of Geotechnical Engineering*, 118(12), 1869–1888.

Stark, T. D., Arellano, D., Horvath, J. S., & Leshchinsky, D. (2004). *Geofoam applications in the design and construction of highway embankments*, NCHRPWeb Document 65. Transp: Res. Board, Wash., DC.

Tawfig, K. S., & Caliendo, J. A. (1993). Laboratory investigation of polythene sheeting as a friction reducer in deep foundation. *Geotextiles and Geomembranes*, 12, 739–762.

Zarnani, S., & Bathurst, R. (2007). Experimental investigation of EPS geofoam seismic buffers using a shaking table tests. *Geosynthetics International*, 14(3), 165–177.

Comprehensive Characteristics of Fresh and Processed MSW Generated in Kanpur City

S. Rajesh

Abstract Integrated solid waste management plan (ISWMP) developed in Kanpur city involves activities related to waste generation, storage, collection, transport to landfill site, processing (compost, incineration), and final disposal. The waste products generated from various phases of ISWMP which have insignificant reuse capabilities (named as processed waste) have been disposed of in engineered landfills. At times, fresh waste is also being disposed of in separate cells of engineered landfill. As the characteristics of municipal solid waste (MSW) play a major role in the design and proper functioning of waste disposal facilities, it is desirable to understand the variation in the characteristics of the fresh and processed MSW. In this study, comprehensive characteristics of fresh and processed MSW generated in Kanpur city are assessed through gradation, compaction, and compressibility behavior. A significant variation in the characteristic behavior has been noticed between fresh and processed wastes.

Keywords Municipal solid waste • Composition • Gradation • Compaction
Primary compression • Secondary compression

1 Introduction

Solid waste management is one of the key environmental challenges in developing countries like India. At present, Indian cities now generate eight times more municipal solid waste (MSW) than they did fifty years back, primarily due to increasing urbanization and changing lifestyles. The amount of MSW generated per capita is predicted to increase at a rate of 1–1.33% annually (Shekdar 1999). A significant increase in population growth rate and per capita income has also resulted in enormous MSW generation which in turn could pose a serious threat to

S. Rajesh (✉)

Department of Civil Engineering, Indian Institute of Technology Kanpur,
208016 Kanpur, India

e-mail: hsrajesh@iitk.ac.in

the environment if not disposed of carefully. The solid waste management is complex not only because of an increase in the waste generation rate, but also due to the issues related to safe disposal of waste and the land needed for ultimate disposal. Even though unscientific disposal is banned in Indian cities as per Management and Handling Rules (MoEF 2000), still there are many cities which do not have engineered landfills; in those cities, wastes are disposed of in low-lying areas without taking any precautions.

MSW is a complex refuse material composed of various materials with different properties. Some of the components are stable while others degrade as a result of the biological and chemical processes. The composition and the quantity of MSW generated form the basis on which the management system needs to be planned, designed, and operated. Moreover, geotechnical properties of MSW are of prime importance for the design and maintenance of waste containment systems including engineered landfills (Hossain 2002; Rajesh et al. 2015, 2017). Heterogeneity of waste adds the complexity in evaluating the engineering properties and hence to understand deformation behavior of MSW landfills. As the nature of the waste generation, its composition and management plans are site specific, the properties of waste which are to be disposed of in a landfill will also be site specific and hence need to be critically studied to understand the behavior of on-site MSW landfill facilities.

A complete integrated solid waste management plan (ISWMP) has been recently developed in Kanpur, India. The waste products generated from various phases of ISWMP which have insignificant reuse capabilities (named as processed waste) are disposed of in engineered landfills. At times, fresh waste is also being disposed of in separate cells of engineered landfill. In this study, an attempt has been made to evaluate the composition and the characterization of MSW before (fresh MSW) and after processing (processed MSW) in waste management system at Panki landfill, Kanpur. The study area is chosen mainly due to the alarming increase in the waste generation rate and recent initiative in developing an ISWMP in an environment-friendly manner. A special emphasis is given on estimating various engineering properties of fresh and processed MSW collected at Panki landfill.

2 Solid Waste Management Plan at Panki Landfill

The integrated solid waste management (ISWM) involves activities related to generation, storage, collection, transport, processing, and disposal of solid wastes. The practice of reduction, recycle, and reuse of waste along with waste containment system fits very well within the sustainable development concept. It should be recognized that waste reduction and recycling programs have a positive impact in reducing the quantities of waste generated and disposed, respectively. The compost and incinerator ash forms major by-products of ISWM. In recent times, ash from incineration process is being used as alternative geomaterials, hence not being landfilled. The waste products generated from various phases of SWM will be

disposed of in engineered landfills. The final disposal in engineered landfills continues to be the most widely used disposal method of MSW and industrial waste. The primary objective of waste containment systems is to contain solid, liquids, and gases present in the landfill and then with careful monitoring, leachate and gases are allowed to be discharged safely for treatment in various treatment plants.

The study area chosen for the present work is Kanpur, the largest industrial city in Uttar Pradesh, India, with a total area of 261 km², which is located about 435 km east of New Delhi. Kanpur city has a population of 2.76 million (Census 2011). Increased population and per capita income had resulted in the generation of enormous solid waste, subsequently, posing a serious threat to the environment. The waste generation rate in Kanpur city has increased from 0.4 to 0.64 kg/capita/day over a period of ten years (CPCB 2004). The alarming rise in the per capita generation rate of MSW and its disposal had made the Kanpur Municipal Corporation develop an integrated solid waste management plan in an environment-friendly manner. It involves activities associated with waste generation, storage, collection, transport, processing, and disposal of solid wastes.

The waste generated from Kanpur city was dumped in a temporary platform within the landfill sites. As the segregation of waste was not done at the collection site, the fresh waste from the temporary platform was screened by rotary trammels. Small-size waste particles (size less than 100 mm) having a higher percentage of the organic component were kept in windrows for 28 days. After 28 days, waste was screened through 4-mm sieve. The material of size less than 4 mm termed as pure compost is used as manure for agriculture purposes, and material of size greater than 4 mm is used for energy generation. Large-size particle retained on rotary trammels was passed through a drier and then to ballistics separator. The materials other than inert and non-combustible materials were incinerated for energy generation. After incineration, the weight of incineration ash is about 20–30% of the weight the MSW before incineration. Thus, there is a significant reduction in the weight of the residuals to be disposed of the ash produced from the incineration process (namely fly ash and bottom ash) that are utilized as alternative geomaterials for construction-related application. The inert materials and the final residuals from the incineration and compost processes are disposed of in an engineered landfill. The final residue meant for disposal in a landfill is hereby termed as processed MSW.

3 Methods and Materials

The evaluation of engineering properties of fresh and processed waste is highly essential for the design and maintenance of landfill. The key difference between the behavior of soil and MSW is due to biodegradation of MSW and the loss of organic content waste with time. Several researchers adopted sample size of fresh and processed MSW similar to that of soils (Tay and Goh 1991; Reddy et al. 2009b). Few researchers have shredded the MSW to estimate the engineering properties of

MSW (Reddy et al. 2009a) while others adopted larger size samples (Dixon and Jones 2005). Fresh and processed MSW samples obtained from Panki landfill have 60% of the particle sizes smaller than 10 mm, and D_{75} of specimens excluding bulky construction and demolition waste is less than 4.75 mm. In the present study, as the bulky inert materials are not included in the testing program, sample sizes adhering to soils can be used without inducing major sample size error on engineering properties.

The gradation analysis for MSW residue was performed in the laboratory after oven drying at 65 °C using sieve analysis and hydrometer analysis, in general accordance with ASTM D422 (2007). Standard Proctor compaction tests were conducted in accordance with ASTM D698 (2012) using a 102-mm-diameter mold. Oven dry MSW residue (at 65 °C) first equilibrated to a room temperature of 26 °C followed by compacting it in three layers, each layer compacted with 25 number of blows using a standard hammer at a free fall of 300 mm.

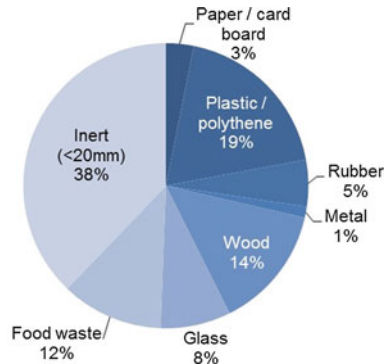
Compressibility characteristics of MSW specimens were determined by performing one-dimensional consolidation test, in general accordance with ASTM D2435 (2011). The MSW specimen was extracted from the standard Proctor compaction mold at a desired unit weight and moisture content. The sample was loaded using a lever arm arrangement, and the compression of the specimen was measured using LVDT. A seating load of 5 kPa was applied to have good contact between porous stone and plunger and to build up initial hydraulic gradient for pore pressure dissipation during consolidation. The load on the specimen was then increased by adopting load increment ratio of unity, with loading steps of 10, 20, 50, 100, 200, 400, and 800 kPa. The properties relevant to primary compression of MSW sample were estimated by allowing the sample to consolidate under each stress increment for 24 h. The secondary compression of MSW specimen was assessed by 1D consolidation test with a distinction of allowing complete dissipation of excess pore pressure for each incremental stress (beyond 24 h) until the variation in the LVDT reading ceases and the next incremental vertical pressure was placed.

4 Results and Discussion

4.1 Waste Composition

At Panki landfill, MSW is a mixture of wastes from the residential and commercial origin. Nine representative fresh MSW samples of 40 kg each at three different locations were used to evaluate the composition of fresh MSW. Figure 1 shows the composition of fresh waste. It can be noticed that nearly 40% of the fresh MSW comprises of inert material. Next major share goes to plastic and their related products, followed by wood and food wastes. An insignificant fraction of metal, paper products, and rubber products was present. This could be due to the removal

Fig. 1 Typical composition of fresh MSW at Panki landfill site, Kanpur, expressed as weight percentage



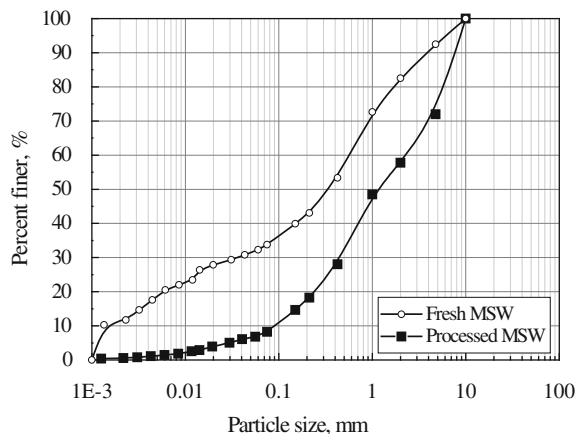
or reuse of these components at the collection sites. Waste generated in Kanpur city has relatively higher percentage of food and inert wastes and a lesser percentage of metal and plastic wastes when compared to the waste generated in Western countries. The organic content in terms of total carbon concentration is found to be 25 and 8% for fresh and processed MSW.

4.2 Particle Size Distribution

In situ gradation analysis was conducted on fresh MSW using a set of four large sieves with an opening size of 100, 36, 16, and 4 mm. The average gradation of fresh MSW determined from more than three representative samples each weighing 100 kg each reveals that the fresh MSW has higher percentage of particle sizes less than 4 mm (35%) followed by bulky particles of size greater than 100 mm (25%); and rest lies within the range of 4–16 mm. The particle size less than 4 mm contains primarily food and organic kind of wastes which are easily biodegradable. Laboratory gradation analysis was performed in general accordance with ASTM D 422 (2007) on fresh and processed MSW samples passed through 10-mm sieve size, as shown in Fig. 2. The smooth S-shaped curve for fresh and processed MSW confirms the well-graded nature of material sizes. The upward shift in the grain size distribution of fresh MSW over processed waste implies for any percentage fines, the particle size of fresh MSW was lower than processed waste. This could be due to the relatively greater percentage of fines present in the fresh MSW was removed during processing.

The in situ gravimetric water content of the fresh and processed MSW was determined using four representative bulk samples greater than 5 kg each. The oven temperature was maintained at 65 °C to avoid combustion of volatile materials. The average in situ water content and the dry unit weight of fresh and processed MSW were found to be $30 \pm 2\%$ and $10 \pm 1\%$ kN/m³; $28 \pm 2\%$ and $11 \pm 1\%$ kN/m³, respectively.

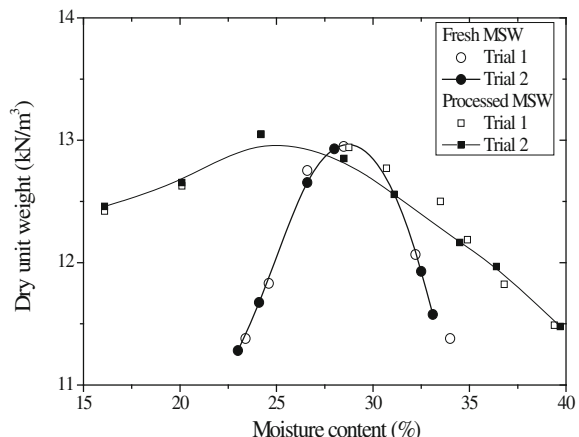
Fig. 2 Particle size distribution of fresh and processed MSW dry unit weight of fresh and processed MSW



4.3 Compaction Characteristics

Figure 3 shows the compaction curve of fresh and processed MSW performed on two representative samples. A good repeatability of the test results can be noticed. The maximum dry unit weight and optimum moisture content (OMC) of fresh MSW were found to be 12.94 kN/m^3 and 28.5%, respectively. Reddy et al. (2009a) reported the maximum dry unit weight and OMC of fresh waste for Orchard hills landfill as 4.12 kN/m^3 and 70%, respectively; however, under the confined condition, the dry unit weight of MSW was found to increase from 5.9 to 6.1 kN/m^3 . The higher value of maximum dry unit weight and significantly lower value of OMC of the fresh waste from Panki landfill when compared to Orchard hills landfill could be due to differences in composition, maximum waste component size, nature of waste, biodegradability as well as component size distribution.

Fig. 3 Variation of dry unit weight of fresh and processed MSW with water content

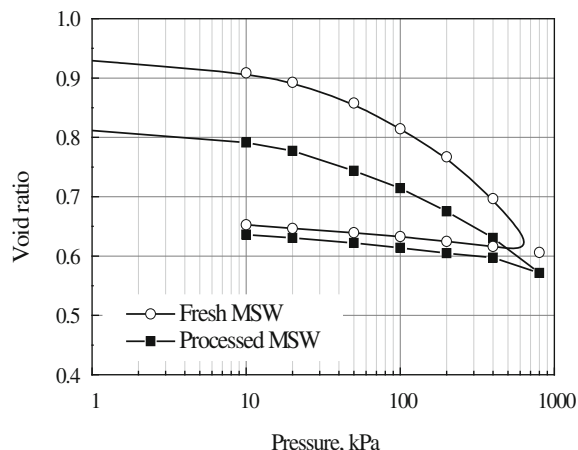


The maximum dry unit weight and OMC for processed waste were found to be 13 kN/m³ and 24%, respectively. Even though the dry unit weight of the fresh and processed waste was close to each other, there is a considerable shift in the OMC. A higher value of OMC for fresh waste could be due to the presence of a higher percentage of organic and fine content. Flatter shape of compaction curve for processed waste relates to the behavior of silty soil where the material is primarily inert/non-plastic in nature. In contrast, the shape of the compaction curve of fresh MSW resembles a fine-grained soil which has a higher percentage of fines and compressibility nature. A significant variation in the engineering properties of the waste can be anticipated due to marked variation in the compaction characteristics.

4.4 Primary Compression Characteristics

Quantifying compressibility characteristics in MSW residue is more complex than doing so in soils due to its heterogeneity and the interaction of a variety of non-uniform particles. Figure 4 shows the variation of the void ratio of fresh and processed waste with vertical pressure in semi-log scale for the complete loading–unloading cycle. The samples were prepared at placement density and moisture content. A considerable decrease in the void ratio can be noticed after loading the sample. The initial void ratio of the fresh waste was found to be greater than processed waste. The compression curve plotted using a semi-logarithm plot exhibits a bilinear shape. The primary compression index C_c is commonly used in engineering practice to characterize the compressibility of a soil specimen and can be obtained from the slope of the virgin compression curve. The primary compression index of fresh and processed wastes was found to be 0.225 and 0.164, respectively. This clearly shows the high compressibility nature of fresh waste when compared to processed waste.

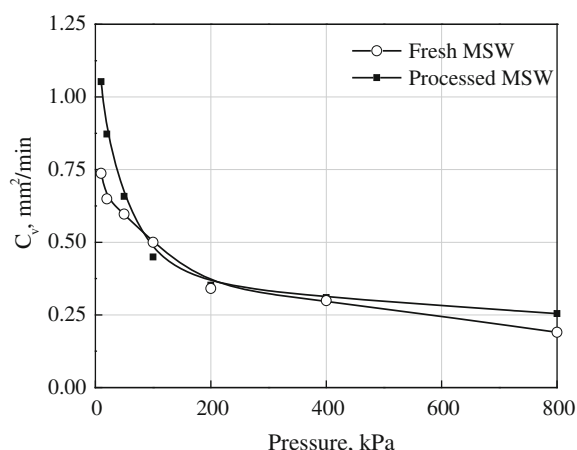
Fig. 4 Variation of void ratio of fresh and processed MSW with vertical pressure



The modified compression index [$C_c/(1 + e_o)$] of fresh and processed wastes was found to be 0.116 and 0.1, respectively. The slope of the unloading curve represents the recompression index, C_r . The recompression index for fresh and processed wastes was found to almost same. However, change in the void ratio between loading and unloading cycle was found to be significantly higher for fresh waste compared to processed waste, irrespective of the applied pressure. The modified compression index of MSW residue is approximately within the range of values between 0.1 and 0.35 reported in the published literature (Landva and Clark 1990; Hossain 2002; Reddy et al. 2009a; Basha et al. 2016). Moreover, the ratio of C_r to C_c was found to be within the range reported in the other research literature (Reddy et al. 2009a).

The coefficient of consolidation C_v was determined using Taylor's square root of time-fitting method as the 90% degree of consolidation is sufficient enough to predict the time taken for primary compression. The time taken for achieving 90% degree of consolidation for both fresh and processed wastes varies between 2 and 5 h; the maximum compression occurs within this period. Even though the 90% degree of consolidation happens well before 24 h, in the present study, next incremental loading on samples was applied only after 24 h. The exact demarcation of time taken for primary and secondary compression for MSW is still debatable. Hence, it is more logical to adopt this approach. The variation of C_v for various vertical pressure is shown in Fig. 5. It can be noticed that with an increase in the vertical pressure, C_v was found to decrease. Nevertheless, the variation of C_v with vertical pressure was found to have a steeper slope up to certain vertical pressure, beyond which, reduction in the coefficient of consolidation was found to be insignificant. It can also be noticed that at lower stress level, C_v was found to be higher for processed waste compared to fresh; however, with the increase in the stress level, the behavior reversal can be observed. Thus, based on the stress level experienced by the waste material, the corresponding C_v may be adopted for precise estimation of the time required for anticipated settlement.

Fig. 5 Variation of coefficient of consolidation of fresh and processed MSW for various vertical pressures



4.5 Secondary Compression Characteristics

In the present study, secondary compression characteristics of fresh and processed MSW were estimated using 1D consolidation test adhering to the test protocol mentioned earlier. Figure 6 shows the variation of the cumulative settlement of fresh and processed MSW samples with time for each incremental stress. It can be noticed that as soon as vertical pressure is applied, a significant primary compression occurs, and with time, the rate of settlement decreases and about 20 days of sustained loading, the settlement measured at an interval of 12 h was found to be less than 0.01 mm. For the same intensity of loading, fresh waste tends to experience higher secondary settlement compared to processed waste. Time frame adopted for the each loading may not account complete secondary settlement; however, it can be noticed that with time, the rate for settlement was found to decrease significantly. The rate of secondary compression of the fresh and processed MSW varied within the range of 0.004–0.028 depending on the time frame and applied stress level. The rate of secondary compression (i.e., the slope of the linear portion of the curve relating strain and time) for soils may be assumed to be constant, irrespective of time, the thickness of soil layer, and load increment ratio

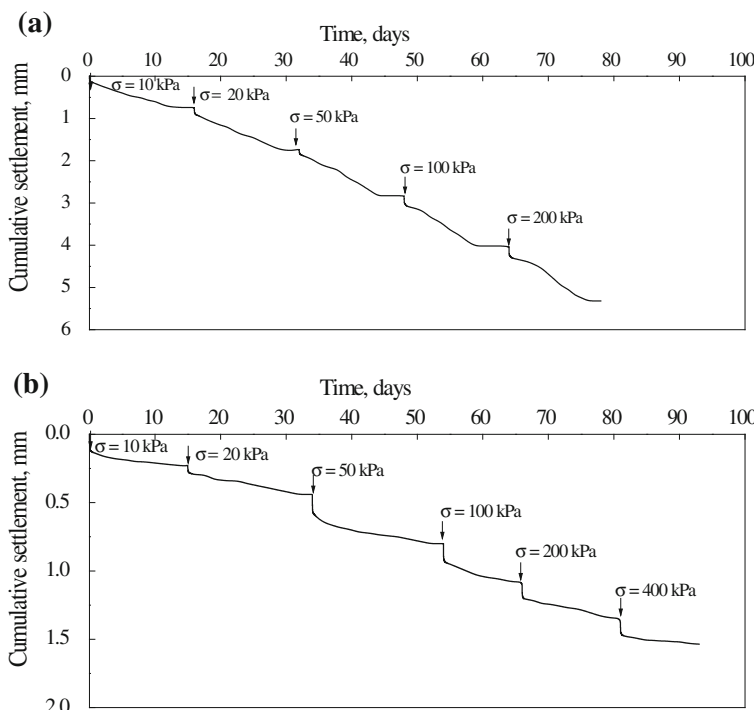


Fig. 6 Variation of cumulative settlement of **a** fresh and **b** processed MSW with time for various vertical pressures

(Holtz and Kovac 1981). The results confirm that rate of secondary compression of MSW samples is not a unique value but depend on vertical pressure and time. The obtained secondary compression ratio of MSW residue was found to be within the range (0.009–0.03) reported in the literature (Gabr and Valero 1995; Chen et al. 2010; Basha et al. 2016).

5 Conclusion

Based on the experimental study performed on fresh and processed MSW, the following conclusions may be drawn:

- Results from standard Proctor compaction reveals that maximum dry unit weight of the fresh and processed wastes was found to be almost same, but optimum moisture content was found to be higher for fresh waste compared to processed waste. This could be due to the presence of a higher percentage of organic and fine content.
- The initial void ratio of the fresh waste was found to be higher than processed waste. The primary compression index of fresh and processed wastes was found to be 0.225 and 0.164, respectively. This clearly shows the high compressibility nature of fresh waste when compared to processed waste.
- At lower stress level, the coefficient of consolidation was found to be higher for processed waste compared to fresh; however, with the increase in the stress level, the behavior reversal can be observed.
- The rate of secondary compression of the fresh and processed MSW varied within the range of 0.004–0.028 depending on the time frame and applied stress level. The results confirm that rate of secondary compression of MSW samples is not a unique value but depend on vertical pressure and time.

Acknowledgements The author wishes to thank A2Z group of companies for providing the access to the Panki landfill and allowing us to perform in situ gradation test on fresh and processed MSW. The author would like to acknowledge his former postgraduate students, Mr. Paras Ram Puniya and Mr. Aniruddhu Kumar Yadav, for their contributions.

References

ASTM. (2007). *D422: Standard test method for particle—Size analysis of soils*. West Conshohocken, PA, USA: American Society for Testing and Materials (ASTM).

ASTM. (2011). *D2435: Standard test methods for one-dimensional consolidation properties of soils using incremental loading*. West Conshohocken, USA, PA: American Society for Testing and Materials (ASTM).

ASTM. (2012). *D698: Standard test methods for laboratory compaction characteristics of soil using standard effort (600 kN m/m³)*. West Conshohocken, PA, USA: American Society for Testing and Materials (ASTM).

Basha, M., Parakalla, N., & Reddy, K. R. (2016). Experimental and statistical evaluation of compressibility of fresh and landfilled municipal solid waste under elevated moisture contents. *International Journal of Geotechnical Engineering*, 10(1), 86–98.

Census. (2011). <http://www.census2011.co.in/census/city/131-kanpur.html>.

Chen, Y., Ke, H., Fredlund, D. G., Zhan, L., & Xie, Y. (2010). Secondary compression of municipal solid wastes and a compression model for predicting settlement of municipal solid waste landfills. *Journal of Geotechnical and Geoenvironmental Engineering*, ASCE, 136(5), 706–717.

CPCB. (2004). *Management of municipal solid waste*. New Delhi, India: Ministry of Environment and Forests.

Dixon, N., & Jones, D. R. V. (2005). Engineering properties of municipal solid waste. *Geotextiles and Geomembranes*, 23, 205–233.

Gabr, M. A., & Valero, S. N. (1995). Geotechnical properties of municipal solid waste. *Geotechnical Testing Journal*, 18(2), 241–251.

Holtz, R. D., & Kovacs, W. D. (1981). *An Introduction to Geotechnical Engineering*. NJ: Prentice Hall.

Hossain, M. S. (2002). *Mechanics of compressibility and strength of solid waste in bioreactor landfills*. PhD Dissertation, Department of Civil Engineering. North Carolina State University at Raleigh, NC.

Landva, A. O., & Clark, J. I. (1990). *Geotechnics of waste fills—Theory and practice* (pp. 86–113). ASTM STP 1070, Philadelphia.

MoEF. (2000). *Municipal solid waste management and handling rules*. New Delhi: Ministry of Environment and Forests, Government of India.

Rajesh, S., Babel, K., & Mishra, S. K. (2017). Reliability based assessment of municipal solid waste landfill slope. *Journal of Hazardous, Toxic, and Radioactive Waste*, ASCE, 21(2), 040160161–11.

Rajesh, S., Rao, B. H., Sreedep, S., & Arnepalli, D. N. (2015). Environmental geotechnology: An Indian perspective. *Environmental Geotechnics*, ICE Publishers, 2(6), 336–348.

Reddy, K. R., Hettiarachchi, H., Parakalla, N. S., Gangathulasi, J., & Bogner, J. E. (2009a). Geotechnical properties of fresh municipal solid waste at Orchard Hills Landfill, USA. *Waste Management*, 29(2), 952–959.

Reddy, K. R., Hettiarachchi, H., Gangathulasi, J., Bogner, J. E., & Lagier, T. (2009b). Geotechnical properties of synthetic municipal solid waste. *International Journal of Geotechnical Engineering*, 3(3), 429–438.

Shekdar, A. V. (1999). Municipal solid waste management—The Indian perspective. *Journal of Indian Association for Environmental Management*, 26(2), 100–108.

Tay, J.-H., & Goh, A. T. C. (1991). Engineering properties of incinerator residue. *Journal of Environmental Engineering*, 117(2), 224–235.

Physico-Chemical Effects on Behaviour of Unsaturated Soils

T. Thyagaraj

Abstract Physico-chemical interactions play a key role in understanding the behaviour of clay soils in wide range of geotechnical and geoenvironmental engineering applications. Its significance on the behaviour of clay soils reconstituted from slurries has been well demonstrated in the literature. Compacted soils and natural soil deposits which are unsaturated also come in contact with contaminants in these applications. Therefore, this paper examines the effect of physico-chemical factors on the structure, compressibility and collapse behaviour of compacted soil. Physico-chemical effects were incorporated using sodium chloride and calcium chloride salt solutions as pore fluid and interacting fluid in different combinations. The changes in the soil structure due to the physico-chemical changes were studied using scanning electron micrographs. The experimental results were analysed and discussed with the aid of Barcelona expansive model (BExM) framework in this paper.

Keywords Compacted soils · Osmotic flow · Soil structure · Matric suction · Loading-collapse curve · Collapse

1 Introduction

Physico-chemical effects arise in geoenvironmental engineering applications such as clay liners in waste containment landfills, buffers in nuclear waste repositories, oil and gas borehole stability. In these applications, the chemical contaminants come in contact with either the natural deposit of soils or man-made compact layers of soil. This results in the interactions between the pore fluid present in the soil and the chemical contaminant, and the pore fluid and clay particles. These physico-chemical interactions affect the behaviour of soils by two distinct mechanisms—*osmotic consolidation/swelling* and

T. Thyagaraj (✉)

Department of Civil Engineering, IIT Madras, Chennai 600036, India
e-mail: ttraj@iitm.ac.in

osmotic-induced consolidation/swelling. Osmotic consolidation (or swelling) occurs at the particle level due to the alterations in the diffuse ion layer thickness around the clay particles owing to the changes in the pore fluid concentration and ion exchange reactions. Osmotic consolidation occurs due to reduction in interparticle repulsive stresses when the pore fluid concentration increases, whereas the interparticle repulsive stresses increase when the pore fluid concentration decreases, leading to *osmotic swelling* (Barbour and Fredlund 1989; Thyagaraj and Rao 2015). *Osmotic-induced consolidation* (or *swelling*) is related to osmotic flow due to the osmotic gradients induced between the pore fluid and inundating fluid (interacting fluid). The occurrence of osmotic flow depends on the ability of clay soils to behave as semi-permeable membranes, and the extent of osmotic flow is defined by the osmotic efficiency of clay soils. The induced osmotic suction, $\Delta\pi$, is given by van't Hoff Eq. (1) as (Thyagaraj and Das 2017):

$$\Delta\pi = i(M_P - M_I)RT \quad (1)$$

where i is the van't Hoff factor (2 for sodium chloride (NaCl) and 3 for calcium chloride (CaCl₂) solutions, Glasstone 1974), M_I and M_P are molar concentrations of the inundating fluid and pore fluid, respectively, $R = 8.32$ litre.kPa/mol K (universal gas constant), and T is the absolute temperature (Kelvin). When the clay soil is inundated with a solution of greater concentration than the pore fluid, osmosis is induced which leads to the outward osmotic flow from the clay soil, leading to the development of negative pore fluid pressures in the pore fluid. This results in the decrease in volume owing to the increase in the effective stress which is termed as *osmotic-induced consolidation*. When the concentration of the pore fluid is greater than the inundating fluid, the inward osmotic flow is induced which leads to an increase in pore water pressure with a consequent decrease in effective stress that in turn results in the increase in volume of clay soil. The increase in volume is termed as *osmotic-induced swelling* (Thyagaraj and Rao 2015).

Extensive research has been carried out in bringing out the significance of physico-chemical effects on the engineering behaviour of clay soils reconstituted from slurries, especially on the compressibility, swelling and hydraulic behaviour, over the last few decades (Bolt and Miller 1955; Bolt 1956; Warkentin et al. 1957; Aylmore and Quirk 1962; Mesri and Olsen 1971; Barbour and Fredlund 1989; Moore 1991; Di Maio 1996; Musso et al. 2003, 2013; Rao and Thyagaraj 2007a, b; Mokni et al. 2014). However, in geoenvironmental engineering applications the clay soils are used as either natural soil barriers or compacted clay liners and are unsaturated. Further, the structure of natural deposits and compacted clay soils is characterized by double structure, whereas monomodal structure characterizes the clay soils reconstituted from slurries. Thus, the behaviour of compacted clay soils would be quite different from the behaviour of specimen reconstituted from slurries owing to the differences in soil structure and unsaturated state. Unlike reconstituted clay soils, the unsaturated soils in geoenvironmental engineering applications are subjected to both physico-chemical and capillary effects. In addition, the physico-chemical factors also influence the

capillary suction via soil structure of compacted clays and thus the behaviour of compacted clay soils.

Therefore, this paper summarizes the recent research findings (Thyagaraj and Salini 2015; Das and Thyagaraj 2016; Thyagaraj and Das 2017) on the effect of pore fluid osmotic suction on matric and total suctions of compacted expansive soil and compressibility characteristics of compacted clayey soil. Further, the effect of physico-chemical variables on the collapse behaviour of compacted clay soils is discussed.

2 Effect of Osmotic Suction on Matric and Total Suctions

Compacted soils are characterized by double structure, namely microstructure and macrostructure. According to the framework proposed by Gens and Alonso (1992) for active clay soils, the microstructural deformations are reversible and independent of macrostructural deformations and occur due to the physico-chemical interactions at the clay particle level. The physico-chemical changes primarily alter the double-layer thickness which in turn alters the soil structure by the changes in soil aggregation and thus the size and volume of micropores and macropores. As the matric suction is associated with the capillary actions in the soil structure, an attempt is made to establish the effect of pore fluid osmotic suction on matric and total suctions. In order to demonstrate the stated objective, an expansive soil from Chennai, India, was selected as the clay soils respond well to the physico-chemical changes. Table 1 presents the properties of the expansive soil. Expansive soil was mixed, separately with distilled water and NaCl and CaCl₂ salt solutions of select concentrations, to attain moisture contents ranging from dry of optimum to wet of optimum and statically compacted to a dry unit weight of 14.13 kN/m³. Additional set of specimens was used for squeezing the pore fluid. The filter paper method was used for the determination of matric and total suctions of compacted specimens and osmotic suction of pore fluid as per ASTM method. Detailed protocols and the discussion are provided in Thyagaraj and Salini (2015).

Figure 1a, b shows the variations of matric and total suctions with pore fluid osmotic suction (using NaCl and CaCl₂ solutions) of compacted specimens at optimum, dry and wet of optimum moisture contents. It is clear from Fig. 1a, b that both matric and total suctions increased with the increase in the osmotic suction owing to the structural changes induced by the pore fluids. Figure 2 shows the structural changes induced by the pore fluids at moisture content of 27%. Compacted specimen prepared with distilled water exhibits dispersed structure. While the compacted specimens prepared with 4 M NaCl and CaCl₂ solutions display aggregated structure, it leads to an increase in the size of macropores owing to the reduction in the size of micropores. It is also evident from Fig. 2 that the aggregations increased with the increase in cation valence and osmotic suction as per the diffuse double-layer theory. This increase in the size of macropores results in the reduction in degree of saturation in the macropore with the increase in pore

Table 1 Properties of expansive soil and clayey soil (after Thyagaraj and Salini 2015; Thyagaraj and Das 2017)

Physico-chemical properties	Expansive soil	Clayey soil (red soil)
pH	7.71	7.80
Cation exchange capacity (meq/100 g)	60.80	2.41
• Calcium	28.27	1.23
• Sodium	6.79	0.02
• Potassium	1.16	0.80
• Magnesium	24.58	0.36
<i>Index and engineering properties</i>		
Specific gravity, G_s	2.72	2.67
Liquid limit (%)	81	35
Shrinkage limit (%)	9	15
Plasticity index (%)	56	18
<i>Grain size distribution (%)</i>		
• Sand	12	62
• Silt	23	14
• Clay	65	24
Unified soil classification symbol	CH	SC
<i>Compaction characteristics</i>		
• Maximum dry unit weight (kN/m ³)	14.13	19.03
• Optimum moisture content (%)	27	12

fluid osmotic suction. This in turn leads to an increase in matric suction with the increase in pore fluid osmotic suction in compacted specimens as the matric suction is related to the macropore degree of saturation. In addition, this increase in matric suction with pore fluid osmotic suction is also attributed to the greater hydration forces in specimens mixed with salt solutions than the specimens mixed with distilled water at the same placement condition (Thyagaraj and Salini 2015).

Further, the total suction increased with the increase in pore fluid osmotic suction owing to the increase in both matric and pore fluid osmotic suctions. Tang et al. (1997) observed that the difference between the total suctions of specimens mixed with NaCl solution and distilled water was greater than the pore fluid osmotic suction of NaCl solution. This supports the present experimental finding that the matric suction of the specimen mixed with salt solutions increases due to the changes in the soil structure. The research finding also reinforces the results of Krahn and Fredlund (1972) that the suction components are additive irrespective of the pore fluid osmotic suction.

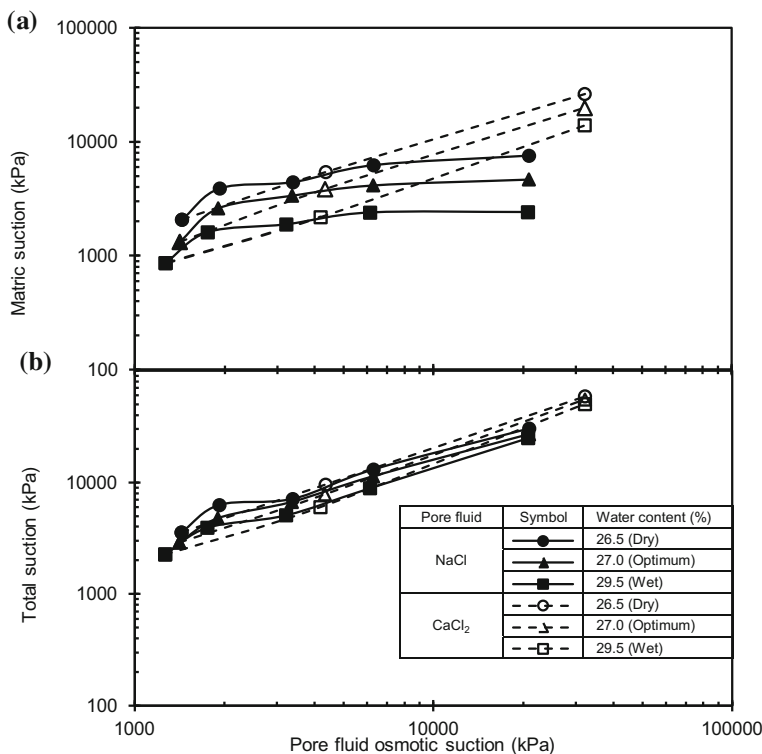


Fig. 1 Variation of **a** matric suction and **b** total suction with pore fluid osmotic suction of compacted expansive soil specimens at optimum, dry and wet of optimum moisture contents ($\gamma_d = 14.13 \text{ kN/m}^3$; after Thyagaraj and Salini 2015)

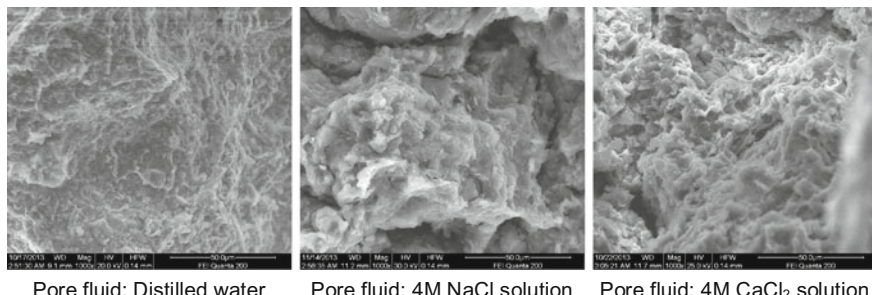


Fig. 2 SEM images of compacted expansive soil specimens (1000 \times magnification; $\gamma_d = 14.13 \text{ kN/m}^3$ and $w = 27\%$)

3 Physico-Chemical Effects on Compressibility Characteristics

The previous section brought out that the physico-chemical changes have significant effect on the microstructure of clay soil which affects the macrostructure and matric suction. As the physico-chemical changes have significant effect on the matric suction, it is also expected to have significant effect on the compressibility behaviour of clay soils. Therefore, this section brings out the physico-chemical effects on the compressibility of compacted clayey soil. The properties of the clayey soil (called hereafter as red soil) used for the compressibility studies are summarized in Table 1. The red soil specimens for the compressibility studies were prepared by mixing the red soil, separately with distilled water and salt solutions of different concentrations, to attain a moisture content of 12% and statically compacted to a dry unit weight of 16.19 kN/m^3 . The compacted specimens were assembled in the conventional oedometer setups and incrementally loaded in unsoaked condition. The yield stress was determined by two tangent methods. Detailed protocols and the discussion are provided in Thyagaraj and Das (2017).

Figure 3 shows the comparison of the compressibility plots of compacted red soil specimens prepared with distilled water and calcium chloride salt solutions of different pore fluid osmotic suctions ($\gamma_d = 16.19 \text{ kN/m}^3$ and $w = 12\%$). It can be seen from Fig. 3 that the initial path followed by the compacted specimens was same in spite of the differences in pore fluid osmotic suction. This is as expected as the microstructural deformations are elastic and independent of matric and osmotic suctions (Alonso et al. 1990; Ferrari et al. 2013; Das and Thyagaraj 2016). However, the yield stress of compacted specimens shows dependence on the pore

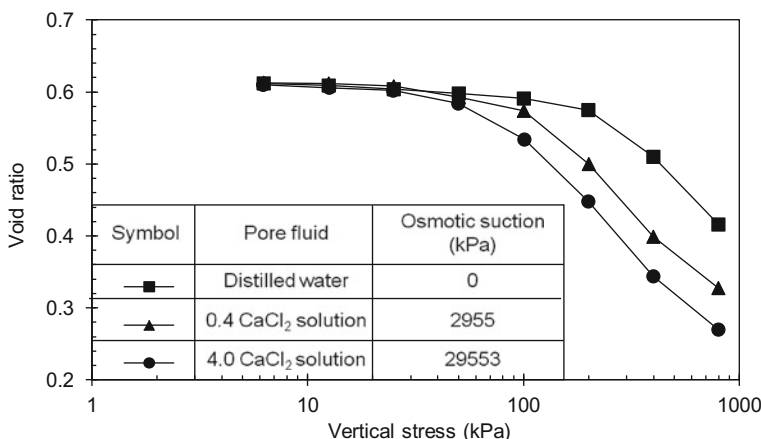


Fig. 3 Compressibility plots of compacted red soil specimens prepared with distilled water and calcium chloride salt solutions of different pore fluid osmotic suctions ($\gamma_d = 16.19 \text{ kN/m}^3$ and $w = 12\%$; after Thyagaraj and Das 2017)

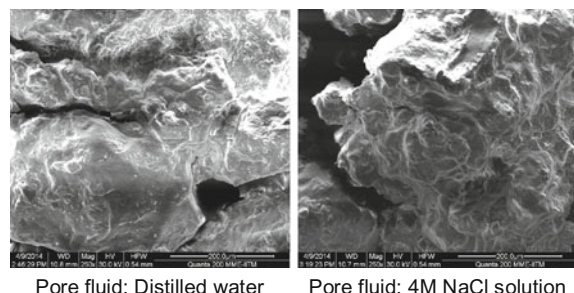
fluid osmotic suction. The yield stress decreased with the increase in pore fluid osmotic suction owing to the decrease in the repulsive-minus-attractive ($R - A$) forces which occurs at the microstructural level. For the microstructural level, Guimaraes et al. (2013) defined an effective stress which is termed as chemically modified effective stress of microstructure, ψ , given in Eq. (2):

$$\psi = p + \chi s_m + \psi_c \quad (2)$$

where p = net mean stress, χ = varies between 0 and 1, s_m = total suction of microstructure and ψ_c = chemical component of chemically modified effective stress. The increase in chemically modified effective stress with the pore fluid osmotic suction results in the decrease in the volume of micropores with a corresponding increase in the volume of macropores. This discussion is supported with scanning electron microscope (SEM) images shown in Figs. 2 and 4 (Thyagaraj and Das 2017). The increase in volume of macropores with the increase in pore fluid osmotic suction causes the reduction in yield stress. Similar findings were reported by Witteveen et al. (2013).

The reduction in yield stress with the increase in pore fluid osmotic suction should also be true at other water contents (i.e. matric suctions) but with the same dry unit weight of 16.19 kN/m^3 . In order to verify this, additional compressibility tests were conducted on soil specimens mixed with calcium chloride salt solutions of different pore fluid osmotic suctions to yield different water contents but compacted to the same dry unit weight of 16.19 kN/m^3 . Plot of the variation in yield stress with matric suction for a particular pore fluid osmotic suction is called as the loading-collapse (LC) curve for that particular pore fluid osmotic suction. Figure 5 shows the effect of pore fluid osmotic suction on the LC curves of compacted red soil using calcium chloride solutions. It is clear from Fig. 5 that the yield stress decreased with the increase in pore fluid osmotic suction at all the matric suctions. Thus, the LC curves shifted towards left with the increase in pore fluid osmotic suction owing to the reduction in volume of micropores and a corresponding increase in the volume of macropores. This indicates that the pore fluid osmotic suction could significantly affect the behaviour of unsaturated soils as well.

Fig. 4 SEM images of compacted red soil specimens (250 \times magnification; $\gamma_d = 16.19 \text{ kN/m}^3$ and $w = 12\%$)



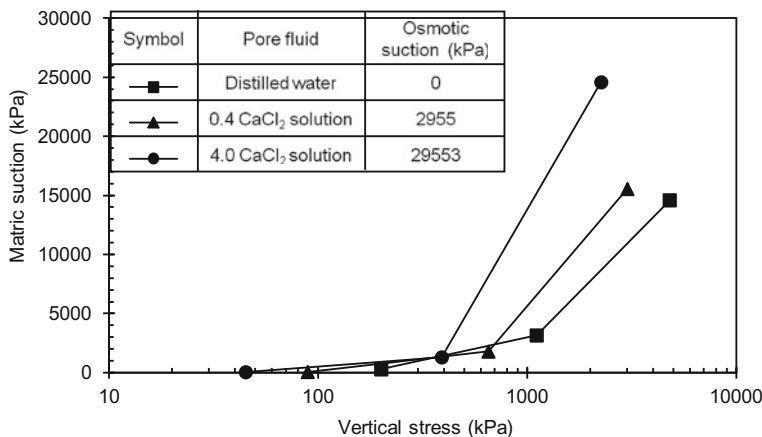


Fig. 5 Comparison of loading-collapse yield curves of compacted red soil using calcium chloride solutions of different pore fluid osmotic suctions ($\gamma_d = 16.19 \text{ kN/m}^3$ and $w = 12\%$; after Thyagaraj and Das 2017)

4 Physico-Chemical Effects on Collapse of Clayey Soil

According to Thyagaraj and Rao (2015), three contaminant situations may arise depending on the relative concentrations of pore fluid and interacting fluid at typical sites where the geotechnical and geoenvironmental engineering problems have to be addressed. In these situations, the osmotic flow direction can be outward, inward and no flow condition. Outward osmotic flow is induced when the osmotic suction of the interacting fluid is greater than the pore fluid. When the osmotic suction of the interacting fluid is lower than the pore fluid, the inward osmotic flow is induced. No osmotic flow situation is also possible where the osmotic suctions of pore fluid and interacting fluid are same. This section brings out the effect of physico-chemical changes on the collapse behaviour of compacted red soil. In order to bring out the physico-chemical effects on collapse behaviour, red soil was mixed with distilled water and, compacted to a dry unit weight of 16.19 kN/m^3 , and then set up in oedometer assemblies and incrementally loaded to 200, 400 and 800 kPa vertical stress in separate oedometer assemblies. Then, the compacted specimens were inundated with salt solutions of different pore fluid osmotic suctions. This induces outward osmotic flow condition owing to the osmotic suction difference between the pore fluid and inundating (interacting) fluid. Similarly, inward osmotic flow condition is induced by mixing the red soil with salt solution and inundating with distilled water. Detailed protocols and the discussion pertaining to this section are provided in Thyagaraj and Das (2017).

Figure 6 shows the comparison of the variation of collapse potential with vertical stress of compacted red soil specimens prepared with distilled and inundated with distilled water and calcium chloride solutions. It is clear from Fig. 6 that the

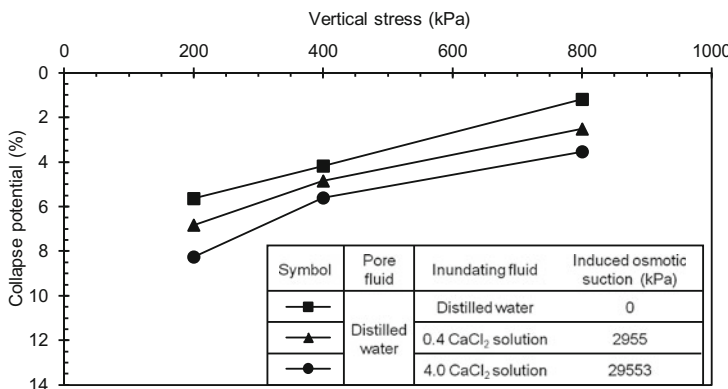


Fig. 6 Effect of induced osmotic suction on collapse potential of compacted red soil specimens subjected to outward osmotic flow condition with calcium chloride solutions ($\gamma_a = 16.19 \text{ kN/m}^3$ and $w = 12\%$; after Thyagaraj and Das 2017)

collapse potential of both specimens inundated with distilled water and calcium chloride solutions decreased with the increase in vertical stress as the specimens are inundated in the plastic region (Lawton et al. 1992; Thyagaraj and Das 2017). Further, it can be observed that the collapse potential of specimens increased with the increase in the osmotic suction difference between the pore fluid and inundating fluid. The osmotic suction difference dissipates by salt diffusion into the soil, osmotic flow out of the specimen and advective flow into the specimen owing to the dissipation of matric suction. All the processes occur simultaneously and lead to an increase in the pore fluid osmotic suction. As discussed earlier, the $R - A$ forces between the clay particles decrease owing to the increase in pore fluid concentration and lead to a reduction in volume which is termed as *osmotic consolidation* (Barbour and Fredlund 1989; Thyagaraj and Rao 2017). Additionally, the osmotic flow induced develops the negative pore water pressures in the soil and increases the effective stress, which also causes a volume reduction which is termed as *osmotic-induced consolidation*. The magnitude of volume reduction by both processes depends on the osmotic efficiency of the clay soil. Thus, the collapse potentials of specimens inundated with salt solutions are greater than the specimens inundated with distilled water.

As discussed in the previous section, the *osmotic consolidation* occurs at the microstructural level and decreases the volume of micropores which increases the volume of macropores accordingly. This increase in the volume of macropores (i.e. chemical softening) leads to irreversible volumetric strains, and it is reflected as a reduction in the yield stress and loading-collapse yield surface. However, both reduction in volume of micropores and increase in volume of macropores occur over a period of time during wetting path and so is the chemical softening. Thus, this chemical softening effect can be considered equivalent to the leftward shift of initial LC curve, as depicted in Fig. 7. This leftward shift of the LC curve increases

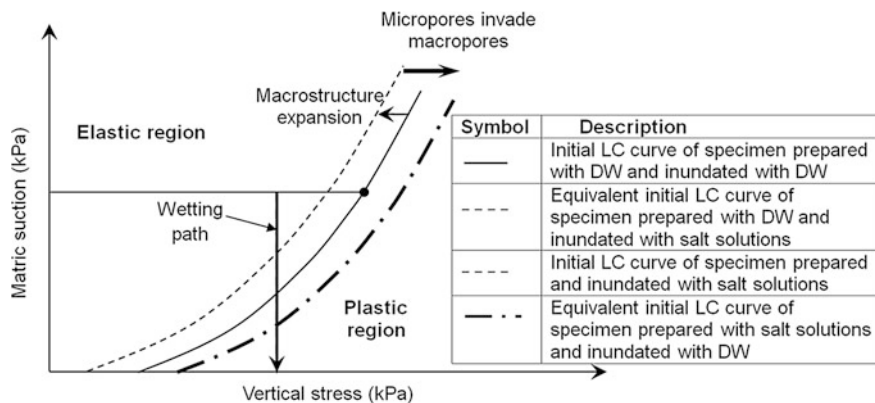


Fig. 7 Schematic diagram depicting the LC curves for compacted specimens subjected to different osmotic flow conditions (after Thyagaraj and Das 2017)

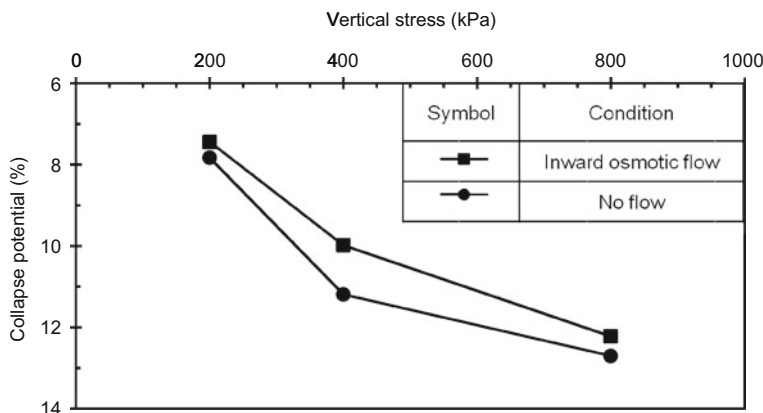


Fig. 8 Comparison of collapse potentials of compacted specimens subjected to no flow and inward osmotic flow conditions using sodium chloride solution (Thyagaraj and Das 2017)

with the increase in the induced osmotic suction and reduces the distance between the inundation path and LC curve. This reduces the elastic region and increases the plastic region, and thus, the collapse potential increases with the increase in the induced osmotic suction owing to the greater plastic strains.

Figure 8 shows the comparison of variation of collapse potential with vertical stress of compacted specimens subjected to no flow and inward osmotic flow conditions. When the concentration of the pore fluid is greater than the inundating fluid, the induced osmotic suction dissipates through outward salt diffusion, inward flow due to osmosis and matric suction dissipation. It should be noted here that all the three processes decrease the pore fluid concentration simultaneously and cause *osmotic swelling* of the microstructure due to increase in electrostatic R – A forces.

In addition, the inward osmosis decreases the effective stress and leads to *osmotic-induced swelling* (Thyagaraj and Rao 2015). Both *osmotic swelling* and *osmotic-induced swelling* increase the volume of micropores and decrease the volume of macropores correspondingly. The decrease in the volume of macropores (i.e. chemical hardening) is reflected as an increase in the yield stress and loading-collapse yield surface. However, both increase in volume of micropores and decrease in volume of macropores occur over a period of time during wetting path and so is the chemical hardening. Thus, this chemical hardening effect can be considered equivalent to the rightward shift of the initial LC curve, as depicted in Fig. 7. This rightward shift of the LC curve increases with the increase in the induced osmotic suction, and also, the distance between the inundation path and LC curve also increases. This increases the elastic region and decreases the plastic region, and thus, the collapse potential of compacted specimens subjected to inward osmotic flow decreases with the increase in the induced osmotic suction owing to the lower plastic strains.

Contrastingly, there is neither diffusion nor the osmotic flow as the concentrations of both inundating fluid and pore fluid are same in the case of no flow condition. The volume of micropores remains unchanged in the specimens prepared with salt solution upon inundation with the same salt solution. Therefore, neither the chemical hardening nor the chemical softening of the macrostructure occurs. However, collapse strains occur in metastable soils upon inundation with salt solutions due to dissipation of matric suction alone. Since the volume of macropores in specimens mixed and inundated with salt solutions is relatively greater than the specimens mixed with salt solutions and inundated with distilled water, the collapse potentials of specimens mixed and inundated with salt solutions are relatively greater than the specimens mixed with salt solutions and inundated with distilled water. This is also illustrated with the aid of LC curves. From Fig. 7, it is shown that the distance between the wetting path and LC curve in case of specimens mixed and inundated with salt solutions is shorter in comparison with the specimens mixed with salt solutions and inundated with distilled water. Therefore, the plastic strains experienced by the specimens subjected to no osmotic flow condition are greater than the specimens subjected to inward osmotic flow.

5 Summary and Conclusions

In this paper, an attempt has been made to demonstrate the physico-chemical effects on the structure of compacted soils. The compacted soils are characterized by double structure comprising a microstructure and a macrostructure. The physico-chemical effects directly control the microstructure of the compacted soil as per the double-layer theory and indirectly control the macrostructural features owing to the changes in the microstructure. This paper experimentally demonstrates the significance of physico-chemical effects on the behaviour of compacted soils by invoking the changes to the macrostructure by the microstructure. The experimental

results showed that the matric suction increased with the increase in pore fluid osmotic suction and cation valence owing to the increase in macropore size as the matric suction is a characteristic of macropore degree of saturation. Further with the increase in pore fluid osmotic suction, the yield stress and loading-collapse yield surface size also reduced.

In compacted specimens mixed with distilled water and inundated with salt solutions, the osmotic gradient induces the outward osmotic flow condition. The osmotic gradient dissipates by salt diffusion into the soil, outward osmotic flow and advective flow into the specimen in response to dissipation of matric suction. The pore fluid osmotic suction increases in the specimen as the osmotic gradient dissipates and leads to chemical softening from microstructural suppression and macrostructural expansion. Thus, the specimens subjected to outward osmotic flow condition experience greater collapse potentials than the specimens inundated with distilled water. In the case of compacted specimens mixed with salt solutions and inundated with distilled water, the inward osmotic flow condition is induced. The induced osmotic gradient dissipated by salt diffusion from the soil, inward osmotic flow and advective flow into the specimen in response to matric suction dissipation, which decreased the pore fluid osmotic suction as the osmotic gradient dissipates and results in the chemical hardening of the macrostructure from the microstructural swelling. Thus, the specimens subjected to inward osmotic flow experience reduced collapse potentials than the specimens subjected to no osmotic flow condition with salt solutions.

References

Alonso, E. E., Gens, A., & Josa, A. (1990). A constitutive model for partially saturated soils. *Géotechnique*, 40(3), 405–430.

Aylmore, L. A. G., & Quirk, J. P. (1962). The structural status of clay systems. In *Clays and clay minerals: Proceedings of the Ninth National Conference on Clays and Clay Minerals* (pp. 104–130). New York: Elsevier.

Barbour, S. L., & Fredlund, D. G. (1989). Mechanisms of osmotic flow and volume change in clay soils. *Canadian Geotechnical Journal*, 26(4), 551–562.

Bolt, G. H. (1956). Physico-chemical analysis of compressibility of pure clays. *Géotechnique*, 6, 86–93.

Bolt, G. H., & Miller, R. D. (1955). Compression studies of illite suspensions. *Soil Science Society of America Journal*, 19(3), 285–288.

Das, A. P., & Thyagaraj, T. (2016). Effect of pore fluid on compressibility and collapse of clayey sand. *Environmental Geotechnics* (Ahead of print).

Di Maio, C. (1996). Exposure of bentonite to salt solution: Osmotic and mechanical effects. *Géotechnique*, 46(4), 695–702.

Ferrari, A., Eichenberger, J., & Laloui, L. (2013). Hydromechanical behaviour of a volcanic ash. *Géotechnique*, 63(16), 1433–1446.

Gens, A., & Alonso, E. E. (1992). A framework for the behaviour of unsaturated expansive clays. *Canadian Geotechnical Journal*, 29(6), 1013–1032.

Glasstone, S. (1974). *Textbook of physical chemistry*. New Delhi, India: Macmillian.

Guimaraes, L. D. N., Gens, A., Sanchez, M., & Olivella, S. (2013). A chemo-mechanical constitutive model accounting for cation exchange in expansive clays. *Géotechnique*, 63(3), 221–234.

Krahn, J., & Fredlund, D. G. (1972). On total, matric and osmotic suction. *Soil Science*, 114(5), 339–348.

Lawton, E. C., Fragaszy, R. J., & Hetherington, M. D. (1992). Review of wetting-induced collapse in compacted soil. *Journal of Geotechnical Engineering*, 118(9), 1376–1394.

Mesri, G., & Olson, R. E. (1971). Consolidation characteristics of montmorillonite. *Geotechnique*, 21(4), 341–352.

Mokni, N., Romero, E., & Olivella, S. (2014). Chemo-hydro-mechanical behaviour of compacted boom clay: Joint effects of osmotic and matric suctions. *Géotechnique*, 64(9), 681–693.

Moore, R. (1991). The chemical and mineralogical controls upon the residual strength of pure and natural clays. *Géotechnique*, 41(1), 35–47.

Musso, G., Morales, E. R., Gens, A., & Castellanos, E. (2003). The role of structure in the chemically induced deformations of FEBEX bentonite. *Applied Clay Science*, 23(1–4), 229–237.

Musso, G., Romero, E., & Della Vecchia, G. (2013). Double-structure effects on the chemo-hydro-mechanical behaviour of a compacted active clay. *Géotechnique*, 63(3), 206–220.

Rao, S. M., & Thyagaraj, T. (2007a). Role of direction of salt migration on the swelling behaviour of compacted clays. *Applied Clay Science*, 38(1–2), 113–129.

Rao, S. M., & Thyagaraj, T. (2007b). Swell–compression behaviour of compacted clays under chemical gradients. *Canadian Geotechnical Journal*, 44(5), 520–532.

Tang, G. X., Graham, J., & Fredlund, D. G. (1997). Effects of osmotic suction on strength of unsaturated highly plastic clays. In *Proceedings of the 50th Canadian Geotechnical Conference, Golden Jubilee* (pp. 641–648). Ottawa.

Thyagaraj, T., & Das, A. P. (2017). Physico-chemical effects on collapse behaviour of compacted red soil. *Géotechnique*, 67(7), 559–571.

Thyagaraj, T., & Rao, S. M. (2015). Osmotic flow in compacted expansive clay. *Environmental Geotechnics*, 2(2), 87–94.

Thyagaraj, T., & Salini, U. (2015). Effect of pore fluid osmotic suction on matric and total suctions of compacted clay. *Géotechnique*, 65(11), 952–960.

Warkentin, B. P., Bolt, G. H., & Miller, R. D. (1957). Swelling pressures of montmorillonite. *Soil Science Society of America Journal*, 21(5), 495–497.

Witteveen, P., Ferrari, A., & Laloui, L. (2013). An experimental and constitutive investigation on the chemo-mechanical behaviour of a clay. *Géotechnique*, 63(3), 244–255.

Crack Initiation—Propagation and Failure Modes in Rocks

V. B. Maji and Sivakumar G.

Abstract Failure and fracturing occur in the rocks when the stresses exceed the threshold limit with the formation of micro-cracks. Subsequent coalescence of several micro-cracks forms a macro-crack leading to failure. The ultimate failure in rocks largely depends on the fracture process and corresponding failure mode. In the present paper, observations on the crack initiation and propagation based on the analysis of failure modes and fracture patterns are reported. Failure strength of the rocks varies with the failure modes and corresponding fracture patterns. Theoretical criteria for rock failure based on crack growth against experimental observations greatly advocated recent years. Moreover, numerical studies on crack initiation and propagation in rocks became very popular in the last decade. This paper presents the complex failure mechanism of rocks with details on crack initiation and propagation characteristics with pre-existing flaws. The study discusses different failure modes in brittle rocks through some laboratory investigation. This paper also discusses some of the numerical simulation results while analysing the crack growth.

Keywords Rock mass · Failure mode · Crack initiation · Crack propagation · Numerical simulation

1 Introduction

Strength and deformation of rock mass is directly governed the presence of joints and bedding planes, fissures and fractures, mineralogical variations, etc. There are numerous microscopic discontinuities, like micro-defects, intergranular cracks and micro-flaws which governs the variability in rocks and in turn the mode by which a rock fails (Szwedzicki and Shamu 1996). Variations in the failure strength in

V. B. Maji (✉) · Sivakumar G.

Department of Civil Engineering, Indian Institute of Technology Madras,
Chennai 600036, India

e-mail: vbmaji@gmail.com

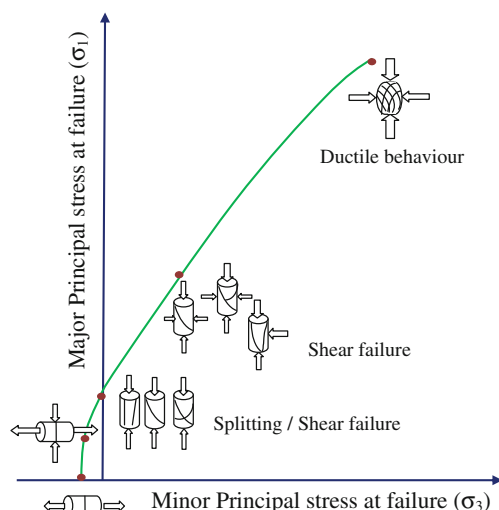
rocks can also be due to the sampling errors, sample preparation methods and testing procedures. Even with identical samples of same rock with similar mineral compositions may result in variation of mechanical properties due to the existence of microscopic discontinuities (Szwedzicki 2007). Many researchers worked on the failure mode of rocks and its effect on overall strength, namely Peng and Johnson (1970), Farmer and Kemeny (1992), Reinhart (1966), Paul and Gangal (1966), Fairhurst and Cook (1996), Szwedzicki (2007), Maji (2011), Basu et al. (2013). It is understood that fractures occur in a rock at a certain point when the stresses cross the threshold value. The rock fails with the coalescence of several micro-cracks leads to different failure modes and corresponding peak strength values. The accurate prediction of failure would significantly reduce the costs involved in construction and improve safety. The existence of discontinuities can alter the state of stress and their distribution in the rock mass when compared with isotropic rock mass. As in nature, rocks usually come with flaws or pre-existing fractures like faults, joints, fissures, etc. Assuming rock as isotropic cannot always give the exact strength and deformation characteristics. Moreover, when the load is applied, new cracks start to form/grow at or near the tips of pre-existing cracks and propagate towards the direction of the major principal stress, leading to macroscopic failure. The prediction of failure modes in rocks and corresponding crack initiation and propagation would help in better understanding of the strength and deformation behaviour of rocks and rock masses. Crack initiation and propagation in rocks and corresponding failure mechanics has tremendous application in rock engineering. The present study is an attempt to review and understand the fracture initiation, growth and pattern, leading to the macroscopic failure in rocks.

With the help of theories of fracture mechanics, it is possible to analyse crack growth to describe their fracture process. And for a better understanding of material failure behaviour in both macroscopic and microscopic senses, analysis at the crack initiation and corresponding growth is necessary. Over the past few decades, many researchers have developed theoretical criteria for crack growth based on experimental observations. Notable contributions were made from Reyes and Einstein (1991), Sagong and Bobet (2002), Wong and Einstein (2009a, b), Park and Bobet (2009, 2010) and Lee and Jeon (2011). Researchers also attempted to numerically capture the crack growth phenomenon using FEM, namely Ingraffea and Heuze (1980), Xu and Yuan (2011), Da Silva and Einstein (2013), Xie et al. (2016), Lee and Jeon (2011) and Vasarhelyi and Bobet (2000). In this paper, crack growth in rocks and corresponding stresses by experimental investigation are also discussed. Numerical simulation on crack growth with extended finite element (XFEM) is also investigated and presented.

2 Failure Modes in Rocks

The stress-strain curve for brittle rock material under uniaxial loading can be divided into four major phases, namely crack closure, elastic compression, stable cracking and unstable cracking. At peak, the micro-cracks join to form macro-crack with sliding happens along macro-cracks. As failure modes of rocks could provide useful information, the examination of failed specimens would be very helpful in design. The relative predominance of the failure modes depends on the strength, anisotropy, brittleness and grain size of the crystalline aggregates. Based on the failure mode of the rock, the values of the UCS obtained in extension are found to be high, whereas the values obtained due to shear are lowest. The most common failure types were failure by axial splitting and shear along single plane (simple shear). As per Gramberg (1989), the common modes of failure in uniaxial compression are axial cleavage and conjugate shear. The failure mode of a brittle rock changes on the application of confining pressure because usually under unconfined compression a rock tends to deform elastically until failure occurs abruptly. With moderate amount of confining pressure, longitudinal fracturing is suppressed and failure occurs with clearly defined plane of fracture. At very high confining pressure, rock may become fully ductile. Figure 1 shows the common failure characteristics/envelope of intact rock in terms of major and minor principal stresses with the depiction of corresponding failure modes in cylindrical specimens. It can be noted that, for uniaxial loading, failure modes are mostly axial splitting, simple shear or multiple shears. With moderate confinement, mode mostly remains with shear and usually seen as Y- or V-shaped failure. For very high confinement, rock may behave like a ductile material. Mode of failure also depends upon the degree of the end constraints of the sample offered by the platens of the testing machine and

Fig. 1 Common failure characteristics of intact rock in terms of major and minor principal stresses



the surface quality of the parallel ends of the sample (Szwedzicki 2007). Samples are likely to fail in shear if the friction between the platens and the specimen is more (Jumikis 1983). Extension fractures develop perpendicular to the minimum principal stress direction and usually follow the orientation of the maximum principal stress. Peng and Johnson (1970) highlighted fracture propagation in specimens of Chelmsford granite subjected to various end-boundary conditions and confining stresses. They reported that the failure theories such as Mohr–Coulomb and Irwin–Griffith's theory fail to explain or predict the exact nature of the fracture development and the orientation of faults in the brittle elastic materials. Santarelli and Brown (1989) discussed the relation between the failure pattern and the internal micro-structure of the rock and developed a qualitative model based on the concept of micro-crack development. Klien et al. (2001) discussed the micro-structural observations of the failure modes in sandstone at different confining pressures ranging from 10 to 350 MPa and reported about the fracture propagation and the stress–strain relations of the rock in brittle–ductile transition. Prudencio and Van Sint Jan (2007) found that the failure modes and maximum strengths of rock with non-persistent joints depend on the geometry of the joint systems, the orientation of the principal stresses and the ratio between principal stresses. Basu et al. (2009) discussed the relation between mechanical behaviours of granite under uniaxial compression based on weathering grades. The effect of internal discontinuities of the rock, angle between the plane of loading and the layer orientation in the rock sample on the failure modes and the fracture patterns are reported by Tavallali and Vervoort (2010).

Experimental investigation was also carried out on cylindrical rock specimens for both uniaxial and triaxial loading in the civil engineering laboratory of IIT Madras. Figure 3 shows some typical failure modes of granulite rock specimens observed using 200T compression testing machine (Fig. 2). The schematic of common failure modes in brittle rocks under compression is shown in Fig. 4. It was found that most of the rock specimens that failed in longitudinal splitting gave maximum strength. Some tested rock samples observed to be failed in simple shear

Fig. 2 200T compression testing machine (CTM) with Hoek triaxial cell of 70 MPa capacity





Fig. 3 Some typical failure modes of granulite rock specimens observed after axial compression testing

or multiple shears and gave relatively lower strength compared to longitudinal splitting. The effect of confining pressure on the strength and failure mode of a rock sample is studied by conducting triaxial compression tests. Failure strength of the rock samples found to be varying based on the failure modes and fracture patterns of the rock samples. Figure 5 shows some typical failure modes of granulite rock specimens observed after triaxial compression testing. As shown in Fig. 5, most of the samples failed in simple shear or with Y-/V-shaped shear failure pattern. Li et al. (2017) attempted to study failure modes of sandstone specimens at different confining stress levels (Fig. 6). They found that, at low confining pressures, rock specimens usually fail in splitting mode, representing brittle failure. With moderate level of confinements, failure mode observed to be transformed into shear failure. Even with high confining pressures, failure remains as shear with some traces of tension. With very high confining pressures, the failure angle with the major principal plane starts reducing, and at pressures of 45 MPa and beyond, failure plane becomes almost flat. Crushing of rock along the shear plane was observed due

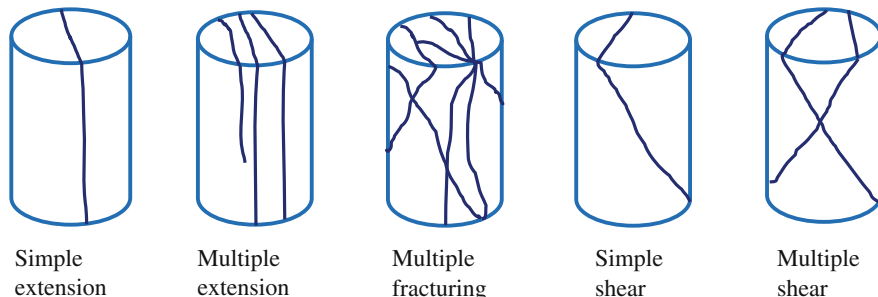


Fig. 4 Common modes of failure in rock sample under axial compression

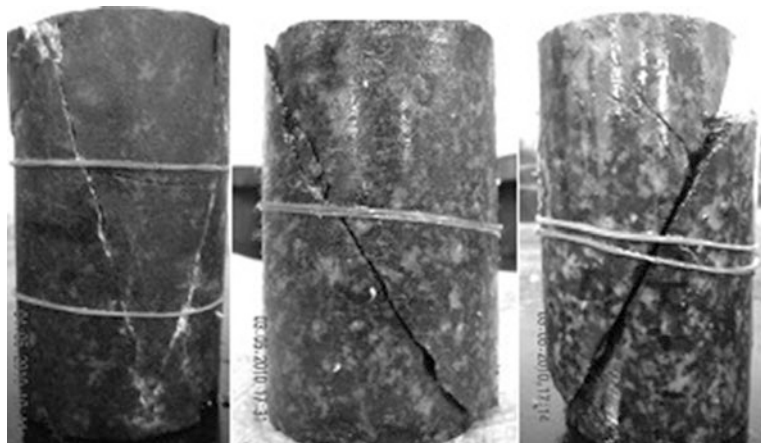
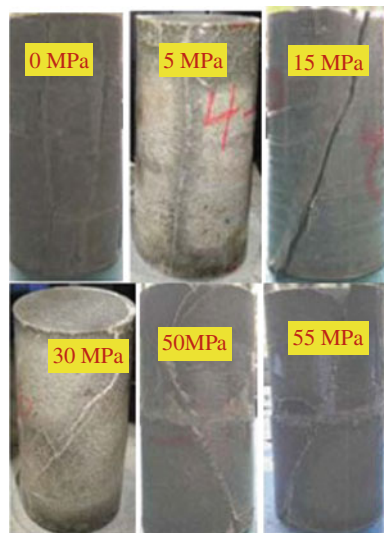


Fig. 5 Some failure modes of granulite specimens after triaxial compression testing

Fig. 6 Failure modes of sandstone specimens at different confining stress levels (after Li et al. 2017)



to shear failure. Many a times, rock tends to fail along some foliation planes which substantially reduces the peak strength. Shear strength along the foliation line plays a crucial role in such cases. Basu et al. (2013) observed that the rock with foliation planes like schists may fail along those foliations when the plane is at an angle to the loading direction. Failure plane can also be affected by specimen sizes. The existence of microscopic discontinuities is responsible for those “scale effects”, i.e. strength reduction with increased sample size. The larger the sample, the higher is the probability that the discontinuities will affect the strength and the sample may fail in shear mode.

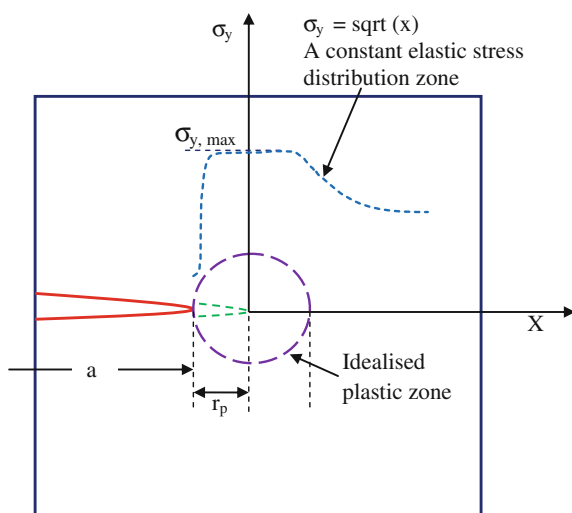
3 Crack Initiation and Propagation in Rocks

Though the effect of loading environment, end conditions, microscopic flaws, etc., contributes in characteristics strength and corresponding failure mode, a better understanding of material failure behaviour both in macroscopic and microscopic senses would depend on crack tip stress. In this respect, analysis of pre-existing crack and their corresponding growth becomes necessary. In reality, the crack tip is surrounded by the fracture process zone (FPZ) where plastic deformation occurs. FPZ is the zone in which there is small-scale yielding, micro-cracking and void initiation takes place. It is observed that plastic deformation occurs at the crack tip as a result of the high stresses. To estimate the extent of this plastic deformation, Irwin equated the yield strength to the y -direction stress along the x -axis and solved for the radius. The radius value determined was the distance along the x -axis where the stress perpendicular to the crack direction would equal to the yield strength (σ_y). Irwin found that the extent of plastic deformation was

$$r_p = \frac{1}{2\pi} \left(\frac{K}{\sigma_{y,\max}} \right)^2$$

where K is stress intensity factor. Subsequent investigations have shown that the stresses within the crack tip region are lower than the elastic stresses and that the size of the plastic deformation zone in advance of the crack is between r_p and $2r_p$. Models of an elastic, perfectly plastic material have shown that the material outside the plastic zone is stressed as if the crack were centred in the plastic zone. Figure 7 describes a schematic model of the plastic zone and the stresses ahead of the crack tip. Usually, a real crack gets blunted as a result of plastic deformation. To represent

Fig. 7 Small-scale yield model for restricted crack tip plastic deformation



the plastic deformation at the crack tip, Dugdale (1960) developed a microscopic plasticity model for ductile materials. The cohesive zone model (CZM) which is direct extension of the Dugdale (1960) and Barenblatt (1962) model considers the plasticity in linear elastic fracture mechanics. The cohesive zone model have a pre-assumption of the crack path, where crack only propagates along the boundaries of elements (FE) and the applications mainly limited to mode-I loading cases. But in the actual engineering problems, the materials are subjected to mixed-mode loading which usually advances along an unknown curved path (Xu and Yuan 2011). Using extended finite element methods (XFEM), one can simulate crack nucleation at an arbitrary material point and crack propagation in an arbitrary direction without introducing extra nodes and elements. Moreover, it allows multi-cracks nucleation, growth and coalescence without remeshing. For the present study, the finite element (FE) software “ABAQUS” is adopted with “Traction-Separation Law” that follows cohesive zone model (CZM) approach. The adopted model is subsequently verified with laboratory experiments using gypsum plaster specimens with incorporation of flaws. Figure 8 presents the generalised crack propagation patterns observed in a specimen with pre-existing flaw with clear depiction of primary (wing) crack and shear crack. Figure 9 shows the crack pattern observed with the typical experimental study for single and double flaws under uniaxial compression in gypsum plaster specimens. Figure 10 shows a typical crack pattern observed with the numerical analysis for single flaw under uniaxial compression. Figure 11 depicts the various possible modes of failure with two flaws in 2D under uniaxial compression. Figure 12 shows the corresponding FE simulation for crack initiation and propagation in gypsum plaster under uniaxial loading. Similar to the laboratory experiments, the tensile and shear cracks could be captured clearly using FE simulation. The failure happens by coalescence of micro-crack with formation of tensile and shear crack. Figure 12 clearly demonstrates the coalescence of two flaws under uniaxial loading with formation of shear and tension cracks. The failure mode is found to dependent on how crack gets interconnected to the adjacent flaws (Basu et al. 2013).

4 Summary and Conclusions

Different failure modes in rock are possible, which provides great information for safe and economic design of any structures in rocks. The ultimate failure in rocks largely depends on the fracture/crack initiation and propagation and subsequent coalescence to form a macro-crack. Rock specimens failing with longitudinal splitting show maximum strength where as specimens failing in simple or multiple shear give relatively lower strength. Confining pressure found to have significant role on deciding the failure modes. With increasing confining pressure, samples usually fail in shear. It is understood that failure mode is very significant to decide upon the true strength of rocks that in turn depends upon the crack initiation and propagation. Theoretical criteria for rock failure based on crack growth against

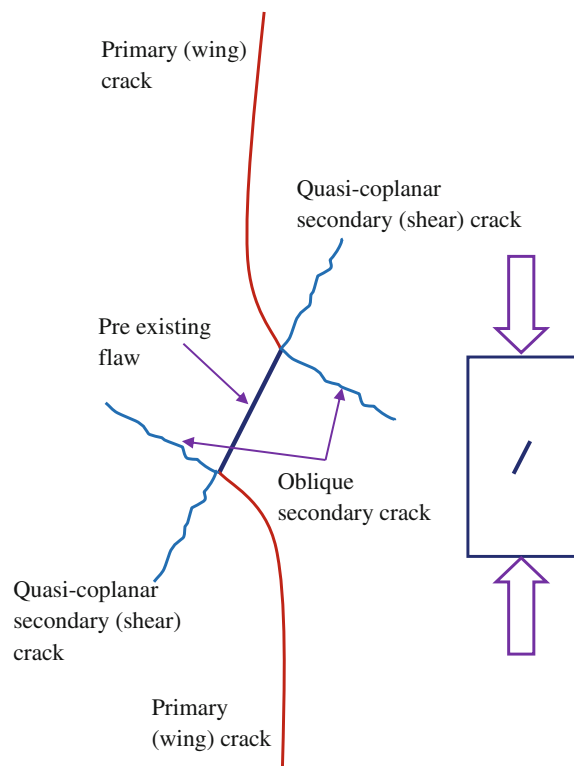


Fig. 8 Crack growth study in gypsum plaster specimen with pre-existing flaw under uniaxial loading



Fig. 9 Crack growth study in gypsum plaster specimen with pre-existing single and double flaws under uniaxial loading

Fig. 10 FE simulation of crack propagation in rock for a single pre-existing flaw

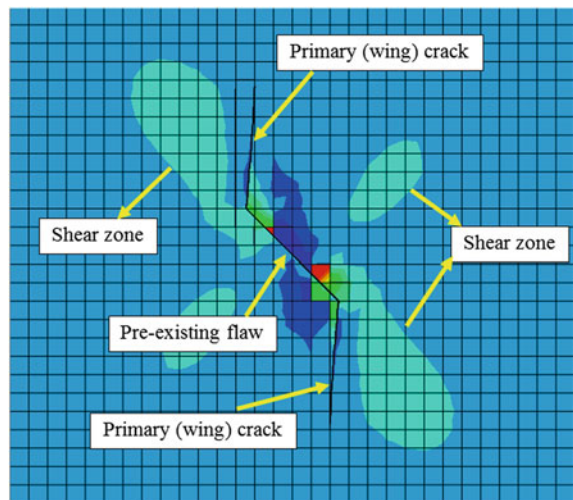


Fig. 11 Mode of failure with two flaws in 2D under uniaxial compression

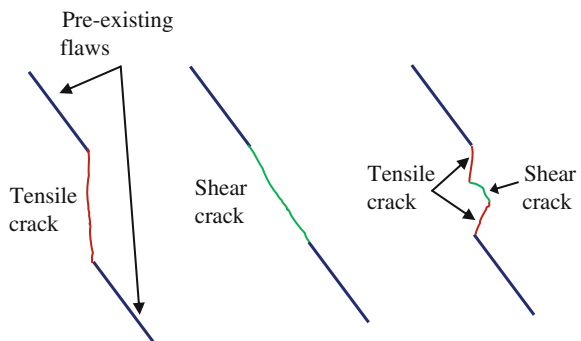
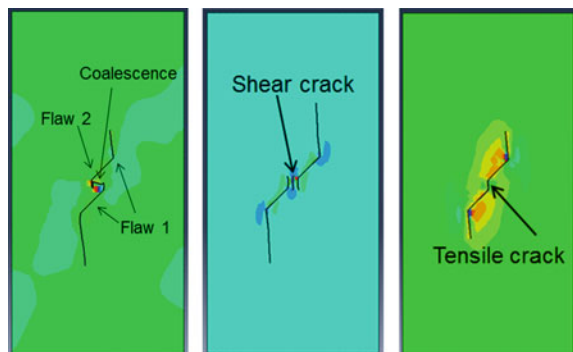


Fig. 12 FE simulation of coalescence of two flaws under uniaxial compression



experimental observations greatly advocated recent years. Moreover, numerical study on crack initiation and propagation has also significantly progressed in the last few decades. This paper presents some details on the complex failure mechanism of rocks with crack initiation and propagation characteristics. The study discusses different failure modes of brittle rock under varying stress conditions. Paper also highlighted some of the FE simulation results for analysing the crack growth.

References

Barenblatt, G. I. (1962). The mathematical theory of equilibrium of cracks in brittle fracture. *Advances in Applied Mechanics*, 7, 55–129.

Basu, A., Celestino, T. B., & Bortolucci, A. A. (2009). Evaluation of rock mechanical behaviours under uniaxial compression for different weathering grades. *Rock Mechanics and Rock Engineering*, 42(1), 73–79.

Basu, A., Mishra, D. A., & Roychowdhury, K. (2013). Rock failure modes under uniaxial compression, Brazilian, and point load tests. *Bulletin of Engineering Geology and the Environment*, 72, 457–475.

Dugdale, D. S. (1960). Yielding of steel sheets containing slits. *Journal of the Mechanics and Physics of Solids*, 8, 100–104.

Fairhurst, C., & Cook, N. G. W. (1996). The phenomenon of rock splitting parallel to the direction of maximum compression in the neighbourhood of a surface. In *Proceedings of the 1st Congress on the International Society of Rock Mechanics*, Lisbon (pp. 687–692).

Farmer, I. W., & Kemeny, J. M. (1992). Deficiencies in rock test data. In *Proceedings of the International Symposium on Eurock '92*, London (pp. 298–303).

Gonçalves da Silva, B., & Einstein, H. H. (2013). Modeling of crack initiation, propagation and coalescence in rocks. *International Journal of Fracture*, 182, 167–186.

Gramberg, J. (1989). *A non-conventional view on rock mechanics*. Rotterdam: Balkema.

Ingraffea, A. R., & Heuze, F. E. (1980). Finite element models for rock fracture mechanics. *International Journal for Numerical and Analytical Methods in Geomechanics*, 4, 25–43.

Jumikis, A. R. (1983). *Rock mechanics* (2nd ed.). Clausthal: Trans Tech Publications.

Klien, E., Baud, P., Reuschle, T., & Wong, T. F. (2001). Mechanical behavior and failure mode of Bentheim Sandstone under triaxial compression. *Physics and Chemistry of the Earth (A)*, 26, 21–25.

Lee, H., & Jeon, S. (2011). An experimental and numerical study of fracture coalescence in pre-cracked specimens under uniaxial compression. *International Journal of Solids and Structures*, 48(6), 979–999.

Li, Z., Shi, J., & Tang, A. (2017). An investigation of failure modes and failure criteria of rock in complex stress states. *The Southern African Institute of Mining and Metallurgy*, 117, 245–255.

Maji, V. B. (2011). Understanding failure mode in uniaxial and triaxial compression for a hard brittle rock. In *Proceedings of the 12th ISRM International Congress on Rock Mechanics* (pp. 723–726). Leiden: CRC Press/Balkema.

Park, C. H., & Bobet, A. (2009). Crack coalescence in specimens with open and closed flaws: A comparison. *International Journal of Rock Mechanics and Mining Sciences*, 46(5), 819–829.

Park, C. H., & Bobet, A. (2010). Crack initiation, propagation and coalescence from frictional flaws in uniaxial compression. *Engineering Fracture Mechanics*, 77(14), 2727–2748.

Paul, B., & Gangal, M. (1966). Initial and subsequent fracture curves for biaxial compression of brittle materials. In *Proceedings of the 8th US Symposium on Rock Mechanics*, Baltimore (pp. 131–141).

Peng, S., & Johnson, A. M. (1970). Crack growth and faulting in cylindrical specimens of chelmsford granite. *International Journal of Rock Mechanics and Mining Sciences*, 9, 37–86.

Prudencio, M., & Van Sint Jan, M. (2007). Strength and failure modes of rock mass models with non-persistent joints. *International Journal of Rock Mechanics and Mining Sciences*, 44, 890–902.

Reinhart, J. S. (1966). Fracture of rocks. *International Journal of Fracture Mechanics*, 2, 534–590.

Reyes, O., & Einstein, H. H. (1991). Failure mechanism of fractured rock-a fracture coalescence model. In *Proceedings of the Seventh International Congress on Rock Mechanics* (vol. 1, pp. 333–40).

Sagong, M., & Bobet, A. (2002). Coalescence of multiple flaws in a rock-model material in uniaxial compression. *International Journal of Rock Mechanics and Mining Sciences*, 39, 229–241.

Santarelli, F. J., & Brown, E. T. (1989). Failure of three sedimentary rocks in Triaxial and hollow cylinder compression tests. *International Journal of Rock Mechanics and Mining Sciences & Geomechanics Abstracts*, 26(5), 401–413.

Szwedzicki, T. (2007). A hypothesis on modes of failure of rock samples tested in uniaxial compression. *Rock Mechanics and Rock Engineering*, 40(1), 97–104.

Szwedzicki, T., & Shamu, W. (1996). Detection of planes of weakness in rock samples using non-destructive testing method. In *Proceedings of '96 International Symposium on Mining Science and Technology*, China (pp. 759–763). Rotterdam: AA Balkema.

Tavallali, A., & Vervoort, A. (2010). Effect of layer orientation on the failure of layered sandstone under Brazilian test conditions. *International Journal of Rock Mechanics and Mining Sciences*, 47, 313–322.

Vasarhelyi, B., & Bobet, A. (2000). Modeling of crack initiation, propagation and coalescence in uniaxial compression. *Rock Mechanics and Rock Engineering*, 33(2), 119–139.

Wong, L. N. Y., & Einstein, H. H. (2009a). Crack coalescence in molded gypsum and Carrara marble: Part 1—Macroscopic observations and interpretation. *Rock Mechanics and Rock Engineering*, 42(3), 475–511.

Wong, L. N. Y., & Einstein, H. H. (2009b). Crack coalescence in molded gypsum and Carrara marble: Part 2—Microscopic observations and interpretation. *Rock Mechanics and Rock Engineering*, 42(3), 513–545.

Xie, Y., Cao, P., Liu, J., & Dong, L. (2016). Influence of crack surface friction on crack initiation and propagation: A numerical investigation based on extended finite element method. *Computers and Geotechnics*, 74, 1–14.

Xu, Y., & Yuan, H. (2011). Applications of normal stress dominated cohesive zone models for mixed-mode crack simulation based on extended finite element methods. *Engineering Fracture Mechanics*, 78, 544–558.

Retrofitting of N–W Corner of Kolkata High Court Heritage Building Through Micropiles and Grouting

Satyendra Mittal and G. L. Sivakumar Babu

Abstract Monumental buildings keep experiencing the distresses due to weathering effects or other reasons. Micropiling had been found very useful for retrofitting works (Srivastava et al. in stability analyses of 18 m deep excavation using micropiles. IGC, N, Delhi, 2016). Kolkata High Court building is a beautiful, majestic building, built in 1872, over a large area, along Hooghly River. The North–West (N–W) corner of the building had experienced some settlement in the year 2014–2015. Authors had inspected the building in December 2015 and again in February 2016. The site visit report indicated that there was differential settlement of shallow foundation of building in its N–W corner. Ingress of Hooghly River water up to foundation was one of the possibilities of distress in foundation. The micropiling followed by grouting was found the most appropriate solution for the site. The site solutions shall be instrumented also over a period of 10 years or so, to periodically monitor the settlement, if any, of building after the treatment.

Keywords Micropile · Ground improvement · Retrofitting · Grouting
Monumental building

1 Introduction

Kolkata High Court building is one of the monumental buildings of Kolkata and is founded on soft soils. Its construction work was completed in 1872. In the year 2014, the building experienced distress in the form of cracks in the super structure at different locations, due to settlement of the foundations.

S. Mittal (✉)

Department of Civil Engineering, IIT Roorkee, Roorkee 247667, India
e-mail: satyendramittal@gmail.com

G. L. Sivakumar Babu

Department of Civil Engineering, IISC Bangalore, Bangalore, India
e-mail: glsivakumar@gmail.com

Authors of this paper visited the site in the months of December 2015 and May 2016 to probe into the reasons of settlement of building. It was decided to get the soil investigation done at this site. The PWD authorities confirmed that there was no event like earthquake, etc., at this site. However, ingress of water into foundation from Hooghly River could not be ruled out as it was flowing hardly 300 m away from the N to W corner of the high court building. Based on the detailed soil investigation report and the site visits, micropiling and grouting were found the most appropriate solutions for this site. It was informed by site officials that the stresses due to vertical loads were in the range of 22–24 t/m². During the site visit, it was noted that differential settlements were in the range of 8 mm or so. The damages are shown in Figs. 1, 2, 3 and 4.

Fig. 1 A view of cracks in wall (outer view of N–W wall)



Fig. 2 Damage seen on the wall



Fig. 3 Distinct cracks seen on wall (N-W) side



Fig. 4 Differential settlement in floor



2 Subsoil Conditions

The soil investigations were performed by Civil Engineering Department of Jadavpur University Kolkata. Information from six number of boreholes, including field testing using SPT and laboratory tests, has been used to understand the type of soils, location of water table, etc. Results in general show that the soil profile is variable in nature and the groundwater table is at around 2.3 m level (during non-monsoon period) and around 1.5 m (during monsoon period). Typical foundation has width of 2.13 m and is resting on filled up compacted soil varying from 1.5 to 5 m. It is followed by soft clay of undrained strength varying in the range of

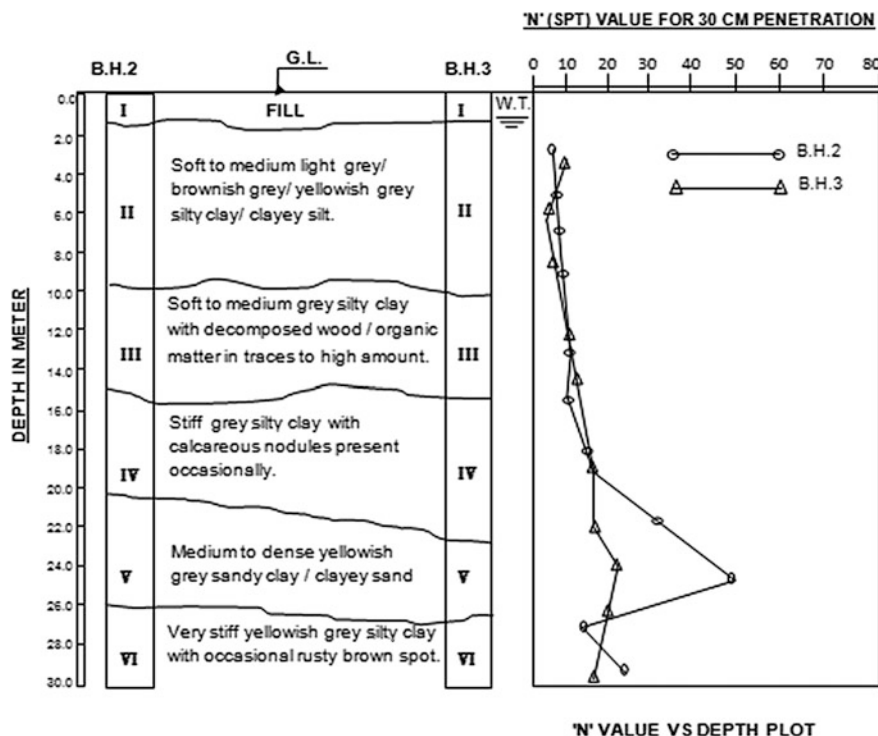


Fig. 5 Soil profile log at Kolkata High Court site

3.6 t/sqm. Typical soil has stiffness of about 8–10 MPa (evaluated from consolidation tests) and is considered to be low to medium and is expected to lead to settlements when there is increase in loads (Mittal and Shukla 2014). The representative bore log of site is shown in Fig. 5.

3 Possible Solutions for the Site

It was informed by site officials during the site visit that the stresses due to vertical loads were in the range of 22–24 t/m². During the field visit, it was noted that differential settlements were in the range of 8 mm (at three locations, the settlements were in the range of 6, 7 and 8 mm, respectively) over a period of about six months and are the clear indication of excessive distresses noted. Hence, immediate ground improvement of the foundation soil was necessary. It was proposed that in addition to the micropiles suggested, grouting should also be used to improve the ground below the foundations. For the purpose of analysis, properties of micropiles given in Table 1 have been proposed to be used. Figure 6 shows the configuration

Table 1 Properties of the in situ soil and improved soil

	In situ properties	Improved properties
<i>Properties layer 1 (0–3 m)</i>		
Unit weight (kN/m ³)	18	18
Young's modulus (kPa)	20,000	40,000
Poisson's ratio	0.2	0.2
Cohesion (kPa)	10	40
Friction angle (°)	20	30
<i>Properties layer 2 (3–6 m)</i>		
Unit weight (kN/m ²)	18	18
Young's modulus (kPa)	15,000	35,000
Poisson's ratio	0.35	0.35
Cohesion (kPa)	36	60
Friction angle (°)	1	25
<i>Properties layer 3 (6–17 m)</i>		
Unit weight (kN/m ²)	17	17
Young's modulus (kPa)	10,000	25,000
Poisson's ratio	0.35	0.35
Cohesion (kPa)	20	40
Friction angle (°)	1	25

of micropiles. Hollow steel pipes of 125 mm diameter and 3 mm thick at 250 mm spacing (c/c) for 9 m length are suggested as micropiles. In addition, four bars of 20 mm diameter (or 12 mm diameter) made of Fe 500 steel with proper centralizer to keep them at the centre and filling the annular space with M 20 concrete are suggested. The grouting of the foundation soil has also been suggested. As the material is clay, grouting using resins/cement has been suggested. Literature shows that cement/resin grouting improves the strength and stiffness of the soft soils (Mittal 2016). For considering the effect of grouting, the properties of the original ground are assumed to be increased. The improved properties in terms of stiffness, strength, cohesion and friction angle are given in Table 1.

For the sake of analysis (conducted through Plaxis 2010 software), two cases were considered in the current study, one is without ground improvement and other with ground improvement with micropiles. Mohr–Coulomb soil model was provided for all the soil layers. Table 1 shows the properties of soil used for the analysis and also the improved properties of the soil after the ground improvement. As there was excessive mesh deformation when the footing was provided below the surface, the soil above the footing was provided as a surcharge loading. This provided the results slightly on the conservative side. A surcharge loading of 38 kN/m² was provided as the surcharge loading corresponding to 1.9 m overburden soil. Groundwater table was considered to be 3 m depth. A loading of 400 kN/m² was applied as the footing stress, and the loading was provided in increments.

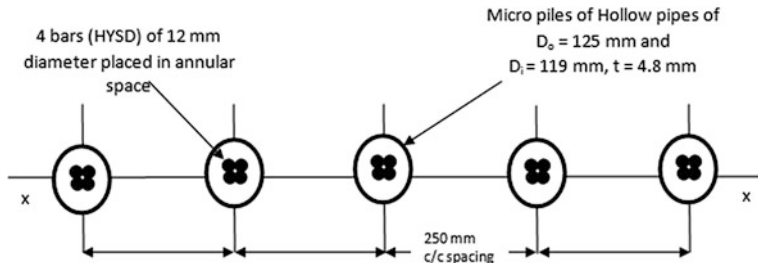


Fig. 6 Scheme for micropiles

Figure 6 shows the scheme for layout of piles. Figure 7 shows the mesh generated for the initial condition without ground improvement, and Fig. 8 shows the model with ground improvement and micropiles. Micropiles were provided at 0.4 m away from the edge of footing. Micropiling is suggested from analysis, up to a depth of 9 m below the footing load. Figures 7 and 8 show the deformed meshes for both the cases. Figure 9 shows the load—displacement curve for both the cases. Boundaries of the mesh have been provided at adequate distance away from the loading point.

The properties of the micropiles were calculated as per Srivastava and Babu (2016). The EI value was taken as $2 \times 10^6 \text{ kN-m}^2/\text{m}$, and EA value taken was 1743 kN/m.

From Fig. 9, it is clear that for in situ condition, the soil fails well below the applied load of 400 kN/m^2 . For the improved ground, the ultimate load is reached when the displacement reaches a value of 36 mm. The existing stress being in the range of 240 kN/m^2 ; the corresponding displacements are less and will take care of further loading as well.

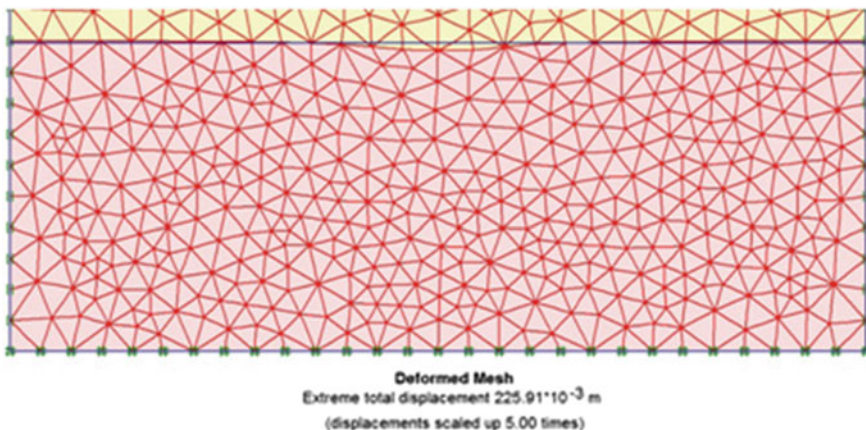


Fig. 7 Deformed mesh after loading (sample fails below ultimate load) in the in situ case without ground improvement

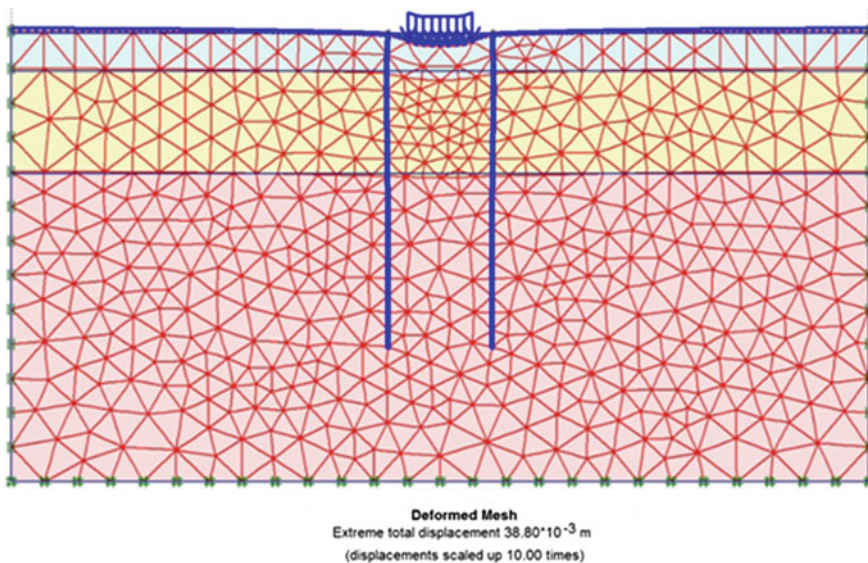


Fig. 8 Deformed mesh after loading for case with ground improvement and micropiling

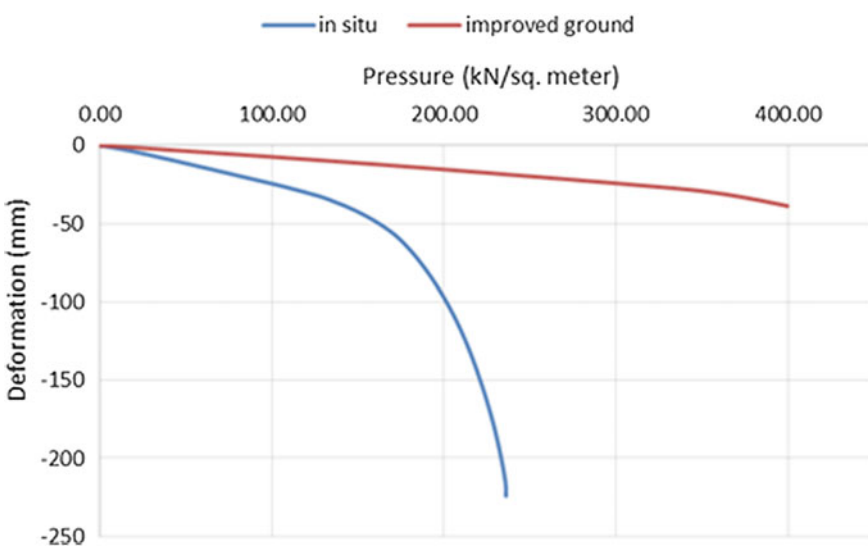


Fig. 9 Load versus displacement curve for in situ soil and improved ground

4 Grouting Technology

At the high court site, the water table is at around 2.3 m depth or so. The River Hooghly is also towards North-West side and is hardly at a crow distance of 250–300 m from high court building. Hence, regular seepage of river water towards high court building cannot be ruled out. Further, in N–W corner only, library of HIGH COURT is situated, where very high loads of periodicals and journals were also noted during site visit of authors. Hence, it has been strongly recommended to do grouting around foundation and up to minimum of 3 m depth below the foundation. The grouting shall be done after construction of micropiles. Since it is steel micropile, it will be very quick to install. The concreting shall also be done (poured) within pipe itself.

5 Construction Methodology

5.1 *Construction of Micropiles*

The micropiles shall be made of hollow pipes with O.D as 125 mm and ID as 119 mm (Mittal 2016). In the pipe, 4 bars of 20 diameter each (or 12 diameter each) shall be placed duly tied up with GI wire and then M 20 concrete slurry shall be poured in the annular space left there. The c/c spacing of vertical micro plies shall be 250 mm as shown in Fig. 6. The distance of micropile shall be 3 times of diameter of micropile (i.e. 375 mm, say 400) from outer edge of foundation as shown below (Fig. 10). The micropile shall have a pointed shoe at the bottom for ease in driving. It is worth mentioning here that micropiling shall be done only outside the building (i.e. on the external side only) and pipe will be left into ground permanently. Thus, it will be sacrificial pipe.

It has also been suggested to protrude micropile 250 mm outside existing floor level of building on its outside, and these protruded portions of all micropiles shall be tied up with a RCC beam or jointed by a channel section of suitable size. This capping beam shall provide additional and composite rigidity.

6 Grouting Process

Grouting shall be done after the micropiling is done. Here, grouting has been proposed with resins (instead of cement slurry). “DRUCSTONE” grout material is one such material and is popular in international market. It is difficult for the authors of this report to provide generic names of grouting material. It is recommended that grouting be done with a very high grout pressure under the supervision of a very competent geotechnical engineer. Grouting shall be done within at least 3 m depth

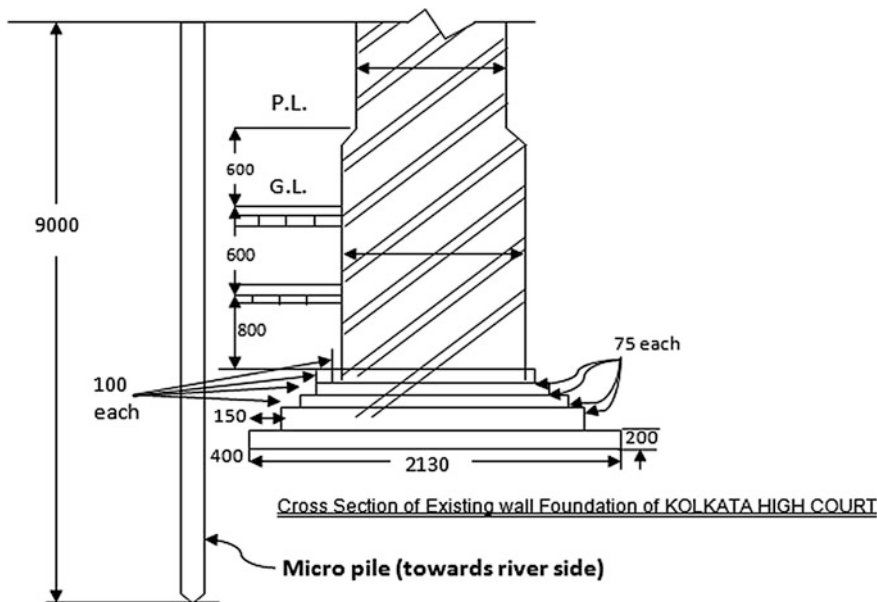
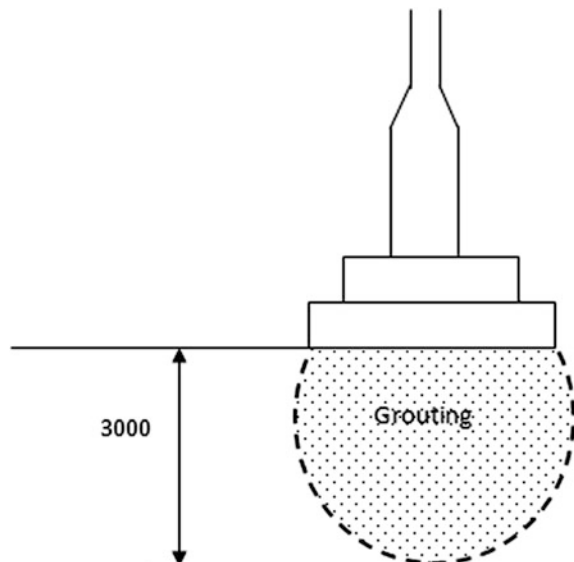


Fig. 10 Schematic of micropile

below the footing level (Fig. 11). The grouting fluid dose should be about 25–50% of wt. of soil present their at site (i.e. wt. of soil present from NGL up to minimum 3 m depth from there to be treated with grout). Thus, after calculating that area,

Fig. 11 Grouting area
(grouting to be done on both
sides of foundation)



the bulk volume of soil can be determined, and thereby weight of in situ soil should be determined. The grouting of in situ soil mass shall help in two ways, e.g.

- (a) Reduction of permeability
- (b) Increasing in situ bearing capacity of soil.

Grouting pressure shall be applied in two stages. In first stage, grout pressure should be minimum 1.5 bar, and at second stage, the pressure shall be around 5 bar. Gradual pressure increment shall be done within 30–40 s in second grade viscosity. Grouting shall be done through perforated pipe with valves and shall be strictly in accordance with ASTM C881 standards. The nozzle diameter of grout tube shall be commensurate with the pressure to be applied for grouting, as per standard practices.

Some pilot tests were conducted in IIT Roorkee Labs to see the effect of grouting on soil mass, and the results were encouraging.

7 Instrumentation

The combination of micropiling and grouting, as discussed above in the report, is believed to control the ingress of water into foundation, provide a confinement to the existing foundation and also increase the bearing capacity of existing foundation. It has been, however, also recommended to do some instrumentation to monitor the results from these proposed solutions. The instrumentation is proposed for following:

- (a) To monitor further sinking of foundation, if any, using VW type settlement system.
- (b) To monitor any possible tilt of building by using vibrating wire tilt meter.
- (c) To monitor developments of new cracks, if any, after adopting all treatment measures, by installing VW crack meter.

8 Concluding Remarks

- (a) For the present case, use of micro piling followed by grouting of the soft soil is suggested for improving the condition of the existing ground. It is quite possible that after the implementation of the ground improvement techniques, further deformations and movements are unlikely. However, to correct the profile of the ground, either the flooring needs to be redone or techniques that correct the profile without disturbing the set-up may be used.
- (b) Before taking of retrofitting work, the excessive load of books in the library needs to be reduced. All the book racks kept in NW directions should be immediately shifted to opposite direction.

- (c) The micropile pipes shall be left into the ground only and shall never be withdrawn from ground.
- (d) The instrumentation shall help in monitoring the performance of foundation of high court building post construction.

References

Mittal, S. (2016). *An introduction to ground improvement engineering*. N. Delhi: SIPL Publications House.

Mittal, S., & Shukla, J. P. (2014). *Soil testing for engineers*. N. Delhi—110006: Khanna Publishers.

Plaxis. (2010). *Plaxis user manual*. The Netherlands: Delft University of Technology & Plaxis bv.

Srivastava, A., Kumar, P., & Babu, G. L. S. (2016). *Stability analyses of 18 m deep excavation using micro piles*. Delhi: IGC, N.

Meethotamulla Landfill Failure Analysis: A Probabilistic Approach

B. Munwar Basha and K. V. N. S. Raviteja

Abstract This paper assesses the possible conditions that might have resulted in the recent catastrophic failure of the Meethotamulla landfill slope at Colombo. This paper presents a probabilistic approach to find the different combinations of parameters that might have caused the collapse of landfill slope. A performance function is formulated, and the reliability of the slope is assessed using first-order reliability method (FORM). The factor of safety associated with various slip surfaces are computed with different combinations of mean and COV. The results obtained from the reliability analysis based on FORM agree closely with the reported post-failure investigations. The analysis elucidated the possible causes of landfill slope failure. The outcome of the analysis can be utilized for finding a remediation with improved knowledge about the shear strength parameters of the solid waste. The probabilistic analysis conducted in the present work reveals that the mean value of shear strength parameters of MSW and its associated variability responsible for the collapse of Meethotamulla garbage dump are friction angle, $\phi = 20^\circ$ and stability number, $c/\gamma H = 0.05$. The reliability analysis proved that the most likely reason for the dump failure is the reduction in shear strength parameters of the MSW. The excessive rainfall might have triggered the reduction in shear strength parameters. The analysis of Meethotamulla garbage dump disaster demonstrated that it is very essential to conduct reliability analysis as realistically as possible to find the conditions that have triggered the collapse.

Keywords Meethotamulla landfill · Probabilistic approach · MSW slopes
Reliability analysis · Variability

B. Munwar Basha (✉) · K. V. N. S. Raviteja
Department of Civil Engineering, IIT Hyderabad, Kandi, Sangareddy, India
e-mail: basha@iith.ac.in

K. V. N. S. Raviteja
e-mail: kvnsravi.teja@gmail.com

1 Introduction

The Meethotamulla garbage dump near Colombo has been collapsed in the early hours of April 14, 2017, killing more than 32 people and injuring several others. Figure 1 shows the failure wedge on the southwest side of the landfill. Nearly 146 houses were buried under the mounds of garbage, and the houses in the nearby area were damaged severely affecting 198 families (NBRO 2017). Approximately 72,342 m³ of waste has been moved during the failure (NBRO 2017), making it as the second major solid waste landslide of this year. Figure 2 shows some of the devastating effects of the landfill slope failure.

Meethotamulla is the largest open dump at Colombo receiving approximately 3,28,500 m³ of solid waste annually. It occupied an area of 78,000 m² spreading 413 m along NW–SE direction and 189 m in NE–SW direction. The height of the dump was varying from 45 to 50 m with an inclination of 35°–60° (SW direction) with the horizontal. At the time of failure, the subsided waste demolished the houses at the bottom running 40 m forward beyond the toe in the SW direction. Figure 3 shows the approximate contours to indicate the movement of failed solid waste mass beyond the toe. Dumping at Meethotamulla site has been commenced before 1998. Over the last 15 years, there is a tremendous increase in MSW quantity at the landfill facility. At the time of failure, the landfill is receiving an average of 850 tons of solid waste per day. It is reported that the slope has undergone progressive failure, which blocked a canal at the southwest side, resulting in the inundation of houses in the southeast direction.

The preliminary studies conducted by NBRO (2017) revealed that there was no proper regulation for disposing the waste at Meethotamulla landfill. Further, there were no proper compaction and working methodologies. It is reported that there were no cover and liners to avoid the infiltration of rainwater, which led to build up



Fig. 1 Meethotamulla solid waste landfill: failed slope in the southwest direction (*Source SLAF media*)



Fig. 2 Meethotamulla landfill slope failure in the southwest direction (Source SLAF media)



Fig. 3 Contours indicating the movement of failed wedge in the southwest direction (Source Google Earth)

the pore pressure within the solid waste mass. A drain is formed naturally in the southwest direction with the generated leachate and rainwater as there is no leachate collection system and drainage system installed in the landfill (NBRO 2017).

Based on the information available from the preliminary studies reported in the literature, the present work investigates the possible causes that may have triggered the slope failure. The solid waste of Meethotamulla landfill comprises high amounts of organic and plastic wastes indicating the lower density profile of waste. The primary objective of the present work is to analyze the causes that triggered the slope failure in the probabilistic framework. The probabilistic analysis is an efficient technique to address the multiple random parameters that affected the failure while accounting the variability. The significance of the probabilistic approaches in addressing the slope failures is well presented in the recent and past by several

researchers (Gilbert et al. 1998; Tang et al. 1999; Zhang et al. 2010; Jahanfar et al. 2017). The probabilistic analysis used in this study advances the vector containing uncertain input variables based on the available information. The distribution type for the shear strength parameters and unit weight of the solid waste were taken from the recent study reported by Basha and Raviteja (2017).

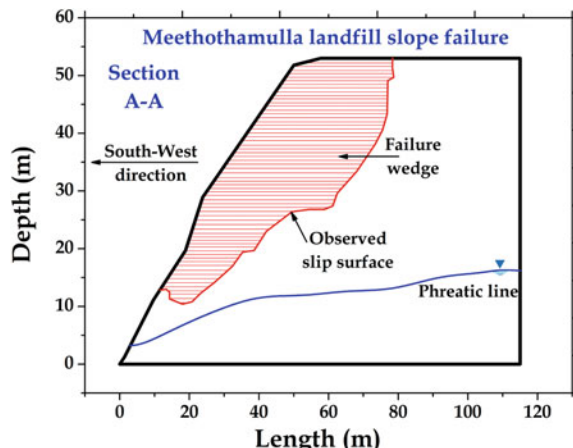
2 Methodology

The geometry of the landfill is shown in Fig. 4, which is digitized from the geometrical model reported by NBRO (2017). Figure 4 shows the cross section of the landfill in the SW direction as indicated in Fig. 3. The amount of solid waste involved the failure was indicated in the figure, and it can be noted that the slip surface is formed above the phreatic line.

It is reported that the waste fill is highly heterogenous, and the parameters of the solid waste were varying considerably within the slope. The bottom section of the landfill comprises highly decayed waste, and the upper section of the landfill comprises highly organic waste similar to every other case. However, the intermediate layers of the landfill are found to be wet due to the precipitation that lasted for weeks. Wet surface was exposed immediately after the failure beneath the failure wedge. Preliminary studies reported that the underlain wet conditions and the steepness of the slope are the major causes for the failure. As the major portion of the landfill comprises the decomposed waste, which is stiff, the failure should be restricted to the crest portion. However, from Fig. 4 it can be depicted that the slip surface is extended almost up to the toe portion of the landfill. Despite all the conditions stated above, the actual cause of the landfill slope failure is unknown.

In this study, the effect of the parameters (c , ϕ , and γ) over the factor of safety (FS) is studied. The stability of the slope is analyzed using Morgenstern–Price

Fig. 4 Sectional geometry of the landfill in the southwest direction (sec A-A) showing observed slip surface and the failure wedge



method using probabilistic framework by assuming that all the input parameters are uncorrelated. The initial mean values and COV ranges of the shear strength parameters are chosen based on the statistical study reported by Basha and Raviteja (2017). Various combinations of mean and COV values associated with shear strength parameters of MSW are analyzed to obtain the most critical slip surface that closely resembles the observed slip surface.

The critical center coordinates (X_{tc} , Y_{tc} , R_{tc}) of the chosen trial runs is checked with the critical coordinates of observed failure surface (X_{oc} , Y_{oc} , R_{oc}) in accordance with the constraints shown in Eq. (1). The corresponding mean and COV values are considered in the further analysis. A few of the trial set combinations are presented in Fig. 5. As the present study deals with the landfill slope that was failed, the mean and COV values that are responsible for the failure can be determined from the reliability analysis. The FS equations for the Morgenstern–Price method of slices and the corresponding performance function are presented in Eqs. (2), (3), and (4), respectively.

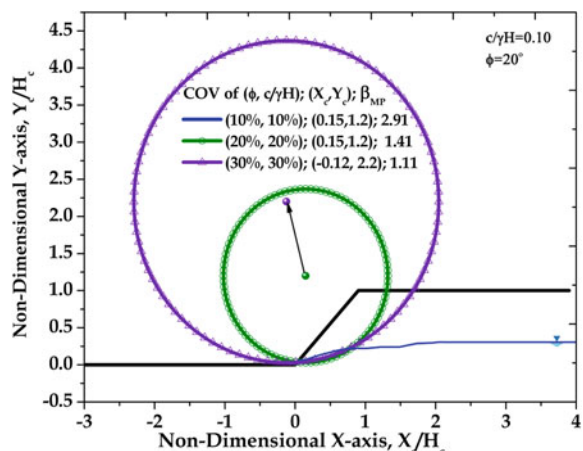
$$\text{Find } (X_c, Y_c, R_c) \left\{ \begin{array}{l} \text{which gives } (X_{tc}, Y_{tc}, R_{tc}) \approx (X_{oc}, Y_{oc}, R_{oc}) \\ \text{subjected to } g_{MP}(X) = 0 \end{array} \right. . \quad (1)$$

The force and moment equilibrium equations are given below:

$$\text{FS}_f = \frac{\sum_{i=1}^n (cdl_i + N'_i \tan \phi) \cos \theta_i}{\sum_{i=1}^n (N'_i + u_i b \sec \theta_i) \sin \theta_i} \quad (2)$$

$$\text{FS}_m = \frac{\sum_{i=1}^n (cdl_i + N'_i \tan \phi) R}{\sum_{i=1}^n w_i R \sin \theta_i} \quad (3)$$

Fig. 5 Combined influence of COV of $(\phi, c/\gamma H)$ on the critical centers and the reliability index against slope failure



The normal force acting at the base of the slice (N'_i) can be written as

$$N'_i = \frac{w_i + X_i - X_{i-1} - u_i b \sec \theta_i \cos \theta_i - \frac{cb \sec \theta_i \sin \theta_i}{F}}{\cos \theta_i + \frac{\tan \phi \sin \theta_i}{F}}$$

where c = mobilized cohesion at the base of the slice, N'_i = normal force acting at the base of the slice, θ_i = base angle of the slice, R = radius of the slip circle, and w_i = weight of the slice.

The performance function for the solid waste slope can be written as:

$$g_{MP}(X) = FS_{MP} - 1 \quad (4)$$

The proposed analysis is based on the first-order reliability method (FORM). The magnitudes of γ , c , and ϕ corresponding to a given target reliability index (β_{MP}) can be written as

$$\gamma = \mu_\gamma - \sigma_\gamma \beta_{MP} \left(\frac{\frac{\partial G}{\partial \gamma} \sigma_\gamma}{\sqrt{\left\{ \frac{\partial G}{\partial \gamma} \sigma_\gamma \right\}^2 + \left\{ \frac{\partial G}{\partial c} \sigma_c \right\}^2 + \left\{ \frac{\partial G}{\partial \phi} \sigma_\phi \right\}^2}} \right) \quad (5)$$

$$c = \mu_c - \sigma_c \beta_{MP} \left(\frac{\frac{\partial G}{\partial c} \sigma_c}{\sqrt{\left\{ \frac{\partial G}{\partial \gamma} \sigma_\gamma \right\}^2 + \left\{ \frac{\partial G}{\partial c} \sigma_c \right\}^2 + \left\{ \frac{\partial G}{\partial \phi} \sigma_\phi \right\}^2}} \right) \quad (6)$$

$$\phi = \mu_\phi - \sigma_\phi \beta_{MP} \left(\frac{\frac{\partial G}{\partial \phi} \sigma_\phi}{\sqrt{\left\{ \frac{\partial G}{\partial \gamma} \sigma_\gamma \right\}^2 + \left\{ \frac{\partial G}{\partial c} \sigma_c \right\}^2 + \left\{ \frac{\partial G}{\partial \phi} \sigma_\phi \right\}^2}} \right) \quad (7)$$

The reliability index against slope failure can be computed as:

$$\beta = \frac{- \sum_{j=1}^n u_k \left[\sum_{i=1}^n \frac{\partial g}{\partial x_k} (\sigma_i) \right]}{\sqrt{\sum_{j=1}^n \left\{ \sum_{i=1}^n \frac{\partial g}{\partial x_k} (\sigma_i) \right\}^2}} \quad (8)$$

The analysis starts with an initial set of parameters and proceeds with various combinations of the parameters until the convergence criteria are met.

3 Results and Discussion

The slip circle that evolves closely with the observed slip surface is considered as the most appropriate failure plane that possesses the set of parameters that might have caused the instability of slope. Figure 5 shows the combined influence of ϕ and $c/\gamma H$ over the formation of slip surfaces and the critical centers. It can be noted from Fig. 5 that for constant mean values of $\phi = 20^\circ$ and $c/\gamma H = 0.10$, the critical slip surfaces are moving toward the crest of the slope when the COV values increase from 10 to 30%. The radius of the slip circle also increases due to the movement of critical centers away from the crest portion. Further, the volume of the solid waste included in the failure wedge increases with increase in the COV due to heterogeneity. Table 1 gives the detailed information about the critical centers and radius of the slip surfaces. The reduction in the reliability index with increase in the COV can be clearly noted from Fig. 5. Moreover, it can be noted from Fig. 5 that a 62% reduction in the magnitude of reliability index when COVs of ϕ and $c/\gamma H$ increase from 10 to 30%. The magnified portion of the slip surfaces within the MSW slope is presented in Figs. 6, 7, and 8. These figures are also used to compare the critical slip surfaces with the observed slip surface.

The influence of mean and COV values of ϕ and $c/\gamma H$ over the slip surfaces is shown in Figs. 6, 7, and 8. The trial slip surfaces are compared with the observed slip surfaces to predict the values of shear strength parameters of MSW at failure condition. Figure 6 shows the sixteen slip surfaces for different mean combinations of ϕ and $c/\gamma H$ and the corresponding values of FS_{MP} and β_{MP} for COV of $\phi = 10\%$ and COV of $c/\gamma H = 10\%$. It can be noted that for higher mean values of ϕ and $c/\gamma H$, the magnitudes of FS_{MP} and β_{MP} are indicating that the slope is safe and stable. The trial slip surface with $c/\gamma H = 0.05$, $\phi = 20^\circ$ is found to closely resemble the actual slip surface. The FS_{MP} and β_{MP} for the trial slip surface are 0.89 and -1.58, respectively, which indicates the probable values at the time slope failure. The selection of trial slip surface is based on the radius, critical centers, mean values, and the practical judgment. Similarly, the trial slip surfaces that closely resemble the observed slip surface are obtained for COVs of ϕ and $c/\gamma H$ with 20 and 30%, respectively, and presented in Figs. 7 and 8. Interestingly, the trial slip surface corresponds to $c/\gamma H = 0.05$ and $\phi = 20^\circ$ that closely resembles the actual slip surface at the same critical centers and same radius for all the COV values. However, the β_{MP} value is not same as it depends on the magnitude of the

Table 1 Combined influence of various sets of COV of ϕ and $c/\gamma H$ on the critical centers of probabilistic slip surfaces and the β_{MP} against landfill slope failure at $c/\gamma H = 0.05$ and $\phi = 20^\circ$

COV of ϕ (%)	COV of $c/\gamma H$ (%)	X_c/H	Y_c/H	R_c/H	β_{MP}
10	10	-0.67	2.00	2.08	-1.58
20	20	-0.67	2.00	2.08	-0.84
30	30	-0.67	2.00	2.08	-0.62

Fig. 6 Comparison of observed slip surface and trial slip surfaces for different combinations of the mean values of $c/\gamma H$ and ϕ for COV of $c/\gamma H = 10\%$ and COV of $\phi = 10\%$

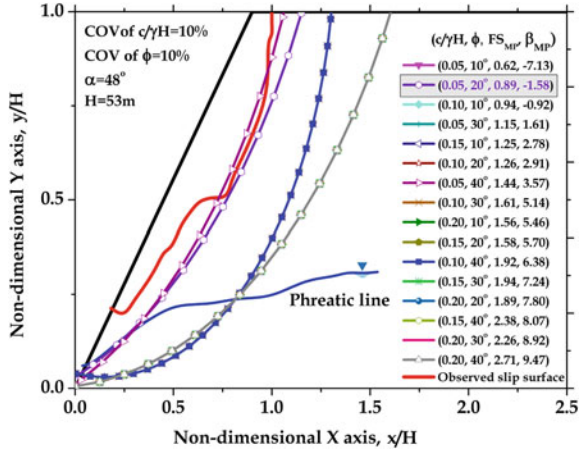
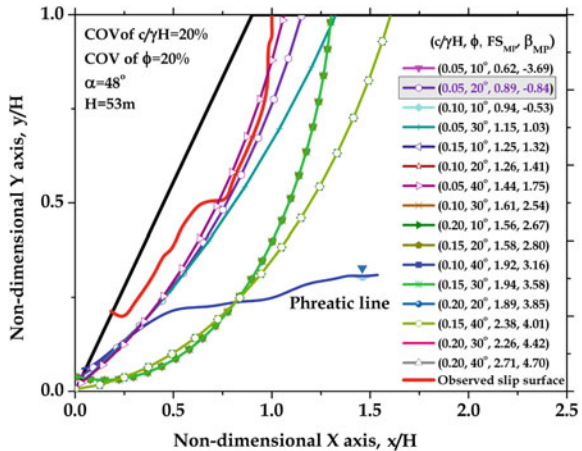


Fig. 7 Comparison of observed slip surface and trial slip surfaces for different combinations of the mean values of $c/\gamma H$ and ϕ for COV of $c/\gamma H = 20\%$ and COV of $\phi = 20\%$



COV. The water table is given due consideration while evaluating the slip surfaces. Figure 6 that the observed slip surface is above the phreatic level.

It can be noted that the β_{MP} in all the three cases is negative, which indicates that the expected performance level is hazardous as per USACE (1997). The magnitude of FS_{MP} also indicates that the slope is not stable. Therefore, it can be concluded from the present study that the mean values of $c/\gamma H = 0.05$ and $\phi = 20^\circ$ are probably mean shear strength parameters of the MSW with COV of 10% associated with the failure.

Further, to study the influence of variability associated with parameters on the slope reliability, design charts are presented with different combinations of mean and COV values. Figures 9, 10, and 11 show the influence of mean values of shear strength parameters on FS_{MP} and combined influence of mean and COVs on the reliability index (β_{MP}).

Fig. 8 Comparison of observed slip surface and trial slip surfaces for different combinations of the mean values of $c/\gamma H$ and ϕ for COV of $c/\gamma H = 30\%$ and COV of $\phi = 30\%$

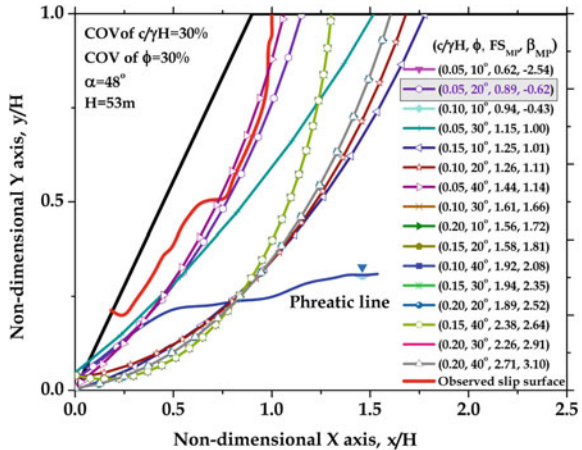
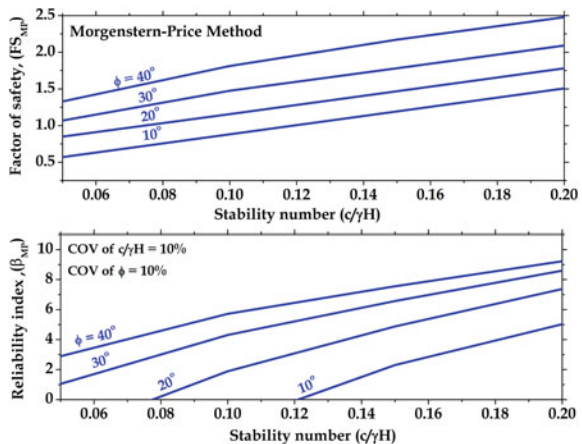


Fig. 9 Influence of mean values of ϕ and $c/\gamma H$ on FS_{MP} and β_{MP} for COV of $\phi = 10\%$ and COV of $c/\gamma H = 10\%$



It is clear to note from Fig. 9 that with increase in the mean value of ϕ from 10° to 40° , there is a considerable increase in the factor of safety (FS_{MP}) as well as reliability index (β_{MP}), for any constant value of $c/\gamma H$. It can also be observed that with increase in $c/\gamma H$ values from 0.05 to 0.20, the factor of safety (FS_{MP}) and reliability index (β_{MP}) are considerably affected. This is due to the fact that increase in the mean values of shear strength parameters enhances the slope stability. However, the increment in the value of β_{MP} is more than the increment in FS_{MP} value as the β_{MP} value is influenced by the mean and COVs of ϕ and $c/\gamma H$ values. Nevertheless, the conventional factor of safety, FS_{MP} , is influenced only by mean values of ϕ and $c/\gamma H$. Similar observations are shown in Figs. 10 and 11 which are presented for the COVs of 20 and 30%, respectively. The reliability approach projects the more realistic conditions and shows a potential change in the slope performance for increased COV values.

Fig. 10 Influence of mean values of ϕ and $c/\gamma H$ on FS_{MP} and β_{MP} for COV of $\phi = 20\%$ and COV of $c/\gamma H = 20\%$

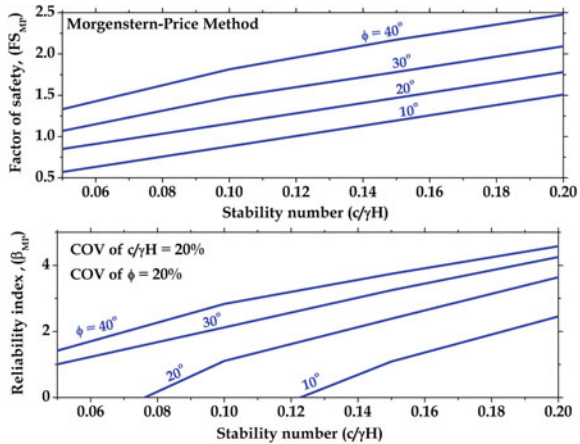
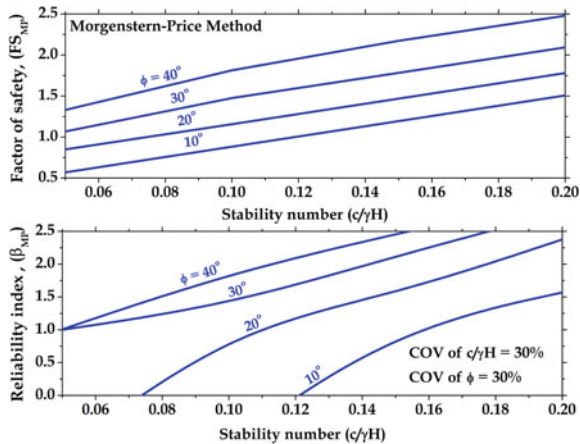


Fig. 11 Influence of mean values of ϕ and $c/\gamma H$ on FS_{MP} and β_{MP} for COV of $\phi = 30\%$ and COV of $c/\gamma H = 30\%$



4 Conclusions

This study emphasizes the probabilistic back analysis, which provides a comprehension of the factors that contributed to slope failure with an insight on variability associated with the shear strength parameters. The present study concludes that the friction angle of 20° , stability number of 0.05, COV of friction angle of 10%, and COV of stability number of 10% are the shear strength parameters of MSW and its associated variability which are responsible for the collapse of Meethotamulla garbage dump. An attempt has been made through this study to predict real field conditions at the Meethotamulla solid waste in terms of its shear strength. The case history highlights the importance of accounting uncertainty of the shear strength of MSW. It is shown that ignoring the uncertainty associated with shear strength parameters of MSW may yield erroneous conclusions.

References

Basha, B. M., & Raviteja, K. V. N. S. (2017). Resistance factor calculations for load resistance factor design (LRFD) of MSW landfill slopes. In *Geoenvironmental practices and sustainability linkages and directions* (pp. 47–56). Berlin: Springer.

Geotechnical Assessment on the Failure at Meethotamulla Waste Fill. (2017). *A report by National Building Research Organization (NBRO)*. Colombo: Ministry of disaster management.

Gilbert, R. B., Wright, S. G., & Liedtke, E. (1998). Uncertainty in back-analysis of slopes: Kettleman hills case history. *Journal of Geotechnical and Geoenvironmental Engineering*, 124 (12), 1167–1176 (ASCE).

Jahanfar, A., Gharabaghi, B., McBean, E. A., & Dubey, B. K. (2017). Municipal solid waste slope stability modelling: A probabilistic approach. *Journal of Geotechnical and Geoenvironmental Engineering*, 143(8), 1–10 (ASCE).

Tang, W. H., Stark, T. D., & Angulo, M. (1999). Reliability in back analysis of slope failures. *Soils and Foundations, JGS*, 39(5), 73–80.

US Army Corps of Engineers. (1997). *Engineering and design: Introduction to probability and reliability methods for use in geotechnical engineering*, Engineering Circular 1110-2-547. Washington, DC: US Department of the Army.

Zhang, J., Tang, W. H., & Zhang, L. M. (2010). Efficient probabilistic back-analysis of slope stability model parameters. *Journal of Geotechnical and Geoenvironmental Engineering*, 136(1), 99–109 (ASCE).

Determination of Anelastic Attenuation Factor (Q) and Decay Factor (K) from Ground Motion Records of the Intra-plate Region

Neelima Satyam, Shambhavi Dube, Raj Banerjee,
Srijit Bandyopadhyay, G. R. Reddy, Suzette Payne
and Justin Coleman

Abstract Attenuation of seismic waves in the frequency domain for near- and far-source sites is the key parameter for inferring source properties, simulating ground motions and hazard analysis. The seismic devastation is directly related to the attenuation characteristics of the medium and the amount of seismic energy released during an earthquake. Based on the detailed literature review, it is observed that studies have been done worldwide to understand the attenuation characteristics by estimating frequency-dependent shear-wave attenuation factor (Q) for inter-plate region but very limited studies have focused on intra-plate region. This research paper focuses primarily on the determination of kappa factor (κ) and quality factor (Q) for intra-plate region as this region has scarcity of observed ground motion data sets. Around 105 recorded ground motions were collected from Canada and USA, monitored by Idaho National Laboratory, USA, during 2005–2015. This data is used to determine the farfield source geometric attenuation, kappa factor and inelastic attenuation of Q -value. An attenuation model of Fourier spectral amplitudes for a shear window for both horizontal and vertical components is also determined. Stochastic simulation of the ground motion records using EXSIM was carried out

N. Satyam (✉)

Department of Civil Engineering, IIT Indore, Indore, India

e-mail: neelima.satyam@gmail.com

S. Dube

Earthquake Engineering Research Centre, IIIT Hyderabad, Hyderabad, India

R. Banerjee · S. Bandyopadhyay

Reactor Safety Division, Department of Atomic Energy, Bhabha Atomic Research Centre, Mumbai, India

G. R. Reddy

Department of Atomic Energy, Bhabha Atomic Research Centre, Mumbai, India

S. Payne

Seismologist, Seismic Research Group, Idaho National Laboratory, Idaho Falls, USA

J. Coleman

Lead, Seismic Research Group, Idaho National Laboratory, Idaho Falls, USA

and very well comparable with the recorded ground motion data. It is also observed that spectral analysis of the ground motions shows a reliable match between the simulated and recorded spectra which supports the validity of the source parameters derived in this study. Also the results show that coefficients developed from vertical components are not applicable for horizontal components. Developed parameters kappa and quality factor are very well comparable with existing relationships from the literature. These parameters developed by considering the large data set from USA and Canada can be used for a wide intra-plate region.

Keywords Anelastic • Attenuation factor (Q) • Decay factor (κ)
Ground motion • Intra-plate

1 Introduction

Majority of earthquakes result from recurrent accumulation and release of strain at contacts between distinctive moving plates. The theory of plate tectonic movement does not readily account for earthquakes located at interiors of oceanic and continental plates. Such intra-plate earthquakes present fundamental challenges in understanding accumulation of strain and the associated seismic potential and hazard. Large areas of Australia, North America, Asia and Europe experience intra-plate earthquakes, some of which are catastrophically large. The seismic risk because of intra-plate earthquakes especially for important structures like high-rise buildings, bridges, natural gas storage tanks, nuclear power plants has been a critical concern. The 2011 Tohoku earthquake with Mw of 9.0 struck off Japan's north-eastern shore which is considered as the most powerful earthquake ever recorded in Japan, generating gigantic tsunami waves widespread across miles of shoreline reaching 40 meters high. This event costs billions of dollars and thousands of lives. One of the important concerns for reliable seismic hazard analysis is the accurate prediction of ground motion at a site as a function of magnitude and distance. This can be obtained by deriving ground motion prediction equation (GMPE) using available large ground motion data sets. But availability of ground motion prediction equations based on observed data is always questionable for a region with scarcity of observed ground motion data such as intra-plate region. However in such a case, synthetic data generation by simulations based on regional seismic parameters can be used as an alternative for deriving GMPEs. In this paper, an attempt is made to find out the value of seismic source and site parameters by analysing the dependence of earthquake peak ground acceleration including characteristic of seismic source, path condition and local site effects. Further, these parameters can be used to generate a ground motion prediction equation for the region which provides peak ground velocity, peak ground acceleration and spectral accelerations for a wide frequency range.

In seismic response analysis of critical structures, acceleration time histories are required as inputs. In most of intra-plate region, the recorded ground motions are sparse; thus, synthetic acceleration time histories are utilized. This paper explains

the detailed procedure for estimating spectral decay factor (kappa: κ) and attenuation of seismic energy also known as quality factor (Q) for generating synthetic ground motions. In this method, the characteristics of seismic source, path attenuation and local soil condition are well considered while generating synthetic ground motions. From the extensive literature survey, it is found that these parameters vary with each earthquake record though it is in intra-plate region. Seismic time history data sets monitored by Idaho National Laboratory (INL), USA, were considered for the analysis. Based on the available strong motion data of the region, epicentral distance and clear S-phase, path and source parameters were analysed and a MATLAB code was developed for calculating the quality factor. The outputs were further used for generating synthetic time histories for different sites where sufficient data sets are not available. These results can further be used for generating a ground motion prediction equation for intra-plate region.

2 Literature Review

From the past research, it is clear that source and site parameters vary according to the characteristics of seismic source, path attenuation and local soil condition. The amplitude and shape of the Fourier amplitude spectrum of strong ground acceleration data are found to be useful for numerous applications to earthquake engineering (McGuire 1978). A widely employed model by Brune (1970) relates the coefficient of this ω^2 trend to the seismic moment, M_0 , and relates the corner frequency (f_0) where this ω^2 trend terminates to a stress drop parameter at the source. Above the corner frequency, Trifunac (1976) and McGuire (1978) have carried out empirical regressions for the shape of the acceleration spectrum. According to Hanks (1979, 1982), generally, the acceleration spectrum is flat above the corner frequency up to a second corner frequency (f_{\max}). Above f_{\max} spectrum starts decaying rapidly. The model developed by Anderson and Hough (1984) for the origin of the spectral decay parameter envisions a frequency independent contribution to the attenuation parameter Q which modifies the shape of source displacement spectrum obeying an ω^{-2} which possesses asymptotic behaviour at high frequencies. The cut-off frequency, f_{\max} , is an important parameter as it controls the peak ground acceleration (PGA). The wave energy is directly driven by *S*-waves at a hypocentral distance (R) less than approximately 60 km (Burger et al. 1987), whereas at distances between 200 and 1000 km, the dominant phase is the *Lg* phase which consists of multiple postcritical reflections of *S*-waves (Kennett 1986). Various seismologists (Burger et al. 1987; Frankel et al. 1990; Boatwright 1994; Hatzidimitriou 1995; Del Pezzo et al. 1995; Zhao 2010) have studied these effects to envisage the strong ground motion for various earthquake engineering purposes. The ground motion amplitudes of a region are affected by geometrical spreading which accounts for diminution of wave amplitude caused by wave scattering, anelastic attenuation which is characterized by Q wave transmission quality factor and scattering attenuation. The geometric spreading factor (kappa: κ)

is found to be unaffected by anelastic attenuation and scattering at short epicentral distances at lower frequency level. Geometric spreading is identified as independent of both wave frequency and earthquake magnitude (Herrmann and Kijko 1983; Atkinson and Mereu 1992; Atkinson and Boore 1995). The frequency independent bilinear (Herrmann and Kijko 1983) and frequency independent trilinear form (Atkinson and Mereu 1992; Atkinson and Boore 1995) are widely used.

Attenuation is a petrophysical parameter sensitive to lithology and physical properties like pressure, temperature, saturation with fluid, gas (Toksöz et al. 1979). An estimate of attenuation provides an idea about characteristics of the medium. The estimated value of quality factor, Q , was found to be frequency-dependent (Aki and Chouet 1975; Aki 1980; Gupta et al. 1995; Mandal et al. 2001). Numerous studies conducted globally relates attenuation characteristics by estimating Q based on P -waves (i.e. Q_α), S -waves (i.e. Q_β) and coda waves (i.e. Q_c). Minimal work has been carried out for intra-plate region to estimate attenuation properties of the medium. Paul et al. (2003) estimated the frequency-dependent coda Q relationship as $(92 \pm 4.73) f^{1.0 \pm 0.023}$ by using single back scattering model proposed by Aki and Chouet (1975). An effective algorithm for obtaining quality factor (Q) from strong motion data has been described by Joshi (2010) and calculated estimated value of frequency-dependent quality factor Q as $(112) f^{0.97}$ for Garhwal Himalaya (Joshi 2006) and the value of Q as $(30) f^{1.45}$ for Pithoragarh region of Kumaon, Himalaya (Joshi 2010). Using source and path parameters, GMPEs have been derived successfully by some researchers in the past and are in use for engineering purposes (Atkinson and Boore 1995).

3 Tectonic and Seismicity Details of the Study Area

Compared to earthquakes near plate boundaries, intra-plate earthquakes are not well understood, and the hazards associated with them may be difficult to quantify. In this paper, study sites monitored by Idaho National Laboratory are located along the Snake River Plain in south-eastern Idaho and towards western USA, which is within the North American plate (Fig. 1). Eastern Snake River Plains (ESRPs) are the track of the Yellowstone hotspot. ESRP is located in the northern region of the basin, and the study area considered falls under intra-plate region. The geological map of INL region along with the local soil conditions is shown in Fig. 2. Also geological details of the stations monitored by INL are shown in Table 1.

3.1 *Location of Stations Monitored Earthquake from 2005 to 2015*

The Idaho National Laboratory (INL) accumulated earthquake data for 40 years (1972–2012). The paper focuses on earthquake activity from 2005 to 2015. The

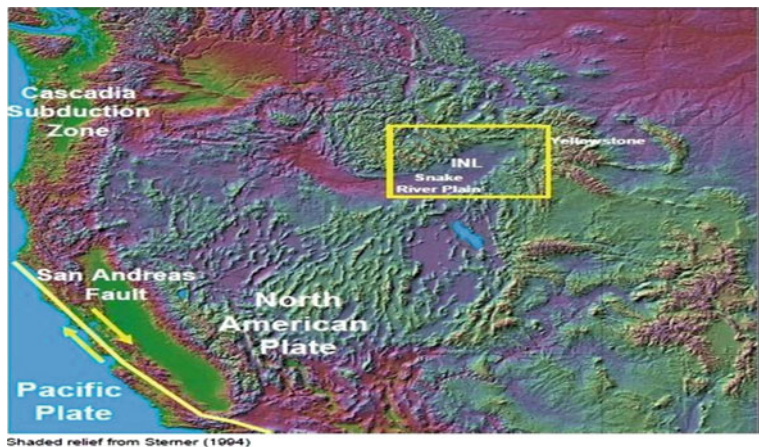
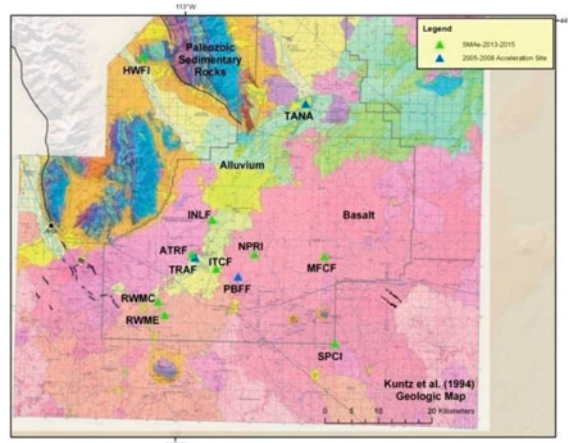


Fig. 1 Location of the study region

Fig. 2 Geological map of INL region along with the local soil conditions (INLF—basalt rock with sedimentary interbeds is 500 m thick; NPRI—basalt rock with sedimentary interbeds is 1100 m thick; at other stations thickness of basalt rock with sedimentary interbeds is unknown)



sites surrounding Eastern Snake River Plain (ESRP) and near INL were considered for the analysis. It discusses the earthquake activity that has occurred around the local region and within 161 km of the INL and centred at $43^{\circ} 39' 00''\text{N}$, $112^{\circ} 47' 00''\text{W}$. The recorded earthquakes from 2005 to 2008 and from 2013 to 2015 are shown in Fig. 3a, b respectively.

INL has supported a seismic monitoring programme and has monitored seismic activity on the Snake River Plain since 1972 which consists of 33 seismic stations classified as broadband, short period and single and three components. In this paper, 33 strong motion data measured both at the bedrock and on free field conditions

Table 1 Geological details of the stations and local site conditions

Station	Latitude N (D)	Latitude N (M)	Longitude W (D)	Longitude W (M)	Elevation (m)	Local site conditions
ATRF	43	35.71	-112	58.34	1502	20 ft alluvium over basalt rock
INLF	43	39.25	-112	55.67	1476	Basalt rock
ITCF	43	34.3	-112	54.89	1490	Basalt rock
MFCF	43	35.79	-112	39.92	1583	Basalt rock
NRVF	43	37.24	-112	56.8	1489	Basalt rock
CNCI	43	55.7	-113	27.13	1896	Palaeozoic limestone
NPRI	43	35.85	-112	49.63	1513	Basalt rock
COMI	43	27.71	-113	35.63	1890	Rhyolite
BCYI	44	18.65	-113	24.31	2194	Palaeozoic limestone
GRRI	42	56.28	-111	25.3	2207	Palaeozoic limestone
HWFI	43	55.54	-113	5.84	1743	Palaeozoic limestone
PTI	42	52.22	-112	22.21	1670	Cambrian limestone
SPCI	43	27	-112	38.22	1530	Basalt rock
TRAF	43	35.36	-112	57.86	1498	35 ft alluvium over basalt rock
NRFF	43	39.11	-112	55.2	1475	40 ft alluvium over basalt rock
TANA	43	51.17	-112	42.95	1480	125 ft playa sediments over basalt rock
PBFF	43	33.56	-112	51.85	1517	Basalt rock
RWMC	43	30.85	-113	2.87	1533	Basalt rock
RWME	43	29.51	-113	1.93	1543	Basalt rock

were considered for the analysis. The seismic data contains three components, two horizontal and one vertical. Figure 4 shows the locations of the seismic stations monitored.

4 Estimation of Seismic Source Parameters

For the estimation of seismic source parameters, 22 recorded seismic events from 2005 to 2015 which are predominant because of normal faulting with magnitudes ranging from 3.3 to 5.9 were considered for the analysis. The horizontal components in east and north direction and vertical components recorded at different stations with epicentral distance ranging from 50 to 300 km are shown in Fig. 5. The strong motion data has been filtered using bandpass Butterworth filter of fourth order with frequency range of 0.4 Hz (f_c) to 25 Hz (f_{max}) Newmark (1965) and baseline corrected up to second order.

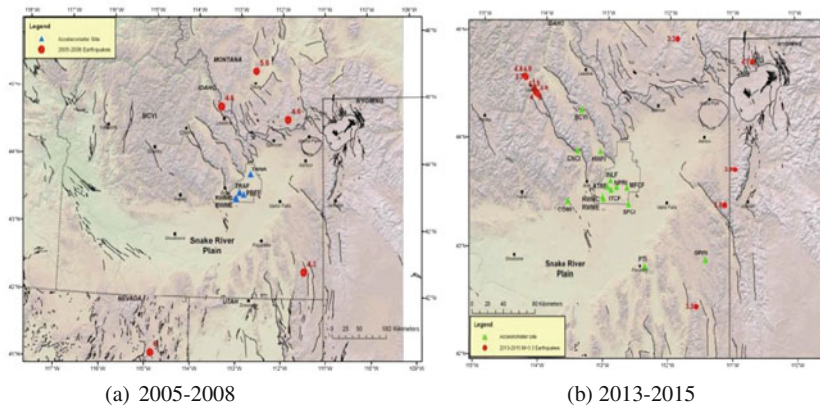


Fig. 3 Stations monitored by INL and earthquake occurrence map

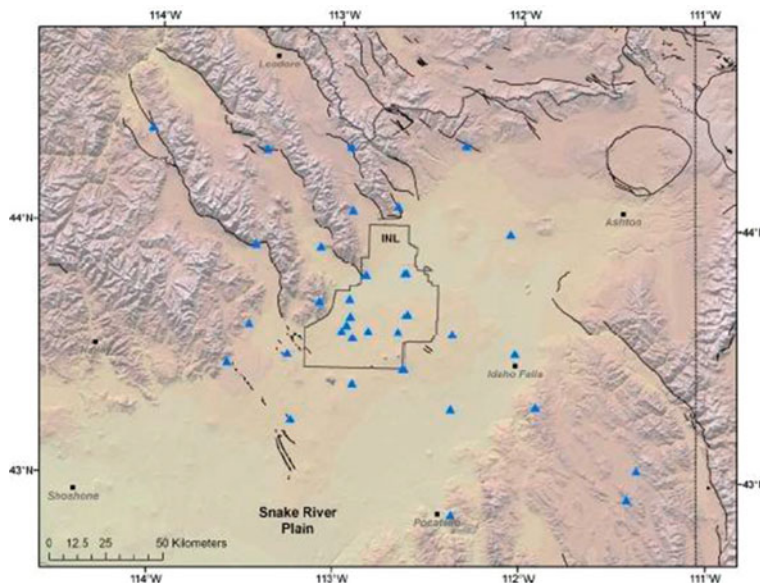


Fig. 4 Seismic stations monitored by INL

Fast Fourier transform of all the strong motion data is plotted with log of frequency at X -axis and log of spectrum at Y -axis (Fig. 6). Fourier amplitude spectrum of acceleration for the horizontal and vertical components of the station accelerogram, INL, for all earthquake events (log-log axes) is calculated. The procedure adopted to calculate the value of spectral decay factor (kappa: κ) is shown below at two stations (Fig. 7).

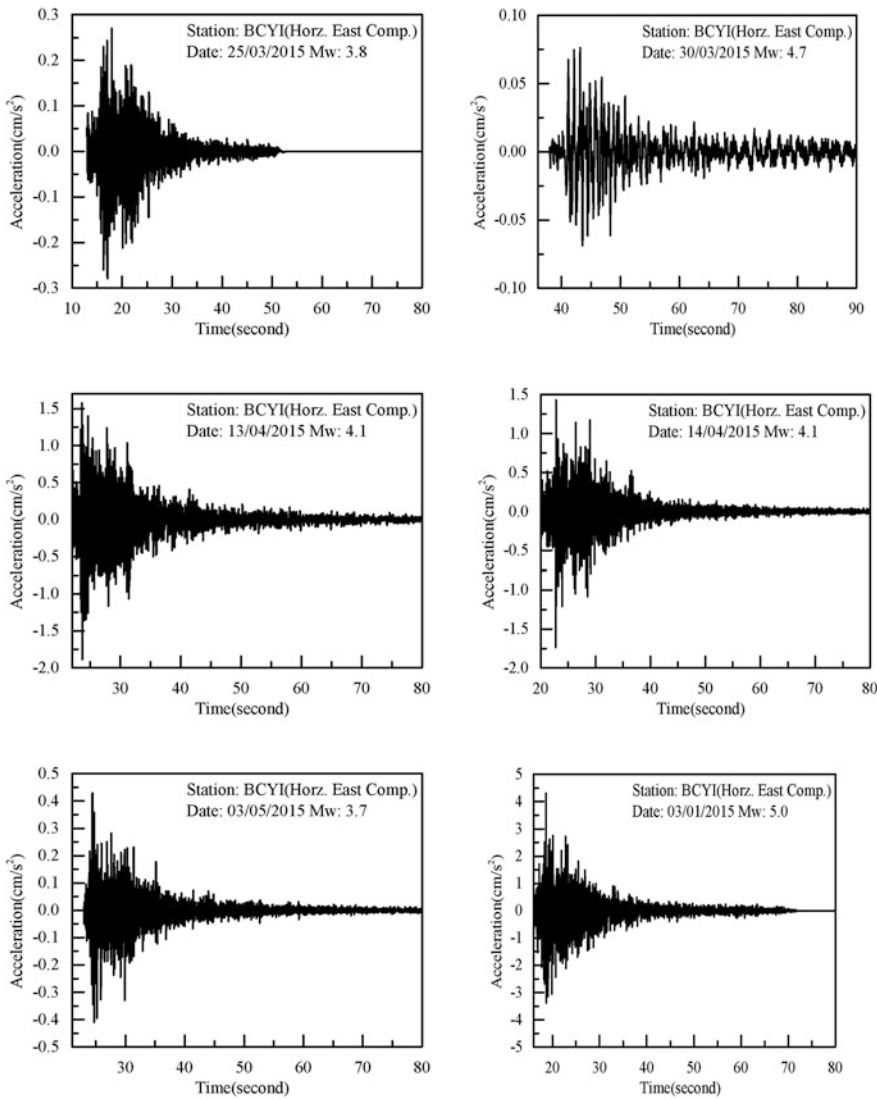


Fig. 5 Strong ground motion data sets at different stations for INL region

Table 2 shows the details of spectral decay factor kappa value calculated for all the seismic events considered. An empirical relationship between kappa value and epicentral distance was developed for stations in limestone site as shown below in Eq. (1) (Fig. 8).

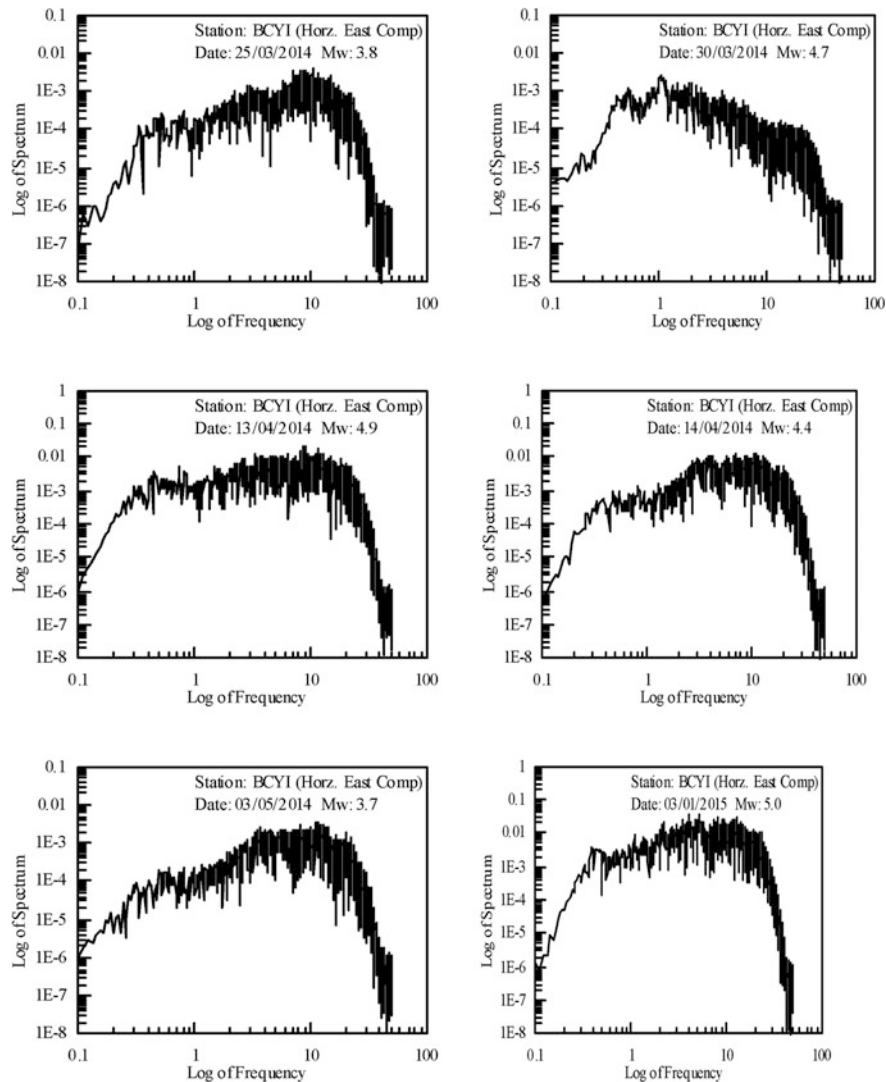


Fig. 6 Fast Fourier transform of strong motion data sets at different stations for INL site

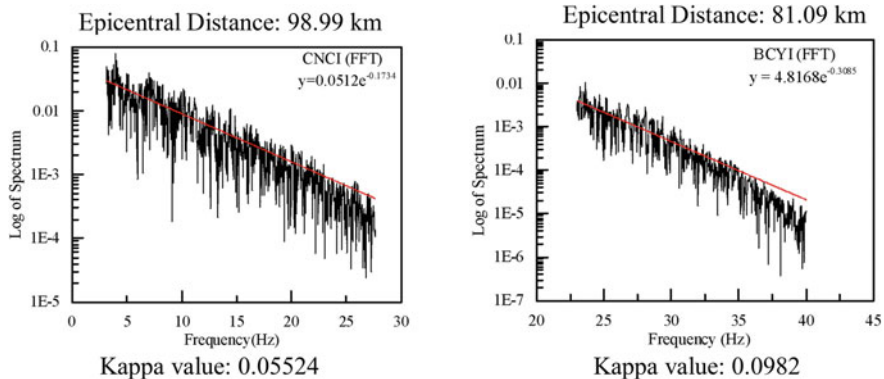


Fig. 7 Kappa factor at two different stations

$$y = 0.0002759x + 0.01456 \quad (1)$$

where x is the epicentral distance (Km) and y is the corresponding value of kappa: κ with the epicentral distance.

It is clear that the zero distance kappa value for limestone site is 0.01456 which gives good match with available literature.

4.1 Q Factor as per Joshi (2006)

The acceleration spectrum used to describe the frequency content of strong ground motion at any place is the function of mainly source spectrum and path spectrum. The source spectrum can be estimated by ω -square model according to which there is decay at the rate of ω -square for high frequencies greater than corner frequency f_c . The source acceleration spectrum can be estimated from acceleration record after correcting it with diminution function, which accounts for geometrical spreading and anelastic attenuation (Joshi 2006). The algorithm to determine this anelastic attenuation also known as quality factor (Q) has been adapted from Joshi (2006), and a MATLAB code is generated to calculate the value of frequency-dependent quality factor. This study uses S-phase of baseline corrected and filtered 105 strong motion data of different sites monitored by Idaho National Laboratory, USA. The geometrical spreading factor term was considered as $1/R$ for strong motion studies of worldwide earthquakes by Boore (1983), Atkinson and Boore (1995), Joshi et al. (2001), Joshi and Midorikawa (2004) and Joshi (2006) for inter-plate as well as intra-plate earthquakes. As the spectral acceleration at a particular station is considered to be dependent on the geometrical spreading term, the value of this term has a direct influence on the obtained results. Therefore, the use of the geometrical term other than $1/R$ needs to be validated before using any data in a new region. In

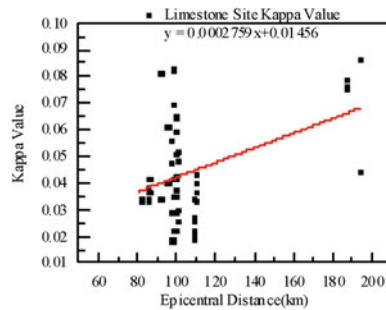
Table 2 Calculated value of kappa factor (κ) at different seismic stations for limestone site

Site	Earthquake event	Epicentre distance (km)	Kappa value (κ)
BCYI_HNE	25/03/2014	85.270	0.042
BCYI_HNE	03/05/2014	85.159	0.101
BCYI_HNE	30/03/2014	94.395	0.096
BCYI_HNE	13/04/2014	85.594	0.076
BCYI_HNE	14/04/2014	85.635	0.089
BCYI_HNE	03/01/2015	81.091	0.030
BCYI_HNN	25/03/2014	85.271	0.037
BCYI_HNN	03/05/2014	85.159	0.049
BCYI_HNN	13/04/2014	85.594	0.042
BCYI_HNN	14/04/2014	85.635	0.048
BCYI_HNN	03/01/2015	81.091	0.068
GRRI_HNE	11/11/2014	95.011	0.046
GRRI_HNE	03/01/2015	186.958	0.078
GRRI_HNN	11/11/2014	95.011	0.040
HWFI_HNE	25/03/2014	108.697	0.023
HWFI_HNE	03/05/2014	108.487	0.022
HWFI_HNE	23/12/2014	98.560	0.025
HWFI_HNE	24/12/2014	97.363	0.023
HWFI_HNE	1/4/2015 (event 3)	99.694	0.023
HWFI_HNE	13/04/2014	109.301	0.036
HWFI_HNE	03/01/2015	99.167	0.034
HWFI_HNE	1/4/2015 (event 1)	98.450	0.037
HWFI_HNE	1/4/2015 (event 2)	100.696	0.019
HWFI_HNN	25/03/2014	108.697	0.035
HWFI_HNN	03/05/2014	108.487	0.027
HWFI_HNN	23/12/2014	98.560	0.033
HWFI_HNN	24/12/2014	97.363	0.033
HWFI_HNN	1/4/2015 (event 3)	99.694	0.032
HWFI_HNN	30/03/2014	123.201	0.031
HWFI_HNN	10/04/2014	108.697	0.032
HWFI_HNN	13/04/2014	109.301	0.042
HWFI_HNN	14/04/2014	109.377	0.043
HWFI_HNN	1/4/2015 (event 2)	100.696	0.036
CNCI_HNE	24/12/2014	97.192	0.059
CNCI_HNE	1/4/2015 (event 3)	99.515	0.044
CNCI_HNE	03/01/2015	98.989	0.063
CNCI_HNE	1/4/2015 (event 1)	98.275	0.075
CNCI_HNE	1/4/2015 (event 2)	100.514	0.059
CNCI_HNN	24/12/2014	97.192	0.069
CNCI_HNN	1/4/2015 (event 3)	99.515	0.073

(continued)

Table 2 (continued)

Site	Earthquake event	Epicentre distance (km)	Kappa value (κ)
CNCI_HNN	03/01/2015	98.989	0.082
CNCI_HNN	1/4/2015 (event 1)	98.275	0.093
CNCI_HNN	1/4/2015 (event 2)	100.514	0.060

Fig. 8 Relationship between kappa (κ) and epicentral distance (R) for INL limestone site

this study, geometrical spreading term has been considered as $1/R$. The values of the parameters radiation factor $R\theta\varphi$ and amplification due to free surface FS are used as 0.55 and 2.0, respectively (Kramer 1996).

The value of frequency-dependent Q factor has been calculated using a MATLAB code for all the strong ground motion data at different stations as shown in Fig. 9, and an average value of Q factor has been obtained as $Q(f) = 35^{0.96}$ for INL intra-plate region. The values of Q obtained at all other stations are similar because of similar tectonic and geological units. The relationship of frequency-dependent quality factor is directly used for the simulation of strong motion data at different magnitude and distance using various simulation techniques. Calculated value of Q factor serves dual purpose of attenuation properties for a region as well as used for generating ground motion prediction equation for INL region which can further be used in analysis of important engineering structures.

Also the quality factor (Q) values calculated are validated with that of recorded strong motion data using Fourier amplitude spectrum, and it is observed that there is a reliable match between the two, which validates the calculated values of quality factor (Q) and decay factor (kappa: κ) as shown in Fig. 10.

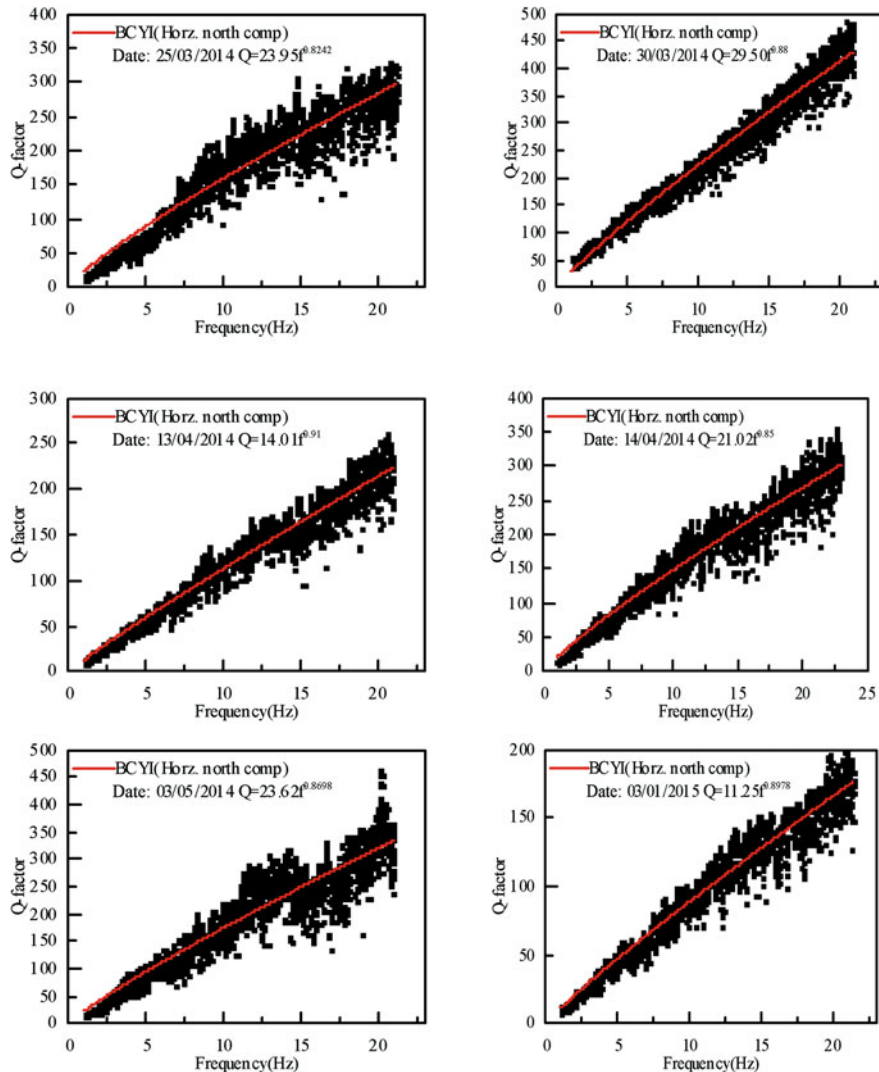


Fig. 9 Relationship between quality factor (Q) and frequency (f) for INL site

5 Simulation of Ground Motions Using EXSIM

The simulation of ground motion has been performed using EXSIM, a finite fault stochastic model developed by Atkinson (2005) and later modified by Boore 2009 which is specifically used for simulating higher frequency ground motions which is of high interest to engineers (Boore 2009). This method is very useful for the intra-plate regions where recording of motion from potentially damaging

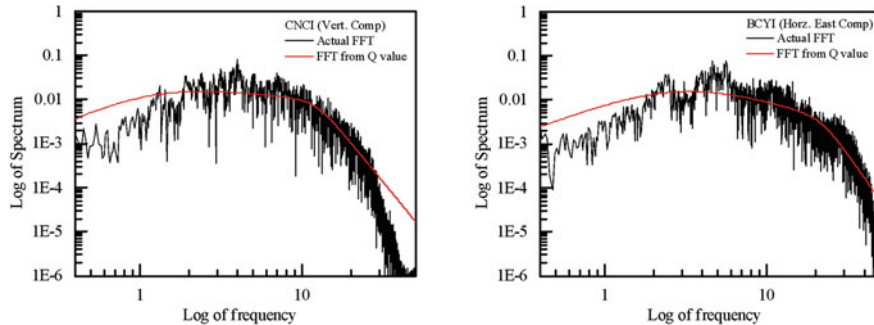


Fig. 10 Validation of the results using estimated frequency-dependent average value of quality factor (Q) for INL site

earthquakes is not available. One of main features of the method is that it distils the various factors affecting ground motions (source, path and site) into simple functional forms. Several methods available use stochastic representations of some or all of the physical processes responsible for ground shaking (Papageorgiou and Aki 1983; Zeng et al. 1994). In this paper, shape of source spectral has been considered as $S(f) = S_a(f) * S_b(f)$, and a model given by Frankel et al. (1996), which is a ω -square model, has been used to calculate the factors S_a and S_b , which are the function of corner frequency. EXSIM is used and verified by many researchers like Atkinson and Assatourians (2015), and results are comparable with that of the average spectral amplitude for different range of magnitude and epicentral distances. Source and path parameters are calculated for INL region using Fourier amplitude spectrum, and these parameters are further used to simulate the ground motion data varying from magnitude 3.3 to 5.9 and distance range between 50 and 300 km. The comparison between the simulated ground motion generated using EXSIM and the available original strong ground motion data set for INL site shows a reliable match which can be interpreted from Fig. 11, and this also validates the computed values of source and path parameters.

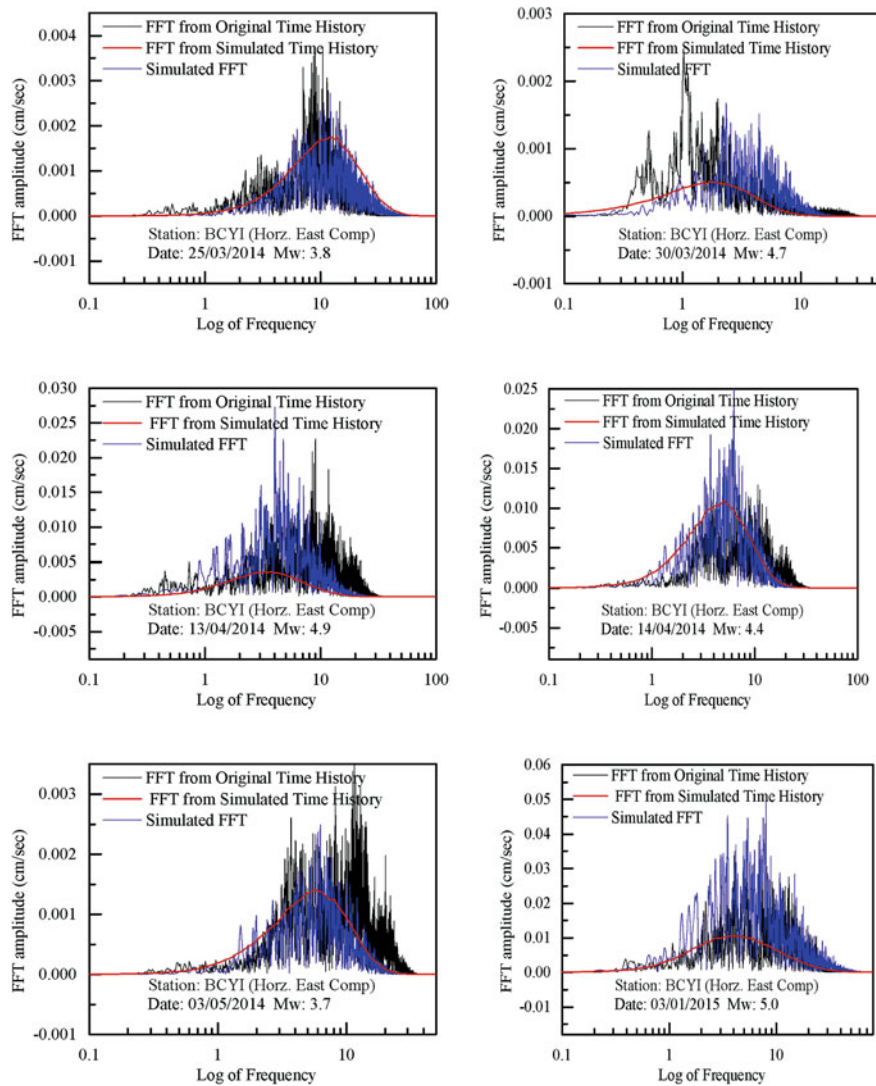


Fig. 11 Generation of synthetic Fourier amplitude spectra using EXSIM

6 Conclusions

Around 105 strong motion records observed by INL sites in USA are studied and considered for estimation of anelastic attenuation factor or quality factor (Q) and spectral decay factor (kappa: κ) which falls under intra-plate region. Seismic analysis has been carried out for this data, and following specific conclusions are drawn from the present study:

- Corner frequency (f_c) and cut-off frequency (f_{\max}) are the important parameters to calculate source and path amplitude spectrum, respectively.
- Spectral analysis of the ground motions shows a reliable match between the simulated and recorded spectra which supports the validity of the source parameters derived in this study.
- Results show that coefficients developed from vertical components are not applicable for horizontal components as horizontal components have predominant site amplification effects.
- Estimated value of spectral decay factor (kappa: κ) and quality factor (Q) is very well comparable with existing values from the literature.
- The relation of $Q(f) = 35f^{0.96}$ obtained from calculations is valid for a wide frequency range of 0.2–25 Hz.
- This attenuation relationship developed considered large amount of data set from USA, so it can be used for a wide intra-plate region.
- The value of calculated source and site factors can further be used to generate synthetic ground motions using stochastic methods of simulation in the INL and other intra-plate region.

References

Aki, K., & Chouet, B. (1975). Origin of Coda Waves: Source, Attenuation and Scattering Effects. *Journal of Geophysical Research*, 80(23), 3322–3342.

Aki, K. (1980). Attenuation of Shear Waves in the Lithosphere for Frequencies from .05 to 25 Hz. *Physics of the Earth and Planetary Interiors*, 21(1), 50–60.

Anderson and Hough. (1984). A model for the shape of the fourier amplitude spectrum of acceleration at high frequencies. *Bulletin of the Seismological Society of America*, 74(5), 1969–1993.

Atkinson and Assatourians. (2015). Implementation and validation of EXSIM (a stochastic finite-fault ground-motion simulation algorithm) on the SCEC broadband platform. *Seismological Research Letter*, 86, 48–60.

Atkinson, G. M., & R. F. Mereu (1992). The shape of ground motion attenuation curves in southeastern Canada. *Bulletin of the Seismological Society of America*, 82, 2014–2031.

Atkinson, G. M., & Boore, D. M. (1995). Ground Motion Relations for Eastern North America. *Bulletin of the Seismological Society of America*, 85(1), 17–30.

Boatwright, J. (1994). Regional propagation characteristics and source parameters of earthquakes in eastern North America. *Bulletin of the Seismological Society of America*, 84, 1–15.

Boore, D. M. (1983). Stochastic Simulation of High-Frequency Ground Motions Based on Seismological Models of the Radiated Spectra. *Bulletin of the Seismological Society of America*, 73(6A), 1865–1894.

Boore, D. M. (2003). Simulation of ground motion using the stochastic method. *Pure and Applied Geophysics*, 160(2003), 635–676.

Boore, D. M. (2009). Comparing stochastic point-source and finite-source ground motion simulations: SMSIM and EXSIM. *Bulletin of the Seismological Society of America*, 74(5), 1969–1993.

Boore, D. M., & Atkinson, G. M. (1987). Stochastic prediction of ground motion and spectral response parameters at hard-rock sites in Eastern North America. *Bulletin of the Seismological Society of America*, 77(2), 440–467.

Brune, J. N. (1970). Tectonic stress and the spectra of seismic shear waves from earthquakes. *Journal of Geophysical Research*, 75, 4997–5009.

Burger, R., Somerville, P., Barker, J., Herrmann, R., & Helmberger, D. (1987). The effect of crustal structure on strong ground motion attenuation relations in eastern North America. *Bulletin of the Seismological Society of America*, 77, 420–439.

Del Pezzo, E., Ibanez, J., Morales, J., Akinci, A., & Maresca, R. (1995). Measurements of intrinsic and scattering seismic attenuation in the crust. *Bulletin of the Seismological Society of America*, 85, 1373–1380.

Frankel, A., McGarr, A., Bicknell, J., Mori, J., Seeber, L., & Cranswick, E. (1990). Attenuation of high-frequency shear waves in the crust: Measurements from New York state, South Africa, and southern California. *Journal of Geophysical Research*, 95(B11), 17441–17457.

Frankel, A., et al. (1996). National Seismic Hazard Maps: Documentation. U.S. Geological Survey Open-File Report, pp. 96–532, 69 p.

Ghofrani, et al. (2013). Stochastic finite-fault simulations of the 2011 Tohoku, Japan, earthquake. *Bulletin of the Seismological Society of America*, 103(2B), 1307–1320.

Gupta, S. C., Singh, V. N., & Kumar, A. (1995). Attenuation of Coda Waves in the Garhwal Himalaya, India. *Physics of the Earth and Planetary Interiors*, 87(3–4), 247–253.

Hanks, T. C. (1979). b-values and ω^2 seismic source models: implications for tectonic stress variations along active crustal fault zones and the estimation of high-frequency strong ground motion. *Journal of Geophysical Research*, 84, 2235–2242.

Hanks, T. C. (1982). fmax. *Bulletin of the Seismological Society of America*, 72, 1867–1880.

Hatzidimitriou, P. M. (1995). S-wave attenuation in the crust in northern Greece. *Bulletin of the Seismological Society of America*, 85, 1381–1387.

Herrmann, R. B., & A. Kijko (1983). Modeling some empirical vertical component Lg relations, *Bulletin of the Seismological Society of America*, 73, 157–171.

Joshi, A. (2006). Use of acceleration spectra for determining the frequency-dependent attenuation coefficient and source parameters. *Bulletin of the Seismological Society of America*, 96(6), 2165–2180.

Joshi, A. (2010). Use of strong-motion data for frequency-dependent shear wave attenuation studies in the Pithoragarh Region of Kumaon Himalaya. *ISET Journal of Earthquake Technology, Paper No. 508*, 47(1), March 2010, pp. 25–46.

Joshi, A., & Midorikawa, S. (2004). A simplified method for simulation of strong ground motion using rupture model of the earthquake source. *Journal of Seismology*, 8(4), 467–484.

Joshi, A., Singh, S., & Giroti, K. (2001). The simulation of ground motions using envelope summations. *Pure and Applied Geophysics*, 158(5–6), 877–902.

Kennett, B. (1986). Lg waves and structural boundaries. *Bulletin of the Seismological Society of America*, 76, 1133–1141.

Kramer, S. L. (1996). *Geotechnical earthquake engineering*. Pearson Education.

Mandal, P., Pandhy, S., Rastogi, B. K., Satyamarayana, V. S., Kousalya, M., Vijayraghavan, R., & Srinivasan, A. (2001). Aftershock activity and frequency-dependent low Q_c in the epicentral region of 1999 Chamoli earthquake of M_w 6.4. *Pure and Applied Geophysics*, 158(9–10), 1719–1736.

McGuire, R. K. (1978). A simple model for estimating Fourier amplitude spectra of horizontal ground acceleration. *Bulletin of the Seismological Society of America*, 69, 803–822.

Motazedian, D., & Atkinson G. M. (2005). Stochastic finite fault modelling based on a dynamic corner frequency. *Bulletin of the Seismological Society of America*, 95, 995–1010.

Newmark, N. M. (1965). Effects of earthquakes on dams and embankments. *Geotechnique*, 15, 139–160. <https://doi.org/10.1680/geot.1965.15.2.139>.

Papageorgiou, A. S., & Aki, K. (1983). A Specific Barrier Model for the Quantitative Description of Inhomogeneous Faulting and the Prediction of Strong Ground Motion. I. Description of the Model. *Bulletin of the Seismological Society of America*, 73(3), 693–722.

Paul, A., Gupta, S. C., & Pant, C. C. (2003). Coda Q Estimates for Kumaun Himalaya. *Proceedings of the Indian Academy of Sciences (Earth and Planetary Sciences)*, 112(4), 569–576.

Toksöz, M. N., Johnston, D. H., & Timur, A. (1979). Attenuation of Seismic Waves in Dry and Saturated Rocks—I. Laboratory Measurements. *Geophysics*, 44(4), 681–690.

Trifunac, M. D. (1976). Preliminary empirical model for scaling Fourier amplitude spectra of strong ground accelerations in terms of earthquake magnitude, source to station distance, and recording site conditions. *Bulletin of the Seismological Society of America*, 66, 1343–1373.

Zeng, Y., Anderson, J. G., & Yu, G. (1994). A Composite Source Model for Computing Realistic Synthetic Strong Ground Motions. *Geophysical Research Letters*, 21(8), 725–728.

Zhao, Z. X. (2010). Geometric spreading functions and modeling of volcanic zones for strong motion attenuation models derived from records in Japan. *Bulletin of the Seismological Society of America*, 100, 712–732.

Uncertainties in Site Characterization Using Surface Wave Techniques and Their Effects on Seismic Ground Response

Ravi S. Jakka and Narayan Roy

Abstract Surface wave methods which utilize the dispersion property of Rayleigh waves are widely used for subsurface site characterization. As a non-invasive method of site characterization, it has many advantages over the invasive methods of geotechnical site characterization. Surface wave methods determine the small strain shear modulus of near-surface materials, and this shear modulus is the key input in the evaluation of the soil response under dynamic/seismic loading. So, the accuracy of testing is very important, otherwise it may lead to significant consequences on the seismic hazard studies. There are different uncertainties associated with surface wave methods. These uncertainties can be broadly classified into three categories: Model-based uncertainty, Data measurement uncertainty, and Inversion uncertainty. Model-based uncertainty basically contains the near-field effects which lead to the underestimation of Rayleigh wave phase velocity. Data measurement uncertainty is another major source of uncertainty, which arises while conducting the surface wave tests due to the noise present in the surroundings in the form of continuous or transient signals. Noise results in a scatter in the measured dispersion curve and this scatter in the dispersion curve may provide different velocity profiles, which are falling in the range of measured data variation. Inversion uncertainty deals with non-unique solution of inversion. Non-unique solution may results into several equivalent velocity profiles, with a good fit with the experimental dispersion curve. Now, the consequence of this data measurement and inversion uncertainty may show significant variation on ground response analysis.

Keywords Surface wave · Inversion non-uniqueness · Ground response
Dispersion curve · Site characterization

R. S. Jakka (✉)

Department of Earthquake Engineering, IIT Roorkee, Roorkee, India
e-mail: rsjakka@gmail.com

N. Roy

Department of Civil Engineering, Jadavpur University, Kolkata, India
e-mail: narayan.roy04@gmail.com

1 Introduction

Site characterization is the very important aspect of any seismic hazard analysis. Site characterization using shear wave velocity (V_S) from surface wave testing is gaining popularity nowadays. Surface wave methods provide small strain shear modulus and damping of near-surface materials. These methods are non-invasive and can characterize a large volume of soil within a very short duration of time. So, surface wave testing can serve as the best alternative for the characterization of sites where driving of borehole and other geotechnical testing are not possible. The applications of surface waves to solve engineering problems started in the 1950s with the steady-state Rayleigh method (Jones 1958), but their revolution has arrived only in the last two decades with the proposition of the Spectral Analysis of Surface Wave (SASW) method (Nazarian et al. 1983) and the Multichannel Analysis of Surface Wave (MASW) method (Park et al. 1999; Xia et al. 1999).

Presently different types of surface wave methods are being used for the seismic site characterization, which is the main basis of the other earthquake geotechnical studies like ground response analysis and microzonation. Active-source tests in which waves are generated using an active seismic source (Stokoe et al. 1994) and passive-source tests, which utilize the constant earth's vibrations or microtremors (Louie 2001; Strobbia and Cassiani 2011), are the most commonly used surface wave methods. Active-source surface wave tests generally provide information of high-frequency components, whereas passive-source tests provide information of low-frequency components. Again, these low- and high-frequency components are directly related to the depth of penetration, lower frequencies penetrate deeper depth reflecting the properties of deeper subsurface, whereas higher frequencies provide the information about shallow subsurface material. Sometimes both active and passive-source surface wave tests are combined to get information up to a reasonable range of frequency band. Once we obtain the dispersion curve, inverse problem solution is used to extract the shear-wave velocity profile of the site, which is used later in seismic hazard analysis.

Surface wave methods are although routinely used in seismic site characterization, they suffer from several uncertainties at the time of data acquisition and during data processing (Foti et al. 2009; Lai et al. 2005; Boaga et al. 2012, 2014; Roy et al. 2013a, b; Jakka et al. 2014, 2015). Uncertainties associated with surface wave testing can be categorized into three different categories: (a) Model-based uncertainty, (b) Data measurement uncertainty, and (c) Inversion uncertainty, although the available literature deals with only model-based uncertainty and data measurement uncertainty. Here, inversion uncertainty is categorized and studied separately. Model-based uncertainty basically consists of near-field effects and lateral heterogeneity. Near-field effect results in the underestimation or overestimation of Rayleigh wave phase velocity (Yoon and Rix 2009; Bodet et al. 2009; Roy and Jakka 2017b) and may arise due to the testing setup configuration, type of source used to generate waves, and subsurface soil profiles. Some studies have been

carried out to study the effect of lateral heterogeneity (Lin et al. 2007; Boaga et al. 2012). These uncertainties play an important role in the resulting shear wave velocity profiles which may lead to different seismic site responses. On the other hand, data measurement uncertainty which may arise from the noise present in the recorded signals, sometimes lead to erroneous determination of Rayleigh wave phase velocity. It largely depends on the type of soil profiles and receiver configurations. Data measurement uncertainty results in a scatter in the field experimental dispersion curve and mainly arises from the noise in the recording signal. Propagation of this data measurement uncertainty on the resulting shear wave velocity profiles after inversion and on seismic site response analysis has been studied by several researchers (Marosi and Hiltunen 2004; Lai et al. 2005; Jakka et al. 2014; Teague and Cox 2016). After generating the experimental dispersion curve, another challenge is to extract a representative V_s profile for a particular site from inverse problem solution. The inverse problem solution suffers from inversion non-uniqueness and may lead to several velocity profiles which are equivalent in terms of experimental dispersion curve. The consequences of this inversion uncertainty on seismic ground response analysis have been studied by several researchers but the conclusions differ among different school of thoughts (Foti et al. 2009; Boaga et al. 2011; Roy et al. 2013a, b). Hence, a comprehensive study is required to address all these uncertainties. Active research is going on how to account the above-mentioned uncertainties and their consequences on other studies.

In this article, an attempt has been made to rigorously study these uncertainties associated with surface wave methods using numerical simulations along with field studies and their effects on seismic ground response analysis. First, a study on model-based uncertainty to study the near-field effects is presented using numerical simulations. Then, a study on data uncertainty and inversion uncertainty is presented along with the consequences on seismic ground response analysis.

2 Model-Based Uncertainty

To study model-based uncertainty, a numerical simulation is performed to simulate near-field effects for varying subsurface scenarios. A normally dispersive S-wave velocity model with four different half-space scenarios has been used in this regard. The simulation mainly considers two different scenarios of Rayleigh wave propagation. First, PLAXIS finite element software is used to model the wave propagation for full wave field due to a point load on the surface and then to model the wave propagation for Rayleigh wave only, i.e., only surface wave in a layered medium. Mat_Disperse program has been used to generate effective Rayleigh wave phase velocity curve by the superposition of multiple modes of plane Rayleigh waves and does not include contributions from body waves. Errors due to near-field effects are quantified using two normalized parameters introduced by Yoon and Rix (2009). Surface waves for full wave field are modeled using 2D axisymmetric

model with PLAXIS finite element program with a point load on the free surface. The equation of motion of N degrees of freedom system subjected to an impact loading can be written as follows:

$$M\ddot{u}(t) + C\dot{u}(t) + Ku(t) = F(t) \quad (1)$$

where M , C , and K are the $N \times N$ mass, damping, and stiffness matrixes, respectively. $\ddot{u}(t)$, $\dot{u}(t)$, and $u(t)$ are the acceleration, velocity, and displacement vectors, respectively. By using the implicit time integration scheme of Newmark, the displacement and the velocity at the point in time $(t + \Delta t)$ is calculated, where Δt is the time step. Impulse loading is simulated using a half-sine pulse acting for a short duration. The load is acting for a short duration of 0.012 s with a peak load of 12 kN. Total time duration of the simulation has been kept 1 s with a time step of 0.001 s.

Initially, the model is validated before starting the main simulation. For validation, one 2D axisymmetric model for a normally dispersive soil profile is developed in PLAXIS. Figure 1a represents the normally dispersive profile used for the validation and Fig. 1b represents the developed 2D finite element model.

Absorbent boundaries are introduced at the bottom and right-hand side of the model. Meshes near to the surface are refined to capture the high-frequency information accurately. Surface wave is modeled due to an impulse loading on the surface for a short duration of 0.012 s with a peak load of 12 kN. Velocity time histories have been computed at 1 m interval for a near offset distance of 1 m. At total 96 receiver positions, velocity time histories have been generated with a far offset of 96 m. After generating the seismogram of velocity time histories at 96 receiver locations, these data are further processed to generate the dispersion spectra to extract the dispersion curve. Figure 2a represents the dispersion image for the considered normally dispersive S-wave velocity model and Fig. 2b represents the

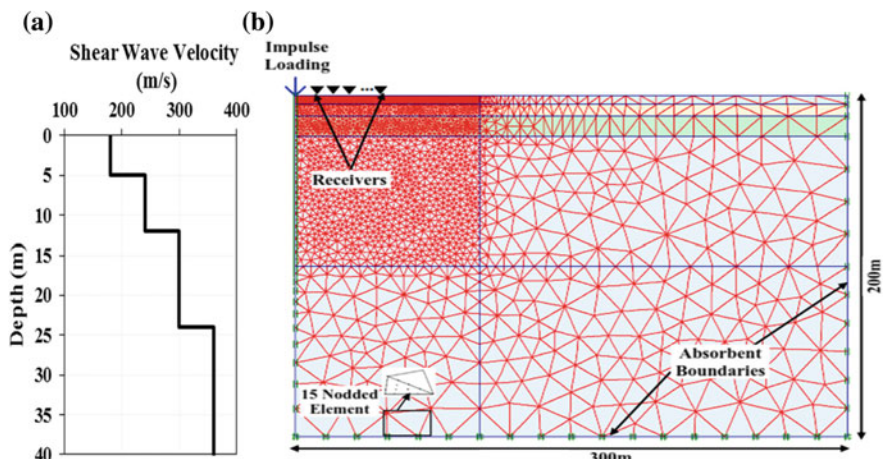


Fig. 1 Finite element model: a velocity profile, b finite element model

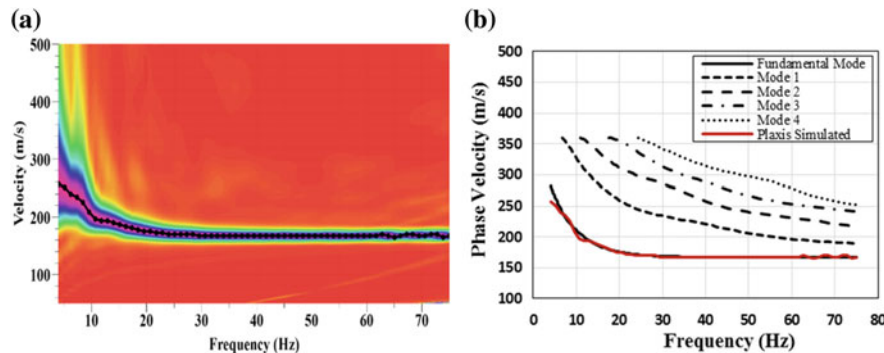


Fig. 2 **a** Dispersion curves after frequency-wave number analysis; and **b** comparison of dispersion curves from PLAXIS and modal dispersion curves

comparison of picked dispersion curve with the theoretical modal dispersion curves. The comparison shows excellent agreement between the theoretical and numerical analysis.

The main simulation is performed for a normally dispersive profile with four different varying half-space velocities. Four different half-space velocities have been chosen to assess the effect of different impedance scenarios on the near-field effects. Table 1 shows the details of soil layer properties for the considered normally dispersive soil profile. Three layer plus half-space soil layer model has been selected. Considered four different half-space velocities, i.e., Case-I(a) to Case-I(d), are 360, 500, 700, and 1000 m/s, respectively. Now, these soil profiles have been modeled in PLAXIS and velocity time histories are generated at four different far-field distances. Far-field distances 10 m, 15 m, 20 m, and 30 m have been selected for this. The generated velocity time histories are taken out and Geopsy Program is used to generate dispersion spectra for full wave field cases. Apparent dispersion curves, i.e., for plane Rayleigh wave cases, have been generated using Mat_Disperse Program for the similar four different far-field cases.

Figure 3a–d show the comparison of the dispersion curves of full wave field for Case-I(a), Case-I(b), Case-I(c), and Case-I(d), respectively. In each figure, a

Table 1 Details of soil layer properties

Thickness (m)	Case-I					
	I(a)	I(b)	Density, ρ (kN/m ³)	I(c)	I(d)	Density, ρ (kN/m ³)
	V_s (m/s)	V_s (m/s)		V_s (m/s)	V_s (m/s)	
5	180	180	18.0	180	180	18.0
7	240	240	18.0	240	240	18.0
12	300	300	18.0	300	300	18.0
Half-space	360	500	18.0	700	1000	20.0

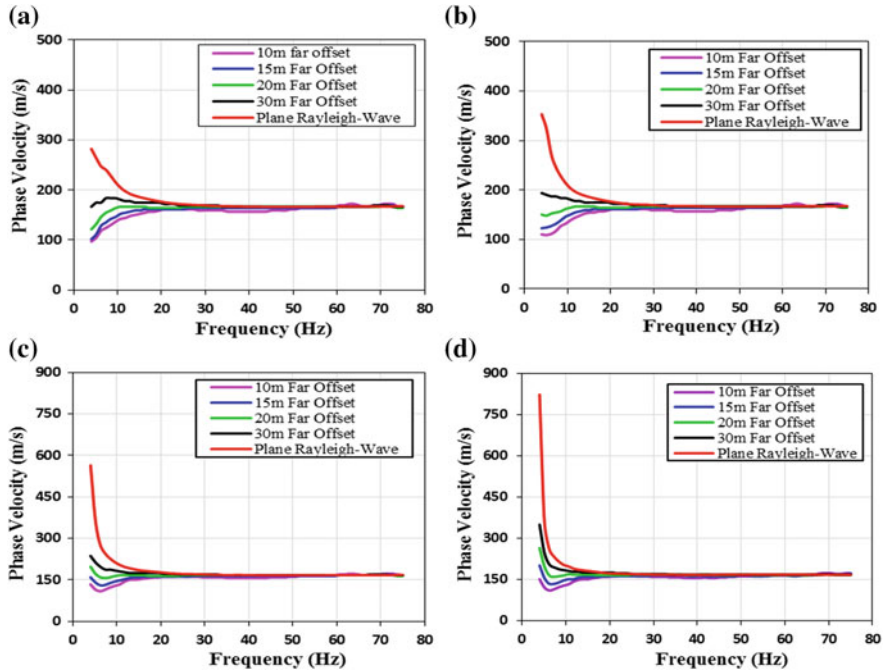


Fig. 3 Comparison of dispersion curves for full wave field with a half-space velocity of **a** HS-360, **b** HS-500, **c** HS-700, and **d** HS-1000 m/s

reference plane Rayleigh wave curve has also been superimposed just to show the extent of level of underestimation. It is very much evident from these plots that the level of underestimation is very much prominent for high impedance case (Fig. 3d). As the far-field distance increases, full wave dispersion curve reach closer to the plane Rayleigh wave velocity and level of underestimation is very high for lower far-offset distances. Once the dispersion curves for full wave field and plane Rayleigh waves are calculated, near-field effects are expressed in terms of two normalized parameters proposed by Yoon and Rix (2009): normalized array centre distance and normalized Rayleigh wave velocity. Normalized array center distance can be written as follows:

$$\frac{\bar{x}}{\lambda_R} = \frac{\frac{1}{N} \sum_{n=1}^N x_n}{\lambda_R} = \frac{\left(\frac{1}{N} \sum_{n=1}^N x_n\right) f}{V_R} \quad (2)$$

where \bar{x} is the mean distance of all receivers in an array with respect to the source, λ_R is the wavelength of the Rayleigh wave, N is number of channels in an array, x_n is the distance of the n th receiver from the source, V_R is the Rayleigh wave phase velocity, and f is the frequency. Normalized Rayleigh wave velocity is expressed as below:

$$\frac{V_R}{V_{R, \text{Plane}}} \quad (3)$$

where V_R is Rayleigh wave phase velocity considering near-field effects, and $V_{R, \text{Plane}}$ is the plane Rayleigh wave velocity, i.e., without near-field effects.

It is very much evident from Fig. 4 that the underestimation increases as impedance contrast increases (Fig. 4a-d). Far-offset distances are having a pronounced effect in the underestimation, lower is the underestimation for higher far-offset distances. For all the impedance cases, it is observed that for a normalized array centre distance 1, the underestimation reduces significantly and leads to a better estimation of Rayleigh wave phase velocity.

To investigate the reason behind the higher underestimation when the half-space impedance is very high (i.e. 700 and 1000 m/s), dispersion curves for full wave field and plane Rayleigh wave are superimposed on modal dispersion curves. Figure 5 shows the comparison for half-space velocity of 700 (Fig. 5a) and 1000 m/s (Fig. 5b). The comparison exhibits an interesting observation that for these two high impedance cases mode jump occurs at the lowest frequency. But usual practice with limited far-offset distances such kind of jump cannot be observed due to the poor resolution in dispersion spectra. Roy and Jakka (2017b) presents an indepth study on near-field effects in site characterization using MASW technique for a wide range of varying subsurface scenarios.

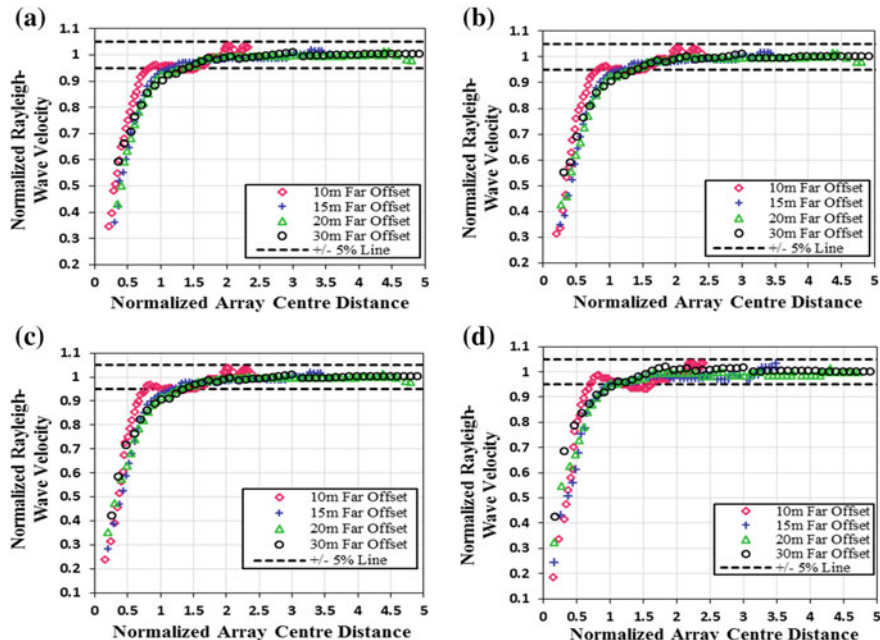


Fig. 4 Near-field effects for Case-I S-wave velocity models with a half-space velocity of; **a** HS-360, **b** HS-500, **c** HS-700, and **d** HS-1000 m/s

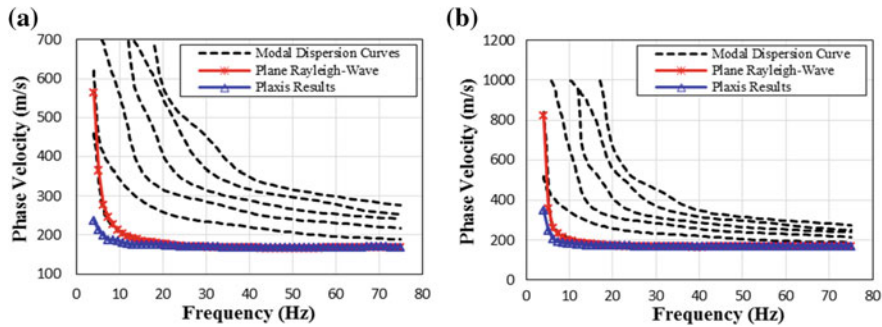


Fig. 5 Comparison of modal dispersion curves with plane- and PLAXIS-simulated dispersion curves for half-space velocity of **a** 700 m/s **b** 1000 m/s

3 Inversion and Data Measurement Uncertainty, Consequence on $V_{S,30}$ Estimation

Surface wave methods suffer from data measurement uncertainty and inversion non-uniqueness. An attempt has been made to separate out the inversion and data measurement uncertainty and their effect on $V_{S,30}$ is studied. A relaxation to the minimum misfit value is introduced to quantify the consequence of inversion uncertainty, whereas data variation up to one standard deviation is considered to study the effect of data uncertainty. In inversion with Neighborhood algorithm, profiles are generated within the bounds defined by misfit relaxation, in case of inversion uncertainty or within the bounds of \pm one standard deviation, in case of data uncertainty. Figure 6 describes the concept of inversion and data measurement uncertainty. Figure 6a shows an assumed mean curve with standard deviation; Fig. 6b presents the inversion uncertainty concept and Fig. 6c shows the data uncertainty concept. Roy and Jakka (2017a) present a detailed and comprehensive study on these inversion and data measurement uncertainty along with the consequence on $V_{S,30}$ estimation.

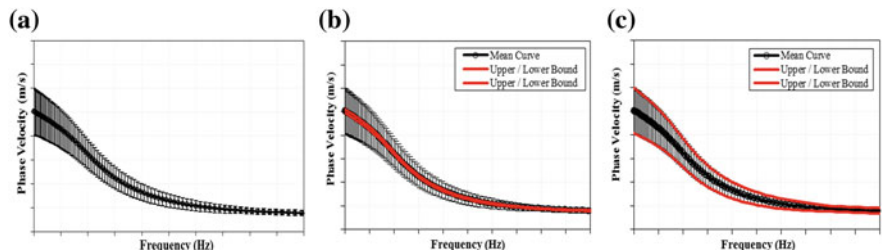


Fig. 6 **a** Mean dispersion curve with data uncertainty, **b** concept of inversion uncertainty, and **c** concept of data measurement uncertainty

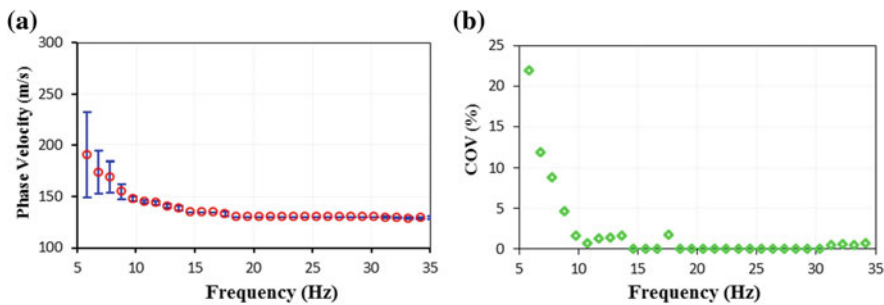


Fig. 7 **a** Mean dispersion curve with data uncertainty, **b** variation of COV

The concept is applied to a site-specific field study of MASW testing. The data has been collected from Solani River site with 24 channel seismograph and automated drop weight of 80 kg. Figure 7a shows the generated mean dispersion curve with standard deviation of the measure data. Figure 7b presents the COV of the data variation which exhibit higher uncertainty at the lower frequencies. A relaxation of 1 and 5% has been assigned to study the inversion uncertainty. Figure 8 presents the results of inversion uncertainty, with increase in relaxation the $V_{S,30}$ variation is also found to increase. A COV value of 0.19% for 1% relaxation and a COV value of 0.36% are observed for 5% relaxation. In data measurement uncertainty, data variation up to one standard deviation is considered. In this case, higher COV is observed, i.e., 3.4%. Figure 9 shows the results of data measurement uncertainty.

4 Consequence of Data and Inversion Uncertainty on Ground Response Analysis

Consequence of data measurement uncertainty and inversion uncertainty has been studied for two site-specific data sets. Similarly like inversion uncertainty case, inversion is performed with Neighborhood algorithm and few profiles covering the entire uncertainty band have been selected to perform ground response analysis using SHAKE2000. Figure 10 presents the results of data uncertainty on ground response analysis. Figure 10a shows the mean field dispersion curve with measured data uncertainty (Fig. 10a1) at LBS ground site, the generated dispersion curves (Fig. 10a2) and velocity profiles (Fig. 10a3) after inversion within the uncertainty bound. Figure 10b shows the results of ground response analysis of those selected generated profiles in terms of amplification spectra (Fig. 10b1), response spectra (Fig. 10b2), and COVs (Fig. 10b3) of amplification and response spectra. Results of ground response analysis reflect high values of COVs of response and amplification spectra.

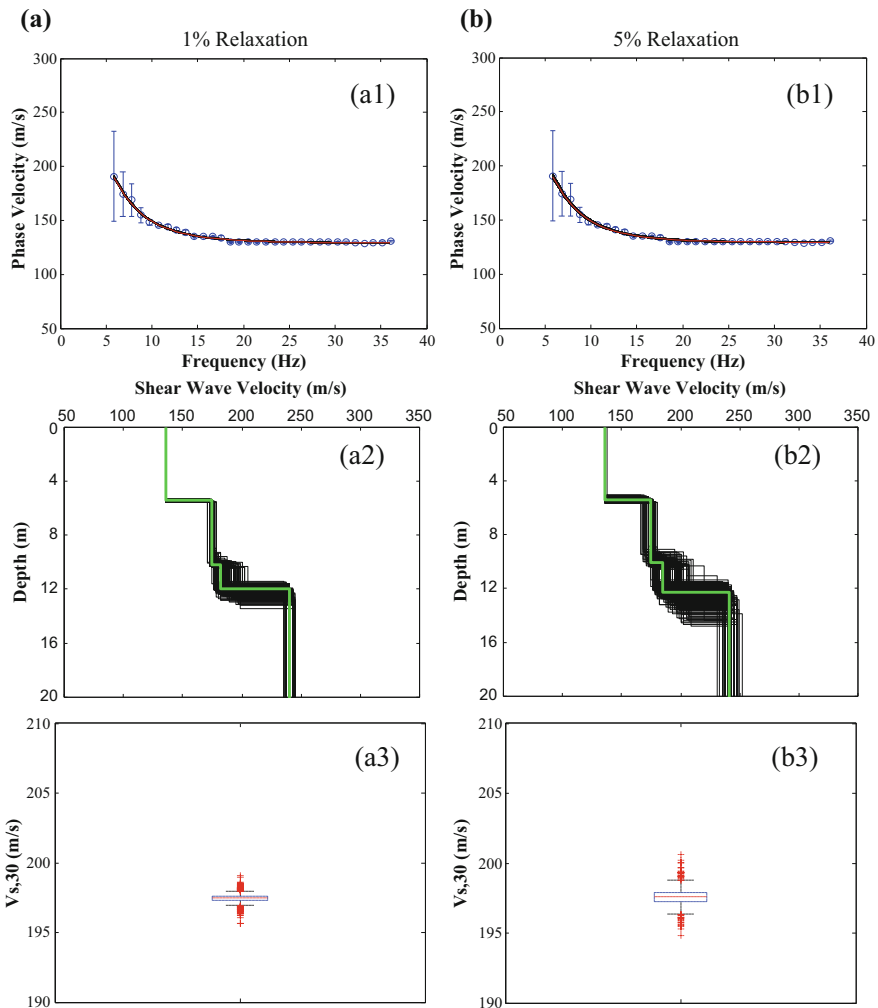


Fig. 8 Generated velocity models at Solani river site by giving **a** 1% relaxation and **b** 5% relaxation

Consequence of inversion uncertainty on ground response has been studied by selecting 15 best fitting profiles after the inversion of dispersion data of Solani river site. Ground response analysis results of those selected velocity profiles have been presented in terms of amplification spectra and response spectra (Fig. 11).

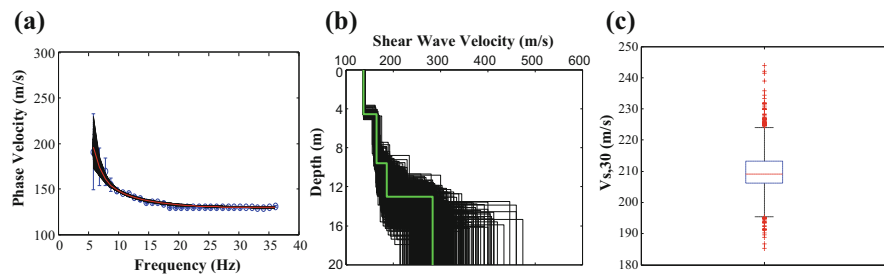


Fig. 9 **a** Dispersion curve generated within the error bounds, **b** selected velocity profiles and **c** distribution of $V_{s,30}$ values of those selected profiles

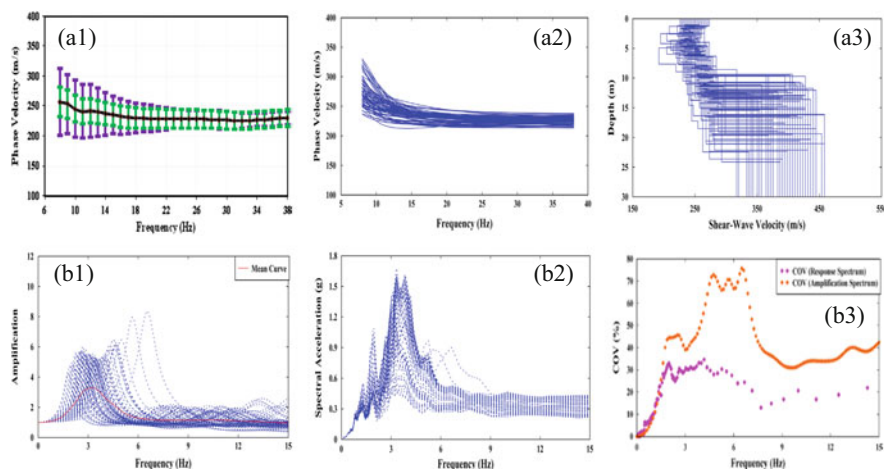


Fig. 10 **a1** Mean dispersion curve with uncertainty, **a2** selected dispersion curve after inversion, **a3** selected Vs profiles, **b1** amplification spectra of selected profiles, **b2** response spectra, **b3** comparison of COVs

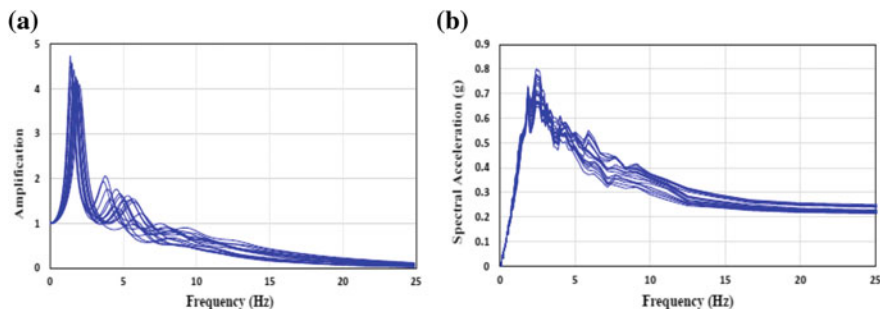


Fig. 11 **a** Amplification spectra and **b** response spectra of first 15 best fitting profiles after inversion at Solani river site

5 Conclusions

Proper attention must be given to the uncertainties involved in surface wave methods in order to make an accurate and reliable estimation of seismic hazard. A proper array centre distance should be maintained while acquiring the surface wave data in the field, and proper care in the field data analysis should also be taken particularly for the sites having inversely dispersive profiles. If the significant data variation is observed during field testing, data variation should be quantified properly and then the consequence of data measurement uncertainty on $V_{S,30}$ and ground response analysis is to be studied to increase the reliability of the hazard analysis. The problem of inversion non-uniqueness should also be taken into the consideration so as to increase the efficiency of application of surface wave methods.

Acknowledgements Financial support received from the SERB/DST, Government of India under Young Scientist Scheme (No. ET-016412014) to carry out the research work presented in this paper, is gratefully acknowledged.

References

Boaga, J., Renzi, S., Vignoli, G., Deiana, R., & Cassiani, G. (2012). From surface wave inversion to seismic site response prediction: Beyond the 1D approach. *Soil Dynamics and Earthquake Engineering*, 36, 38–51.

Boaga, J., Vignoli, G., & Cassiani, G. (2011). Shear wave profiles from surface wave inversion: The impact of uncertainty on seismic site response analysis. *Journal of Geophysics and Engineering*, 8, 162–174.

Boaga, J., Vignoli, G., Deiana, R., & Cassiani, G. (2014). The influence of subsoil structure and acquisition parameters in Masw mode mis-identification. *Journal of Environmental and Engineering Geophysics*, 19(2), 87–99.

Bochet, L., Abraham, O., & Clorennec, D. (2009). Near-offset effects on Rayleigh-wave dispersion measurements: physical modelling. *Journal of Applied Geophysics*, 68, 95–103.

Foti, S., Comina, C., Boiero, D., & Socco, L. V. (2009). Non-uniqueness in surface-wave inversion and consequences on seismic site response analyses. *Soil Dynamics and Earthquake Engineering*, 29, 982–993.

Jakka, R. S., Roy, N., & Wason, H. R. (2014). Implications of surface wave data measurement uncertainty on seismic ground response analysis. *Soil Dynamics and Earthquake Engineering*, 61–62, 239–245.

Jakka, R. S., Roy, N., & Wason, H. R. (2015). Reply on “Implications of surface wave data measurement uncertainty on seismic ground response analysis”. *Soil Dynamics and Earthquake Engineering*, 74, 92–95.

Jones, R. B. (1958). In-situ measurement of the dynamic properties of soil by vibration methods. *Geotechnique*, 8(1), 1–21.

Lai, C. G., Foti, S., & Rix, G. J. (2005). Propagation of data uncertainty in surface wave inversion. *Journal of Environmental and Engineering Geophysics*, 10(2), 219–228.

Lin, C. P., & Lin, C. H. (2007). Effect of lateral heterogeneity on surface wave testing: Numerical simulations and a countermeasure. *Soil Dynamics and Earthquake Engineering*, 27, 541–552.

Louie, J. N. (2001). Faster, better: Shear-wave velocity to 100 meters depth from refraction microtremor arrays. *Bulletin of the Seismological Society of America*, 91(2), 347–364.

Marosi, K. T., & Hiltunen, D. R. (2004). Characterization of SASW shear wave velocity measurement uncertainty. *Journal of Geotechnical and Geoenvironmental Engineering*, 130(10), 1034–1041.

Nazarian, S., Stokoe, K. H.-I. I., & Hudson, W. R. (1983). Use of spectral analysis of surface waves method for determination of moduli and thicknesses of pavement systems. *Transportation Research Record*, 930, 38–45.

Park, C. B., Miller, R. D., & Xia, J. (1999). Multi-channel analysis of surface waves. *Geophysics*, 64(3), 800–808.

Roy, N., Jakka, R. S., & Wason, H. R. (2013a). Effect of surface wave inversion non-uniqueness on 1-D seismic ground response analysis. *Natural Hazards Journal*, 68(2), 1141–1153.

Roy, N., Jakka, R. S., & Wason, H. R. (2013b). Reply to comment on “Effect of surface wave inversion non-uniqueness on 1D seismic ground response analysis”. *Natural Hazards Journal*, 75(1), 983–989.

Roy, N., & Jakka, R. S. (2017a). Effect of data uncertainty and inversion non-uniqueness of surface wave tests on $V_{s,30}$ estimation. *Soil Dynamics and Earthquake Engineering* (Under review).

Roy, N., & Jakka, R. S. (2017b). Near-field effects on site characterization using MASW Technique. *Soil Dynamics and Earthquake Engineering*, 97, 289–303.

Strobbia, C., & Cassiani, G. (2011). Refraction microtremors (ReMi): Data analysis and diagnostics of key hypotheses. *Geophysics*, 76(3), MA11–MA20.

Stokoe II, K. H., Wright, S. G., Bay, J. A., & Roessel, J. M. (1994). Characterization of geotechnical sites by SASW method geophysical characterization of sites. In R. D. Woods (Ed.) (pp. 15–25). New Delhi: Oxford & IBH Publishing.

Teague, D. P., & Cox, B. R. (2016). Site response implications associated with using non-unique V_s profiles from surface wave inversion in comparison with other commonly used methods of accounting for V_s uncertainty. *Soil Dynamics and Earthquake Engineering*, 91, 87–103.

Xia, J., Miller, R. D., & Park, C. B. (1999). Estimation of near-surface shear-wave velocity by inversion of Rayleigh wave. *Geophysics*, 64(3), 691–700.

Yoon, S., & Rix, G. J. (2009). Near-field effects on array-based surface wave methods with active sources. *Journal of Geotechnical and Geoenvironmental Engineering*, 135, 399–406.

Impact of Flooding on Roadways

Rajib Basu Mallick, Mingjiang Tao and Nivedya M. K.

Abstract Flooding can cause extensive damages in roadways, particularly in those with granular base layers and thin asphalt mix surface layers. The objective of this paper is to present a summary of work conducted on the evaluation of the impact of flooding on pavements. Research shows that flood-induced damage occurs through various ways—weakening and washing away of granular base and soil subgrade layers, washing away of thin surface layers such as seals, and through erosion of subsurface materials near flowing water. Dislocation of concrete slabs due to washing away of subgrade soils during flooding has also been noted. Several models and frameworks have been developed to predict change in structural and surface properties such as roughness due to the impact of flooding. A number of models relating resilient modulus of soil to saturation and matric suction have been proposed. Researches have used both finite difference and finite element models to simulate flow of water through pavements. It has been confirmed that flow under unsaturated conditions is the dominant drainage mechanism in pavements. The role of base course material properties, trench backfill material, and drainage systems has been found to be crucial for drainage. The importance of considering the soil water characteristic curve information and an understanding of change in hydraulic conductivity for different saturation conditions has been emphasized.

Keywords Pavement drainage · Resilient modulus · Flooding
Road damage · Saturation · SWCC

R. B. Mallick (✉) · M. Tao · Nivedya M. K.
Civil and Environment Engineering Department,
Worcester Polytechnic Institute (WPI), Worcester, MA, USA
e-mail: rajib@wpi.edu

M. Tao
e-mail: taomj@wpi.edu

Nivedya M. K.
e-mail: nmadankarakottay@wpi.edu

1 Introduction

In most parts of the world, roadways are responsible for the transportation of the majority of passengers and a significant amount of commodities. Road closures due to damages and failures cause delay, rerouting, and consequent loss of time and money and may endanger the lives of citizens. Finally, premature failure of roadways and resultant need for repair can lead to significant expense for road authorities and inconvenience for the road users.

One of the primary causes of road failures is the ingress of water into the roadway pavement structure. Water is responsible for the reduction in the structural capacity of pavements through a variety of ways. For example, it can damage the bituminous layers, reduce the load-bearing capacity of the underlying layers, reduce the support in concrete pavements, or cause a combination of all of these effects, and wash away stretches of roadways (Fig. 1). The net result is a roadway structure with a significantly reduced load-bearing capacity. Such a reduction in the capacity may persist for a short or long period of time, depending on the amount of water and the time it takes for it to drain out.

Flooding may cause inundation of roadways under large amounts of water and for extended periods of time, and/or subject roadways near streams or rivers to rapidly flowing water. Generally, floodwaters entering the roadway persist for a relatively long time because of slowing down of flow of water out of the pavement structure. Quite often, they persist in the underlying layers long after the floodwaters have receded from the surface of the pavement. This presence of water keeps the pavement structure vulnerable to traffic loading, which may go unnoticed by



Fig. 1 Road section washed away by flooding

road authorities if they, as it happens in most cases, depend solely on visual observation. The opening of such a roadway to traffic can lead to two serious consequences—lives of employees working to clear roads of flood debris and travelers can be endangered, and the roadway can fail prematurely, well before the design life causing unforeseen requirement of budgets for repairing and road closures and further delay for the travelers.

The objective of this paper is to present a review of recent work that has been conducted on impact of flooding on roadways. The organization of the paper is as follows: an overview, followed by reviews of relevant literature, and finally conclusions and recommendations from the reviews.

2 Overview of the Problem

Water in hot-mix asphalt (HMA) mixes can lead to detachment of asphalt binder from aggregate surface (stripping), create loose aggregate particles, and subsequently lead to the formation of potholes and disintegration of the layer. Water in Portland cement concrete (PCC) pavements can lead to an acceleration of cracking, leaching of chemicals, and corrosion of reinforcements and dowels. Water can also dissolve some types of carbonate aggregates and cause localized sinkholes and can cause swelling of expansive soils in the subgrade. Presence of water causes pumping of subgrade materials from beneath slabs, leading to premature failure of PCC pavements at joints. Fast-flowing water near streams can cause erosion of materials at different layers, such as chip seals and base courses, and weaken the foundation of the top layers, and thus cause overall failure of the pavement structure. A number of researches have pointed out the vulnerabilities of pavements to flooding—significant and widespread failures, specifically for thin surface asphalt pavements.

Among all of the different types of effects, the most significant effect that has been identified with the impact of flooding is that on the geo-materials (aggregates and soil). These geo-materials provide the bulk of the structural strength or the foundation of most pavements—base, subbase, and subgrade. Floodwater can reduce the strength/stiffness of these layers significantly due to increase in saturation for long periods of time (see Fig. 2, for example), which leads to excessive strains and deformations under traffic loading and consequently premature failure of the pavement. The extent of damage depends on the vulnerability of the pavement to ingress of surface water, the amount of water the inundation period, and the drainage features of the pavement. High water tables, clogged ditches, absence of properly maintained underdrain systems, and the presence of unsaturated conditions within layers can reduce the hydraulic conductivities significantly, resulting in poor drainage conditions. Undetected high saturation levels in the underlying layers can make a pavement highly vulnerable to traffic loading immediately after flooding. Understanding the impact of moisture, on soil properties specially those related to pavements, has been the topic of many researches. Also, advanced and more

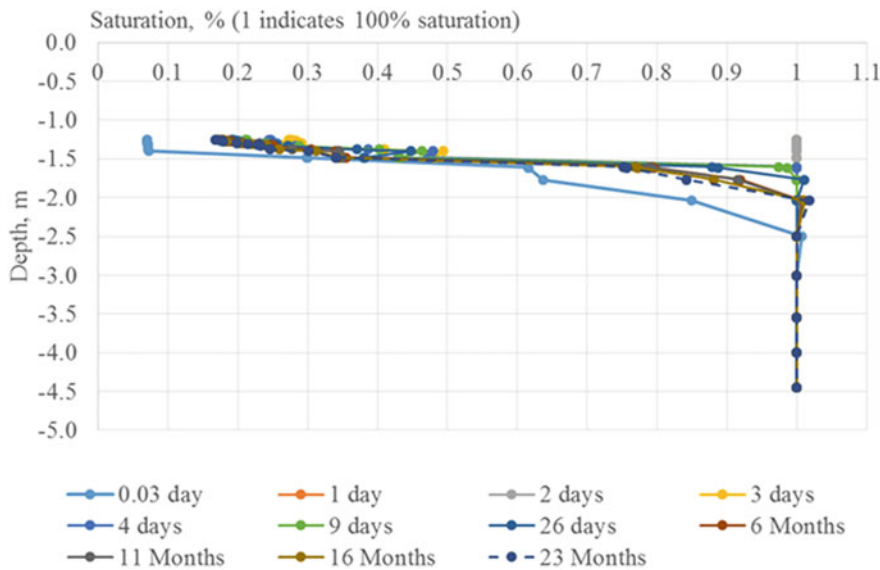


Fig. 2 Example of plot of time versus degree of saturation in base layer due to flooding (Nivedya et al. 2017)

accurate models have been developed and implemented in different pavement structural design methods.

Accurate and timely detection of intensity and extent of flood-induced damage in pavements is a topic of serious concern. Research has been carried out in the recent past on developing guidelines and framework for evaluation of pavements after flooding, using nondestructive testing, hydraulic analyses, and predictive equations, as well as Artificial Neural Network (ANN). Simultaneously, research has been carried out to develop models for deterioration of pavement surface/ride and structural condition as a result of flooding, which could be incorporated in pavement management systems for adopting proper pre- and post-flood strategies.

3 Literature Review—Impact of Flooding on Pavements

Gaspard et al. (2007) carried out a quantitative analysis of loss of pavement strength from data collected from 238 lane miles of roadways in New Orleans, Louisiana, after floods caused by Hurricane Katrina. They observed relatively greater damage for thinner pavements, and voids at joints and deterioration of joint transfer efficiencies in PCC pavements. They noted that the average structural strength loss for thinner PCC pavements (<10.5 in.) was 0.43 and 0.48 in. of HMA, for deterioration of the pavement and the subgrade, respectively, and an average loss of 0.5 in. of HMA for composite pavements.

Helali et al. (2008) evaluated pavement conditions after Hurricane Katrina and Rita in Louisiana. They concluded that flooding caused significant damage to pavements, and the loss of structural strength in asphalt pavements amounted to those equivalent to >50 mm of HMA layer.

Zhang et al. (2008) reported another study of evaluation of flooded pavements in Louisiana, in which a suite of nondestructive testing tools and Geographical Information System (GIS) maps were utilized to evaluate the extent and intensity of damage. The authors concluded that pavements in low-lying areas and those with thin structures suffered the most damage while damage to PCC pavements was very limited.

Kreibich et al. (2009) conducted a study in Germany on the effect of flow velocity on flood damage of structures, including buildings and roads. They used hydraulic parameters such as flow velocity and depth, and their combinations such as intensity (velocity*depth) as predictors of damage. Their study showed that flow velocity is a significant predictor of road damage and stressed the need for further studies to develop models for relating flow velocity to road damage.

Vennapusa et al. (2013) conducted a study on using advanced technologies to rapidly assess the flood-induced damage to secondary roadways, and developing effective repair and mitigation strategies and solutions. The authors noted the following primary modes of damage in pavements: voids at shallow and deeper depths due to failure of underlying base materials and erosion of shoulders close to water line in paved roadways (both flexible and rigid) and rutting and erosion of materials in unpaved roadways. They provided a catalog of different available evaluation and assessment techniques and a framework for the selection of assessment and mitigation techniques.

The primary reasons of concrete slab movements during flooding in Iowa (such as on I 680 and IA2) were washing away of subgrade/subbase as well as concrete slabs by rapidly flowing floodwater, moving in a perpendicular direction to the highways (Omundson 2013). In cases where the flow was parallel to the highway (such as in I 29), scouring of pavement foundation materials (up to a width of 3 ft and depth of 4 ft in the driving lane) was observed in a few cases.

Daniel and Mallick (2014) noted from a survey that more than 90% of the states in the US rely on visual inspection for assessment of flooded pavements, although about 30% conduct nondestructive test also, and about 10% conduct hydraulic analyses. Only a few states were reported to conduct remaining life analyses for flooded pavements.

Deterioration of pavement conditions and their probabilistic modeling has been the subject of extensive work by Khan et al. (2014, 2015, 2016) in Australia. Using field data and modeling, they have predicted increase in roughness (International Roughness Index, IRI) and rutting as a consequence of flooding. Their models relate pavement damage with the probability of flooding in specific projects locations. The researchers have utilized their models along with HDM-4 to develop optimum pavement maintenance strategies to reduce the impact of flooding.

Wang et al. (2015) have presented a study on the evaluation of structural damage of asphalt pavements due to flooding. They used the results of tests with a subgrade

soil (in Hong Kong) to estimate the reduction in modulus with an increase in saturation and then utilized mechanistic empirical principles. Using transfer functions that relate allowable traffic repetition to response under traffic (strain), they estimated the damage in a flooded pavement that is inflicted by traffic, in terms of damage in a normal pavement (no flood scenario). They were able to demonstrate significant flood-induced damage, specifically in asphalt pavements with thin surface HMA layer.

Mallick et al. (2015) have developed a system dynamics-based tool to evaluate the vulnerability of pavements to flooding. Their model uses the Green-Ampt equation (Green and Ampt 1911) to determine the time for flood (of a specific inundation and duration) water to infiltrate to the base course of a pavement with a specific structure and materials and compares the time (T_{critical}) to the actual time of flooding. The model takes into account the condition of the surface layer (cracked or uncracked), through the use of the Global Aging System (GAS) model (Mirza and Witczak 1995) for asphalt mixes, for prediction of permeability at different times after construction under different climatic conditions, and the eroding effect of fast-flowing water, using the Briaud model (Briaud 2008). The results of their simulation show the important positive impact of thicker surface layer, base layer, and compaction density in reducing the vulnerability of asphalt pavements to the impact of flooding.

Based on data from roads affected by floods in Australia, Sultana et al. (2016) developed a model for short-term post-flooding structural condition of pavements. The researchers' utilized FWD data from pre- and post-flooded pavements and utilized the data to estimate modified structural number for the pavements. Their model predicted a deterioration of structural strength in the post-flooded condition.

Mallick et al. (2017) presented a framework and a tool for estimating the structural condition of pavements after flooding by using a combined hydraulic and structural analysis. They estimated the flow conditions through the underlying layers, utilized the hydraulic conductivity to estimate the saturation of the base layer at different times, and finally used the resilient modulus–saturation relationships to predict the overall structural capacity of the pavement in terms of predicted deflection under various types of loads. Their results showed a reduction in capacity to different extents and for different periods, depending on the hydraulic conductivities of the underlying layers.

Qiao et al. (2017) developed a Bayesian Decision Tress-based approach for making decisions to open or close a road after flooding, on the basis of probabilities and assumed risks and payoffs for specific events. Their method could be utilized by road authorities to consider different options such as conduct hydraulic analysis or nondestructive testing of pavement after flooding, compare the relative merits and demerits, and then select the option with the most payoff potential. The approach is based on minimizing the risk of opening the road when it is in a damaged or unsafe condition or closing the road when it is in an undamaged condition, based on visual inspection only.

4 Impact of Moisture on Granular Materials Used in Pavements

For unbound geo-materials, such as those used in base or subbase and subgrade of a pavement, moisture content plays an important role in their behavior. Resilient modulus (M_R) is a fundamental material parameter that characterizes elastic response of pavement materials under traffic loading and has been used for pavement design, performance evaluation, distress diagnosis, and rehabilitation (AASHTO 1993; NCHRP I-37A 2004). For example, in a gravel soil a 50% decrease in resilient modulus due to a change in saturation from 70 to 96% was reported by Haynes and Yoder (1963). Hicks and Monismith (1971) observed that the resilient modulus decreases steadily as the moisture content increases above its optimum value. During flooding, water infiltrates into the subsurface layers, and the degree of saturation in these layers can increase significantly or reach its maximum value (i.e., 100%); consequently, the load-bearing capacity of the flooded pavement is reduced significantly.

Drumm et al. (1997) proposed a method for predicting the change in the resilient modulus of fine-grained soils caused by increased degree of saturation, with $M_{R(opt)}$ as a reference value. This model was based on the linear relationship observed between resilient modulus and degree of saturation for 11 soils throughout Tennessee. In addition, an empirical equation was proposed for the rate of change of resilient modulus with change of degree of saturation, as a function of AASHTO soil classification and $M_{R(opt)}$. It was found that an increase in gravimetric moisture content of 1.5% would result in a change in degree of saturation of 4.75% and a decrease in resilient modulus by a factor of two (e.g., 130–70 MPa).

$$M_{R(wet)} = M_{R(opt)} + dM_R/dS \Delta S$$

$$dM_R/dS = 1690 - 194(CLASS) - 11.2M_{R(opt)}$$

where $M_{R(wet)}$ = resilient modulus at increased post-compaction saturation; $M_{R(opt)}$ = resilient modulus at optimum moisture content and maximum dry density; dM_R/dS = gradient of resilient modulus with respect to saturation (or slope of M_R versus degree of saturation curve); and ΔS = change in post-compaction degree of saturation expressed as a decimal. CLASS = AASHTO classification expressed as a real number (e.g., for A-4, CLASS = 4.0; for A-7-5, CLASS = 7.5); and = resilient modulus (MPa) at optimum moisture content and maximum dry density for $\sigma_c = 41$ kPa (6 psi) and $\sigma_d = 28$ kPa (4 psi).

A sigmoid model was proposed for both fine-grained and coarse-grained soils by Witczak et al. (2000):

$$\log M_R/M_{Ropt} = a + (b - a) / (1 + \exp(\beta + k_s \cdot (S - S_{opt})))$$

where $M_R/M_{R_{opt}} =$ resilient modulus ratio; $M_R =$ resilient modulus at a given degree of saturation; $M_{R_{opt}} =$ resilient modulus at optimum moisture content and maximum dry density; $a =$ the minimum of $\log(M_R/M_{R_{opt}})$; $b =$ the maximum of $\log(M_R/M_{R_{opt}})$; $\beta =$ location parameter that is obtained as a function of a and b by imposing the condition of a zero intercept $\beta = \ln(-b/a)$; regression parameter; $S - S_{opt} =$ variation of degree of saturation in decimal. The resilient modulus predicted using the aforementioned model is only a function of the degree of saturation while the direct effect of the state of stress (or effective stress) is not considered.

Yang et al. (2005) found that the combination of high subgrade moisture content and poor compaction results in sharp decreases in subgrade resilient modulus. Based on the effective stress concept for unsaturated soils (Bishop's equation), they proposed a deviator stress-matric suction model as follows:

$$M_R = k_5(\sigma_d + \chi(u_a - u_w))^{k_6}$$

where k_5 and k_6 are regression constants; χ is a parameter in the Bishop's equation and thought to be a function of degree of saturation ($\chi = 0$ for dry soils, $\chi = 1$ for saturated soils); σ_d is deviator stress.

Liang et al. (2008) proposed a model that is capable of considering the influence of both state of stress and water content (or matric suction) on resilient modulus.

$$M_R = k_1 p_a (\theta + \chi_m \psi_m / p_a)^{k_2} (\tau_{oct} / p_a + 1)^{k_3}$$

where $\psi_m =$ matric suction that is the difference in pore air pressure and pore water pressure of unsaturated soils; $\chi_m =$ Bishop's effective stress parameter that ranges from 0 to 1 and represents the contribution of matric suction to the effective stress.

4.1 Assessment of Pavement Condition After Flooding

One of the big challenges that road authorities face after floodwaters have receded is in making a rational decision regarding opening the road to traffic or closing it for further investigation. A way to forecast the condition of the pavement after flooding will be very helpful to avoid the dangerous conditions. This can be done by combining hydraulic analysis with structural analysis (Mallick et al. 2017) (see Fig. 3). The method starts with the estimation of hydraulic properties of the base course materials, which consists of saturated hydraulic conductivity and Soil Water Characteristics Curve (SWCC) data. The gradation of the base course materials, specifically D60, can be used as a predictor of saturated hydraulic conductivity. Based on the flooding scenario, using the hydraulic properties, the saturation level at different depths at different times can be estimated. This estimation can be carried out with various methods such as a finite difference method (for example,

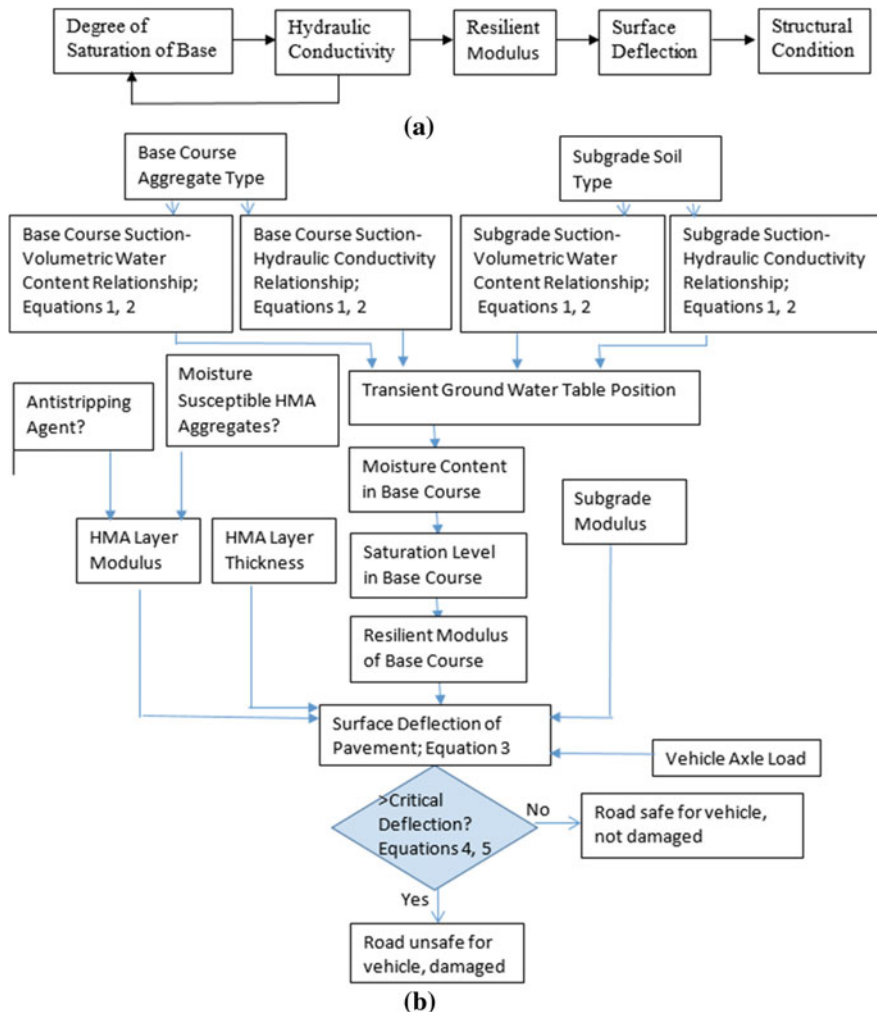


Fig. 3 **a** Overview of model; **b** details of the model. Note Critical deflections for damaged road (500 μm) and unsafe road (750 μm) are different (Mallick et al. 2017)

MNDrain) or finite element method (for example, GeoStudio 2016). Next, using the saturation values and the resilient modulus versus saturation models the modulus of the base course at different depths at different times can be estimated. These moduli values can then be used to estimate any structural response under traffic that is indicative of the condition of the pavement. Using this framework, the condition of the pavement after flooding can be predicted, and the impact of different materials and layer thicknesses can also be evaluated.

5 Numerical Simulations on Water Movement in Pavement Structures

Stormont and Zhou (2005) investigated water movement in pavement sections using VS2DHI, which is a finite difference model that solves Richard's equation for flow in one or two dimensions.

$$\frac{\partial \theta}{\partial t} = \frac{\partial}{\partial z} \left[K(\theta) \left(\frac{\partial \psi}{\partial z} + 1 \right) \right]$$

where θ = volumetric water content; $K(\theta)$ = unsaturated hydraulic conductivity as a function of soils' water content; ψ = suction of the soil; t = time; and z = vertical coordinate taken positive downward.

The simulation results indicate that unsaturated flow is the dominant flow pattern of the water movement in the pavement section from the surface infiltration, and the drainage efficiency depends on the base course and edge drain configurations, as well as trench backfill materials. The following specific conclusions were drawn from this study: (i) While the materials with high saturated hydraulic conductivity are desirable, the magnitude of saturated hydraulic conductivity does not warrant good drainage performance; (ii) Greater drainage efficiency can be achieved by designing for unsaturated flow, which implies less water in pavement layers at any time; and (iii) Pavement drainage should aim to not only limit positive water pressure, but mitigate moisture increase in pavement sections from unsaturated water movement as well.

Ariza and Birgisson (2002) used SEEP/W and FHWA DRIP software to analyze data collected at the Minnesota Road Research project. Their simulation results indicated that most modeled materials would drain under saturated conditions in just a few minutes while it would take days or is unachievable under unsaturated conditions. Their study also indicated that SWCC, hydraulic conductivity curve, and air entry potential of pavement materials play important roles in governing flows throughout pavement systems.

6 Conclusions

Flooding has been found to impact roadways adversely in a significant way. The different mechanisms of flood-induced damage include washing away of bituminous seal layers and granular material from base and subbase, creating voids, erosion of layers in pavements near streams, and saturation of granular layers. The most impacted pavements are those with granular layers and thin bituminous surfacing, although loss of concrete slabs have also been noted as a result of washing away of underlying subgrade layers. The potential of damage can be estimated from velocity and depth of floodwater, and the extent of damage to the pavement can be

estimated by knowing the saturation, the resilient modulus and the corresponding pavement repose under expected traffic. The degree of compaction of the subgrade soil has been found to be critical for defining equilibrium moisture content, and hence the behavior of the soil with increased moisture content. Advanced models have been proposed that consider the effects of both the stress state and the moisture content (or suction) on resilient modulus. Models have been proposed to predict the surface and structural conditions after flooding from statistical analyses of data collected from pre- and post-flooded pavements. A numerical approach has also been proposed through a combination of hydraulic and structural analyses, utilizing finite element methods and layered elastic analyses. Analyses have confirmed that flow of water in pavements is mostly under unsaturated conditions, and the flow is much slower than that during saturated conditions.

7 Recommendations for Research

Based on the review of the literature, the following recommendations are made regarding the evaluation of impact of flooding on pavements. (1) Investigate the SWCC behavior of the materials that are typically used in different pavement layers; (2) Evaluate the combined effects of the properties of the pavement layers and the drainage structures (ditch, trenches, pipes) on the drainage; (3) Investigate the impact of different types of scenarios such as rainfalls, typical and atypical, and flooding, on the drainage; (4) Investigate the impact of existing water tables/groundwater levels on the drainage; (5) Combine hydraulic analyses with structural analyses to estimate the impact of flooding and heavy rainfall on the structural performance and deterioration, and remaining life of the pavement.

Considering the recent increase in the use of recycled layers in pavements, research is needed in the understanding of drainage through these layers, to ensure the proper functioning of these pavements under flooding and heavy rainfall, and hence the realization of the environmental and cost benefits of recycling.

References

AASHTO. (1993). *Guide for design of pavement structures*. Washington, D.C.

Ariza, P., & Birgisson, B. (2002). *Evaluation of water flow through pavement systems*. Final report for Minnesota Department of Transportation, University of Florida.

Briaud, J. L. (2008). Case histories in soil and rock erosion: Woodrow Wilson Bridge, Brazos River Meander, Normandy Cliffs, and New Orleans Levees. *Journal of Geotechnical and Geoenvironmental Engineering*, 134(10), 1425–1447.

Daniel, J. S., & Mallick, R. B. (2014). *Flooded pavement assessment*. Quarterly Report to FHWA, p. 15.

Drumm, E. C., Reeves, J. S., Madgett, M. R., & Trolinger, W. D. (1997). Subgrade resilient modulus correction for saturation effects. *Journal of Geotechnical and Geoenvironmental Engineering*, 123(7), 663–670.

Gaspard, K., Martinez, M., Zhang, Z., & Wu, Z. (2007). *Impact of Hurricane Katrina on roadways in the New Orleans area*. Technical Assistance Report No. 07-2TA, p. 73.

Geostudio. (2016). *GEO-SLOPE*, Calgary, Alberta, Canada.

Green, W. H., & Ampt, G. (1911). Studies of soil physics, part I—The flow of air and water through soils. *Journal of Agricultural Science*, 4, 1–24.

Haynes, J. G., & Yoder, E. J. (1963). Effects of repeated loading on gravel and crushed stone base course materials used in the AASHO road test. *Highway Research Record*, 39.

Helali, K., Robson, M., Nicholson, R., & Bekheet, W. (2008). Importance of a pavement management system in assessing pavement damage from natural disasters: A case study to assess the damage from Hurricanes Katrina and Rita in Jefferson Parish, Louisiana. In *Proceedings of the 7th International Conference on Managing Pavement Assets* (p. 10).

Hicks, R. G., & Monismith, C. L. (1971). Factors influencing the resilient properties of granular materials. *Highway Research Record*, 345, 15–31.

Khan, M., Mesbah, M., Ferreira, L., & Williams, D. J. (2014). Developing a new road deterioration model incorporating flooding. *Proceedings of the Institution of Civil Engineers Transport*, 167(5), 322–333.

Khan, M., Mesbah, M., Ferreira, L., & Williams, D. J. (2015). Development of a post-flood road maintenance strategy: Case study Queensland, Australia. *International Journal of Pavement Engineering*. <https://doi.org/10.1080/10298436.2015.1121781>.

Khan, M., Mesbah, M., Ferreira, L., & Williams, D. J. (2016). Pre-flood road maintenance strategy for a road authority. *Journal of Transportation Engineering*, 142(12), [https://doi.org/10.1061/\(asce\)te.1943-5436.0000901](https://doi.org/10.1061/(asce)te.1943-5436.0000901).

Kreibich, H., Piroth, K., Seifert, I., Maiwald, H., Kunert, U., Schwarz, J., et al. (2009). Is flow velocity a significant parameter in flood damage modelling? *Natural Hazards and Earth System Sciences*, 9(5), 1679–1692.

Liang, R., Rabab'ah, S., & Khasawneh, M. (2008). Predicting moisture-dependent resilient modulus of cohesive soils using soil suction concept. *Journal of Transportation Engineering, ASCE*, 134(1), 34–40.

Mallick, R. B., Tao, M., Daniel, J. S., Jacobs, J. S., & Veeraragavan, A. (2015). Development of a methodology and a tool for the assessment of vulnerability of roadways to flood-induced damage. *Journal of Flood Risk Management*. <https://doi.org/10.1111/jfr3.12135>.

Mallick, R. B., Tao, M., Daniel, J. S., Jacobs, J., & Veeraragavan, A. (2017). A combined model framework for asphalt pavement condition determination after flooding. *Transportation Research Record (TRR): Journal of the Transportation Research Board*. <https://doi.org/10.3141/2639-09>.

Mirza, M. W., & Witczak, M. W. (1995). Development of a global aging system for short and long term aging of asphalt cements. *Journal of Association Asphalt Paving Technologies*, 64, 393–430.

NCHRP 1-37A. (2004). *Guide for mechanistic-empirical design of new and rehabilitation pavement structures*. Final Report, Part 2, Design Inputs. Washington, D.C.: National Cooperative Highway Research Program (NCHRP).

Nivedya, M. K., Tao, M., Mallick, R. B., Daniel, J. S., & Jacobs, J. M. A. (2017). Framework for the assessment of resilience of pavement to flooding. *Transportation Research Board Annual Meeting*.

Omundson, J. (2013). *Personal communication*. Feb 5, 2013.

Qiao, Y., Medina, R. L. M., Mallick, R. B., & Daniel, J. S. (2017). Decision-tree for post-flooding roadway operations. *Transportation Research Record (TRR): Journal of the Transportation Research Board*. <https://doi.org/10.3141/2604-15>.

Stormont, J. C., & Zhou, S. (2005). Impact of unsaturated flow on pavement edgedrain performance. *Journal of Transportation Engineering*, 131(1), 46–53.

Sultana, M., Chai, G., Martin, T., & Chowdhury, S. (2016). Modeling the postflood short-term behavior of flexible pavements. *ASCE Journal of Transportation Engineering*, 142(10). [https://doi.org/10.1061/\(asce\)te.1943-5436.0000873](https://doi.org/10.1061/(asce)te.1943-5436.0000873).

Vennapusa, P., White, D., & Miller, K. (2013). *Western Iowa Missouri river flooding—Geo-infrastructure damage assessment, repair, and mitigation strategies* (p. 269). Iowa State University.

Wang, Y., Huang, Y., Rattanachot, W., (Woody) Lau, K. K., & Suwansawas, S. (2015). Improvement of pavement design and management for more frequent flooding caused by climate change. *Advances in Structural Engineering*, 18(4), 487–496.

Witczak, M., Dragos, A., & Houston, W. (2000). *Guide for mechanistic-empirical design of new and rehabilitated pavement structures. Appendix DD-1: Resilient modulus as function of soil moisture—Summary of predictive models*. Final report to National Cooperative Highway Research Program, Report, (1-37A).

Yang, S.-R., Huang, W. H., & Tai, Y. T. (2005). Variation of resilient modulus with soil suction for compacted subgrade soils. *Transportation Research Record: Journal of the Transportation Research Board*, 1913(1), 99–106.

Zhang, Z., Wu, Z., Mark, M., & Kevin, G. (2008). Pavement structures damage caused by Hurricane Katrina flooding. *Journal of Geotechnical and Geoenvironmental Engineering*, 134(5), 633–643.

A Quantitative Framework for Sustainability and Resilience in Geotechnical Engineering

Dipanjan Basu and Mina Lee

Abstract Civil infrastructure systems, especially geotechnical assets, are vulnerable to climate change, and natural and man-made disasters. Resilience, which is the ability of a system to absorb, recover from, and adapt to disruptions so that the consequences are minimized, introduces a new paradigm to overcome challenges related to infrastructure vulnerability against disasters. Consideration of sustainability in conjunction with resilience in infrastructure asset management ensures that human interventions of building resilient infrastructure systems are in harmony with the natural environment and with the aspirations of the present and future generations. A quantitative framework for the assessment of resilience and sustainability of geotechnical infrastructure is developed based on the Driver–Pressure–State–Impact–Response (DPSIR) framework. The new framework is demonstrated through an example problem based on a selected road network in the province of Ontario, Canada.

Keywords Sustainability assessment · Resilience metrics · DPSIR framework · Transportation network · Geotechnical infrastructure

1 Introduction

Over the last decade, the importance of sustainability in the built environment has been emphasized because of the growing awareness that there are limited resources on earth to fulfill human needs. The effort of the current generation to sustain and carefully consume available resources with the consideration of intergenerational equity has been a norm for sustainable development. In the recent past,

D. Basu (✉) · M. Lee
Department of Civil and Environmental Engineering,
University of Waterloo, Ontario, Canada
e-mail: dipanjan.basu@uwaterloo.ca

M. Lee
e-mail: m65lee@uwaterloo.ca

the increased frequency and magnitude of extreme events (i.e., natural and man-made disasters), mostly because of climate change, have led to the realization that it is necessary to build resilience in civil infrastructure systems, ecosystems, communities, and other critical systems that are vital for fulfilling human needs and maintaining quality of life. Incorporation of resilience theory and sustainability science during the design, construction, operation, and maintenance of critical infrastructure systems ensures that consequences of extreme events are minimized and, at the same time, adverse environmental and socioeconomic impacts are reduced so that sustainable development is achieved.

Geotechnical assets (e.g., embankments, tunnels, retaining structures, bridge foundations, dams, and pipelines), being important components of civil infrastructure systems, must be properly designed and maintained with resilience and sustainability considerations so that these are not only robust against climate change effects and extreme events, but also sustainable from social, economic, and environmental perspectives. To practically determine if geotechnical assets of interest are resilient and promote sustainability goals, a quantitative framework is required that assesses resilience and sustainability in an integrated manner.

The purpose of this paper is to present a brief overview of sustainability and resilience in connection with geotechnical engineering, with particular emphasis on the concepts of resilience. The theories of sustainability and resilience are compared to find their similarities and contrasts and to understand the fundamental connections between the two. Finally, a quantitative framework for the assessment of resilience and sustainability of geotechnical assets and infrastructure is presented, which is philosophically based on the Driver–Pressure–State–Impact–Response (DPSIR) framework used in the assessment of socio-environmental problems.

2 Sustainability: Brief Overview

Degradation of earth's life-supporting capacity, environmental problems, socio-economic issues especially on poverty and inequality and impacts of current generation's decision-making on future generations are the key aspects of sustainability (Hopwood et al. 2005; Gibson 2006). The first articulation of the key to contemporary sustainability was introduced in the well-known Brundtland report, *Our Common Future*, in 1987. In the Brundtland report, sustainability is defined as the development that "*meets the needs of the present without compromising the ability of future generations to meet their needs*" (Brundtland 1987). Further, the report introduced the concept of triple bottom line (TBL) which suggests that sustainability should be evaluated with reference to the interaction of three fundamental criteria—environment, economy, and equity (three E's). For civil engineering applications, sustainability can be understood as a dynamic equilibrium between four E's—engineering practice, economy, environment, and equity—an extension of the TBL. More details on sustainability and its connection with civil and geotechnical engineering are given in Basu et al. (2015).

3 Concepts of Resilience

The concept of resilience was first introduced in ecological studies by Holling (1973) in which resilience was defined as “*the measure of the persistence of systems and of their ability to absorb change and disturbance and still maintain the same relationships between populations or state variables.*” Simply put, resilience is understood as the ability of a system to “bounce back” from a change or shock and continue to function. Key characteristics of resilience are adaptation and transformation. Adaptation relates to the decision-making processes, collective actions, and learning capabilities to adjust a system to potential shocks, stresses or other changing conditions in order to maintain essential system functioning and allow continuous development (Nelson et al. 2007; Folke 2006). On the other hand, transformability is the capacity of people to create a fundamentally new system when ecological, political, social, or economic conditions make the existing system untenable (Walker et al. 2004). In short, adaptation relates to an adjustment of a system in response to threats, whereas transformation relates to a more pervasive and radical action when the system is near a threshold because of a major threat (Redman 2014).

For civil engineering applications, the concept of resilience can be characterized by robustness, rapidity, resourcefulness, and redundancy (Bruneau et al. 2003). Robustness is the ability to absorb and withstand external shocks. Rapidity is the speed of recovery from being disrupted or damaged to achieve an acceptable level of functionality. Resourcefulness is the capacity to identify problems, establish priorities, and mobilize resources (i.e., monetary, physical, technological, and informational resources). Redundancy indicates the extent to which existing elements or systems are substitutable. Many engineering systems are inextricably connected to the social, environmental, and economic systems (Basu et al. 2015); therefore, consideration of multiple dimensions of resilience is necessary to enable a holistic conceptualization of resilience from an interdisciplinary perspective (Rogers et al. 2012). Thus, the four characteristics of resilience (i.e., robustness, rapidity, resourcefulness, and redundancy) can be improved in four different dimensions comprising technical, organizational, social, and economic domains (Bruneau et al. 2003; O'Rourke 2007).

In general, resilience can be quantified in terms of change in the system performance with respect to time, given by:

$$R = \frac{1}{t_h} \int_{t_d}^{t_d + t_h} Q(t) dt \quad (1)$$

where R is the resilience, $Q(t)$ is the system functionality or performance function, t is time, t_d is the time when disruption occurs, and t_h is the total inspection time.

4 Similarities and Contrasts of Sustainability and Resilience

Many studies suggest that resilience is a prerequisite to sustainable development because a resilient system has the capability to avoid surprises and continue to provide the goods and services that support the quality of life (Gunderson and Holling 2002; Rodriguez-Nikl 2015; Walker and Salt 2006). Natural (e.g., climate change and natural disasters) and human-made (e.g., technological and geopolitical) changes will disrupt the cycles of materials and energy flows. Therefore, civil infrastructure systems and geotechnical assets, which consume a vast amount of resources (e.g., natural and monetary resources), will be affected by such changes and impact the sustainability (Basu et al. 2015; Fiksel 2007). A resilient civil infrastructure system ensures that the system has the capability to recover from a disrupted state in response to global changes and extreme events so that a desirable configuration can be maintained over a long period. If the goods and services are able to serve desirable development over extended periods of time, and the development does not jeopardize the functions of the system, then sustainability can be achieved (Folke et al. 2002; Xu et al. 2015). Moreover, a resilient infrastructure system is capable of remaining at an equilibrium state even under the stress of external factors (e.g., extreme weather and disruptive human activities), and this equilibrium state not only relies on the technical stability of the infrastructure system but also on the stock of natural resources, and social and economic well-being, which are consistent with the four Es of sustainability (Xu et al. 2015).

Sustainability envisions a continuously desirable future; however, resilience is not necessarily always desirable. A system in an undesirable state may exhibit high resilience and resist all efforts to shift the system out of that state (Walker and Salt 2006). For example, polluted water supplies, political dictatorships, and fossil fuel-based energy systems, which are not in favor of social welfare, can be highly resilient (Carpenter et al. 2001; Xu et al. 2015). While sustainability focuses on examining future options to reach more desirable and durable futures, resilience focuses on the process to build adaptive capacity to cope with unknown futures (Gibson 2006; Redman 2014). In other words, sustainability can be deemed to be the desirable objective of human development, whereas resilience thinking contributes in providing specific and practical ways to reach that goal (Xu et al. 2015). Table 1 summarizes the contrasts between resilience theory and sustainability science approach in terms of their origin, objectives, and perspectives.

Table 1 Comparison between resilience theory and sustainability science

Resilience theory approach	Sustainability science approach
Origin in ecology	Origin in social sciences
Change is normal for social-ecological systems and is considered stable. A system may exist in multiple stable states	Envision the future Human interventions to make the desirable future happen
Result of change is open-ended and emergent	Desired results of change are specified in advance
Concerned with maintaining system dynamics	Focus is on interventions that lead to sustainability
Experience adaptive cycle gracefully	Utilize participatory governance
Stakeholder input focused on desirable dynamics	Stakeholder input focused on desirable outcomes

Adapted from Redman (2014)

5 Integrated Resilience and Sustainability Assessment Framework

An integrated framework for the assessment of resilience and sustainability is presented in this paper. The structural thinking of the Driver–Pressure–State–Impact–Response (DPSIR) framework, developed by the European Environment Agency (EEA), is adopted for the development of the new framework. The DPSIR framework helps to provide an overview of a problem or a system by structuring information in accordance to five categories: drivers, pressures, states, impacts, and responses, and the framework helps to identify important relations between the five categories.

The objectives of the new assessment framework for geotechnical engineering include the following: (i) to simulate hazard scenarios and quantify the response of geotechnical assets in terms of their limit states, (ii) to capture the impacts of damaged geotechnical assets to critical infrastructure systems and societies, (iii) to quantitatively assess the resilience of geotechnical assets considering the key aspects of resilience (i.e., robustness, rapidity, resourcefulness, redundancy, adaptability, and transformability), and (iv) to evaluate the effectiveness of response strategies implemented for improving the resilience of geotechnical assets.

The reinterpretation of the five components of DPSIR framework for the new assessment framework is discussed in the following sections along with an application in the form of an example problem of a transportation network, consisting of road embankments, that connects two cities, London and Toronto, in the province of Ontario, Canada. In this hypothetical case study, seven different geometric sections of embankments are considered. Figure 1 shows the schematic of the transportation network considered.

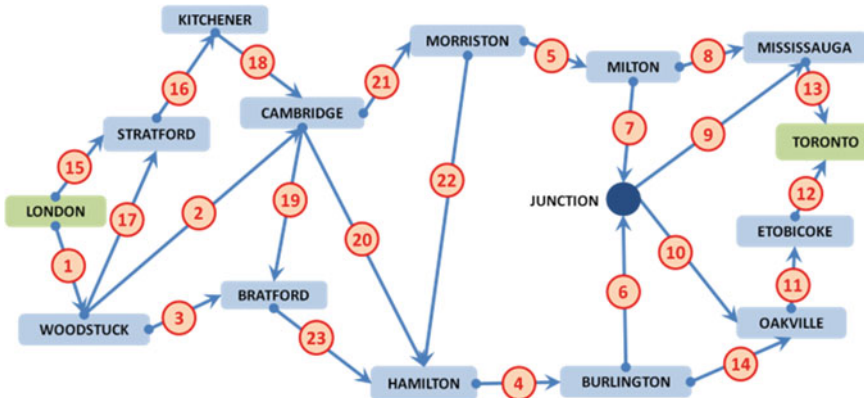


Fig. 1 Schematic of London-Toronto transportation network

5.1 Drivers: Identification of Driving Forces

The drivers can be understood as the fundamental causes that change the pressures to the geotechnical infrastructure. Indicators for drivers should describe the social, demographic, and economic developments in societies (Gabrielsen and Bosch 2003). For example, there are economic driving forces, which fulfill human needs for food and raw materials, water, shelter, health, security, infrastructure, and culture. Social driving forces fulfill human needs for social relations, equity, governance, and cultural identity (Bradley and Yee 2015).

The primary function of a transportation network is to provide mobility to the public. Therefore, for the case study problem, the driving forces are the factors that motivate human to attain mobility of passengers and goods to the destination point. Mobility can be affected by the user's behavior (i.e., travel distance and frequency of trips) and choice of transportation mode (i.e., private car ownership and use of public transport), which are also influenced by the demographics, economic needs (e.g., employment), leisure activities (e.g., tourism), development of technologies (e.g., satellite tracking for traffic conditions), energy availability (e.g., vehicle fuels), production and trade of goods, and policy making (Akhyani 2015). Identification of the drivers can help select the most important transportation networks within a jurisdiction that require resilience assessment. In this particular case, the choice of the network is made based on the fact that London–Toronto corridor is very important in Ontario from a socioeconomic point of view.

5.2 Pressures: Hazard Scenarios

The driving forces result in pressures, which are hazards or threats to the selected geotechnical infrastructure over its lifespan. The pressures can be identified according to the eight categories of possible threats that physical civil infrastructure may encounter: (i) gradual deterioration from ageing, (ii) damage from surface loading or stress relief, (iii) severely increased demand and ever-changing demands, (iv) the effects of climate change, (v) the effects of population increase, (vi) funding constraints, (vii) severe natural hazards, and (viii) terrorism (Rogers et al. 2012). Different hazard scenarios based on the identified pressures can be generated for a comprehensive analysis.

For the case study, the generation of hazard scenarios is focused on the natural hazards in Ontario. The study focuses only on floods mainly because it is the most frequent natural hazard in Ontario, and hydraulic inputs and outputs to soil and water system are directly significant to geotechnical failures (Vardon 2015). In the case study, five network links (i.e., link Nos. 2, 10, 17, 20, and 21 in Fig. 1) are assumed to be affected by a flood scenario with 100 mm/hr of rainfall intensity, 6 h of rainfall duration, and 100-year return period. It is also assumed that only 1/3 of the entire length of road embankments is affected.

5.3 States: Characteristics of Resilience

In the proposed framework, the states indicate metrics that represent the resilience of geotechnical infrastructure, which can be represented by the robustness, rapidity, redundancy, and resourcefulness aspects of resilience. Robustness of geotechnical infrastructure can be represented by the ultimate limit state (ULS) and serviceability limit state (SLS) of the geotechnical infrastructure affected by the hazard scenarios. Geotechnical analyses are performed to calculate the changes in ULS and SLS caused by the hazard scenarios generated described in Sect. 5.2. Rapidity is characterized by the recovery in the limit states (from failed conditions) of geotechnical infrastructure with respect to time. Redundancy can be quantified by the number of substitutable or redundant components within the network of the geotechnical infrastructure. Resourcefulness can be represented by the costs required for construction, maintenance, mitigation, and repair of the geotechnical infrastructure with respect to an available budget.

Robustness of road embankments can be quantified in terms of the change in the ultimate limit state (ULS) and serviceability limit state (SLS) of embankments, which are represented by the factor of safety (FoS) against slope stability and excessive settlement, respectively. The rapidity aspect of resilience for the road embankments can be measured by the recovery of FoS and reduction in settlement with respect to time. Resourcefulness can be quantified by the ratio of construction costs required for implementing a response strategy to the government budget on

highway management. The redundancy aspect of resilience can be represented by how “distributed” the highway network is and can be measured by its network entropy (Xie and Levinson 2011). The more distributed the network, the higher the entropy, and the greater the redundancy. The network entropy is calculated using the Shannon entropy.

5.4 Impacts

The impacts are interpreted as the effects of damaged geotechnical components to the associated infrastructure systems and societies. Many civil infrastructure systems, especially transportation networks, are highly dependent on the geotechnical components (e.g., embankments, slopes, foundations, and retaining structures). Therefore, the states of the geotechnical components, which are disrupted by the hazard scenarios, directly affect the functionality of the associated infrastructure system and eventually affect the communities. The impacts can be measured from technical, economic, social, and environmental points of view, and relevant sustainability indicators/tools can be used for quantification.

For the case study, the impacts are quantified based on technical, environmental, economic, and social viewpoints using appropriate indicators. Table 2 briefly summarizes the description of the different impacts and the methodology used for the quantification.

5.5 Responses

Mitigation and rehabilitation actions are institutional efforts to cope with the hazards and disrupted geotechnical infrastructure. Mitigation measures aim for the prevention and reduction of the impacts of hazards, whereas rehabilitation actions target for recovery of the disrupted infrastructure in a timely manner. The rehabilitation actions can be implemented to improve the adaptability or transformability of the disrupted geotechnical infrastructure. If complete failure of geotechnical components has not reached, retrofitting or reinforcement of

Table 2 Description and quantification methods of impacts

Impact	Description	Methodology
Technical	Change in traffic volumes and travel times	Network flow optimization
Environmental	Air pollution	Life cycle assessment (LCA)
Economic	Construction costs for mitigation and repair	RSMeans (2014) estimates
Social	Human health damage	LCA
	Change in leisure time	Network flow optimization

geotechnical infrastructure can be undertaken to partially repair the damage and improve their adaptability. However, if partial repair is no longer possible because the damage is severe, then the damaged geotechnical components can be completely rebuilt to transform into a new system. Several mitigation and rehabilitation strategies can be planned and combined to generate different response scenarios. The effectiveness of the response scenarios can be evaluated based on the metrics and the impacts determined in Sects. 5.3 and 5.4, respectively.

Five possible scenarios for the road embankments of the case study are outlined in Table 3 to cope with floods. As a mitigation measure, toe berms can be constructed to improve the stability of road embankments. Rehabilitation can be practiced either by retrofitting (i.e., partial repair) to improve adaptability or by reconstruction (i.e., full repair) to achieve transformation.

5.6 Case Study Results

The effectiveness of the five different response scenarios was evaluated based on (i) the resilience of the transportation network by considering performance functions like FoS, settlement, network entropy, and leisure time and (ii) the impacts of flooded road embankments that affect sustainability.

Normalized FoS, settlement, network entropy, and leisure time over 100 days of inspection and for different response scenarios outlined in Table 3 are shown in Figs. 2a, b, c, and d, respectively. These functions were used as performance functions, $Q(t)$, to calculate the resilience of the transportation network using Eq. (1), and the results are summarized in Table 4.

Figure 3 shows the construction costs of mitigation and rehabilitation actions for the response scenarios. Figure 4 shows the normalized environmental impacts from construction activities such as the haulage and operation of machineries and haulage of embankment fills. It is evident that the haulage of fills dominates the environmental impacts. Human health impacts portray the same results as shown in Fig. 4.

Considering all the characteristics of resilience, it is apparent that the response scenarios 4 and 5 are the most resilient options (Table 4). However, from the sustainability point of view (i.e., considering the environmental and human health impacts), scenario 4 appears to be the best.

Table 3 Response scenarios

Response scenario	Mitigation	Rehabilitation
1	No action	Retrofitting
2	No action	Reconstruction
3	Berm construction	No action
4	Berm construction	Retrofitting
5	Berm construction	Reconstruction

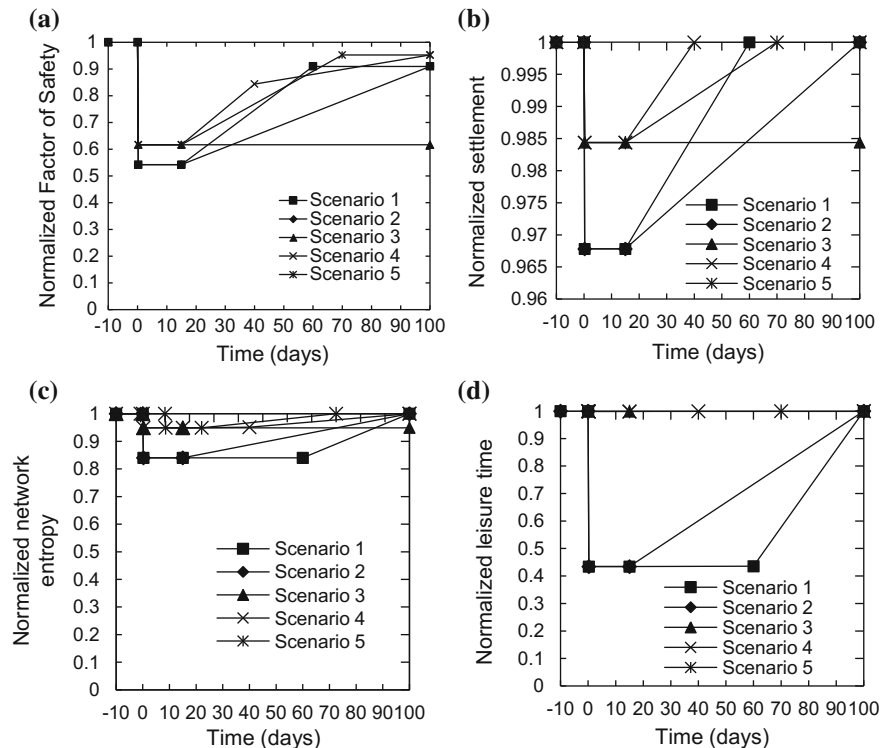


Fig. 2 **a** Normalized factor of safety of road embankments, **b** normalized settlement of road embankments, **c** normalized network entropy of transportation network, and **d** normalized leisure time of road users

Table 4 Resilience of transportation network

Response scenario	Resilience [Eq. (1)]			
	FoS	Settlement	Network entropy	Leisure time
1	0.772	0.988	0.904	0.662
2	0.699	0.982	0.908	0.675
3	0.617	0.984	0.949	0.999
4	0.814	0.996	0.963	0.999
5	0.810	0.993	0.978	0.999

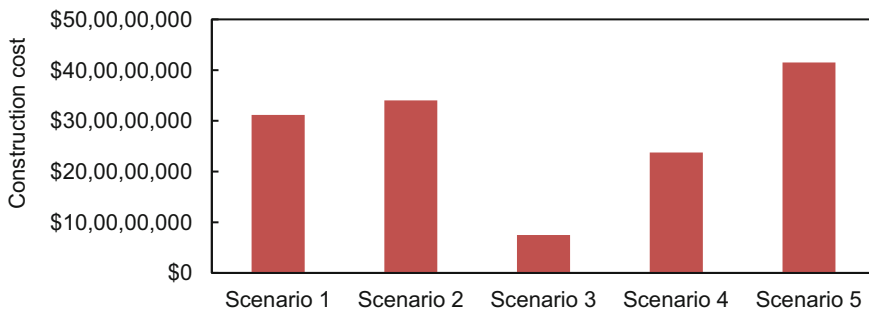


Fig. 3 Construction costs for road embankments

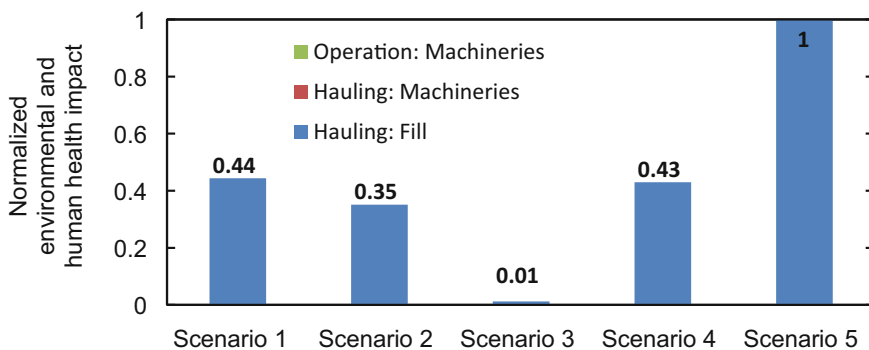


Fig. 4 Normalized environmental and human health impacts

6 Concluding Remarks

Sustainability envisions a desirable future where intergenerational equity, with respect to environmental, social, and economic perspectives, is maintained while fulfilling the needs of current generations. Resilience, on the other hand, specifically focuses on the ability of a system to respond, adapt, and evolve to changes in order to minimize the consequences caused by the changes. These two concepts need to be concurrently considered in infrastructure management, as there is an increasing probability of exposure of infrastructure networks to extreme events and climate change. Resilient infrastructure systems have the ability to prepare, mitigate, and respond to disasters and climate change in a timely and economical manner so that consequences to communities are minimized; thereby, sustainable development can be achieved by reducing expenditures to maintain and repair the consequences. Incorporation of sustainability and resilience in geotechnical engineering is particularly important as many critical infrastructure networks consist of geotechnical assets. Failure of these geotechnical assets can cause significant impacts to the performance of infrastructure networks. Hence, there is a strong need for

developing an assessment framework that considers both resilience and sustainability of geotechnical infrastructure in order to plan, mitigate, and prepare for threats.

A quantitative framework for the assessment of resilience and sustainability of infrastructure systems affected by geo-hazards is presented in this paper. The framework is developed based on the DPSIR framework. The framework considers resilience metrics and sustainability indicators in the decision-making process for determining the best response strategy against the geo-hazards. An example problem on a transportation network, consisting of road embankments that are subjected to a flood scenario, is used to demonstrate the application of the new framework. In the case study, the resilience metrics and sustainability indicators are utilized to evaluate the effectiveness of five different response strategies with different combinations of mitigation and rehabilitation actions. The assessment results can be useful in determining the areas of improvement for designing robust geotechnical infrastructure against extreme events and climate change, for building resilient communities, and, finally, for sustainable development.

References

Akhyan, R. (2015). *Resilience of geotechnical assets*. University of Birmingham.

Basu, D., Misra, A., & Puppala, A. J. (2015). Sustainability and geotechnical engineering: Perspectives and review. *Canadian Geotechnical Journal*, 52(1), 96–113.

Bradley, P., & Yee, S. (2015). *Using the DPSIR framework to develop a conceptual model: Technical support document*.

Brundtland, G. H. (1987). *Our common future: Report of the 1987 world commission on environment and development*. Oxford, UK.

Bruneau, M., et al. (2003). A framework to quantitatively assess and enhance the seismic resilience of communities. *Earthquake*.

Carpenter, S., et al. (2001). From metaphor to measurement: Resilience of what to what? *Ecosystems*, 4(8), 765–781.

Fiksel, J. (2007). Sustainability and resilience: Toward a systems approach. *IEEE Engineering Management Review*, 35(3), 5.

Folke, C. (2006). Resilience: The emergence of a perspective for social-ecological systems analyses. *Global Environmental Change*, 16(3), 253–267.

Folke, C., et al. (2002). Resilience and sustainable development: Building adaptive capacity in a world of transformations. *Ambio*, 31(5), 437–440.

Gabrielsen, P., & Bosch, P. (2003). *Environmental indicators: Typology and use in reporting*.

Gibson, R. B. (2006). Sustainability assessment: Basic components of a practical approach. *Impact Assessment and Project Appraisal*, 24(3), 170–182.

Gunderson, L. H., & Holling, C. (2002). *Panarchy: Understanding transformations in human and natural systems*. Washington, DC: Island Press.

Holling, C. S. (1973). Resilience and stability of ecological systems. *Annual Review of Ecological Systems*, 4, 1–23.

Hopwood, B., Mellor, M., & O'Brien, G. (2005). Sustainable development: Mapping different approaches. *Sustainable Development*, 13, 38–52.

Nelson, D. R., Adger, W. N., & Brown, K. (2007). Adaptation to environmental change: Contributions of a resilience framework. *Annual Review of Environment and Resources*, 32(1), 395–419.

O'Rourke, T. D. (2007). Critical infrastructure, interdependencies, and resilience. *The Bridge: Linking Engineering and Society*, 37(1), 22–29.

Redman, C. L. (2014). Should sustainability and resilience be combined or remain distinct pursuits? *Ecology and Society*, 19(2).

Rodriguez-Nikl, T. (2015). Linking disaster resilience and sustainability. *Civil Engineering and Environmental Systems*, 32(1–2), 157–169.

Rogers, C. D. F., et al. (2012). Resistance and resilience—paradigms for critical local infrastructure. *Proceedings of the ICE—Municipal Engineer*, 165, pp. 73–83.

RSMeans, (2014). *Heavy construction cost data*. Norwell: RSMeans.

Vardon, P. J. (2015). Climatic influence on geotechnical infrastructure: A review. *Environmental Geotechnics*, 2(3), 166–174.

Walker, B., et al. (2004). Resilience, adaptability and transformability in social—ecological systems. *Ecology and Society*, 9(2), 5.

Walker, B., & Salt, D. (2006). *Resilience thinking: Sustaining ecosystems and people in a changing world*. Washington, DC: Island Press.

Xie, F., & Levinson, D. (2011). *Evolving transportation networks*. New York: Springer Science & Business Media.

Xu, L., Marinova, D., & Guo, X. (2015). Resilience thinking: A renewed system approach for sustainability science. *Sustainability Science*, 10(1), 123–138.

Case Studies—Prediction of Offshore Jack-up Leg Penetrations

C. R. Parthasarathy

Abstract The utilization of Jack-up rig for offshore exploration is significantly higher over the last decade and hope to increase in future despite the low oil prices for the last couple of years. Good prediction of spudcan bearing resistance in a problematic soil profile can shed light on precautionary measures that a rig contractor can adopt to facilitate a safe installation of spudcan. Nonetheless, the accuracy of the prediction is limited by the reliability of the interpreted soil strength parameters, lateral variability as well as the validity of the design method currently in use. It is imperative that high quality of sampling and testing methods is adopted, to evaluate the stratification/strength and arrive at a reasonable design profiles. This in aid of geophysical surveys will assist in evaluating the potential risks and the measures to mitigate the same.

Keywords Jack-up · Spudcan · Bearing capacity · Punch through
Rapid penetration · Integrated survey

1 Introduction

Incidents of foundation failure of Jack-ups occur frequently, while the safety records of other jack-up activities, viz. towing, drilling, structural fatigue, collusion, fire and blowouts, have improved significantly (Osborne et al. 2006). The Jack-up rig installation depends on the nature of the subseabed as the spudcan penetrates into it. Often, the presence of problematic seabed profiles challenges the stability of the rig during spudcan installation. Amongst these, the stiff overlying (STRONG) soft soil (WEAK) profile or SAND (STRONG) overlying soft CLAY (WEAK) is commonly found to be the main cause of spudcan punch through (Fig. 1). The stiff CLAY overlying soft CLAY is prevalent in offshore Southeast Asia and formed during the worldwide lowering of sea level in the last major glacial episode in which part of the

C. R. Parthasarathy (✉)

Sarathy Geotech & Engineering Services Pvt. Ltd., Bangalore, Karnataka, India
e-mail: partha@sarathygeotech.com

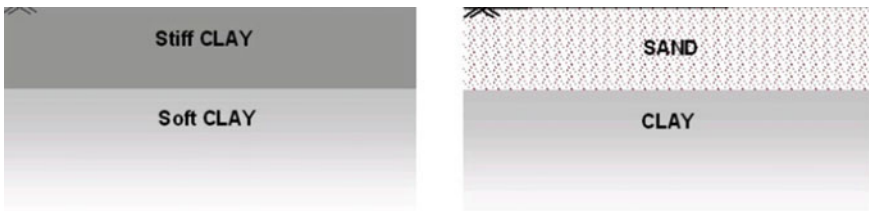


Fig. 1 Strong over weak profile



Fig. 2 Failure of jack-up units

surface CLAY was exposed and subjected to desiccation (Leung et al. 2006). In other parts of the world beyond South East Asia, with active oil and gas drilling exploration works, Osborne and Paisley (2002) defined the incident of spudcan punch through as “an unexpected jack-up footing rapid settlement resulting in consequential lost drilling time” and reported that the consequence of punch through often involves serious structural damage of the Jack-up rig, as shown in Fig. 2.

2 Spudcan Leg Penetration Analysis

It is necessary to estimate the leg penetrations, and the Jack-up rig achieves during preload. This is useful in evaluating the adequacy of the leg length and thus the suitability of the proposed rig for the particular location, in addition to assessing the potential risk—punch through and rapid leg penetration. The spudcan analysis can be assessed based on general bearing capacity theory (standard limit equilibrium approach) as per the guidelines laid out in SNAME (1994), API (1993) RP2A, DNV (2001), CLAROM (1993) etc., that are appropriate to the soil types encountered at a particular location using Skempton (1951) approach. These bearing capacity predictions assist the rig operator for the suitability of a particular jack-up rig at a site or can modify the installation procedures to minimize potential risks.

The degree of reliability of prediction depends on the accuracy of the geotechnical information and thus the derived ground model. The geophysical information is vital for assessing the geohazards. Hence, an integrated approach

performing geophysical survey and geotechnical survey is very useful to assess and mitigate all the potential risks that will be detrimental to the safety of Jack-up installation.

3 Case Studies

Four case studies on prediction of spudcan penetrations for offshore jack-up sites located in Indonesia, Vietnam, east and west coast of India have been presented in this paper. The spudcan analysis was assessed based on general bearing capacity theory and modified where applicable, based on back analysis of several observed penetration of similar foundations in similar soils together with the calibrated strength factors appropriate to the soil sampling and testing methods employed. In all the four cases, the author involved in the survey and desktop studies, assisted the rig mover during preloading and recorded the observed penetrations.

3.1 Site A—Offshore Indonesia

This site is located in offshore Indonesia. The review of geophysical information indicated the absence of anchor/drag scars and jack-up footprints except for few pockmarks in the vicinity. No other seabed hazards/obstructions is visible that is detrimental for jack-up rig emplacement. The subbottom profiles indicated no crossing of channel flanks. The review of geotechnical information indicated very soft-to-firm CLAY up to 7.0 m below seabed followed by 2.0-m-thick very stiff silty CLAY, which is underlain by stiff silty CLAY layers up to 14.0 m. Below 14 m, a 7-m-thick very stiff CLAY layer is encountered, which is underlined by stiff CLAY layer up to 31.0 m. The presence of 2.0-m-thick crust over the firm to stiff silty CLAY layer warrants the potential for rapid penetration or punch through of spudcan to be analysed for strong layer over weak layer case. The design profile considered for the bearing capacity analysis is summarized in Table 1.

The predicted and observed spudcan penetrations are summarized in Table 2, while bearing capacity versus spudcan penetration curve is presented in Fig. 3.

3.2 Site B—Offshore Vietnam

This site is located in offshore Vietnam. The topography within the site is generally smooth with low-to-moderate sonar reflective sediments as the ambient seabed. The absence of variation in acoustic reflectivity across the area indicates little variation in superficial sediment. Numerous seabed (trawl or anchors) scars were observed. The presences of numerous scars indicate regular previous trawling activities. No

Table 1 Site A—soil parameters

Sl. no.	Depth (m)	Soil type	Undrained shear strength (kPa)	ϕ (°)	Unit weight (kN/m ³)
1	0.0 2.0	Very soft CLAY	2 ^{LB} –8 ^{UB}	–	5.0
2	2.0 7.0	Firm CLAY	30 ^{LB} –40 ^{UB}	–	7.0
3	7.0 9.0	Very stiff silty CLAY	120 ^{LB} –140 ^{UB}	–	7.0
4	9.0 10.8	Stiff silty CLAY	75 ^{LB} –95 ^{UB}	–	7.0
4	10.8 14.0	Stiff silty CLAY	60 ^{LB} –75 ^{UB}	–	8.0
5	14.0 16.5	Very stiff silty CLAY	120 ^{LB} –140 ^{UB}	–	8.0
6	16.5 21.0	Very stiff silty CLAY	(100–120) ^{LB} (125–145) ^{UB}	–	8.0
7	21.0 31.0	Stiff silty CLAY	65 ^{LB} –85 ^{UB}	–	8.0

Table 2 Site A, spudcan penetrations

Leg	Estimated penetration (m)	Observed penetration (m)
Bow	8.7–15.0	15.0
Port		16.2
Star board		15.5

items of debris or man-made objects, which could impede Jack-up emplacement, have been found. No significant rock outcrop has been identified within the site. The review of geotechnical information indicated medium-to-dense fine sandy SILT and fine SAND up to 15.8 m below seabed underlain by stiff to very stiff silty CLAY up to 25 m. The presence of medium-to-dense SAND layers followed by stiff to very stiff CLAY layers was unlikely to pose a risk of rapid spudcan penetration. The design parameters considered for the bearing capacity analysis are summarized in Table 3.

The predicted and observed penetrations are summarized in Table 4, while bearing capacity versus spudcan penetration curve is presented in Fig. 4.

3.3 Site C—Offshore East Coast of India

This site is located in offshore east coast of India. There was no site survey planned, and the rig was already at the location. With the onset of monsoon and cyclones

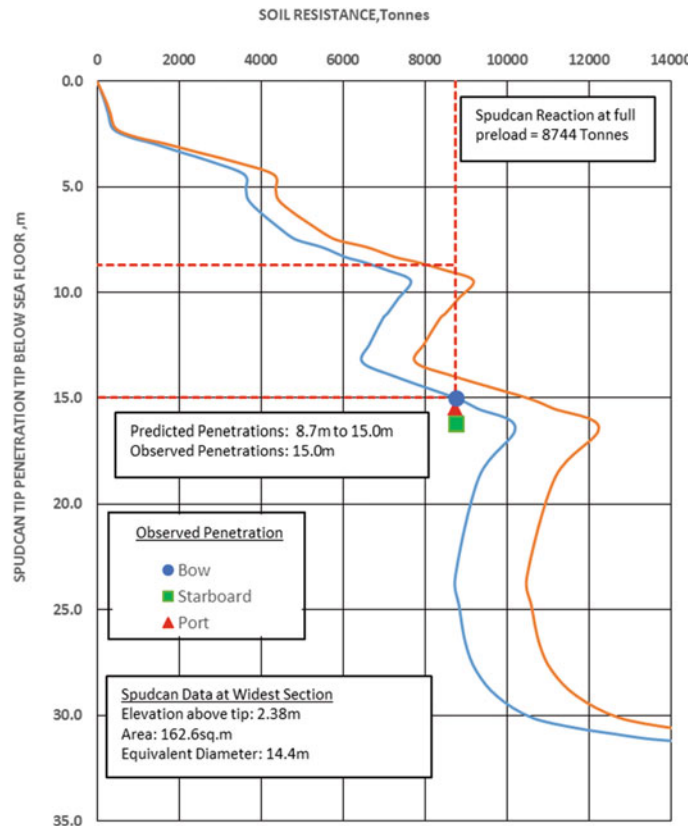


Fig. 3 Site A: bearing capacity versus spudcan penetration

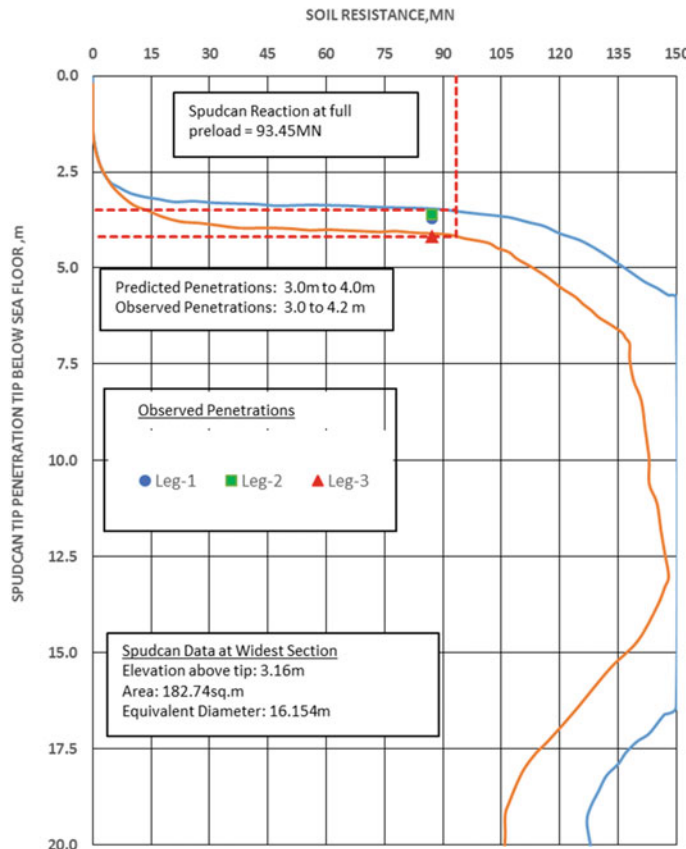
Table 3 Site B—soil parameters

Sl. no.	Depth (m)	Soil type	Undrained shear strength (kPa)	φ (°)	Unit weight (kN/m ³)
1	0.0 3.5	Sandy SILT		25	9.0
2	3.5 15.8	Silty SAND	—	25 ^{LB} –30 ^{UB}	9.5
3	15.8 21.2	Stiff to very stiff silty CLAY	80 ^{LB} –110 ^{UB}	—	9.0
4	21.2 25.0	Very stiff silty CLAY	100 ^{LB} 130 ^{UB}	—	7.0

prevalent, the client decided to carry out rig-based coring utilizing the drilling infrastructure of the jack-up rig. The rig was soft pinned, and the boring/sampling operations were carried out. The review of geotechnical information indicated very

Table 4 Site B, spudcan penetrations

Leg	Estimated penetration (m)	Observed penetration (m)
1	3.0–4.0	3.2
2		3.0
3		4.2

**Fig. 4** Site B; bearing capacity versus spudcan penetration

soft CLAY up to 4 m, followed by loose clayey SAND up to 7 m underlain by medium-to-dense, fine-to-coarse SAND up to 31 m. The design parameters considered for the bearing capacity analysis are summarized in Table 5.

The predicted and observed penetrations are summarized in Table 6, while bearing capacity versus spudcan penetration curve is presented in Fig. 5.

Table 5 Site C—soil parameters

Sl No.	Depth	Soil type	Undrained shear strength (kPa)	φ (°)	Unit weight (kN/m ³)
1	0.0 4.0	Very soft CLAY	3 ^{LB} –12 ^{UB}	–	4.0
2	4.0 7.0	Clayey SAND	–	15 ^{LB} –20 ^{UB}	7.0
3	7.0 13.0	SAND	–	25	8.0
4	13.0 31.0	SAND	–	35	10.0

Table 6 Site C, spudcan penetrations

Leg	Estimated penetration (m)	Observed penetration (m)
Bow	7.8–9.0	8.8
Star board		8.6
Port		8.9

3.4 Site D—Offshore West Coast of India

Unlike overseas offshore practice, it is not customary in India to perform thorough geophysical investigation prior to geotechnical investigation as such, and only geotechnical investigation information was available for this location. This site is located in offshore west coast of India. The review of geotechnical information indicates very soft CLAY up to 9 m, followed by loose SAND up to 10.5 m underlain by a 2-m-thick firm to stiff CLAY layer. This is followed by a 4-m-thick firm CLAY layer underlain by stiff CLAY layers up to 28.6 m. The 2-m-thick firm to stiff CLAY layer overlying firm CLAY layer might pose a risk of rapid penetration or punch through. The design parameters considered for the bearing capacity analysis are summarized in Table 7.

The predicted and observed penetrations are summarized below in Table 8, while bearing capacity versus spudcan penetration curve is presented in Fig. 6.

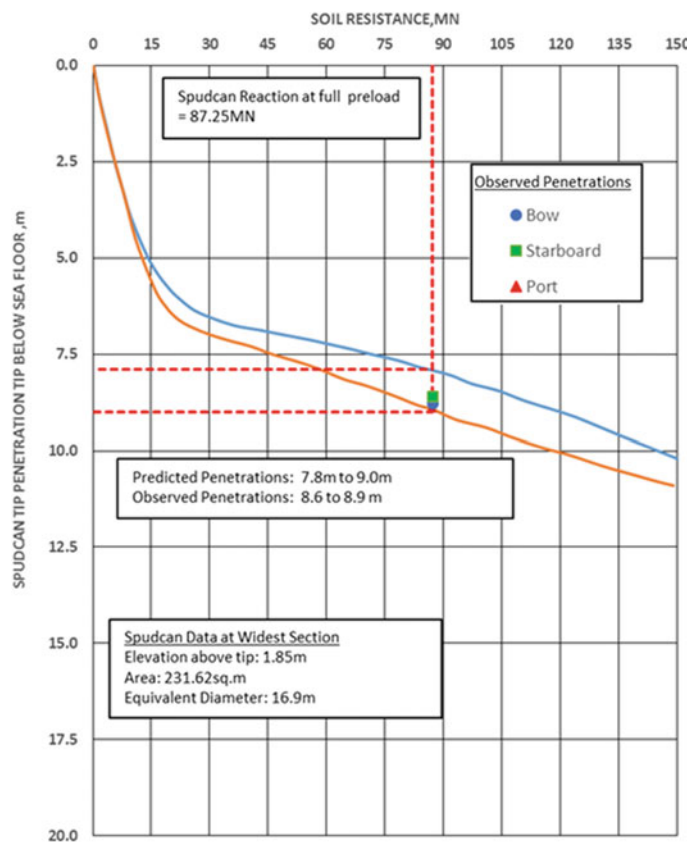


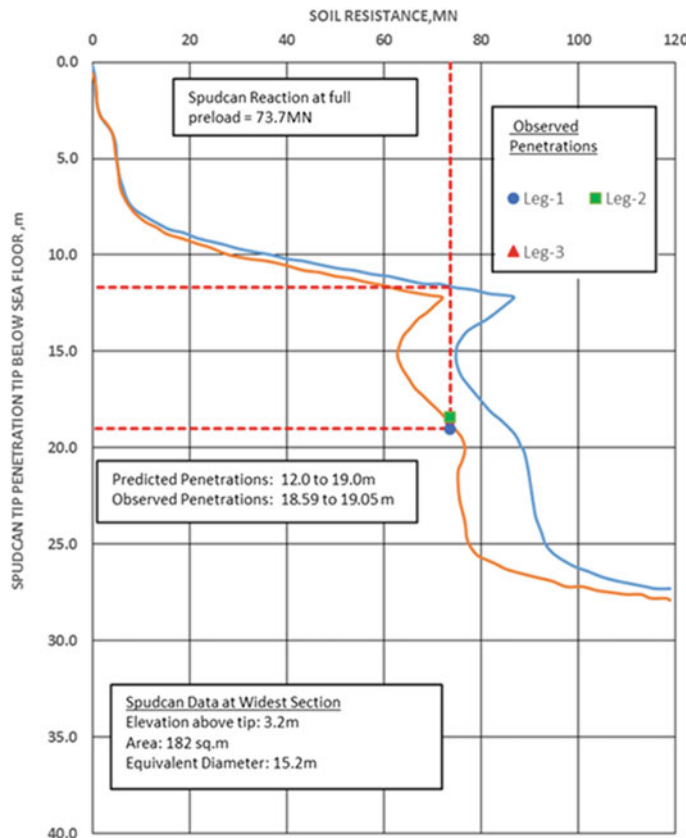
Fig. 5 Site C; bearing capacity versus spudcan penetration

Table 7 Site D—soil parameters

Sl. no.	Depth	Soil type	Undrained shear strength (kPa)	φ (°)	Unit weight (kN/m ³)
1	0.0 9.0	Very soft CLAY	3 ^{LB} –12 ^{UB}	–	4.5
2	9.0 10.5	SAND	–	15 ^{LB} –20 ^{UB}	8.5
3	10.5 12.5	Firm to stiff CLAY	42 ^{LB} –62 ^{UB}	–	8.0
4	12.5 16.7	Firm CLAY	38 ^{LB} –51 ^{UB}	–	8.0
5	16.7 17.7	Stiff CLAY	60 ^{LB} –80 ^{UB}	–	8.0
6	17.7 28.6	Stiff CLAY	50 ^{LB} –60 ^{UB}	–	8.0

Table 8 Site D, spudcan penetrations

Leg	Estimated penetration (m)	Observed penetration (m)
1	12.0–19.0	19.05
2		18.41
3		18.59

**Fig. 6** Site D; bearing capacity versus spudcan penetration

4 Conclusions

Site-specific geotechnical investigations, including appropriate soil sampling prognosis coupled with high-quality testing, is necessary for accurate estimation of spudcan penetrations. It is advised to carry out investigations at every leg location to account for lateral variations in soil profile and at locations susceptible for punch

through. Geophysical site survey will supplement geotechnical investigation in identifying potential risks and mitigate measures for safe emplacement of Jack-up rigs. The accuracy of predictions relies on the accuracy of the ground model and risk parameters derived for location.

At all the four locations, the predicted range of spudcan penetrations is in agreement with the observed penetration.

Acknowledgements The author acknowledges the efforts of his colleagues Mr. Gangisetty Ramesh and Mr. Katakam Pramod in assisting with the preparation of this manuscript.

References

API. (1993). Recommended practice for planning, designing and construction fixed offshore platforms. API Recommended Practice 2A (RP2A) 11th Edition, 1979, 20th Edition, 1993.

CLAROM. (1993). Stability and operations of Jackups, edited by Pierre Le Tirant and Christian Perol.

DNV. (2001). Rules for the classification of mobile offshore units. Class Notes 30.4.

Davis, E. H., & Booker, J. R. (1973). The effect of increasing strength with depth on the bearing capacity. *Geotechnique*, 23(4), 551–563.

Leung, C. F., Teh, K. L., Chow, Y. K., Foo, K. S., & Quah, M. (2006). *Evaluation of SNAME methods in predicting spud can punch through*. PETROMIN—Jack-up Asia conference and exhibition, Singapore.

Osborne, J. J., & Paisley, J. M. (2002). *SE Asia punch through—The way forward*. SUT Conference, London.

Osborne, J. J., Pelly, D., Nelson, C., & Hunt, R. (2006). *Unpredicted Jack-up foundation performance*. PETROMIN—Jack-up Asia conference and exhibition, Singapore.

Skempton, A. W. (1951). The bearing capacity of clays. In *Proceedings of Building Research Congress* (Vol. 1, pp. 180–189). London: Institution of Civil Engineers.

The Society of Naval Architects and Marine Engineers. (1994). *Guidelines for site specific assessment of mobile Jack-up units* (First ed.). Technical & research bulletin 5-5A.

Forensic Study on the Causes of Failure of Stone Columns Under Water Storage Tanks and Possible Remedial Measures

Kaushik Bandyopadhyay

Abstract Water storage tanks of diameter 30 m and height 14.50 m were erected at a site near the coastal region of West Bengal. Detailed soil exploration work revealed that the deposit consisted of typical soft marine clay with standard penetration (SPT) values lying in the range of 2–6 up to 28.0 m depth below the ground level. Varying percentage of decomposed vegetation and laminated silt was observed between 11.50 and 28.00 m depth below EGL. Overall ground improvement was proposed, and accordingly, stone columns were installed up to the depth of 10.00 m below EGL. After one year of installation, total settlements of 800 mm and differential settlement of about 150 mm were observed and these have been continuing unabated. Subsequently, detailed forensic investigation was made, and it was observed that the stone columns had showed telltale signs of failure, and consequently, huge settlement resulted. The present paper discusses on the various causes of failure and suggests some remedial measures for arresting the settlements.

Keywords Storage tanks · Soft clay · Stone columns · Failure
Forensic study · Remedy

1 Introduction

Stone columns are essentially a method of soil reinforcement. By installation of these, soft cohesive soil is replaced at discrete points by compacted stone or crushed rock in pre-bored vertical holes to form ‘columns’ or ‘piles’ within soil (Som and Das 2003). Stiffness of stone columns being higher than that of the surrounding soil causes a considerable portion of the vertical load to be transferred to the columns. As a consequence, the entire soil below a foundation acts as a reinforced soil with higher load carrying capacity than the virgin ground. In the present case under

K. Bandyopadhyay (✉)

Department of Construction Engineering, Jadavpur University,
Block-LB, Plot-8, Sector-III, Salt Lake, Kolkata 700098, India
e-mail: drkaushik99@gmail.com

consideration, it was found that even after installation of the stone columns, considerable amount of settlement had occurred and the soil below the foundation was on the verge of shear failure. Detailed study including field and laboratory work was conducted to investigate the causes of failure. Subsequently, some remedial measures were suggested to arrest the settlements.

2 Objective of Present Study

The objective of the present study consisted of the following.

- (a) Determination of the subsoil profile.
- (b) Evaluation of the causes of failure of the stone columns.
- (c) Suggestion of remedial measure and recommendations.

Evaluation of Sub-soil Profile

Soil exploration study was conducted at the site by conducting three numbers of boreholes up to the depth of 50 m by shell and auger technique. Brief description of different soil layers is presented in Fig. 1. Results of laboratory test are summarized in Table 1.

Engineering Properties of Soil

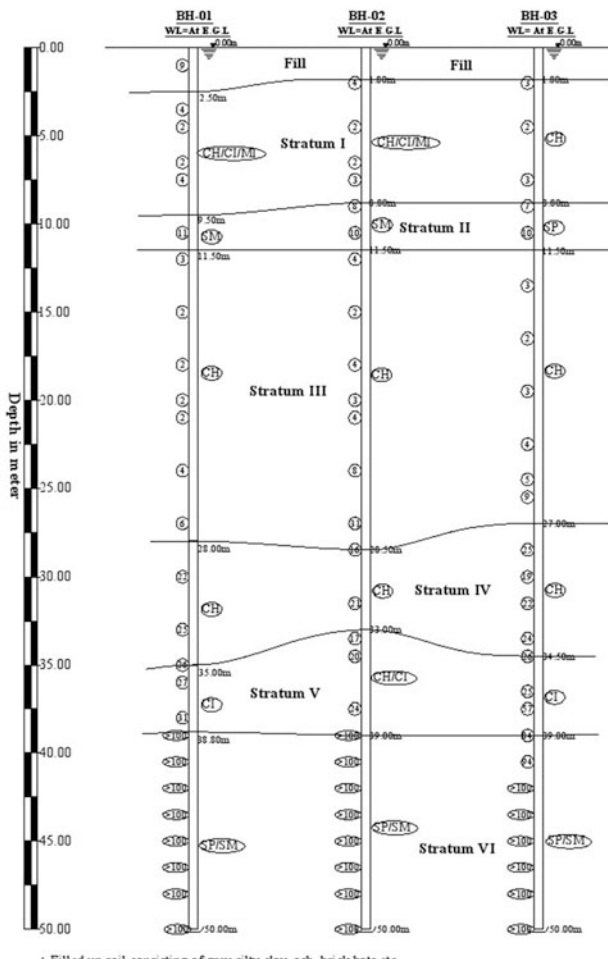
Results of laboratory tests are summarized in Table 1.

3 Results and Discussions

The field exploration study revealed that the top layer consisted of a fill of 2 m thickness followed by a 7 m thick soft clay layer. This layer was underlain by a sand layer of 2 m thickness. Below the sand layer, there was a very soft to soft clay layer which extended up to the depth of 28 m below the ground level. This deep soft layer is underlain by a stiff clay layer of 3 m thickness followed by a dense sand layer up to the depth of exploration.

3.1 Installation of Stone Column and Its Performance

At the present site under consideration, stone columns of length 10 m were installed with the sole purpose of overall ground improvement. Diameter and spacing of stone columns are 800 mm and 2 m c/c, respectively. Schematic of stone column layout is provided in Fig. 2.



Fill : Filled up soil consisting of grey silty clay, ash, brick bats etc.
Stratum I : Very soft to soft brownish grey to grey silty clay / clayey silt.
Stratum II : Loose to medium dense grey silty sand with mica.
Stratum III : Very soft to soft grey silty clay with varying percentage of decomposed wood noticed.
Stratum IV : Stiff to very stiff bluish grey to grey silty clay with rusty brown spots and varying percentage of sand.
Stratum V : Very stiff greyish brown silty clay with varying percentage of sand.
Stratum VI : Dense brownish grey silty sand with mica.

Fig. 1 General soil profile of the site

It was decided that the stone columns would be supported on the thin sand layer of limited thickness. Plates 1 and 2 show the photographs of the tanks during recent times and accumulation of water around the tanks. These also show the ground subsidence of the sand pad foundation endangering the life of the steel tanks due to corrosion in contact with water.

An approximate analysis was made to determine the present state of degree of consolidation which revealed that 90% of primary consolidation had already taken place. Still, settlements continued at a faster rate. The reason behind this could be

Table 1 Results of laboratory test

Stratum	<i>N</i> value	Bulk density (kN/m ³)	Cohesion (kN/m ²)	Angle of internal friction (°)	<i>m_v</i> (m ² /kN)
Filled up soil consisting of grey silty clay, ash, brick bats, etc.	—	18.50	—	—	—
Very soft to soft brownish grey to grey silty clay/clayey silt (CH/CI)	3	18.10	22.0	—	0.000642
Loose to medium dense grey silty sand with mica (SM/SP)	10	18.40	—	30	—
Very soft to soft grey silty clay with varying percentage of decomposed wood (CH/CI)	4	17.20	18.0	—	0.000451
Stiff to very stiff bluish grey to grey silty clay with rusty brown spots and varying percentage of sand (CH)	22	19.25	98.0	—	—
Very stiff greyish brown silty clay with varying percentage of sand (CI)	28	19.35	123.0	—	—
Dense brownish grey silty sand with mica (SM/SP)	36	21.00	—	35	—

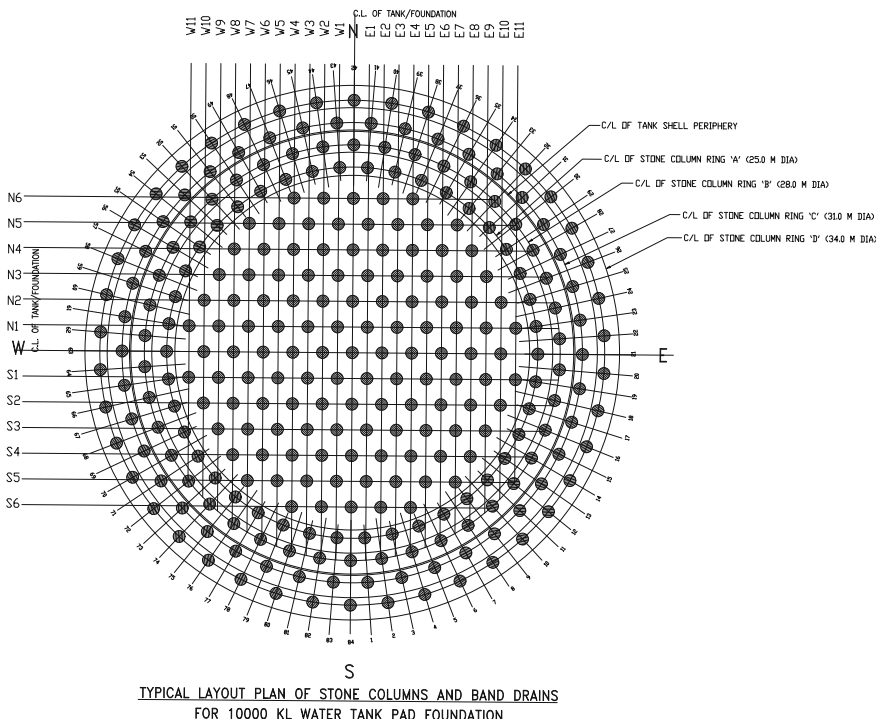
**Fig. 2** Typical layout plan of stone columns



Plate 1 Photograph of the tanks during recent times



Plate 2 Photograph showing accumulation of water around the tanks and subsidence of the sand pad foundation below the ground

attributed to many factors. First of all, the stone columns could restrict the settlement of the top layer, but they were not able to do so of the deep bottom clay layer owing to their limited length. Secondly, when the tanks were filled for the first time, loading applied was to the tune of 150 kPa. Sudden application of this load caused considerable settlement of ground along with dissipation of pore pressure. As the thickness of the supporting sand layer below the stone columns was not sufficient, chances are there that the stone columns penetrated through this layer into the bottom clay layer. As a result, the stone columns were unable to perform their designated functions. Load tests on the stone columns indicated non-compliance of test results as well. All these factors provided evidence towards failure of the stone columns.

As a consequence of the reason described above, the top clay layer along with the stone columns acted as a surcharge for the bottom clay layer giving rise to one-dimensional consolidation settlement of the latter one. Besides, the pore water

which is released cannot find any way out as the only drainage layer lies at the bottom. This is why the settlement continues unabated.

Last but not the least, the spacing of the three water tanks was not much and consequently when the tanks were loaded, they gave rise to concentration of stress at points of overlap of pressure bulbs. This might have caused some additional settlements.

IS 15284-1 (2003) on guidelines for design and construction of stone columns recommends the acceptable settlement criteria from the load test results as 25–30 mm settlement at the design load for a three column group test. In the present case under consideration, the load test results show that most of the settlements have exceeded this limit impairing the satisfactory performance of the stone columns.

3.2 *Tilt and Angular Distortion*

Settlement data below the centre of the tank could not be collected owing to inaccessibility. As a result, exact values of angular distortion and tilt could not be obtained from field measurements. Some approximate values are obtained from observed settlement at periphery and theoretical one at centre.

$$\text{Tilt } \frac{\delta}{R} = \frac{\delta_2 - \delta_1}{R} \quad (1)$$

where δ = difference of settlement at centre (δ_2) and edge (δ_1) of tank, and R is the radius of the tank.

Here, δ_1 (observed) = 0.727 m and δ_2 (calculated) = 0.776 m and R = 15 m

$$\therefore \text{Tilt } \frac{\delta}{R} = \frac{0.776 \text{ m} - 0.727 \text{ m}}{15 \text{ m}} = 0.00327 < \frac{1}{50}$$

For satisfactory performance of the tank, tilt should lie between 1/30 and 1/50. In the present case, it is well within this limit.

Also, angular distortion = Differential settlement between the two extreme ends of the tank \div Diameter of the tank

$$= \frac{0.141 \text{ m}}{30 \text{ m}} = 0.0047 > \frac{1}{300}$$

As per IS 1904 1986, value of angular distortion should lie within 1/300 to 1/500, and here, it is more than the higher permissible value (1/300). Hence, the tank fails in angular distortion.

4 Remedial Measures

To tackle the settlement problem, some remedial measures have been suggested, e.g. cement grouting, lime column and chemical grouting.

Authors have opined cement grouting below the tank foundation as one of the methods for arresting settlement. But, in the present case under consideration, the soil is predominantly clayey and the permeability is very low. As results, the effectiveness of using cement grouts will be doubtful and the outcome of this method of ground improvement for controlling settlement may not be satisfactory.

Another suitable alternative is by installation of lime column below the tank foundation. Laboratory research was conducted in line with work by Mittal (2015) using lime column. Besides, the work by Poorooshashb and Meyerhof (1997) is also noteworthy in this respect. In the present case, it is suggested that inclined lime column may also form an alternative form of ground improvement to arrest further settlement. Table 2 quantifies the extent of settlement reduction which shows the success of the treatment to reduce settlement to the tune of 50% of the untreated ground.

4.1 *Recommendation*

The most suitable alternative is by application of chemical grouts. Here, a combination of sodium silicate and ethyl acetate is recommended for the site as this combination works well in clayey soil.

Sodium silicate comes in the form of a heavy syrupy liquid with a pH of about 11 and viscosity varying with the ratio of $\text{SiO}_2:\text{Na}_2\text{O}$ and water content (Shroff and Shah 1992). Since SiO_2 is a weak acid, sodium silicate is a basic. Silicate precipitates as a soft gel on neutralization with a strong or weak acid, acidic salts, sulphate salts, etc., by forming a hard gel with ethyl acetate, ethyl alcohol and acetic acid. This hard gel subsequently neutralizes sodium silicate by the saponification process. This silica gel is a resultant of the reaction obtained by the addition of bivalent or trivalent cations, causing poly-condensation which ultimately leads to a three-dimensional network structure. Besides, sodium silicate is considered non-toxic and non-corrosive and hence free from health hazards and environmental effects (Shroff and Shah 1992). The similar mix of sodium silicate and ethyl acetate has also been successfully applied for filling voids in clayey soils and arresting water seepage during initial stages of Calcutta Metro construction (Som and Das 2003).

Here, it is proposed that various trials at laboratory and field be made to arrive at an optimum design mix for the two materials. Some initial trials at the laboratory were also made, and it was observed that factors affecting the syneresis of hardened gels were mostly density of the grout mix and environmental changes. Similar findings are also reported by Shroff and Shah (1992).

Table 2 Calculation of settlement ratio as per Porooshash and Meyerhof (1997)

Soil		Lime column				C = Constant	Diameter, $2b = C \times Sa$	Modulus (Ec) (kPa)	(UDL) (kPa)	Settlement Ratio, $\eta = (UDL/Es)/(\delta L)$ $= 1 + Ar(Ec/Es-1)$
Cohesion Cu (kPa)	Modulus (Es) = 500 Cu (kPa)	Cohesion (Cu) (kPa)	Diameter (2a) (mm)	Depth (m)	Actual spacing from centre to centre of columns (Sa) (m)					
20	1000	150	500	10	1.4	1.05	1.4	12.76	9500	145

Settlement Ratio, $\eta = \text{Settlement of untreated Soil}/\text{Settlement of the treated soil} = 2.09$ say 2.0

Settlement of treated ground = $\frac{1}{2}$ of settlement of untreated ground

But due to space constraint, this method may also not be viable from construction point of view

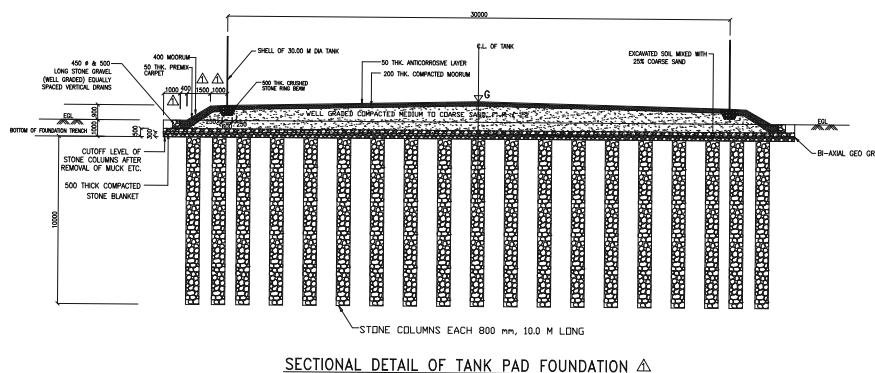


Fig. 3 Schematic drawing of remedial measure of tank foundation

Before commencing the grouting work, the tanks should be raised from the ground level by hydraulic jacks. Subsequently, the sand pad foundation should be freshly prepared and relaid in layers with geotextile sheets placed at suitable intervals. Afterwards, the tanks may be placed on the sand pad by removing the jacks. Schematic drawing of the remedial measure is presented below in Fig. 3.

Settlement monitoring should be continued to ensure effectiveness of the technique.

5 Conclusion

Design scheme of any ground improvement technique should be judiciously selected after due consideration of the actual sub-soil condition, depth of the various layers, loading condition and mechanism of load transfer. The final design scheme should be chosen keeping in mind that the benefits of the installation technique reach all the vulnerable layers, and the chosen technique helps arrest the problem rather than becoming a deterrent.

References

IS:15284-1. (2003). *Design and construction for ground improvement-guidelines, Part 1, stone columns*. New Delhi: Bureau of Indian Standards.

IS: 1904. (1986). *Code of practice for design and construction of foundations in soils: General requirements*. New Delhi: Bureau of Indian Standards.

Mittal, S. (2015). *An introduction to ground improvement engineering*. New Delhi, India: Scientific International Pvt. Ltd.

Poorooshashb, H. B., & Meyerhof, G. G. (1997). Analysis of behavior of stone columns and lime columns. *Computers and Geotechnics*, 20(1), 47–70 (Elsevier Science Ltd.).

Shroff, A. V., & Shah, D. L. (1992). *Grouting technology in tunnelling and dam construction*. Delhi: Oxford & IBH Publishing Co. Pvt. Ltd.

Som, N. N., & Das, S. C. (2003). *Theory and practice offoundation design*. Delhi: Prentice Hall of India Pvt. Ltd.

Runout of Flow Landslides

J. Kim, Z. Q. Liu, S. Lacasse, S. Nordal and V. Thakur

Abstract Risk assessment and management of flow landslides require a reliable estimate of the runout of the landslide masses. This paper introduces empirical and analytical models for the prediction of the runout of flow landslides. The numerical model uses an extension of the Bing model in Eulerian coordinates with two-space dimensions and implements the full Herschel–Bulkley rheology to dynamically compute the depth of the moving material and shear layer. The models are validated by comparing them to the observed runout values for the Kattmarka flow landslide that took place in Norway in 2009. In particular, the analytical model, although still under development, shows promise.

Keywords Flow landslides · Runout · Herschel–Bulkley rheology
Sensitive clays · Kattmarka

J. Kim
University of Washington, WA, USA
e-mail: jhkim2@uw.edu

J. Kim · Z. Q. Liu · S. Lacasse
Norwegian Geotechnical Institute, Oslo, Norway
e-mail: Zhongqiang.Liu@ngi.no

S. Lacasse
e-mail: Suzanne.lacasse@ngi.no

J. Kim
University of Oslo, Oslo, Norway

S. Nordal · V. Thakur (✉)
Norwegian University of Science and Technology, Trondheim, Norway
e-mail: Vikas.Thakur@ntnu.no

S. Nordal
e-mail: Steinar.Nordal@ntnu.no

1 Introduction

Flow landslides, for example, debris flows, debris avalanches, earth flows, sensitive clay slides, mining waste failure, and snow or rock avalanches are among the most dangerous and damaging of all landslide phenomena. Their runout potential is essential when assessing the associated consequences and risk (Fig. 1). Runout parameters include the maximum distance reached, flow velocities, thickness and distribution of deposits, and behavior in bends and at obstacles in the flow's path (Fell et al. 2000; Crosta et al. 2003; Rickenman 2005; Hungr 2005, 2016; Lacasse 2013, 2016; Lacasse et al. 2017). Different analytical and empirical models for estimating retrogression (L) and runout distances (L_u) can be found in the literature. These prediction methods are based on travel distance ($L + L_u$) and event magnitude, volume balance, mass point methods, remolding energy, or other limiting criteria such as critical slope angle. Empirical relationships usually fall short because they involve several simplifications and approximations. Therefore, analytical dynamic runout models for flow landslides may be a better alternative. This paper presents a new empirical method established to predict the runout of landslides in Scandinavian sensitive clay deposits, and a new continuum-based model numerical to predict the runout of flow landslides. The empirical model was developed as part of the intergovernmental NIFS research program in Norway (www.naturfare.no). The new numerical runout model is under development as part of the ongoing R&D project *GeoFuture II*, with the support of the Research Council of Norway (www.geofuture.no). The new model will help assess the runout distance (L_u) and can visualize the runout over an area in full 3D. In this paper, the empirical and numerical models are used to back-calculate for the Kattmarka flow landslide that took place in Norway in 2009.

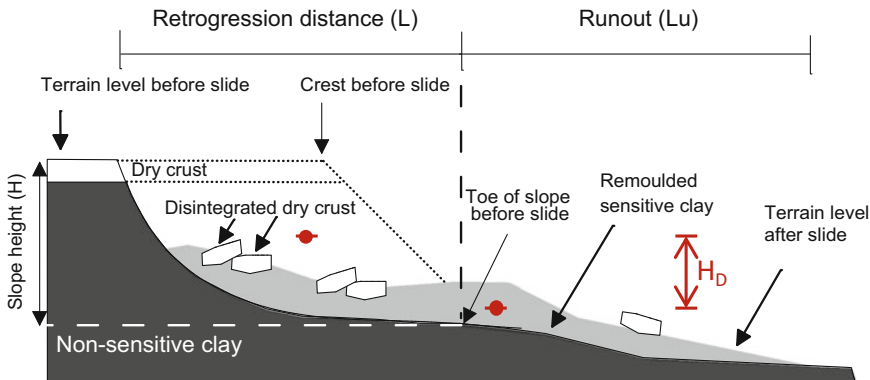


Fig. 1 Schematics and definition of terms of a flow landslide (after Strand et al. 2017)

2 Assessment of the Runout of Landslides with Empirical and Analytical Methods

Empirical relationships are the most commonly used techniques for estimating the runout distance of slide debris. Numerous empirical correlations for estimating the runout distance for various geomaterials are reported in the literature, for example, Rickenmann (1999) proposed an expression based on a worldwide dataset that includes 154 debris-flow events. This function shows that the maximum runout distance (L_u) is mainly linked with the vertical drop (H_D) and the debris-flow volume (V). Here, H_D is the vertical distance between the center of gravities of the soil body subject to landslide and the deposit of slide debris in the downstream side.

$$L_u = 1.9 V^{0.16} H_D^{0.83} \quad (1)$$

Corominas (1996) compared a dataset of 52 debris flows, debris slides, and debris avalanches using the following relationship:

$$L_u = 1.03 V^{-0.105} H_D \quad (2)$$

Locat et al. (2008) and L'Heureux (2012) proposed correlations to estimate the runout distance for Canadian and Norwegian sensitive clays, respectively. The upper limits of L_u were given as follows:

For Canadian sensitive clays:

$$L_u = 1.3 (V/W_{avg})^{0.73} \quad (3)$$

For Norwegian sensitive clays:

$$L_u = 9 (V/W_{avg})^{0.73} \quad (4)$$

Here, W_{avg} is the average width of landslide.

Locat et al. (2008) suggested a maximum runout distance for Canadian landslides as follows:

$$L_u = 8.8 L^{0.8} \quad (5)$$

Scheidegger (1973) proposed an estimate for the runout distance of rock falls as follows:

$$L_u = L (1 - H_D L^{-1}) \tan \varphi_m \quad (6)$$

Here, the reach angle (φ_m) is expressed by $\arctan (H_D/L)$.

An approach based on energy balance was suggested by Thakur and Degago (2017a, b) to estimate runout for a flow landslide in sensitive clays along a channelized terrain,

$$L_u = (E^P - E^R)^{5/3} \quad (7)$$

Here, E^P and E^R refer to the total available potential energy and the remolding energy per unit volume, respectively. The potential energy (E^P) per unit volume can simply be calculated using $2\rho g H/3$. Here, ρ is the mass density of sensitive clay and g is the gravitational acceleration. The remolding energy (E^R) can be determined using the laboratory or field testing-based methods described by Tavenas et al. (1983) and Thakur et al. (2017). Alternatively, the empirical equation: $E^R = 16 \cdot c_{ui} \cdot I_p$ proposed by Leroueil (2001) can be used. Here, c_{ui} is the average undrained shear strength and I_p is the plasticity index.

3 New Empirical Model to Predict Runout of Flow Landslides

Strand et al. (2017) presented empirical relationships based on the data from 51 landslides in sensitive clays Norway. The recommendations are given in Fig. 2. The recommendations are for estimating the runout (L_u) of landslides in sensitive clay deposits onshore (as opposed to underwater slides). The empirical model distinguishes between flow landslides in channelized terrain (where debris are confined), flow landslides in open terrain, and flake or rotational landslides.

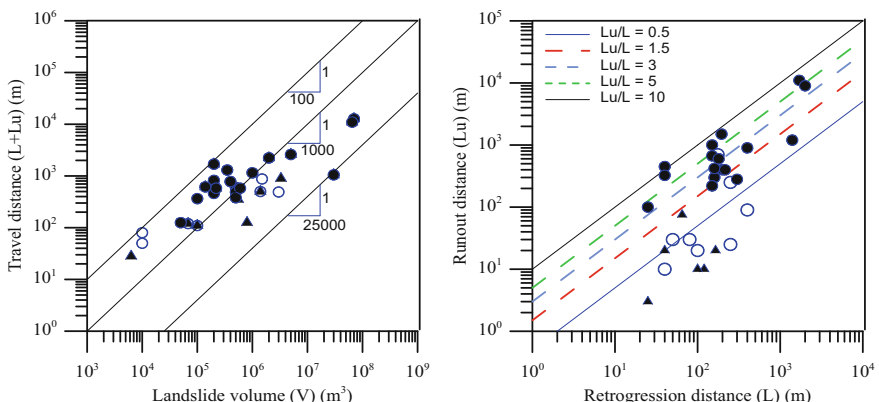


Fig. 2 Empirical model with relationships between travel distance ($L + L_u$) and landslide volume (V) (left) and runout distance (L_u) and retrogression distance (L) (right), with observed values for 51 landslides in Norwegian sensitive clays (Strand et al. 2017)

Flow landslide in channelized terrain is the following:

$$L_u = 3.0 L \quad (8)$$

Flow landslide in open terrain is the following:

$$L_u = 1.5 L \quad (9)$$

Flakes or rotational landslides are the following:

$$L_u = 0.5 L \quad (10)$$

The major advantage of these empirical relationships is their simplicity. The only required input data are the longitudinal profile of the flow path and the landslide volume. In contrast, the empirical relationships are often established using large datasets of observed debris flows without considering the specific characteristics of the sliding debris or topographical aspects that may influence the dynamic behavior and trajectory (Strand et al. 2017; Lacasse et al. 2017).

For flow landslides, the deposit width can be estimated assuming the concept that the volume of material involved in the landslide is the same as the volume of slide debris along the runout path outside the toe of the slope.

For flow landslides in channelized terrain (where the debris materials are confined), the width of deposited debris (B_u) can be obtained from the following:

$$B_u = 1/3 \times D/D_u \times B \quad (11)$$

For flow landslides in open terrain, B_u can be obtained from the following:

$$B_u = 2/3 \times D/D_u \times B \quad (12)$$

where D is the depth of the sliding surface, D_u the average thickness of the debris along the runout path, and B the width of the slope in the release area. The values of D_u and B_u are influenced by the terrain in the runout area. Equations 9 and 10 have no dependence on the release area shape, terrain inclination, and remolding behavior and flow of remolded debris materials.

4 New Numerical Model to Predict Runout of Flow Landslides

A new model, called *BingClaw*, was developed to predict the runout of flow landslide. This model is an extension of the Bing model (Imran et al. 2001) in Eulerian coordinates in two horizontal space dimensions. Locat and Demers (1988) and Grue et al. (2017) suggested that the Herschel–Bulkley rheology is suitable for

sensitive clays. This rheology was used for the dynamic computation. Due to the limited space, only selected governing equations of the BingClaw model is presented here. Readers are encouraged to refer to Kim et al. (2017) for a more detailed description of the new BingClaw model.

For simple shear conditions, the Herschel–Bulkley rheological model can be described as the following (Kim et al. 2017):

$$\left| \frac{\dot{\gamma}}{\dot{\gamma}_r} \right|^n = \begin{cases} 0, & \text{for } |\tau| \leq \tau_y, \\ \left(\frac{\tau}{\tau_y sgn(\dot{\gamma})} - 1 \right), & \text{for } |\tau| > \tau_y. \end{cases} \quad (13)$$

where $\dot{\gamma}$ is strain rate; $\dot{\gamma}_r$ reference strain rate ($= (\tau_y / \mu)^{1/n}$) with dynamic viscosity μ and exponent n ; and τ and τ_y the shear and yield stress. The exponent n is taken between 0 and 1, and $n = 1$ represents the Bingham fluid case.

The model accounts for the plug and shear layers. The mass balance is integrated over the flow's depth, and two separate momentum balance equations are integrated over the plug and shear layer. Figure 3 (left) illustrates the Herschel–Bulkley model with a constant velocity profile for the plug and parabolic velocity profile for the shear layer. The viscosity measurement done by Grue et al. (2017) (right in Fig. 3) showed that remolded Norwegian sensitive clay behaves as a shear thinning fluid and can be characterized using the Herschel–Bulkley rheology.

Sensitive clay debris materials have a peculiar characteristic; they disintegrate from an intact state to a fully remolded state during the landslide process (Thakur and Degago 2013; Thakur et al. 2017). Accordingly, an expression for the remolding is proposed as follows:

$$\tau_y(\gamma) = \tau_{y,\infty} + (\tau_{y,0} - \tau_{y,\infty}) e^{-\Gamma\gamma} \quad (14)$$

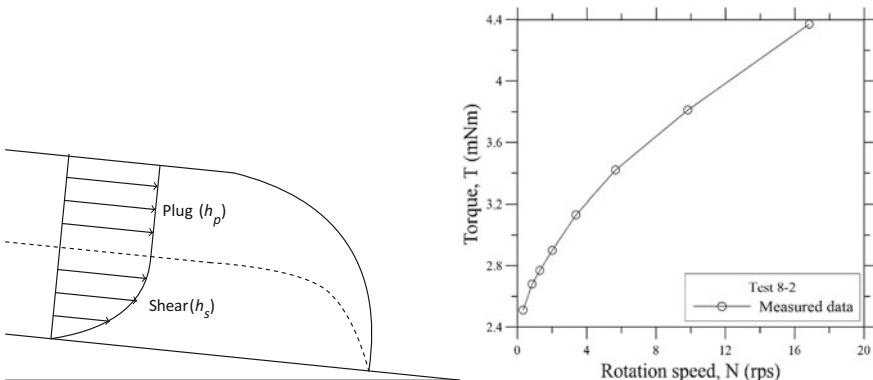


Fig. 3 Schematic Herschel–Bulkley model of plug and shear (Kim et al. 2017-left); observed behavior of a Norwegian sensitive clay in laboratory (Grue 2015-right)

where $\tau_{y,0}$ and $\tau_{y,\infty}$ are the initial and residual yield stress, and Γ (dimensionless) is a coefficient describing the remolding. The change in τ_y because of remolding is directly proportional to $-e^{\Gamma y}$. Small Γ values imply that large accumulated shear is needed for remolding. Because the remolding process is assumed to be a non-reversible process, the average yield stress decreases in time. The proposed model calculates the runout distance, maximum velocity over the flow domain, and the average deposit height over the runout area. The numerical implementation, using a finite volume method, has three steps: (1) the earth pressure is compared to the yield stress in each cell. If the yield stress is larger than the earth pressure, no motion is allowed. If the two adjacent cells do not deform, there is no displacement at the interface; (2) if one of the cells deforms, the equations without friction terms are solved. At each cell interface, a Riemann problem is solved with the wave propagation algorithm of the finite volume method, and (3) the friction forces are then included using a Godunov fractional step method (Kim et al. 2017).

5 Back-Calculation of the Kattmarka Flow Landslide

5.1 The Kattmarka Flow Landslide

On March 13, 2009, in Kattmarka near Namsos, which is north of Trondheim in Norway, a slide occurred, moving about 500,000 m³ of material in a scar of about 100 m wide by 300 m long. The slide destroyed a highway and damaged four permanent dwellings and six summer residences. Seven persons who had been transported on the slide were rescued by helicopter. Figure 4 is an aerial photograph taken right after the flow landslide. Figure 5 (upper left) shows a 3D representation of terrain of Kattmarka before the landslide and the blast site where the initial took place. The lower left Fig. illustrates the post-failure situation with a 3D representation of the extent of the runout zone and the locations of some of the houses, which were moved along with the slide debris. Figure 5 (right) illustrates the sequence of the movements (from 1 to 5) based on observations and eyewitness accounts. The slide started about 30 s after the blasting of rock as part of nearby highway construction. The second slide occurred 2 min after the first, and thereafter, three more slides occurred. The sliding activity lasted between 6 and 10 min (Lacasse 2013).

The nearby construction project was a widening of the road that involved removing some of the mountainside, along with adding sidewalks and upgrading the sewers and pavement. The soil investigations post-landslide revealed the presence of sensitive clay with lenses of silt and sand. The clay thickness was between 10 and 20 m above bedrock. There was a thin layer of moraine above the bedrock. The soil consisted of clay layers, some more silty than others, with thin sand lenses at irregular intervals. The water content was above the liquid limit. The overconsolidation ratio in the clay below a drying crust of about 2.5 m thick



Fig. 4 An aerial view of the Kattmarka flow landslide. *Source* L. A. Holme

decreased from 2.5 at a depth of 3 m to 1.5 at a depth of 14 m (Nordal 2009; Lacasse 2013). The average shear strength of the sensitive clay deposit was around 30 kPa, and the remolded shear strength was measured to be between 0.6 and 1.0 kPa.

5.2 Runout Prediction

The back-calculation of the runout of the Kattmarka flow landslide was done with both the new empirical model (Eq. 7) and the new numerical model. Table 1 lists the input parameters for both models. The observed runout distance (L_u) was a maximum of 280 m. It is worth mentioning that the landslide retrogressed sideways and therefore L is probably approximately 300 m.

The numerical calculations were done using the best estimate of the parameters (see Table 1) that also made the results fit the observations. As illustrated in Fig. 6, the initial slide and the subsequent stages of the movement (Fig. 5) were successfully reproduced by the new BingClaw model. The back-calculated depositional height in the runout zone varied between 1 to 3 m (Fig. 6 left), the runout velocity was as high as 2 m/sec (Fig. 6 center), and the runout of the remolded debris is shown in Fig. 6 right. A 3D terrain model the landslide after 1 and 20 min is shown in Fig. 7.

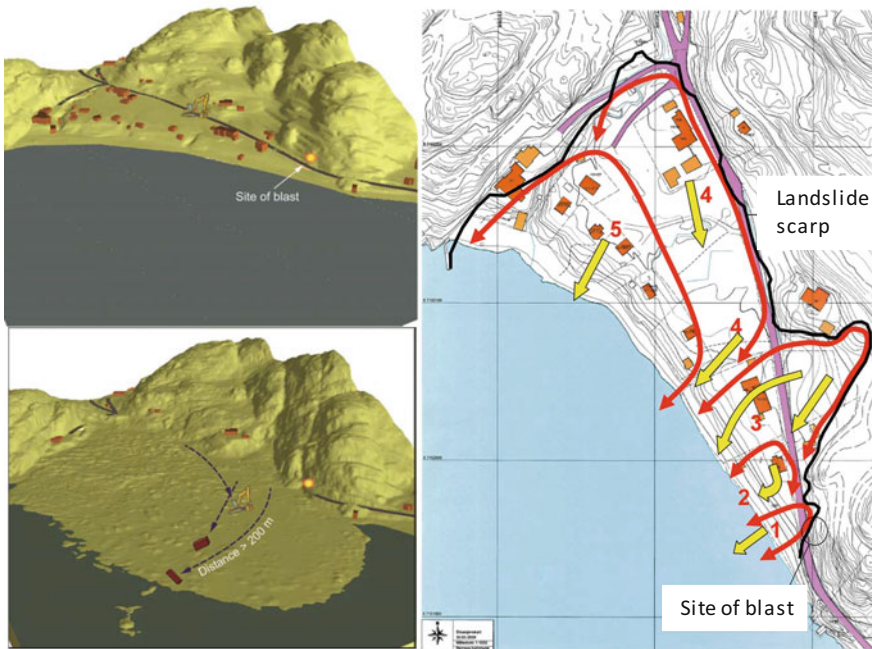


Fig. 5 (Left) A 3D representation of the area subjected to landslide and the runout zone. “Site of blast” is the located where the landslide initiated (left); reconstruction of the landslide into five stages based on witness accounts (right—grid size is $100\text{ m} \times 100\text{ m}$ (Lacasse 2013; Nordal 2009)

Table 1 Input parameters for the back-calculation of the Kattmarka flow landslide

Parameters	$\tau_{y,0}$	$\tau_{y,\infty}$	Γ	L	D	D_u
Values	30 kPa	0.80 kPa	0.09	300 m	10 m	3 m

The numerically obtained runout distance and runout zone are essentially identical to the observations. However, the results are sensitive to the parameter selection. The parametric study performed for the Kattmarka flow landslide suggests that runout distance decreases with increasing residual yield stress, deposit height increases with increasing residual yield stress, and maximum velocity decreases with the increasing product of initial yield stress and parameter Γ .

The *BingClaw* model has been applied to six sensitive clay landslides in Norway. Liu et al. (2017) back-calculated the Rissa landslide and showed that the overestimation of runout distance may happen if one assumes the entire sliding mass as sensitive clay. With such depth-averaged model as this new numerical model, the residual yield stress should have been given a somewhat higher value to account for the non-sensitive material above the sensitive clay. This would give

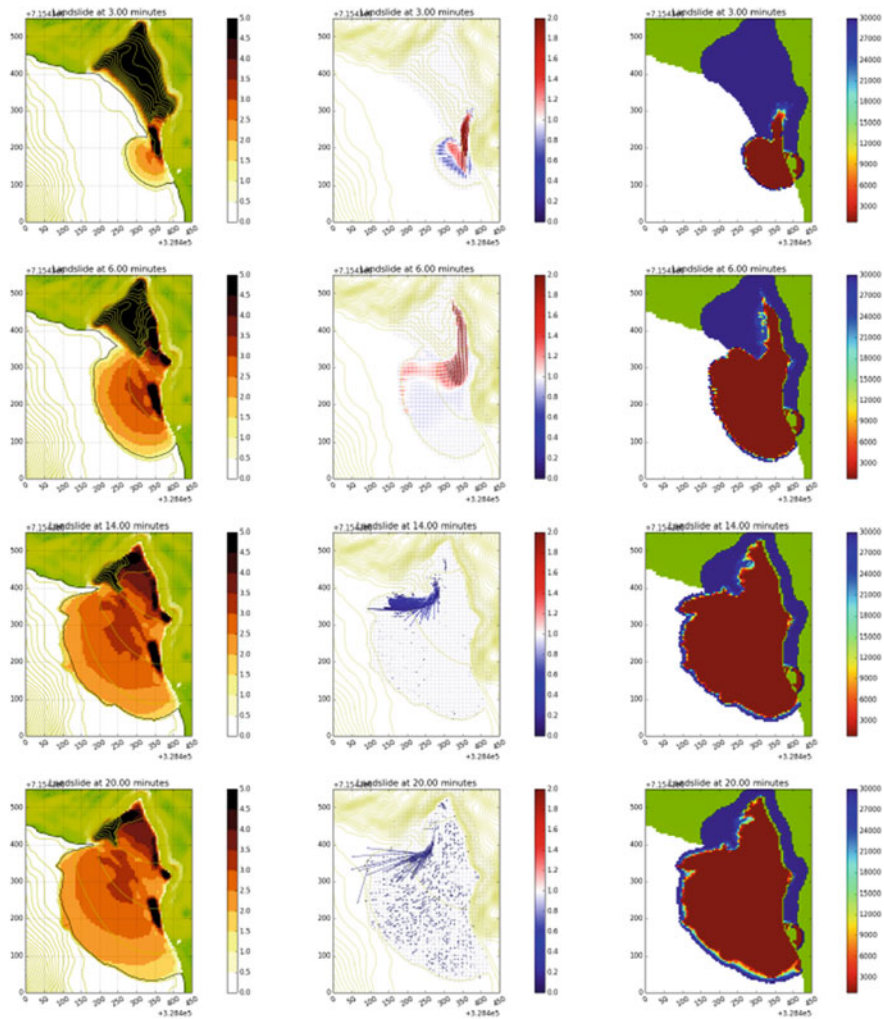


Fig. 6 Results of numerical modeling of runout after 3, 6, 14, and 20 min after the initiation of the flow landslide. Left: depositional height of slide debris; Center: average velocity over flow domain; Right: spatial distribution of shear resistance, with blue the average intact shear strength ($\tau_{y,0} = 30,000$ Pa or 30 kPa) and brown the fully remolded shear strength ($\tau_{y,\infty} = 800$ Pa or 0.8 kPa)

shorter runout and higher deposit height. Liu et al. (2017) combined the numerical results with probabilistic analyses with Monte Carlo simulations to provide a range of runout distance, deposit height, and average velocity. Such analyses are useful because one could then estimate the runout as a mean \pm one standard deviation of the predicted values for the ensuing consequence analysis.

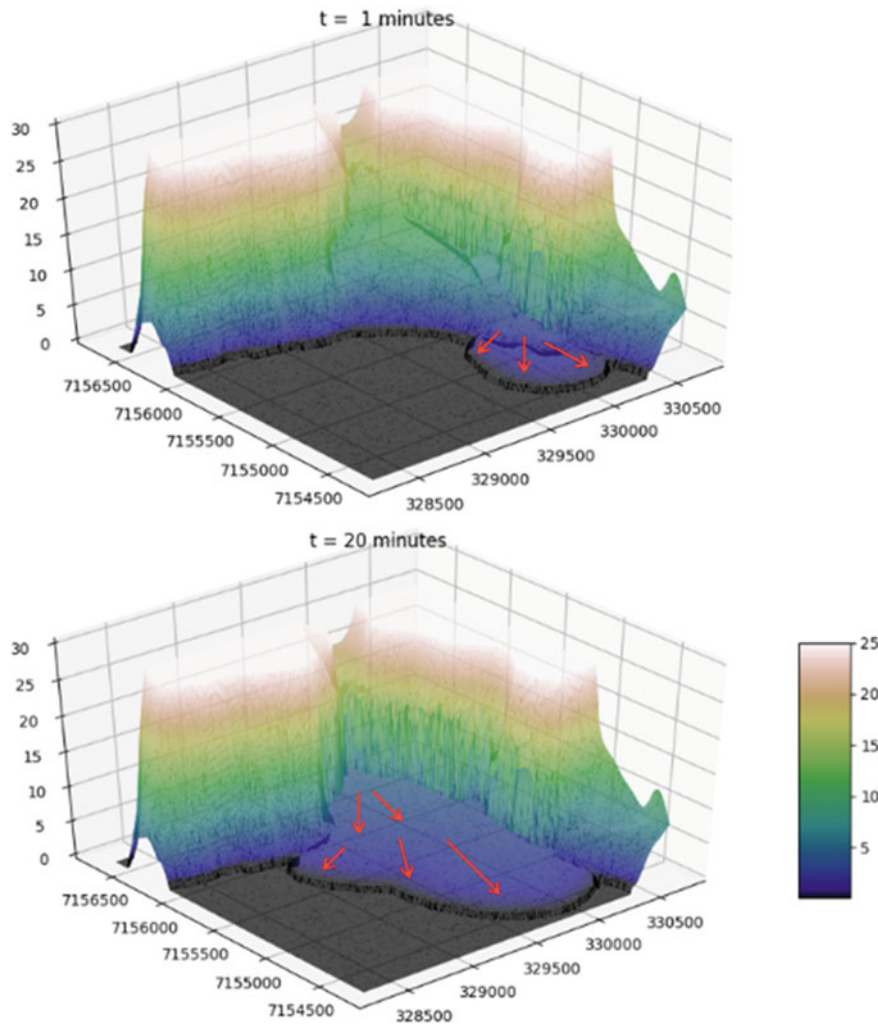


Fig. 7 Terrain model of the Kattmarka flow landslide after 1 and 20 min. The legend represents the height in meters

Using the empirical model proposed by Strand et al. (2017), the runout distance for the Kattmarka landslide is calculated as $1.5 \times 300 \text{ m} = 450 \text{ m}$. The width of the runout zone (B_u) is obtained as 2.22 times the width of landslide (B) assuming that $D = 10 \text{ m}$ and $D_u = 3 \text{ m}$. These estimates are conservative side as anticipated. The model was made to give runout parameters on the high side.

6 Summary and Conclusions

Runout of flow landslides needs to be predicted with reasonable reliability for landslide hazard and risk assessment, particularly the identification of the elements at risk and the impact of the landslide on these elements at risk. The runout is usually predicted by either empirical/statistical methods or analytical dynamic methods. The two new models gave reasonably good estimates of the observed runout distance and maximum velocity over the flow domain for the Kattmarka flow landslide, with the empirical method overestimating the runout distance as it is meant to be. Both models provided reasonable results, and each has its domain of application. In particular the *BingClaw* model, although still under development, offers promise.

Acknowledgements The cooperative research program «Natural Hazards: Infrastructure for Floods and Slides (NIFS)» and the GeoFuture II project are acknowledged for the support. The authors wish to acknowledge Dr. Hans Petter Jostad (NGI) and Dr. Finn Løvholt (NGI) for their contributions.

References

Corominas, J. (1996). The angle of reach as a mobility index for small and large landslides. *Canadian Geotechnical Journal*, 33(2), 260–271.

Crosta, G. B., Cucchiaro, S., & Frattini, P. (2003). Validation of semi-empirical relationships for the definition of debris-flow behavior in granular materials. In *3rd International Conference on Debris-Flow Hazards Mitigation* (pp. 821–831). Davos: Millpress.

Fell, R., Hungr, O., Leroueil, S., & Reimer, W. (2000). Geotechnical engineering of the stability of natural slopes, and cuts and fills in soil. *GeoEngineering*, 2000(1), 21–120.

Grue, R., Issler, D., L'Heureux, J. S., & Thakur, V. (2017). Viscometric tests of sensitive clay from Byneset, Norway, and fit to the Herschel–Bulkley model. In *Natural hazards book: Advances in natural and technological hazards research* (pp. 155–166) (ISSN: 1878-9897).

Grue, R. H. (2015). *Rheological parameters of Norwegian sensitive clays, focusing on the Herschel–Bulkley model* (Master's thesis). Department of Civil and Transport Engineering, Norwegian University of Science and Technology (NTNU). URL <http://hdl.handle.net/11250/2349972>.

Hungr, O. (2005). Classification and terminology. In *Debris-flow hazards and related phenomena* (pp. 9–24). Chichester: Springer (ISBN 3-540-20726-0).

Hungr, O. (2016). A Review of landslide hazard and risk assessment methodology. In *Landslides and engineered slopes. Experience, theory and practice: Proceedings of the 12th International Symposium on Landslides*. Italy: Napoli.

Imran, J., Parker, G., Locat, J., & Lee, H. (2001). 1D numerical model of muddy subaqueous and subaerial debris flows. *Journal of Hydraulic Engineering*, 127(11), 959–968.

Kim, et al. (2017). A first coupled analysis on the giant 8100 BP Storegga slide and tsunami studies by new landslide source models. Subm. *Journal of Geophysical Research*.

L'Heureux, J. S. (2012). A study of the retrogressive behaviour and mobility of Norwegian quick clay landslides. In *Proceedings of 11th NASL* (Vol. 1, pp. 981–988). Banff, Canada.

Lacasse, S. (2013). 8th Terzaghi oration protecting society from landslides—the role of the geotechnical engineer. In *18th International Conference on Soil Mechanics and Geotechnical Engineering*. Paris, France.

Lacasse, S. (2016). 55th rankine lecture hazard, risk and reliability in geotechnical practice. *Geotechnique*.

Lacasse, S., Liu, Z., Kim, J., Choi, J. C., Nadim, F. (2017). Reliability of Slopes in Sensitive Clays. In Thakur, V., L'Heureux, J. S., Locat, A. (Eds.), *Landslides in Sensitive Clays. Advances in Natural and Technological Hazards Research*, Vol 46. Cham: Springer. https://doi.org/10.1007/978-3-319-56487-6_45.

Leroueil, S. (2001). Stability of natural slope and cuts. *Geotechnique*, 51(3), 197–243.

Liu, Z. Q., Lacasse, S., L'Heureux, J. S., Kim, J., & Thakur, V. (2017). Modelling of the runout of the Rissa landslide. In *Canadian Geotechnical Conference*. GeoOttawa.

Locat, J., & Demers, D. (1988). Viscosity, yield stress, remolded strength, and liquidity index relationships for sensitive clays. *Canadian Geotechnical Journal*, 25, 799–806.

Locat, P., Leroueil, S., & Locat, J. (2008). Remaniement et mobilité des débris de glissements de terrain dans les argiles sensible de l'est du Canada. In *Proceedings of the 4th Canadian Conference on Geohazards: From Causes to Management* (pp. 97–106). Québec.

Nordal, S., Alén, C., Emdal, A., Jendeby, L., Lyche E., & Madshus, C. (2009). Skredet i Kattmarkvegen i Namsos 13. mars 2009. Rapport fra undersøkelsesgruppe satt ned av Samferdselsdepartementet.

Rickenmann, D. (1999). Empirical relationships for debris flows. *Natural Hazards*, 19–1, 47–77.

Rickenmann, D. (2005). Run-out prediction methods. In M. Jakob & O. Hungr (Eds.), *Debris-flow hazards and related phenomena* (pp. 305–324). Berlin: Springer.

Scheidegger, A. E. (1973). On the prediction of the reach and velocity of catastrophic landslides. *Rock Mechanics*, 5, 231–236.

Strand, S. A., et al. (2017, June). Runout of landslides in sensitive clays. In *2nd International Workshop on Landslides in Sensitive Clays* (pp. 289–300). Trondheim: Springer.

Tavenas, F., Flon, P., Lerouil, S., et al. (1983). Remolding energy and risk of slide retrogression in sensitive clays. In *Proceedings of the Symposium Slopes on Soft Clays* (pp. 423–454). Linköping, Sweden.

Thakur, V., & Degago, S. A. (2013). Disintegration of sensitive clays. *Géotechnique Letters* (3–1), pp. 20–25.

Thakur, V., & Degago, S. A. (2017a). Role of remoulding energy in the post failure movements of landslides. In *19th International Conference on Soil Mechanics and Geotechnical Engineering*. Seoul, South Korea.

Thakur, V., & Degago, S. A. (2017b). Role of remolding energy in the post failure movements of landslides. In *9th International Conference on Soil Mechanics and Geotechnical Engineering*. (19th ICSMGE), Seoul.

Thakur, V., Degago, S., Selänpää, J., & Länsivaara, T. (2017). Determination of remoulding energy of sensitive clays. In *Natural hazards book: Advances in natural and technological hazards research* (pp. 97–106). (ISSN: 1878-9897) (Print) 2213-6959 (Online). <https://doi.org/10.1007/978-3-319-56487-6>.

Quantification of Soil State Variables Using Electromagnetic Methods

Alexander Scheuermann, Thierry Bore, Partha Narayan Mishra,
Habibullah Bhuyan, Guanxi Yan, Tilman Bittner and Rolf Becker

Abstract The possibility to quantitatively measure changes in state variables both in laboratory and in situ is the key for the comprehensive assessment and understanding of many problems in geotechnical engineering. The analysis of the processes in unsaturated soils, for example, requires not only pore water pressures but also the information on the water content and the porosity to capture the field soil–water retention relationships. In saturated soils, knowledge of the temporal evolution of the soil density allows a much better understanding of the consolidation and shrinkage behavior, especially with respect to soft soils. Electromagnetic measurement methods allow the quantification of not only the water content but also the porosity of granular and cohesive soils. In particular, the porosity, which determines the dry density of a soil in combination with the specific gravity, is a key parameter influencing many mechanical and hydraulic processes and their governing

A. Scheuermann (✉) · T. Bore · P. N. Mishra · H. Bhuyan · G. Yan · T. Bittner
School of Civil Engineering, The University of Queensland,
St Lucia, QLD 4072, Australia
e-mail: a.scheuermann@uq.edu.au

T. Bore
e-mail: t.bore@uq.edu.au

P. N. Mishra
e-mail: p.mishra@uq.edu.au

H. Bhuyan
e-mail: h.bhuyan@uq.edu.au

G. Yan
e-mail: g.yan@uq.edu.au

T. Bittner
e-mail: t.bittner@uq.edu.au

R. Becker
Faculty of Communication and Environment, Rhine-Waal University
of Applied Sciences, 47475 Kamp-Lintfort, Germany
e-mail: rolf.becker@hochschule-rhein-waal.de

parameters. The presented contribution introduces different measurement methods in the laboratory and the field for determining water content and density using a variety of sensors.

Keywords Water content · Density · Less invasive · Mixing rules
Electromagnetic method

1 Introduction

Basically, all processes in soil mechanics and geotechnical engineering are accompanied by changes in the soil state variables. From the hydraulic point of view, this concerns the pore water pressure, which can be either positive or negative relative to the atmospheric pressure and the water content. From a mechanical perspective, stress and deformation are the state variables of interest defining the stress state in the soil. While pore water pressures are simple to measure, the quantification of the water content already requires specialized instrumentation (Robinson et al. 2003) which in part is commercially available. Total stresses are usually measured point-wise using flat jacks only if absolutely required and only at selected locations. Deformations are usually only available as a cumulative value in form of settlement at the surface or as distribution in the ground as measured using the extensometer. The observation of the changes in soil density in the ground usually eludes our observation. As a localized form of deformation, shear zones can be identified using inclinometers.

Electric and electromagnetic measurement methods provide an alternative solution for measuring the soil state variables. These methods have been already used for decades for measuring the water content in the soil, as the targeted electric parameters, electrical conductivity, and the dielectric permittivity are directly correlated with this soil state variable (O'Connor and Dowding 1999). Originally, and still today, simple sensor designs in form of rod probes or circuit boards as sensors are used to quantify the moisture content for partly saturated soils at a single location, since smallest changes in water content can already cause large variations in the targeted electric parameter. New sensor designs in combination with more sophisticated measuring methods and analysis procedures allow the observation of water content profiles along elongated sensors (Scheuermann et al. 2009) and the quantification of changes in solid concentration at water-saturated conditions (Chung and Lin 2011). Equally, other sensor designs allow for the measurement of other soil state variables or changes in the ground connected to deformation and stress (O'Connor and Dowding 1999; Scheuermann and Huebner 2009).

In the following, this contribution provides an overview of some electromagnetic measurement methods used for quantifying the water content together with selected examples from latest developments to improve these methods for targeted soil state variables.

2 Electric and Electromagnetic Measurement Methods

There are numerous methods available for measuring the water content in soils. These methods differ from each other mainly in terms of the way how the measurement is conducted and the consequential frequency range covered by the method. In principle, two methods can be differentiated, namely time domain and frequency domain methods. Although the resulting dielectric parameters differ in their information content, the fundamental concepts to derive the water content from the dielectric parameters are more or less the same.

2.1 Time Domain Reflectometry (TDR)

The time domain reflectometry method is probably the most well-known method in soil-related disciplines for measuring water contents in soils. In this method, a step-pulse is launched by the TDR device into a transmission line consisting of a 50Ω coaxial cable as a feeding line connected to a sensor as a waveguide. Mostly non-insulated rod probes are used as sensors, but also insulated rod probes or ribbon cables are applied for this task (Huebner et al. 2005). The step-pulse travels along the transmission line creating an electromagnetic field that is shielded and encapsulated within the coaxial cable but reacts to the changes in the physical properties of the soil while traveling along the sensor.

The TDR device that consists of a pulse generator and a sampling oscilloscope has an internal wave resistance of 50Ω . Since the wave resistances of the device and the coaxial cable are the same, there is nearly no reflection at the transition from device to the coaxial cable. At the transition from coaxial cable to the waveguide, however, the wave resistance changes considerably, leading to a distinct reflection of a part of the signal at the beginning of the sensor. The residual part travels along the sensor where it is fully reflected at the open end of the sensor in the case that there is no other cable connected to the sensor. The reflections of the signal travel back to the TDR device, where they are measured as changes in voltage in the time domain also called the TDR trace.

The reflections at the beginning and the end of the sensor can easily be identified in the TDR trace. The so-called tangent method is used to calculate the resulting travel time of the signal, which also contains the travel time in the sensor head forming the transition from coaxial cable to the sensor. Strictly speaking, only the sensor in direct contact with the soil is considered as the waveguide sensing the soil parameters. Therefore, the travel time in the sensor head usually needs to be determined based on calibration measurement with materials of known dielectric permittivity, such as air, water (at different temperatures), or other liquids (e.g., methanol).

Once the travel time t_s along the sensor has been identified, the effective dielectric permittivity ϵ_{eff} can be directly determined for non-insulated sensors based on the equation

$$\epsilon_{\text{eff}} = \left(\frac{c_0 \cdot t_s}{2 \cdot L_s} \right)^2 \quad (1)$$

with c_0 being the speed of light and L_s the length of the sensor. For the case that the sensor is insulated, the inductance L' as an additional parameter is required to calculate the mean capacitance C' based on the velocity of the signal along the sensor

$$v_s = \frac{2 \cdot L_s}{t_s} = \frac{1}{\sqrt{L' \cdot C'}} \quad (2)$$

The mean capacitance C' depends directly on the effective dielectric permittivity ϵ_{eff} . Depending on the geometry and the way how the sensor is insulated, different functions of the capacitance model are used to determine C' (Huebner et al. 2005).

A sophisticated method on how to analyze TDR traces is the inversion, which allows the determination of the profile of the effective dielectric permittivity along the sensor. Several methods have been developed (e.g., Leidenberger et al. 2006; Norgren and He 1996) of which the one of Schlaeger (2005) is the one used for most of the presented studies.

2.2 Frequency Domain Reflectometry (FDR)

As simple as it may sound, the basic difference between time domain methods and frequency domain methods is the measuring domain. In both methods, the propagation of the electromagnetic wave along the transmission line is subject to exactly the same influences. The difference is that in TDR a signal is launched into the transmission line containing a limited frequency content that even changes while traveling along the sensor. In frequency domain methods, a sinusoidal signal with given frequency and amplitude is sent, and reflections and transmissions are observed. The basic measurements taken describe changes in amplitude and phase shift that are described by the so-called scattering parameters. Based on calibrations, these scattering parameters can be recalculated into a real part ϵ' and an imaginary part ϵ'' of the complex dielectric permittivity.

Conventional FDR methods cover a restricted frequency range to provide a mean dielectric permittivity over this frequency range. However, dielectric spectroscopy covers a large frequency range that allows the determination of the frequency-dependent values for ϵ' and ϵ'' . With suitable analysis methods based on

the Debye theory, relaxation processes happening over different frequency ranges can be identified and related to different soil parameters, such as soil density and the content of the bound water phase.

3 Examples of Soil State Variables Measurements

Subsequently, examples from various completed and ongoing research studies are presented in which electromagnetic measurement methods are used to determine one or the combination of the major state variables, namely the water content, density/porosity, and the total earth pressure.

3.1 *Measurement of Water Content Distributions*

The measurement of water content distributions requires the application of elongated sensors. Sufficient sensor lengths can only be achieved by insulating the rods or the wires forming the sensor. With blank sensors, the electromagnetic signal would attenuate too fast, with the consequence that the inversion of the TDR trace is not feasible. In most of the presented applications, flat ribbon cables are used as insulated sensors. The advantage of using flat ribbon cables as sensors is that measurements from both ends of the sensor can be conducted. Measurements from both ends of the sensor allow for the determination of not only C' but also the conductance G' that is directly related to the electrical conductivity of the soil (Schlaeger 2005). In this way, the influence of the electrical conductivity on the wave propagation is considered in the inversion. Another advantage of using flexible flat ribbon cables as sensors is that they can be easily installed during construction.

3.1.1 Rod Sensor Measurements in a Lysimeter

Becker et al. (2008) used insulated rod sensors of 70 cm length to observe water content distributions within a lysimeter filled with silty soil. Artificial precipitation test has been conducted aiming at improving the characterization of the hydraulic parameter of the soil based on transient infiltration tests. Since measurements from only one end of the sensor could have been conducted, a relationship between G' and C' was introduced and calibrated to allow the inversion of the measurements under consideration of the conductance G' .

3.1.2 Water Content Distributions Within a Model Dyke

The first large-scale application of TDR in combination with flat ribbon cables as sensors for measuring water content distributions (spatial TDR) was a natural-scaled dyke model (Scheuermann et al. 2009). Twelve flat ribbon cables of different lengths have been installed vertically inside the dyke body. Flood simulation tests have been conducted, and water content changes during water infiltration observed. Based on these measurements, the influence of the initial water content distribution on the transient seepage through levees could be proven.

3.1.3 Combination of Spatial TDR and ERT

Electrical resistivity tomography (ERT) is a useful tomographic geophysical method to be combined with spatial TDR. At the above-mentioned dyke model, ERT was applied to observe the transient seepage during a flood simulation test (Rings et al. 2008). Based on in situ calibrations between the electric resistivity and the water content measured using spatial TDR, ERT measurements could be analyzed in terms of water contents. The same approach was chosen by Fan et al. (2015) to investigate the groundwater recharge processes on vegetated sand islands. In this study, two different soil horizons were considered and calibrated. The combination of ERT with spatial TDR allowed the observation of 2D water content distributions over one year.

3.1.4 Characterization of Soil Hydraulic Parameters

The possibility of transiently measuring water content distributions allows the in-depth characterization of the hydraulic parameters of the soil, especially the soil retention behavior. First attempts to quantify the soil water retention curve using spatial TDR measurements based on multi-step-inflow and multi-step-outflow experiments have been presented by Scheuermann and Bieberstein (2005). These tests showed for the first time the step-wise accumulation of water with repeated imbibition/drainage cycles (hydraulic ratcheting, Galindo-Torres et al.). In latest investigations, spatial TDR is used to measure the water content distribution in soil columns of 2 m height to be compared with test results from conventional axis translation tests for measuring the soil water retention curve (Yan et al. 2017). At equilibrium conditions, both curves should match each other.

3.2 *Measurement of Density or Porosity*

The density state influences both the shear strength and the stiffness of a soil. While stresses can easily be assessed based on the assumption of geostatic conditions, the

density state is usually unknown and difficult to be assessed. Any information provided on temporal changes in density would allow the improvement of the understanding of underlying processes related to, e.g., the deformation of soils due to consolidation or as a result of cyclic loading. Furthermore, many constitutive relationships require the changes in porosity as input parameter, for example, to determine the hydraulic conductivity or the stiffness of a soil. In the following, some examples for measuring the density or porosity of a soil using electromagnetic measurement methods are presented.

3.2.1 Measurement of Dry Unit Weight in Coarse Grained Pavement Materials

Quality control is essential during earthworks. One important task is to determine the dry density and water content after compaction to make sure that the required density condition is achieved. As a fast measurement method, nuclear density gauges are usually used. However, the operation of these devices is allowed only by specially trained personal and under strict safety conditions allowing an investigation depth of 300 mm maximum. An alternative method was developed by Drnevich et al. (2005), which is even suggested by ASTM for measuring water content and dry density in granular materials (ASTM D6780 2003). A further developed method with correction for the temperature was suggested by Yu and Drnevich (2004). For monitoring of pavements, Bhuyan et al. (2017) introduced a robust method for determining not only moisture content of unbound road materials but also the field dry density using a standard rod sensor.

3.2.2 Porosity Distributions During Erosion Tests

The process of internal erosion is always accompanied by structural changes of the soil skeleton visible in form of porosity changes. Fine particles are either washed out of the soil skeleton, or they are mixed with coarse soils leading to a change in the porosity. Knowledge of these porosity changes during erosion is essential to better understand the underlying processes and to provide important data for the verification of numerical tools. Scheuermann (2012) has used spatial TDR in combination with five rod probes for the first time to measure porosity distributions in water-saturated granular materials. This method was further developed and is used now with a coaxial line cell for investigating the contact erosion of soils. An experimental setup was developed to allow the parameterization of the coupled hydraulic, mechanic, and dielectric parameters under flow conditions using a large open-ended sensor (Bittner et al. 2017).

3.2.3 Measurement of Density Changes During Shrinkage and Compaction

A laboratory shrinkage test usually starts at water contents slightly higher than the liquid limit at water contents very close to saturation. As dewatering of the sample starts, the soil deforms and undergoes different deformation stages. The evolution of shrinkage follows a saturation line along the zero air void line until the shrinkage limit is reached. At the water content defining the shrinkage limit, air entering into the pore system of the soil occurs, and the stiffness increases substantially leading to residual shrinkage with further reduction of the water content. Dielectric measurements during shrinkage help in interpreting structural changes during desiccation (Bore et al. 2017). Dielectric measurements during compaction tests show that in principle it is possible to quantify the density based on the frequency-dependent dielectric permittivity.

3.3 *Measurement of Total Stress*

One of the first applications of TDR was the identification of shear zones in moving slopes (O'Connor and Dowding 1999). In principle, a coaxial cable is vertically buried in the ground supported by grouting. At locations, where the cable is deformed, peaks in the TDR trace become visible which allows the identification of the depth of the deformation. Scheuermann and Huebner (2009) presented a new sensor design for quantifying the stresses along the sensor based on spatially distributed TDR measurements. The deformation of the sensor changes the inductance directly. As the sensor is deformed without or minimally changing the dielectric of the sensor, the propagation speed v_s of the electromagnetic signal is nearly unchanged. As a consequence, a direct relationship between inductance L' and conductance C' can be derived. The influence of the conductance G' is minimal and can be neglected. A first practical application was the observation of changes in TDR traces along 4-m-long sensors during the installation of auger displacement piles. From a geotechnical engineering point of view, this kind of sensor provides the possibility to observe stress distributions along elongated elements, such as sheet pile walls, pile raft systems, and along tunnels.

4 Discussion and Conclusion

All processes in soil mechanics and geotechnical engineering are accompanied by changes in the soil state variables. Knowledge of the changes in these soil state variables is essential for improving the understanding and modeling of the underlying mechanic and hydraulic processes. The paper briefly introduces

electromagnetic measurement methods and examples of studies aiming at measuring one or several of these soil state variables.

Electric and electromagnetic measurement methods provide the possibility to quantify conditions which were hidden so far. These methods include the sensor, the measuring device, and the analysis procedures, and they will play an important role in future for geotechnical and geoenvironmental engineering applications.

References

ASTM. (2003). *Standard test method for water content and density of soil in place by time domain reflectometry (TDR)*. D6780, West Conshohocken, PA.

Becker, R., et al. (2008). *Spatial time domain reflectometry (Spatial TDR)–principles, limitations and accuracy* (pp. 181–187). London: Taylor & Francis.

Bhuyan, H., et al. (2017). Use of time domain reflectometry to estimate moisture and density of unbound road materials. *Transportation Research Record: Journal of the Transportation Research Board*, 2655, 71–81.

Bittner, T., et al. (2017). Experimental investigation of the dielectric properties of soil under hydraulic loading. *Measurement Science & Technology*, 28(4), 44001.

Bore, T., et al. (2017). Broadband electromagnetic analysis of compacted kaolin. *Measurement Science & Technology*, 28(1), 14016.

Chung, C.-C., & Lin, C.-P. (2011). High concentration suspended sediment measurements using time domain reflectometry. *Journal of Hydrology*, 401(1–2), 134–144.

Drnevich, V. P., et al. (2005). Time domain reflectometry for water content and density of soils: Study of soil-dependent calibration constants. *Canadian Geotechnical Journal*, 42(4), 1053–1065.

Fan, J., et al. (2015). Quantifying spatiotemporal dynamics of root-zone soil water in a mixed forest on subtropical coastal sand dune using surface ERT and spatial TDR. *Journal of Hydrology*, 523, 475–488.

Huebner, C., et al. (2005). Advanced measurement methods in time domain reflectometry for soil moisture determination. *Electromagnetic Aquametry*, 317–347.

Leidenberger, P., Oswald, B., & Roth, K. (2006). Efficient reconstruction of dispersive dielectric profiles using time domain reflectometry (TDR). *Hydrology and Earth System Sciences Discussions*, 10(2), 209–232.

Norgren, M., & He, S. (1996). An optimization approach to the frequency-domain inverse problem for a nonuniform LCRG transmission line. *IEEE Transactions on Microwave Theory and Techniques*, 44(8), 1503–1507.

O'Connor, K. M., & Dowding, C. H. (1999). *Geomeasurements by pulsing TDR cables and probes*. Boca Raton: CRC Press.

Rings, J., et al. (2008). Soil water content monitoring on a dike model using electrical resistivity tomography. *Near Surface Geophysics*, 6(2), 123–132.

Robinson, D. A., et al. (2003). A review of advances in dielectric and electrical conductivity measurement in soils using time domain reflectometry. *Vadose Zone Journal*, 2(1996), 444.

Scheuermann, A. (2012). Determination of porosity distributions of water saturated granular media using spatial time domain reflectometry (spatial TDR).

Scheuermann, A., & Huebner, C. (2009). On the feasibility of pressure profile measurements with time-domain reflectometry. *IEEE Transactions on Instrumentation and Measurement*, 58(2), 467–474.

Scheuermann, A., et al. (2009). Spatial time domain reflectometry and its application for the measurement of water content distributions along flat ribbon cables in a full-scale levee model. *Water Resources Research*, 45(4).

Schlaeger, S. (2005). A fast TDR-inversion technique for the reconstruction of spatial soil moisture content. *Hydrology and Earth System Sciences*, 9, 481–492.

Yan, G., et al. (2017). *An experimental platform for measuring soil water characteristic curve under transient flow conditions advances in laboratory testing and modelling of soils and shales (ATMSS)* (pp. 231–238). Berlin: Springer.

Yu, X., & Drnevich, V. P. (2004). Soil water content and dry density by time domain reflectometry. *Journal of Geotechnical and Geoenvironmental Engineering*, 130(9), 922–934.

Diverse Applications of Geocells for Highways—Two Case Studies from the North-East

Shahrokh P. Bagli

Abstract Geocells are geosynthetics which are essentially three dimensional and have a rhomboidal cellular profile. Geocells with engineering applications, now made in India, are fabricated from textured HDPE straps which are welded together. For major applications, the geocells are judiciously perforated for drainage/porewater pressure relief and cell-to-cell infill interaction. The geosynthetic is versatile and can be utilised for a variety of geotechnical applications, broadly load bearing and protection against erosion. The profile of geocells for these two broad applications differs; the geocell for load bearing is deeper and has closer weld spacing. This paper highlights application of geocells in roads, specifically rehabilitation of a road, and embankment slope protection, both cases in Assam, Churaibari and Bogibeel. Both these studies relate to corrective measures taken after a series of fiascos, one of these of a major nature. In both cases, geocells were quite rapidly installed. While the solutions were executed on an emergency basis, no further work was required to be done and the solutions proved to be long term. This paper also attempts to highlight that geocells need not be a part of a disaster management system but can and should play a major role as part of the designed system for highways with several inherent advantages.

Keywords Cellular confinement • Geocells • Pavements • Drainage
Weak subgrade • Embankment slopes • Erosion

1 Geocells

Geocells are a category of geosynthetics which are truly three dimensional, that have lent to many an innovative application. All their applications are based on one fundamental premise, confinement of material within the cells.

S. P. Bagli (✉)
Strata Geosystems (India) Pvt. Ltd., Mumbai, India
e-mail: shahrokh.bagli@strataindia.com



Fig. 1 Geocell panels folded for storage, transportation, and expanded at project location

Individual cells of a geocell panel have a rhomboidal cellular profile and have depth. Geocells used for engineering applications are essentially fabricated from high-density polyethylene (HDPE) straps judiciously held together by ultrasonic welding. The cell HDPE walls are textured and perforated. The pattern of perforation would vary with the depth of the geocell and weld spacing, and the array is astutely designed to optimise the tensile strength of the strap that forms the cell wall. The geocell panel can be folded for ease of storage and transportation and can be expanded at the location as a panel, as shown in Fig. 1.

2 The Mechanics of Geocells

The basic functions of geocells are two and rather diverse:

- Spread the imposed load.
- Prevent erosion of the underlying material due to wind and surface run-off water.

2.1 *Spread of Imposed Load and Improved Resilient Modulus*

Geocells filled with nonplastic material form semi-rigid mats capable of distributing imposed loads over larger area. The mechanics of how the load spread occurs is explained by Avesani Neto et al. (2013).

With reference to Fig. 2, the vertical imposed pressure p is reduced to p^* at the base of the geocell panel. The pressure p within the cell generates lateral stress on the wall of the cell, which is approximately equivalent to

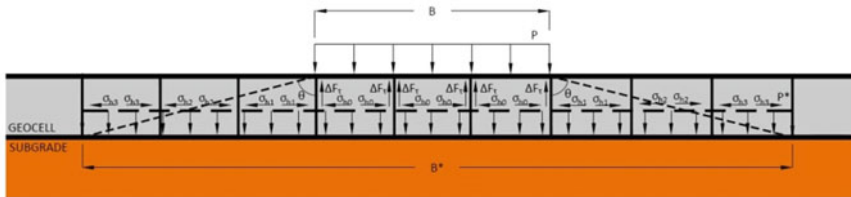


Fig. 2 Load spread mechanics within a geocell panel

$$\sigma_0 = k * p \quad (1)$$

where

σ_0 is the lateral pressure on the cell wall

k is the coefficient of earth pressure at rest, equivalent to $(1 - \sin \varphi)$, φ being the internal friction angle of the infill material.

Lateral forces are also generated in congruent cells as reaction. The confinement increases the shear strength of the soil. With slightest deflection of geocell panel, frictional forces are generated along geocell walls which tend to reduce the pressure at the base. These help in creating a “rigid mattress” which distributes the load over a larger area signified by B^* in Fig. 2. The distribution over area is also on the principle of equilibrium of forces where

$$(p * B) = (p^* * B^*) \quad (2)$$

It has also been significantly proven through field and laboratory tests and theoretically that geocells improve the load-carrying capacity of a geotechnical system (Basu and Soni 2013; Rajagopal et al. 2014; Hegde 2017); whether the system is a flexible pavement or a foundation system for flexible structures such as embankments or reinforced soil structures, or footings for structures.

Besides in a flexible pavement system, it has been proven by several researchers including Rajagopal in several of his treatises including the above mentioned that the resilient modulus M_R of an engineered soil layer significantly improves when the material is confined within geocells. The magnitude of improvement varies with researchers, but improvement there is, along with the reduction in stresses below the system. As a result, thickness of the pavement components and as a corollary, the overall thickness of the pavement reduces. The end result is a major saving in cost and time of construction, besides improved life cycle costs and increased life of the pavement in terms of million standard axles (msa) that it can take on over its life. These points are the crux of deployment of geocells to salvage a dire situation that arose on NH-44 in 2016 on an emergency basis, being highlighted in this paper.

2.2 Erosion Control

Embankment side slope erosion of the soil along highways is a major issue particularly in areas of heavy rainfall. Stone pitching has been commonly used, and Fig. 3 is a common enough sight along roads.

Stone pitching has inherent disadvantages. It is difficult to lay pitching on a slope steeper than 1V:2H. Besides there are restrictions on quarries, and pitching proves to be expensive when leads are long. Skilled craftsmen are hard to come by, and laying stone pitching is slow. Besides, as can be seen in Fig. 3, regular maintenance is required.

The mechanics of support of geocells on slopes is highlighted in Fig. 4. The infilled geocell is shown with the typical activating forces down the slope and resisting forces by virtue of friction along the slope which is a function of the friction between the slope soil and the infill, and the downward force normal to the slope surface. Generally one targets for a safety factor of 1.5 against sliding. However, this can be difficult to achieve and invariably steel, timber or PVC stakes are provided for safety for achieving the required safety factor. Sometimes an anchor trench is provided at the top of the embankment for suitable resistance against net (balance) factored sliding forces. The mechanics of stakes will be brought out in a *future* paper accepted for publication during the 11th International



Fig. 3 Typical stone pitching damage

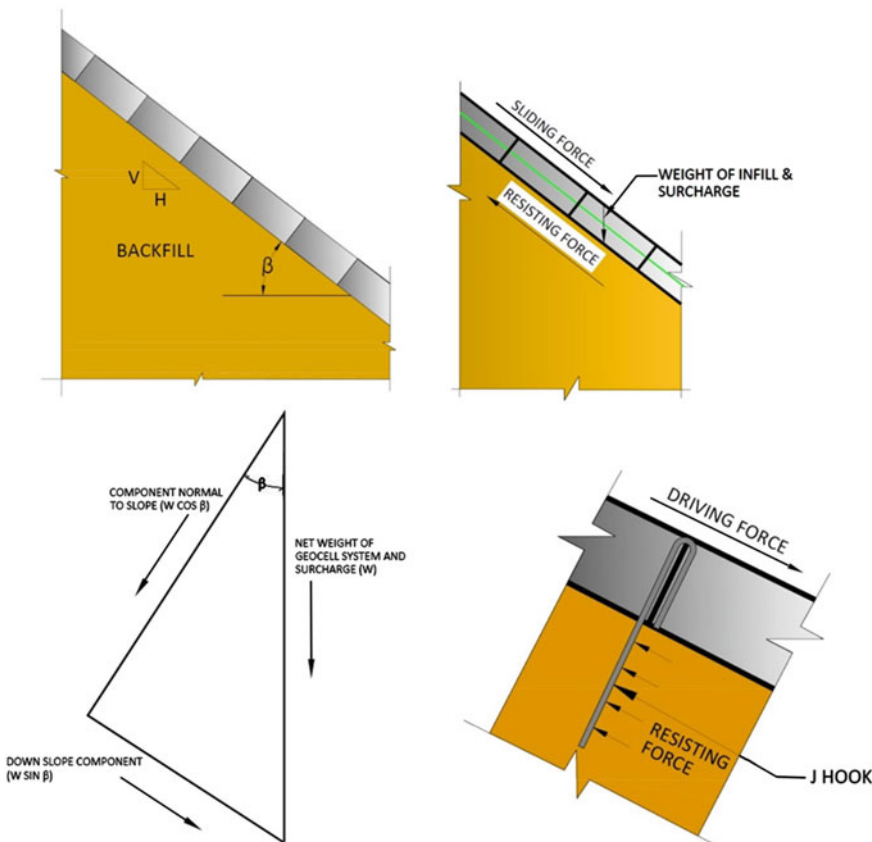


Fig. 4 Mechanics of stability of an infilled geocell along a slope

Conference on Geosynthetics, September 2018, Seoul, Korea (Design of Geocell Stakes along Slopes using Analogy of Laterally Loaded Piles; Guda, Vedpathak, Patil, Dalmia and Bagli).

3 Case Studies from the North-East

Two case studies are discussed herein. One is the case of highway NH-44 that had to be rehabilitated on an emergency basis at Churaibari, and the other is the NH-52B highway embankment at the Brahmaputra river crossing at Bogibeel. These are two diverse applications of geocells for highways.

3.1 NH-44 at Churaibari

The National Highway NH-44 is a major artery for the North-East states of India. The stretch between Malidoor at the Assam–Meghalaya border and Churaibari at the Assam–Tripura border is crucial for Tripura. Because of Tripura's peculiar geography, NH-44 is its crucial lifeline for supplies and victuals, the only land connect with the rest of the country.

The NH-44 near Churaibari on the Assam side of the Assam–Tripura border traverses forested and undulating terrain. The subgrade of the highway is highly plastic but weak clayey soil. The plastic subgrade with its low permeability compounded with the terrain complexed matters related to drainage. The Assam–Tripura region experienced exceptionally heavy rainfall since March 2016, which completely damaged the stretch and reduced it to a swampy mass (Fig. 5). Conventional repairs were attempted which were unsuccessful, and it was difficult for vehicles to ply even a stretch of about 500 m. This strangulated free flow of traffic. With the bottleneck of stranded vehicles, the situation turned chaotic and untenable with blockage of all goods to Tripura and virtual isolation from the rest of the country. The pictures in Fig. 5 highlight the impossible conditions faced where goods vehicles were hauled by bulldozer, tractors and front loaders.

The problem was referred to Strata Geosystems (India) Pvt. Ltd. by the Assam Public Works Building and National Highway Department. There were two essential issues to be addressed:

- Drainage of the pavement section and its subgrade;
- Strengthening the pavement section.

Both these issues were addressed while designing a pavement section with geocells within the pavement section. With a CBR as low as 0.5% and a traffic of 20 msa, a section was designed and adopted as in Fig. 6. Strata's geocells of Style StrataWeb® SW 356-150 were recommended (weld spacing 356 mm and depth 150 mm). The geocells improved the elastic modulus (conservatively considered as twice) and confined the granular material while ensuring drainage of ingressed



Fig. 5 Condition of NH-44 near Churaibari during the March–July 2016 rains

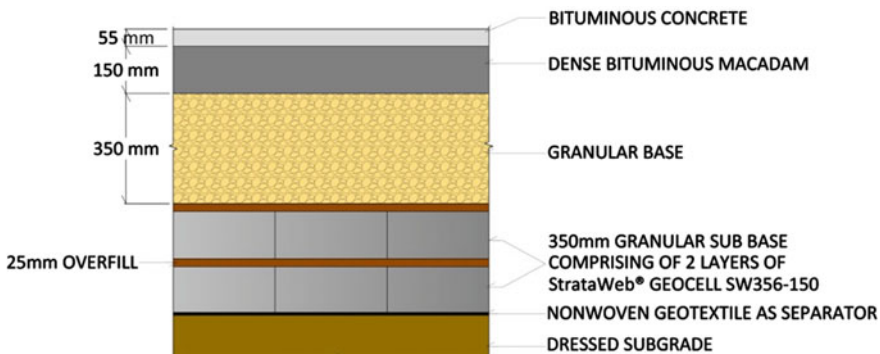


Fig. 6 Pavement section designed with geocells

water. The mechanistic-empirical pavement design method was used to design the section as shown in Fig. 6. The section was enhanced by necessary detailing.

The subgrade was dressed to the extent possible. Considering that the soil was weak and plastic, even dressing was difficult. A nonwoven geotextile of grammage exceeding 400 GSM was laid over the subgrade as separation (Fig. 7). The first layer of geocell was placed and infilled with granular material. The geocells were overfilled, and the layers were compacted with a vibratory compactor (Fig. 7). The overfill of 25 mm was topped by another panel of geocells, also infilled with granular material and compacted, overtopped by 25 mm. The geocell panel and its overfill were topped by 350 mm compacted granular base material, to be followed by 150 mm dense bitumen mix and 55 mm bituminous wearing course.

It must be noted that owing to emergency conditions and continuing inclement weather, traffic was allowed to ply immediately on laying the 350 mm granular base course (Fig. 8a). In any case, the wet conditions were not conducive to laying the bituminous courses. This also served as a visual inspection of the performance of



Fig. 7 Construction of pavement with geocells



Fig. 8 **a** Heavy vehicles plying over the granular base over the geocells. **b** The repaired stretch in July 2017

the geocell-reinforced pavement. It may be noted that there is scarcely any rutting in spite of heavy vehicle movement in wet conditions.

It is significant to note that the geocells could reach the site only during the last week of July 2016 due to difficult logistics prevailing, but the pavement (constructed up to the granular base course) was ready to receive traffic of all classes of vehicles by 15 August 2016. Figure 8b shows the highway in July 2017, after the bituminous wearing course has been laid. The pavement has survived the 2017 floods well.

The NH-44 case study highlights how a pavement can be rapidly reconstructed in an emergency situation, and yet can be used for long-term applications. The pavement was used for all classes of traffic even up to the granular base level without distress. The bituminous toppings were constructed after weather conditions were more conducive and the surface is dry enough to receive the bitumen courses, yet without interruption to regular traffic.

Besides the above, geocells in pavements have several other advantages. These include the following:

- Pavement sections incorporating geocells are leaner in section and hence more economical. The economics also lie in reduced life cycle costs owing to less maintenance and periods in between maintenances.
- With the confinement effect of the geocells, the effective shear strength of the infill is improved. Hence, locally available nonplastic material can be used. Economies in design are also effected with the reduced consumption of raw

material and reduction in project time owing to less material to be handled and worked upon.

- Geocells can be stored and transported in flat conditions occupying little space, as compared to the final volume being laid out. Hence, there is economy in storage and transportation.
- Installation can be carried out even in inclement weather conditions as was proven by the NH-44 case study. No specialised construction equipment was required, and the local unskilled labour was mobilised for the work which was completed in record time. There are also other cases where geocells have proven themselves in emergency/disaster situations.
- The material of fabrication, HDPE, is carbon treated and is UV-proof. Its manufacture leaves a low carbon footprint due to minimal resource requirements and minimised transportation.

3.2 Brahmaputra Bridge Approach of NH-52B at Bogibeel

The road-cum-rail crossing across the Brahmaputra on the NH-52B is located at Bogibeel, about 17 km downstream of Dibrugarh in Assam. The location is an area of high-intensity rainfall. During heavy rains, the surface run-off along the embankment slopes erodes the surface soil, forming rills and gullies down the slope, which widen with more run-off. Figure 9 illustrates the situation in October 2016.

The issue was essentially that of drainage and several measures for drainage of water from the highway, and cattle barriers were designed (and now implemented) by the Assam Public Works Building and NH Department. Besides these measures, the PWD decided to protect the side slopes further with geocells. The geocells would be infilled with compacted local soil and turfed with local “Uloo” grass. Strata were approached for design of the geocell system and supply of StrataWeb® Style SW 445 100, i.e. weld spacing 445 and 100 mm depth. This style of geocell (for slope protection) is quite different in profile as compared to the style used for NH-44 since the applications are diverse, though based on the principle of confinement of material within the cells. The design is illustrated in Fig. 10.



Fig. 9 Embankment slopes in October 2016, eroded by run-off during rainfall

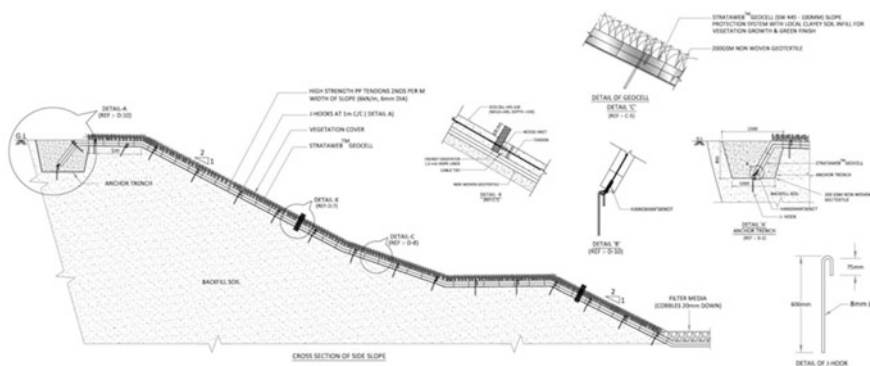


Fig. 10 Design and detailing of slope protection with geocells

The geocell efficacy was demonstrated over a stretch of 20 m where rain cuts and side slope erosion were observed to be the highest in the flood inundated area, at the south bank of the Brahmaputra. The geocells were laid as per the drawing (Fig. 10). After the infilling was done, Uloo grass was planted on the geocells.

It is reported that the site which was continuously devastated has shown no signs of degradation notwithstanding heavy rains and floods. Conditions in June 2016, during the heavy rains and floods, are highlighted in Fig. 11. It has also been reported that the geocells have performed well even during the 2017 flood season.

Some of the advantages cited for geocells in pavements also hold for geocells for slope and ground protection against erosion. The other advantages include:

- Geocells are good for slopes up to 1V:1H (as long as slope stability is maintained).
- Geocells infilled with locally available soil are an excellent replacement for stone pitching.
- Installation is eight to ten times faster than conventional methods and is easy to transport owing to its flat and collapsible structure.



Fig. 11 20 m geocell protected stretch (circled) and a profile of the turfed slope

- Geocell slope protection lends to aesthetics. Geocells support development of vegetation where water is available in plenty. In arid areas where watering is not practical, the infill may be gravel or concrete.
- The HDPE of geocells is long lasting and resistant to extreme soil and weather conditions.
- No skilled manpower is required, and even the labour requirement is small.

4 Conclusions

Geocells are three-dimensional geosynthetics that can be used for highways, both within the pavement section as well as for slope erosion protection.

As highlighted by the NH-44 case study, geocells are invaluable for rehabilitation of pavements in emergency situations including damage by floods and where the CBR have been reduced to very low values. Moreover, the rehabilitation is also a long-term solution which is a major advantage.

Confinement characteristics of geocells help protect slopes against erosion. While in the Bogibeel case study, geocells have been infilled with soil and vegetated, other options include infilling with gravel when it is difficult to sustain vegetation due to climatic conditions or maintenance issues. Concrete infilling is also common particularly for reservoir side slopes or where flow characteristics in canals need to be appropriately maintained.

Acknowledgements The author takes this opportunity to express his deep gratitude to the Assam Public Works Building and National Highways Department for giving Strata the opportunity to lend its ideas towards the success of these projects and in particular the NH-44 case, where we jointly got an opportunity to prove the worth of geocells in an emergency. And of course, his sincere thanks to Strata Geosystems (India) Pvt. Ltd. for allowing publication of these case studies.

References

Avesani Neto, J. O., Bueno, B. S., & Futai, M. M. (2013). A bearing capacity calculation method for soil. *Geosynthetics International*, 20(3), 129–142 (Thomas Telford Ltd.).

Basu, C., & Soni, J. K. (2013). Design approach for geocell reinforced pavements. *Highway Research Journal*, 1–7.

Hegde, A. (2017). Geocell reinforced foundation beds-past findings, present trends and future prospects: A state-of-the-art review. *Construction and Building Materials*, 154, 658–674 (Elsevier).

Rajagopal, K., Chandramouli, S., & Parayil, A. (2014). Studies on geosynthetic reinforced road pavement structures. *International Journal of Geotechnical Engineering*, 8(3), 287–298 (W. S. Maney & Son Ltd.).